CRANFIELD UNIVERSITY

ADRIANA ENCINAS-OROPESA

A STUDY OF HOT CORROSION OF SINGLE CRYSTAL SUPERALLOYS AND PLATINUM-ALUMINIDE COATINGS.

2005

SCHOOL OF INDUSTRIAL AND MANUFACTURING SCIENCE

Ph.D. THESIS

CRANFIELD UNIVERSITY

SCHOOL OF INDUSTRIAL AND MANUFACTURING SCIENCE

Ph.D. THESES

ACADEMIC YEAR 2005

ADRIANA ENCINAS-OROPESA

A STUDY OF HOT CORROSION OF SINGLE CRYSTAL SUPERALLOYS AND PLATINUM-ALUMINIDE COATINGS.

SUPERVISORS: Professor J.R. Nicholls, Dr. N.J. Simms

October 2005

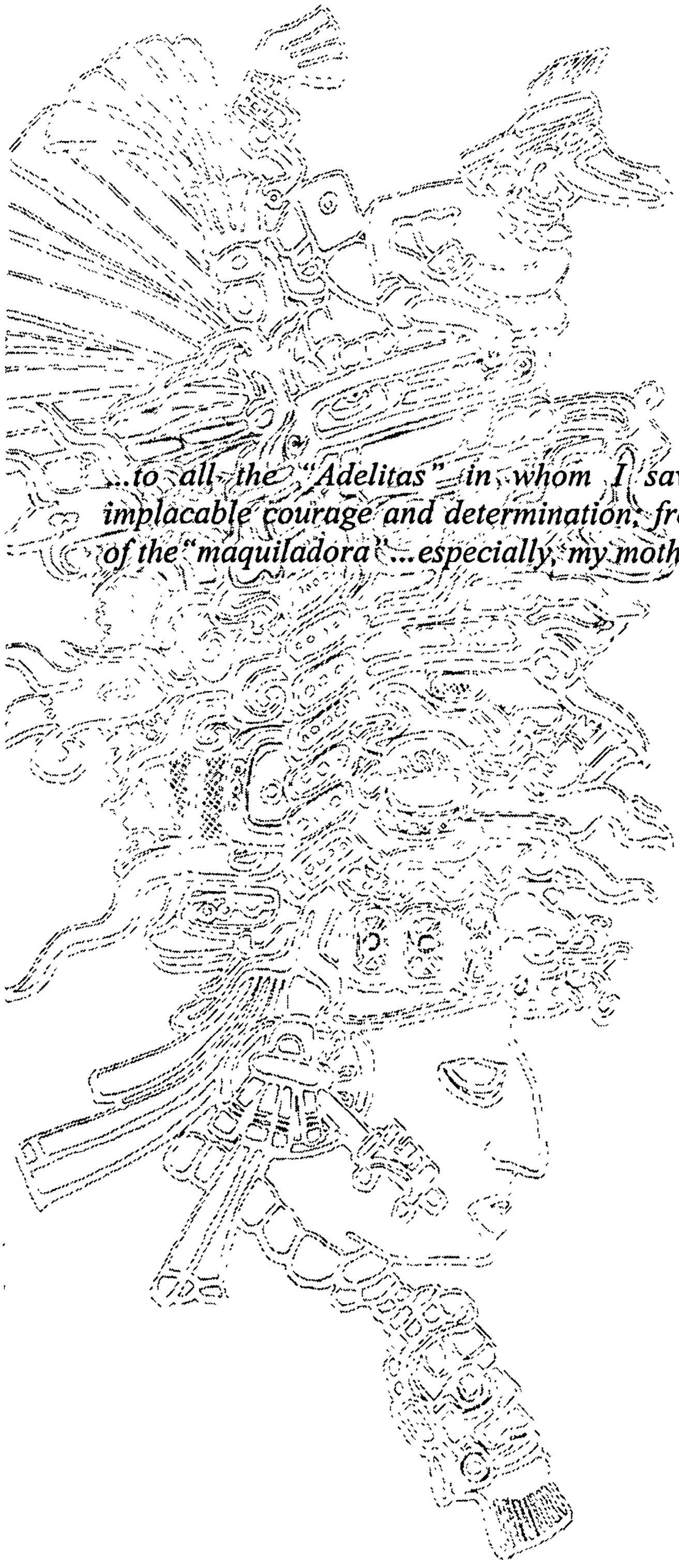

...to all the "Adelitas" in whom I saw an inspiration for their implacable courage and determination; from Sor Juana to the women of the "maquiladora"...especially, my mother.

Acknowledgements

The author would like to express her gratitude to the European Commission for the funding of this work under the Advanced Long Life Turbine Coating Systems project (ALLBATROS), contract number ENK5-CT2000-00081 and the European Coal and Steel Community (ECSC) with project number 7220-PR/053.

I have had the pleasure of working in a very nice environment, both the National High Temperature Surface Engineering and the Power Generation Technology Centre, where anybody I asked for help, someone always kindly helped me. I greatly appreciate the patience shown on my slow learning process of the English language ever since I started. However, I would like to thank especially the people I have bothered the most:

Professor John Nicholls for believing in me by giving me the opportunity to work in this project, his thorough guidance and constructive discussions.

Dr Nigel Simms, who always had time for my doubts, for his guidance and support and for all the things I have learnt since I started working with him.

John Oakey, Borja Arias, Paul Kilgallon, Andrew Potter, Steve Mabbutt, Nigel Legrave, Jim Norton, all of whom helped me at some point of this work. Rachel Newton, who always offered her help during the experimentation part of this project (and always ended up weighing samples), Gemma Grasa-Adiego who made the time and effort to study and explain to me what looked impossible to understand, and Peter West who often was overloaded with my work so I could make time for this thesis.

Tim Pryor, who taught me and helped me with the laborious set up of the experiments in the laboratory, to start them on time and keep them going. Andrew Dyer, who taught me to prepare the samples correctly and to make proper use of the equipment (and for fixing my mistakes).

Suzie Chadwick in the computer centre for her nice support every time I panic because I messed up my work on the computer. The kind ladies of the library who help me to find information that often, was just under my nose and to Heather for her support in the Procite use.

The Community Development Centre, Margaret and Lynn, for making life easier and all those lovely gestures of support and care on difficult and happy times…

I would like this opportunity to thank those people who have had a great influence during my academic/professional formation, since they provide me with the means to cope with the unknown: Professor Cristina Oliviera who taught me to *"organize my thoughts, not to think..."* Don Julio Giovine who

taught me that *"engineering means... to be ingenious"* and Cuco Navajas who told me *"...what do I have?... and the qualite of the executant"*...

I am also very grateful to my friends with whom I have spend hours and hours of reflexion, adventure and fun, those whom have been happy for me, and I will thank them personally.

To my brothers, Armando y Alberto whom in retrospective, in my nicest memories, you both are always there...and because the Atlantic has made our bond closer and stronger...

To my father; for being my *maestro* and example, his advice, support and encouragement.

To mi greatest friend, Isidro...for his unconditional love, care and support... because I feel very lucky to have coincided in life and for sharing my life with you...

And to my little "*moon light*"...*Itzel,* for all those extraordinary feelings you give me with your smile every day...

Sincerely

Adriana Encinas Oropesa

Abstract

At the present time, combined cycle systems for power generation (e.g. IGCC), offer increased efficiency of power generation and lower environmental emissions, specifically CO_2, SO_x, and NO_x, as well as being adaptable to most fossil fuels. Economic factors, such as the cost of the materials must be considered. Materials influence the service lifetime in the required operational environment. Solid fuels like coal and biomass produce different combustion environments containing a range of contaminants that, when they reach their melting points, may cause accelerated corrosion, affecting directly the service life time of the gas turbine constructional materials. This accelerated corrosion is known as Hot Corrosion.

The aim of this study was to develop, an understanding of the influence of these environmental factors on rate of hot corrosion of modern turbine materials, i.e. the single crystal alloys CMSX4 the SC^2, both uncoated and PtAl coated that are needed for a gas turbine blade and vanes operating in a range of hot corrosion environments expected in an IGCC plant.

To achieve this aim, a series of laboratory corrosion tests was planned to simulate the same corrosion environment as in industrial high temperature gas turbine operation. Following established procedures for corrosion testing, samples were exposed in a controlled atmosphere furnace to a mix of gases (air/SO_2/HCl) with a cyclic exposure time of 50 and/or 100h duration. Each cycle, samples were removed to be recoated with an alkali salt mixture to a total exposure time of 500h and or 1000h. Cross sections were examined by SEM/EDX to identify the mode of hot corrosion attack. To quantify the rate of corrosion, samples were measured pre-exposure and post-exposure, and this corrosion data was statistically assessed.

Finally, from this quantitative data, life prediction models were developed to describe/predict the onset of hot corrosion and the corrosion rates observed under different gas compositions, and various deposition fluxes, both at typical type I and type II hot corrosion temperatures in terms of incubation and propagation periods. Separate models have been developed for the two single crystals superalloys: CMSX4 and SC^2, in both the uncoated and platinum aluminide coated condition. The goodness of fit as defined by the regression coefficient varies from 0.88 to 0.99 for the propagation models at 700 and 900°C. The incubation models are as precise at 700°C but less precise at 900°C with regression coefficients of 0.78-0.94.

Table of Contents

List of Figures

List of Tables

List of Equations

1 Introduction

At the present time, there are many different processes used for electricity generation. Clean coal technologies, such as combined cycle systems offer, over conventional coal-fired power generation systems, increased efficiency of power generation and lower environmental emissions, specifically lower CO_2, SO_x, and NO_x [1], as well as being adaptable to most fossil fuels.

Gas turbines are at the heart of such power stations, usually as part of combined cycle systems fired on natural gas. It is anticipated that gas turbines will be used even more widely in the future, with increasing numbers of natural gas fired combined cycle systems being installed and as new solid fuels, i.e. coal, biomass, waste combined cycle power generation systems move from development through demonstrations to commercialisation [2; 3; 4]. However, in a combined cycle system for power generation, there are important economic factors to be considered, such as the capital cost of the plant, maintenance, operating cost, and materials of its components. The choice of materials is relevant as their service lifetime in the required operational environment, their success or failure, affects the overall efficiency of the process. The combined cycle process achieves its efficiency by working together a steam turbine technology (bottom cycle) and a high temperature gas turbine technology (top cycle).

Solid fuels, like coal and biomass, through combustion and gasification technologies, can be used in combined cycles. The different gases produced by these processes contain contaminants that are extremely corrosive to the turbine components (blades and vanes), resulting in a gradual loss of efficiency and/or reliability. It is the performance of the materials of this high temperature gas turbine technology that is of interest in this present study.

The constitution of the gases from the combustion of coal and biomass gasifier derived fuel gas includes a mix of sulphurous oxides of SO_2/SO_3 and HCl generated from fuel gas combustion in an oxygen excess. Additionally, this gas includes significant quantities of vaporised alkali metal salts, based on Sodium and Potassium, as well as Calcium, Magnesium, Lead and Zinc in lower quantities which are deposited on the surface of a blade or vane turbine as metal sulphates, and/or chlorides. When they reach their melting points they may cause accelerated corrosion and degradation, affecting directly the service life time of the gas turbine constructional materials.

This accelerated corrosion is known as Hot Corrosion, and has been classified in two generic types: type I in a range from 800 to 950°C (high temperature hot corrosion) and type II in a range from 600 to 800°C (low temperature hot corrosion).

As the high temperature gas turbine (top cycle) of an integrated gasification combined cycle power generation (IGCC) operates in the range from 550 to 900°C, both types of hot corrosion have been considered in plant operation and therefore are studied in this work.

Extensive studies have provided materials (metal superalloys based on nickel or cobalt) with good mechanical performance at increasing operating temperatures in order to have more efficient plant, e.g. the development of the single crystal superalloys. However, these materials do not always have satisfactory corrosion resistance.

Hence, the development of coating systems and surface treatments, used for the first time during the 1950s, and since then, under constant study, development and improvement. These coating systems offer a range of alternatives within the two main coating families: diffusion coatings and overlay coatings, to select a suitable one for a given function in a specific application or environment. The Platinum Aluminides (PtAl) are diffusion coatings, formed through diffusional interaction between the constituents of coating material (e.g. aluminium, and platinum) and the alloy. These are widely used given their easiness of production and relatively low cost.

Thus, the aim is to study the hot corrosion of modern turbine materials, the single crystal alloy in current use CMSX4 and the new SC^2 alloy; both in the uncoated and PtAl coated condition. These materials and coatings are used for gas turbine blades and vanes operating in a range of hot corrosion environments expected in an IGCC plant.

To achieve this aim, a series of twelve laboratory corrosion test were undertaken to simulate samples under the same corrosion environment as expected in industrial high temperature gas turbine operation as part of a IGCC plant following the established procedures for corrosion testing. The experimentation was carried out in tests of 500h or 1000h duration, to a total of 9000h, involving 136 samples in two main stages:

- The aim of stage 1, was to examine the behaviour of a hot corrosion resistant alloy (IN738LC), and a single crystal alloy (CMSX4), both uncoated and coated with platinum/aluminium diffusion coatings in realistic hot corrosion environments.

This stage comprised six hot corrosion tests to examine the effect of changing the deposit composition at the same temperature but in different gas compositions, and to investigate the effect of using the same gas composition at a range of different temperatures.

- Stage 2 aimed to examine the effect of three different model gas compositions, but using only one deposit composition, deposited at a range of deposition fluxes. The materials investigated in this stage were two single crystal alloys (CMSX-4 and SC^2) and a corrosion resistance alloy (IN792) again both uncoated and coated with a platinum aluminide diffusion coating. During the experimentation time, sample mass changes were recorded for further quantitative assessment.

After having completed the exposure times, the samples were metallographically prepared, observed through an optical microscope to produce a series of photomicrographs able to show the main characteristics of the hot corrosion attack per sample (that is material/coating/environmental combination) and measured through microscopy/image analyses. A selection of samples was examined by SEM/EDX to identify the mode of hot corrosion attack that took place per material system.

Since the hot corrosion attack results in a non-uniform morphology (e.g. presence of pits for type II hot corrosion), it is necessary to adopt methods to quantify the rate of corrosion on components when the corrosion process results in areas of local attack. This is achieved through the accurate measurement of pre-exposure and post-exposure samples, coupled with the statistical assessment of the corrosion data, using normal distributions and extreme value statistics (Gumbel distribution) to determine the rate of growth of maximum areas of attack. From these quantitative data and the early measured mass change data, life prediction models have been developed that describe/predict the onset of the hot corrosion failure under defined conditions such as gas composition and concentration, various deposition flux concentrations and material types, both in the type I and type II hot corrosion temperature regimes.

These models have been developed for the two single crystals superalloys studied, CMSX4 and the new SC^2 alloy both uncoated and platinum/aluminide coated, and the corrosion resistant polycrystals IN738LC and IN792, which are chosen as references.

Using these models coupled with the identification of the alloy/coating degradation mode, future improvements in the materials system are recommended for overall power generation plant efficiency.

2 Literature Review

2.1 Power Generation Systems

The first source of artificial power was the energy extracted from the water of rivers by hydro-mechanical means. Energy became an all-pervading social and economic factor when the use of electricity permitted work, heat and light to be broadly distributed, making the benefits of the hydraulic or other power sources available to mankind almost everywhere on our planet. The main source of heat was, and still is, the combustion of fossil fuels. For example, Figure 2.1 shows the consumption of fuel in the United Kingdom in 1990 and 2001.

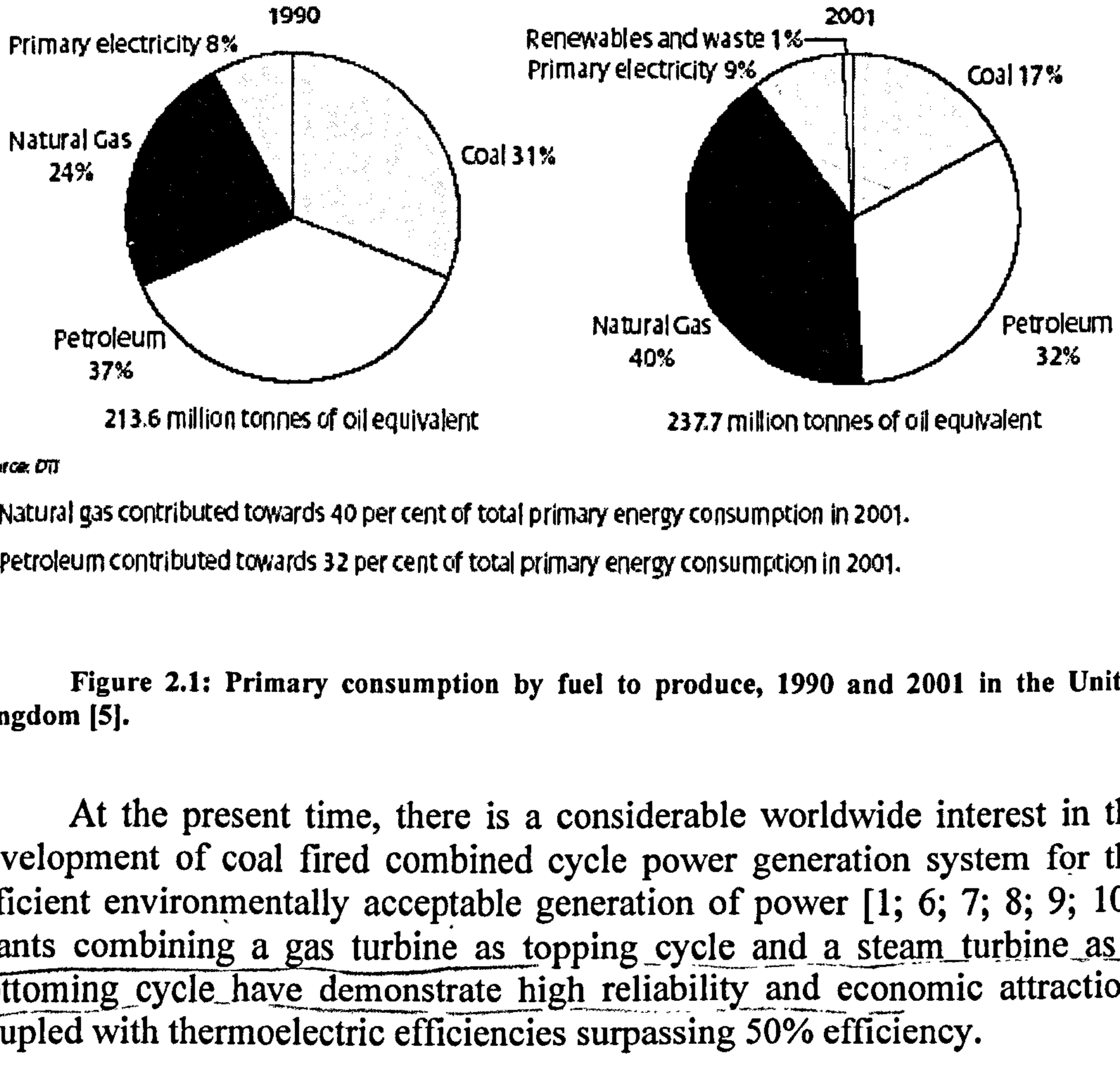

Figure 2.1: Primary consumption by fuel to produce, 1990 and 2001 in the United Kingdom [5].

At the present time, there is a considerable worldwide interest in the development of coal fired combined cycle power generation system for the efficient environmentally acceptable generation of power [1; 6; 7; 8; 9; 10]. Plants combining a gas turbine as topping cycle and a steam turbine as a bottoming cycle have demonstrate high reliability and economic attraction, coupled with thermoelectric efficiencies surpassing 50% efficiency.

Combined-cycle technology can be adapted for most fossil fuels and to meet increasingly stringent low-pollution requirements. The history of the development of high thermal plant efficiency is illustrated in Figure 2.2.

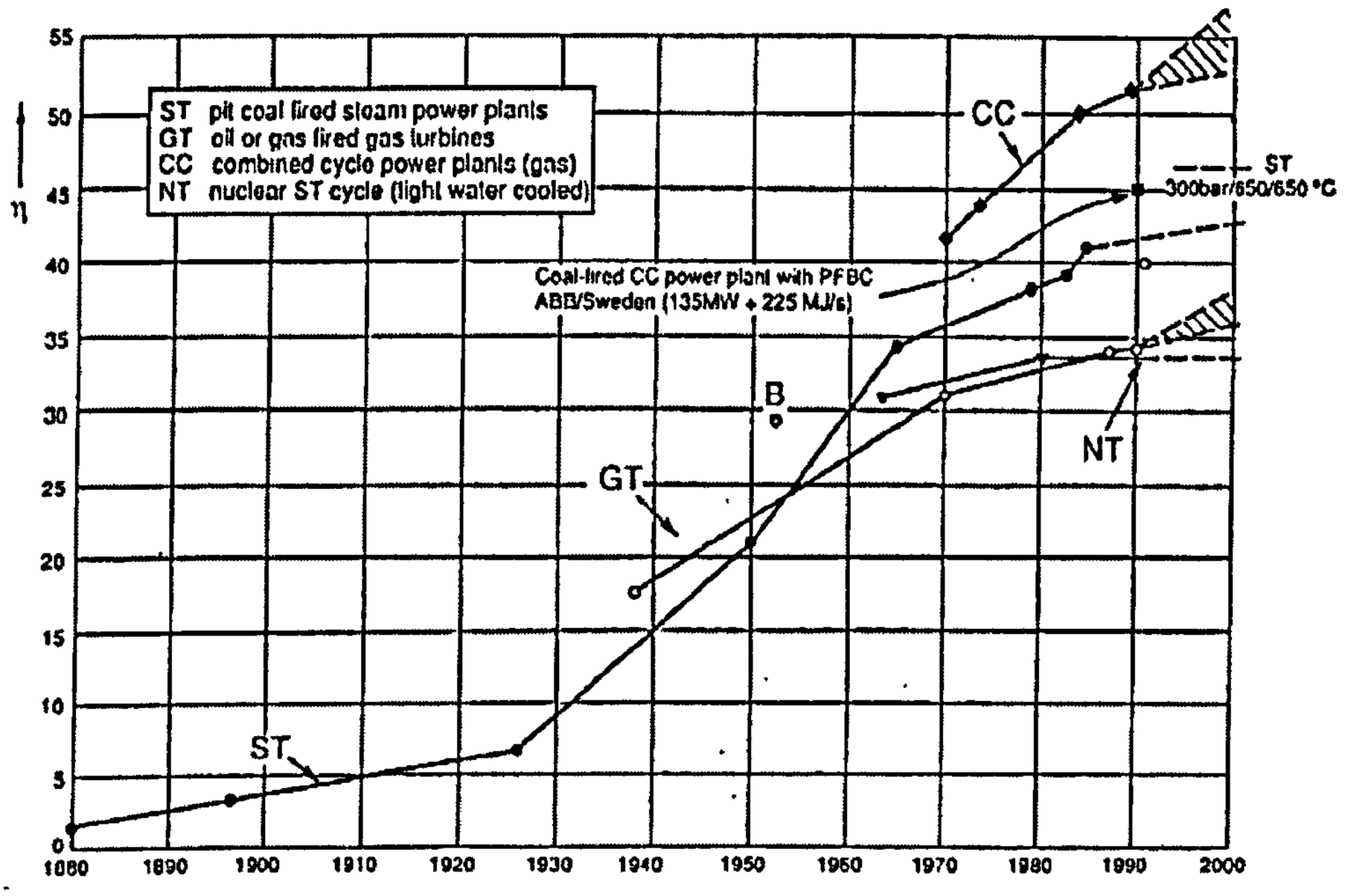

Figure 2.2: Historical Evolution of Power Plant Efficiency [10].

The first thermal plant steam cycle (curve ST in Figure 2.2) was built around 1880 with an efficiency of a few percent. In the years after 1950, a step increase can be noted (Figure 2.2) leading to the present values around 40%. The use of gas turbines (curve GT Figure 2.2) for electricity generation begins in 1938 and reflects the progress made in the development of high-temperature alloys and in the development of turbine blade cooling techniques. The efficiency of the simple open-cycle gas turbine has reach 36%-38%.

Nuclear steam turbines cycles (curve NT), have an efficiency around 33% which remains practically constant due to safety and political reasons. The efficiency of a power generation plant is measured by its thermal energy capacity, which cannot be completely converted to work (second law of thermodynamics). The maximum theoretically achievable conversion rate with a given heat source is called *Carnot efficiency* η_c ,where:

$$\eta_c = (T_{max} - T_{min}) / T_{max}$$

and T_{max} is the maximum temperature in the cycle in Kelvin degrees, and T_{min} is the minimum temperature. For example, according to Allen and Stringer [11], for a conventional utility steam cycle with T_{max} =811° K and

T_{min} =300° K or so, η_c= 0.63. In practice, the overall efficiency of the system will be approximately half of this.

The corresponding value for a simple cycle gas turbine with an inlet temperature of 1450° K and an exhaust temperature of 600° K, η_c is 0.59, and again, for practical engines, the efficiency is approximately half of this. The difference is due to undesirable, but unavoidable, dissipative processes taking place in real fluids and to the fact that generally, neither the heat addition nor the rejection can take place at a constantly high or constantly low temperature level.

Higher cycle efficiencies, exceeding about 40 to 42%, are now being reached by steam cycles, only possible using near critical or supercritical pressures (in the range of 250 to 320 bar) and peak superheat temperatures of the order of 900°K (600 to 650° C). For example, in Japan, such improvement in steam conditions is largely attributed to material development [12].

Gases like air, or the combustion gas resulting from burning fuels in air, can be readily heated to very high peak temperatures without necessarily reaching excessively high pressures. However, both heat addition and heat rejection will cause a continuous change in fluid temperature, keeping the cycle efficiency much below the η_c value calculated from the highest and lowest temperature reached in the cycle.

The development of the combustion turbine cycle (or gas turbine cycle) consists in a steady striving for higher peak combustion temperatures, in order to make the mean temperature of heat addition as largely different from the mean level of heat rejection as possible.

The combined cycle approach is to place another cycle in series with the steam cycle or the gas turbine cycle to recover some of the otherwise unavailable energy. One cycle, termed the topping cycle, is energized by the heat source and rejects heat to the second cycle; the latter, also termed the bottoming cycle, converts part of the heat obtained from the first cycle to work and rejects the rest to the heat sink. Normally, the fluids are selected such that both cycles operate in a technically convenient range of pressure and temperature.

Examples of combined cycles in the general sense are e.g.: gas/steam, mercury/steam, steam/ammonia or gas/organic-fluid cycles, where the first fluid refers to the topping and the latter to the bottoming cycle. Of these combined cycle systems (some in operation commercially, others as development plant and/or at the research and proof of concept phase), the gas/steam cycle is of greatest importance and it is the combination of interest for the present work.

The majority of combined cycle power plants are energized by the heat liberated from the combustion of fossil fuels; such as coal, oil or natural gas. Coal has been the most used fuel due its availability and even distribution all over the world [4; 13] two thirds of all electricity is generated by coal; hence, many countries are using the development of clean coal technologies.

There are three main categories of combined cycle clean-coal technologies:

- AFBC or atmospheric fluidised-bed combustion,
- PFBC or pressurized fluidised-bed combustion and
- IGCC or integrated-gasification combined cycle.

These categories vary significantly in detail and offer, over conventional coal-fired power generation systems, increased efficiency of power generation and lower environmental emissions, specifically CO_2 , SO_x, and NO_x [1], as well as being adaptable to most solid fuels. An example of IGCC is illustrated in Figure 2.3, which is the clean coal technology that the present study is focused on.

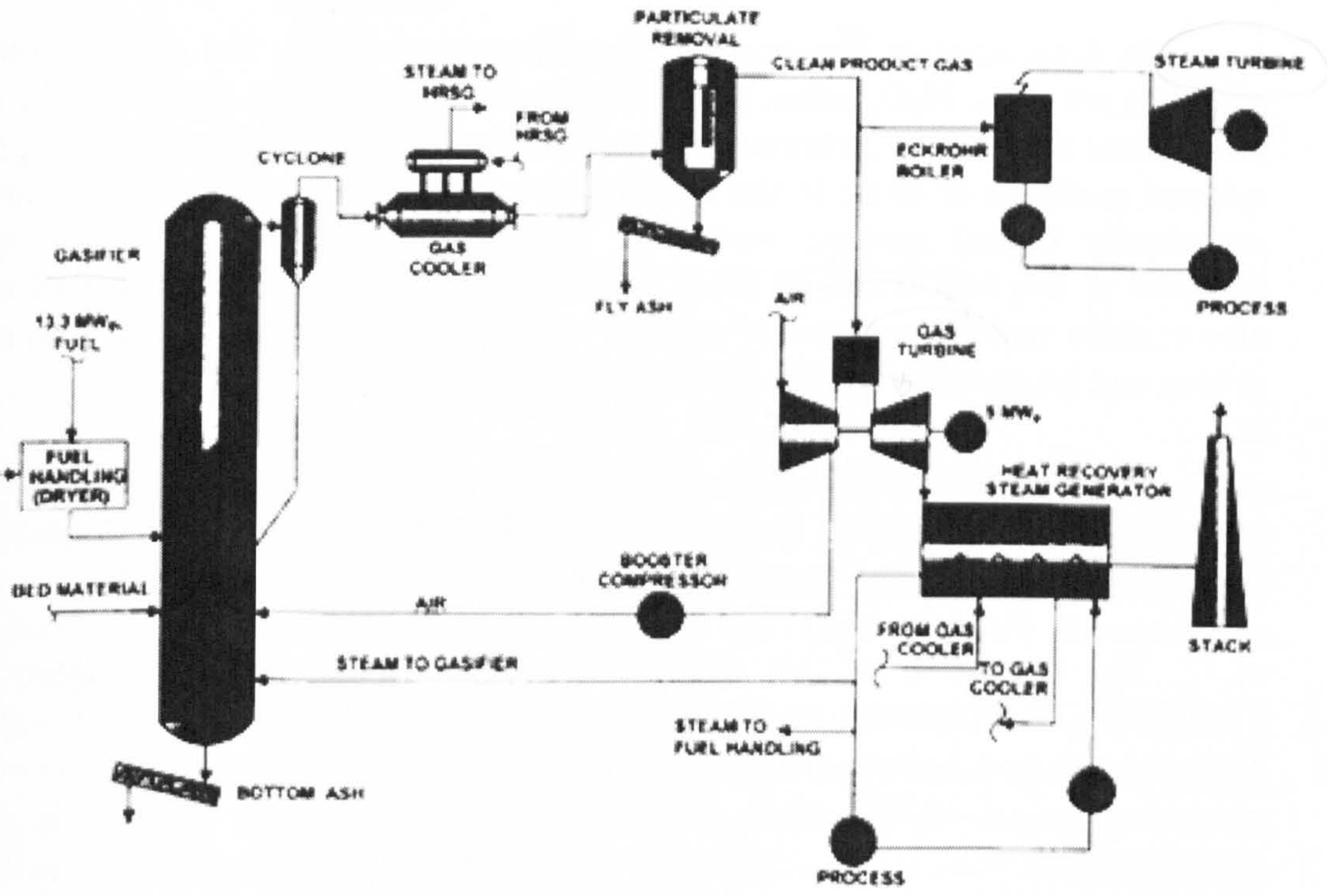

Figure 2.3: Simplified flow sheet of the process of Integrated Gasification Combined Cycle Power Generation [14].

2.2 Contaminants in a Coal/biomass Fired Gas Turbine

In the combined cycle systems previously described, the performance of the gas turbine is vital to the overall plant efficiency and economic viability. Within these systems, corrosion and/or erosion, creep and fatigue are life limiting for gas turbine vanes and blades in the short and long term [15; 16; 17; 2; 3]. The environments found within the hot gas path of gas turbines depend on the contaminants present in the fuel and air entering the turbine, as well as the gas turbine operating conditions.

Industrial gas turbines have been developed to fire on a wide variety of fuels; however, the levels of contaminants are different [18]: fuel gases derived from solid fuels such as coal, biomass and their mixes have the potential to generate low melting point deposits which, within a certain temperature range, can cause degradation of the component materials that may directly affect their service life time. These degradation processes are known as hot corrosion (see section 2.5.2.).

In the complete combustion of coal and petroleum, the main reaction products are CO_2, H_2O, ashes and various salts arising from impurities in the fuels. Coal consists of carbonaceous material and mineral matter. Some of the mineral matter is intrinsic to the coal itself, as relatively small inclusions or as organically bound species, and some is extrinsic, deriving from the rock adjacent to the coal seam, or from faults within the seam. Coal and fuel oils also contain various amounts of sulphur which, on combustion, yields SO_2 and in turn can be partially oxidised to SO_3 (see Figure 2.4).

At low temperature, SO_3 and water vapour react and form sulphuric acid. NaCl (present either as impurities in the fuel or in the air) reacts with SO_3 and $H_2O_{(g)}$ at high temperature to yield Na_2SO_4 and $HCl_{(g)}$.

The formation of this alkali sulphate has been studied in detail by Tschinkel [19]. Experiments by Gibb [20] showed that chlorine is released as HCl. Spacil and Luthra [21] considered possible reactions at temperatures characteristic of PFBC plant for chloride levels of 0.01 and 0.1% and calculated that ppm levels of chloride vapour could be released at 800-900°C, increasing rapidly with temperature, as shown in Figure 2.5.

A review of the species having significant influence on the hot corrosion processes are outlined by Stringer [22] as: alkali sulphates, sulphur and sulphur oxides and chlorine.

Table 2.1 shows a list of the common minerals found in coal. The majority of the mineral matter is incombustible, except the pyrite, iron sulphide, which burns to form SO_2 and iron oxide [23; 24].

Name	Formula	Approximate Vickers hardness
Clay minerals		
Montmorillonite	$Al_2Si_4O_{10}(OH)_2 \cdot H_2O$	
Illite	$KAl_2(AlSi_3O_{10})(OH)_2$	
Kaolinite	$Al_4Si_4O_{10}(OH)_8$	50–79
Sulphide minerals		
Pyrite	FeS_2	585–795
Marcasite	FeS_2	
Sulfate minerals		
Gypsum	$CaSO_4 \cdot 2H_2O$	
Anhydrite	$CaSO_4$	
Jarosite	$(Na,K)Fe_3(SO_4)_2(OH)_6$	
Carbonate minerals		
Calcite	$CaCO_3$	92
Dolomite	$(Ca,Mg)CO_3$	
Siderite	$FeCO_3$	171–236
Ankerite	$(Ca,Fe,Mg)CO_3$	148–171
Chloride minerals		
Halite	NaCl	
Sylvite	KCl	
Silicate minerals		
Quartz	SiO_2	1081
Albite	$NaAlSi_3O_8$	
Orthoclase	$KAlSi_3O_8$	
Fayalite	Fe_2SiO_4	795
Oxide minerals		
Hematite	Fe_2O_3	287–585
Magnetite	Fe_3O_4	
Rutile	TiO_2	585–795

Table 2.1: Common minerals found in coal [23].

Thus, hot corrosion can result from the combined effects of the gaseous species (e.g. SO_x and HCl) and deposits formed by condensations from the vapour phase (e.g. alkalis and other trace metal species) and/or particle impactation and sticking. The corrosion damage mode is highly dependent on the local component environment.

Conventionally, the metal vapour species of most concern were alkalis in gas turbines fired on clean fuels (either as fuel contaminants or via the combustion air) or vanadium from heavy fuel oils. In a coal fired system such as a PFBC, significant levels of SO_x and HCl combustion derived gases tend to influence the levels of sodium and potassium (much greater quantities of Na are released than K [24]), whereas gasifier derived fuel gases such as IGCC or ABGC systems (when used with hot gas cleaning processes) have higher levels of heavy metals such as lead and zinc [25].

Co-firing with biomass or waste fuel changes the levels of all the contaminants, e.g. for trace metals, wheat straw has higher potassium levels and sewage sludge has higher zinc levels [25]. The effects of different fuels on the levels of contaminant vapour phase species, deposition fluxes and deposits composition (e.g. melting points) are considered in this present work.

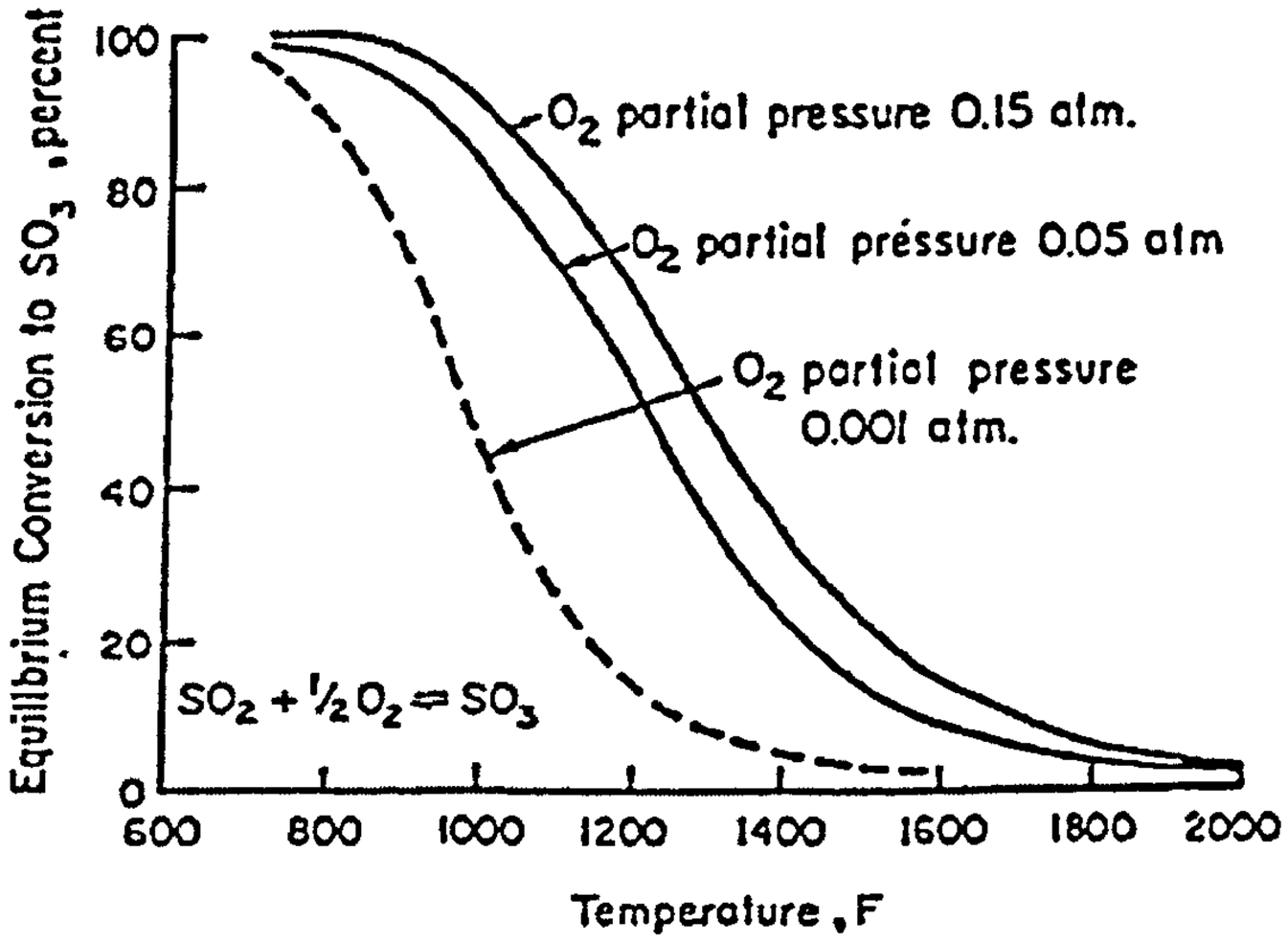

Figure 2.4: Variation of equilibrium levels of SO_2/SO_3 with temperature as refereed in [26].

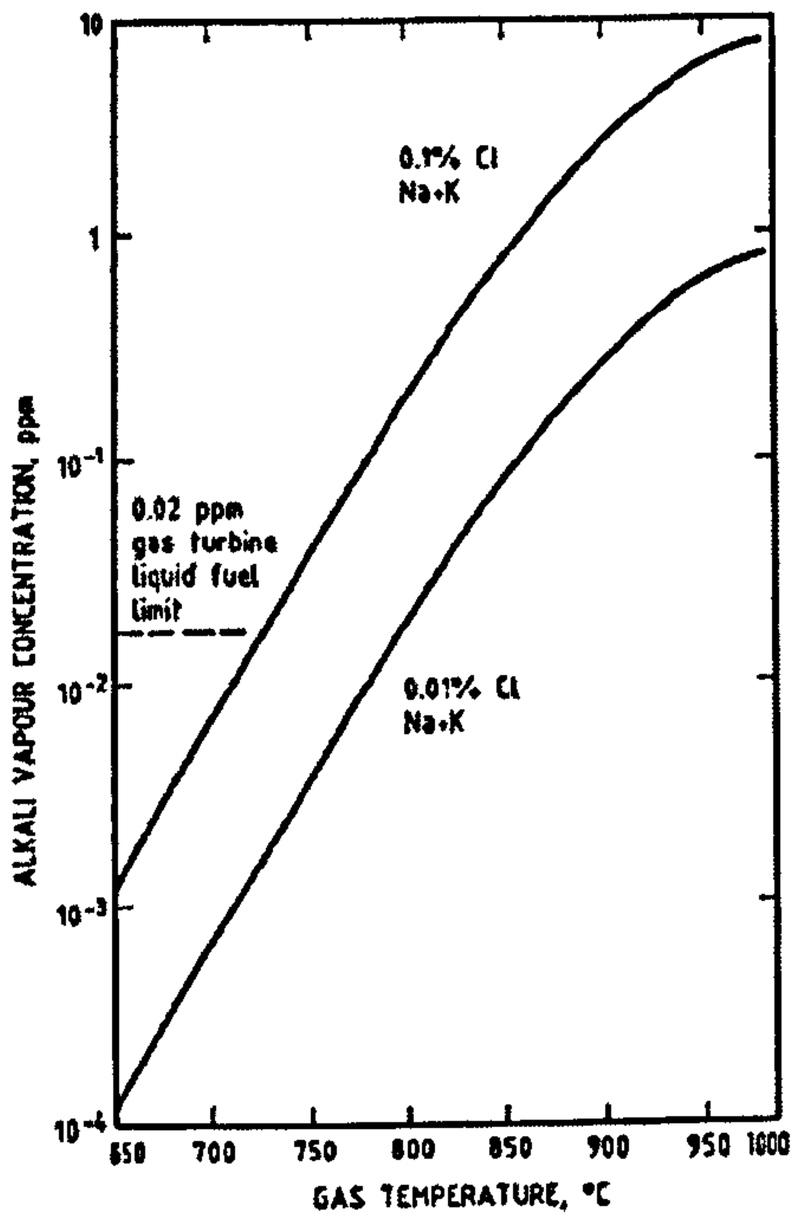

Figure 2.5: Equilibrium alkali chloride (Na + K) vapour concentration as function of gas temperature for PFBC conditions [24].

2.3 Materials Impact on the Industrial Gas Turbines

2.3.1 Introduction

In a combined cycle system for power generation, there are important economic factors to be considered, such as the capital cost of the plant, reliability, maintenability, operating cost and materials of its components.

Corrosive attack reduces the useful life of equipment, industrial products and general consumables. The total cost of corrosion includes both direct and indirect costs, for repairs, replacements, inspection, maintenance, provision of reserve equipment and overseeing to allow for corrosion. It is important to study and develop special materials, new methods of prevention and new products and processes for protection.

The identification of corrosion and protection problems, and the costs which are associated with them, is an essential part of the process of technical and economic choice in the field of materials [27; 28; 29]. The influence of materials is relevant due their service lifetime in the required operational environment; their success or failure affects the overall viability as well as efficiency of the process.

The development of gas turbines has been regulated by the availability of materials, the ability to process them into useful shapes and their capacity to perform under demanding combinations of stress and temperature in a high velocity gas that may contain the contaminants described in the previous section. Such materials must possess mechanical and physical properties to suit the individual requirements for specific areas of the turbine. Historically, the progress of the development of these alloys is well known: a comprehensive description is contained in Sims, Stoloff and Hagel [30] and a more recent paper by Molloy [31].

High temperature alloys for gas turbines generally contain cobalt or nickel as base metals. In order to obtain improved high temperature corrosion resistance, alloy additions of chromium, aluminium and silicon are important as they may (depending upon the alloy composition and exposure conditions) form protective oxide scales of Cr_2O_3, Al_2O_3 and SiO_2 (these phenomena will be addressed in the next chapter).

2.3.2 Superalloys

A superalloy is an alloy developed for elevated temperature service, usually based on group VIIIA elements, where relatively severe mechanical stressing is encountered, and where high surface stability is frequently required. Superalloys are divided in three classes: nickel-base superalloys, cobalt–base superalloys and iron-base superalloys. In addition to aircraft, marine, industrial and vehicular gas turbines, superalloys see service in space vehicles, rocket engines, nuclear reactors, submarines, steam power plants, and petrochemical equipment. Many (perhaps 15-20%) have been developed for utilization in corrosion-resistant applications [30]. Nickel-base superalloys are of the interest of this study.

2.3.3 Nickel-Base Superalloys

Nickel-base superalloys are the most complex and widely used for the hottest gas turbine parts. The physical metallurgy is complex and the relationship of properties to structure in this system is the best known of all materials for use in the 650-1100°C range. From 1940 to 1965, the properties given the most attention for applications such as aircraft engine blades were high-temperature tensile strength, creep rupture strength to 5000h and oxidation resistance.

Conversely, industrial gas turbine designers required blade alloys with known longer time creep rupture properties and good hot corrosion resistance. Thus, aircraft engines for advanced transport systems aimed at 20,000-50,000h life and industrial turbines aimed at up to 100,000h life require consideration of many factors to ensure high performance and reliability [32]. An example of a nickel-base blade used in industrial gas turbines is shown in Figure 2.6 (a), and with severe corrosion damage in Figure 2.6 (b).

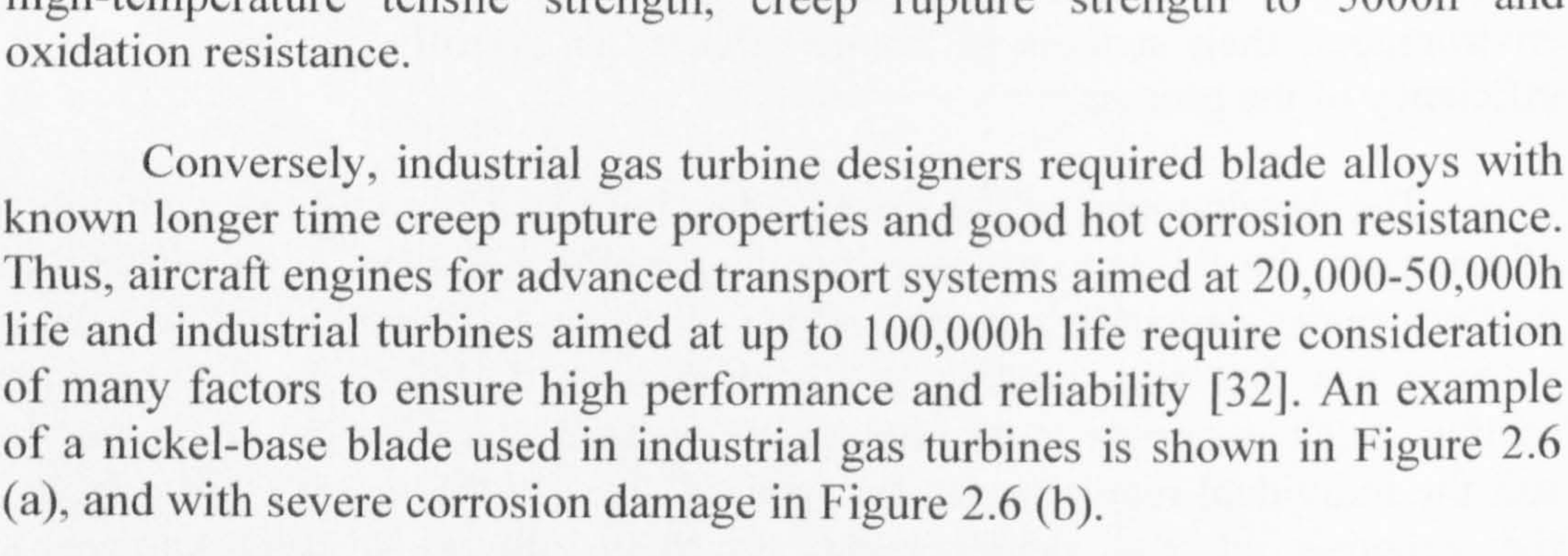

Figure 2.6: Example of a gas turbine blade for power generation systems (a) and severely damaged (b).

2.3.4 Chemical composition

The composition of many types of nickel-base alloys include at least 12-13 important elemental constituents which are controlled. Most nickel-base alloys contain 5-20% chromium, up to 8% aluminium and titanium, 5-10% cobalt and small amounts of boron, zirconium and carbon. Common additions are molybdenum, tungsten, columbium, tantalum and hafnium. Figure 2.7 illustrates that the alloying elements do tend to be grouped with some commonality in the periodic system. The first class consists of elements that prefer and make up the face-centred cubic (FCC) austenitic (γ) matrix. These are from Groups VIA and VIIIA in Figure 2.7 and include nickel, cobalt, iron, chromium, molybdenum, and tungsten.

The second class of elements partition to and make up the γ' precipitate, Ni_3X. These elements are from Groups III, IV and V and include aluminium, titanium, columbium, tantalum, and hafnium. Boron, carbon and zirconium make up a third class of elements that tend to segregate to grain boundaries. These elements are from groups II, III, and IV and are very odd sized in terms of atomic diameter.

Two subclassifications are beyond these three major classifications. One includes the carbide formers: chromium, molybdenum, tungsten, niobium, tantalum and titanium. The second subclasification comprises the chromium and aluminium oxide formers, which develop adherent diffusion-resistant oxide scales to protect the alloys from the environment. Table 2.2 shows the nominal compositions of the alloys that have been studied during the present work, i.e. two known corrosion resistance superalloys (as references) IN738LC, IN792 and two single crystal superalloys, the already in use CMSX4 and the new SC^2. (In section 3.2, the coatings are given in Table 3.2 and the base/alloy coating combinations are given in Table 3.3).

Alloy		Cr	Co	Mo	W	Ta	Nb	Al	Ti	C	B	Zr	Others
Poly-crystalline	IN 792	12.4	9.0	1.9	3.8	3.9	-	3.1	4.5	0.12	0.020	0.10	
	IN 738LC	16.0	8.5	1.7	2.6	1.7	0.9	3.4	3.4	0.11	0.010	0.05.	
Single Crystal	CMSX-4	6.5	10.0	0.6	6.0	6.0	-	5.6	4.9	1.0	-	-	0.1Hf,2.9 Re
	SC^2	11.8	4.95	0.99	3.93	2.03	-	4.02	4.58	190 ppm	-	-	‹ 5 ppm

Table 2.2: Nominal composition (bal. nickel) of gas turbine alloys (wt.%) [33; 34; 35].

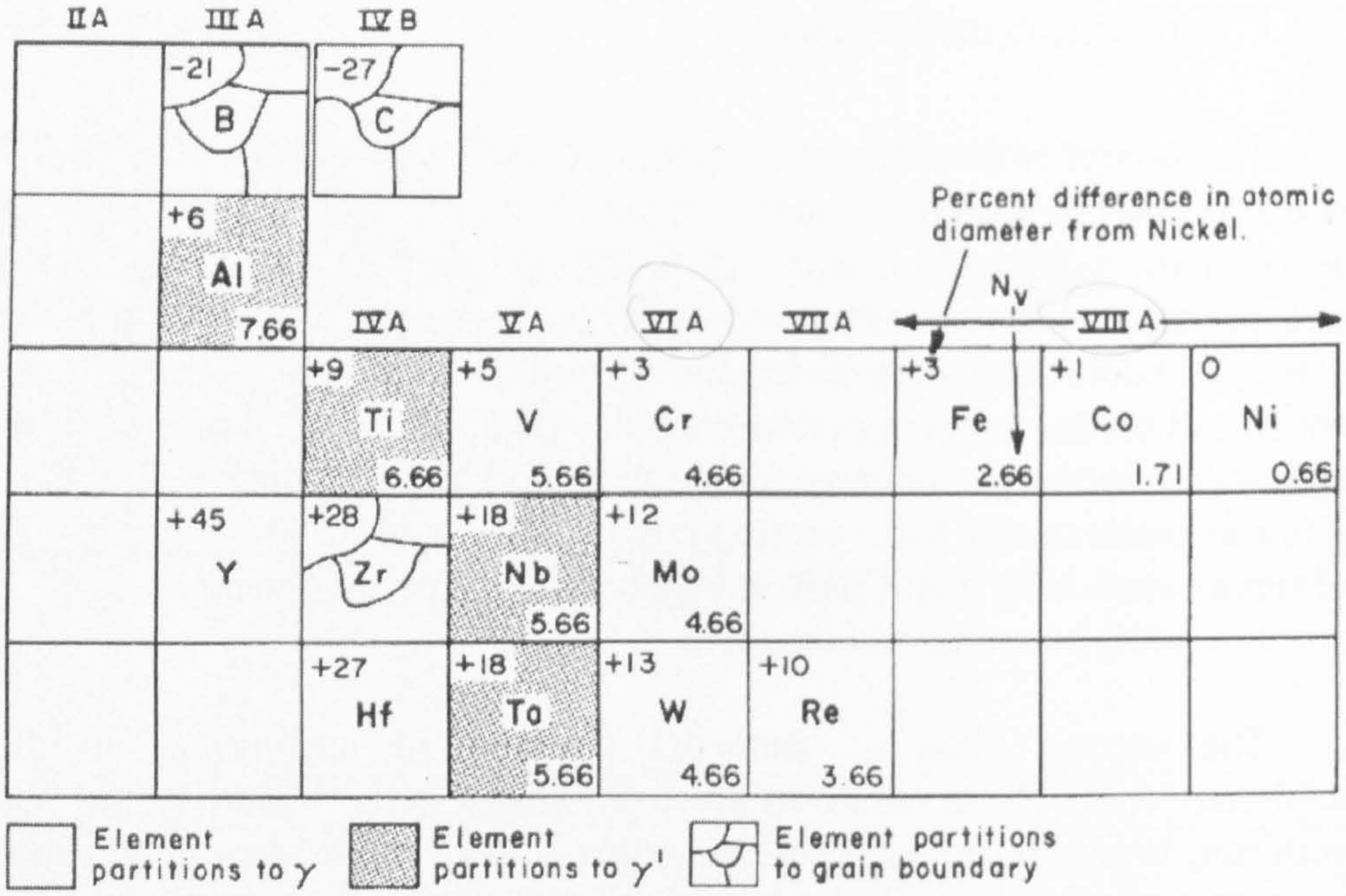

Figure 2.7: Elements important in the constitution of nickel-based alloys [32].

2.3.5 Structure and Microstructure

The major phases present in nickel superalloys are as follows [32]:

1. Gamma Matrix (γ). The continuous matrix is an FCC nickel-base austenitic phase called gamma that usually contains a high percentage of solid-solution elements such as cobalt, chromium, molybdenum and tungsten.

2. Gamma Prime (γ'). Aluminium and titanium, for example, are added in amounts and mutual proportions to precipitate high volume fractions of FCC γ', which invariably precipitates coherently with the austenitic γ matrix.

3. Carbides. Carbon, added at levels of about 0.05-0.2%, combines with reactive and refractory elements such as titanium, tantalum, and hafnium to form MC carbides. During heat treatment and service, these begin to decompose and generate lower carbides, such as M_2C and M_6C, which tend to populate the grain boundaries.

4. Grain boundary γ'. For the stronger alloys, heat treatments and service exposure generate a film of γ' along the grain boundaries; this is believed to improve rupture properties.

5. Borides. Occur as infrequent grain boundary particles.

6. TCP (topologically close packed)-Type Phases. Under certain conditions, plate-like phases, such as σ, μ, and Laves, form; this can result in lowered rupture strength and ductility.

Figure 2.8 is a drafted panoramic sketch (at about 10,000x showing the 50-years development, up to the late 80's, of the nickel superalloys, the appearance, characterizing the microstructures that have made the alloys increasingly strong over time, yet retaining usable ductility, as in the upper two thirds of the picture. The lower part of the figure includes some of the phases that have been found to cause brittleness, have lower strength, or create other problems.

As seen in Figure 2.8, from the 30's to the 50's, alloys were filled with increasing structure to make them stronger. In the 50's, packing with strengthening elements was accelerated but thus led to significant problems created by embrittling phases (such as σ and Laves). Also; in the 50's, very complex grain boundaries, with carbides engloved in γ', created a dispersion-strengthened layer bonding the grains together. By the 1970's, the effects of hafnium had been discovered and the γ' engloved carbide structure was less essential.

Directional solidification (DS) processing then created aligned grain structures, aligned grain boundaries, and even aligned strengthening filaments (such as TaC), shown in Figure 2.8 as they appeared in the 70's and 80's. Finally, the aligned homogeneous single crystal (SX or SC) structures were introduced. Recently, through heat treatment, transverse plates of γ' have been created in single crystals, which gives still further strengthening.

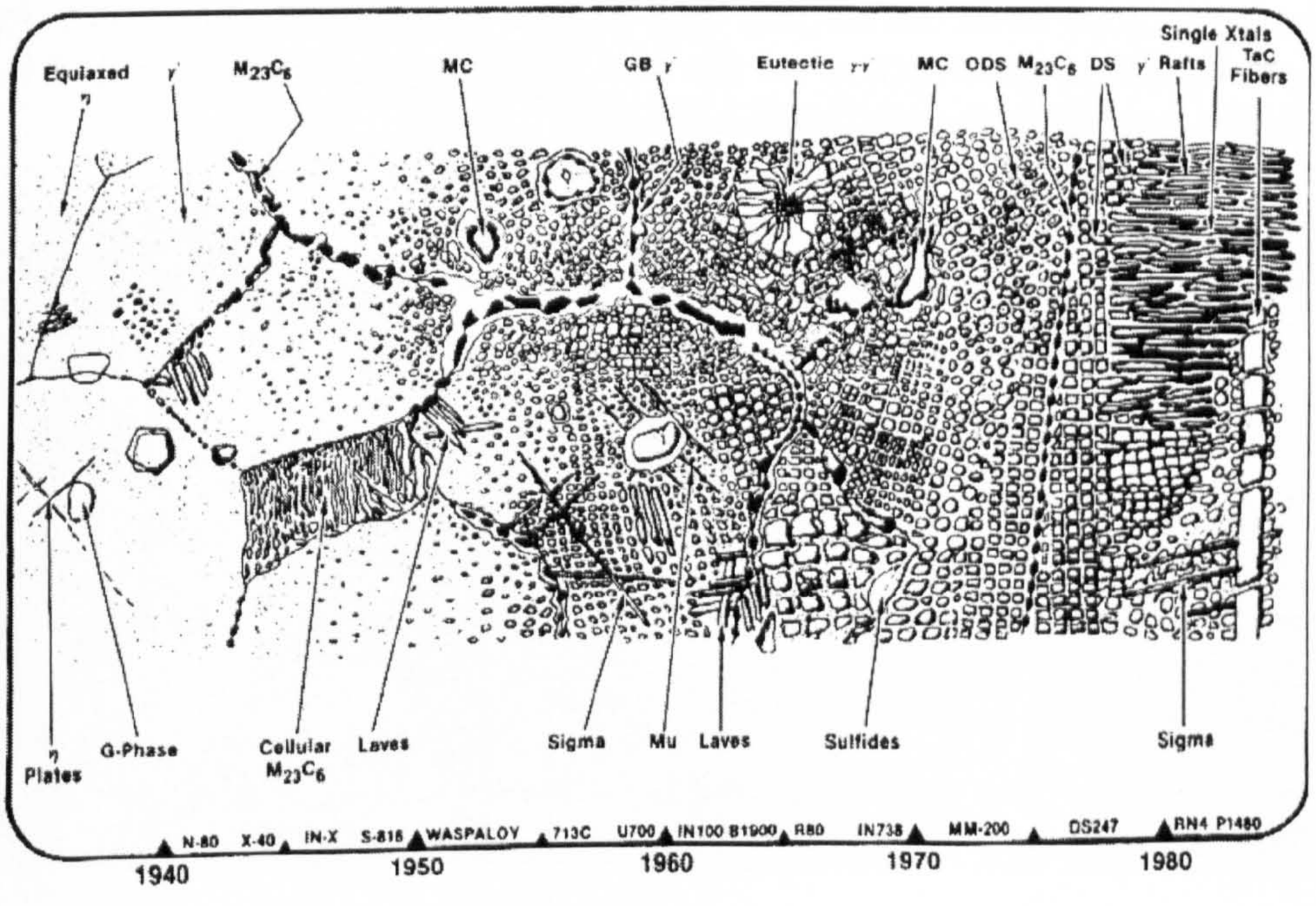

Figure 2.8: Panorama of the development of nickel superalloy microstructure showing both useful and deleterious phases [30].

Directionaly solidified (DS) columnar-grained (CG) and single crystal (SC) superalloys have the highest elevated temperature capabilities of any superalloy. For this reason, they are finding widespread use as turbine airfoils, an application that demands the most in alloy properties at elevated temperatures. There are two primary reasons that explain why DS superalloys are superior to conventionally cast (CC) superalloys:

- Alignment, or elimination, in the case of SC superalloys, of the grain boundaries normal to the stress axis enhances elevated-temperature ductility by eliminating the grain boundary as the failure initiation site. This permits the γ' microstructure to be refined with a solution heat treatment that increases alloy strength.
- The DS process provides a preferred low-modulus (001) texture or orientation parallel to the solidification direction. This results in a significant enhancement in thermal fatigue resistance, so important in elevated-temperature components.

In the absence of grain boundaries, more flexibility in alloying might be achieved that would result in an optimum balance of creep-rupture, fatigue and strength, but with the penalty of decreased hot corrosion resistance. The use of single crystals alloys has been mainly in aircraft engines. In small land based turbines, CMSX-4 alloy has been used since 1990 to date [36]. It is expected that single crystal aero foils will become a standard feature in large industrial turbines within the next few years [36; 11]. However, more corrosion resistance alloys need developing and, in fact are under development. Figure 2.9 shows the microstructure of the two single crystal alloys studied in this work: the new SC^2 (a) and CMSX4 (b).

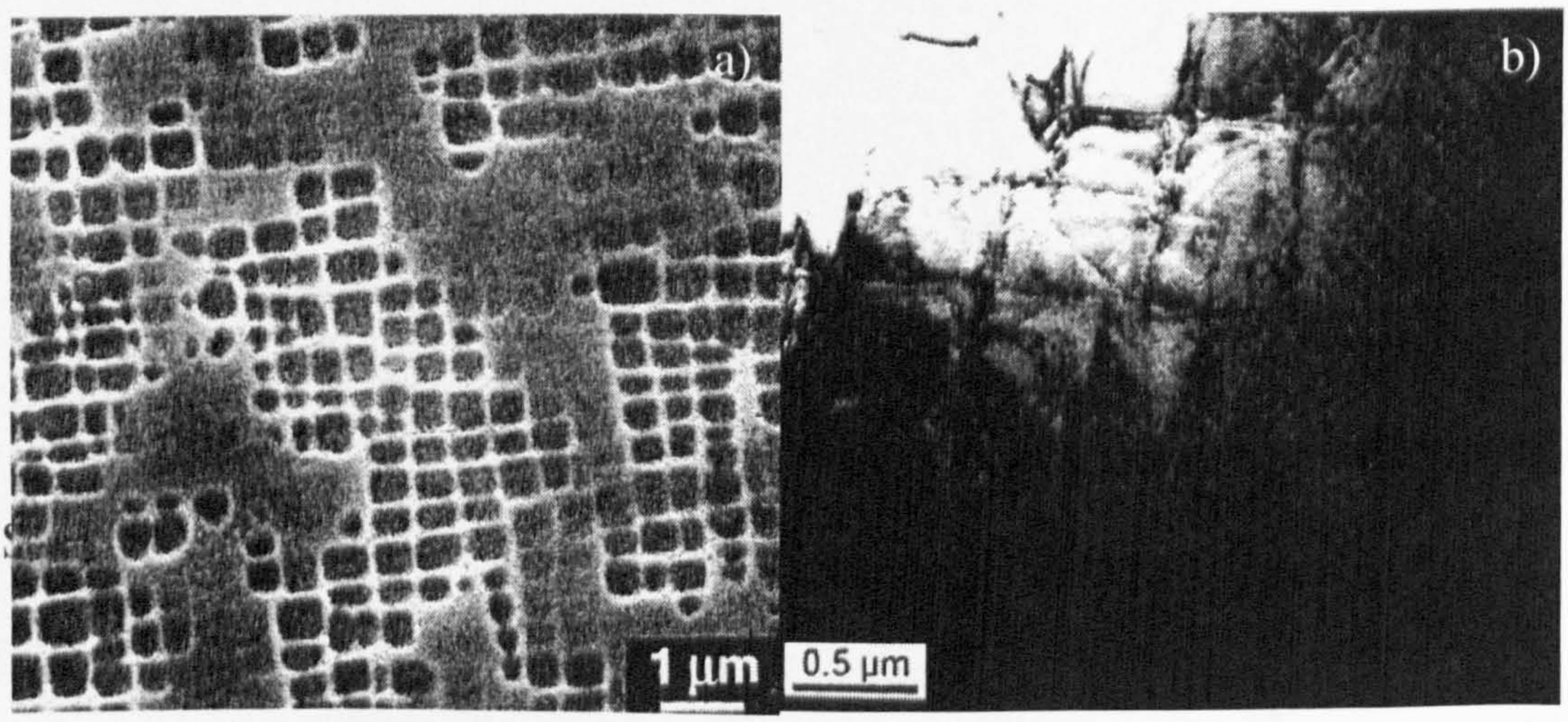

Figure 2.9: Microstructure of the two single crystal alloys studied in this work: a) γ' precipitates in fully heat treated SC^2 superalloy [37] b) typical microstructure of CMSX4, with γ'-NI_3Al grains, embedded in a γ-Ni matrix [38].

2.3.6 Effects of Alloying Elements

Numerous studies have demonstrated the beneficial effects of additions of various elements to the alloy. For example, chromium additions decrease the minimum Al content needed to form a continuous alumina scale [39], while the reactive elements (Y, Hf, Ce, La, etc.) and precious metals, such as Pt [40], decrease the scale growth rate and improve the spallation resistance.

In the NiAl system, the minimum concentration of Al at which alumina is the dominant oxide scale is about 35 at% but, with the addition of 5% Cr, the limit of Al_2O_3 is pushed to about 12 at%. Thus, chromium has a strong effect on the selective oxidation of Al and formation of a continuous Al_2O_3 This occurs by the internal oxidation of Cr in the early, transient stages of oxidation, reducing the O flux into the metal. This is known as a "gettering" effect and is described by the sequence proposed by Giggins and Pettit in Figure 2.10 [39].

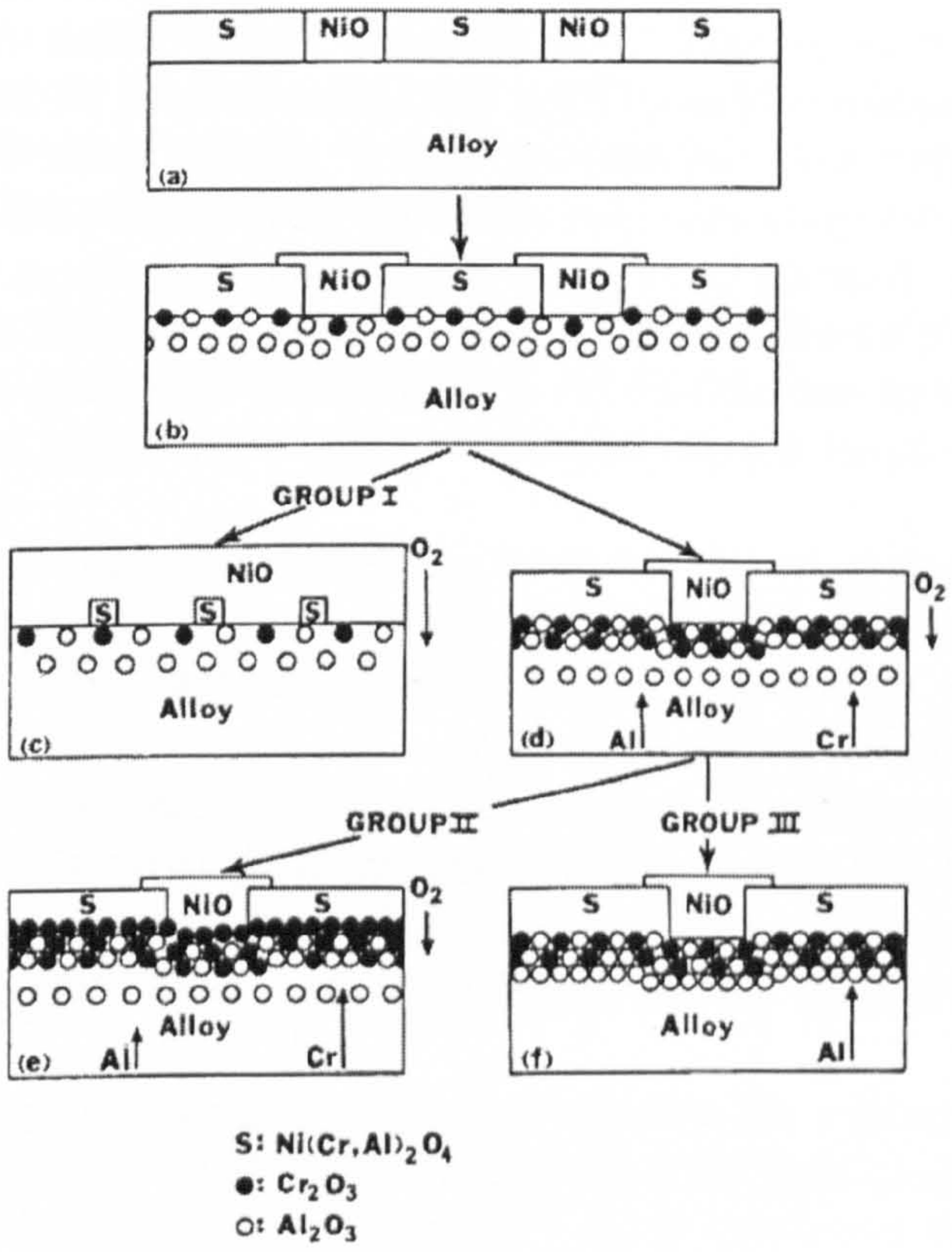

Figure 2.10: Schematic diagram illustrating the oxidation mechanism for Ni-Cr-Al alloys [39].

The first oxide scale that forms on a Ni-Al-Cr alloy will be a mixture, such as NiO-$Ni(Cr,Al)_2$, in proportions that reflect the alloy composition. Since Cr_2O_3 is stable at low oxygen partial pressures, it can form below the

scale. Al_2O_3 is even more stable and forms as internal oxide particles, below the Cr_2O_3 grains. If the Al and Cr contents of the alloy are low, NiO will continue to form (called Group I in Figure 2.10) and no continuous alumina or chromia layers built up. If the Al or Cr contents are higher, a Cr_2O_3 layer forms at the mixed-oxide/alloy interface, reducing oxygen diffusivity. This slows down the grow of both the internal Al_2O_3 grains and the outer NiO-$Ni(Cr,Al)_2O_4$ mixture. However, if the Al content is high enough, a continuous alumina layer appears. This layer becomes rate determining and further oxidation will create Al_2O_3 (Group III). If the Al content in the alloy is lower, Al_2O_3 will remain present as internal oxide precipitates and the continuous duplex layer will be enriched in Cr (Group II). For the continuous alumina layer formation (Group III), steady state is reached after about 1 h at 1000°C.

In addition to Cr and Al, other common alloying elements are manganese, titanium and silicon and the refractory metals, such as molybdenum, tungsten and tantalum. Manganese promotes Cr_2O_3 formation in Ni-20Cr, but up to 30% manganese was not effective in Co-19Cr. Additions of manganese have been shown to maintain Al_2O_3 scales on Fe-Al alloys. Additions of titanium promote Cr_2O_3 formation on both Ni-20Cr and Co-20Cr but do not significantly affect the Cr_2O_3 growth rate. Titanium slightly increases the growth rate of Al_2O_3 scales on β-NiAl and does little to promote exclusive Al_2O_3 formation on γ'-Ni_3Al or γ-Ni(Al) alloys. Titanium has a deleterious effect on adherence on nickel-base superalloys.The isothermal and cyclic behaviour of some Ni-Cr, Fe-Cr and Ni-Al alloys can be improved with silicon so as to equal the performance of exclusive Cr_2O_3 or Al_2O_3 forming alloys.

The refractory metals are used on nickel- or cobalt-base superalloys as strengtheners, participating in γ' formation, carbide formation and through solution effects. Refractory elements can produce three effects on the oxidation of nickel-or cobalt-base alloys:

- These elements can be considered to be oxygen getters and assist in the formation of Al_2O_3 and Cr_2O_3 healing layers (beneficial effect)
- Refractory elements decrease the diffusion of aluminium, chromium and silicon which opposes healing layer formation (deleterious effect).
- The oxides of refractory metals are generally non-protective (i.e. low melting points, high vapour pressure, high diffusivities, etc.) (deleterious effect).

The deleterious effects of the refractory metals outweigh the beneficial effects and therefore, they are not added to superalloys to improved oxidation behaviour. On the other hand, some of these elements do appear to be preferable to others. For example, tantalum does not appear to produce deleterious effects as severe as do tungsten or molybdenum. Tungsten, molybdenum and vanadium are similar [41].

2.4 High Temperature Oxidation

2.4.1 Introduction

By nature, metals are thermodynamically unstable with respect to ambient gases and will react to form oxides, sulphides, carbides, nitrides, etc. For many metals at room or low temperature, this instability is of little or no consequence because rates of reaction are very low. However, the reaction rates increase rapidly with temperature. Therefore, in those industrial processes where metals are required to perform at elevated temperatures, such as gas turbines in power generating plant, oxidation/corrosion resistance becomes a serious issue.

The most common reaction is with the oxygen in the air: oxidation. This occurs when a metal and oxygen combine to form a metal oxide, which may extend to cover the entire surface, creating a thin layer (oxide scale). In some situations (certain metals, oxides and temperature ranges), this layer acts as a "protection barrier" for the underlying metal [42].

When the oxide scale is not continuous or dense enough, the rate of oxide formation increases such that much more material is consumed (metal loss); therefore, a component such as a gas turbine blade, may fail or need to be replaced early.

2.4.2 Thermodynamics of Oxidation

The overall driving force for metal-oxygen reactions is the free energy change associated with the formation of the oxide from the reactants. Thermodynamically, the oxide will be formed only if the ambient oxygen pressure is larger than the dissociation pressure of the oxide in equilibrium with the metal.

The standard free energies of formation of oxides as a function of temperature and the corresponding dissociation pressures of the oxides can be summarised in the form of the Ellingham/Richardson diagram, illustrated in Figure 2.11, [43] (similar diagrams are also available for the formation of sulphides, chlorides, etc. [44]). Such a diagram shows data for oxides that are often encountered in the oxidation of metal and alloys.

The most stable oxides have the largest negative values of ΔG. It may be observed from the oxides shown in Figure 2.11, that for the most important oxide systems in gas turbine technology: Fe_2O_3, CoO, NiO, Cr_2O_3, TiO_2 and SiO_2, Al_2O_3, the stability of the oxides increases from Fe_2O_3 to Al_2O_3.

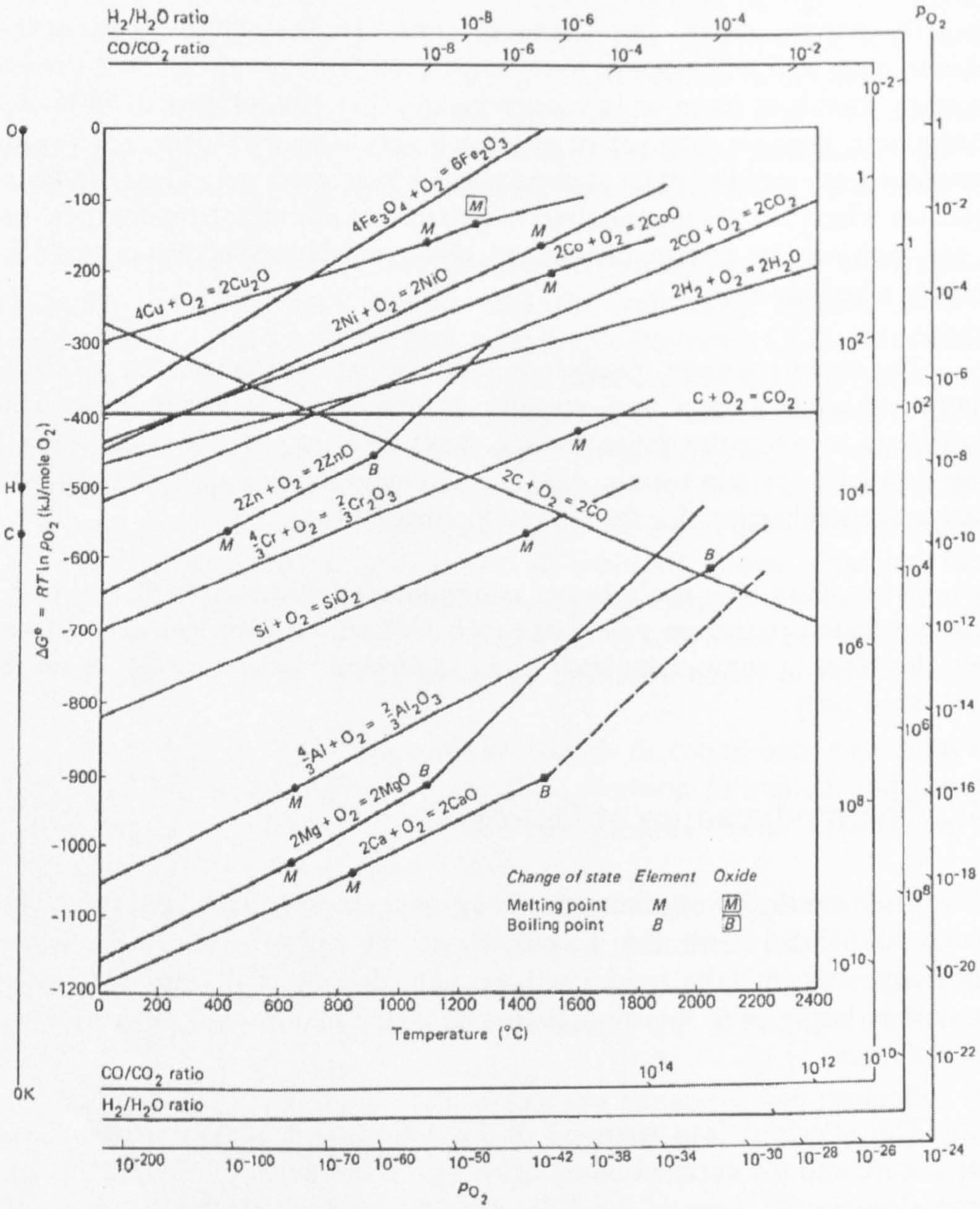

Figure 2.11: Ellingham/Richardson diagram. Standard free energy of formation of selected oxides as a function of temperature [45].

2.4.3 Kinetics of Oxidation: Oxide Scale Formation and Grown

The total chemical reaction of a metal M and oxygen gas O_2 to form the oxide M_aO_b may be written as:

$$aM + (\frac{b}{2})O_2 = M_aO_b$$

Equation 1

Many authors have explained in detail the formation and growth of the oxide scale, [46; 47; 48; 49] are typical reference books on the subject. For example, Kofstad [45; 50] explains that, on a truly clean metal surface, this initial oxidation (by oxygen) and formation of the scale can be divided into three main stages, Figure 2.12.

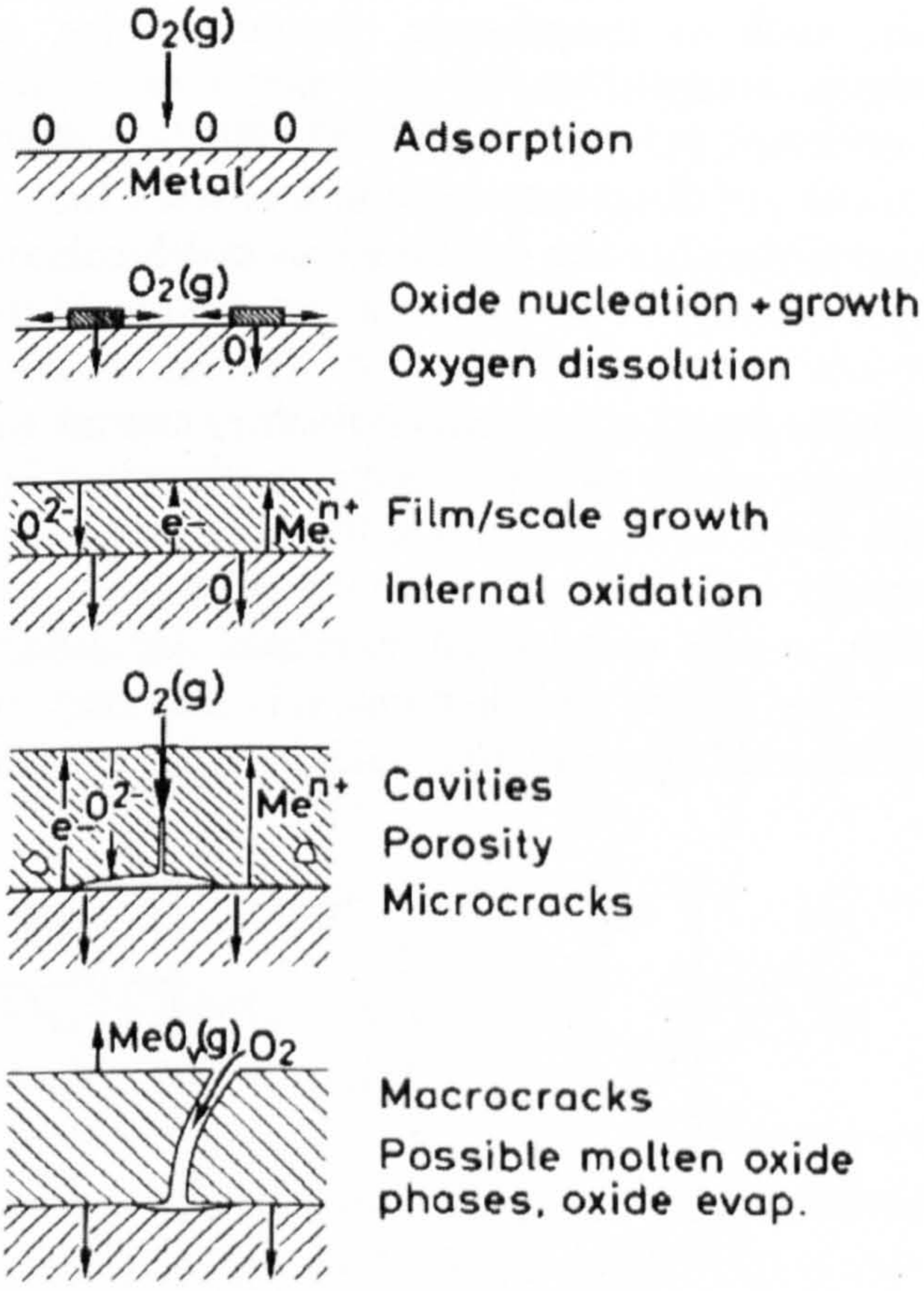

Figure 2.12: Schematic illustration of the main phenomena and part-processes taking place in the reaction of metals with single oxidant gases, e.g. oxygen [50].

Firstly, this metal-oxygen reaction involves the adsorption of gas on the metal surface.

Secondly, as the reaction continues, oxygen may dissolve into the metal, and oxide is formed on the surface either as a film or as separate oxide nuclei, which then grow laterally to form a continuous oxide layer which covers the whole surface. At the same time, the oxidant continues to dissolve in the metal substrate to an extent determined by the solubility and diffusivity of the oxidant in the metal. Both, the adsorption and the initial oxide formation are functions of surface orientation, crystal defects at the surface, surface preparation and impurities in both the metal and the gas. The surface oxide, in turn, separates the metal from the gas.

Finally, further growth of the oxide film occurs normal to the surface. At this stage, when a continuous film covers the surface, the reaction can proceed only through the solid-state diffusion of the reactants through the film. The reaction path and the oxidation behaviour of a metal will depend on a variety of factors, such as temperature, thermal cycles, composition and velocity of the gas, composition of the alloy, etc. These factors have frequently been reviewed [45; 46; 50; 47; 48; 49] over the period from the early 1960's. A review of direct relevance to this work looks at the influence of the oxidation conditions on the development and breakdown of protective oxide scales in coal-derived environments, as reported by Hsu [51].

In order for the reaction to proceed further, neutral atoms or ions and electrons must migrate across the oxide scale, as shown in Figure 2.13. If the oxide scale growth is by cation migration, this will lead to scale formation at the scale-gas interface and, if the scale growth is by anion migration, it leads to scale formation at the metal-scale interface. In order to explain the simultaneous migration of ions and electrons, it is necessary to assume that the oxides formed during oxidation, are non-stoichiometric compounds.

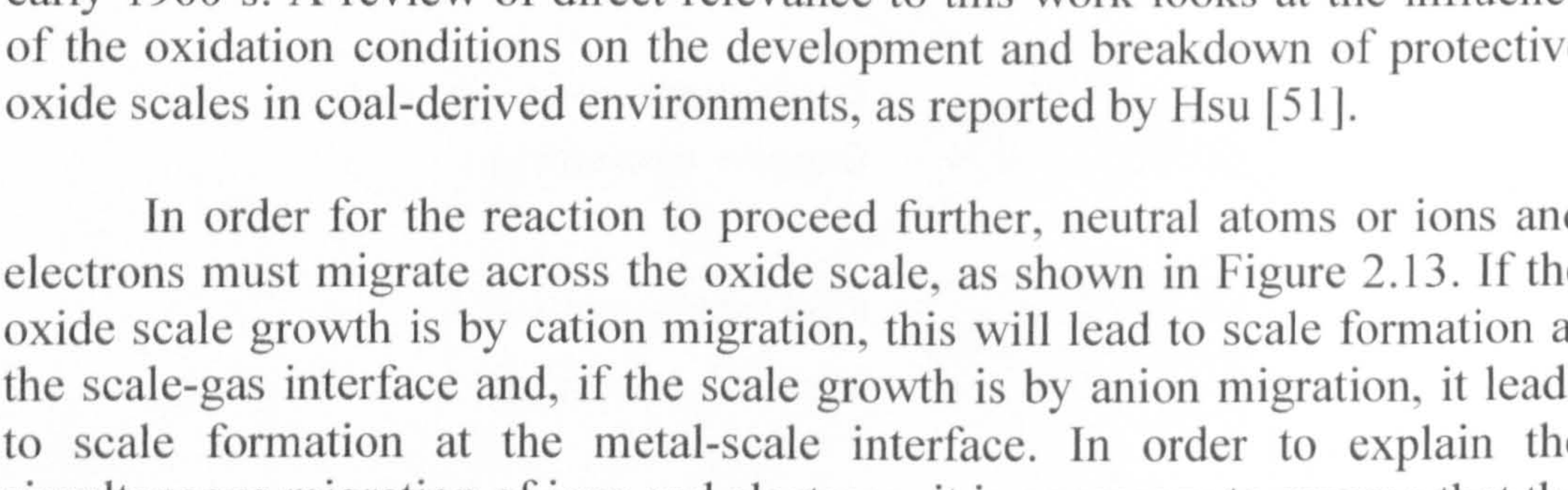

Figure 2.13: Interfacial reactions and transport processes for high temperature oxidation mechanisms (a) cation mobile and (b) anion mobile [49].

The rate of growth of the oxide scale may vary as a function of time and temperature. For high temperature oxidation, it often occurs in three different ways: parabolic, linear and logarithmic, as can be seen in Figure 2.14

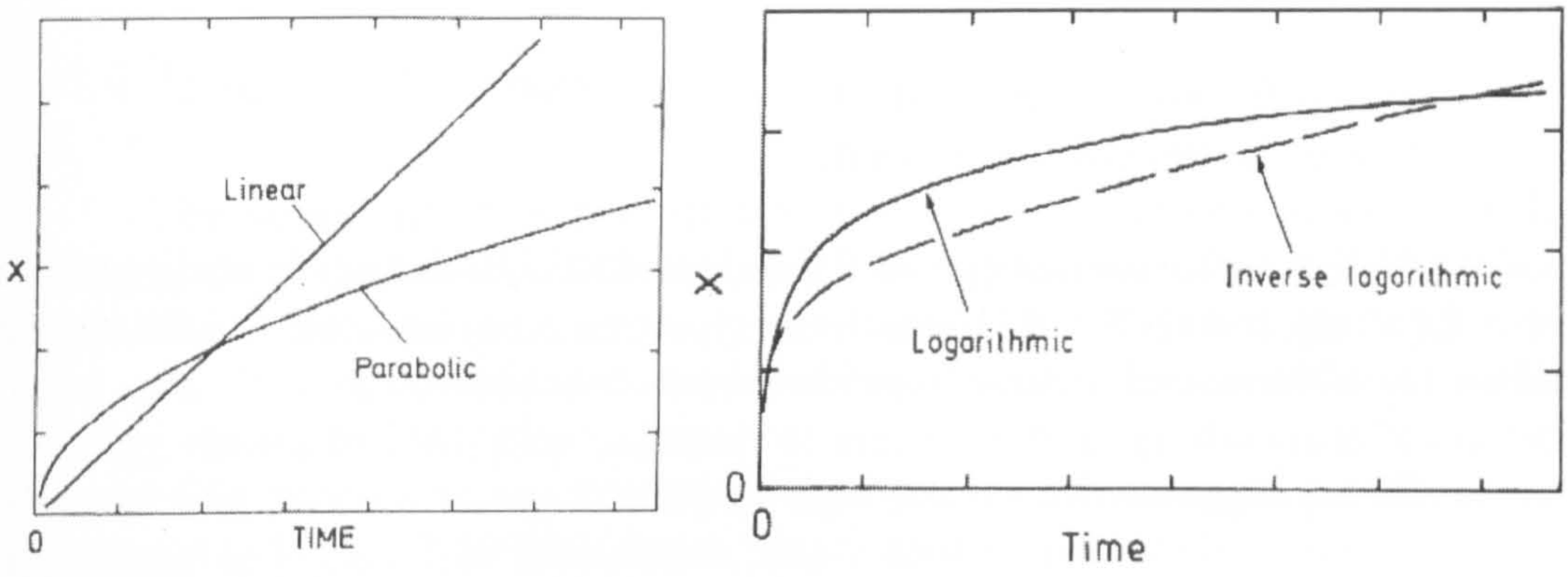

Figure 2.14: Schematic illustration of the variation of x (e.g. oxide thickness) with time for parabolic, linear and logarithmic oxidation [45].

At high temperatures, when the layer of reaction products remains dense and continuous, reactions are governed by diffusional transport of the reactants and electrons through the layer of reaction products. The thin layers grow into thicker scales. As the diffusion paths lengthen with increasing scale thickness, the reaction rate decreases with time. The reaction can be described by a parabolic rate equation as follows:

Differential: $dx/dt = k'_p/x$

Equation 2

Integral: $x^2 = 2k'_p t + C = k_p t + C$

Equation 3

k'_p and $k_p =$ the parabolic rate constant ($k_p = k'_p$).

$C =$ is the integration constant.

Large stresses may build up in the scales, with balancing stresses in the underlying metal; these can cause plastic deformation of the metal or lead to cracking of the scale. If repeated cracking takes place, the scale loses its protective ability. In this case, the reactions may be governed by diffusion through a thin reaction product layer of approximately constant thickness next to the metal or by phase boundary reactions. These reactions are described by a linear equation:

Differential: $dx / dt = k_1$

Equation 4

Integral: $x = k_1 t + C$

Equation 5

$k_1 =$ is the linear rate constant
$C =$ is the integration constant

At low temperatures (generally below 400° C), the oxide scale growth may for many metals follow logarithmic type rate equations, which include the direct logarithmic and inverse logarithmic rate equations:

Direct logarithmic: $x = k_{\log} \cdot \log(t + t_0) + A$

Equation 6

Inverse logarithmic: $1 / x = B - k_{il} \log t$

Equation 7

$x =$ thickness of the oxide scale, the amount of oxygen consumed per unit surface area of the metal, the amount of metal transformed to oxide.
$t =$ time
$k_{\log}$ and k_{il} = rate constants.
A and B = constants.

For practical alloys oxidised at high temperature, parabolic kinetics are the most common, with oxide scales that grow the most slowly, Cr_2O_3, Al_2O_3, SiO_2, being the most desirable, as may be seen in Figure 2.15

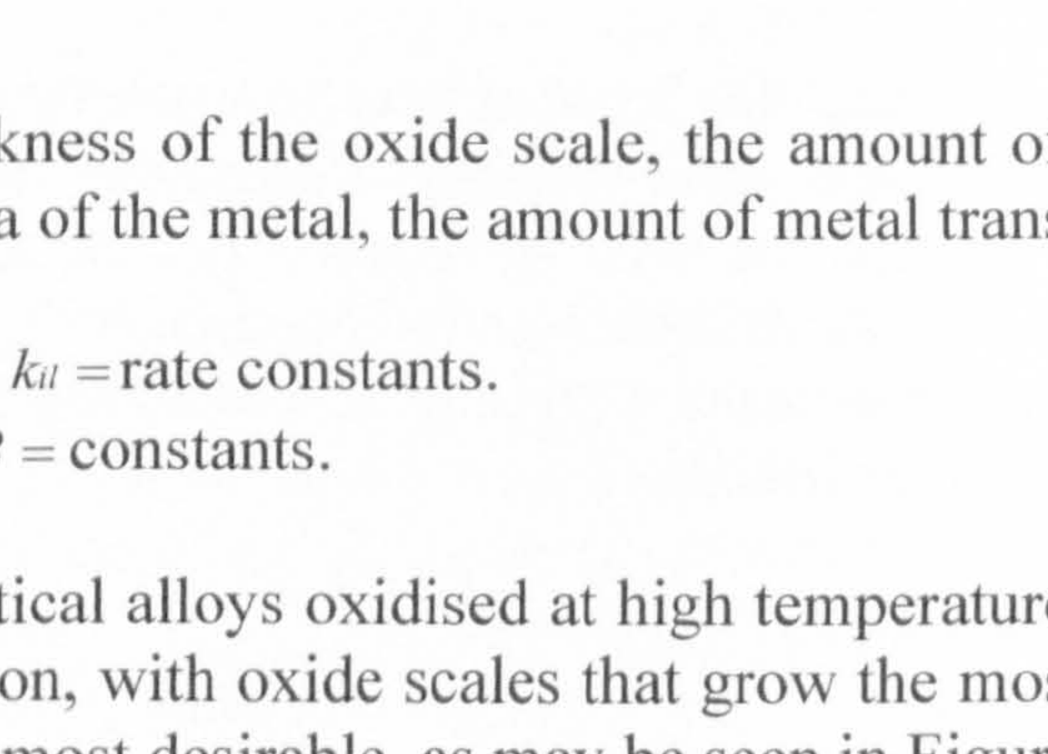

Figure 2.15: Order-of-magnitude parabolic rate constants for the growth of several oxides [49].

High stresses may also cause cavities, cracks or micro cracks in/under the oxide scale, making it fail as a protection shield. These may develop during oxidation as part of the growth of the oxide scale or be a result of thermal cycling (due to the thermal expansion mis-match between the oxide scale and the metal).

2.4.4 Transport mechanisms

The solid state transport of the reactants or electrons takes place by diffusion through the lattice, along grain boundaries and other easy diffusion paths. The diffusional process has been modelled by Wagner [52; 53] for the ideal case. The basic assumption of the theory is that lattice diffusion of the reacting atoms, as ions, plus transport of electrons through the scale is the rate determining process in the oxidation reaction. These transport processes are illustrated in Figure 2.16 for a dense, single phase oxide scale.

It is further assumed that thermodynamic equilibrium is established at the metal-oxide and oxide-oxidant interface. The "driving energy" for the reaction is the free energy change of the reaction between the metal and the oxidant to form the reaction product. The migrating species may alternatively be considered to constitute lattice and electronic defects, i.e. vacancies and interstitial ions and electrons and electron holes, respectively. This is illustrated in Figure 2.16 and the overall reaction follows a parabolic rate.

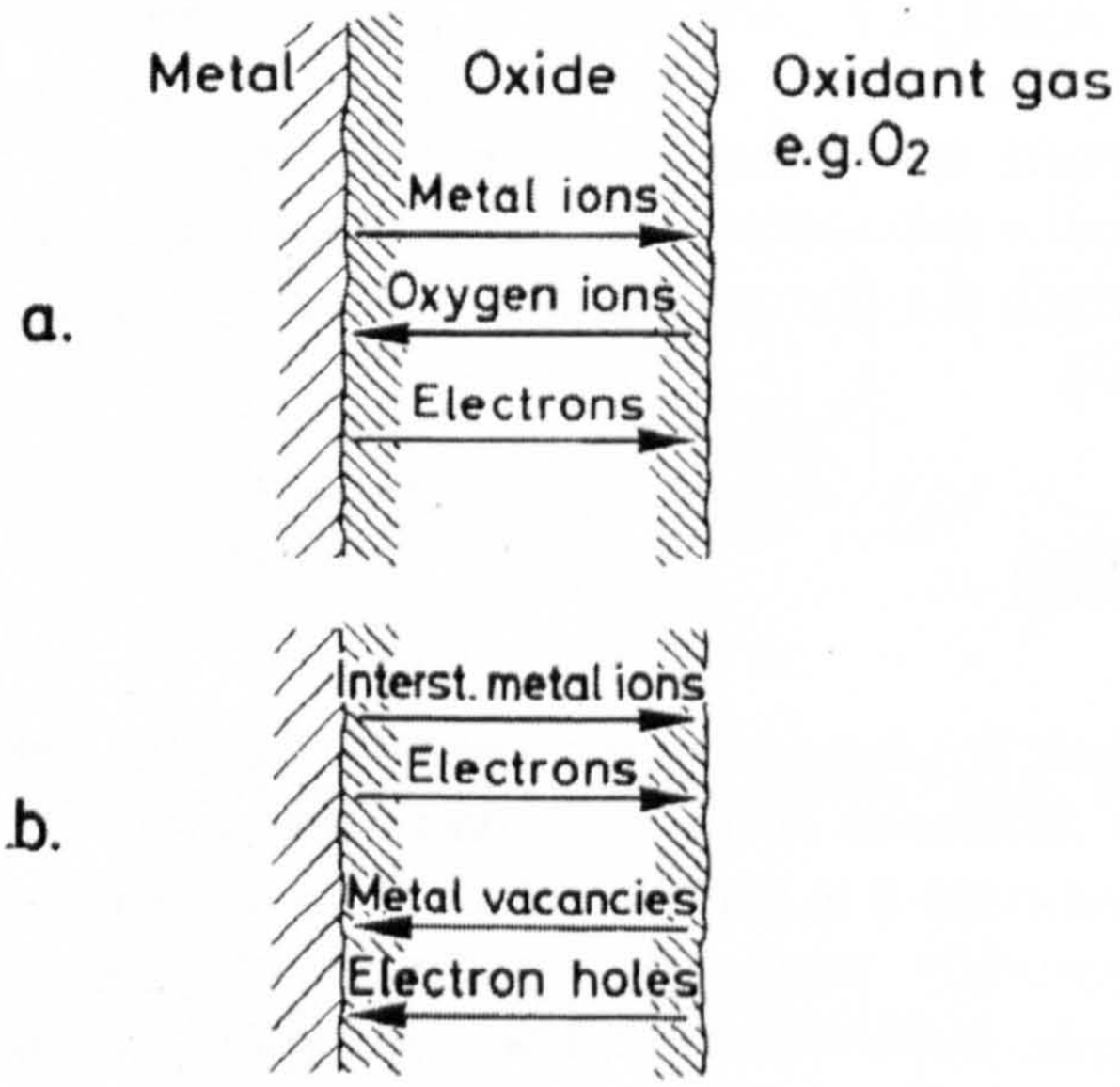

Figure 2.16: (a) Transport processes through scales growing by lattice diffusion.(b) Transport processes in growing scale in terms of lattice and electronic defects, e.g., of metal vacancies and interstitial ions and of electrons and electron holes respectively [50].

2.5 High Temperature Corrosion

2.5.1 Introduction

Corrosion is nature's way of returning processed metals, e.g. steel, copper, zinc, etc., to their native states as chemical compounds or minerals. In the presence of water and oxygen, nature relentlessly attacks the metal, reverting the elemental metal back to an oxide. Thus, metals are very sensitive to the environment in which they perform [54].

The gas from the combustion of coal and biomass contains aggressive species (previously identified in section 2.2) that can be deposited on to the surface of blades or vanes within the turbine hot gas path of a combined cycle power plant, as metal sulphates and/or chlorides. When they reach their melting points, these deposits may cause accelerated corrosion and degradation of the underlying metal. This form of metal damage is often call hot corrosion.

Hot corrosion was first recognise as a serious problem in the 1940's [22; 55; 45] in connection with degradation of fireside boilers tubes in coal-fired steam generating plants. It has since been shown to represent a problem in gas turbines, especially when operated in marine and industrial environments, in fluidized bed combustion, in magnetohydrodynamic systems and in municipal and industrial waste incinerators. Due to the important economic consequences, hot corrosion phenomena have been the subject of extensive research and a substantial effort has been directed to determine the mechanism (s) by which the hot corrosion of superalloys takes place [56; 57; 58; 59; 60; 61; 62; 63].

2.5.2 Hot Corrosion

Once the deposit has formed on the metal surface, the extent to which it affects the corrosion resistance of the alloy will depend on whether or not the deposit melts, how adherent it is and the extent to which it wets the surface. A liquid deposit is generally necessary for severe hot corrosion to occur, although some examples exist where solid deposits apparently have resulted in considerable corrosion [49]. Once the alloy-surface has been partially or completely wetted by the molten salt(s), conditions for severe corrosion can develop.

Pure Na_2SO_4 has a melting point of 884°C, but with dissolved salts, e.g. NaCl or other metal sulphates (e.g. K_2SO_4), the melting point is lowered. The present study is mainly concerned with the deposition of some species mixtures, particularly Na_2SO_4 and K_2SO_4 in the mol ratio 80:20 and 50:50, that, as may be seen in the binary diagram (Figure 2.17), have a melting point of 823° and 850°C respectively. Other corrosive species considered include: $ZnCl_2$ that has a melting point of 283°C, and $PbCl_2$ with a melting point of 497°C [64], both of which are further expected to lower the deposit melting points.

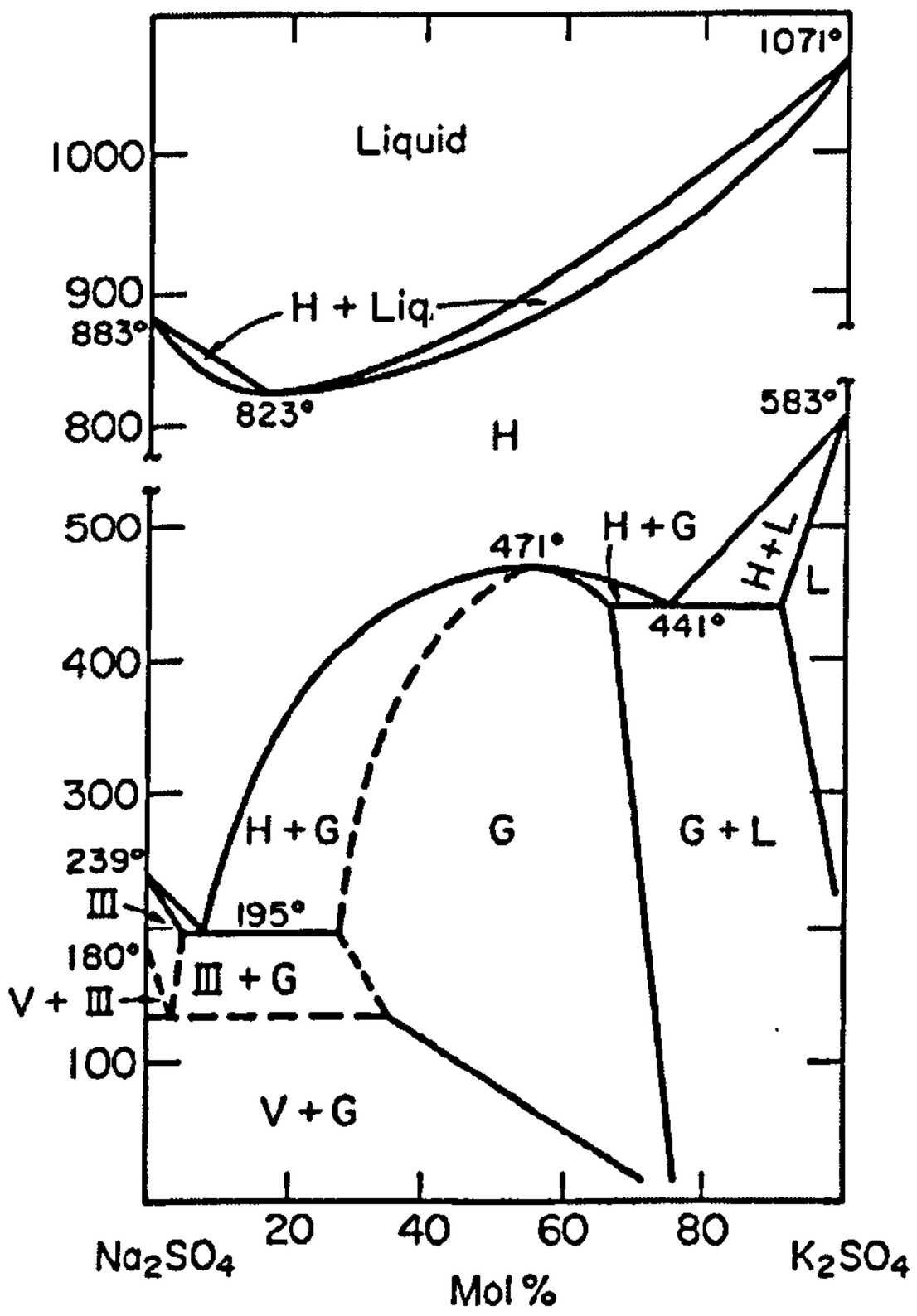

Figure 2.17: Binary equilibrium diagram for system Na_2SO_4-K_2SO_4 [65].

2.5.3 Hot Corrosion Degradation Sequence

Giggins and Pettit, in their Unified Theory [61], propose the "hot corrosion degradation sequence" in which mass change data for hot corrosion as a function of time, appeared to indicate two stages of attack: an initial stage (initiation or incubation) during which the attack is not too severe and a later

stage (propagation) where the attack has considerably increased. The first stage, initiation, corresponds to the growth and dissolution of the protective oxide layer (the growth has previously been described in section 2.4.) and to the formation of the deposits. The reaction rate of the metal surface at this stage is very slow. The second stage, propagation, is characterised by a rapid increase in corrosion rate, usually associated with important changes in the morphology of the corrosion layers, once the oxide layer has broken down.

These two stages are illustrated in Figure 2.18 for three different types of high temperature oxidation/corrosion test. It can be seen that the transition from the initiation to the propagation stage is influenced by factors such as spalling of the oxide scale (cyclic oxidation) and salt deposition (hot corrosion).

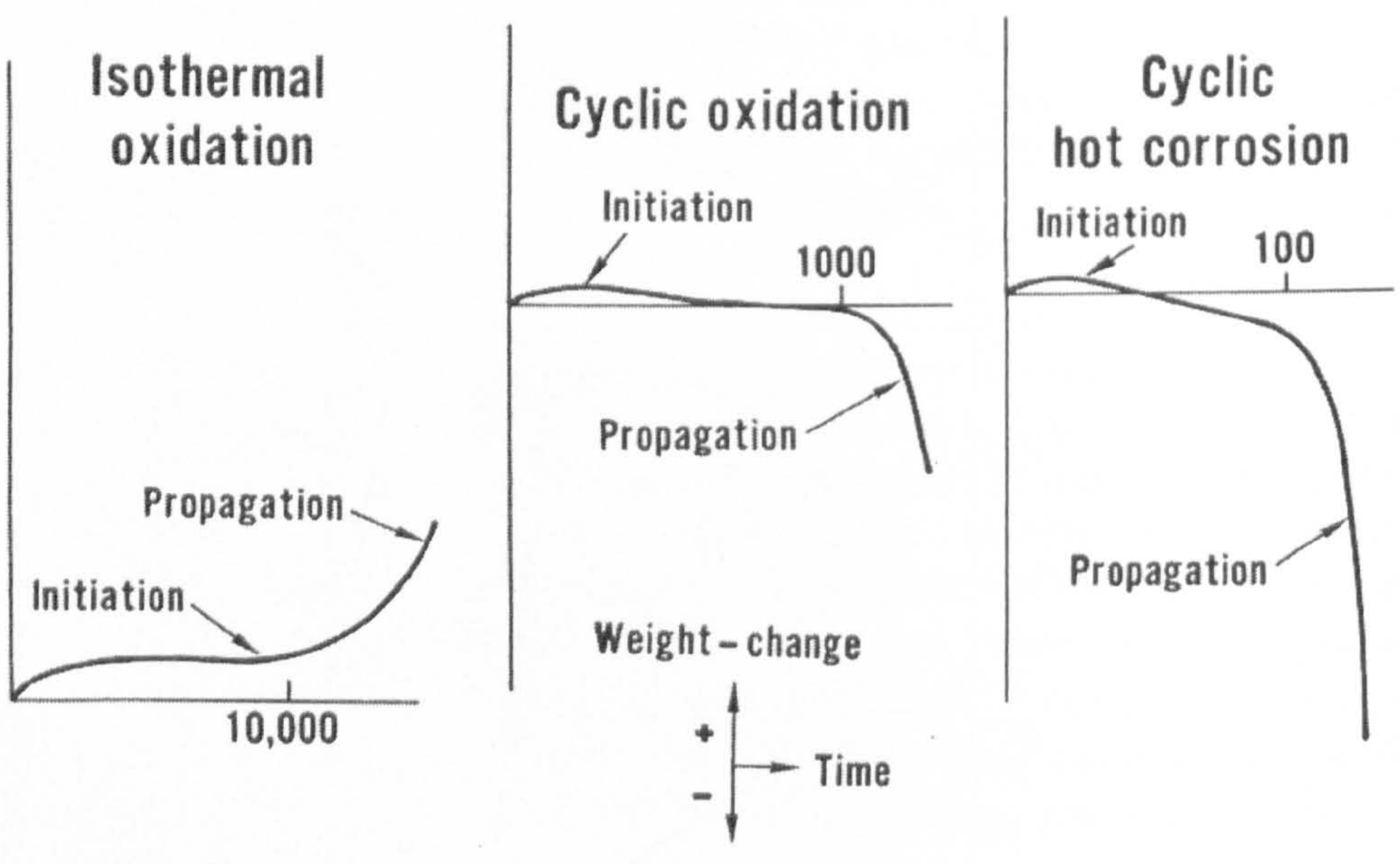

Figure 2.18: Schematic weight change versus time to illustrate that the degradation of corrosion resistant systems consist on an initiation and propagation stage [61].

During the initiation (incubation) stage, the alloy surface and scale growth are being altered to make the alloy susceptible to rapid attack. This alteration may include depletion of the elements responsible for forming the protective scale (usually Al or Cr), formation of sulphides in the alloy due to sulphur diffusion through the scale, dissolution of oxides into the salt and development of growth stresses in the scale.

This alteration also can result in shifts in salt composition towards more corrosive conditions. In many cases, the end of the initiation stage follows the local penetration of the salt through the scale and subsequent spreading along

scale-alloy interface. Figure 2.19 shows an example of the microstructural features that develop during the attack and that these features undergo a marked change as the severity of the attack increases, e.g. the amount of sulphide particles (black arrows) increases until the oxidation of the sulphide phases leads to a significant increase in the rate of attack.

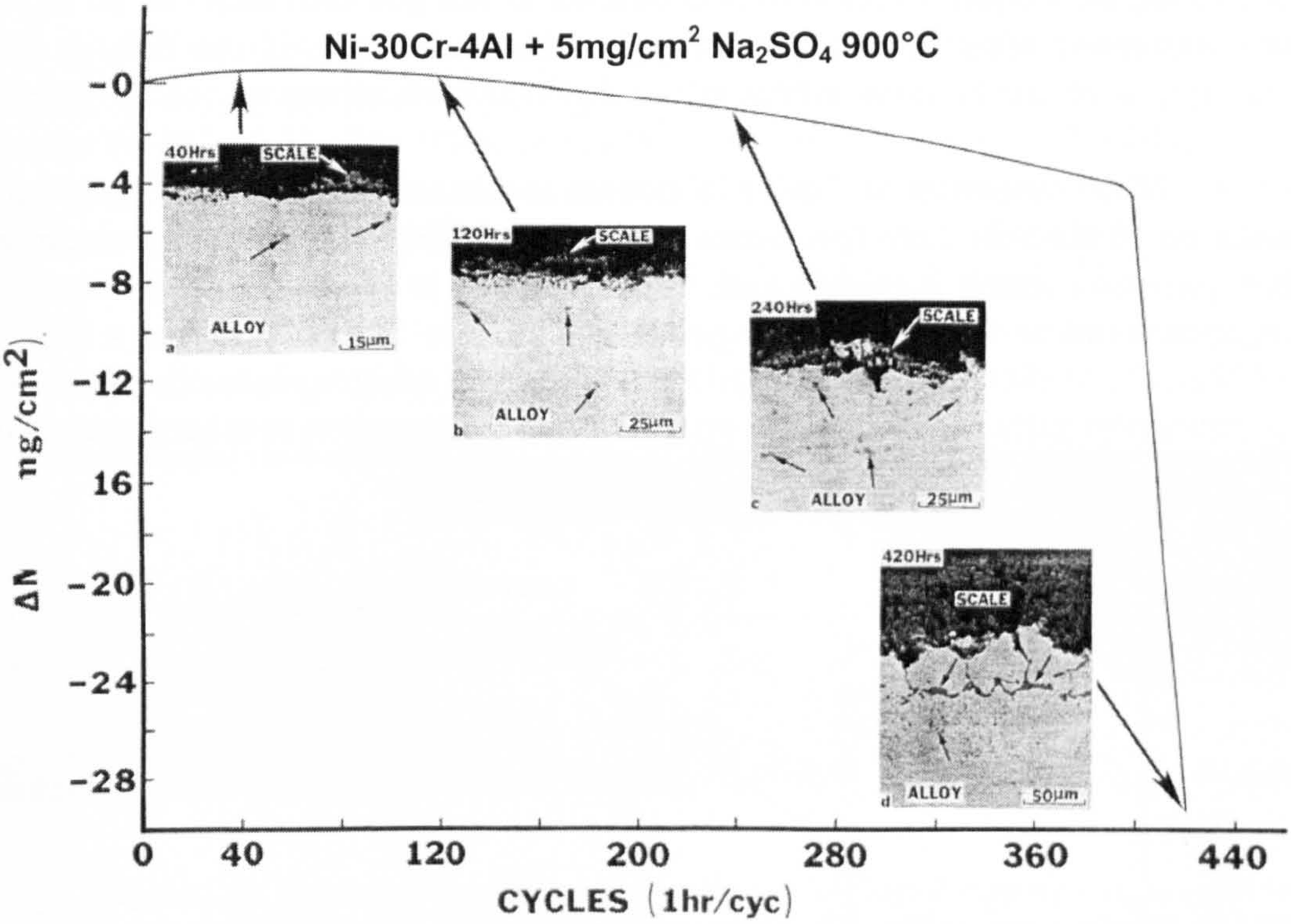

Figure 2.19: Weigh change versus time and corresponding microstructural features for the cyclic hot corrosion of Na_2SO_4 coated Ni-30Cr-4Al [61].

2.5.4 The Initiation Stage of Hot Corrosion Attack

The length of the initiation stage can vary from seconds to thousands of hours. A number of factors have been identified (Figure 2.27) upon which this phenomenon depends; these are related to the service conditions, materials composition and design.

1. Related to the service conditions:

- Temperature: Hot corrosion is a characteristic degradation mechanism in gas turbines in the metal temperature range of 600 to 950°C in a given environment; different mechanisms with different initiation times can be observed at certain temperatures. Hence, rate constants change not only because the kinetics are being influenced by temperature, but also because a completely new reaction mechanism can become operative.

• Composition of the gas: this factor can produce very substantial effects on the initiation and degradation rate of hot corrosion attack [66; 67; 68; 69] e.g. in Figure 2.20, weight change is compared for the oxidation of Na_2SO_4 coated CoCrAlY coatings in oxygen and in oxygen containing SO_3 at 10^{-4} atm. In this study, hot corrosion attack has commenced from the beginning of weight-increase measurements in the gas with SO_3 but no attack was observed after 20h in pure oxygen. The influence of the SO_3 in this example is on the Na_2SO_4, which is not liquid at the temperature of 700° C.

When oxidation of CoCrAlY occurs at this temperature in SO_3, a liquid solution of Na_2SO_4-$CoSO_4$ is formed. SO_3 also influences the rate at which the hot corrosion attack is propagated; as can be seen in Figure 2.20, the attack in oxygen is not as severe as in oxygen with 10^{-4} atm. SO_3, even when a deposit of Na_2SO_4-$MgSO_4$, which is liquid at 700° C in oxygen, is used. Thus, gas composition influences both the initiation and propagation mechanisms of hot corrosion attack, for this coating.

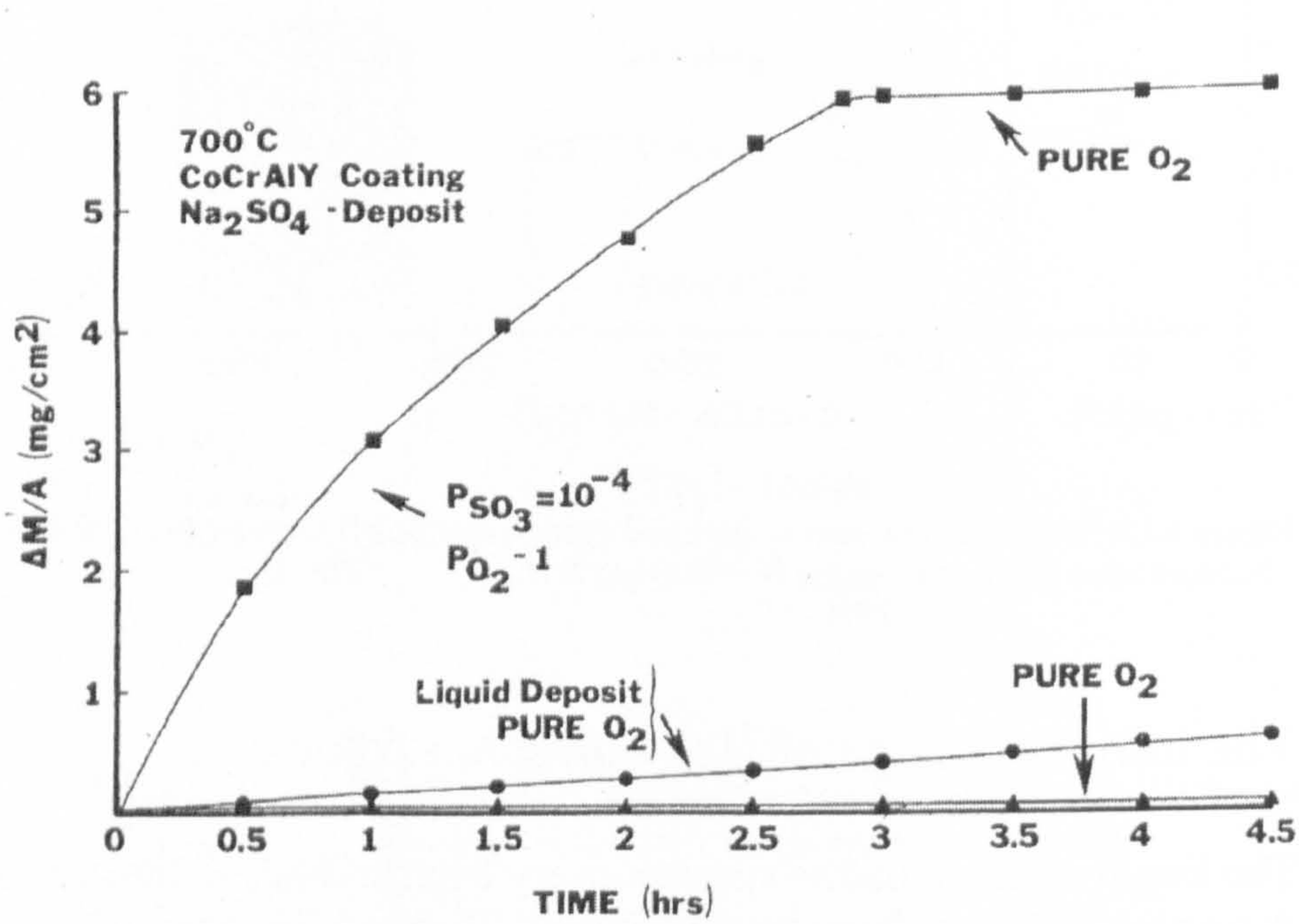

Figure 2.20: Weight change that shows the double influence on hot corrosion attack of the gas composition, either on the initiation of hot corrosion as well as on the propagation (mechanisms) [55].

• Deposit composition: one effect occurs because the deposit transforms from solid to liquid with the compositional change, Figure 2.20; another effect involves changes in the mechanism of the hot corrosion attack,

e.g. in Figure 2.21 photographs are presented to compare the degradation microstructures developed in coatings exposed to Na_2SO_4 containing different amounts of NaCl on CoCrAlY-coated IN738LC at 900°C in air. The degradation becomes more severe as the NaCl concentration in the deposit is increased.

- Deposit deposition rates: for example, for some mechanisms that are not self-sustaining, deposit is consumed and, therefore, the more deposit present, the more is the extent of attack; this effect can be seen in Figure 2.22 for the Ni-8Cr- 6Al alloy when tested with different amounts of Na_2SO_4. Other mechanisms require the salt to have a certain composition before attack commences. This factor has been recognized as relevant to the hot corrosion of materials [70; 71].
- Other factors include: thermal cycles, physical state of the salts, erosion, and velocity of the gas.

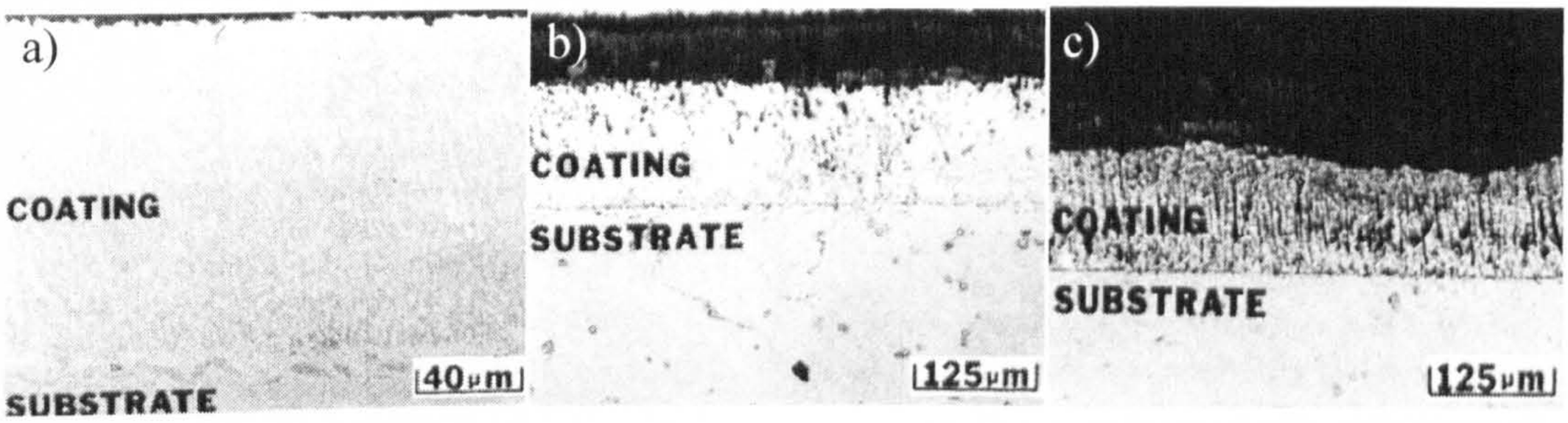

Figure 2.21: Photomicrographs to compare the CoCrAlY coating degradation on IN738 after exposure at 900°C in air to Na_2SO_4 deposits containing different amounts of NaCl. (a) 500h with Na_2SO_4, (b) 500h with Na_2SO_4-5wt% NaCl, (c) 40h with Na_2SO_4-90 wt% NaCl [55].

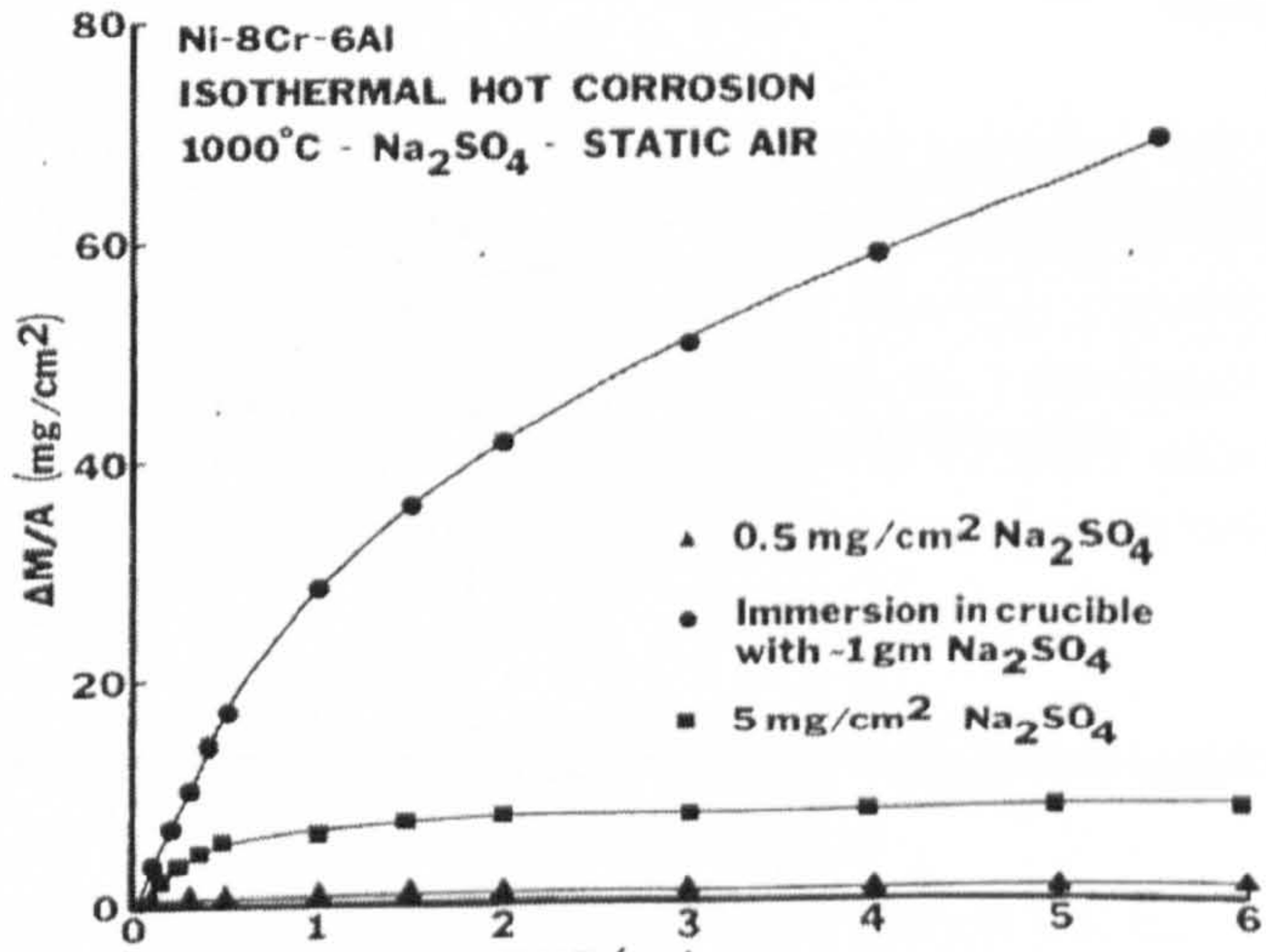

Figure 2.22: Weight change for the hot corrosion attack of Ni-8Cr-6Al specimens with different amount of Na_2SO_4 [61].

2. Related to the material and design:

Composition of the alloy: the data presented in Figure 2.23 show that the length of the initiation stage for hot corrosion induced by Na_2SO_4 in air is increased as the aluminium content of nickel-chromium or cobalt-chromium alloys is increased from 6 to ~11%. It also shows that, in this case (type I hot corrosion, see section 2.5.5), the initiation stage for Co-Cr-Al alloys is longer than that for nickel-base alloys.

- Micro-structural: the presence and/or removal of grain boundaries, changes in composition because of this (i.e. a single crystal superalloy), impurity levels, etc.

- Geometry of the component: for example, it is common to observe spalling of the oxide scale initiating at the sharp angles (edges and corners) of specimens or service hardware.

- Other factors: alloy fabrication conditions and methods.

From all these factors, alloy composition, temperature, gas composition, salt deposition rate and salt composition were considered in planning the experimentation in the present study and their effects are thoroughly discussed in section 5.

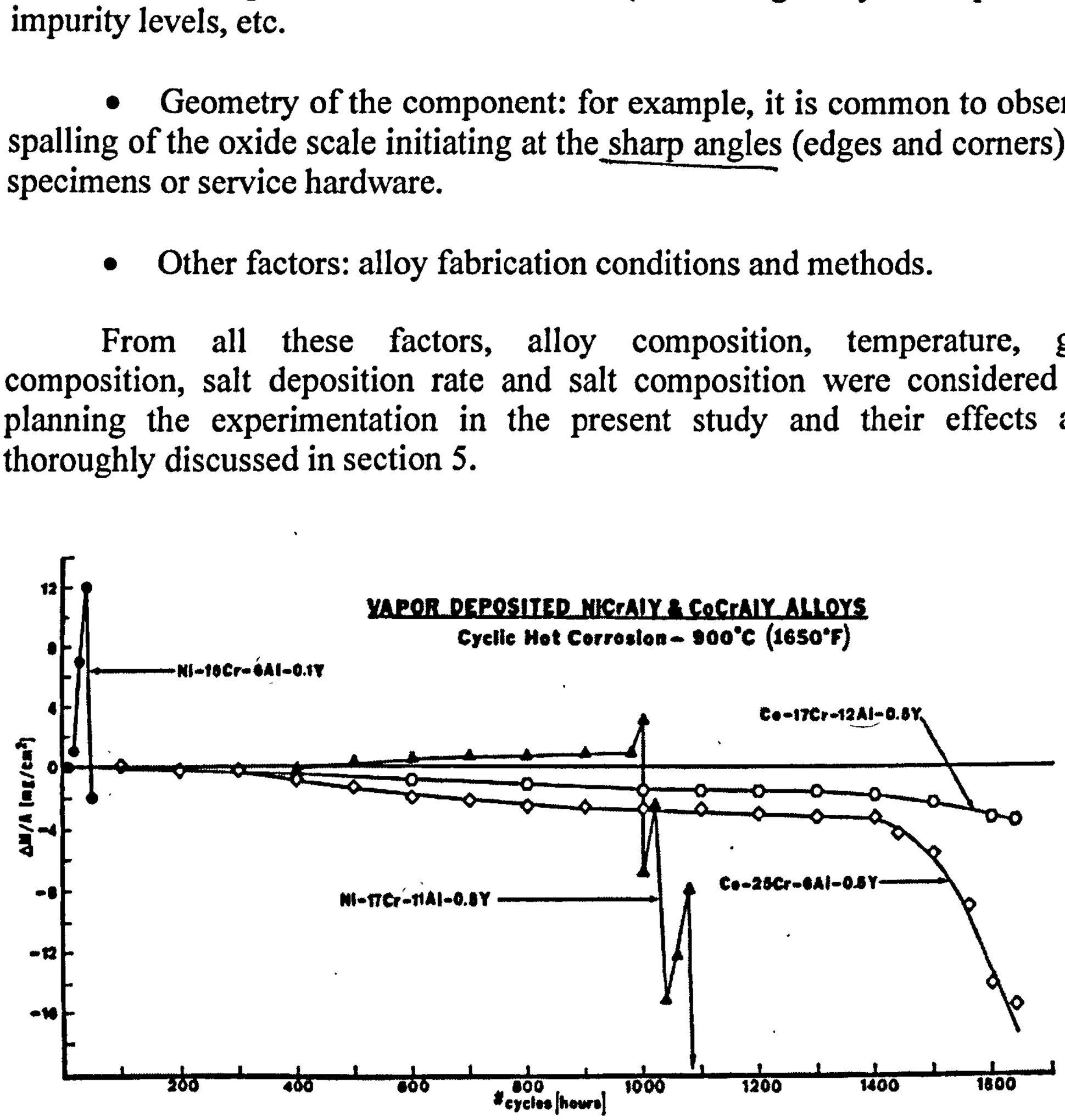

Figure 2.23: The length of the initiation stage for hot corrosion induced by Na_2SO_4 in air is increased as the aluminium content of nickel-chromium or cobalt-chromium alloys is increased [61].

2.5.5 Hot Corrosion: Type I and Type II

At the present time, two types of hot corrosion morphologies have been clearly identified which depend on the temperature of the corrosion environment; the degradation rates due to hot corrosion peak at two different temperatures, as may be seen schematically in Figure 2.24. The first maximum at around 700°C corresponds to low temperature hot corrosion or type II and the second maximum, at around 850°C, corresponds to type I.

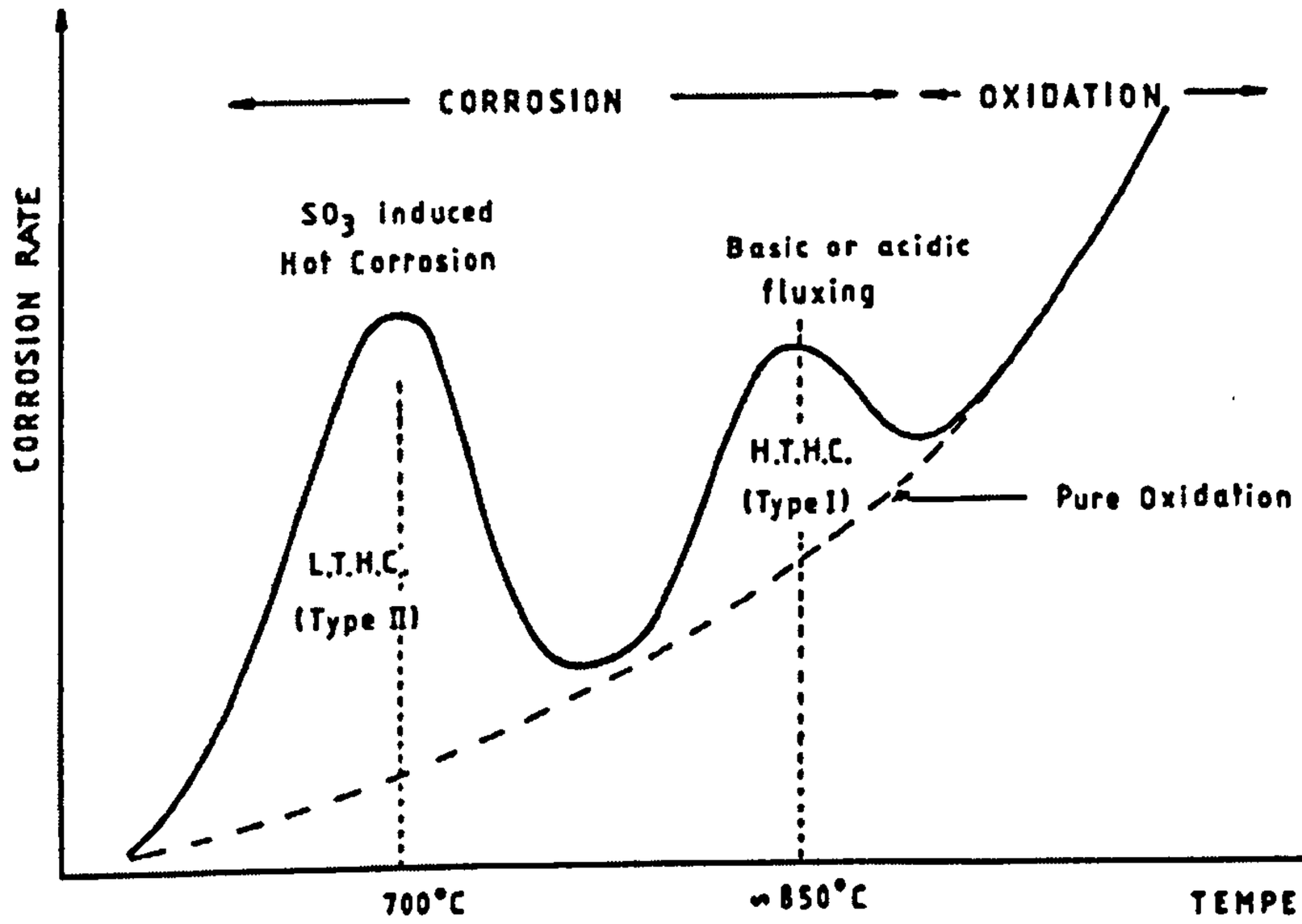

Figure 2.24: Schematic diagram of corrosion rate versus temperature [72].

Type I hot corrosion (or sulphidation) between 800° and 950°C results from a fluxing process (either basic fluxing, alloy-induced acidic fluxing or sulphidation) where modifications of the Na_2SO_4 deposit chemistry permits ingress of sulphur into the underlying metal; this produces localized depletion of the protective elements and progressive internal attack occurs. The net process of type I hot corrosion produces a characteristic pattern of attack which includes:

- A porous oxide scale (sometimes containing metallic particles)
- An irregular metal/scale interface
- Internal attack with preceding metal sulphides.

An example of severe hot corrosion process type I may be seen in the photomicrograph-diagram illustrating the progression from simple oxidation

(I) to severe hot corrosion (IV) for a high chromium nickel-base superalloy, (a) and a micrograph from the present study (b) Figure 2.25.

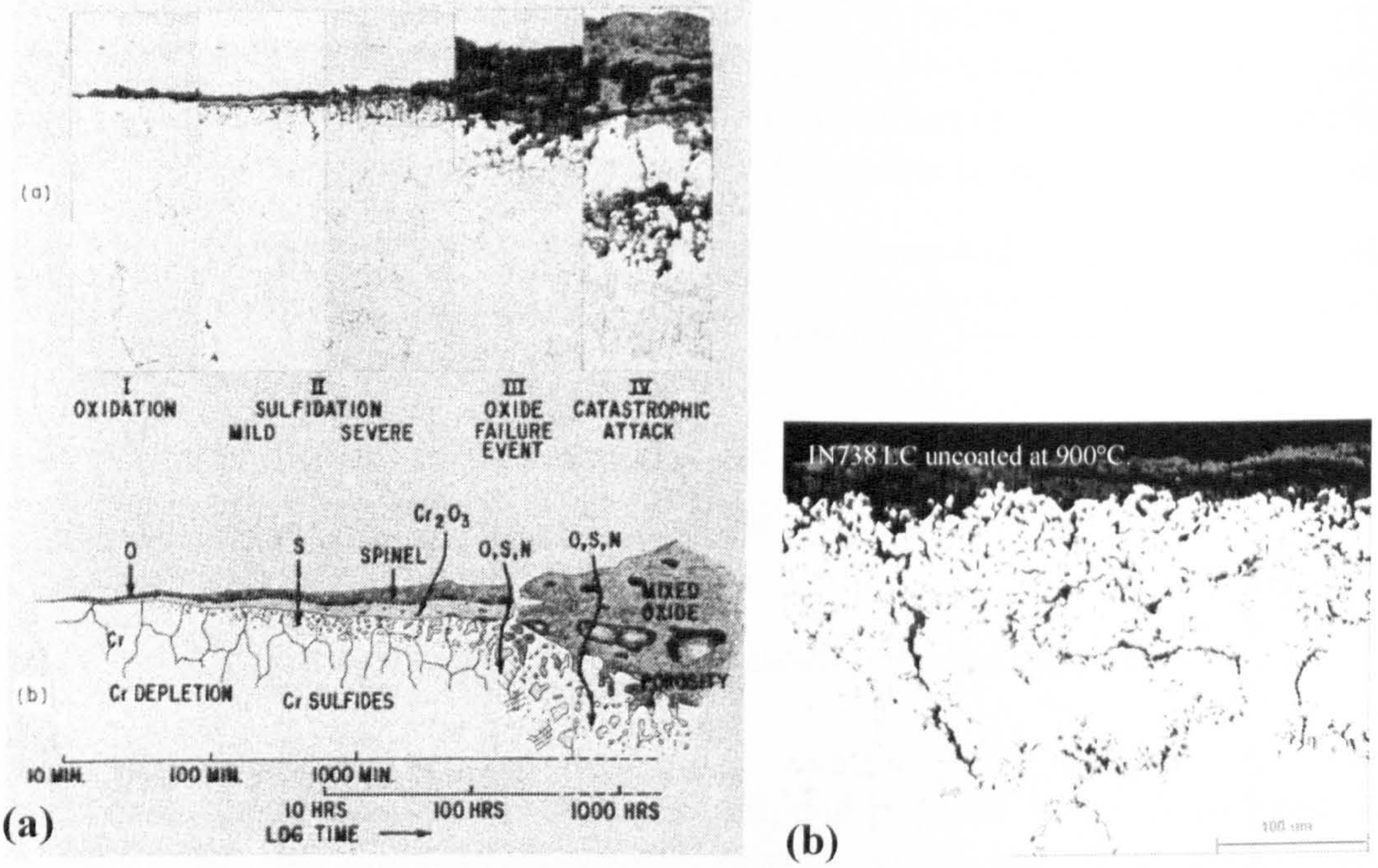

Figure 2.25: Schematic diagram illustrating the progression of the Type I hot corrosion [73] and a micrograph from the present study.

Type II hot corrosion (or low temperature sulphidation) between ~650° and ~750°C requires Na_2SO_4 and sufficient SO_3 to maintain a low melting deposit which readily fluxes the surface oxide. Thermodynamics favour SO_3 formation in the lower temperature range and the low melting point deposit results from a eutectic between Na_2SO_4 and base metal sulphates, produced through dissolution of base metal oxides in the acidic melt. Its characteristic pattern of attack consists of:

- Localised attack occurring by gas-induced acidic fluxing or sulphidation.
- A non-uniform distribution of pits with a lamellar scale rich in sulphur through the progressive fluxing action of the deposits.
- Sulphur not generally entering the alloy to form internal sulphides; but found concentrated at the pit/metal interface.

Type II hot corrosion has a greater effect on alloys and coatings that have chromium content less than ~20%.

An example of the characteristics of this hot corrosion type may be seen in the schematic illustration of Figure 2.26 (a) and in the micrograph from the present work (b).

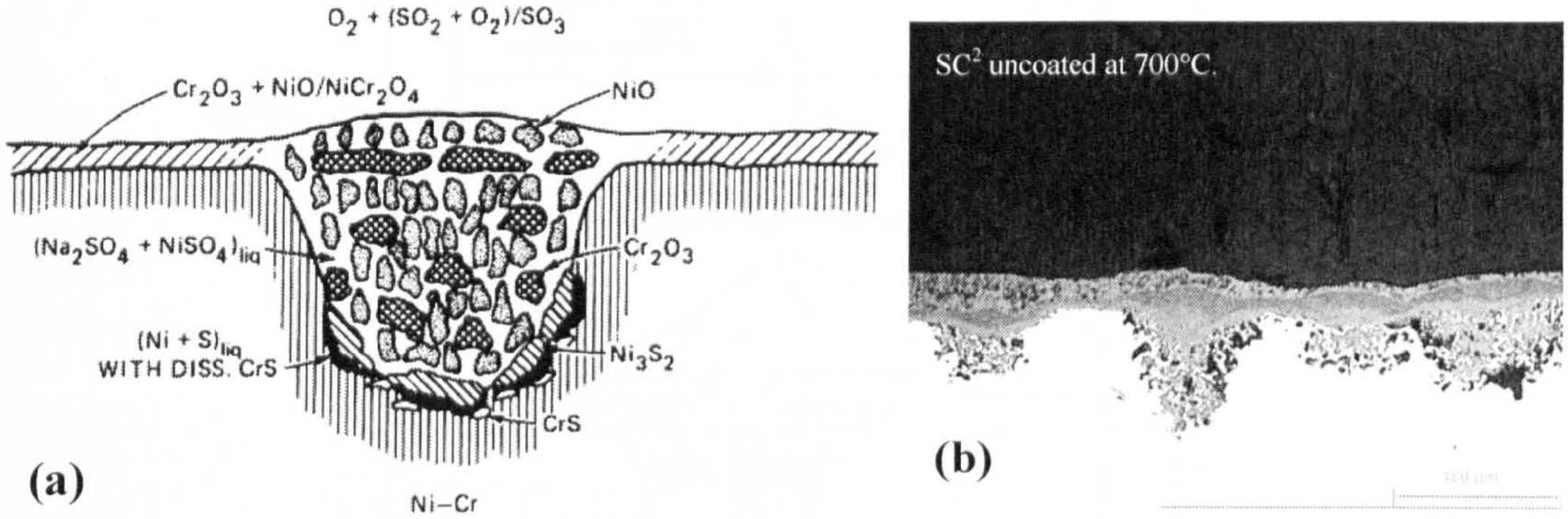

Figure 2.26: Reaction mechanism of low temperature hot corrosion of Ni-Cr and Co-Cr alloys in SO_3 containing gases (a) schematic diagram from [45] and (b) micrograph from this study.

2.5.6 The Propagation Stage of Hot Corrosion

This situation, in which the salt reaches sites of low oxygen activity and is in contact with an alloy depleted in Al or Cr, generally leads to the rapid propagation stage. The propagation stage can proceed by several modes of attack, depending on the alloy and exposure conditions. As indicated in Figure 2.27, the propagation stage for degradation of alloys under deposit can be classified into three general categories.

In one of these categories, the deposit is innocuous and degradation in the propagation stage proceeds by a mechanism determined by the alloy and the gas. Such a situation is likely to occur with porous, solid deposits through which the gas can easily penetrate. Deposit fluxing reactions require the deposit or a product of the deposit-alloy-gas reaction, to be liquid. Reaction between elements in the alloy and components from the gas in the presence of the liquid results in the formation of non-protective reaction products.

The final category, deposit/component-induced hot corrosion (or deposit/component-alloy reactions) involves propagation stages where an elemental component from the deposit diffuses into the alloy, or reacts with the alloy or with its reaction products, such that non-protective reaction product barriers are developed. The species is usually sulphur, but can include P, Cl, etc., or alloy components like Mo and W, etc.

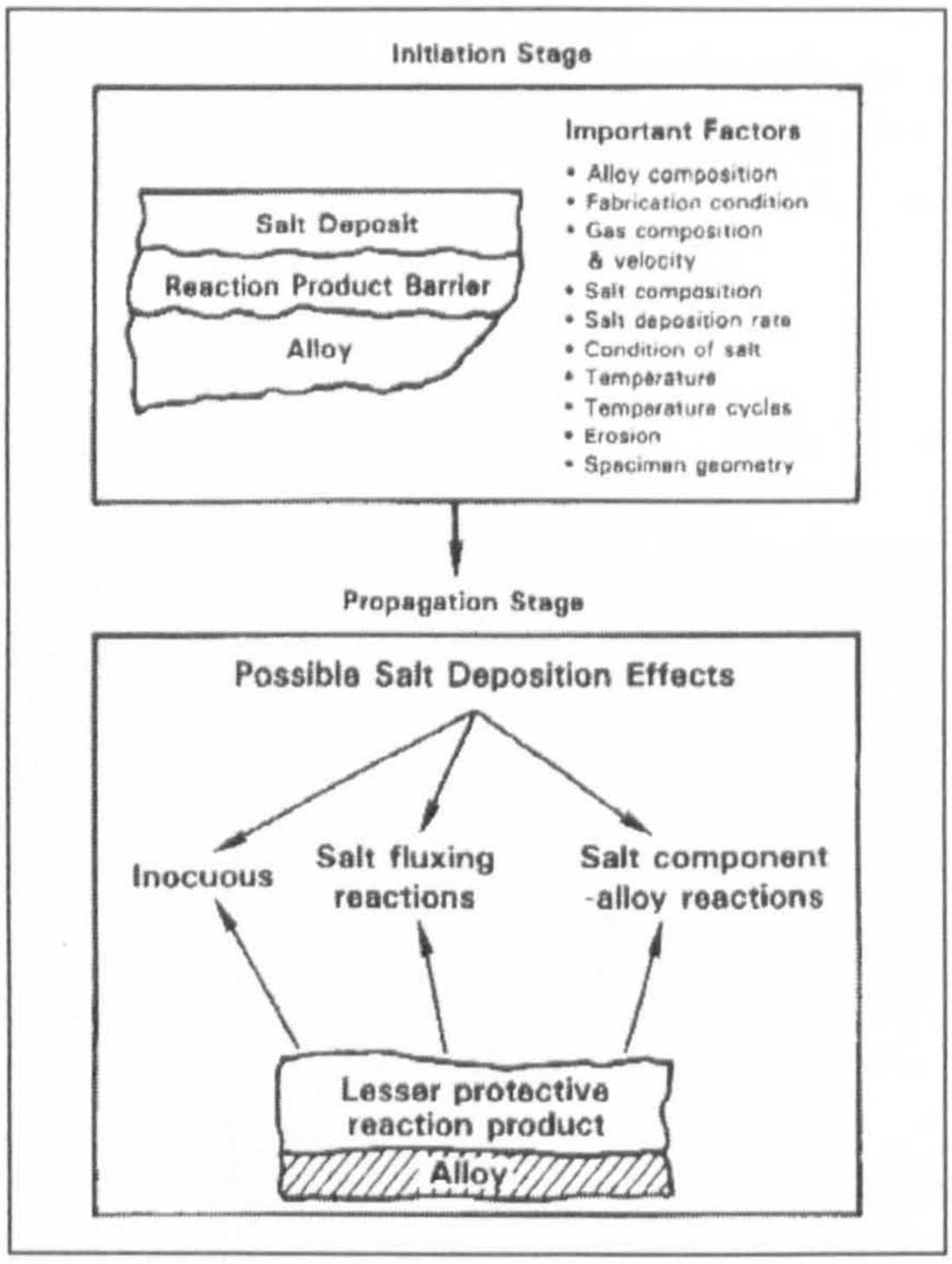

Figure 2.27: Schematic diagram to identify the factors that determine the time at which the transition from the initiation stage to the propagation stage occurs and to illustrate the two general categories of protective scale breakdown [55].

2.5.7 Thermodynamics

As explained in section 2.2, sodium sulphate is of great importance and a major component of deposits that have traditionally induced hot corrosion; hence, attack by Na_2SO_4 has been widely studied and used to explain the hot corrosion mechanism.

When Na_2SO_4 covers the alloy as a layer, components from the gas must diffuse through the Na_2SO_4 to react with the alloy; hence, the composition of the Na_2SO_4 near to the alloy may become different from that in equilibrium with the gas, as indicated with arrows in the schematic phase stability diagram for $Na_2SO_4/SO_3/O_2$ in Figure 2.28.

Three compositional changes of importance can take place: the deposit may become more basic, that means the concentration of oxide ions (O^{2-}), or the activity of Na_2O is increased; on the other hand, if the concentration of oxide ions is decreased, the deposit becomes more acidic, e.g. enriched in SO_3, and it almost always becomes more sulfidizing as a result of the lower oxygen activity.

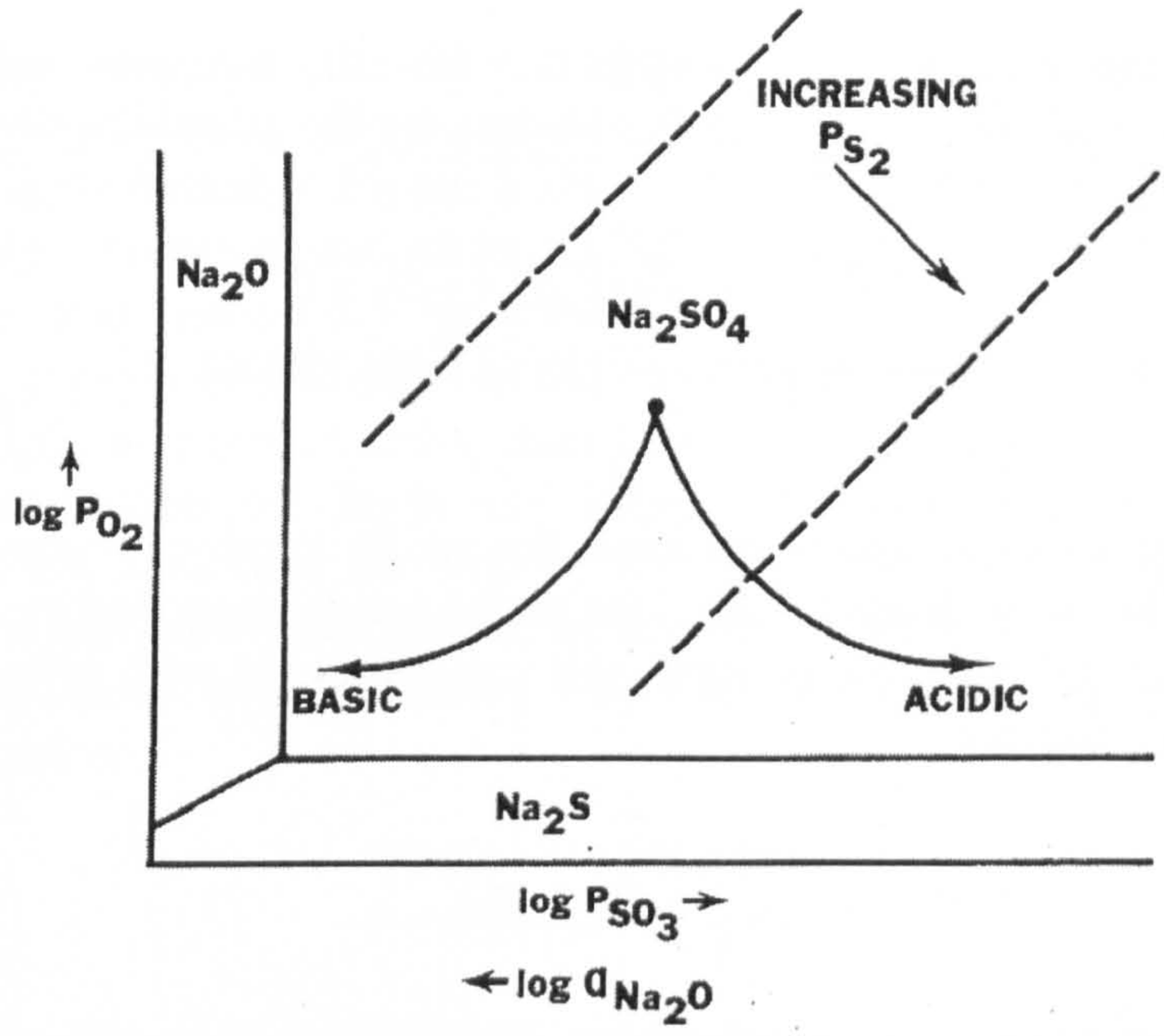

Figure 2.28: Thermodynamic stability diagram for the Na-O-S system showing how the composition of the Na_2SO_4 may change due to reaction of the alloy with the deposit [55].

Oxygen, sulphur, SO_2 and SO_3 are interrelated by the equations:

$$SO_2 + \frac{1}{2}O_2 \leftrightarrow SO_3$$

Equation 8

$$SO_2 \leftrightarrow \frac{1}{2}S_2 + O_2$$

Equation 9

$$\frac{1}{2}S_2 + \frac{3}{2}O_2 \leftrightarrow SO_3$$

Equation 10

Thus

$$p_{O_2}^{3/2}\, p_{S_2}^{1/2} \,/\, p_{SO_3} = K$$

Equation 11

and, by understanding that, if SO_3 is not decreased substantially, the sulphur pressure is increased as the oxygen pressure is decreased, Figure 2.28.

One of the processes by which the Na_2SO_4 becomes more basic involves the removal of sulphur from the Na_2SO_4 by the alloy whereby:

$$SO_4^{2-} \longrightarrow S(alloy) + \frac{3}{2}O_2 + O^{2-}$$

Equation 12

The other process arises because the oxide product formed on the surface of the alloy may donate oxide ions to the salt as proposed by Rapp and Goto [74]; in parallel with this process, salt can also react with existing oxide ions by reactions such as:

$$MO + O^{2-} \longrightarrow MO_2^{2-}$$

Equation 13

This latter reaction is a means by which the salt can become more acidic.

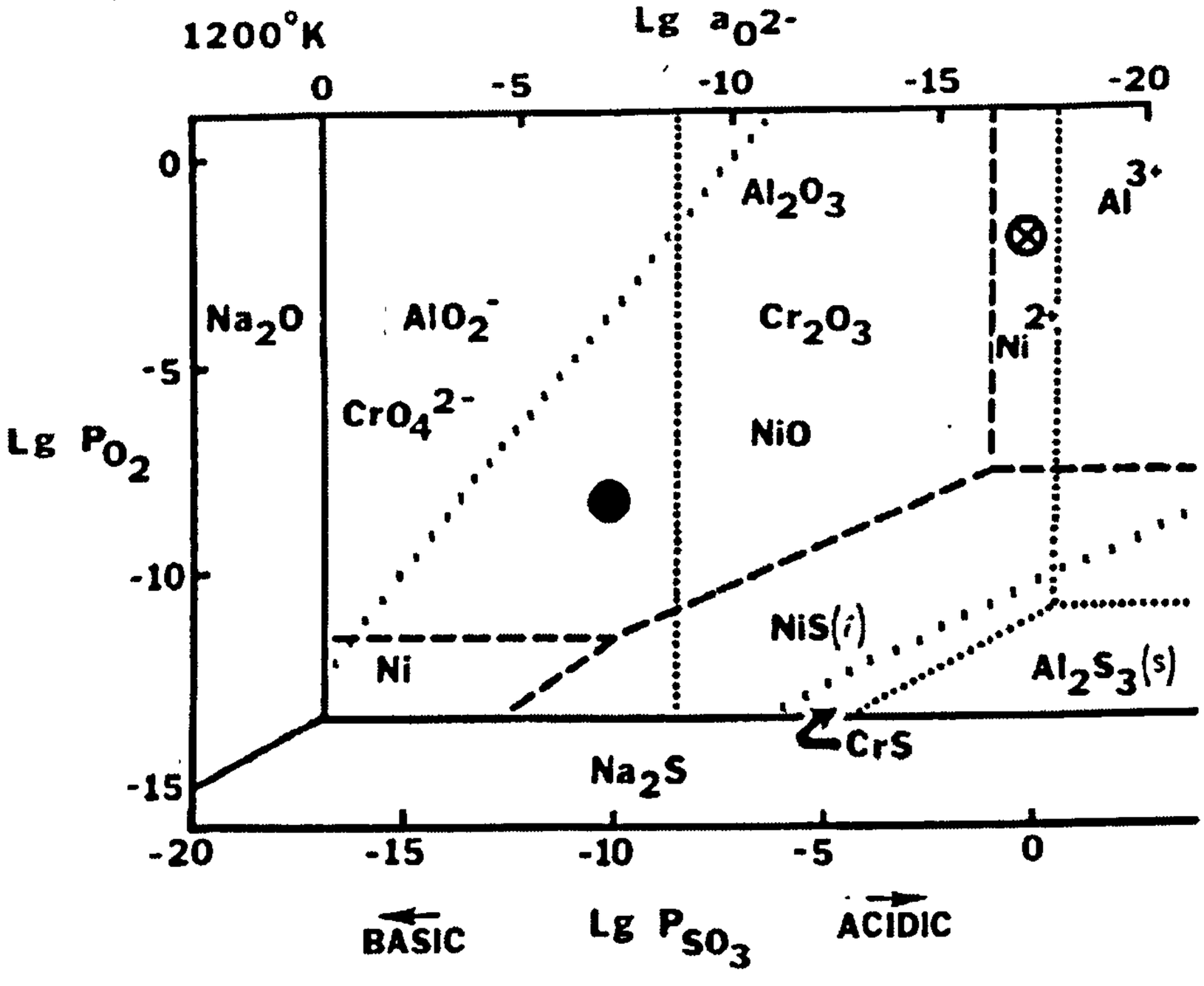

Figure 2.29: Thermodynamic stability diagram to illustrate the phases of Ni (---), Al (...) and Cr (xxx) that can exist in a Na_2SO_4 layer on a Ni Cr Al alloy [55].

Thus, the oxides that begin to be formed on the surfaces of the alloy will make the salt basic or acidic, as determined by the oxide ion concentration of the deposit (defined by that at the deposit-gas interface) and the affinity of the oxides and their metal ions for oxide ions [61].

Thermodynamic stability diagrams have also been used to describe the stability of oxides on alloys beneath deposits of Na_2SO_4. A typical stability diagram is presented in Figure 2.29, where the stabilities of phases containing aluminium, chromium and nickel in Na_2SO_4 are compared. It can be seen that there are acid melts (⊗) for which NiO is more effective than Al_2O_3 in developing basic conditions. On the other hand, there are basic melts (•), for which Al_2O_3 is more effective than Cr_2O_3 in making acidic conditions. From the measurements of Gupta and Rapp [75], examples of the two fluxing reactions are illustrated for NiO by the solubility plot shown in Figure 2.30. There is a minimum solubility at an activity of Na_2O of 10^{-10}. The solubility of NiO increases with increasing Na_2O activity (decreasing p SO_3) according to the reaction:

$$2NiO + O^{2-} + \frac{1}{2}O_2 \longleftrightarrow 2NiO_2^-$$

Equation 14

which corresponds to basic fluxing. The solubility of NiO also increases with decreasing Na_2O activity according to the reaction

$$NiO \longleftrightarrow Ni^{2+} + O^{2-}$$

Equation 15

which corresponds to acid fluxing. Similar solubility behaviour in Na_2SO_4 has been observed for other oxides, e.g. Cr_2O_3 and Al_2O_3, Figure 2.31.

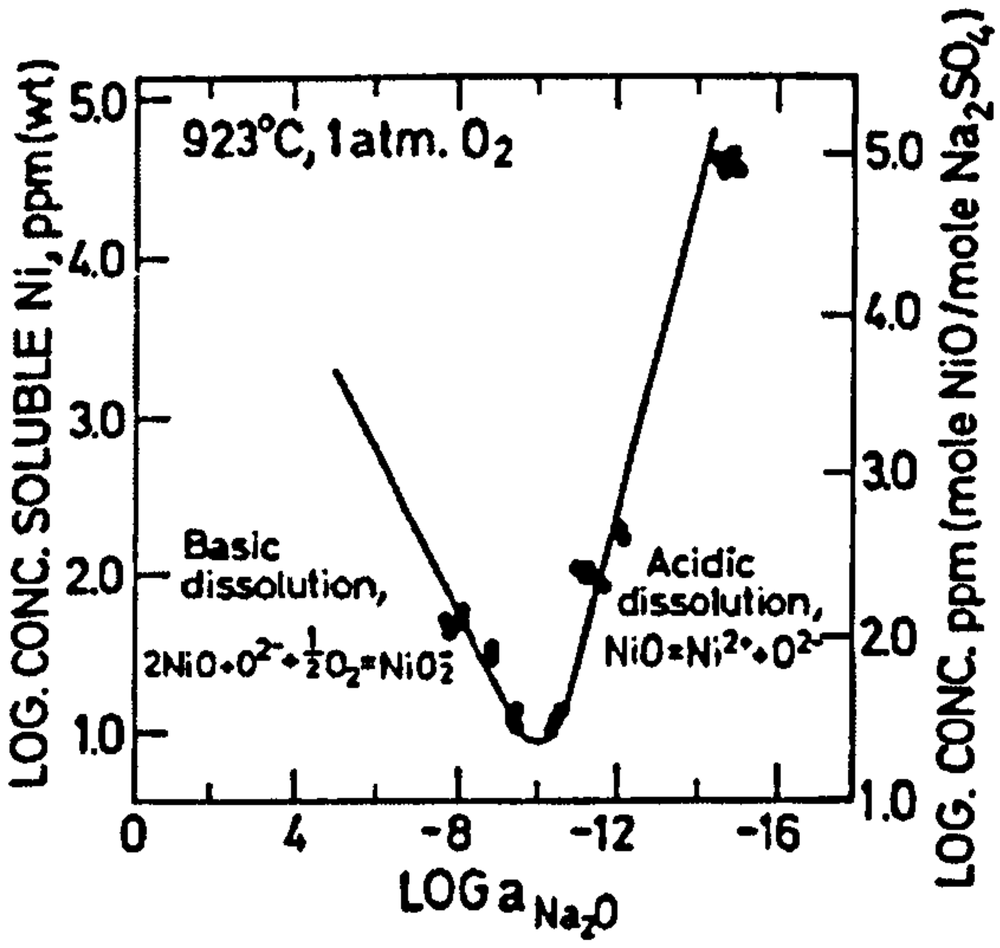

Figure 2.30: The solubility of NiO in Na_2SO_4 at 1 atm O_2 and 927° C as a function of the basicity a_{Na_2O} in Na_2SO_4 [75].

The stabilities of the various complex anions vary and conditions which may lead to the acid fluxing of one oxide could equally cause basic fluxing of another oxide. The terms: acid and basic are relative and refer to the reaction that occurs rather than to just the condition of the melt, i.e., for each oxide, there is a relationship, such as in Figure 2.30, for the condition of acid and basic fluxing. The curves for different oxides are displaced to left or right of each other, depending on the relative stabilities of the compounds involved Figure 2.31. Ni and Co are the bases for the alloys while Cr and Al form stable oxides.

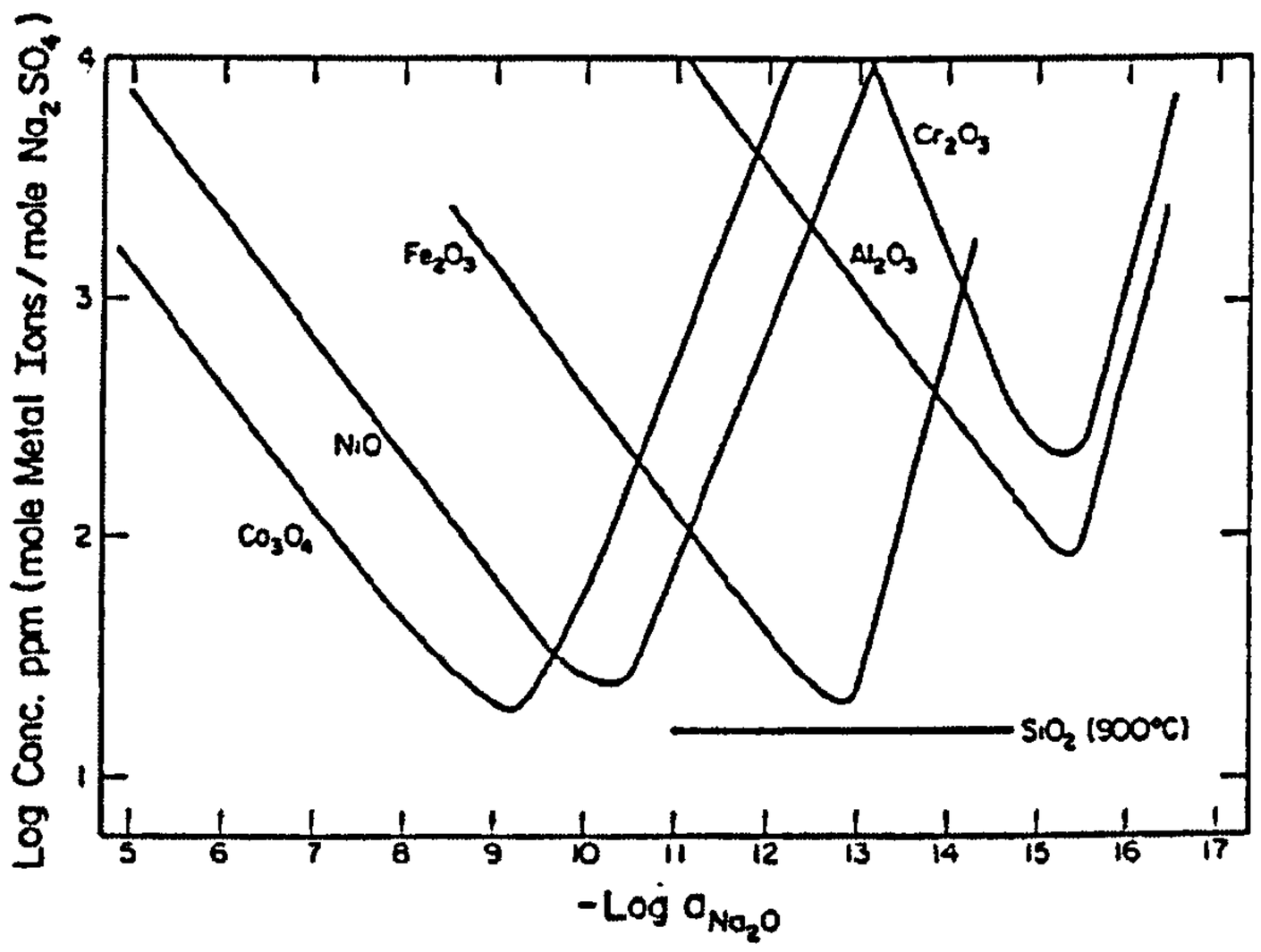

Figure 2.31: Measured oxide solubility in fused Na_2SO_4 at 1200°K and $P_{O_2} = 1.01 \times 10^5 Pa$ [76].

2.5.8 Basic Fluxing

The initial concept of basic fluxing was first proposed by Bornstein and DeCrescente [57; 58; 77] and then described in thermodynamic terms by Goebel and Pettit [59]. Rapp and Goto describe some theoretical mechanisms for the hot corrosion attack [74; 60]. An example of the process of basic fluxing hot corrosion is given in the schematic diagram from Birks and Meier [49], Figure 2.32, illustrating the Na_2SO_4 induced hot corrosion of pure nickel. As explain previously in section 2.4, a thin oxide scale of NiO is formed and is covered by the Na_2SO_4 as it melts; the formation of oxide rapidly lowers the P_{O_2} in the salt, as proposed by Goebel and Pettit [60], and the sulphur potential increases, leading to sulphur transport through the oxide scale and to the formation of sulphides at the scale-metal interface, Figure 2.32 (a).

The exact nature of the sulphur transport has not been verified, but studies by Wooton and Birks [78] suggest that the mechanism could be transport by SO_2 molecules penetrating through defects in the scale, such as microcracks. Further, the diffusivity of S in NiO was studied by Chang et al [79]. The source of SO_2 is the dissociation of the sulphate:

$$SO_4^{2-} \longrightarrow SO_2(g) + \frac{1}{2}O_2(g) + O^{2-\bullet}$$

Equation 16

and, since the SO_2 and O_2 are consumed, the O^{2-} activity in the salt will increase to maintain equilibrium, resulting in the salt becoming more basic. The increase of basicity will be greatest over the areas where sulphides form, i.e. where SO_2 is consumed most rapidly and, in these regions, the NiO scale will react to form soluble nickelate ions in the melt, Equation 14, Figure 2.32 (b). These nickelate ions will diffuse to the salt-gas interface (where the O^{2-} concentration is low) and will reprecipitated as NiO. This dissolution of the scale then allows the salt to penetrate it and spread along the scale-metal interface, lifting and cracking the scale Figure 2.32 (c). This cracking may be initiated by the formation of a Ni-S liquid phase at the scale-metal interface with a greater molar volume than that of the nickel. The cracking of the scale also allows oxygen penetration which oxidises the sulphides, thereby freeing sulphur to penetrate further into the alloy.

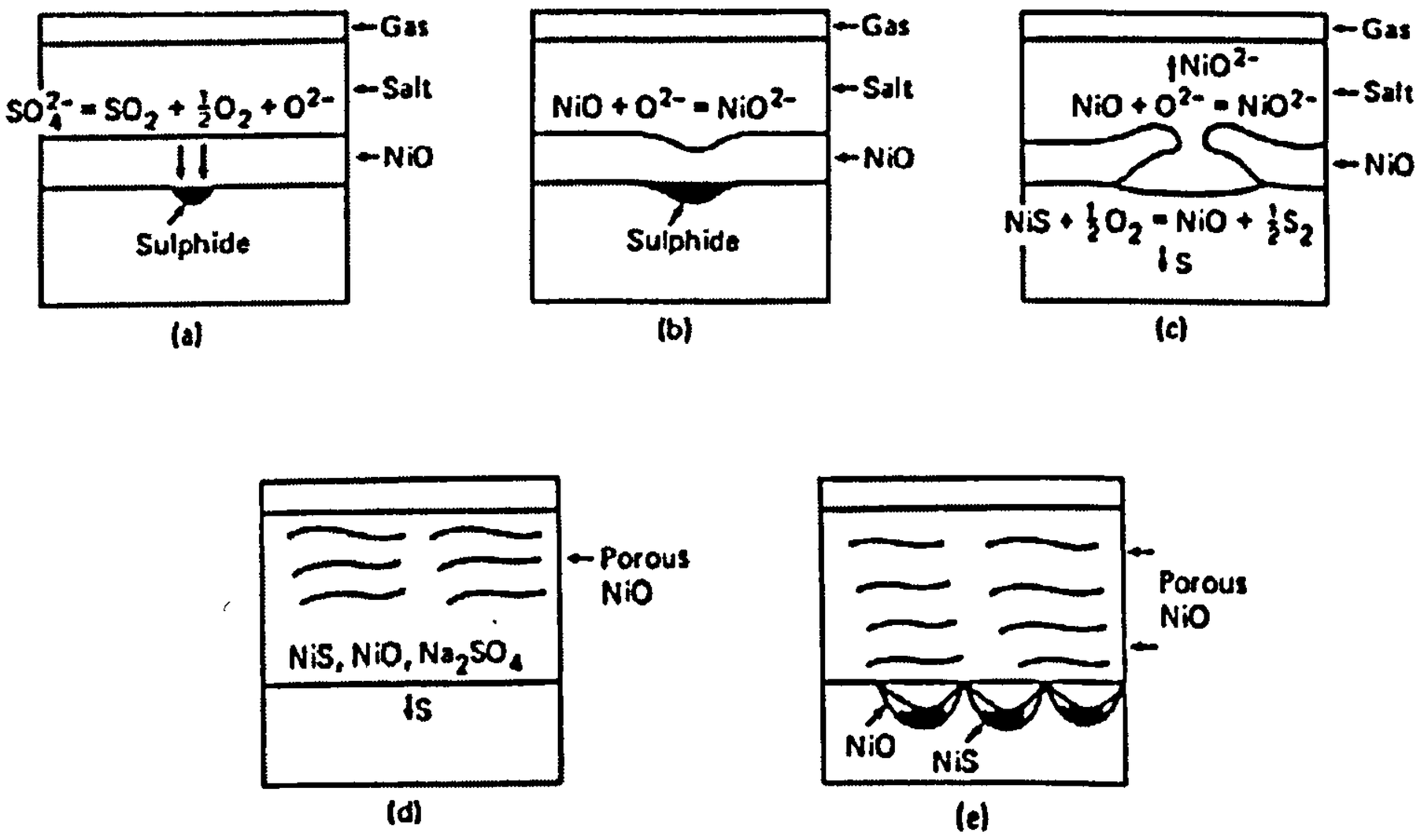

Figure 2.32: Schematic diagram illustrating the Na_2SO_4 induced hot corrosion of pure nickel in 1 atm O_2 [49].

The repetition of this process produces the porous honeycomb-like NiO scale, Figure 2.32 (d), and results in diffusion of sulphur and, subsequently, oxygen along the grain boundaries of the alloy (in the case of poly-crystalline alloy), Figure 2.32 (e). Eventually, as Na_2SO_4 is trapped in the porous scale, the rapid reaction stops and a dense protective NiO layer forms.

The amount of attack depends on the production of oxide ions by the melt; hence, a supply of Na_2SO_4 is necessary for the attack to continue, i.e. this form of hot corrosion is often not self-sustained, but is reliant on a continuous flux of Na_2SO_4 to the corroding surface. Basic fluxing hot corrosion is usually restricted to high temperatures (above 900°C), since the processes that produce oxide ions proceed slowly at lower temperatures [55], and affects alumina-forming alloys having a low chromium content (< 15%).

A similar basic fluxing mode is also observed when the protective oxide scale is Cr_2O_3 or Al_2O_3, as in the hot corrosion of Ni-8Cr-6Al alloys [61]. Birks and Meier [49] explain the basic fluxing of Cr_2O_3 and Al_2O_3 scales as follows: Initial formation of Cr_2O_3 and on Al_2O_3 scales depletes the deposit melt of oxygen and lowers the oxygen potential. Accordingly, from Equation 16, sulphate ions decompose further as $SO_4^{2-} \longrightarrow SO_2(g)+\frac{1}{2}O_2(g)+O^{2-*}$ and, at low oxygen potential, the sulphur activity increases, leading to the formation of nickel sulphides. The low sulphur and oxygen potentials of the deposit, resulting from the formation of oxides and sulphides, lead to an increase in the oxygen ion, or Na_2O, activity in the melt. In this way, conditions are established for the basic fluxing of Cr_2O_3 and Al_2O_3 by the reactions:

$$Cr_2O_3 + O^{2-} = 2CrO_2^{2-}$$

Equation 17

$$Al_2O_3 + O^{2-} = 2AlO_2^{2-}$$

Equation 18

forming chromate and aluminate ions, respectively, in solution in the molten deposit. These ions migrate through the salt layer to sites of higher oxygen potential close to the deposit-atmosphere interface where they precipitate out as Cr_2O_3 and Al_2O_3, releasing oxide ions according to

$$2CrO_2^{2-} = Cr_2O_3 + O^{2-}$$

Equation 19

$$2AlO_2^{2-} = Al_2O_3 + O^{2-}$$

Equation 20

The high oxygen potential at this position drives Equation 16 in reverse such that the oxide ion, or Na_2O, activity becomes too low to support the existence of the complex anions which decompose, as shown above. As in the case of pure Ni, the attack on Cr_2O_3 and Al_2O_3 is not self-sustaining and requires a continuous replenishment of Na_2SO_4. Again, as a result of basic fluxing, sulphide formation occurs in the alloy. The photomicrograph in Figure 2.33 shows an example of hot corrosion degradation via basic fluxing of a Ni-8Cr-6Al alloy.

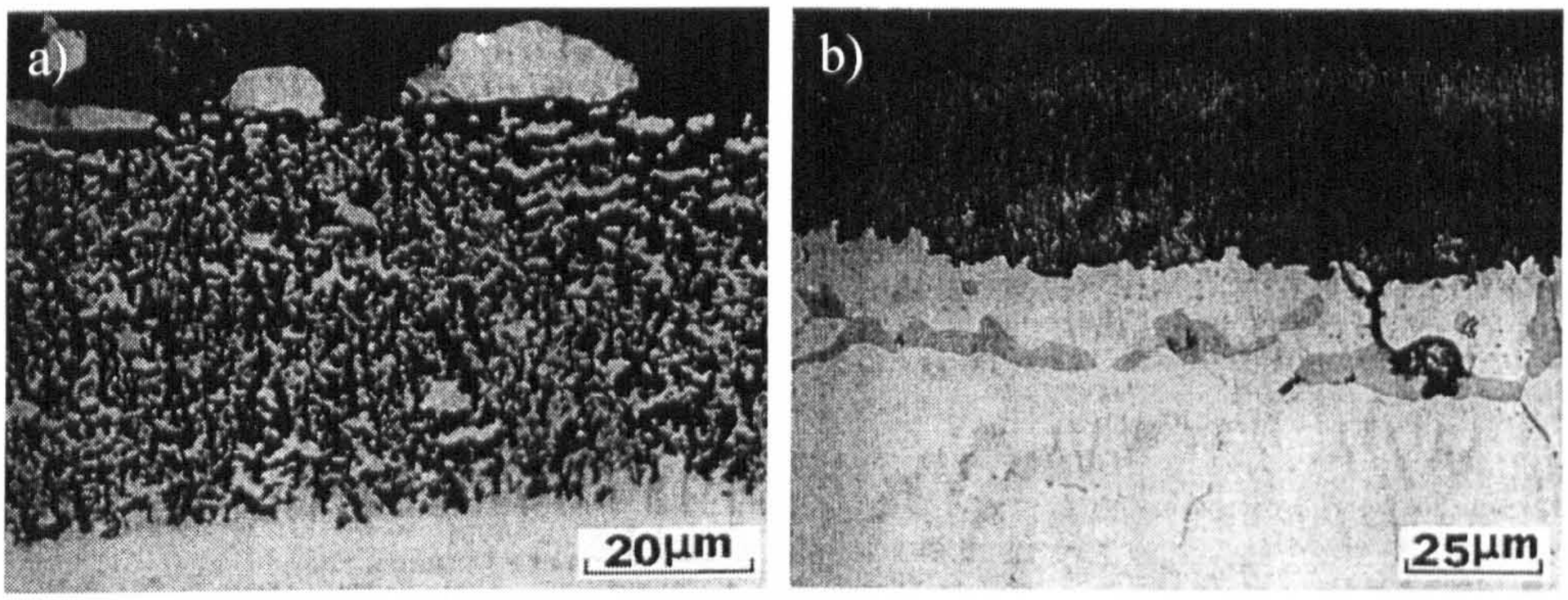

Figure 2.33: Photomicrograph showing features of Ni-8Cr-6Al specimens after exposure at 1000°C in air to 5mg/cm^2 Na_2SO_4 for two minutes, (a), and 1 hour (b). Degradation via basic fluxing is evident after 2 minutes, (a), but the Na_2SO_4 becomes consumed after 1 hr, hence the rapid attack ceases and the microstructure no longer exhibits the basic fluxing features, (b) [61].

2.5.9 Acid Fluxing

A feature of acidic fluxing that differs from the basic fluxing is that acidic-induced attack is sometimes self-sustaining. Deposits can be made acidic by two different processes:

- Alloy-induced acid fluxing: in which the acid conditions in the salt are established by dissolution of species from the alloy which react strongly with Na_2O, and
- Gas induced-acidic fluxing: in which the acid conditions are established by interaction with the gas phase.

Alloy-induced acid fluxing is generally the result of the dissolution of oxides of the refractory metals in the Na_2SO_4, i.e. molybdenum, tungsten and vanadium forming molybdates, tungstates and vanadates respectively, thus lowering the oxide ion concentration of the salt melt. This makes the deposit much more acid and dissolution of oxides in the deposit can occur by dissociation according to Equation 13.

The oxide scale formed on the specimens during this reaction is very porous and thick with a layered texture which peels off on cooling to room temperature [49].

Goebel, Pettit and Goward [59] have suggested a model for alloy-induced acid fluxing, as shown in Figure 2.34 for a Ni-31Al-Mo alloy. These features are also believed to be generally applicable to Na_2SO_4-induced catastrophic oxidation of nickel-base alloys that have been exposed to Na_2SO_4–V_2O_5 salt mixes (for example, for alloys used in environments resulting from combustion of impure oil-derived fuels).

Figure 2.34 shows (a) how oxygen moves from the gas through the Na_2SO_4 to the alloy surface where oxide phases similar to these formed during normal oxidation are developed. The MoO_3 (b) formed by the oxidation of molybdenum-rich phases, as well as MoO_3 formed during the transient period of oxidation prior to the development of a continuous Al_3O_3 scale, react with the Na_2SO_4 which decreases the oxide ion activity of Na_2SO_4 and produces acidic conditions. The acidic condition (c) of the Na_2SO_4 causes the protective Al_2O_3 scale to be destroyed since the Al_2O_3 scale donates oxide ions to the modified Na_2SO_4, i.e.

$$Al_2O_3 \rightarrow 2Al^{3+} + 3O^{2-}$$

Equation 21

However, vaporization of MoO_3 at the melt surface causes the Al_2O_3 to precipitate as a porous network at the Na_2SO_4/gas interface. Rapid oxidation (d) ensues aluminium is preferentially removed from the alloy and the alloy/scale interface becomes irregular. The nickel-rich islands formed because of preferential oxidation of aluminium are converted to NiO. The rapid oxidation is self-sustaining because MoO_3 is continually added to the Na_2SO_4 by oxidation of molybdenum in the alloy. Although very small amounts of salt cause large amounts of attack, the presence of the salt is necessary for the attack to continue. Microstructural features, typical of the alloy-induced acidic propagation mode, are presented in Figure 2.35 for the alloy Co-25Al-12W.

Gas-induced attack occurs when the atmosphere contains relatively high partial pressures of SO_3, the acid component of Na_2SO_4. Under these conditions, the reaction in Equation 13 is forced to the left resulting in a salt melt of low oxide ion, or Na_2O activity.

Luthra and Shores [80] studied the hot corrosion of Co-30Cr and Ni-30Cr by spraying Na_2SO_4 salt in O_2, SO_2 and SO_3 environments between 600° and 900°C; high corrosion rates were obtain due Na_2SO_4–$CoSO_4$ and Na_2SO_4–$NiSO_4$ liquid formation on the respective alloys. It was found that maximum corrosion rates occurred at 650°C to 700°C for the Co-30Cr alloy and peak corrosion rates for the Ni-30Cr alloy at 700°C to 750°C.

Figure 2.34: Model for the Na_2SO_4 alloy-induced acid fluxing of a Ni-31Al-Mo alloy from reference [59].

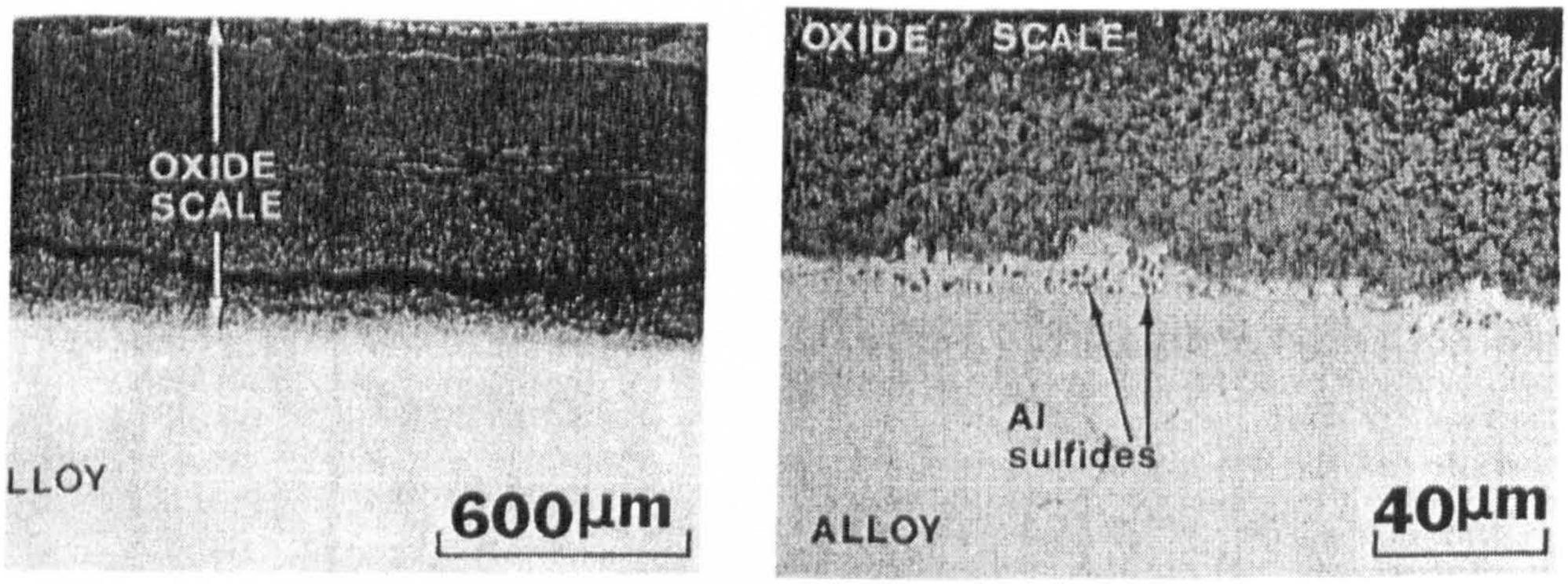

Figure 2.35: Optical micrograph showing the overall oxide scale thickness (a) and the scale-alloy interface (b) of alloy-induced acid fluxing for Co-25Al-12W [61].

Thermodynamic considerations can show that liquid deposits can form with moderate SO_3 levels in the gas, e.g. the $CoSO_4$ forms initially by interaction of Co_3O_4 with SO_3 in the gas. Figure 2.36 shows the minimum SO_3 levels required to stabilize the liquid phase and $CoSO_4$ solid. At temperatures below the melting point of Na_2SO_4 (884°C), very low corrosion rates would be observed at SO_3 levels below the minimum required to stabilize the liquid. At higher SO_3, levels the liquid phase can form. For nickel-base alloys, $NiSO_4$ also form low melting eutectics with Na_2SO_4 but these are much less stable than $CoSO_4$. Consequently, the SO_3 levels required to stabilize liquid phase in the Na_2SO_4-$NiSO_4$ system are much higher than those required for Na_2SO_4 – $CoSO_4$. For example, Figure 2.37 shows the minimum level required to stabilize Na_2SO_4-$NiSO_4$. Similar results have been observed by others authors [81][82; 83].

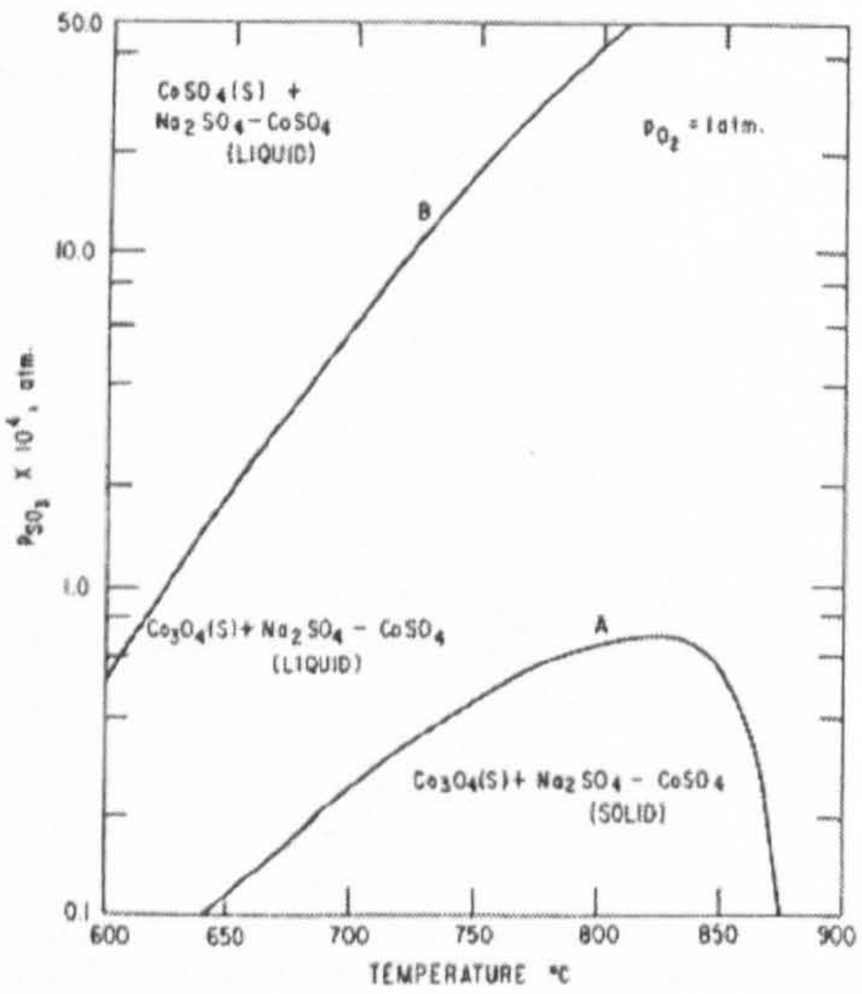

Figure 2.36: Minimum SO_3 levels required to stabilize Na_2SO_4-$CoSO_4$ liquid (curve A) and $CoSO_4$ solid (curve B) from Co_3O_4 [84].

The eutectic temperature of Na_2SO_4+$NiSO_4$, 671°C, is shown in Figure 2.38 (a). A similar phase diagram applies to Na_2SO_4+$CoSO_4$, Figure 2.38(b), with eutectic temperature of 556°C [45; 85].

K_2SO_4 also forms a low melting eutectic with $CoSO_4$ (melting point 538°C) [86].

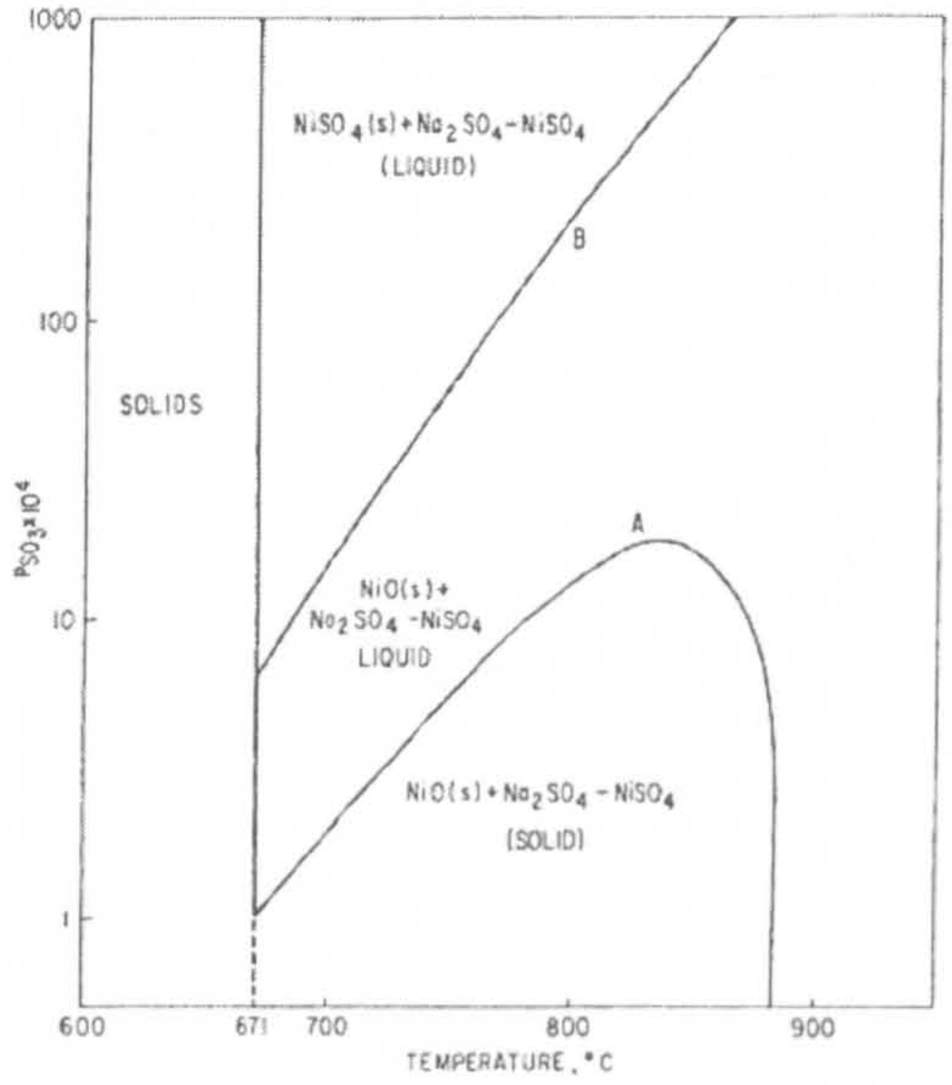

Figure 2.37: Minimum SO_3 require to stabilize Na_2SO_4 –$NiSO_4$ liquid (curve A) and $NiSO_4$ solid (curve B) from NiO [84].

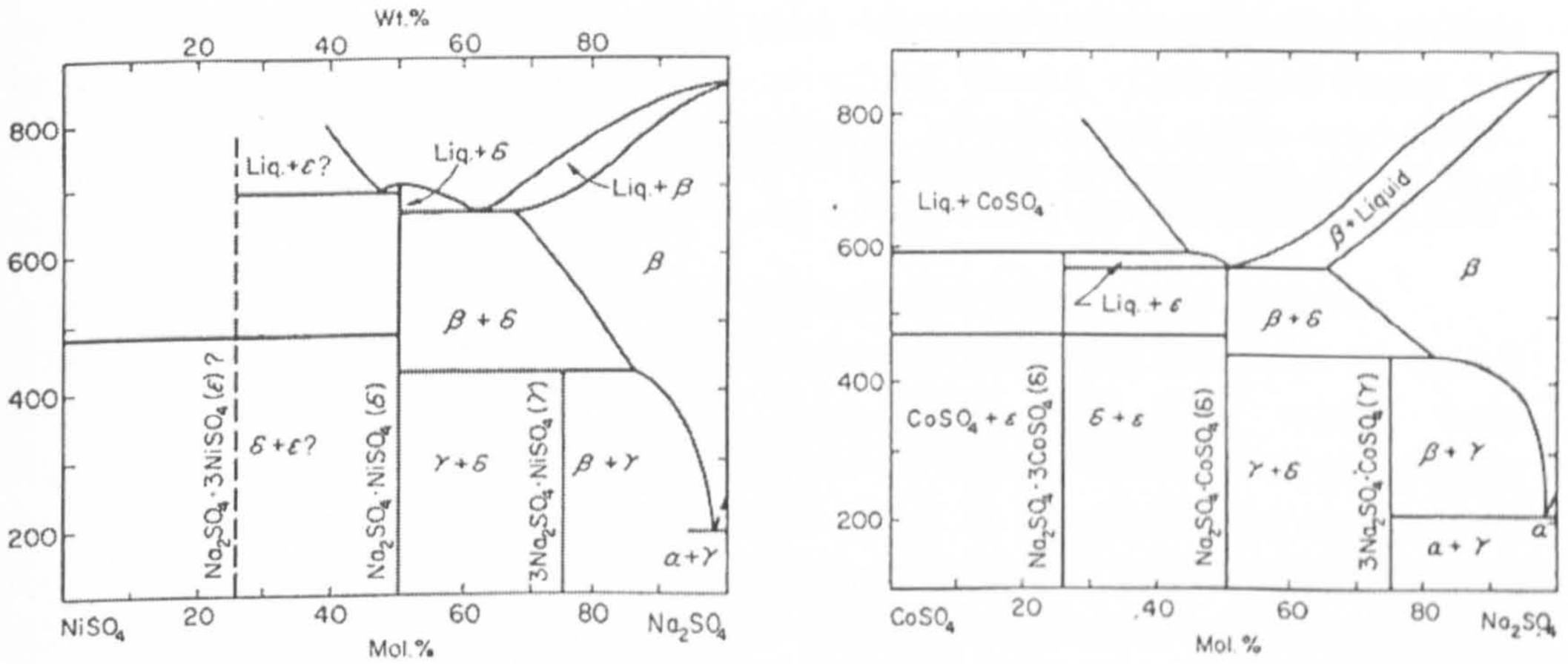

Figure 2.38:Phase diagram of Na_2SO_4-$NiSO_4$ (a) and Na_2SO_4-$CoSO_4$ (b) [85].

Once a liquid film forms on the surface of an alloy, further corrosion results from sulphation (or dissolution) of cobalt and CoO at the scale-salt

interface. During the early stages of the reaction, dissolution of CoO is the predominant process (Case (a)) Figure 2.39. At later times, when the salt is saturated, cobalt dissolves, migrates through the liquid and precipitates as Co_3O_4 and/or $CoSO_4$ in different regions of the liquid salt, depending on P_{SO_3} in the gas and the temperature, cases (b) and (d).

At intermediate levels of SO_3, cobalt dissolves at the scale-salt interface and forms Co_3O_4 near the gas-salt interface (case (b)). At the high levels of SO_3, cobalt dissolves and forms $CoSO_4$ (s) at the gas-salt interface (case (c)) or within the liquid salt (case (d)). At all times, the other alloying elements present in the alloy, including the more reactive elements such as chromium and aluminium, oxidize near the scale-deposit interface.

The mechanism and characteristics of this form of corrosion have been explain by the work of Luthra and co-workers [80; 84], Hocking and Sidky [87] and subsequent work by Luthra [88; 89; 90; 91]. The common and significant features of these studies are as follows:

- The hot corrosion attack is non-uniform and has a pitting-like appearance.
- Liquid solutions of Na_2SO_4+MSO_4 (M= nickel or cobalt) are present on, or in the scale in the regions of the local attack.
- Sulphur in the form of sulphides is present at, or near the interface of the metal and the reaction products.

The reaction products in the pits consist of the sulphate mixture, Cr_2O_3 and/or Al_2O_3 (depending upon the alloy composition). The external region of the reaction products mainly comprises NiO and CoO/Co_3O_4 on nickel- and cobalt-base-alloys respectively. A schematic representation of these features is show in Figure 2.21.

Although the present mechanism was developed for cobalt-base alloys, it may be extended to predict the corresponding corrosion behaviour of nickel-base alloys [90; 92]. Nickel-base alloys exhibit similar corrosion morphologies to these formed on Co-base alloys; for example, in experiments carried out by Chiang et al [93], Ni-Cr and Ni-Cr-Al alloys and, to some extent, Co-Cr alloys, showed features indicative of the classic type II hot corrosion, except for the morphology of attack on the Co-Cr-Al alloys, where a uniform frontal attack is reported.

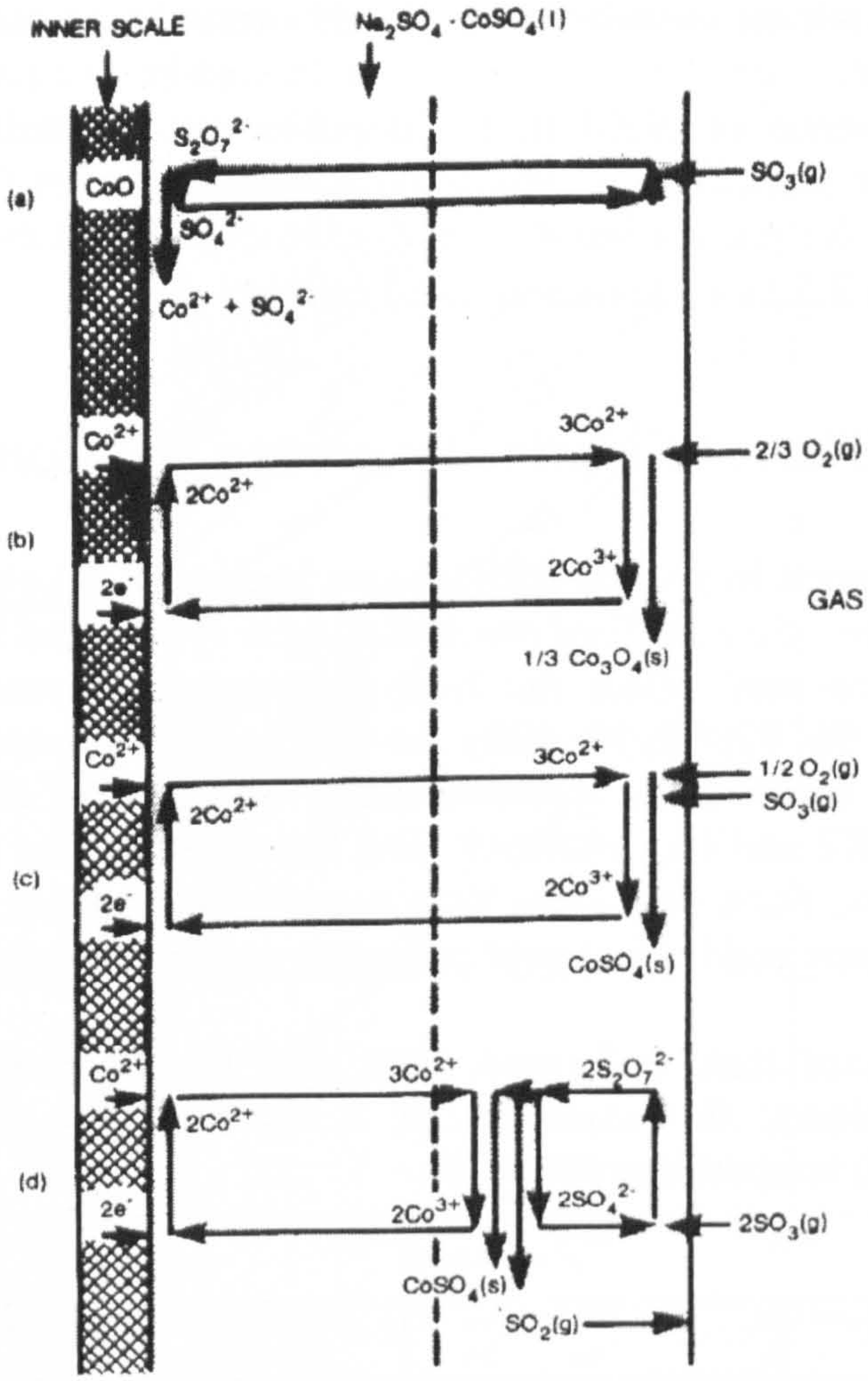

Figure 2.39: Schematic representation of the reaction products formed at different locations and the transport steps involved during the dissolution and precipitation of cobalt in low temperature hot corrosion [90].

2.5.10 Salt Component-Induced Hot Corrosion

As a result of salt deposition, elements from the salt can be introduced into the corrosion product or the surface regions of alloy and eventually affect their oxidation behaviour. The components of greatest importance are sulphur, carbon and chlorine. The extensive sulphidation of elements, such as Cr and Al, that are needed to form protective oxide scales often results in the formation of non-protective oxide layers. Carbon, formed at some phase of the combustion process, often accelerates hot corrosion by decreasing the oxygen

pressure and increasing the sulphur pressure in the salt. This accelerates those mechanisms which are sensitive to these conditions: basic and acid fluxing.

The presence of NaCl in the deposits can markedly accelerate hot corrosion. Since the effects of chlorine-containing species (HCl, NaCl) have been studied in the present work, a more extended explanation is presented in the next section 2.5.11 on halide-induced effects.

2.5.11 Effect of Chlorine Species on Hot Corrosion

As explained in section 2.2, gaseous hydrogen chlorine is encountered in the gas turbine of a coal-fired combined cycle system and it has been shown that its presence may affect the high temperature corrosion resistance of metals [94; 95; 96; 97; 98; 99; 100]. As well as the salt corrosion products, it is important to consider the thermodynamic stabilities of the likely products formed from HCl and Cl_2. Hancock [96] has collected the data presented in Table 2.3 below. Such data show that, except for fluorides, the halides have low melting points and high vapour pressures compared to the oxides.

This means that, if formed, they may be expected to cause severe corrosion problems; the existence of a liquid phase generally leads to accelerated high temperature corrosion.

Compound	Fluorides		Chlorides		Bromides		Iodides		Oxides	
	Tm	T4	Tm	T4	Tm	T4	Tm	T4	Tm	T4
FeX_2	1020	906	676	536	689	509	594	476	1420	
FeX_3	1027	673	303	167		157			1565	
NiX_2	1450	939	1030	607	965	580	780		1990	
CoX_2	1250	962	740	587	678		515		1935	
CrX_2	894	928	820	741	842	716	869	702	-	-
CrX_3	1404	855	1150	611	> 800	616	> 600		2435	
AlX_3	1291	820	190	72	97.5	53	191	145	2050	~2000
NaX_3	992	928	801	742	750	690	660	651	1275	
									Sublines	

Table 2.3: Melting points (Tm) and temperature (T4) at which the vapour pressure of each compound is 10-4 atm. Temperatures in °C [96].

Daniel and Rapp reported [101] that the halogens are less soluble and mobile in metals than are oxygen and sulphur, which suggests that, although the low melting points may cause accelerated corrosion by breakdown of the surface protective scale, pronounced internal attack by internal diffusion of halides may not be a severe problem.

The thermodynamic stabilities of oxides and halides are compared in Figure 2.40; it may be seen that the most stable oxide and halide compounds likely to be present in industrial hot corrosion situations are Al_2O_3, Cr_2O_3, Na_2O and NaCl.

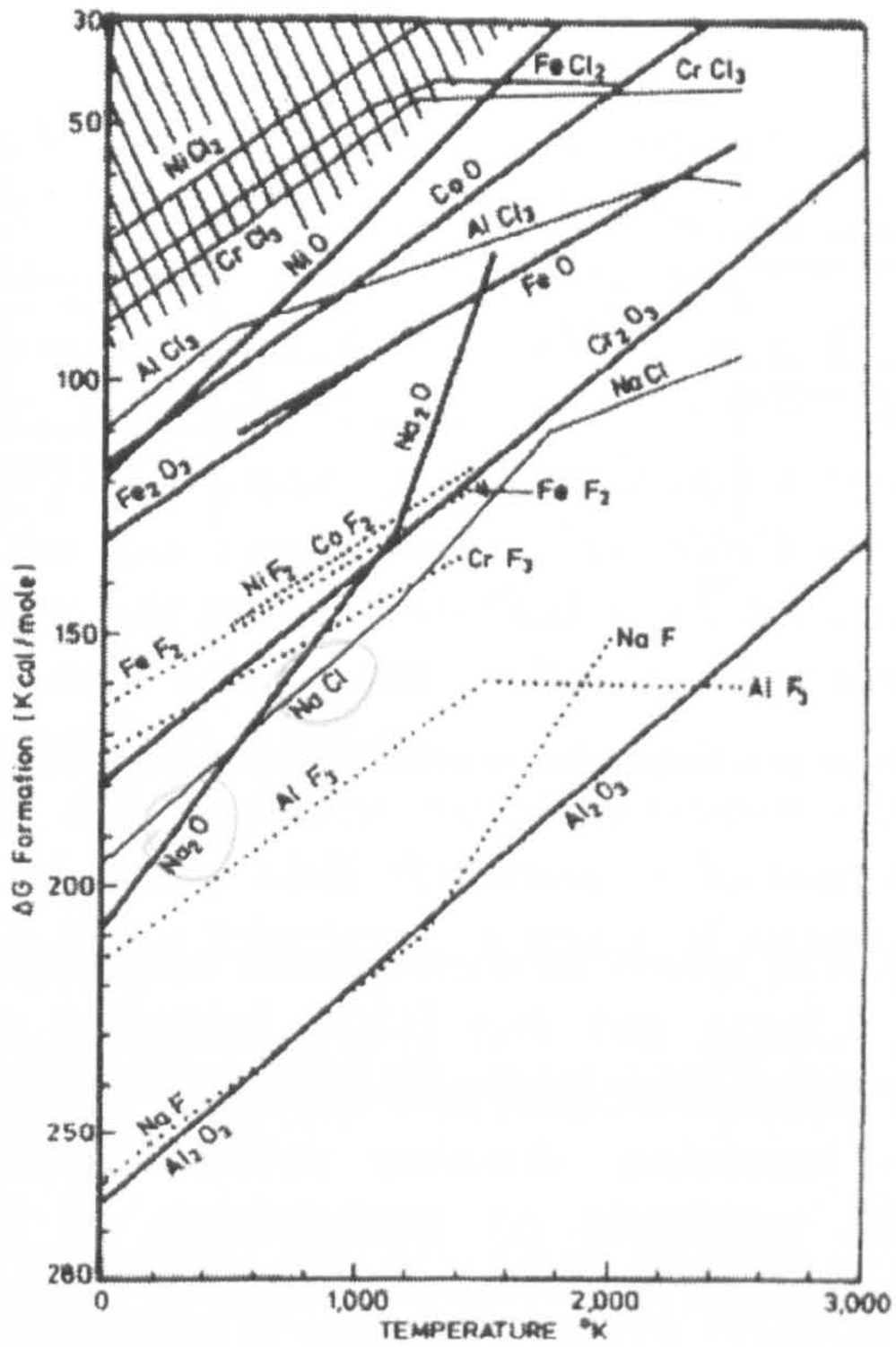

Figure 2.40: Standard free energies of formation of condensed metal halides and oxides from reference [96].

Studies have been carried out in order to understand the mechanisms and effects of chlorine contaminants; some examples are outlined below:

Jacobson et al [102] suggest that the reactions of chlorine and oxygen with metals are dependent on the thermodynamic stabilities of the products, the individual reaction rates for oxidation and chlorination and the reaction conditions. Four reaction schemes have been proposed;

- reaction of chlorine with the oxide,
- chlorine penetration of the oxide scale and reaction with the underlying substrate
- simultaneous oxide growth and chlorination at similar rates and finally,
- gas phase reactions.

These four reaction schemes may be observed in Figure 2.41.

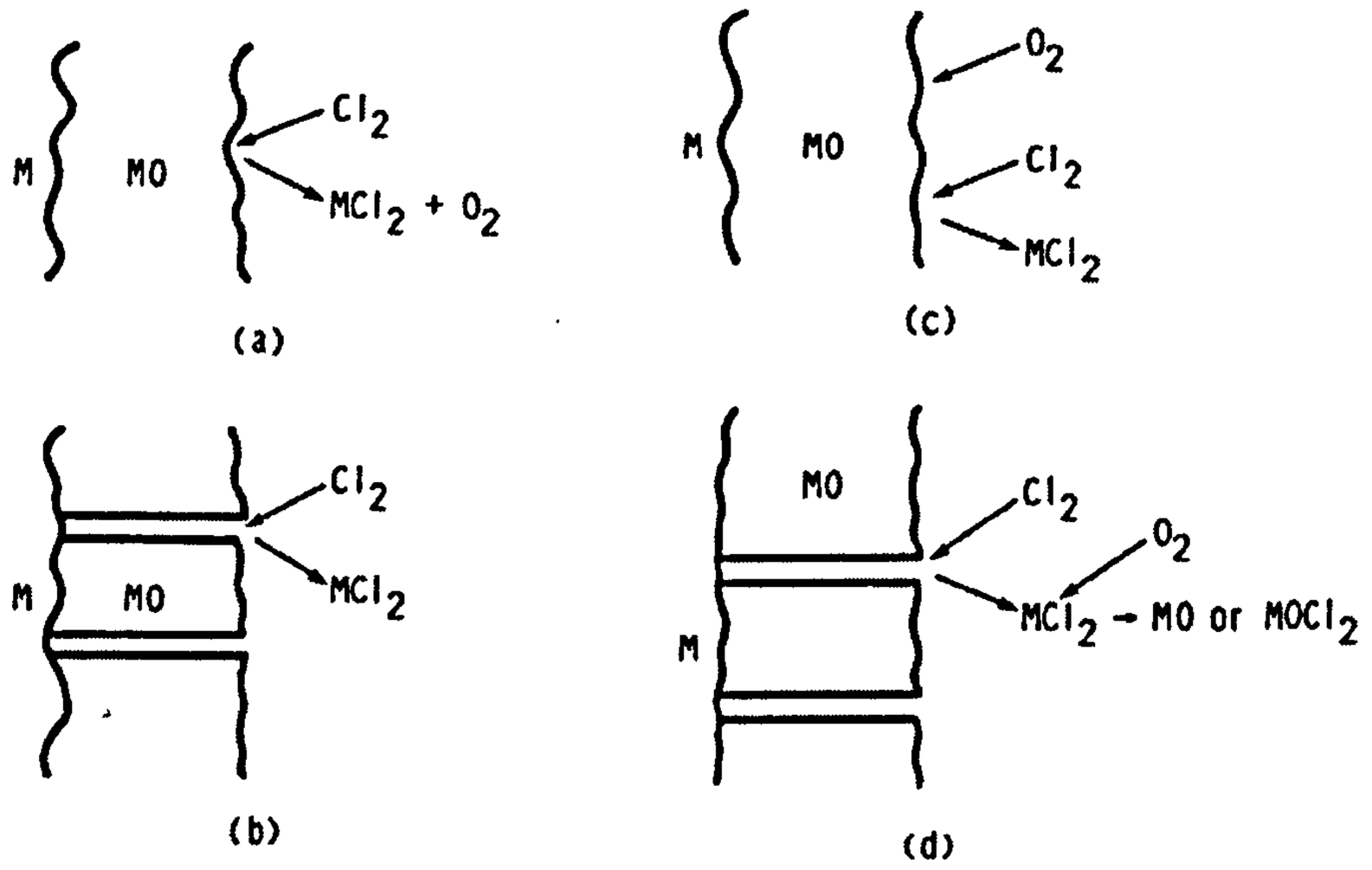

Figure 2.41: Four reactions scheme observed in chlorination-oxidation reactions at high temperatures [102].

The corrosion of alloys in atmospheres containing Cl_2 and /or HCl has been reviewed by Chang and Wei [103], including the effects of gaseous components in the atmosphere (oxygen, air, water vapour, sulphur dioxide and nitrogen) on the corrosion. Another review of corrosion in chlorine environments, with emphasis on performance as well as on materials limitations in such environments was published by Foroulis [104].

Stott and co-workers [105] have studied various alloys in a gas atmosphere of Ar-25vol $\%H_2$ -10HCl-5CO-1CO_2, at 900°C: the rates of attack were fairly low with Al_2O_3-forming alloys being more resistant to attack than Cr_2O_3-forming alloys. There was relatively little metal loss, but, in some alloys, there were significant depths of internal corrosion. Some volatile chlorides were formed following penetration of chlorine-containing species through the oxide scale to the alloy substrate, especially $FeCl_2$.

Previous work by the same authors [106] using the same gas mixture was carried out to study the behaviour of pure metals in the same environment as that to which the alloys were exposed and to determine the nature of the corrosion species. Iron results in rapid corrosion; the extent of corrosion of nickel was much less; cobalt gave very little indication of attack. Cr_2O_3 scales developed on chromium during exposure; however, these were not very protective and chromium chlorides formed at the oxide-alloy interface following penetration of chlorine-containing species through the scale. Molybdenum and tungsten were reasonably inert in this HCl-containing gas.

Rhee et al [107] have studied the corrosion of superalloys in an oxidising environment of argon containing 20% oxygen and 0.25% chlorine at 900°C. They suggested that corrosion occurs by two mechanisms in this environment: metal loss by the formation of volatile chlorides or oxy-chlorides and internal damage.

Ihara et al [108] have studied the kinetics of corrosion for nickel between 400 and 700 °C in hydrogen chloride gas and gas mixtures of hydrogen chloride and oxygen; they concluded that there is no fundamental difference in the corrosion behaviour of nickel over a wide range of gas compositions from pure hydrogen chloride to a gas mixture of 25% hydrogen chloride and 75% oxygen because of the preferential formation of a $NiCl_2$ scale, regardless of the gas composition. The reaction of nickel in gases containing hydrogen chloride can be classified into three temperature regions:

-Up to 450°C, scale sublimation is hardly observed and the reaction proceeds according to parabolic kinetics.

-At 500-550°C, the specimen weight increases almost parabolically until an $NiCl_2$ scale of steady state thickness is formed and, subsequently, decreases according to linear kinetics as a result of evaporation of the $NiCl_2$ scale.

-Above 600°C the sublimation rate is extremely high, and the specimen weight always decreases linearly.

Hossain [109] examined the corrosion resistance of a Ni-12Cr-6Al alloy at 849°C in the presence of chlorides and/or Na_2SO_4. Additions of HCl gas or NaCl vapour to the air stream resulted in an increase in the isothermal oxidation rate of uncoated specimens; although the effect of HCl was fairly small, in both cases, the oxide scale blistered and spalled on cooling or the oxide scale cracked at temperature. In the presence of mixed contaminants, i.e. $NaCl(g)+Na_2SO_4(c)$ or $HCl(g)+Na_2SO_4$, the alloy was attacked more severely than when it was exposed to the corrodents individually. Al_2O_3-forming alloys were more resistant to attack by NaCl(g) and HCl(g) than Cr_2O_3-forming alloys, although the same general mechanism of attack was observed.

The morphologies of oxide scales formed on nickel and cobalt in argon-oxygen-chlorine mixtures at 1000 °K were examined by McNallan et al. [110] These oxide scales were porous and blisters in the cobalt oxide were produced during the early stages of oxidation of clean surfaces.

Hancock [96] reported that iron, nickel and cobalt alloys suffer enhanced attack at high temperature if NaCl is deposited on the surface and/or is present in the vapour phase, especially in the presence of Na_2SO_4.

Hurst et al [111] studied iron, steel and various nickel-base alloys in the temperature range of 600° to 950°C; NaCl was found to cause enhanced oxidation of all the materials examined. When only NaCl was present, internal penetration of the metal occurred, whereas Na_2SO_4 alone did not produce such penetration (950°C).

An important feature of the mechanism of these corrosion processes is that chlorine accumulates at, or near the metal/scale interface suggesting that the chlorine does not migrate inwards in the form of chloride ions [45]. Chlorides cause an increased rate of oxidation, and this may in many cases, be related to mechanical failures of the scale, e.g. blistering, cracking and spalling of the scale, loss of adherence at, or near the metal/scale interface, etc.

2.6 Protective Coatings

2.6.1 Introduction

Studies of high temperature materials have permitted the development of alloys of higher strengths and favourable mechanical properties that allow good performances at increasing operating temperatures. These have been used in a range of plants including those for power generation, chemical processing or component heat treatment. For gas turbine blades and vanes, Ni and Co based superalloys have been developed. These are complex materials containing 11-12 alloying additions (Table 2.2 and section 2.3.4) to achieve specific properties.

However, the alloy composition and microstructures that provide the optimum mechanical properties (e.g. single crystal superalloys) often do not provide satisfactory high temperature corrosion resistance. Hence the vital importance of protective coatings: they are used and are being further developed to allow full exploitation of alloy strength capabilities at high temperatures by reducing the scaling (oxidation) rate of the coated component surfaces.

2.6.2 Coating Requirements

The use of coatings (or surface treatments) allows the total or partial separation of surface and substrate related properties. Thus, coating systems are designed to provide a more optimised environmental protection capability, without the constraints of high strength that are normally place on structural

alloys for load-bearing components. The selection of a suitable treatment or coating for a given application depends on a complex interplay of surface-coating-substrate related properties that are specific to the application. Table 2.4 summarises these properties and forms the framework around which the design requirements of a coating for good oxidation/corrosion resistance can be discussed. The purpose of the coating/surface treatment, is to form a stable, slow-growing surface oxide that provides a shield-barrier between the coating-alloy and the environment in which it operates. In order to achieve this oxide scale, it is necessary to have a reservoir of the component that forms it (i.e. aluminium, chromium or silicon) beneath the scale.

Thus, for high temperature structural alloy design, iron-, nickel- or cobalt-base alloys, containing concentrations of aluminium in excess of about 10 wt. % or chromium in excess of 16wt.%, will form, in an oxidising atmosphere, scales in which alumina and chromia predominate. Apart from being designed to provide oxidation/corrosion resistance, a coating system also needs to have suitable mechanical properties, such as good adhesion and metallurgical stability; having all these qualities in a single coating system leads to the concept of "design surface" and the custom design of the coatings for the most demanding applications. Smart overlay coatings and layered thermal barrier coatings (TBCs) are examples of such custom designed surface engineering.

Coating Property	Requirement	Coating Surface	Mid Coating	Coating/ substrate interface
Oxidation/ corrosion resistance	• Low rates of scale formation	X	...	...
	• Uniform surface attack	X	...	...
	• A thermodynamically stable surface oxide	X	...	...
	• Ductile surface scales	X	...	...
	• Adherent surface scales	X	...	...
	• High concentration of scale forming element within coating to act as reserve for scale repair	X	X	...
Interface stability	• Low rate of diffusion across the interface at operating temperatures	...	...	X
	• Limited compositional changes across interface	...	...	X
	• Absence of embrittling phase formation during service	...	...	X
Good adhesion	• Matched coating and substrate properties to minimise coating mismatch and stress generation at coating/substrate interface	...	X	X
	• Optimum surface condition before coating	...		X
	• Stresses during coating formation should be minimised	...	X	X
Mechanical strength	• Coating must withstand all stress (creep, fatigue, and impact loading) that is generated at component surface during service	...	X	...
	• Well matched thermal expansion coefficients between coating and substrate to minimise thermal stressing and thermal fatigue	...	X	X

Table 2.4: Desirable features of an Oxidation/corrosion Resistant Coating [112].

Several authors have published comprehensive guidelines on commercially available coatings and reviews of advances and/or requirements, e.g. Nicholls [112; 113; 114], Goward [115; 116; 117] Goward and Canon [118] and McMinn [119].

2.6.3 High Temperature Coatings

At the present time, two generic types of metallic coatings are used: diffusion coatings and overlay coatings. Diffusion coatings are formed through diffusional interaction between the constituents of the coating material (aluminium, chromium or silicon) and the substrate alloy. The diffusion coating may either be formed by predominant inward diffusion of the coating material (e.g. aluminium) into the alloy (inward diffusion type), or by outward diffusion of the base materials in an alloy (e.g. nickel in nickel-base alloys) (outward diffusion type). The inward diffusion type of coatings is formed at relatively high aluminium activities at the surface, while the outward diffusion type of coatings is formed at low aluminium activities. Examples of the two types of coatings on a nickel-based alloy are shown in Figure 2.42.

Diffusion coatings can be applied to components using a range of techniques: pack cementation, slurry cementation, overpack chemical vapour deposition (CVD), gas phase CVD, metallising and fluidised-bed techniques. For pack cementation, the deposition rate and morphology of the coating depend on the pack activity, process time and temperature. Similarly, for CVD coatings, the activity of various species in the vapour phase is equally of importance. Hence, the properties of a diffusion coating depend upon the process methodology, as well as the substrate composition and the subsequent heat treatment.

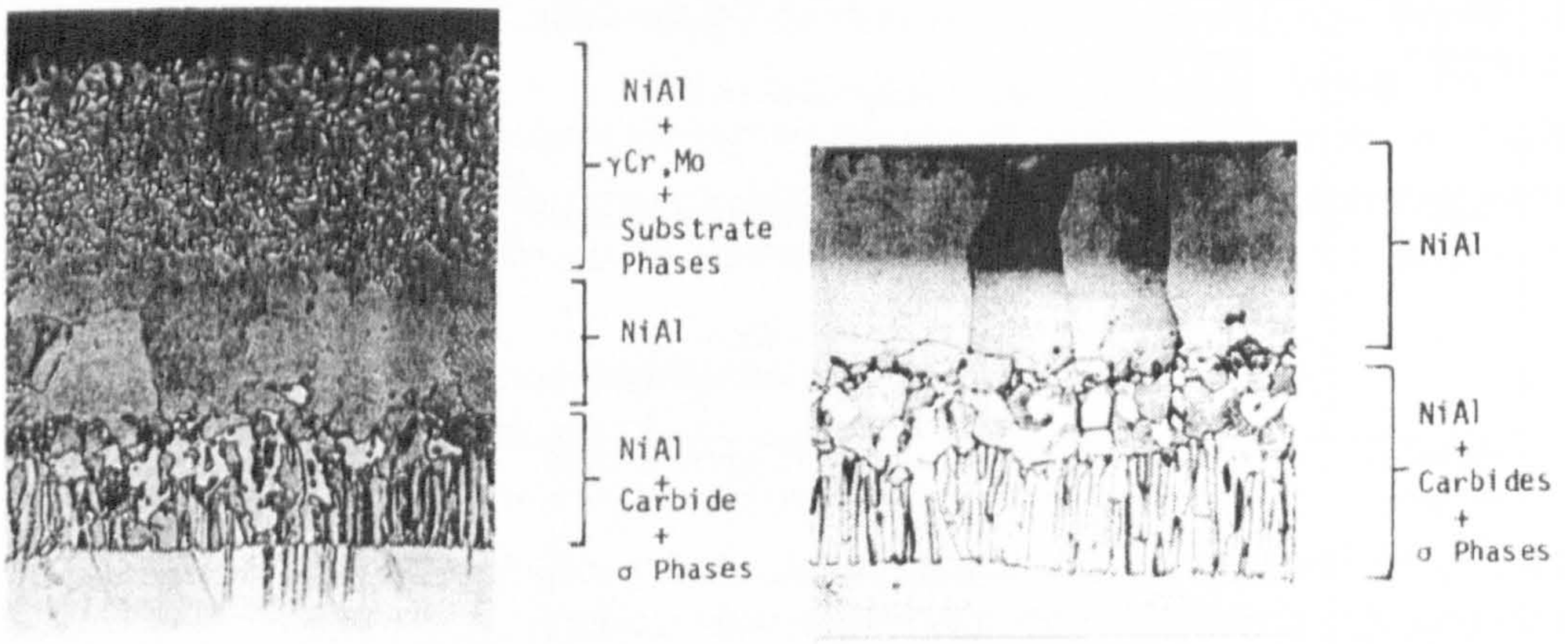

Figure 2.42: Aluminide coatings on the nickel-based alloy Udimet 700: (a) inward diffusion type; (b) outward diffusion type [115].

Diffusion coating processes have been applied for many years to improve the environmental resistance of base alloys by enriching the surface in chromium, aluminium or silicon. Pack chromising was used in the early 1950s to increase oxidation/corrosion resistance of low-alloy steels. Aluminising, developed in the 1960s, was first used for the protection of superalloy gas turbine aerofoils. Siliconizing and silicon-modified diffusion coating were used in the early 1970s, when novel solutions to the low temperature hot corrosion problems associated with contaminants in industrial turbine plants burning impure fuels were required. Of these processes, the two most used are aluminising and chromising.

The traditional route for producing diffusion coatings is based on pack cementation. In this process, components to be coated are buried in a 'pack' contained in a sealed retort, Figure 2.43. The retort is heated to the desired processing temperature under either an inert gas or hydrogen atmosphere to prevent oxidation. The exact process cycle, time and temperature, is dependant on the required coating, coating thickness and subsequent heat treatment. The pack contains a donor alloy that releases solute material at a known rate (and hence determines the pack activity), a halide activator (NaF,NH_4Cl, $NaCl$ or a mixture) that dissociates during the process cycle and acts to transport solute material from the pack to the component to be coated, and an inert oxide dilutent to prevent pack sintering. Typical pack compositions used to produce a range of metallic coatings are given in Table 2.5.

Coating	Pack Deposition Composition (wt.%)	Temp. (°C)
Al	Al_2O_3-2.2 Al-1.2NaF	900-1100
Cr	Al_2O_3.48Cr-4NH_4Cl	850-1050
Ti	77Ti-3NH_4Cl-bal.TiO_2	850-1050
Si	Al_2O_3 -5Si-3NH_4Cl	580-1050

Table 2.5: Typical pack compositions and deposition temperatures for halide-activated pack cementation [120].

Therefore, the diffusion coating is formed as a result of two distinct processing steps:

- The solute elements are brought into contact with the surface of the component to be coated (the role of the halide activator).
- The solute diffuses into the component surface to form a surface alloy or compound of different composition (the coating).

After coating, the component may be subjected to a recovery heat treatment, dependent on the substrate used. Recent developments have focused on overpack CVD and gas-phase CVD processes [120]. Both yield low-activity coatings (more ductility and higher purity), while allowing the coating of internal features, such as cooling passages and cooling holes.

Figure 2.44 is a schematic diagram of a retort that can be used for gas-phase CVD or overpack aluminizing.

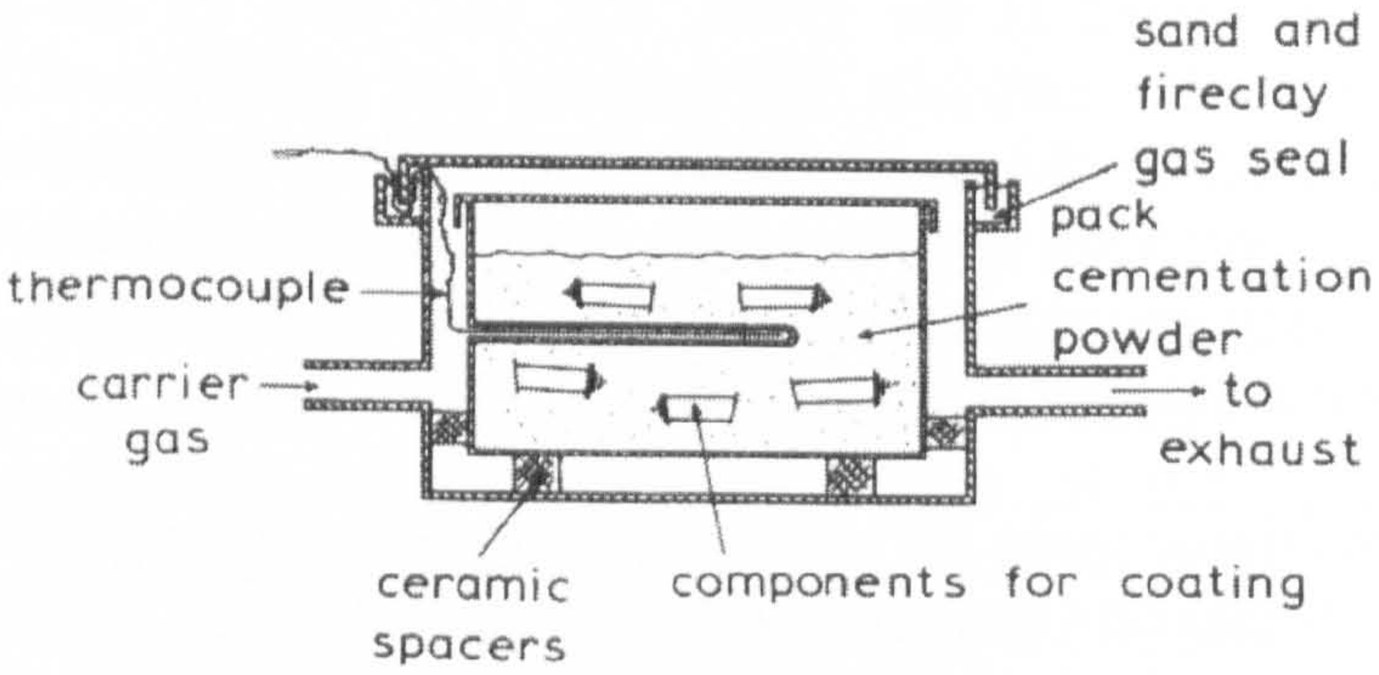

Figure 2.43: Schematic diagram of pack cementation retort [121].

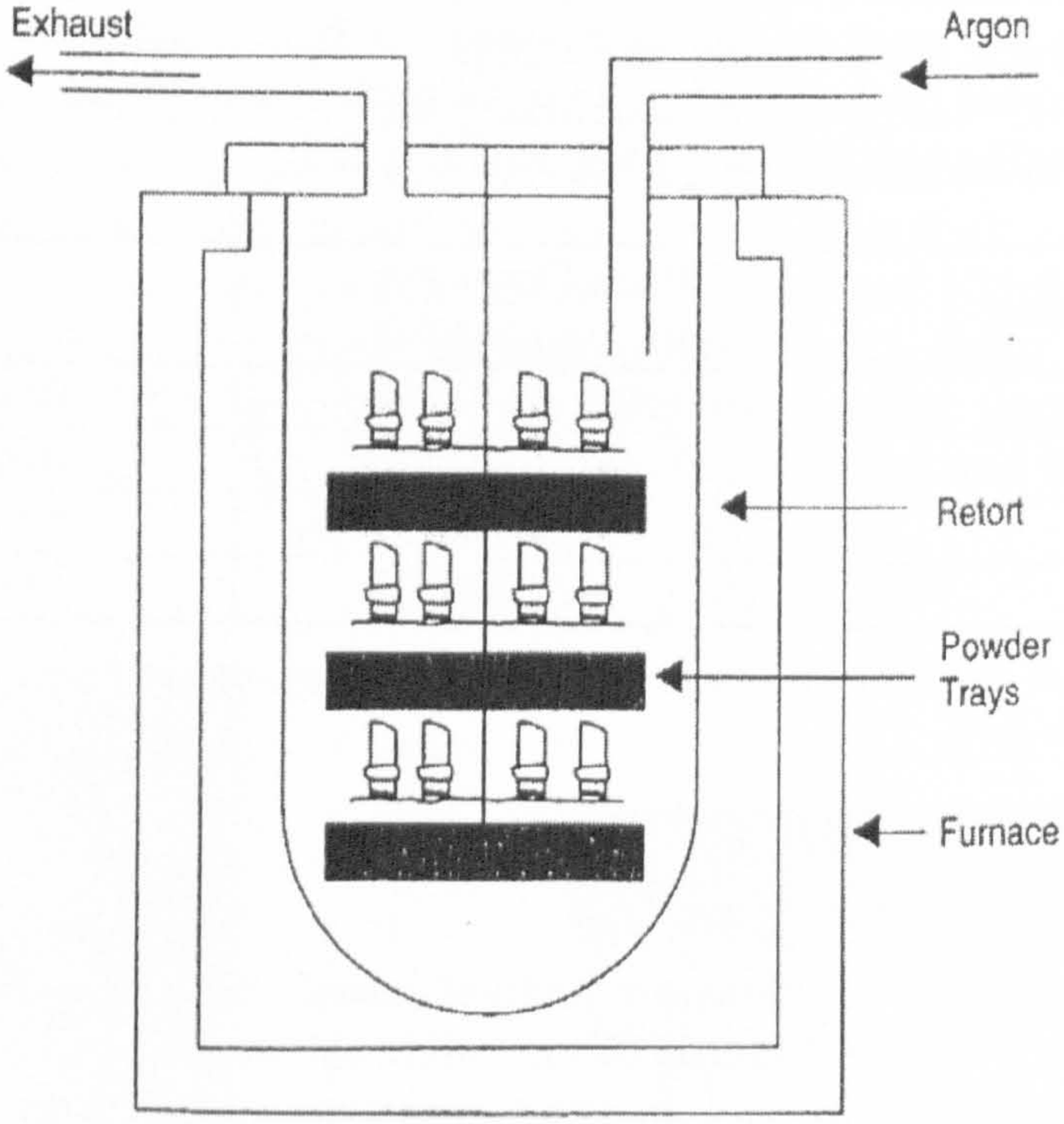

Figure 2.44: Schematic diagram of an overpack aluminizing or gas-phase CVD retort [120].

2.6.4 Aluminising

In the aluminising process, intermetallic compounds are formed on nickel- and cobalt-based superalloys due the reaction of aluminium with the alloy. This results in the formation of an intermetallic coating, primarily NiAl or CoAl, depending on the alloy composition, but containing a certain amount of most of the other elements present in the alloy, either in solution or as dispersed phases, for example, the refractory elements or Cr, which benefit corrosion resistance of the coating [122]. Generally, a uniform coating is produced on all free surfaces, 30-100 μm thick, depending on the type of aluminide formed.

When at temperature, aluminium from the pack reacts with the halide species (X) present to form AlX, via an AlX_3 precursor, which is then transported to the component surface, where the following exchange reactions are believed to occur, depositing aluminium on the alloy surface.

$$9AlX(g)+4Ni(s)\rightarrow 2Ni_2Al_3(s)+3AlX_3(g) \text{ (high activity)}$$

$$3AlX(g)+2Ni(s)\rightarrow 2NiAl(s)+AlX_3(g) \text{ (low activity)}$$

The aluminium then reacts with the base alloy to form the intermetallic aluminide coating, while the halide reaction products are recycled to continue coating deposition.

The morphology of coatings depends on pack activity, with coating processes classified as either 'low activity', when outward diffusion of nickel occurs, or 'high activity' for which an outer layer of Ni_2Al_3 forms by inward diffusion of aluminium. In the latter instance, a further heat treatment, after aluminising, is required to convert the brittle surface Ni_2Al_3 to NiAl.

The corrosion protection of this type of coating relies on the formation of a protective alumina scale, with a reservoir of aluminium should the protective oxide be damaged. Typically, aluminide coatings contain in excess of 30wt % aluminium and are deposited to thicknesses of between 30-100μm, depending on the type of aluminide formed. They offer satisfactory performance for many aviation, industrial and marine gas turbine applications.

Under severe hot corrosion conditions, or at temperatures above 1050°C, aluminide coatings offer only limited protection. To address these issues, modified aluminide coatings and overlay coatings (MCrAlY)

technologies were developed in the 1970's and development in these two areas continues today to combat the increased demands placed on the modern gas-turbine power plants [113].

2.6.5 Modified Aluminide Coatings

Modified aluminides are usually fabricated by one of the following techniques:

- Depositing an interlayer (e.g. 7 μm of platinum by electroplating or PVD to subsequently form a platinum aluminide) prior to the aluminising process.
- Pre-treating the superalloy before aluminizing (e.g. chromising prior to pack aluminizing).
- Co-depositing elements from a pack or slurry, or by blending them in the vapour phase.

Alloying coating additions include Cr, Si, Ta, various earth rare elements and precious metals, with many of these coatings now commercially available.

To improve the high-temperature oxidation performance of aluminides, a significant advanced was made with the development of platinum-modified aluminides. Platinum aluminide diffusion coatings are now an accepted industrial standard, outperforming conventional aluminides [123; 124] under high-temperature oxidation, cycling oxidation and hot-corrosion conditions .

2.6.6 Platinum Aluminide Coatings

Most commercial platinum aluminides are manufactured by first electroplating 5-10 μm of platinum, then heat-treating to diffuse the platinum into the nickel-based superalloy prior to aluminizing. Both high-activity and low-activity aluminising have been used, as have pack cementation, overpack CVD and gas–phase CVD processes. Variations in platinum thickness, heat-treatment, aluminising processes and the substrate result in a wide range of coatings/microstructures broadly known as platinum aluminides.

Depending on the initial Pt layer thickness, diffusion heat treatment and aluminization parameters, Pt modify coatings may have different typical microstructures, schematically described in Figure 2.45. When, besides being present in solid solution in β-NiAl, Pt forms $PtAl_2$, the coating is termed a two-phase coating; otherwise, it is called a single-phase coating.

Despite numerous studies of platinum modified aluminides, the exact mechanism by which platinum improves the coating performance is still a subject of open discussion. However, most researchers concur that platinum promotes the selective oxidation of aluminium and this results in the formation of a purer slower-growing alumina scale [113].

The performance of two current commercially available PtAl coatings, i.e. RT22 and CN91, has been evaluated under hot corrosion conditions in the present work. Figure 2.46 shows an example of the platinum aluminide coating RT22 deposited on SC^2 single crystal (a) as well as an example of an overlay coating, which is described further in this section (b).

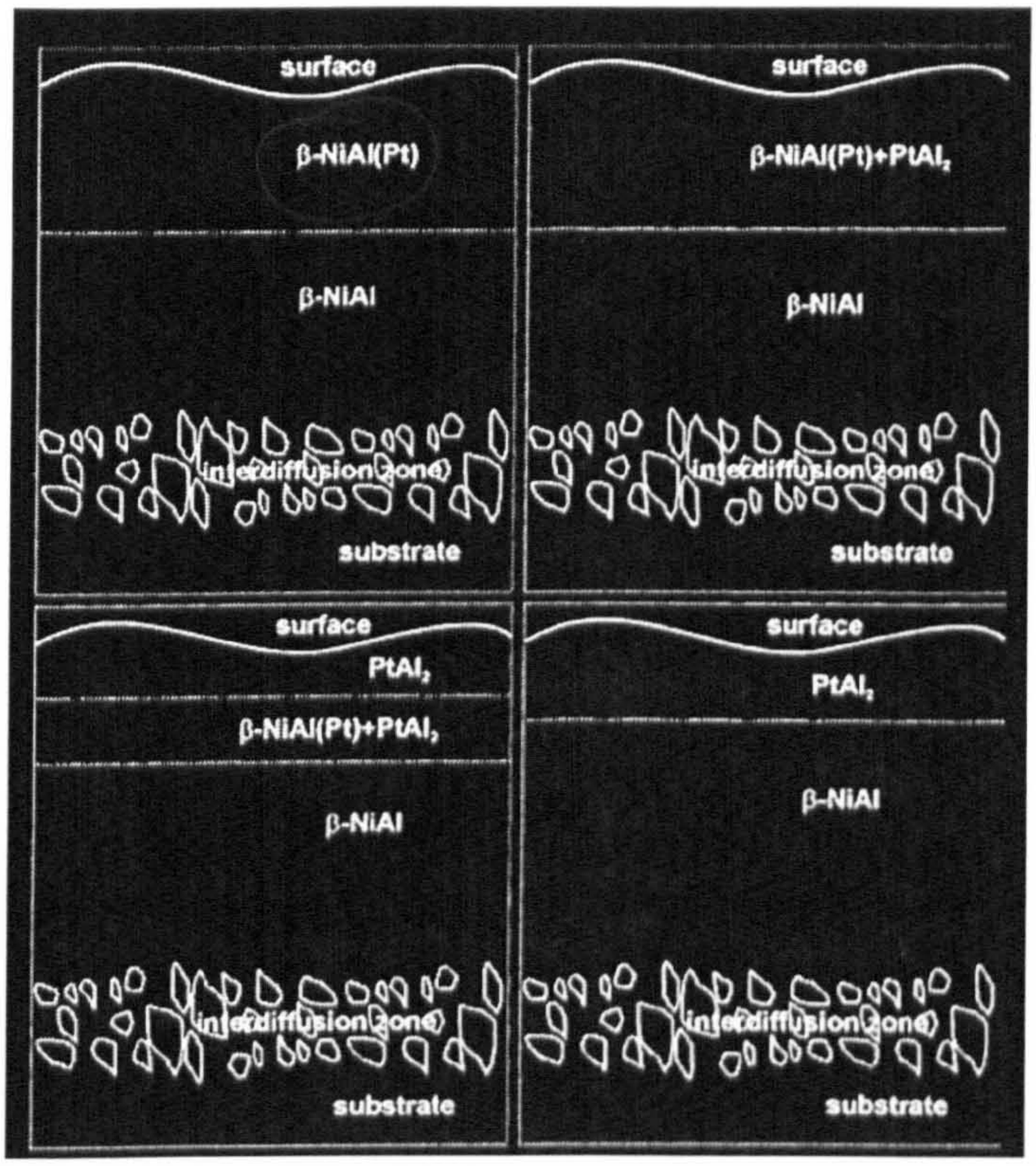

Figure 2.45: Schematic microstructures of different Pt modified aluminide diffusion coatings [38].

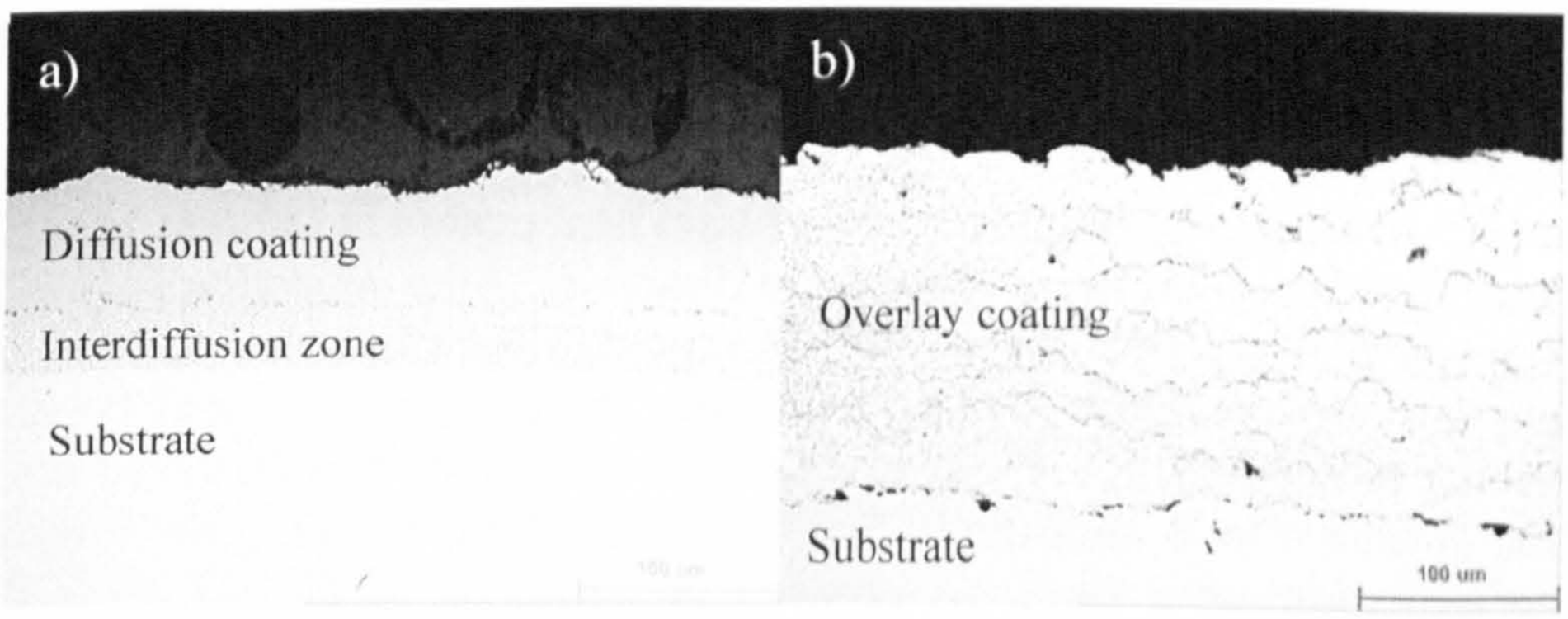

Figure 2.46: a) Example of platinum aluminide coating RT22; b) example of an overlay coating. Both deposited on SC^2 single crystal.

2.6.7 Microstructure of PtAl Modified Coatings

Extensive work by Angenete [38], about oxidation, microstructural and microchemical of PtAl modified coatings, describes the characteristics of as-coated (on nickel-based superalloys (CMSX4)) PtAl coatings RT22, PWA73, MDC150L and SS82A as follows:

- The three inwardly grown (high activity) coatings consist of an outer zone (OZ) containing small precipitates, embedded in a β-NiAl matrix, as seen in Figure 2.47.

- Between the OZ and the substrate, a zone with larger, often more elongated precipitates, is observed. This region is termed the interdiffusion zone (IZ). In the as coated condition, the precipitates in the OZ were identified as α-W, σ, μ and α-Cr phases. The α-Cr phase was predominantly observed in PWA73, while the dominating precipitate phase in the Pt-modified coatings was α-W.

- The outwardly grown (low activity) coating, MDC150L, has a precipitate-free OZ, which is the result of a lower amount of alloying elements from the substrate being incorporated into this coating (Figure 2.47).

- Another important difference between the inward and outward grown coatings is their Al content in the β phase; being high (Al/Ni>1) in the inward grown coatings and low (Al/Ni>1) in the outward grown coating.

- Two of the Pt-modified coatings, RT22 and MDC150L, are called single-phase coatings, i.e. Pt is present in solid solution in β-NiAl. In the other Pt-modified coating, SS82A, Pt is distributed in β-NiAl and $PtAl_2$ phases. This zone is termed the two-phase zone. Whether the $PtAl_2$ phase is present in Pt-modified coatings depends on the heat treatment procedures during coating production, and not on the amount of Pt present in the coating. In fact, after short-term oxidation (50h at 1,050°C), the $PtAl_2$ grains of SS82A are completely dissolved.

- In all four coatings, after short term heat treatment (50h) at 1,050°C all precipitate types except μ-phase were dissolved. After oxidation for 200h, the β phase matrix of RT22 and PWA73 started to transform into γ'-Ni_3Al at the coating surface. Upon further oxidation, these areas grew and become numerous. In MDC150L and SS82A, no such behaviour was observed up to 5,000h. It was also demonstrated that, in all coatings, the IZ grew inwards during oxidation, as a result of outward Ni diffusion to the OZ from the substrate. The depletion in the substrate below the IZ caused further precipitation of μ-phase particles.

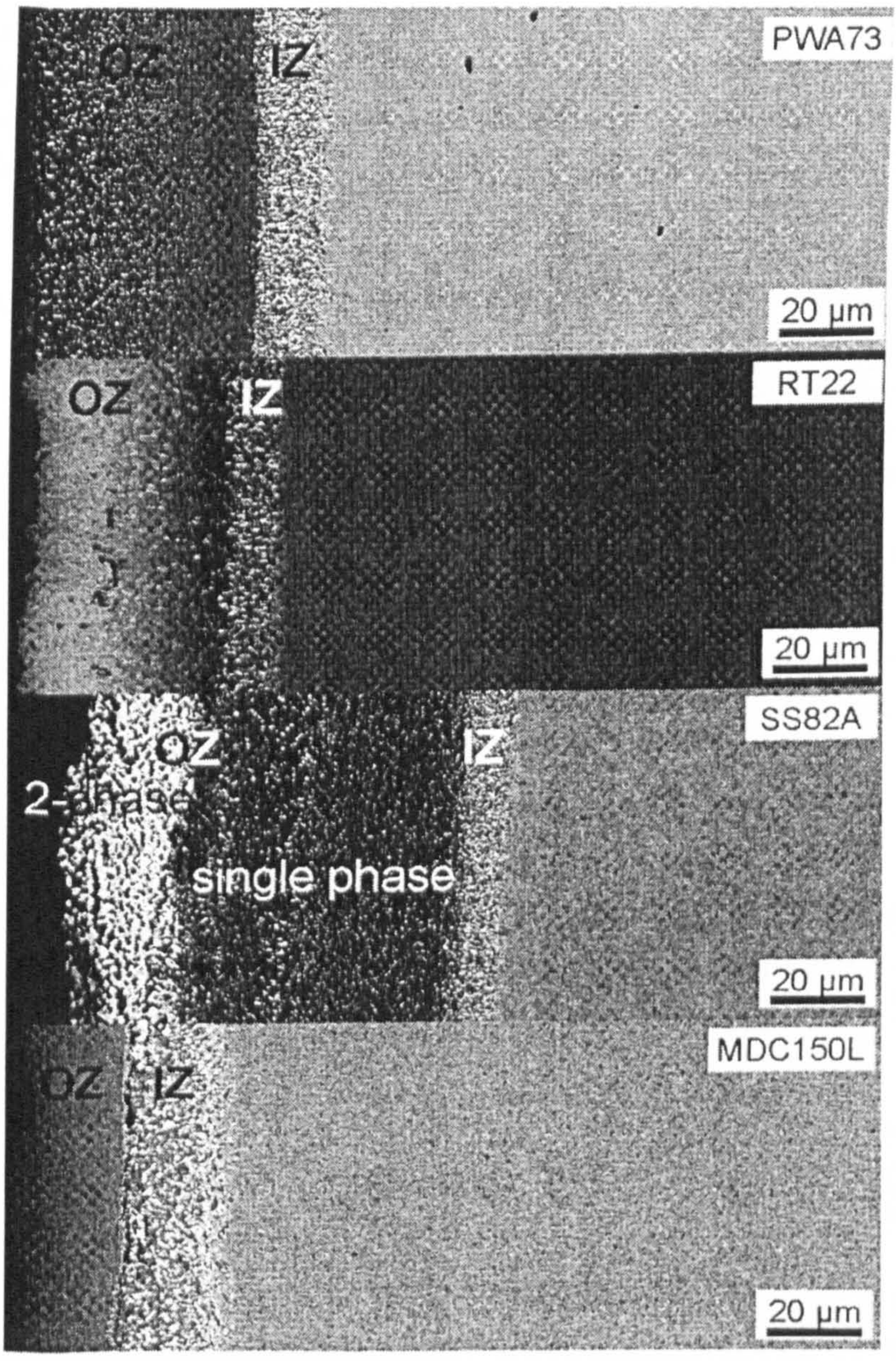

Figure 2.47: Electron backscatter image of the four coating in the as-coated condition on CMSX4 [38].

2.6.8 Overlay Coatings

Overlay coatings are a family of corrosion-resistant alloys specifically designed for high-temperature surface protection and are often referred to as M-Cr-Al-Y coatings, where M is the alloy base metal (normally nickel, cobalt or a combination of these two). Recently, other oxygen-active alloy additions have also been added to the coating such as Hf, Si and Y [113].

These more complex alloys systems are known as M-Cr-Al-X or M-Cr-Al-X-Y systems where X refers to oxygen-active elements other than yttrium. The compositions of overlay systems are selected to provide a good balance between oxidation resistance, corrosion resistance and coating ductility, while the active-element additions are beneficial to oxide-scale adhesion and decrease the oxidation rate. Ni-Cr-Al-Y coatings are generally the most oxidation resistant while Co-Cr-Al-Y systems provide good hot corrosion resistance (Figure 2.48).

The earliest production method was Electron-Beam Physical Vapour Deposition method (EB-PVD, 1970s), but, because its production costs were high, other methods are now preferred, such as: plasma spray methods (argon-shrouded plasma and vacuum-plasma) and, more recently, high velocity oxyfuel (HVOF) spraying, composite electroplating and laser-fusion.

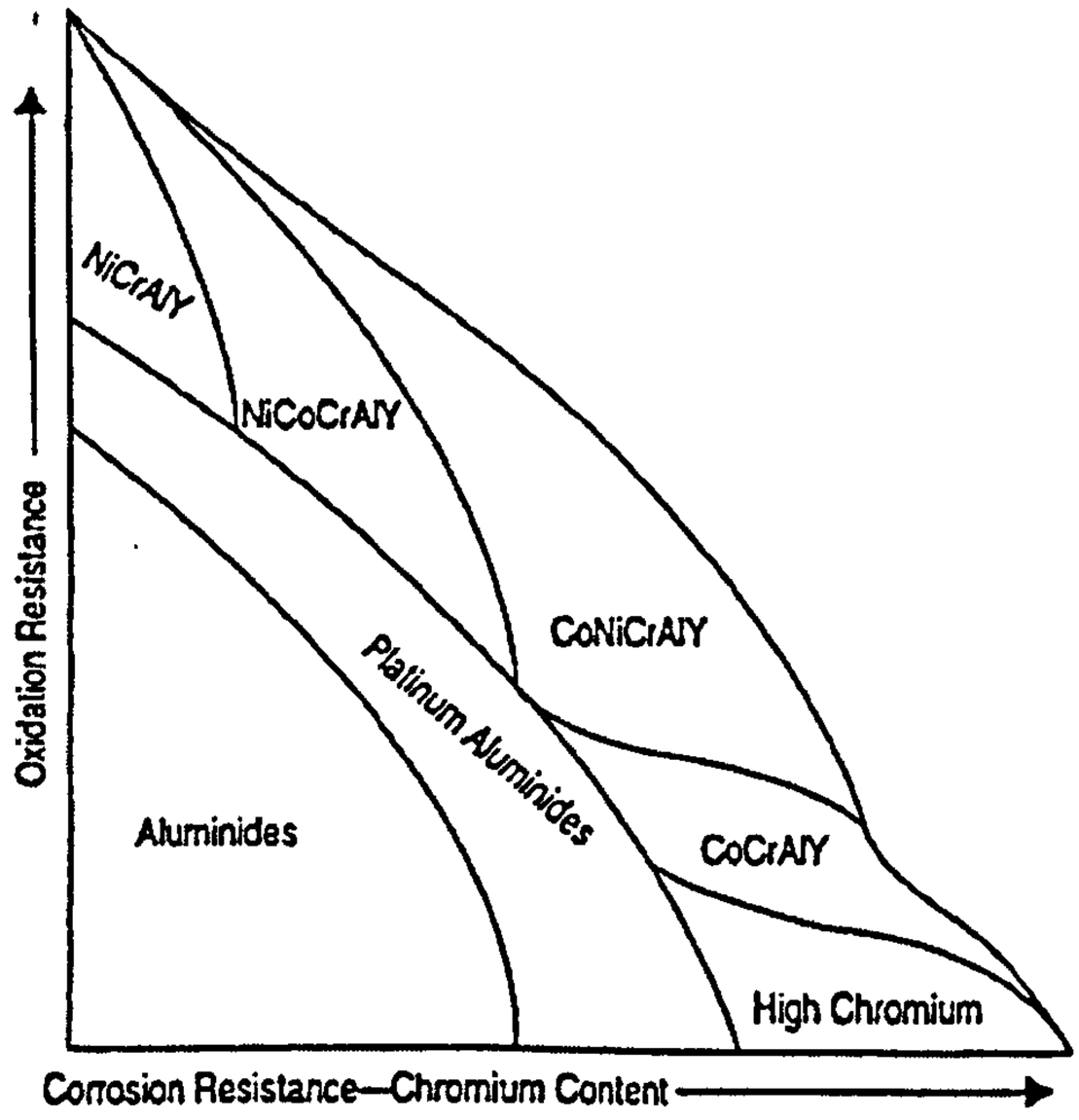

Figure 2.48: Relative oxidation and corrosion resistance of high temperature coating systems . Novack (1994) as cited in reference [120].

Overlay coatings are deposited thicker than diffusion coatings; thus, if they corrode at the same rate, overlay coatings will last proportionally longer than their diffusion equivalent. The EB-PVD process ensures a dense uniform coating and permits some interdiffusion between the coating and substrate during the coating processing cycle for good adhesion. Plasma spraying allows the deposition of metals, ceramics or a combination, generating homogeneous coatings with microstructures consisting of fine equiaxed grains, although it may contain small amounts of porosity (up to 5%) which permits the penetration of the gaseous reactants into, and sometimes through, the coating

and this may result in corrosion within the coating or at/ beneath the coating/substrate interface. These porosity problems can be overcome using post-coating thermo- mechanical treatments. The HVOF spraying process produces a dense coating with a very low porosity. Typical coating thicknesses are in a range of 100-300 μm.

2.6.9 Oxidation and Hot Corrosion of Coatings

As previously explained, hot corrosion problems (type I, II and vanadic corrosion) are a direct result of salt contaminants such as Na_2SO_4, NaCl and V_2O_5, which, in combination, produce low-melting point deposits that dissolve the "protective shield" that is the oxide surface.

Since such degradation processes can be separated into two known stages, initiation and propagation, and if the coating provides for the repair of the protective surface-oxide scale, then the initiation stage can be extended. The length of the extension could be the evaluation criteria upon which the performance of a coating-alloy system could be taken. Ideally, this should be for the design life of the components.

The corrosion performance of a range of diffusion and overlay coatings under high temperature oxidation and type I and II hot corrosion conditions, has been reviewed by Malik et al.[125], Nicholls et al.[120; 113], Goward [116], Barkalow [126] and Stringer [127].

The platinum-modified aluminides perform exceptionally well under high temperature oxidation conditions and type I hot corrosion, but less well under type II hot corrosion conditions [127; 120; 128; 129; 16]. The silicon-containing diffusion aluminides perform well under type II hot corrosion conditions. Chromized and chrome-aluminized coatings also offer protection under type II corrosion conditions, and improved corrosion resistance in a turbine environment.

Classic overlay coatings (with 18-22 % chromium and 8-12 % aluminium) generally perform better at higher temperatures with good adherence of the thin alumina scales.

Generally, under these high temperature oxidising conditions, Ni-Cr-Al-Y and Ni-Co-Cr-A-Y systems outperform cobalt-based systems. At low temperatures where type II corrosion predominates (650°- 800°C), Co-Cr-Al-Y coatings generally outperform Ni-Cr-Al-X coatings, with the high chromium-containing Co-Cr-Al-Y coatings showing the best performance [120].

Methods have been investigated to improve the traditional M-Cr-Al-Y coating by use of a platinum under layer; over layers with additions such as Ti, Zr, Hf, Si and Ta have been examined. Surface modifications by CVD, PVD or slurry-cementation techniques have also been considered, with varying degrees of success. Surface modification results in the formation of a duplex coating structure, and can improved performance. Silicon modifications to the surface of Co-Cr-Al-Y coatings have also been proposed and improve the resistance to low-temperature hot corrosion.

Other important properties of coating systems are mechanical properties and thermal stability. The first one governs the resistance to cracking by thermally induced stresses, and the second one refers to the capacity to maintain their protective qualities over extended periods of time at high temperature.

An alternative strategy to the development oxidation/corrosion-resistant alloys is to design coatings systems that lower the metal surface temperature: Thermal Barrier Coatings (TBC). TBCs offer the potential to drop the metal-surface temperature by up to 150°C in conjunction with component cooling, thus reducing the oxidation rate. The use of TBCs on turbine blades offers at least two benefits: the cooling requirement can be reduced and/or the hot gas temperature can be raised significantly, which means lower specific fuel consumption and higher output powers. From a corrosion point of view, thermal barriers permit the ceramic surface temperatures to increase, reducing the rate of salt deposition due to condensation reactions. In addition, for many corrodents (vanadium being an exception) the TBC may also act as an environmental barrier.

TBC materials must have low heat conductivity and partially stabilised zirconium is the material commonly used in these coatings. 7-8% Y_2O_3-balance ZrO_2 TBCs do not provide long-term corrosion resistance at high temperature, and they must be combined with protective bond coatings between the thermal barrier coating and the substrate alloy. In addition, these bond coatings also serve to reduce the thermal expansion mismatch between the ceramic coating and the alloy substrate.

TBCs have been applied by plasma-spraying since 1950s. Alternatively, EB-PVD produces a strain-tolerant columnar microstructure that allows TBCs to operate successfully on highly stressed turbine components without spalling.

2.7 Application of Statistics to High Temperature Corrosion

It has been stated by Evans [48] that, whereas for the majority of reactions which receive quantitative study from chemists, identical results are obtained on each repetition of an experiment, this is not always the case with corrosion reactions, which often give different results when performed several times.

Under these conditions, the results of an experiment should be quoted as maximum and mean metal loss or corrosion penetration. Data plotted as a bar charts and by alloy system can be ranked as having good, average or poor corrosion resistance. An alternative method of analyzing oxidation and corrosion data, based on the application of statistical methods to maximize the available information from laboratory and burner rig corrosion studies has been presented by Nicholls and Hancock [130; 131]:

Since hot corrosion attack results in a non-uniform morphology (e.g. presence of pits for type II hot corrosion), it is necessary to quantify the rate of corrosion statistically on components when the corrosion processes result in areas of different local attack. This can be achieved through the accurate measurement of samples pre- and post-exposure, coupled with the statistical assessment of the data generated, using normal distribution and/or extreme values statistics to determine the rate of growth of maximum areas of attack.

From this type of data, life prediction models can be developed that accurately predict the onset of hot corrosion induced failure. This statistical approach has been further applied to predicting the high temperature corrosion performance of coatings and alloys, for example in marine service conditions [132; 133], in high temperature power plants [128; 16; 134; 135; 136; 137; 138; 139] and it will be applied in the analysis and discussion of the present study (sections 4 and 5).

3 Experimental Procedures

3.1 Introduction

In any power generation system, it is important that components have adequate, reliable and predictable lives in their required operational environments. In the development of co-fired power systems, it is necessary to demonstrate that adequate component lifetimes will be achieved with the unusual fuels and fuel mixes that are currently being proposed.

The experimentation in the present study has been carried out in two main stages for an aggregate time of 9000 hours involving 136 samples. The aim of stage 1 was to examine the behaviour of a polycrystal alloy (IN738 LC) and a single crystal alloy (CMSX-4). Both alloys were examined uncoated and coated with a platinum aluminide diffusion coating, in different realistic hot corrosion environments. This stage comprised a series of six hot corrosion tests and had two parts:

1. This part comprised tests 1, 2, 3 and 5 to examine the effect of changing the deposit composition at the same temperature but in different gas compositions.

2. This part comprised tests 4, 5 and 6 to examine the effect of using the same gas composition at different temperatures.

Each test consisted of 36 samples, 24 for a total time of 500 h and 12 for 1000 h of exposure. The accumulated test duration of this stage was 6000 h. Every 100h, samples were removed to be re-coated with the required amount of simulated deposit. (It has been recommended that, at least 10 salt recoats are used per test duration [140]). Stage 2 had an accumulated test duration of 3000 hours involving 72 samples. It was aimed at evaluating:

1. The effects of three different model gas compositions using only one deposit composition, but with three deposition fluxes on two single crystal alloys (CMSX-4 and SC^2) and a further polycrystalline alloy (IN792), again both uncoated and coated with a platinum aluminide diffusion coating in realistic hot corrosion environments.

2. The effect of changing temperature on the same materials/coatings: tests 7, 9 and 11 for 700°C and tests 8, 10 and 12 for 900°C.

Each test had 24 samples for a total time of 500 h of exposure. Every 50h, samples were removed, weighed and re-coated with the required simulated deposit (It has been recommended that, at least 10 salt recoats are used per test duration [140]). A matrix of the conditions for each test is given in Table 3.1.

Samples for all these test were cleaned and measured before exposure, exposed, metallographic section prepared after exposure, and these sections were measured according to the procedures detailed later in the present chapter. One unexposed reference sample of each material passed through this whole assessment process for comparison with the exposed samples.

Stage no.		Test no.	Temp (°C)			Gas Composition							Flux/Comp.				Hours	
						SOx / 300	100	300	20	50	500	50						
			650	700	900	HI / 600	100	100	10	-	-	500					500	1000
1	1a	1		•			•						A	C				•
													A	B	C	D	•	
		2		•		•							A	C				•
													A	B	C	D	•	
		3		•					•				A	C				•
													A	B	C	D	•	
		5		•				•					A	C				•
													A	B	C	D	•	
	1b	4			•			•										
															B		•	
		6	•					•										
															B		•	
2		7		•						•			B	B'	B''			
																	•	
		8			•					•			B	B'	B''			
																	•	
		9		•							•		B	B'	B''			
																	•	
		10			•						•		B	B'	B''			
																	•	
		11		•								•	B	B'	B''			
																	•	
		12			•							•	B	B'	B''			
																	•	

Table 3.1: Matrix of two experimentation stages (see Table 3.4 and Table 3.5 for gas and deposit compositions).

3.2 Materials

As described in section 2.3, high temperature alloys for gas turbines generally contain cobalt or nickel as base metals. In order to obtain improved high temperature corrosion resistance, alloying additions of chromium, aluminium and silicon are important as they may (depending upon the alloy composition and exposure conditions) form protective oxide scales of Cr_2O_3, Al_2O_3 or SiO_2. Table 2.2 in section 2.3.4, shows the nominal compositions of the alloys that have been tested during the present work, Table 3.2 shows the coatings and Table 3.3 shows the base/alloy coating combinations

Coating	Composition	Application Route
RT22, CN91	Pt–Al	Electrodeposited Pt followed by over aluminising (different conditions were need to produce proprietary CVD for RT22 and CN91 coatings) and heat treatment

Table 3.2: Diffusion coatings evaluated.

Exp. stage	Base Alloy	Coating
1	IN738LC	uncoated
	IN738LC	Pt–Al
	CMSX-4	uncoated
	CMSX-4	Pt–Al
2	CMSX-4	uncoated
	CMSX-4	Pt–Al
	IN 792	uncoated
	IN 792	Pt–Al
	SC^2	uncoated
	SC^2	Pt–Al

Table 3.3: Base alloy/coating combinations evaluated in the various corrosion test.

3.3 Corrosion Furnaces and Environment

The corrosion tests were carried out in vertical tube furnaces. Prior to starting each test, the furnace was carefully calibrated, such that samples would be exposed in the hot-zone within a range of ± 5°C of the target test temperature. Alumina furniture was used throughout the furnace. This furniture has six crucible holders, each one with four places; thus, every one of the 24 samples can be in the same place throughout the test. At the top of the furnace, a lid supports the alumina furniture as well as providing an inlet and an outlet for the gas.

The gas flow rate was 50 ml min^{-1} (within the recommended gas flow range [140]) and was regulated by a pre-calibrated mass flow controller with an accuracy of ± 1 %. Gases were commercially procured as certified bottle gases containing specified levels of SO_2 and HCl, together with major species (given in Table 3.4). Figure 3.1 shows a diagram of the vertical furnace for controlled atmosphere corrosion tests. The gas is fed through an alumina feed tube to the bottom of the furnace, before flowing back up the furnace around the specimens to the gas outlet. This procedure permits the equilibration of SO_2/SO_3 over the alumina as a catalyst.

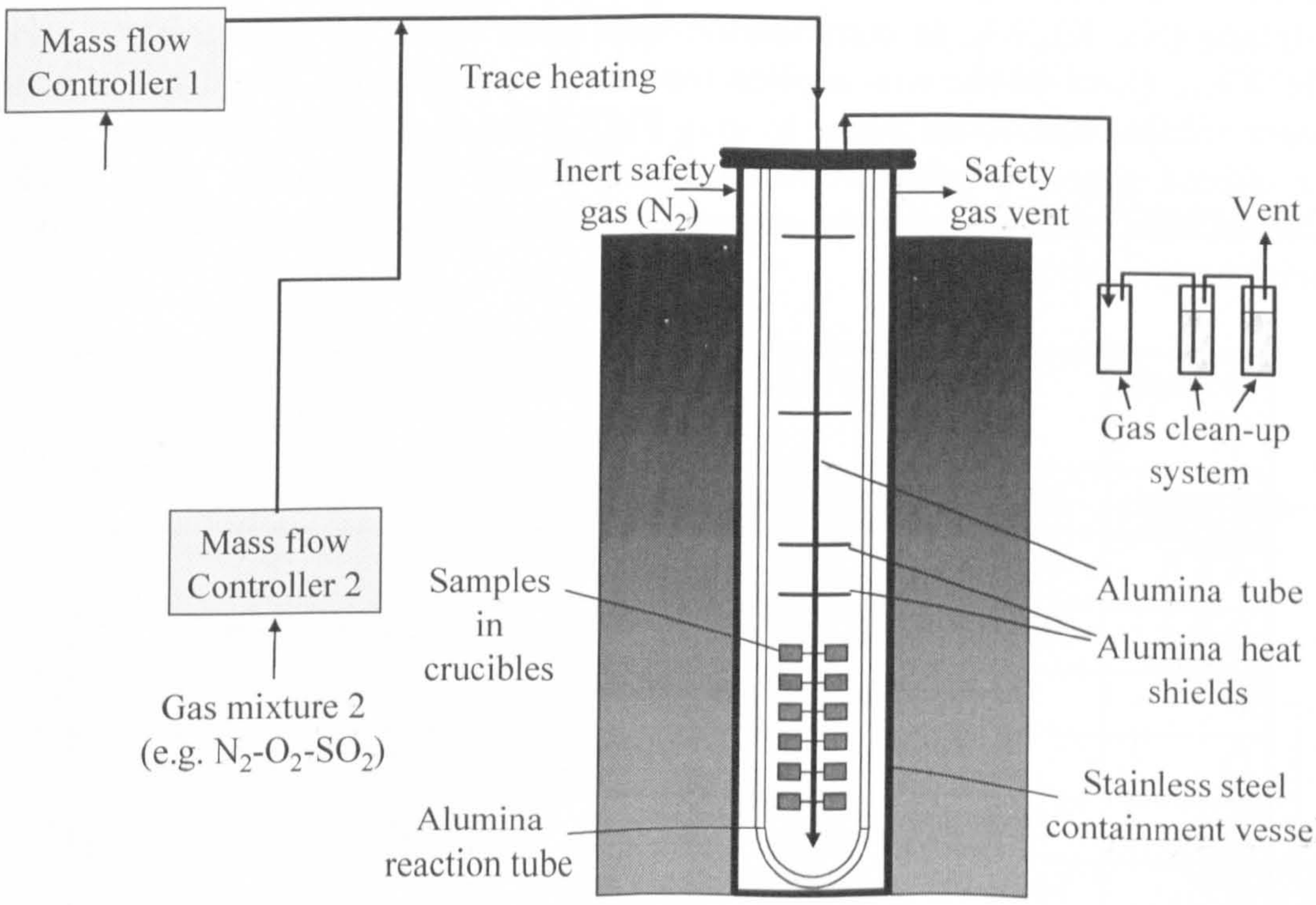

Figure 3.1: Vertical furnace for controlled atmosphere, gas goes in through Al_2O_3 tube to base of furnace[71].

The next table shows gases concentrations used in this study:

Stage no.	SO_2 (vppm)	HCl (vppm)	CO_2 (v%)	O_2 (v%)	N_2 (v%)
Test 1	100	100	5	15	Balance
Test 2	300	500			
Test 3	20	10			
Test 4,5 & 6	300	100			
Test 7,8	50	-	-	20	
Test 9,10	500	-			
Test 11,12	50	500			

Table 3.4: Gas compositions referred to in Table 3.1.

3.4 Corrosion Testing: Deposit Re-coat Test Method in Controlled Atmosphere Furnaces

When samples completed a required thermal cycle (i.e. 50 h or 100h in this study) of exposure in the furnace, they were unloaded, weighed and re-coated with salt. The aim was to deposit a calculated quantity of alkali sulphate $(Na, K)_2SO_4$, in combination with other solutions such as NaCl and $Pb(NO_3)_2$, (lead nitrate was applied instead of lead chloride because this was water soluble and decomposed to give $PbCl_2$).These deposits, combined with the mixed gases, created an environment where hot corrosion attack took place. Table 3.5 shows the target combinations for the deposits, their relative weights, (moles) and fluxes.

Deposit ID	Weight % (mole % in parenthesis)				Flux $\mu g/cm^2/h$
	Na_2SO_4	K_2SO_4	$Pb(NO_3)_2$	NaCl	
A	44.9(50)	55.1(50)	-	-	15
B	76.5(80)	23.5(20)	-	-	
C	-	13.5(16.6)	77.4(50.1)	9.1(33.4)	
D	-	5.6(6.1)	79.5(45.5)	14.9(48.4)	
B'	76.5(80)	23.5(20)	-	-	5
B''	76.5(80)	23.5(20)	-	-	1.5

Table 3.5: Composition of sprayed deposits and flux for each deposit ID (as referred in table Table 3.1).

Deposition of salts onto the samples was achieved using the "deposit re-coat method" [136; 141; 71; 142] that has proved to be an effective way of simulating "in service" deposit conditions within laboratory tests and now forms the basis for EU recommended guidelines for hot salt corrosion testing [141]. This method consists of spraying a mist of solution through an artist's air-brush onto a sample pre-heated to 120°C. Water evaporation from the hot surface of the sample leaves an even layer of deposit on the sample surface.

Figure 3.2 illustrates the spraying application technique, where variables such as distance of air brush from sample, air brush height, air brush nozzle aperture and spray time, have been calibrated and standardised. The deposition quantity (mg) has been calculated by considering the required deposition weights of 15, 5 and 1.5 $\mu g/cm^2/h$ x sample surface area x 100h or 50h depending on test recoat interval. In order to achieve repetitive spray deposition accuracy, a flow diagram for standard operation has been followed for the application of the deposits (Figure 3.3). The repeatability of the salt application method can be seen in the histograms shown in Figure 3.4, where a consistency of ± 0.05 mg has been achieved. This provides a very reliable method on which to base the hot corrosion data.

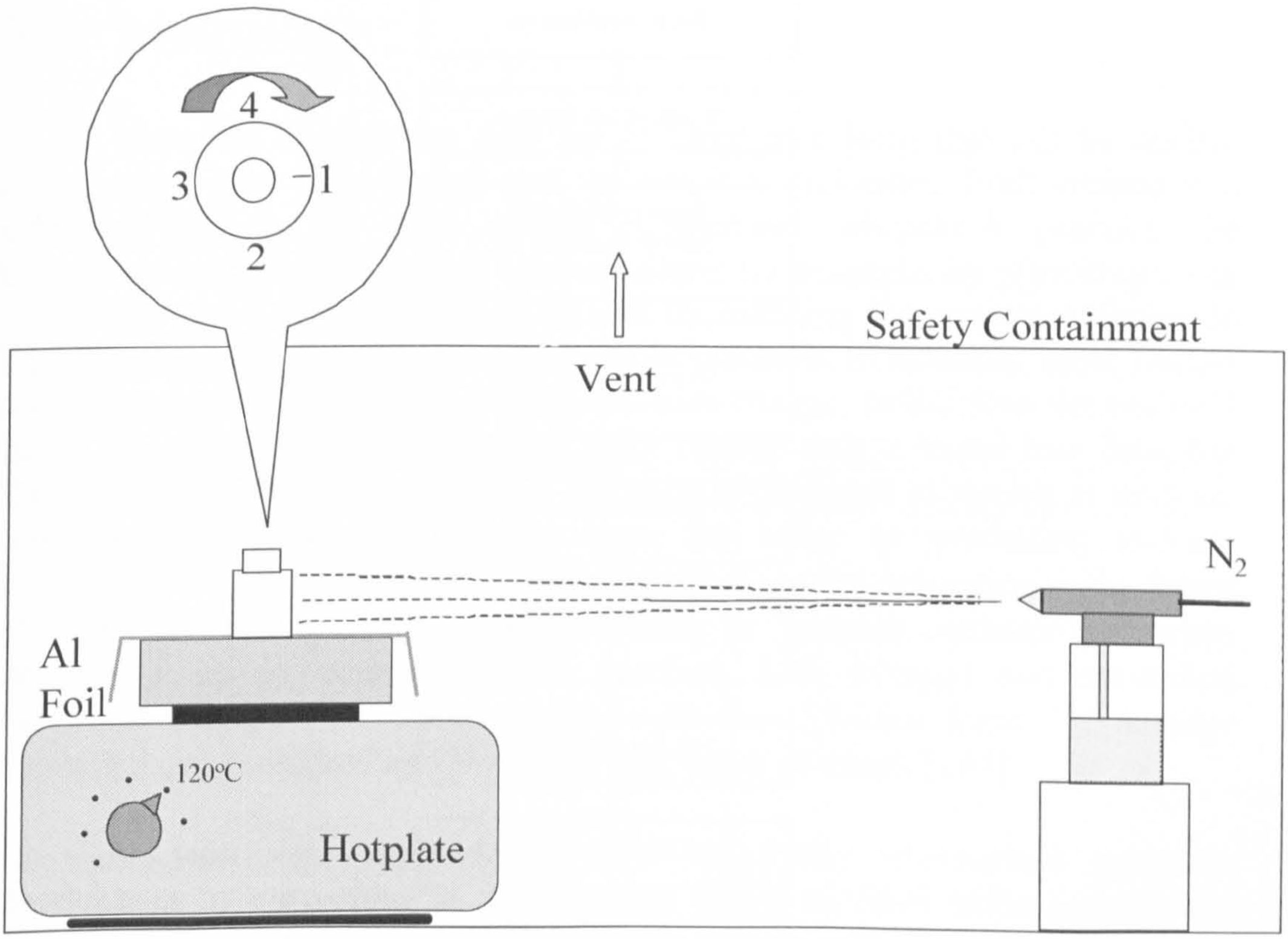

Figure 3.2:Illustration of spraying technique [143].

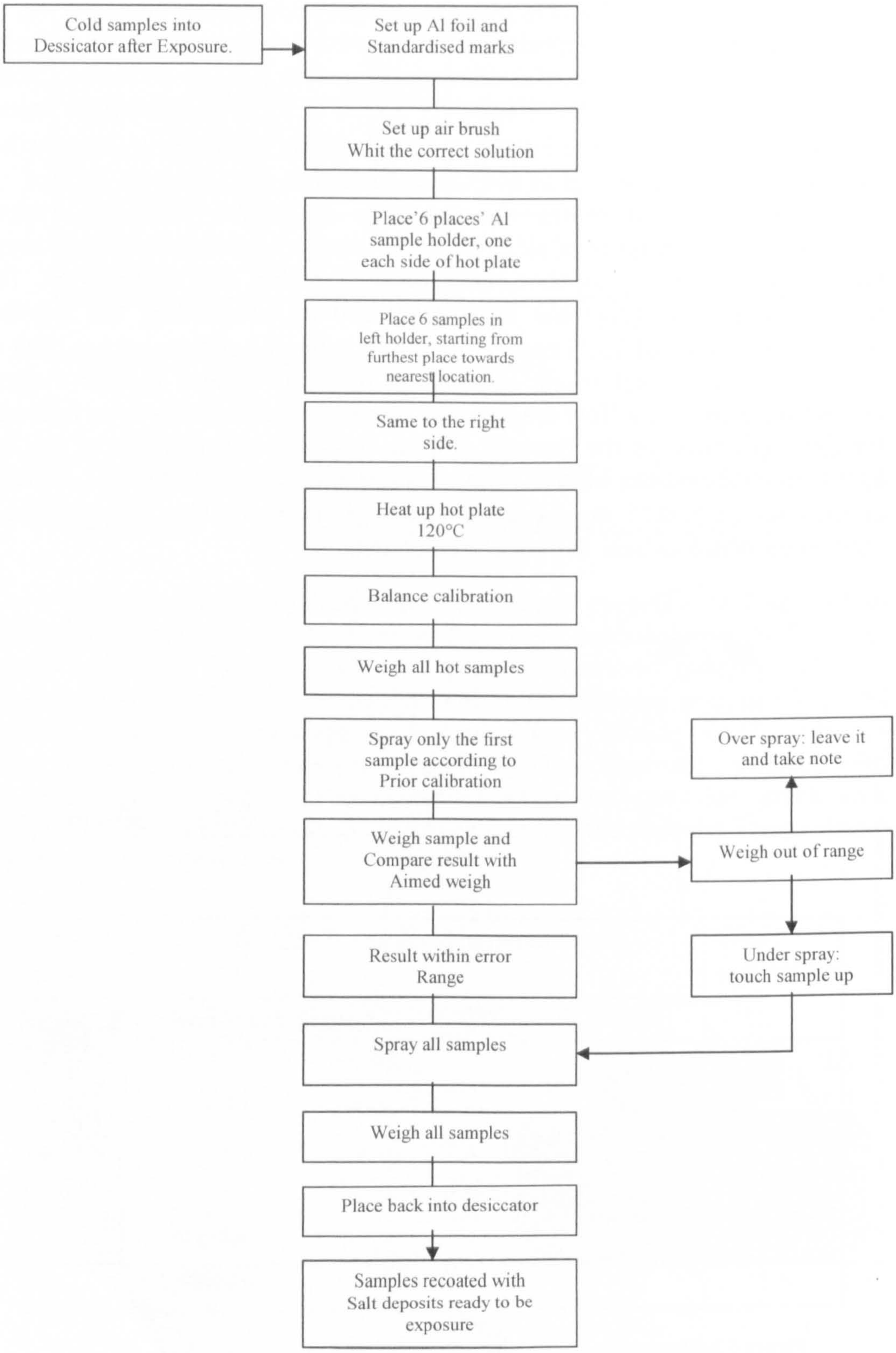

Figure 3.3: Flow diagram for salt deposition procedure.

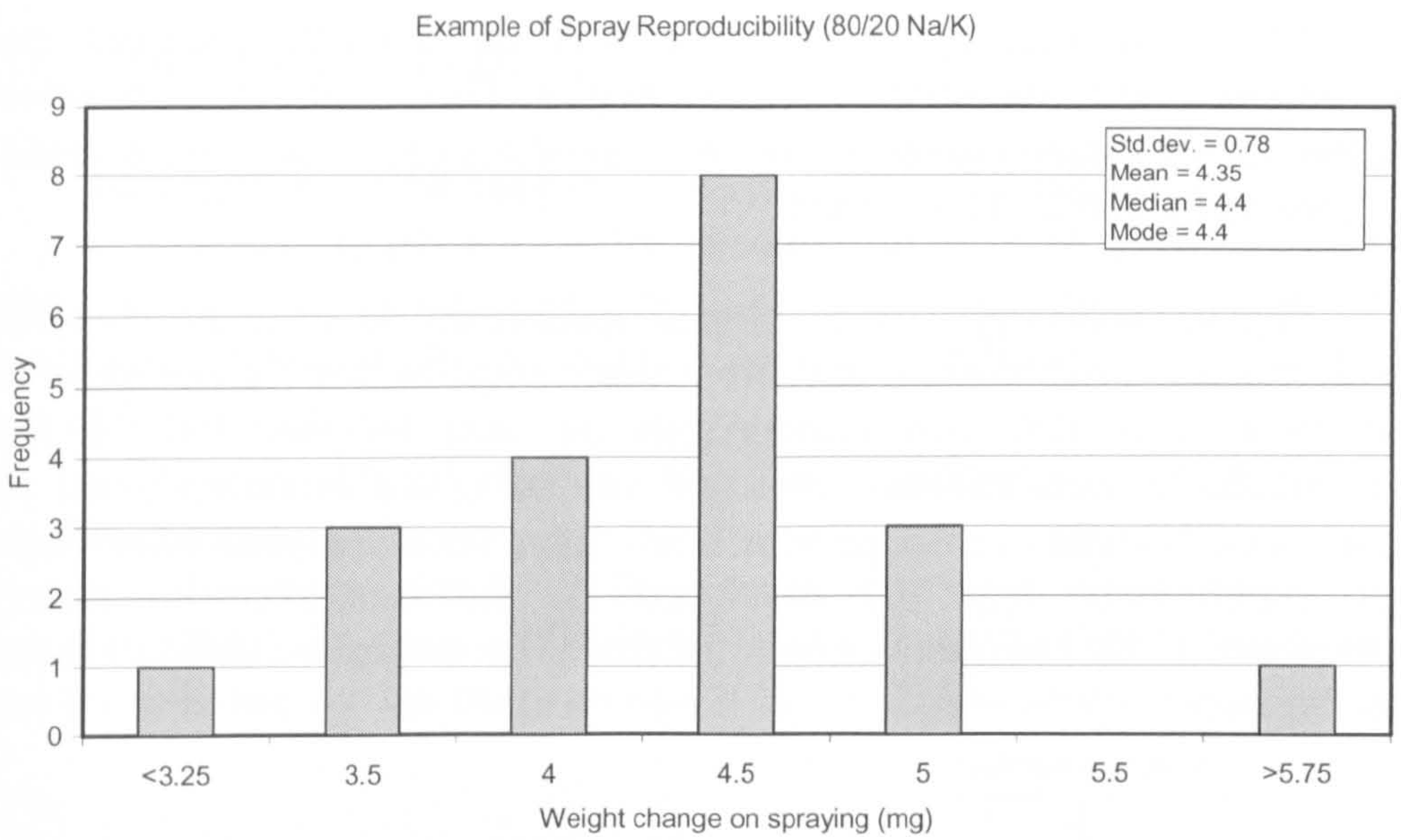

Figure 3.4: Example of spray reproducibility with a deposit of 80/20 $(Na/K)_2SO_4$.

3.5 Metrology

Materials degradation data are required in a form that can be readily incorporated into plant design and maintenance processes. Both erosion and corrosion damage are often quoted as averages, whereas in practice, the regions of deepest damage will lead to failure: for example, by providing a site for fatigue crack initiation (e.g. a pit), or by reducing the section thickness to such an extent that creep rupture failure is possible. In addition, most studies report erosion and corrosion damage as mass change, rather than dimensional metal loss. It is possible to convert mass change data to metal loss data, but this involves several assumptions, the most significant of which is uniform scale growth. Mass change data have the effect of producing average measurements of the damage that are inappropriate for evaluating many forms of corrosion damage (e.g. localised pitting or internal corrosion) or when deposits form on components. In practice, both average and maximum materials damage rate are desirable, with the different forms of damage identified and measured as a thickness loss/depth of attack [144].

A metrology methodology for accurately measuring materials degradation by corrosion (and/or erosion) in gas turbines environments was developed by British Coal, through collaboration with Cranfield University [144], that is based in the accurate measurement of sample dimensions before and after exposure. Contact metrology is use to measure the dimensions of materials samples/ components before exposure (as described in section 3.7).

After exposure, optical measurements on carefully prepared cross-sections are used to measure damaged samples. These methods were selected to allow for semi-automation so that large numbers (≥24) data points could be collected and statistically analysed.

The methodology was developed specifically to generate compatible sets of materials degradation data from laboratory, burner rig and short term plant runs. Such data can subsequently be used for modelling materials performance in such environments and validating the models against plant experiences. Samples in the present study have been analysed following the basic experimental approach developed for the assessment of materials performance [145; 146], that consists of five main stages and follows the next flow diagram :

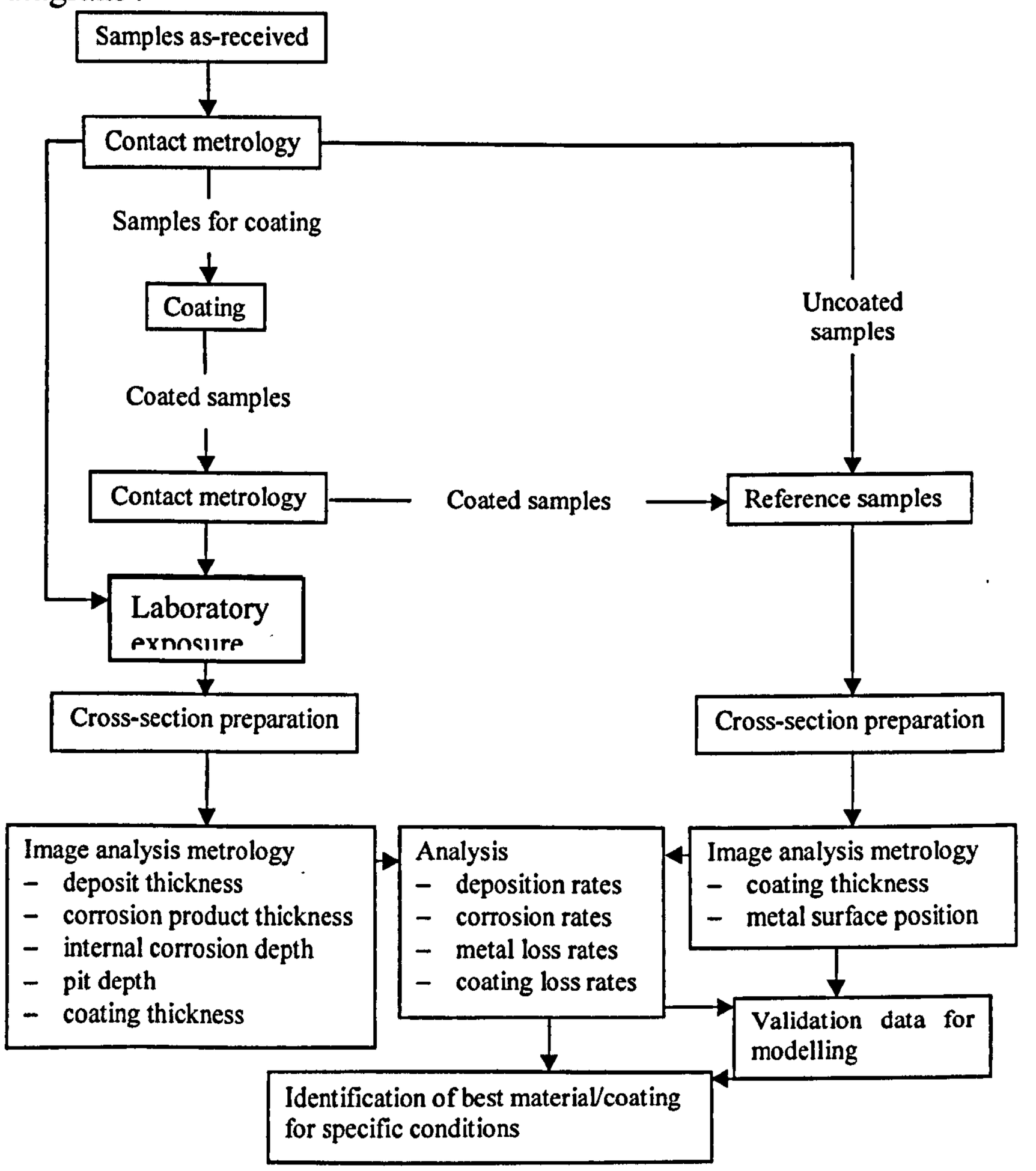

Figure 3.5: Flow diagram of materials metrology process [145].

3.6 Specimen Manufacture

Two features of the sample prior to exposure are important:

- Surface roughness: as the pre-exposure metrology uses a contact method, variability in roughness can lead to errors affecting the reliability of measurement readings; hence, sample surface roughness should be in the range of 0.4-1.6 μm R_a.
- Figure 3.6 illustrates specimen geometry, dimensions and manufacturing precision.
- The rate of change in the sample dimension perpendicular to the measuring plane, since this determines how close to the original measurement plane the polished section needs to be for post-exposure measurement.

3.7 Pre-exposure Metrology

Pre-exposure metrology depends on sample geometry, dimensions and intended use. For solid cylindrical samples as used in the laboratory corrosion tests in the present study, only sample diameters need to be measured. An ~153mm long bar of each metal alloy (from Table 2.2), was machined creating eleven individual cylindrical samples of 10mm long x 10mm ∅, as shown in Figure 3.6. These were coated, where necessary, with the protective coating as shown in Table 3.2.

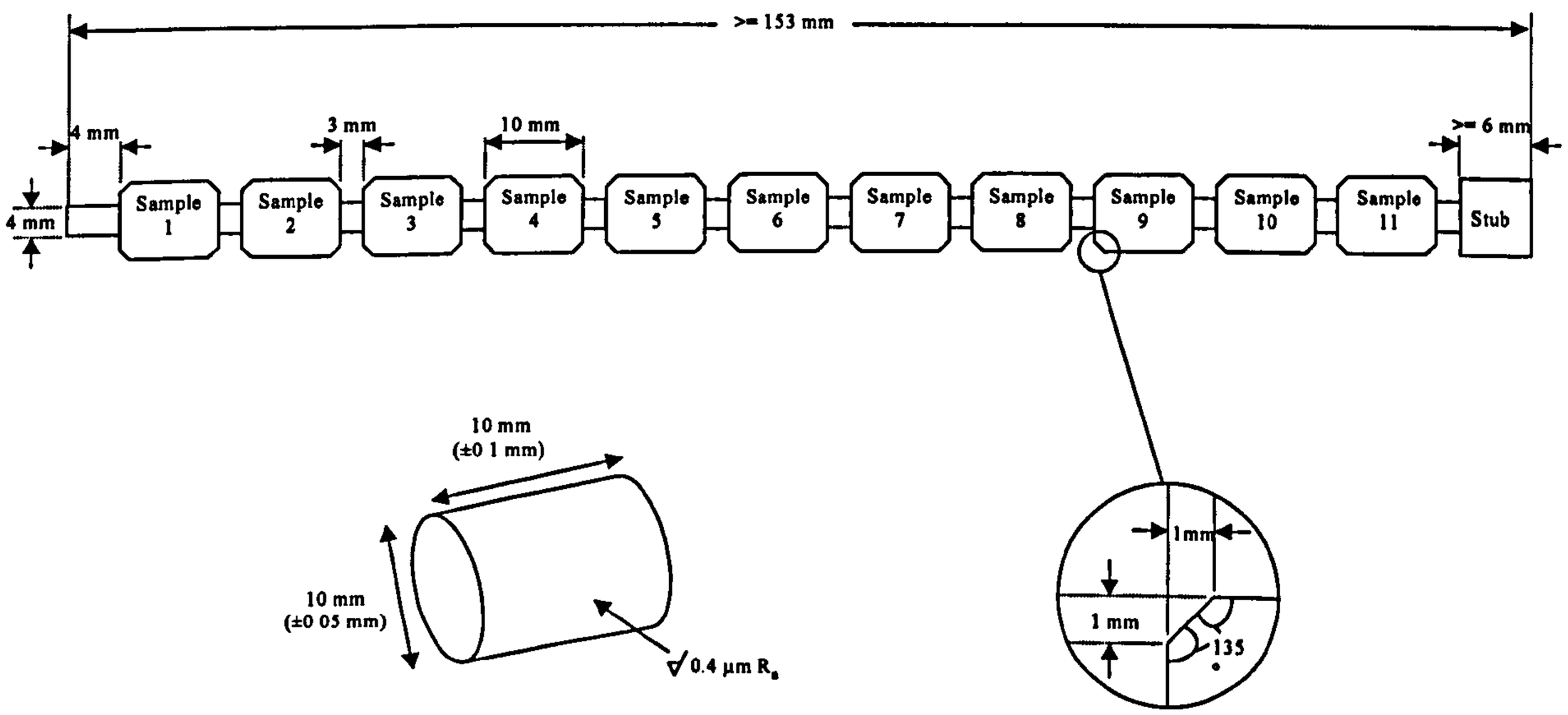

Figure 3.6: Illustration of samples, as received, machined form ~a 53 mm source material bars [143].

Prior to exposure, the following procedure was carried out:

- Cutting: each sample was parted off using a precision cutting machine at approximately 1.0-1.3mm from the end chamfer of the sample, such that a 2mm stub remained at the top of the sample. This was made to facilitate future handling and also for indicating sample orientation.

- Reference mark: it was important to make a groove mark in the top chamfer that was used as a reference point for measurements, salt re-coat procedure, mounting and final image analysis. This groove mark was 1mm deep (Figure 3.7).

- Sample cleaning: samples were thoroughly cleaned by a degreasing treatment. Firstly samples were immersed in volasil 344 in an ultrasonic bath for 15 minutes and then, the same procedure was followed using isopropyl alcohol (IPA). Samples were then placed in individual plastic bags labelled previously.

- Contact metrology: using a vernier gauge (micrometer), with a resolution of ± 0.001mm, each sample was measured diametrically at the centre of its height eight times. In order to gather accurate readings before exposure, an imaginary clock time was used as reference mark so that measurement was always started in the same position (12:45) and followed a clockwise rotation measuring every 45° to completed eight intervals as shown in next Figure 3.7. This means that each diameter is measured twice, thus both measurement errors and variation in diameter can be assessed. A sample of each material was kept as an unexposed reference sample.

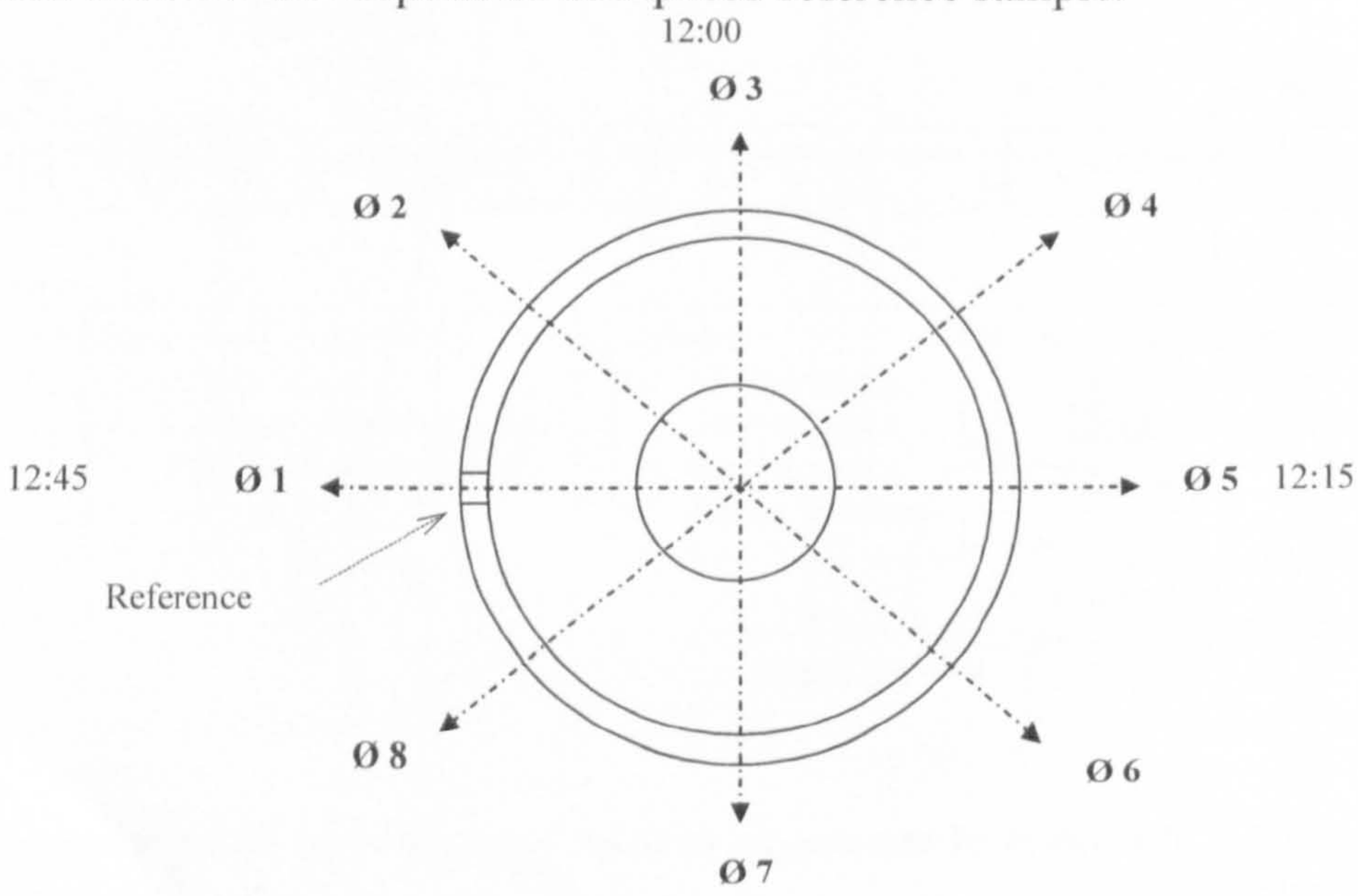

Figure 3.7: Micrometer contact measurements procedure.

- Crucible cleaning: before placing the measured sample into a crucible, the crucible was cleaned firstly with water and then isopropyl alcohol after which it was pre-heated at 1000 °C for 24 hours.

- Mass change: to generate the mass change data, samples were weighed individually every cycle (i.e. every 50 and/or 100h). The crucible was weighed alone, and also the sample plus its crucible were weighed together from the test commencement, using a microbalance with resolution of ± 0.01mg. Prior to the start of the test, the samples and their crucibles were placed in a labelled desiccator.

3.8 Post-exposure Sample Preparation

Metallographic sections of the corroded samples are needed to obtain hot corrosion data through microscopy image measurements. Samples must be mounted vertically to produce flat sections perpendicular to their cylinder axes. For this, a special mounting jig is used. It contains two reference pins and a knife edge which keeps the sample parallel against them, as may be seen in Figure 3.8. The sample is mounted by filling the mould up with epoxy resin [147] in combination with Potters ballotini (0.04–0.07 silica glass powder) and carrying out a vacuum de-gassing during the first stages of epoxy settings.

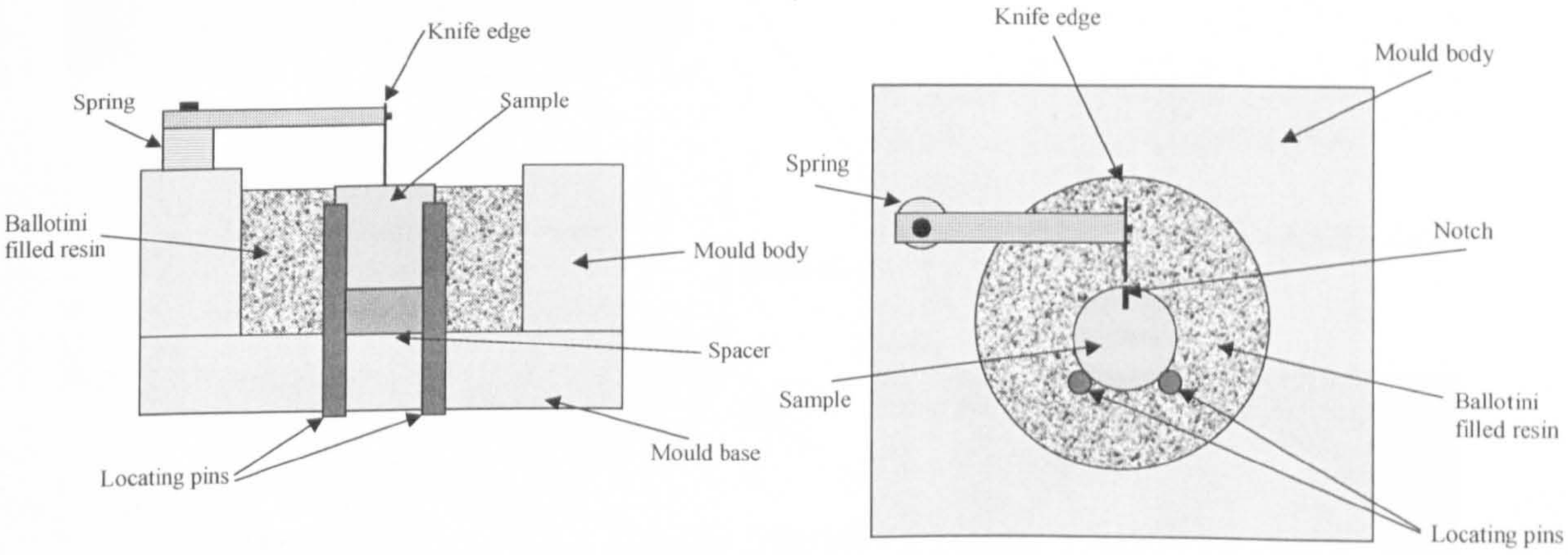

Figure 3.8: Sample mounting jig [71].

The knife edge position must be touching the original reference mark made before exposure (described in the pre-exposure sample preparation section), so that, after metallographic preparation, the knife edge will remain and act as the new reference mark that will indicate the origin position of the pre-exposure sample measurements and the starting position for post-exposure

image measurements. These samples were sectioned close to their mid-point and then metallographically prepared (using mineral oil lubricants to ensure that water soluble species remained in the prepared sections) using semi-automated grinding and polishing machines.

3.9 Post- exposure Metrology

This stage was intended to accurately determine the resulting dimensions of the samples and to characterise the extent of any corrosion damage or other required parameter (e.g. depth of internal penetration, scale thickness, deposit thickness). To achieve this, the carefully prepared cross-sections were measured using reflected light microscopes with a very accurately calibrated x-y stage using a commercial image analysis system. At each location, several parameters could be measured, for example the position of the edge of the metal, the depth of internal corrosion and the deposit thickness. Prior to measuring, optical micro-graphs were produced to visually assess the corrosion damage. Figure 3.9 and Figure 3.10 illustrate how the measurements were made during the post-exposure metrology work in order to generate the data required for materials performance modelling in terms of metal/coating loss under different exposure conditions.

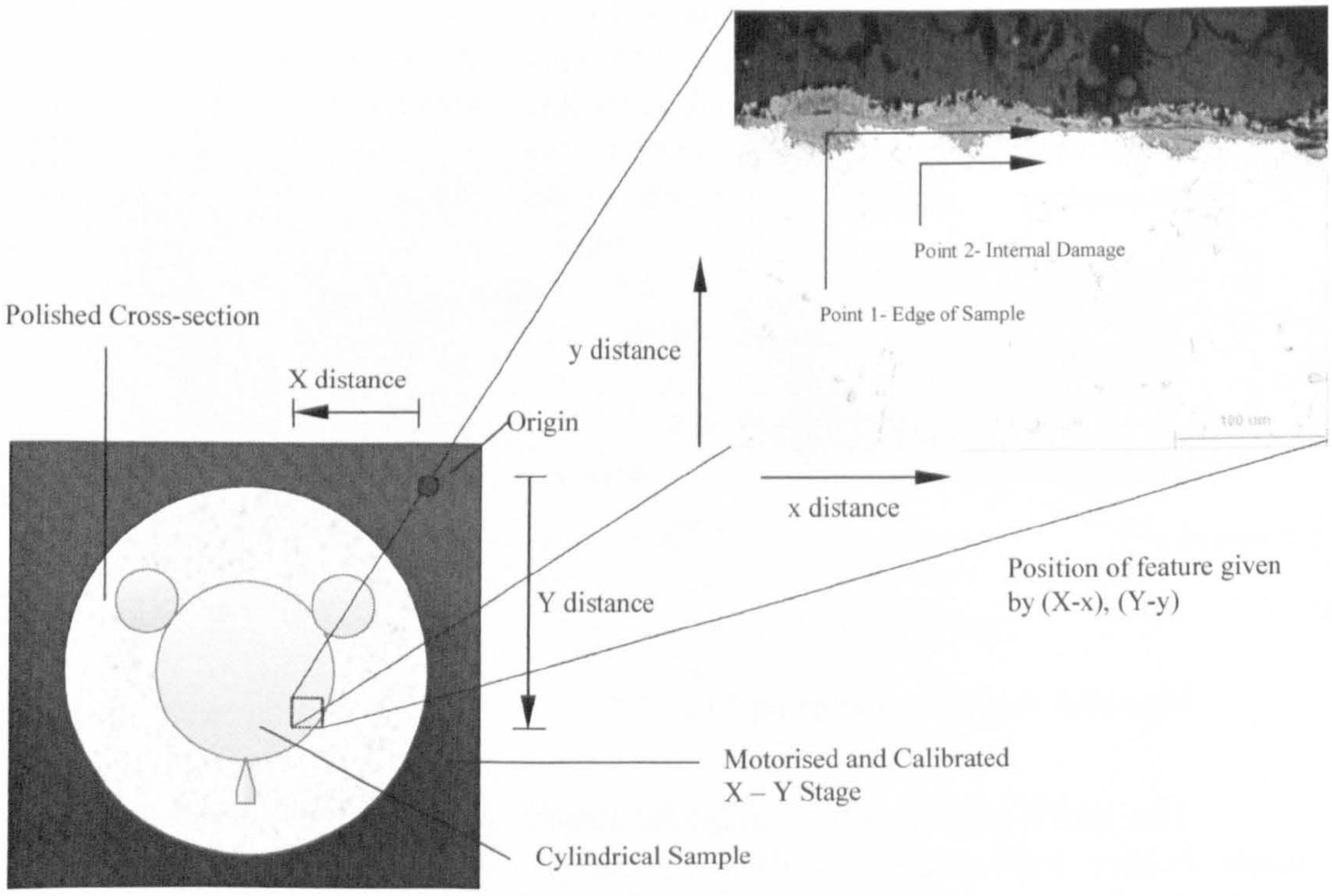

Figure 3.9: Post-exposure measurements process on image analyser system [144].

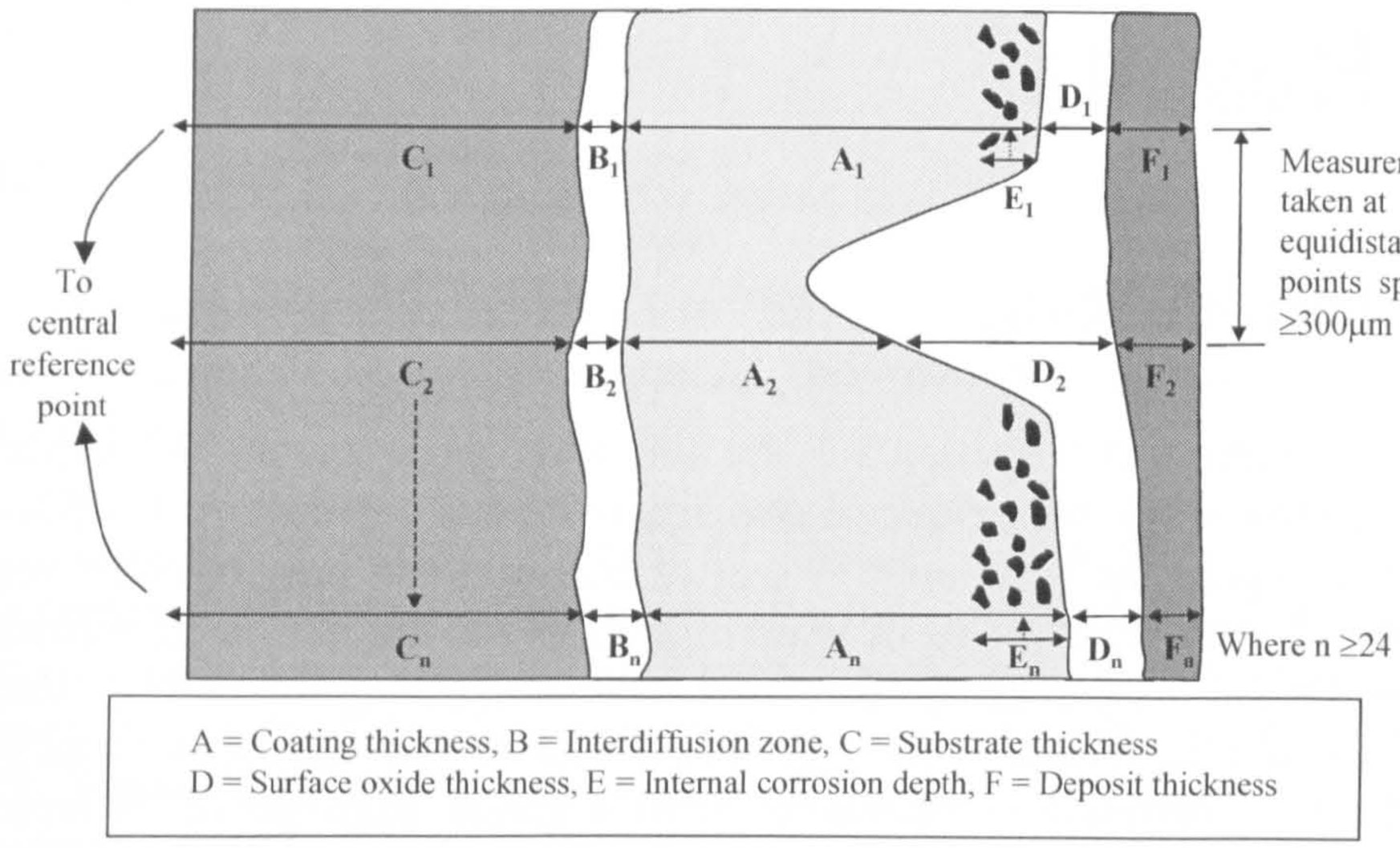

Figure 3.10: Diagram of post-exposure sample metrology procedure used to generate the data required for materials performance modelling [71].

4 Results

4.1 Introduction

As explained in section 3.1, the aim of the experimentation in this study was to examine the behaviour of two single crystal superalloys CMSX-4 and SC^2, to compare the behaviour to that of conventional hot corrosion resistant polycrystal materials, and to develop models of the hot corrosion performance of the single crystal materials. This was carried out for both uncoated materials and materials with a platinum aluminised diffusion coating in a realistic hot corrosion environment with a range from 20 to 500vpm SO_2 and/or in combination with HCl in a range from 10 to 500vpm, together with different deposit compositions. The information gathered from the data obtained from the laboratory tests, is detailed in this chapter and these can be split into four categories:

- mass change,
- optical microscopy,
- metrology and data analysis
- Scanning Electron Microscope (SEM) equipped with an Energy Dispersive X-ray (EDX) analysis system. The results of these observations are given in the discussion part of this thesis for clarity (section 5, Figure 5.8 to Figure 5.18 and Figure 5.24 to Figure 5.31).

4.2 Mass Change

Mass change data are the least useful of the methods for assessing high temperature corrosion damage, as they are not sensitive to localised pitting or internal corrosion damage which are anticipated for type II and I hot corrosion respectively. However, it is useful in giving an indication of the extent of general corrosion damage.

Mass change is produced during the salt deposition process of every test, when the samples are recoated in deposits every 50 or 100 hours. The mass change is calculated after each 50 or 100 h cycle and used to produce a plot of cumulative mass change (mg/cm^2) against time. Sets of this mass change have been produced for the twelve tests carried out in this study and are presented as follows:

4.2.1 Mass change data (Phase 1)

4.2.1.1 Uncoated IN738 LC at 700° C:

The data plotted in Figure 4.1 to Figure 4.4 show that, for this material, the alkali deposits caused higher general corrosion damage than the deposits containing lead.

This trend is observed for each of the four tests at 700°C. With respect to gas composition, as the SO_2 concentration is increased from 20 to 300 vpm, an increase in the observed maximum mass change is noticeable after 500 h of exposure, i.e. from ~0 to 10 mg/cm^2 (test 3,Figure 4.1) to ~60 to 70 mg/cm^2 (test 2, Figure 4.4), with the exception of the 300 vpm SO_2/100 vpm HCl combination (test 5, Figure 4.2) that appear to be less affected than the 100 vpm SO_2/100 vpm HCl combination (test 1, Figure 4.3).

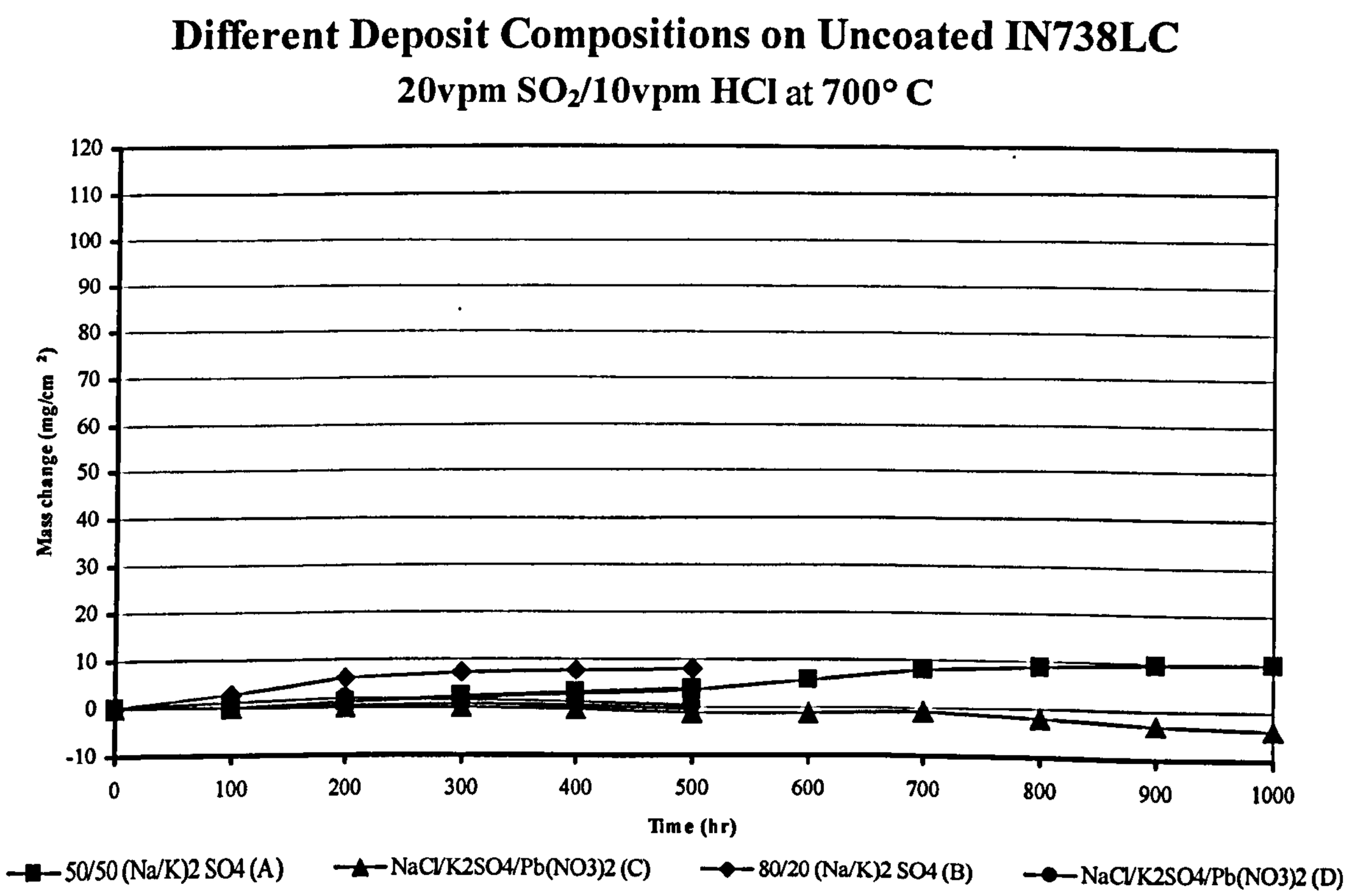

Figure 4.1: Comparison of deposit compositions with a flux of 15µg/cm^2/h, in 20vpm SO_2/10vpm HCl; on uncoated IN738LC at 700°C, from test 3.

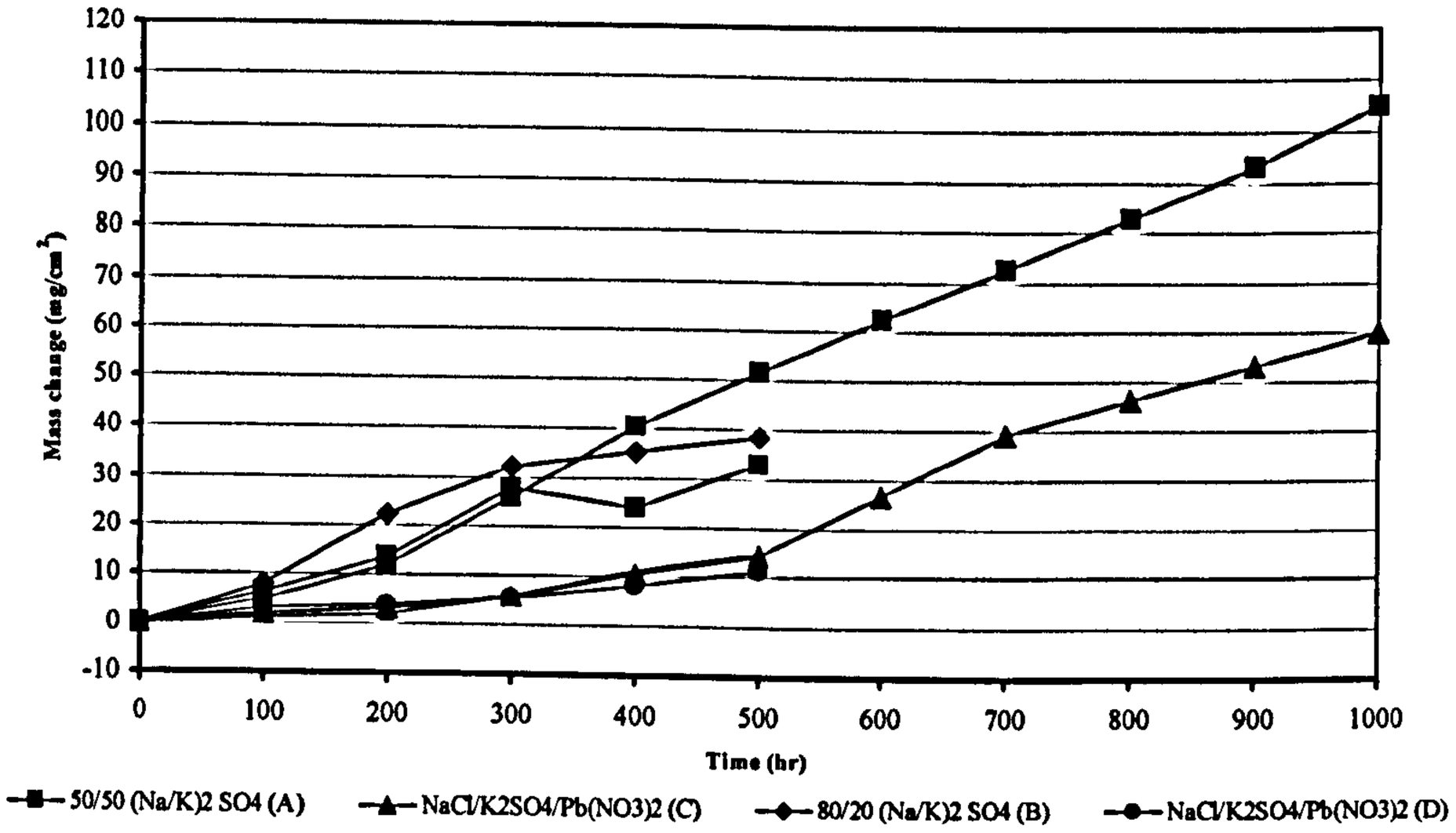

Figure 4.2: Comparison of deposit compositions with a flux of 15µg/cm²/h, in 300vpm SO_2/100vpm HCl; on uncoated IN738LC at 700°C, from test 5.

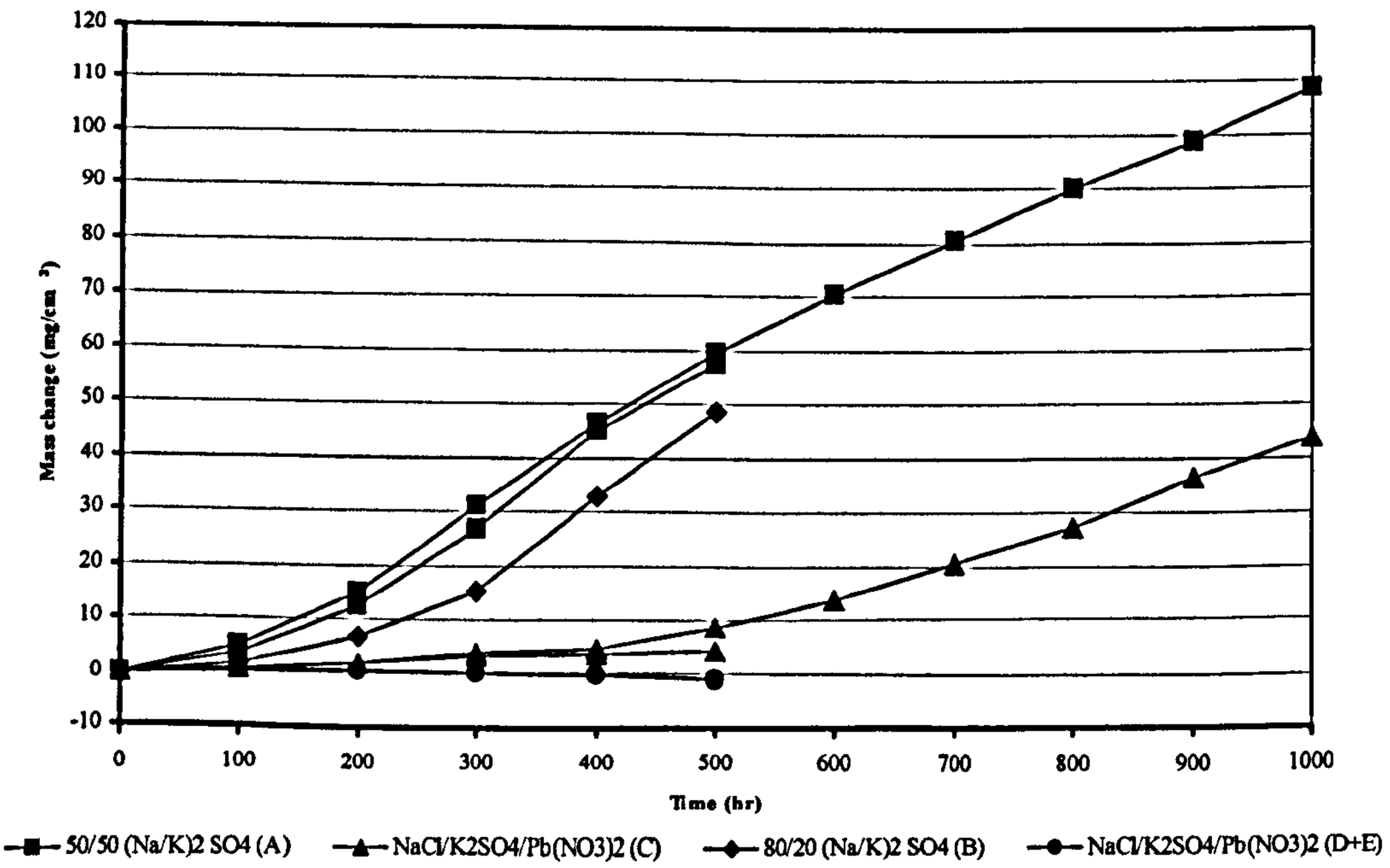

Figure 4.3: Comparison of deposit compositions with a flux of 15µg/cm²/h, in 100vpm SO_2/100vpm HCl; on uncoated IN738LC at 700°C, from test 1.

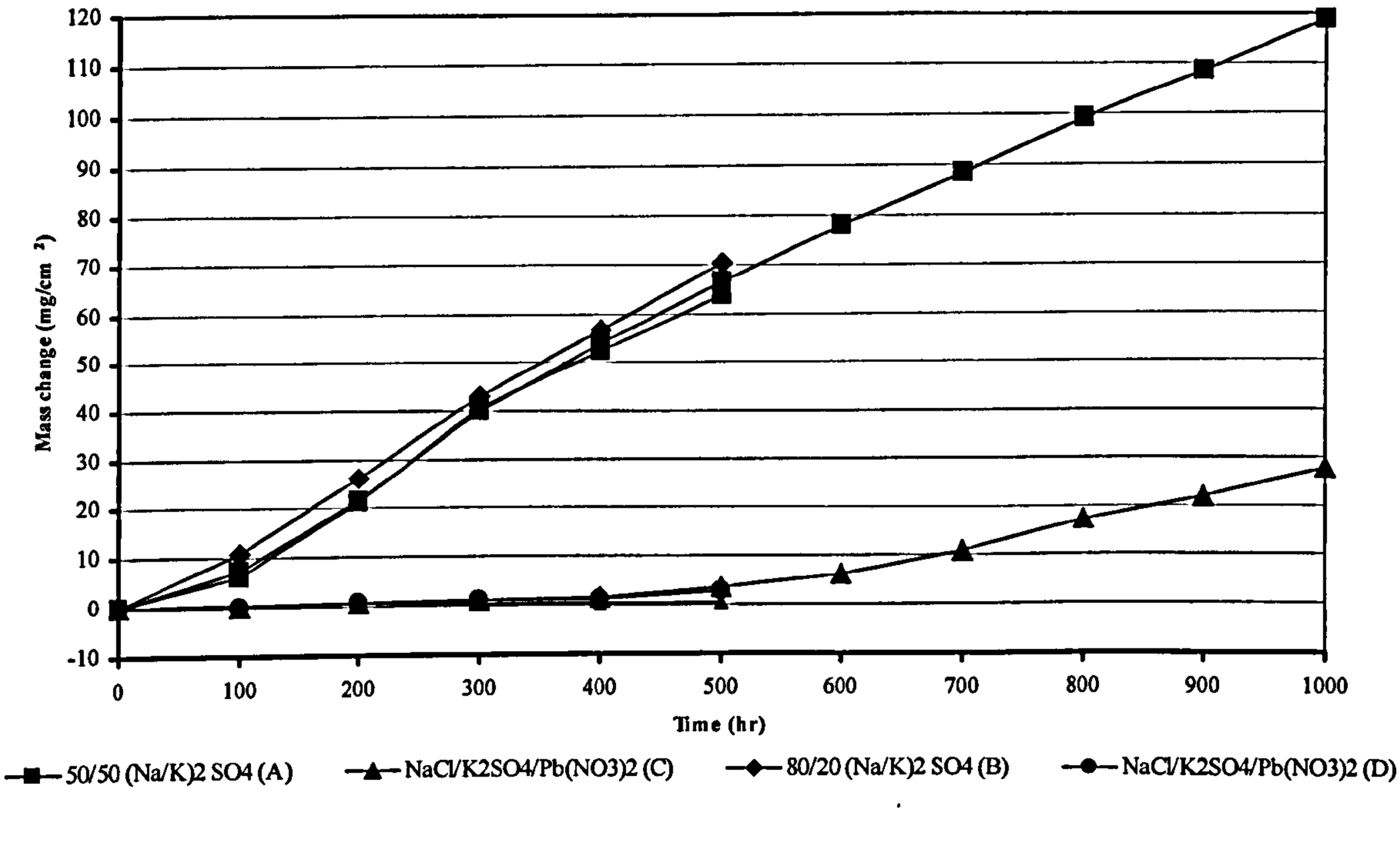

Figure 4.4: Comparison of deposit compositions with a flux of 15µg/cm^2/h, in 300vpm SO_2/500vpm HCl; on uncoated IN738LC at 700°C, from test 2.

4.2.1.2 Platinum aluminised coated IN738 LC:

For the PtAl coated alloy, the alkali deposits also caused higher general corrosion damage that the deposits containing lead (Figure 4.5 to Figure 4.8).

As observed when uncoated, the increase in SO_2 concentration from 20 to 300 vpm, increases the observed maximum mass change after 500 h of exposure i.e. from ~ 0 to 10 mg/cm^2 (test 3, Figure 4.5) to ~ 40 to 50 mg/cm^2 (test 2, Figure 4.8).

In the 20 vpm SO_2/10 vpm HCl gas, the corrosion damage was practically the same for the PtAl coated IN738 as for the uncoated IN738LC (test 3, Figure 4.5 and test 3 Figure 4.1).

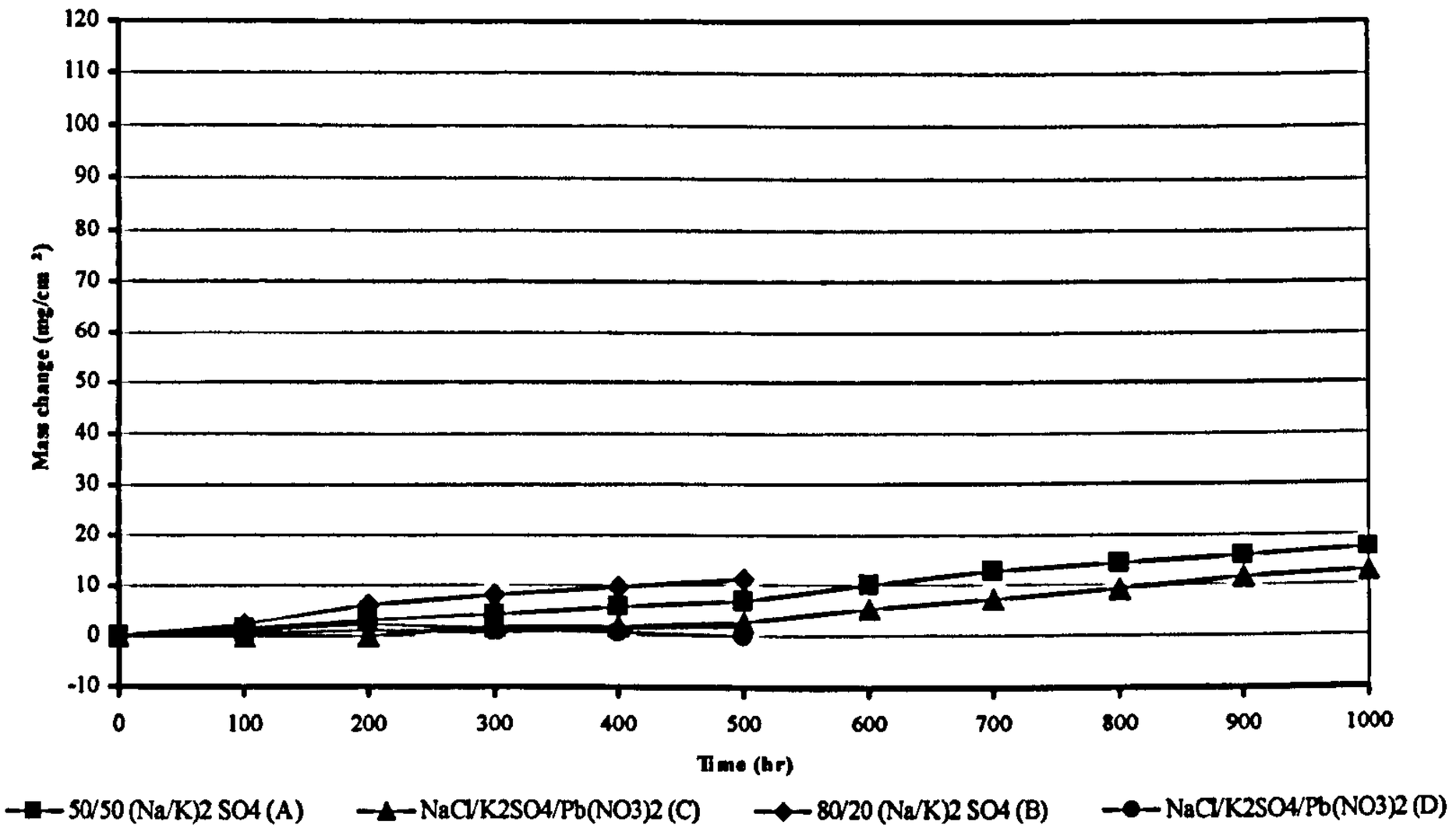

Figure 4.5: Comparison of deposit compositions with a flux of 15µg/cm²/h, in 20vpm SO_2/10vpm HCl; on PtAl coated IN738LC at 700°C, from test 3.

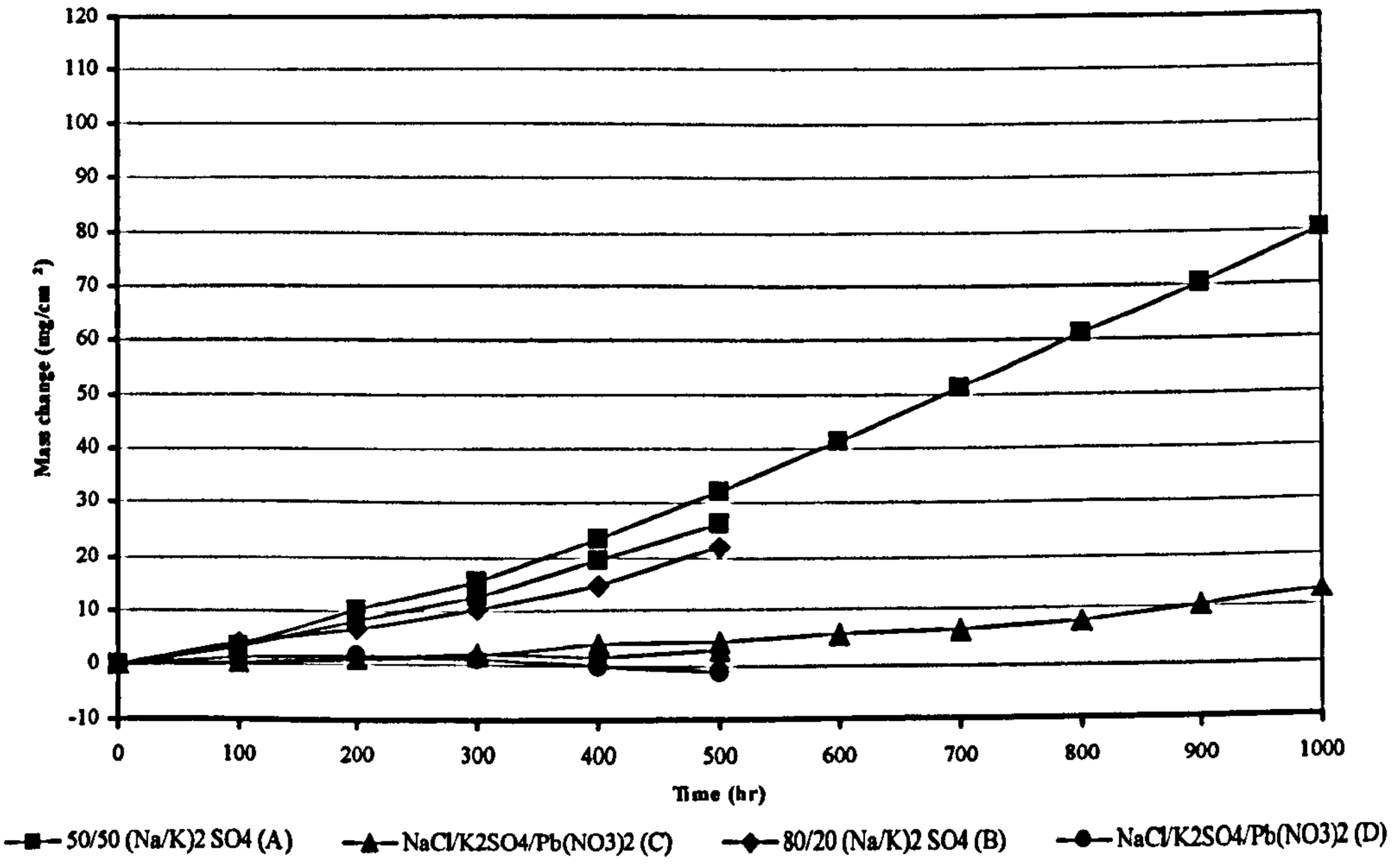

Figure 4.6: Comparison of deposit compositions with a flux of 15µg/cm²/h, in 100vpm SO_2/100vpm HCl; on PtAl coated IN738LC at 700°C, from test 1.

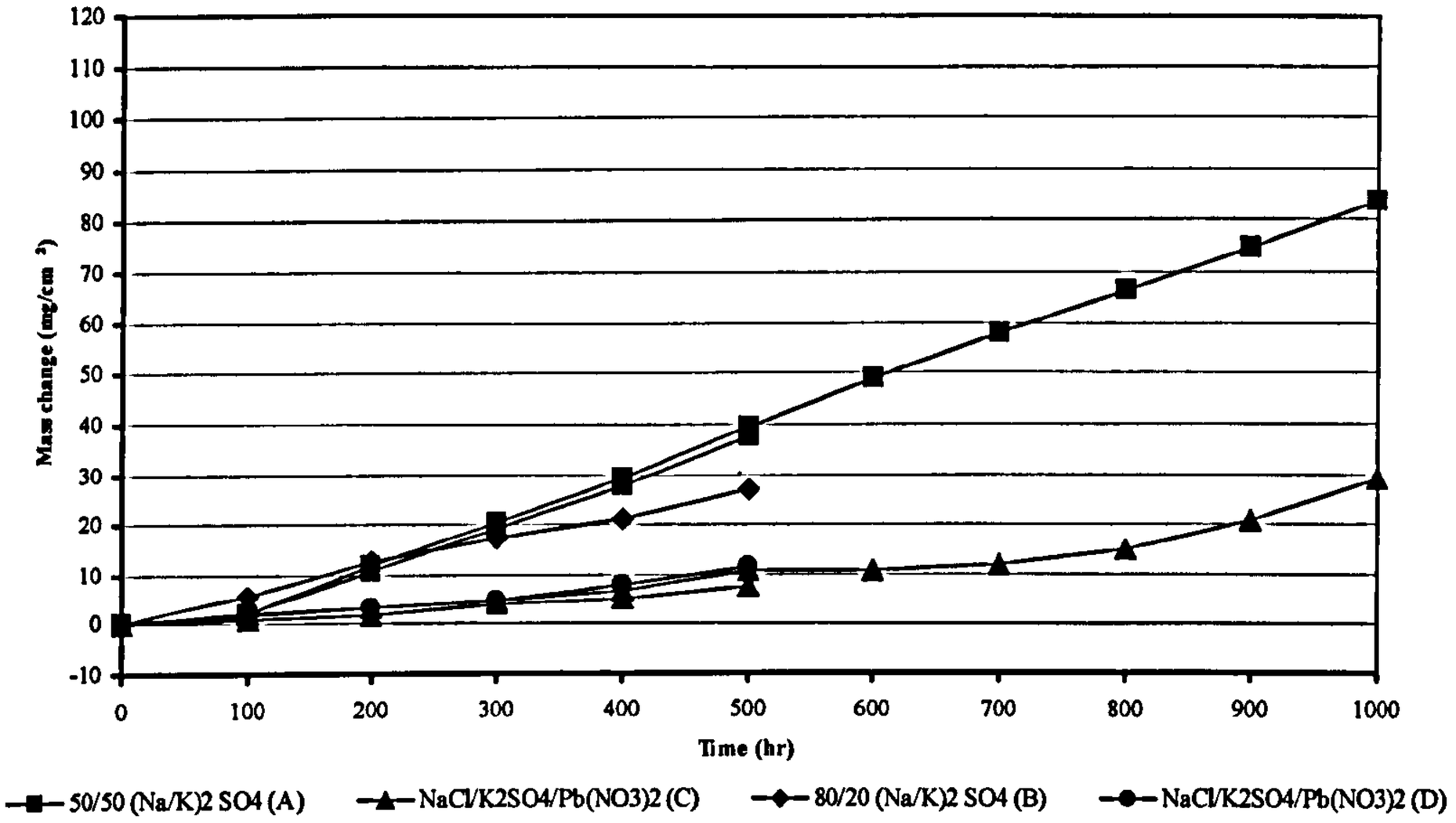

Figure 4.7: Comparison of deposit compositions with a flux of 15µg/cm²/h, in 300vpm SO_2/100vpm HCl; on PtAl coated IN738LC at 700°C, from test 5.

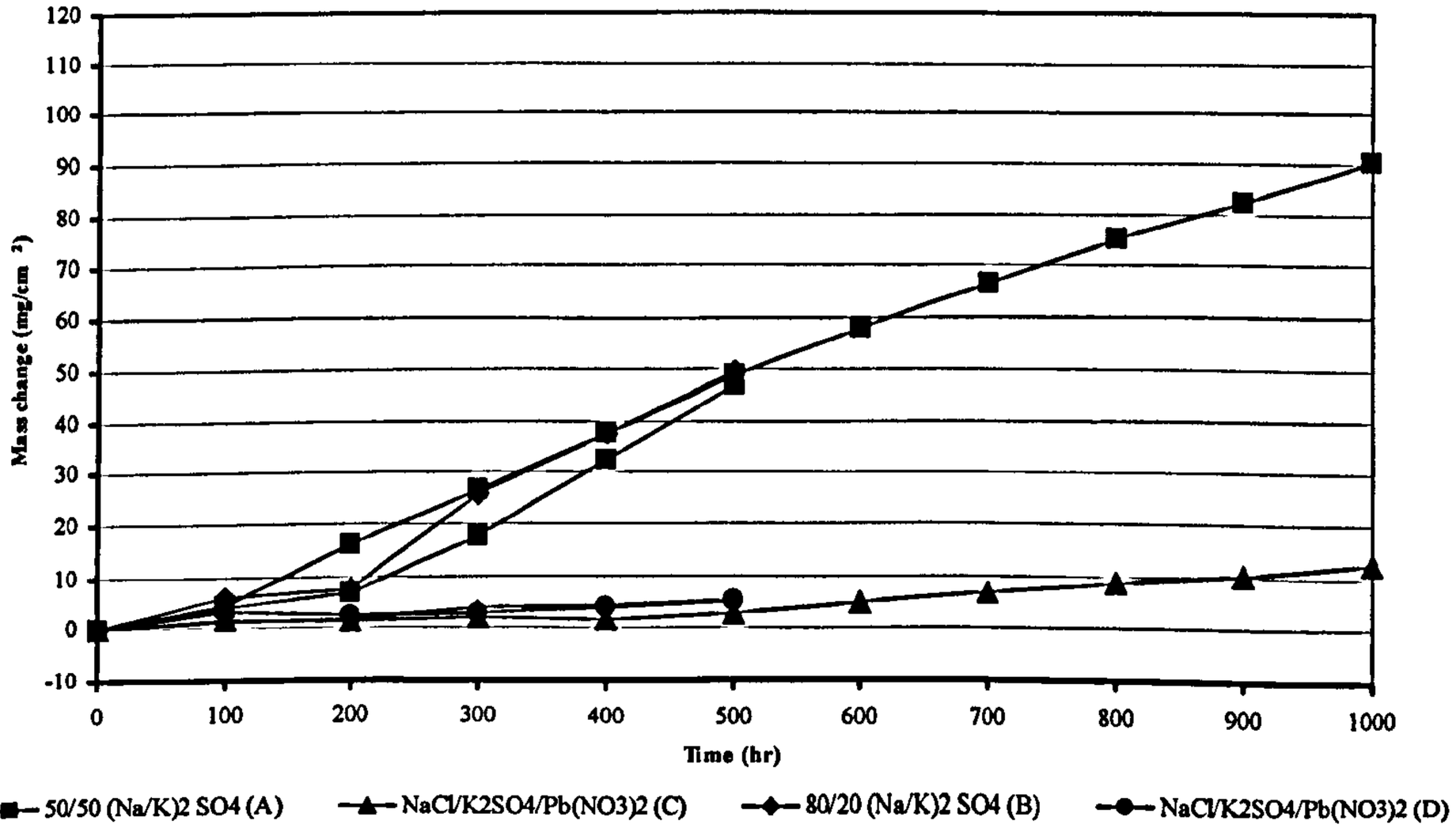

Figure 4.8: Comparison of deposit compositions with a flux of 15µg/cm²/h, in 300vpm SO_2/500vpm HCl; on PtAl coated IN738LC at 700°C, from test 2.

4.2.1.3 Uncoated CMSX-4 at 700°C:

In a general comparison with the IN738LC material when tested in the same environment, i.e. the same gases composition, for this single crystal material, the alkali deposits also caused higher general corrosion damage than the deposits containing lead.

Also, a general increase in maximum mass change was observed; as the SO_2 concentration was increased from 20 to 300 vpm, the increase in the observed maximum mass change was noticeable after 500 h of exposure, i.e. from ~0 to -100 mg/cm^2 (test 5, Figure 4.11) indicating extensive scale/deposit spallation, to ~80 to 90 mg/cm^2 (test 2 Figure 4.12) showing much less spallation. These data are plotted in Figure 4.9 to Figure 4.12.

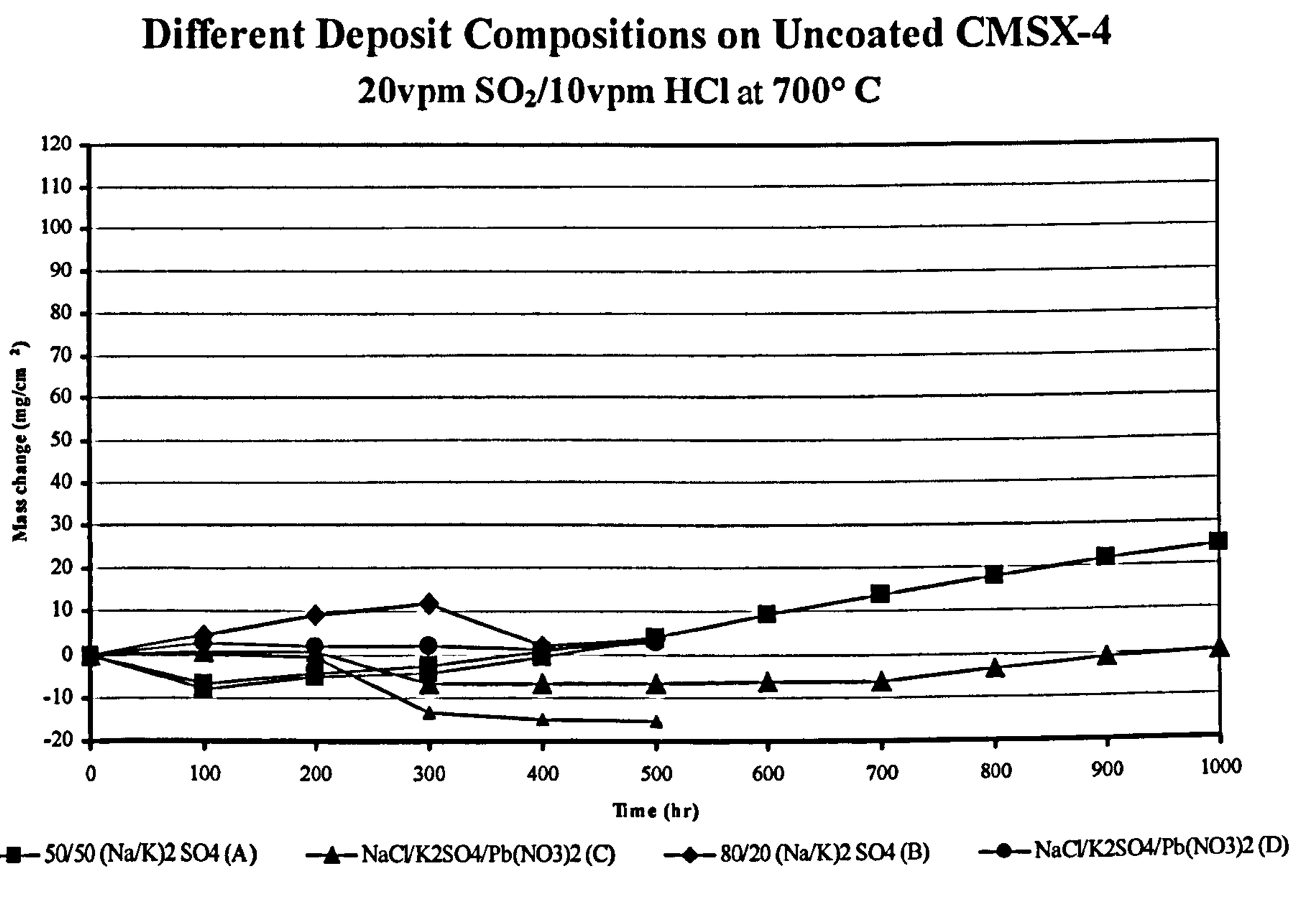

Figure 4.9: Comparison of deposit compositions with a flux of 15µg/cm^2/h, in 20vpm SO_2/10vpm HCl; on uncoated CMSX4 at 700°C, from test 3.

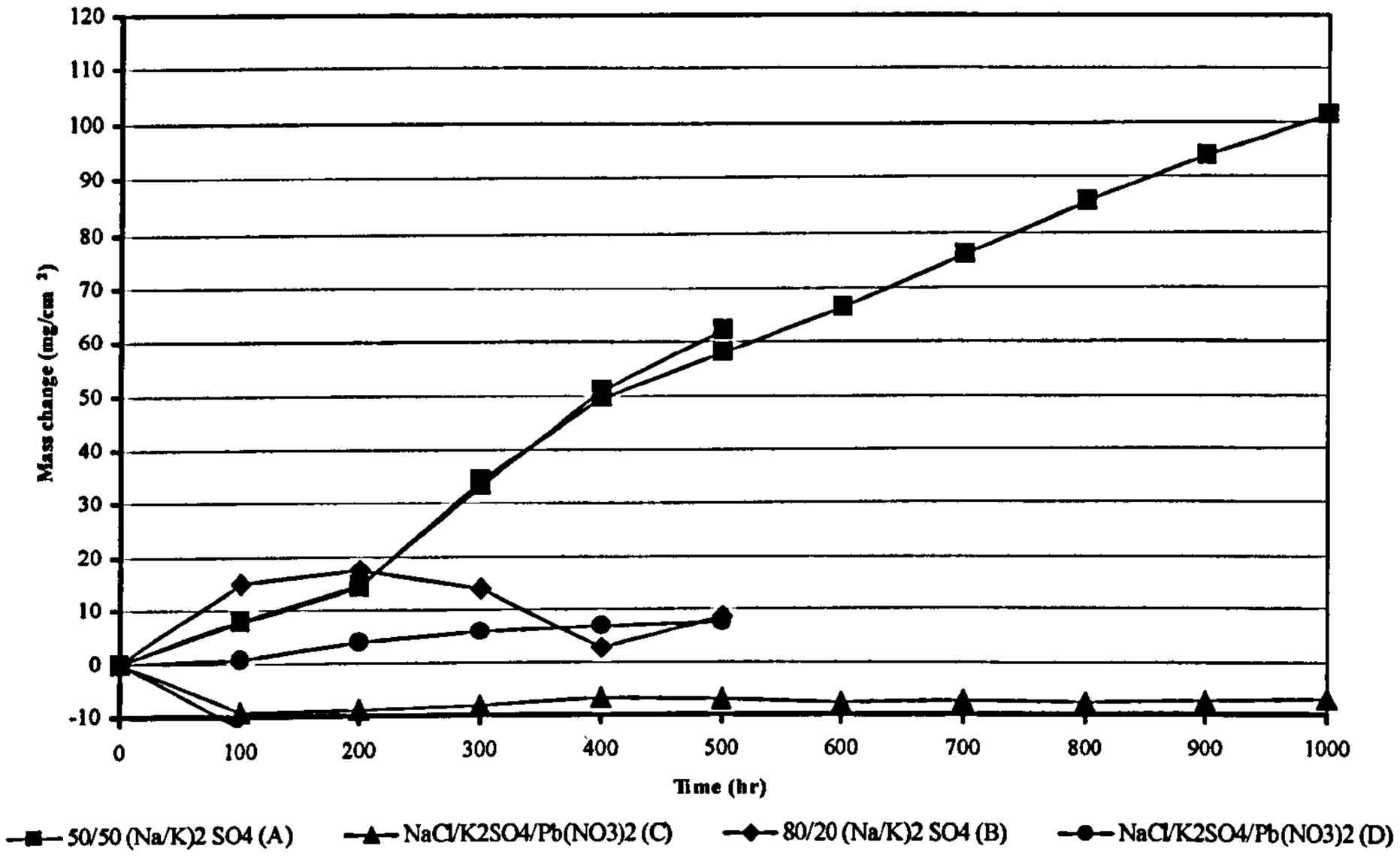

Figure 4.10: Comparison of deposit compositions with a flux of 15µg/cm²/h, in 100vpm SO_2/100vpm HCl; on uncoated CMSX4 at 700°C, from test 1.

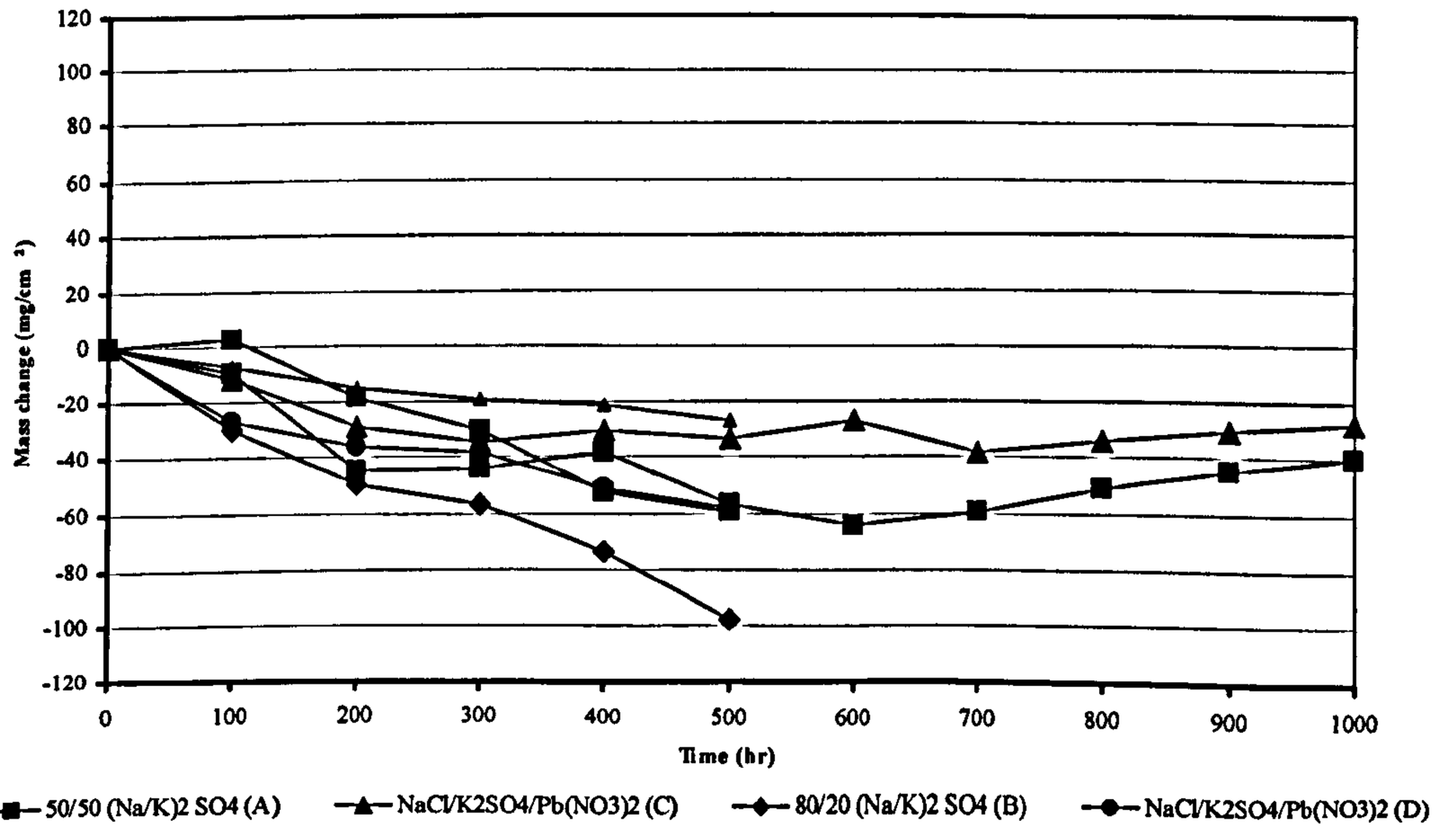

Figure 4.11: Comparison of deposit compositions with a flux of 15µg/cm²/h, in 300vpm SO_2/100vpm HCl; on uncoated CMSX4 at 700°C, from test 5.

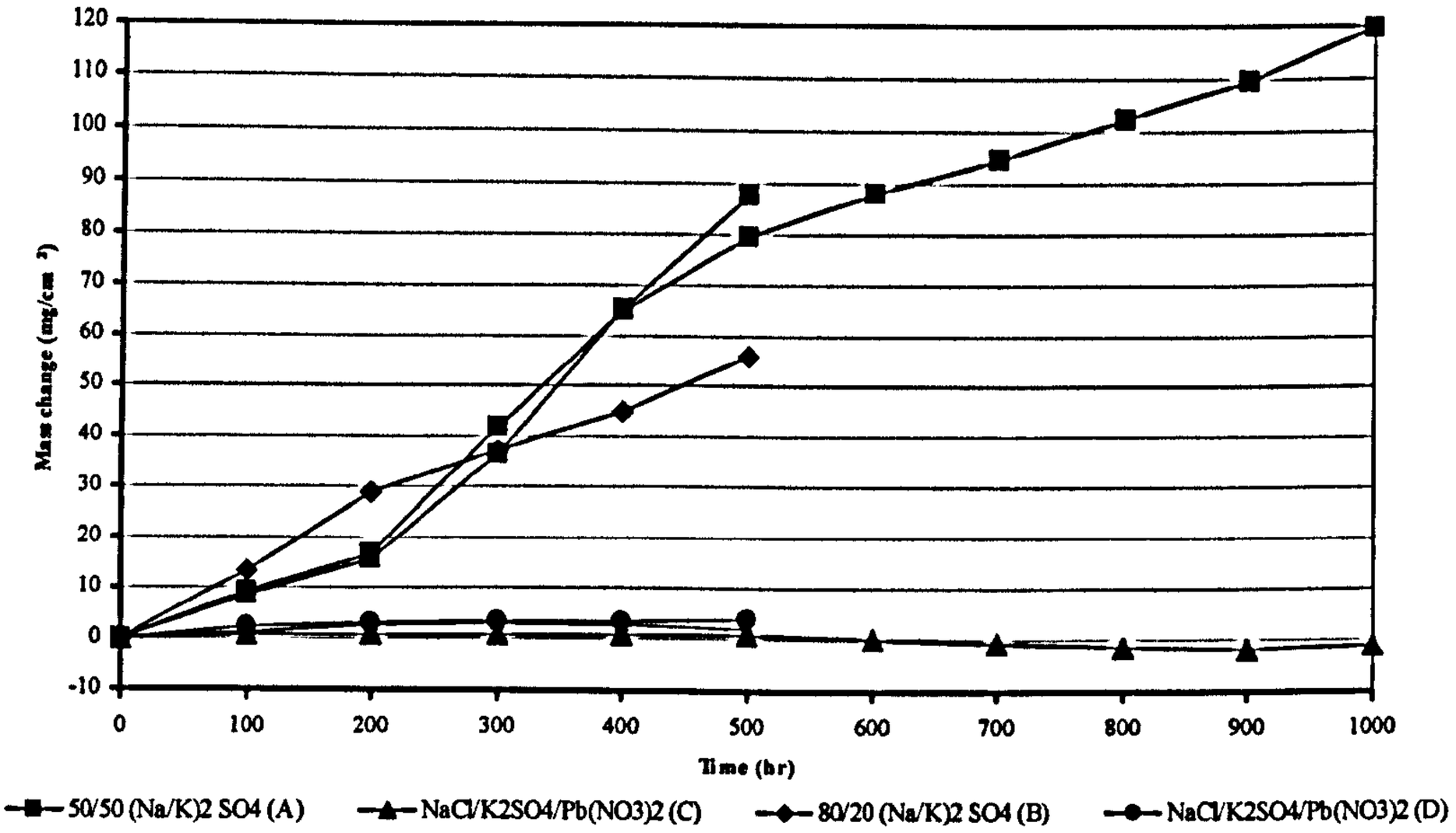

Figure 4.12: Comparison of deposit compositions with a flux of 15µg/cm^2/h, in 300vpm SO_2/500vpm HCl; on uncoated CMSX4 at 700°C, from test 2.

4.2.1.4 Platinum Aluminized coated CMSX-4 at 700°C:

When this single crystal is coated, the alkali deposits also caused higher general corrosion damage than the deposits containing lead. However, the maximum mass change is less than when uncoated, and the graph trend is more uniform. In this case, the SO_2/ HCl concentration did not show much difference in terms of the maximum mass change between the 20 vpm SO_2 /10 vpm HCl combination (test 3, Figure 4.13) and the 100 vpm SO_2 /100 vpm HCl combination (test 1, Figure 4.14), where the maximum mass change was ~ 10 mg/cm^2 after 500 h of exposure. However, at times greater than 500h, the mass change in the 100 vpm SO_2/100 vpm HCl environment was observed to increase for the alkali salt coated sample.

When the SO_2 was increased to 300 vpm in combination with 500 vpm HCl (test 2, Figure 4.15), there was slightly less general corrosion damage (30 mg/cm^2) than for the 300 vpm SO_2/100 vpm HCl gas combination (40 mg/cm^2, test 5, Figure 4.16). Both values were greater than that measured in the 100 vpm SO_2/100 vpm HCl environment.

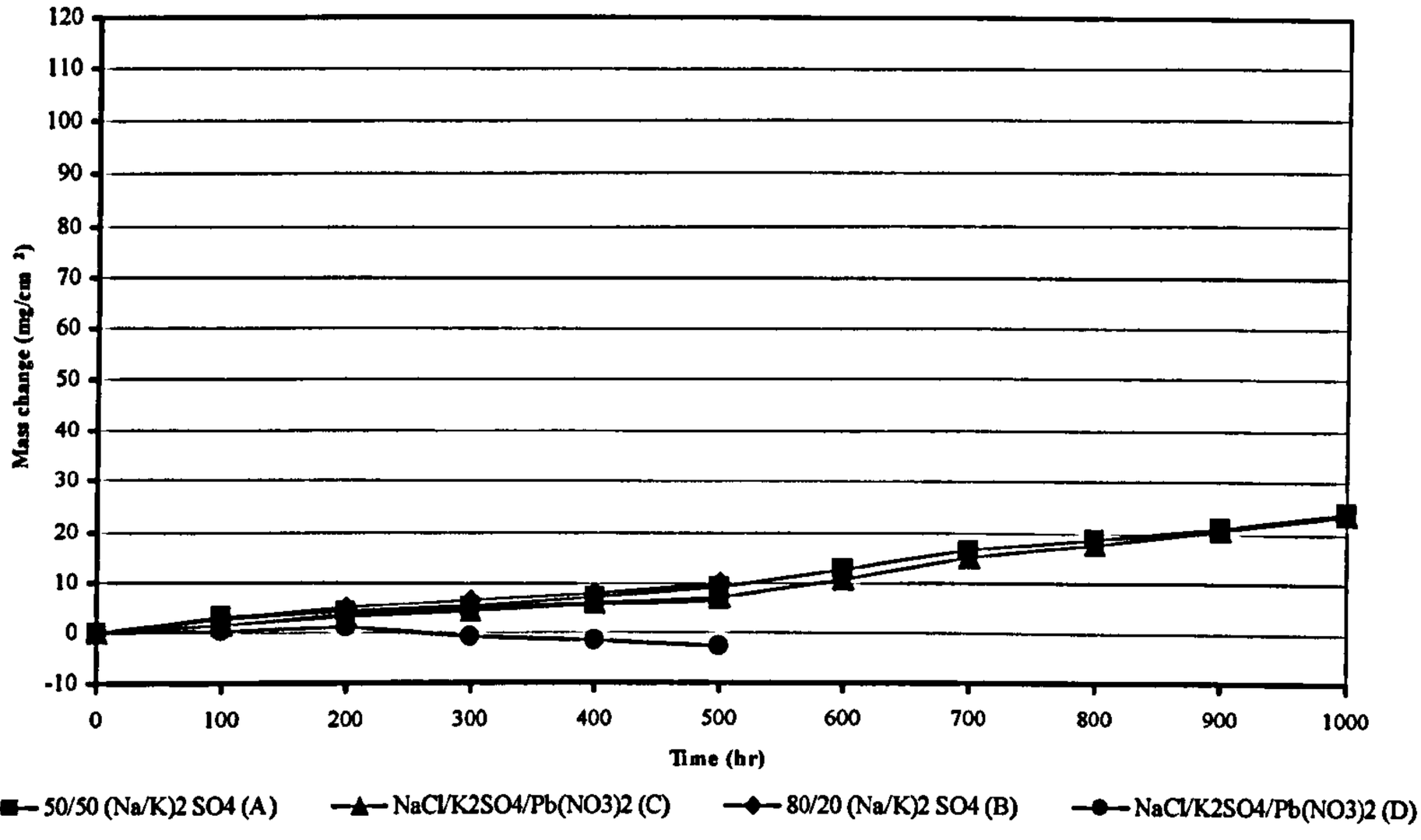

Figure 4.13: Comparison of deposit compositions with a flux of 15µg/cm^2/h, in 20vpm SO_2/10vpm HCl; on PtAl coated CMSX4 at 700°C, from test 3.

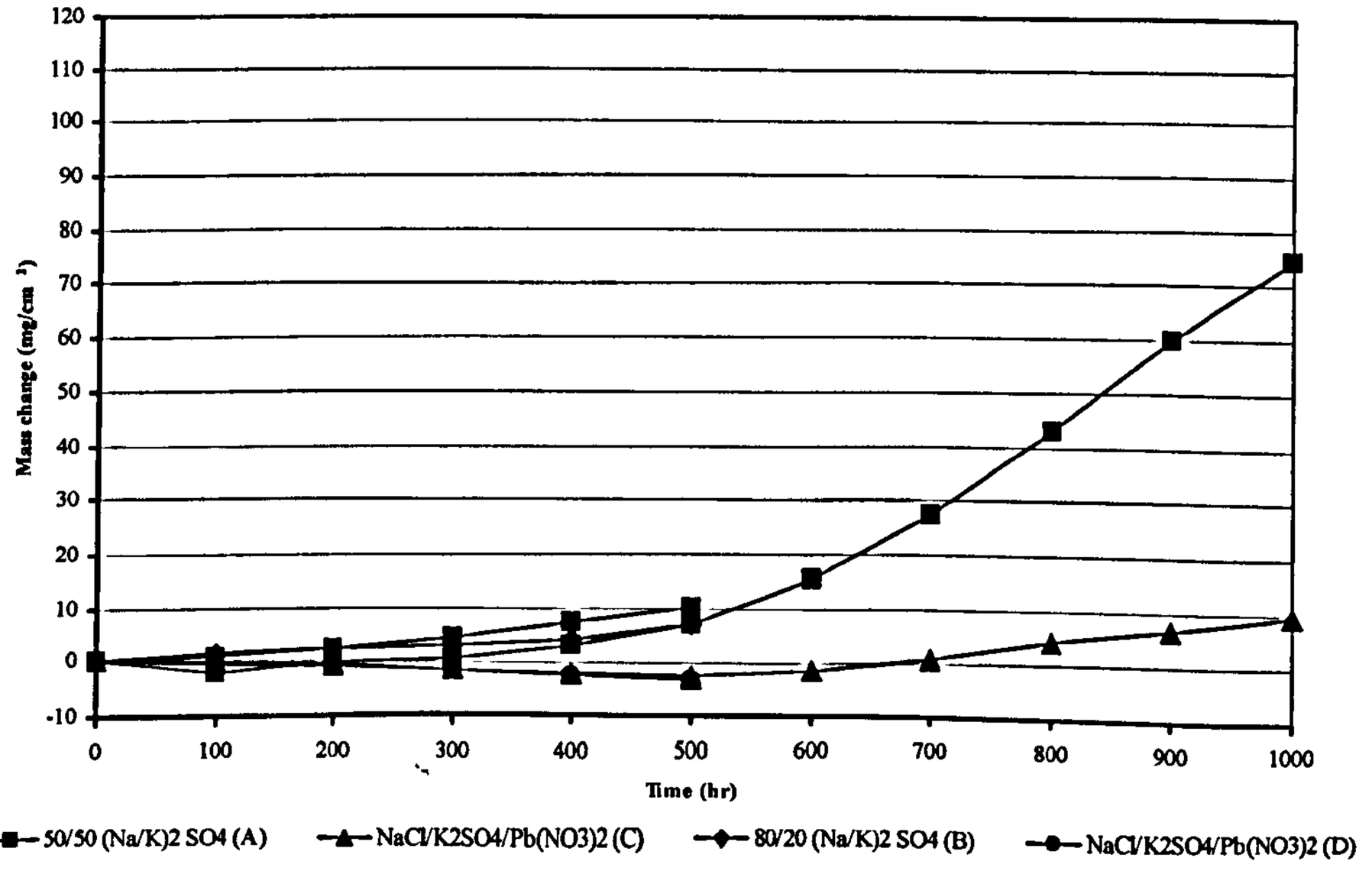

Figure 4.14: Comparison of deposit compositions with a flux of 15µg/cm^2/h, in 100vpm SO_2/100vpm HCl; on PtAl coated CMSX4 at 700°C, from test 1.

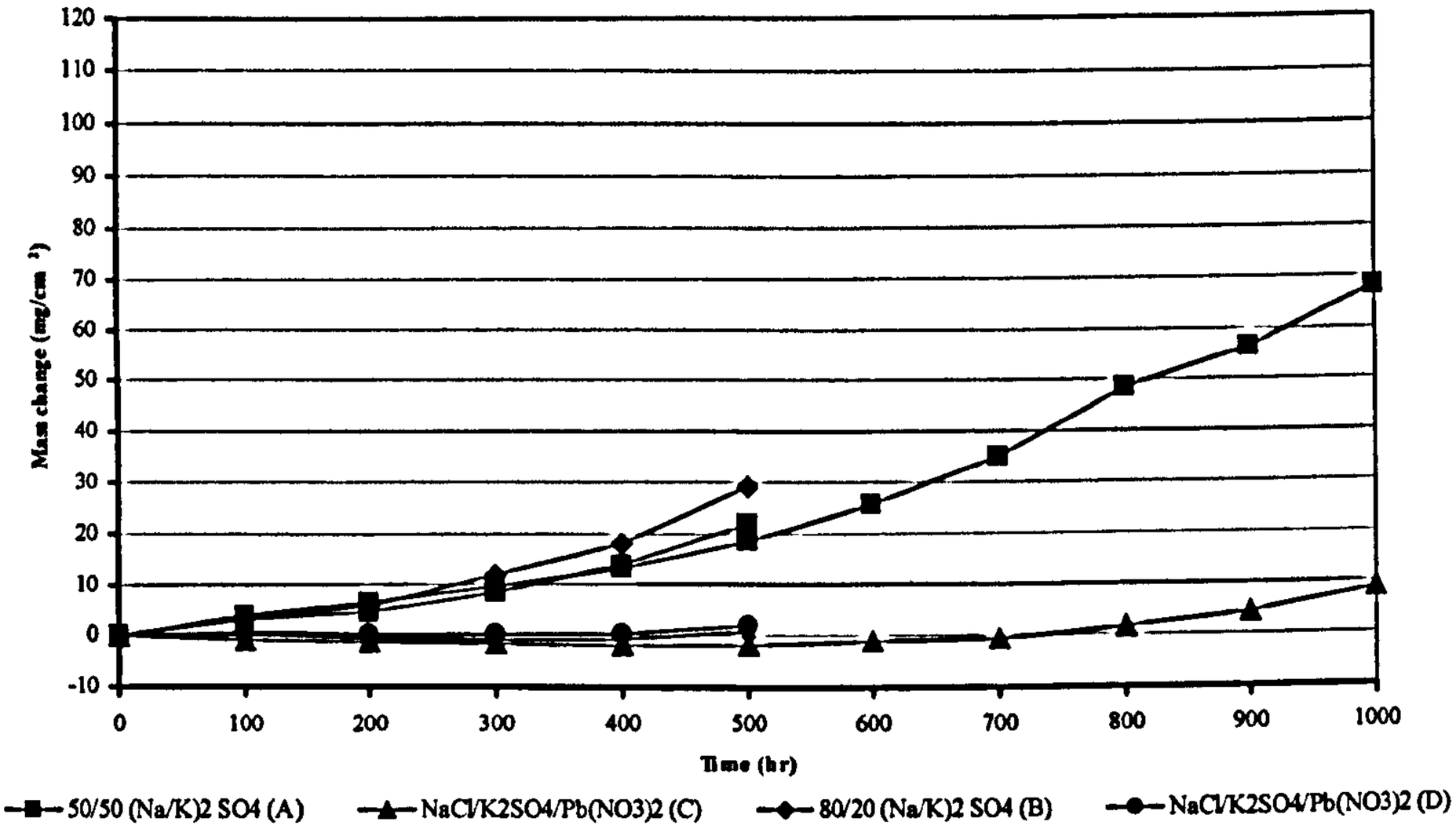

Figure 4.15: Comparison of deposit compositions with a flux of 15µg/cm^2/h, in 300vpm SO_2/500vpm HCl; on PtAl coated CMSX4 at 700°C, from test 2.

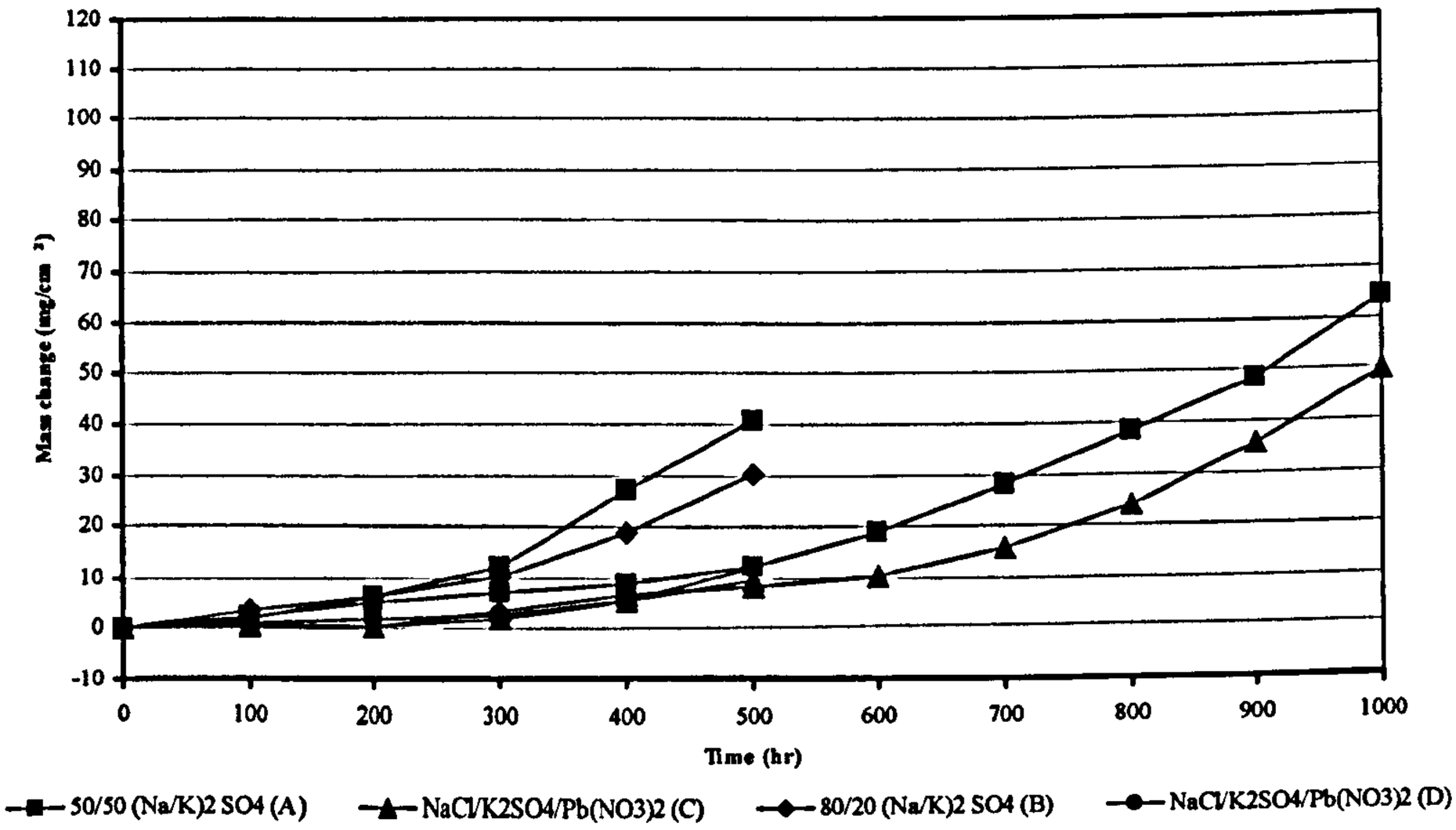

Figure 4.16: Comparison of deposit compositions with a flux of 15µg/cm^2/h, in 300vpm SO_2/100vpm HCl; on PtAl coated CMSX4 at 700°C, from test 5.

4.2.2 Mass change data (Phase 2)

The second part of the general experimentation matrix (Table 3.1, section 3.1) aimed to study the effect of temperature, 700 and 900°C; three different model gas compositions including, SO_2 and HCl, and only one salt composition 80/20 $(Na/K)_2SO_4$ with different flux concentrations from 1.5 to 15µg/cm^2/h were used. The samples were single crystal CMSX-4 and SC^2, both uncoated and platinum aluminised coated. The data obtain from this stage are shown in the next set of graphs regarding mass change; however, the accurate assessment of the performance of the materials in all tests, was determined by the dimensional metrology techniques described in section 3.5, and reported in section 4.4.

4.2.2.1 Mass change on CMSX-4 (uncoated and with a PtAl coating)

At 700°C, the trend for uncoated CMSX-4 shows a negative mass change, probably due to spalling which was observed to increase as the SO_2 concentration was increased from 50 to 500 vpm, Figure 4.18 (test 7) and Figure 4.19 (test 9). However, this tendency changed in the presence of HCl, Figure 4.17 (test 11), where it can be seen that by increasing the flux concentration of the salt deposit from 1.5 to 15µg/cm^2/h, the corrosion damage is increased; this tendency is also observed when the material is PtAl coated.

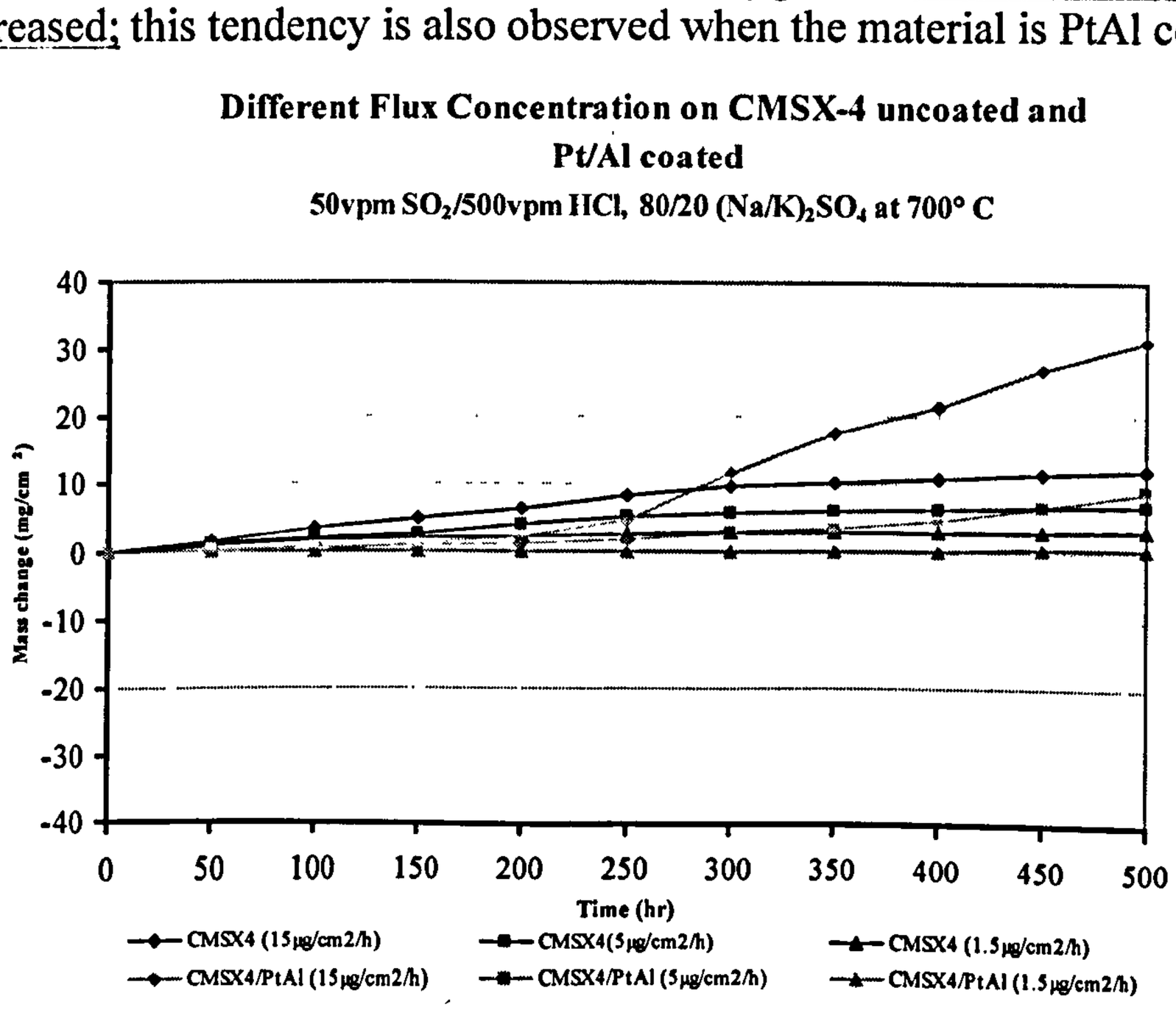

Figure 4.17: Comparison of deposit flux concentration: 1.5, 5 and 15µg/cm ^{2}/h on bare CMSX-4 and PtAl coated in 50 SO_2/500 HCl vpm at 700° C, from test 11.

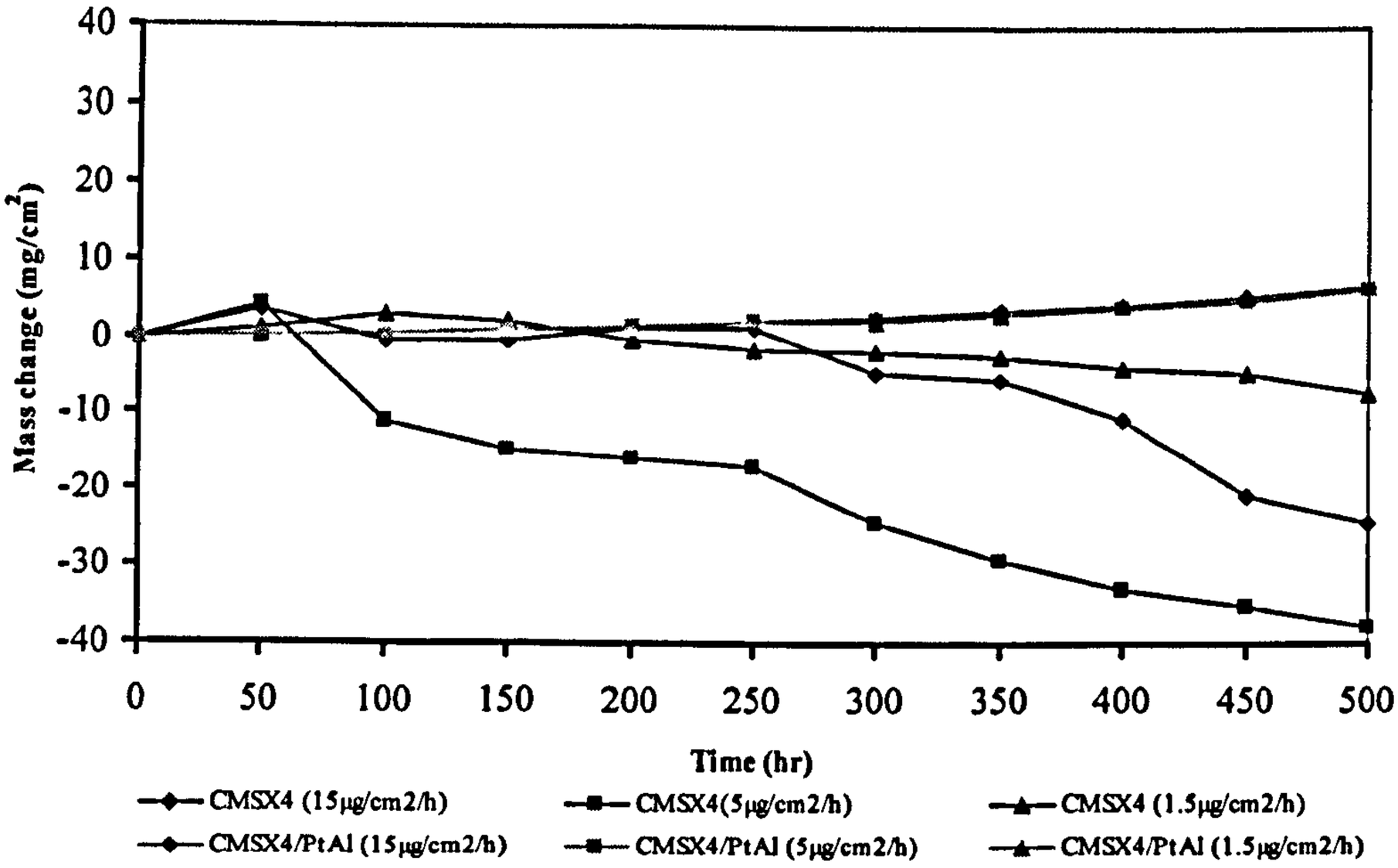

Figure 4.18: Comparison of deposit flux concentration: 1.5, 5 and 15µg/cm ^{2}/h on bare CMSX-4 and PtAl coated in 50 vpm SO_2 at 700° C, from test 7.

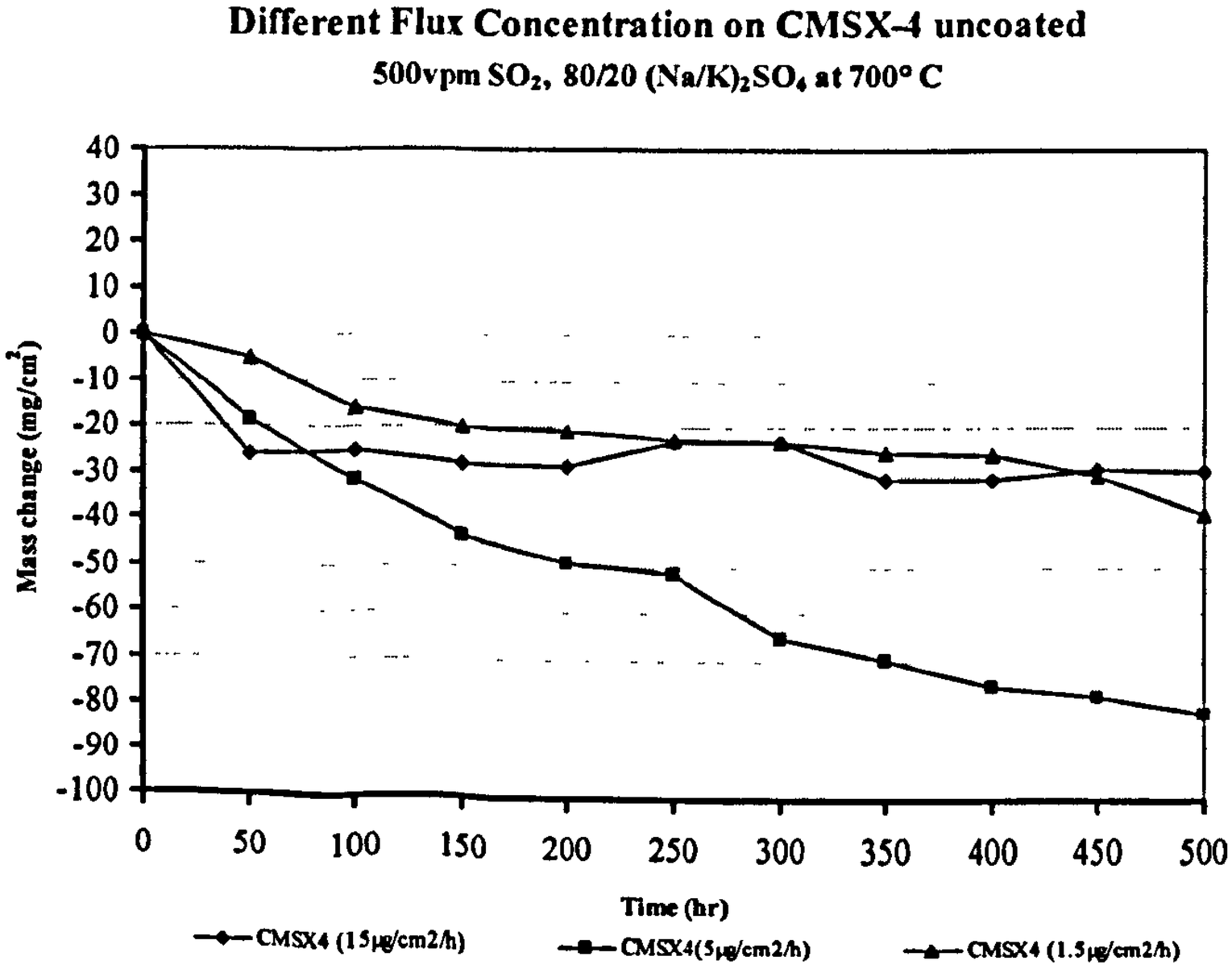

Figure 4.19: Comparison of deposit flux concentration: 1.5, 5 and 15µg/cm ^{2}/h on bare CMSX-4 in 500 vpm SO_2 at 700° C, from test 9.

At 900°C, the trend for uncoated CMSX-4 at 900° C showed negative mass change only in the presence of HCl, Figure 4.20 (test 12). As the SO_2 concentration was increased from 50 to 500 vpm, Figure 4.21 (test 8) and Figure 4.22 (test 10), the total mass change increased from 120 to 160 mg/cm^2 respectively.

It is also seen that, on increasing the flux concentration of the salt deposit from 1.5 to 15µg/cm^2/h, the extent of corrosion damage increased; however, this tendency is only observed in the 500 vpm SO_2 environment Figure 4.22 (test 10) and when the material is PtAl coated, Figure 4.21 (test 8).

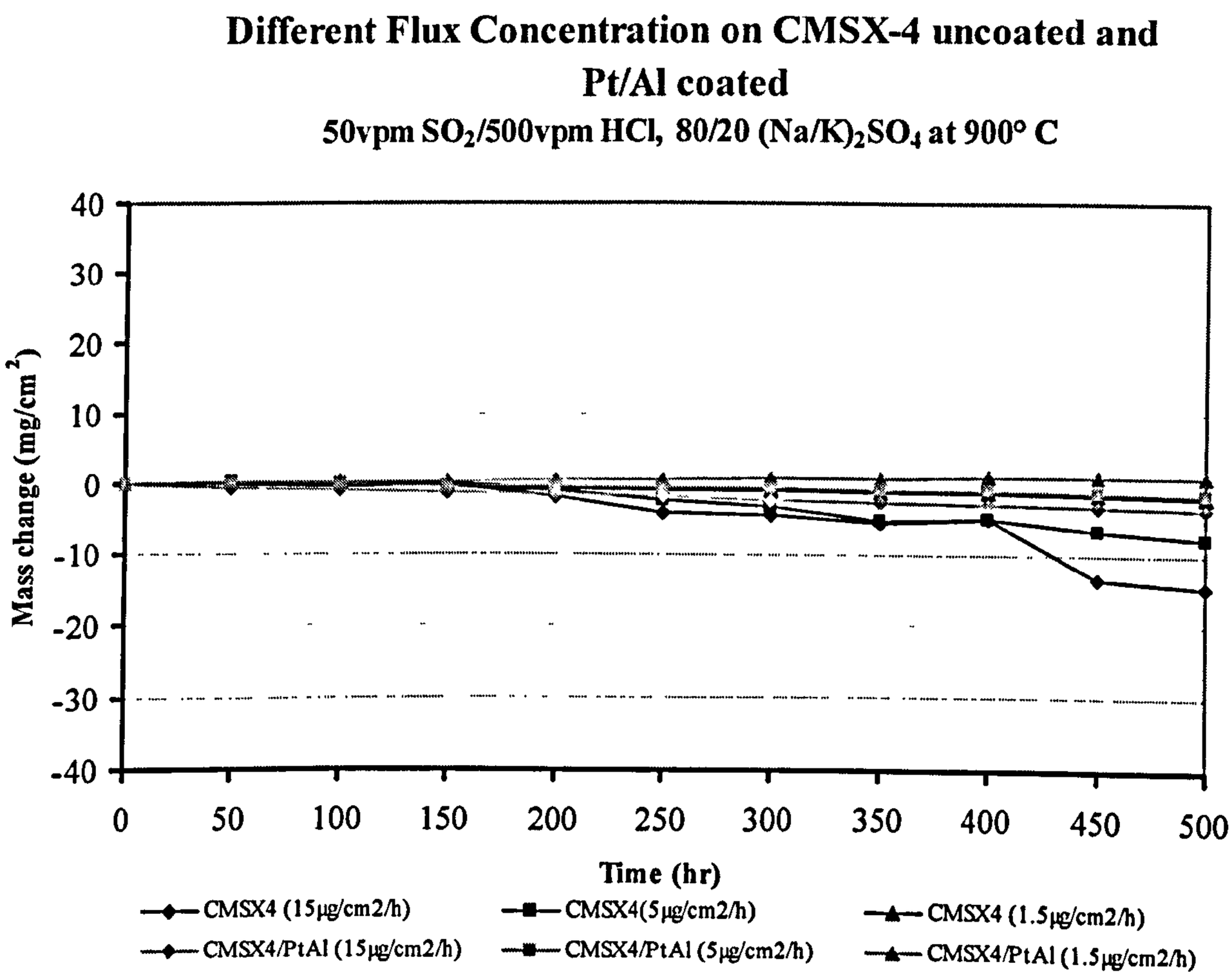

Figure 4.20: Comparison of deposit flux concentration: 1.5, 5 and 15µg/cm ^{2}/h on bare CMSX-4 and PtAl coated in 50 SO_2/ 500 HCl vpm at 900° C, from test 12.

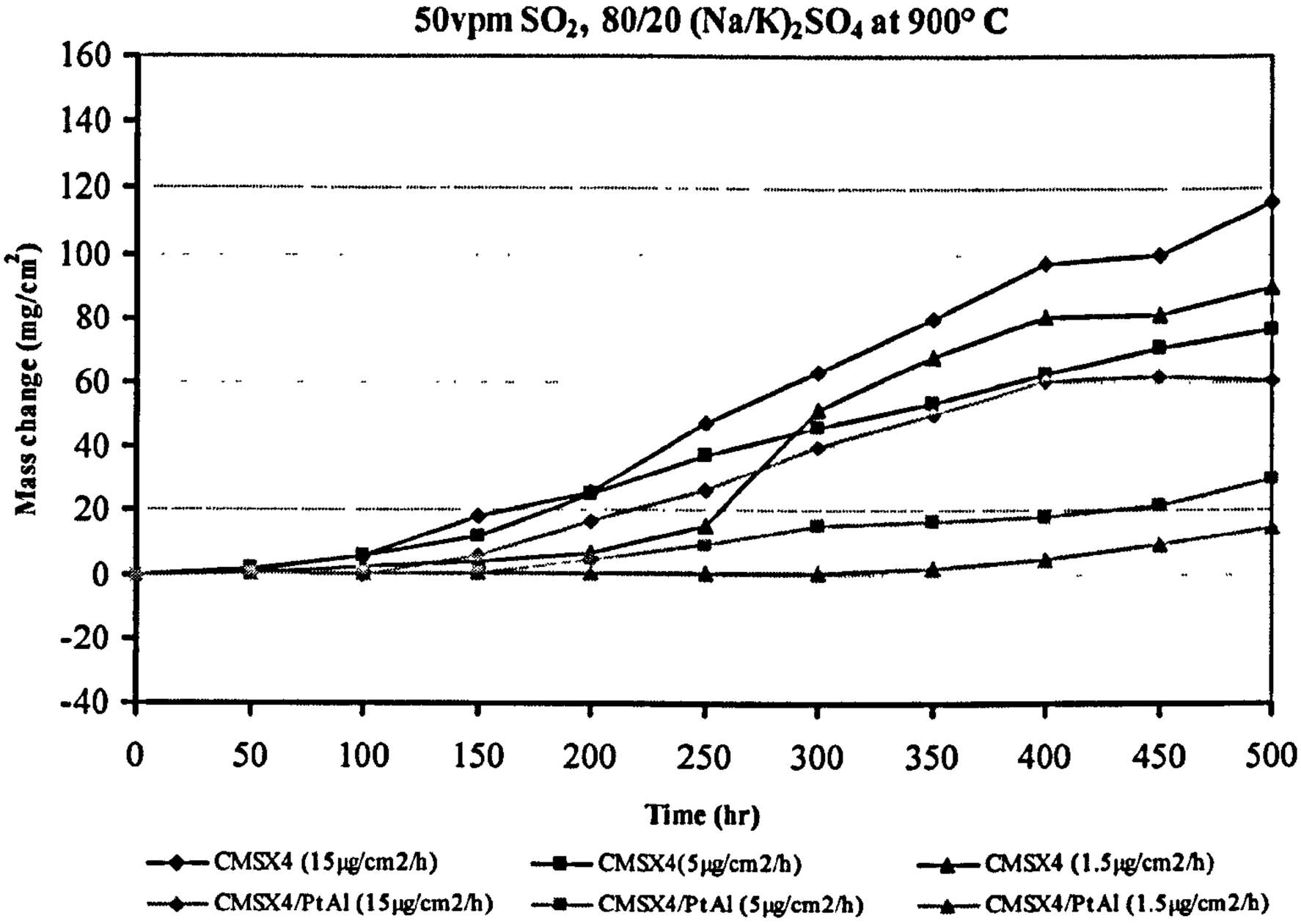

Figure 4.21: Comparison of deposit flux concentration: 1.5, 5 and 15µg/cm ^{2}/h on bare CMSX-4 and PtAl coated in 50 vpm SO_2 at 900° C, from test 8.

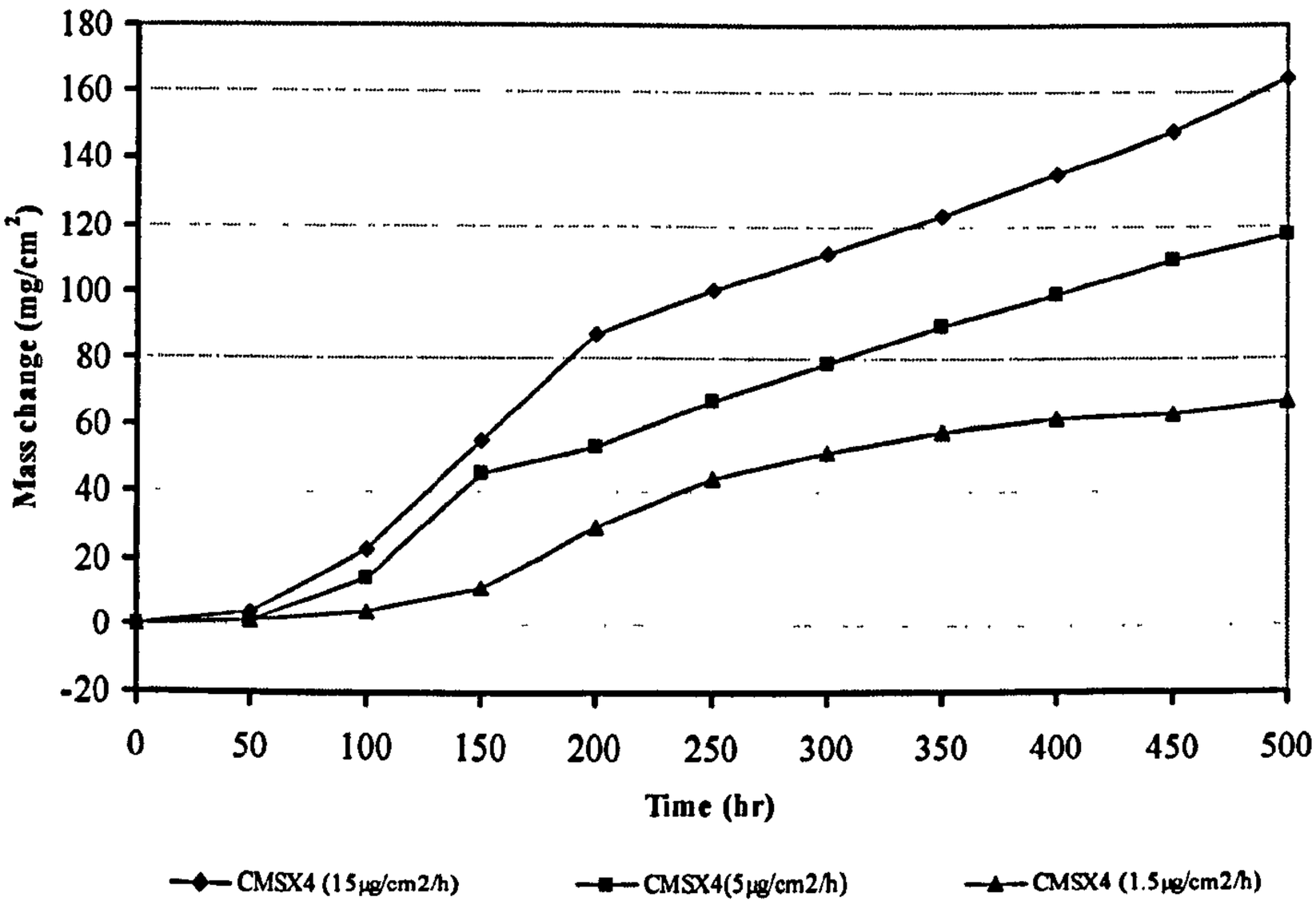

Figure 4.22: Comparison of deposit flux concentration: 1.5, 5 and 15µg/cm ^{2}/h on bare CMSX-4 and PtAl coated in 500 vpm SO_2 at 900° C, from test 10.

4.2.2.2 Mass change on SC^2 (uncoated and with PtAl coating)

At 700°C, the total mass change for the uncoated SC^2 increased as the SO_2 concentration was increased from 50 to 500 vpm, Figure 4.24 and Figure 4.25. There seems to be slightly less corrosion damage in the HCl gas combination atmosphere, and also when this single crystal is PtAl coated. It is also observed that, on increasing the flux concentration of the salt deposit from 1.5 to 15μg/cm^2/h, the extent of corrosion damage increased for both material systems; the only exception was in Figure 4.25 (test 9), where negative mass change due to spalling occurred during the course of the test.

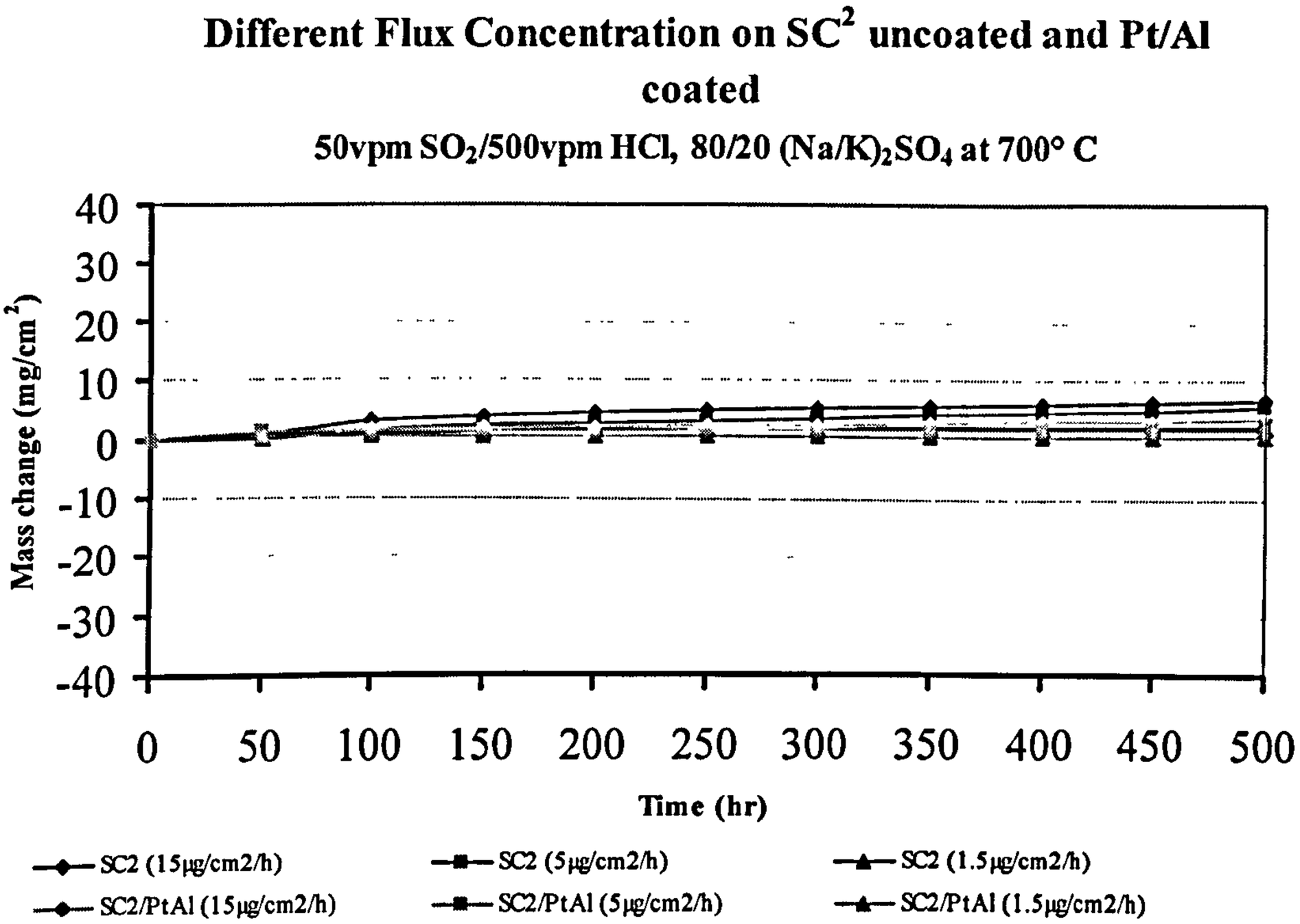

Figure 4.23: Comparison of deposit flux concentration: 1.5, 5 and 15μg/cm ^{2}/h on bare SC^2 and PtAl coated in 50 SO_2/ 500 HCl vpm at 700° C, from test 11.

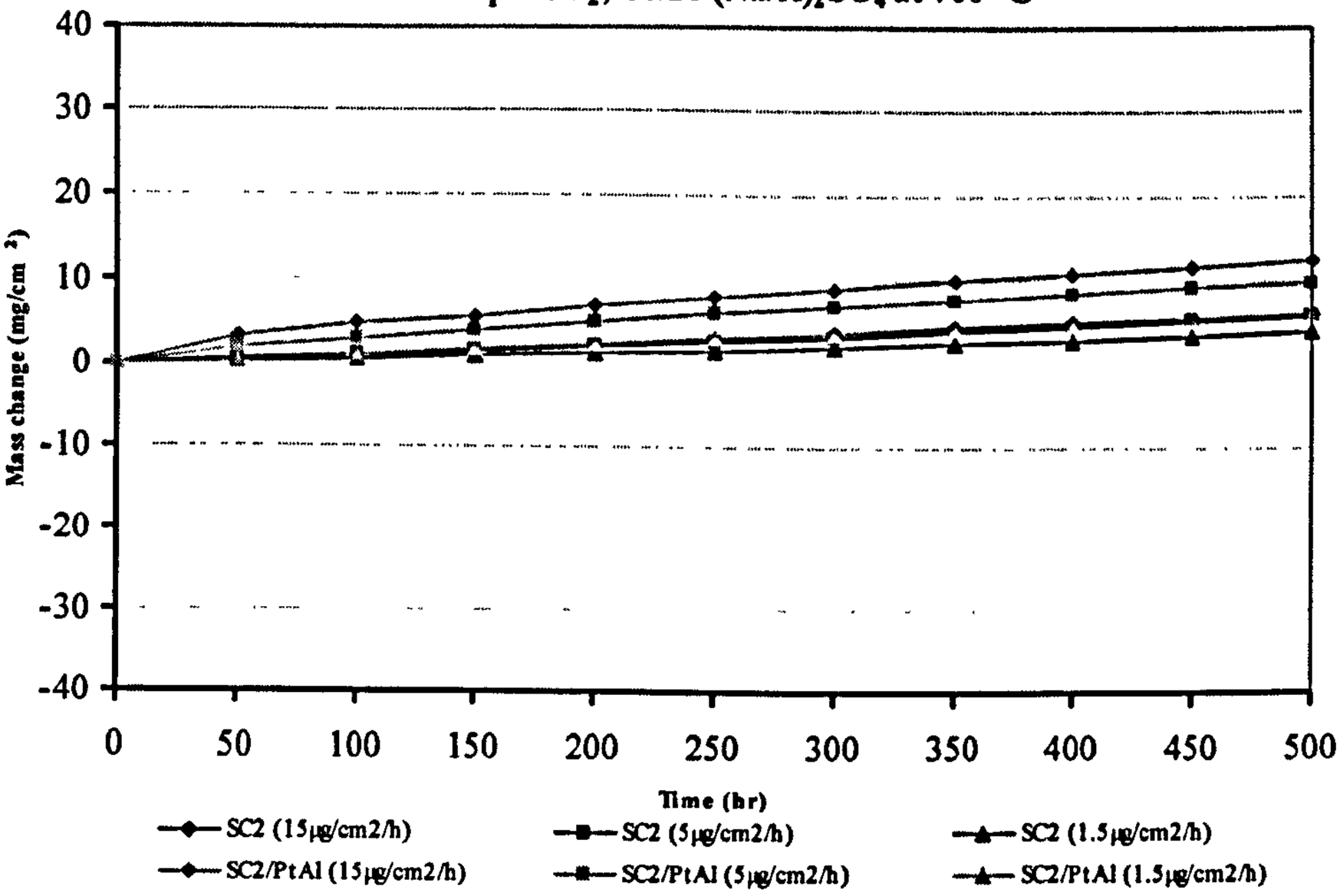

Figure 4.24: Comparison of deposit flux concentration: 1.5, 5 and 15µg/cm ^{2}/h on bare SC^2 and PtAl coated in 50 vpm SO_2 at 700° C, from test 7.

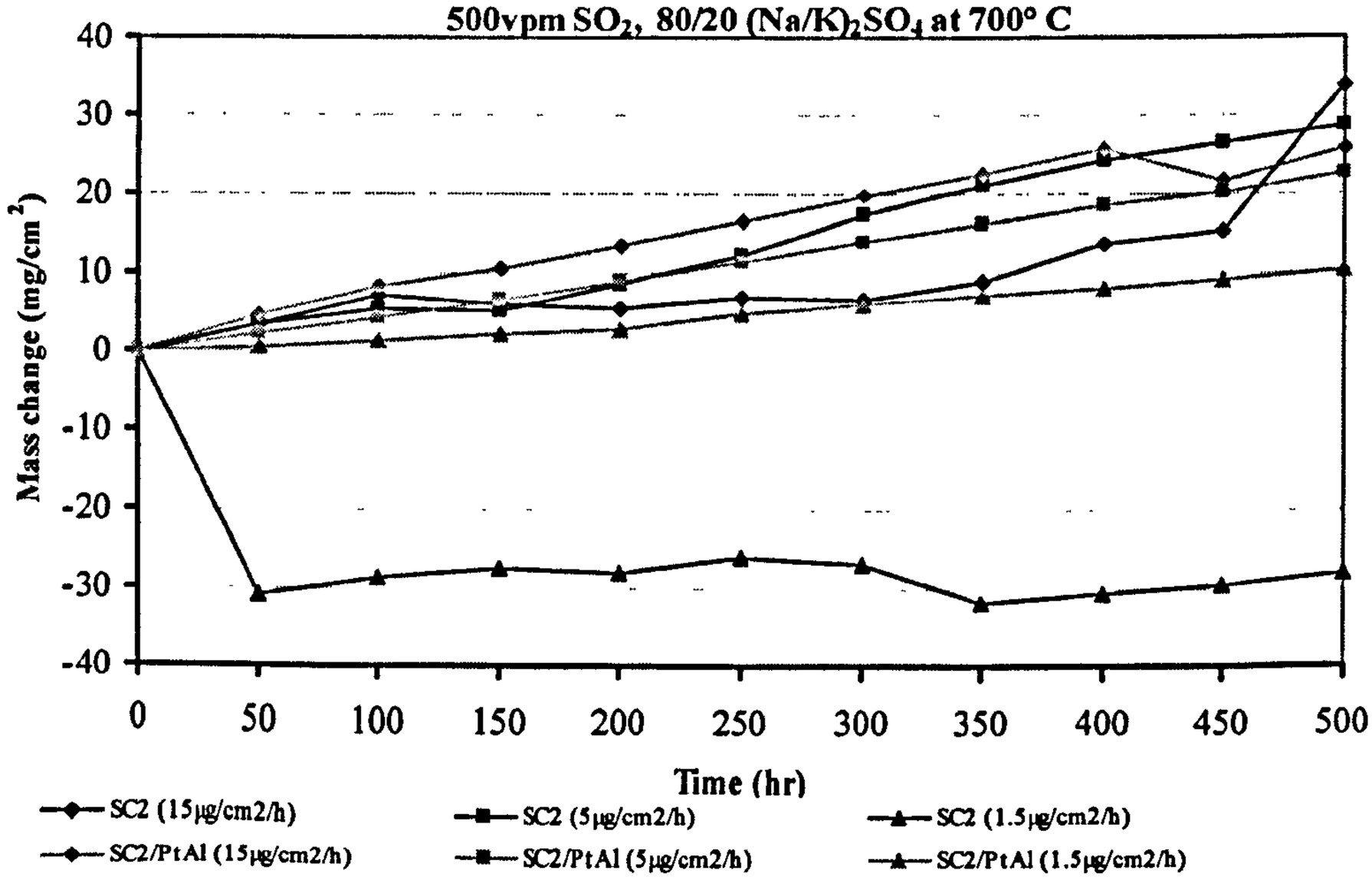

Figure 4.25: Comparison of deposit flux concentration: 1.5, 5 and 15µg/cm ^{2}/h on bare SC^2 and PtAl coated in 500 vpm SO_2 at 700° C, from test 9.

At 900°C, the total mass change for the uncoated SC^2 was considerably increased as the SO_2 concentration changed from 50 to 500 vpm, Figure 4.27 and Figure 4.28. There is notably less corrosion damage in the gas atmosphere with the HCl addition, Figure 4.26, likewise for the case where this single crystal alloy is PtAl coated.

It is also observed that, on increasing the flux concentration of the salt deposit from 1.5 to 15μg/cm^2/h, the extent of corrosion damage was increased for both material systems, with the exception of the 50 vpm SO_2/500 vpm HCl environment, Figure 4.26. These data show that, in general, the systems exposed at 900°C have a longer incubation period and more rapid propagation than those exposed at 700°C.

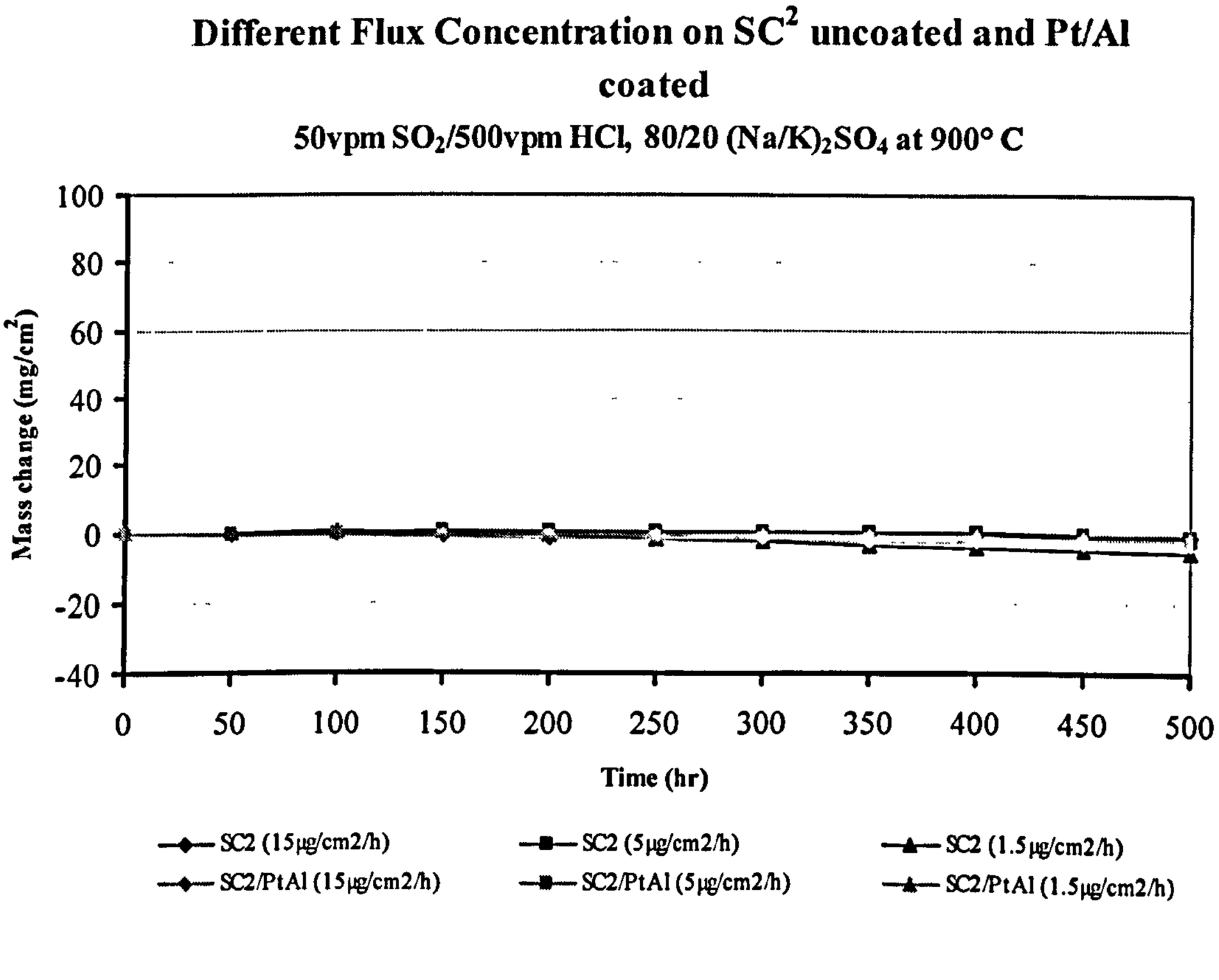

Figure 4.26: Comparison of deposit flux concentration: 1.5, 5 and 15μg/cm ^{2}/h on bare SC^2 and PtAl coated in 50 SO_2/ 500 HCl vpm at 900° C, from test 12.

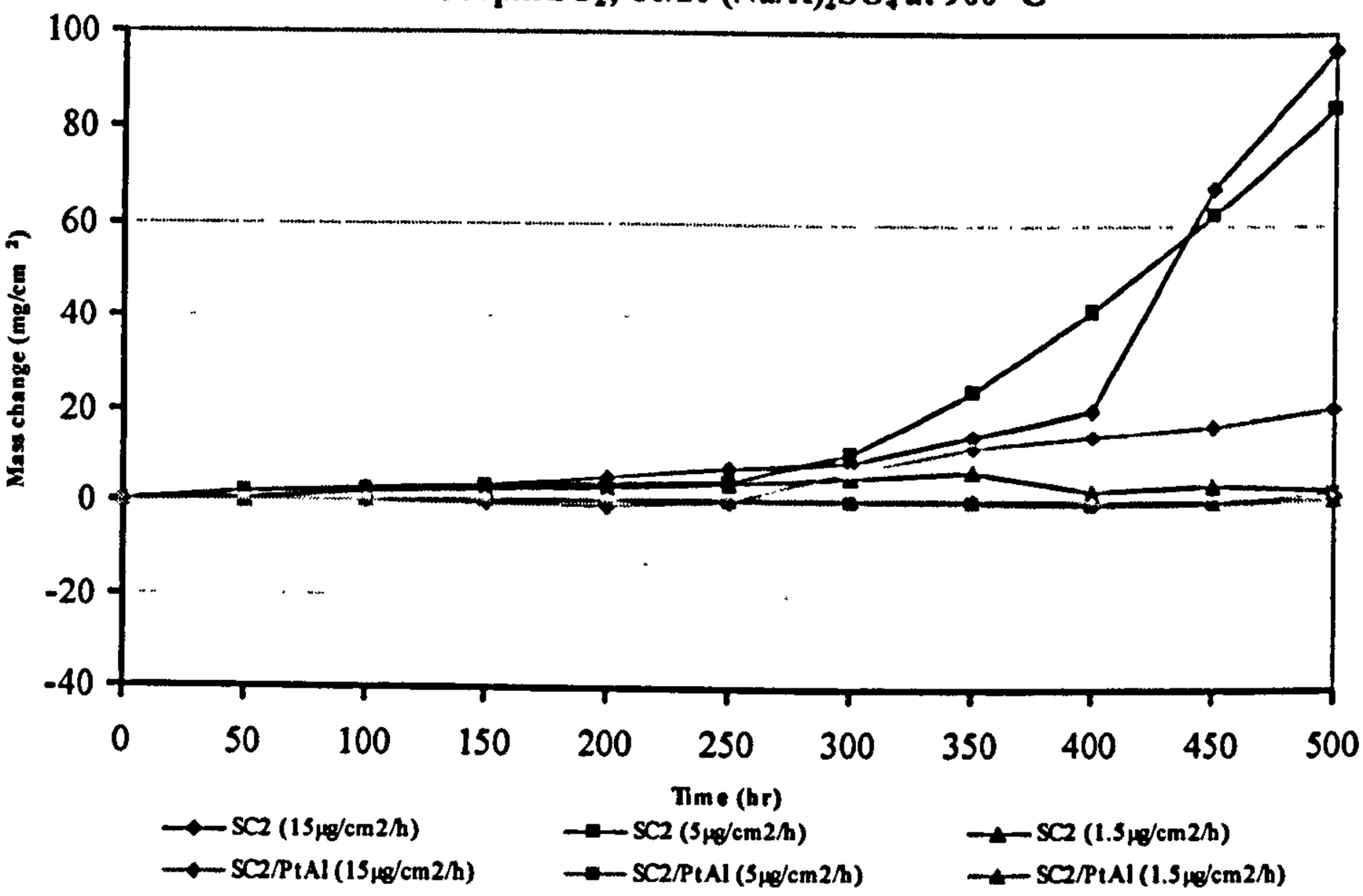

Figure 4.27: Comparison of deposit flux concentration: 1.5, 5 and 15µg/cm ^{2}/h on bare SC^2 and PtAl coated in 50 vpm SO_2 at 900° C, from test 8.

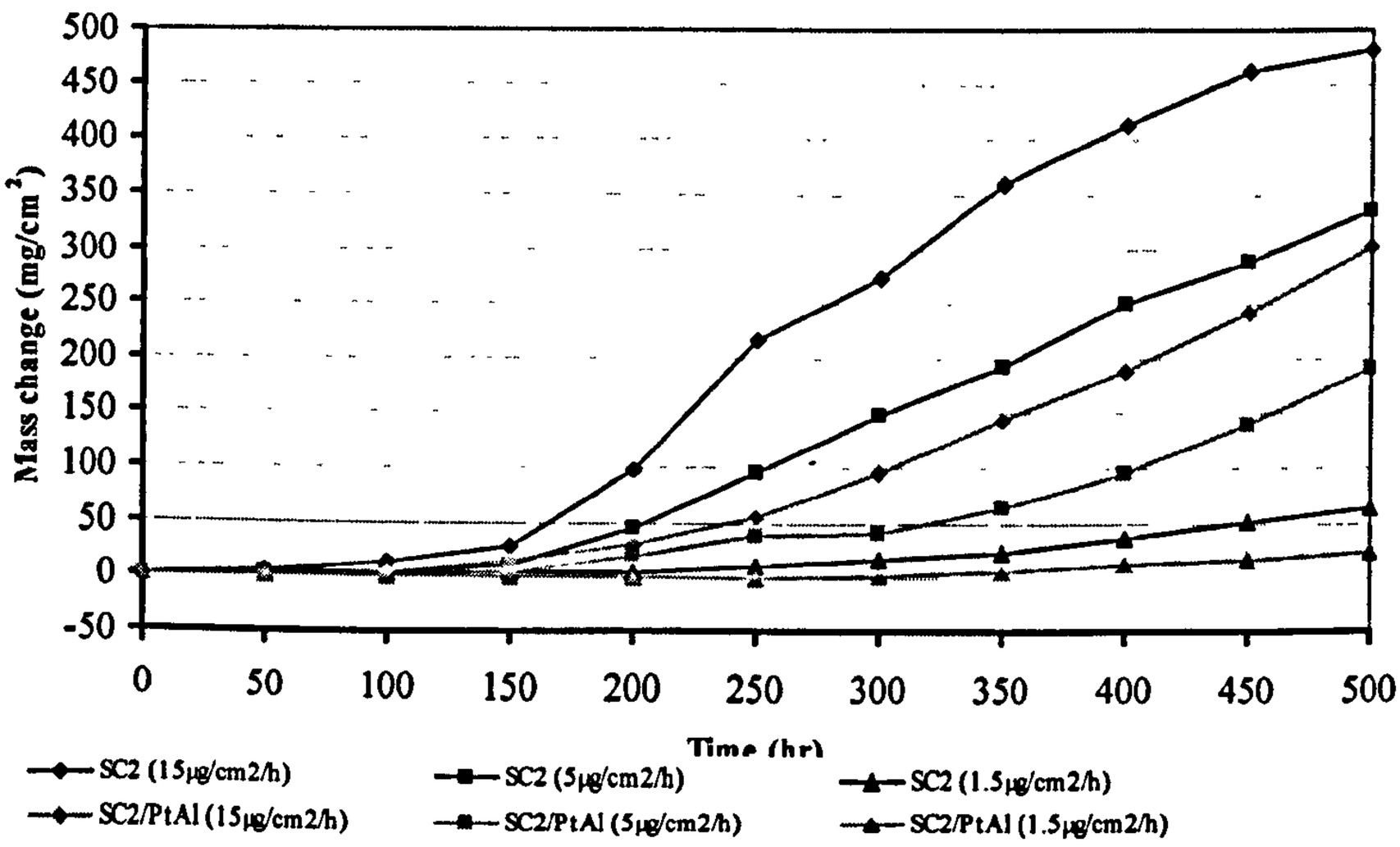

Figure 4.28: Comparison of deposit flux concentration: 1.5, 5 and 15µg/cm ^{2}/h on bare SC^2 and PtAl coated in 500 vpm SO_2 at 900° C, from test 10.

4.3 Optical Microscopy

Cross-sections were prepared from all samples exposed in these tests, according to the methods outlined in section 3.5. These cross-sections were used for both microstructural observations and dimensional metrology. Examination of the damage observed on these samples enables qualitative trends in damage as a function of exposure conditions to be identified. In order to make a visual comparison, the reference samples of the materials studied in this work are shown in Figure 4.29.

Morphological characteristics of the propagation stage of hot corrosion salt fluxing reactions, such as the characteristic non-uniform distribution of the pits formed in type II hot corrosion and the internal penetration during type I hot corrosion can be appreciated through visual comparison of the micrographs presented in this section, as well as the effects of varying conditions such as changing gas and deposit compositions, deposit flux, temperature and material.

4.3.1 Damage Morphologies (Phase 1)

Figure 4.30 shows the results of changing deposit compositions (as outlined in Table 3.5) and the effect of changing the gas composition for the reference material IN738LC at 700°C. The characteristic localized damage (pitting) of type II hot corrosion can be seen, as well as a thin layer of internal sulphidation in all samples exposed to lead deposits (photomicrographs 4, 10, 16, 28, 7, 13, 19, 31) and those exposed to a 20vpm SO_2/10vpm HCl atmosphere (photomicrographs 14, 18, 16, 19) . Some samples, for example the set exposed with 50/50 $(Na/K)_2SO_4$ under different high levels of contaminants (SO_2 and HCl), and gas compositions (see first row horizontally, photos 2, 8, 26), had the same apparent damage, hence the need to quantify the recession of surface of the sample accurately. The result of this analysis is quantified in Figure 4.44 (a) and, for the effect of changing deposits, it is quantified in Figure 4.46 (a).

Figure 4.31 shows the damage morphology for the PtAl coated IN738 LC under the same conditions as for the uncoated materials. In some cases, the coating has been consumed (photos 2, 6, 8, 12, 26, 30, 19) or the corrosion damage has penetrated through to the substrate (photos 10 and 13). This effect has been quantified for the effect of different gases and different deposits in Figure 4.44 (b) and Figure 4.46 (b) respectively.

Figure 4.32 shows the effect of four different deposits and four gas compositions on the performance of uncoated CMSX-4 at 700°C. The damage has a similar appearance, except for those samples showing a thin zone of internal sulphidation (photos 7, 8, 10, 13 and 19); however, measurements in the image analyser for this base alloy, as can be seen in Figure 4.45 (a) and Figure 4.47 (a), show how the deposit composition and gas composition affect the rate of material consumption.

The PtAl coated CMSX-4 type II hot corrosion morphology is shown in Figure 4.33. Unlike the PtAl coated IN738LC (Figure 4.31), the coating has not been completely consumed although, in two samples, photomicrographs 12 and 16, the corrosion damage has reached the substrate. In this set of photomicrographs, the pitting damage typical of type II hot corrosion, can be fully appreciated. Plots of the results from measurements of damage in this material system are given in Figure 4.45 (b) and Figure 4.47 (b).

4.3.2 Damage Morphologies (Phase 2)

Figure 4.34 shows the effect of different deposition fluxes on the single crystal SC^2 uncoated at 700°C. From the even surface of the reference sample (Figure 4.29), progression of the hot corrosion reaction can be appreciated, commencing with low damage for the lowest flux (photos 3, 9), next a clear formation of pits (photos 2, 8), towards severe damage for the highest flux (photos 1, 7). Adding HCl to the SO_2 in the test atmosphere suppresses the typical morphology of type II hot corrosion, but instead internal damage is observed (photos 13, 14, 15). Similar observations were made for the PtAl coated SC^2, Figure 2.41. This set of photographs shows how deeply the corrosion has affected the PtAl coating; clearly, the depth of corrosion increases with flux concentration. This effect can be seen by comparing the sets of photomicrographs 1, 2, 3 or 7, 8, 9 or 13, 14, 15.

At 900° C, catastrophic degradation can be seen, Figure 4.35, when the uncoated SC^2 is exposed to the higher SO_2 concentration (500 vpm) with the medium and higher deposit fluxes (5 and 15 $\mu g/cm^2/h$, photos 10 and 11). A very characteristic damage morphology, typical of type I hot corrosion, is evident in all samples.

PtAl coated SC^2 seems, in general, to perform better at 900°C than at 700°C (Figure 4.36 vs. Figure 4.37), although, at the 500vpm SO_2 concentration, the coating was practically destroyed at the medium and higher deposit flux levels (Figure 2.42; pictures 10 and 11).

Figure 4.38 gives the morphologies of uncoated CMSX-4 exposed to different gases with different deposit concentrations at 700° C. It is clear that pitting is accompanied by internal damage for samples exposed in the 50 vpm SO_2/500 vpm HCl environment. Also, a corrosion sequence from less damage to more damage on increasing the flux concentration (photos 13, 14 and 15) is observed. The rest of the samples in Figure 4.38, apparently, had much the same corrosion damage morphology. However, by quantifying the damage, for example in Figure 4.64 (a), it may be seen that the corrosion damage in 500 vpm SO_2 has increased proportionally to the increasing deposition flux.

The type II hot corrosion morphology for CMSX-4, in Figure 4.38, is in general, different to that for SC^2 (Figure 4.34). This may be due to the different elements/compositions of the two alloys and the effect of these composition differences in modifying the fluxing mechanism. Nevertheless, for both materials, internal damage may be observed when they are exposed in SO_2+HCl gas environments. At 900° C, catastrophic corrosion takes place for the majority of the CMSX-4 samples, Figure 4.39. CMSX-4 seems to be more sensitive to corrodent conditions than SC^2 when both alloys are uncoated (Figure 4.39 vs. Figure 4.35) for type I hot corrosion. The morphologies after exposure in SO_2+HCl gas environments are similar, however, for both materials.

When CMSX4 is PtAl-coated and exposed in the low SO_2 concentration (50 vpm) at 700°C, Figure 4.40, the corrosion damage can be seen to have penetrated through the coating into the substrate under the highest flux deposit (15μg/cm^2/h, photo 1). Under the same conditions, the PtAl-coated SC^2 does not present such deep attack (Figure 4.36 photo 1). Comparison of the group of PtAl-coated CMSX4 (Figure 4.40 photos 1, 2, 3) and PtAl-coated SC^2 (Figure 4.36 photos 1, 2, 3) in 50 vpm SO_2, shows different rates of corrosion degradation and different resulting morphologies (Figure 4.36 photos 3 and 9). The damage has commenced and progressed as far as the base of the outer coating layer. In photo 2 and 8, the damage has extended along the sample and, in Figure 4.36 photos 1 and 7, corrosion approaches and/or penetrates the base metal.

This form of progression of damage, removing the coating layer by layer, suggests an electrochemical form of attack, with the underlying material layer being protected until the outer layer has been removed. This kind of corrosion degradation, as seen in Figure 4.40, shows that the corrosion damage also increases according to flux concentration. Pits are observed to commence in the outer layer of the coating, (photo 3) and continue to penetrate inwards through the coating, (photo 2), towards the substrate to produce deep localized damage in the alloy; (photo 1).

Both systems, PtAl on CMSX4 and PtAl on SC^2, when exposed to 500 vpm HCl (photos 13, 14, 15 for both figures), show smaller pits with internal damage that proportionally increase with the flux concentration. The micrographs of PtAl-coated CMSX4 at 900° C are given in Figure 4.41; the coating appears to have protected the substrate material, although some internal damage, characteristic of type I hot corrosion, can be seen in those samples exposed with the highest flux of 15µg/cm^2/h in the various corrosive environments (photos 4, 10, 16).

4.3.3 Damage morphologies (Phase 3)

The effect of changing test temperature on hot corrosion of the different materials systems is illustrated in Figure 4.42. At 650 and 700° C, pitting can be seen in the PtAl-coated CMSX-4, photos 36 and 30. At 900° C, typical internal damage of type I hot corrosion is observed, e.g. photos 24, except for PtAl-coated CMSX4. The quantification of corrosion damage for these systems may be seen in Figure 4.48 (a) and (b) and Figure 4.49 (a) and (b).

All these photographs corroborate the importance of the metrology method, as corrosion damage can be quantified, including pitting and the extent of internal damage; neither can be assessed using mass change data.

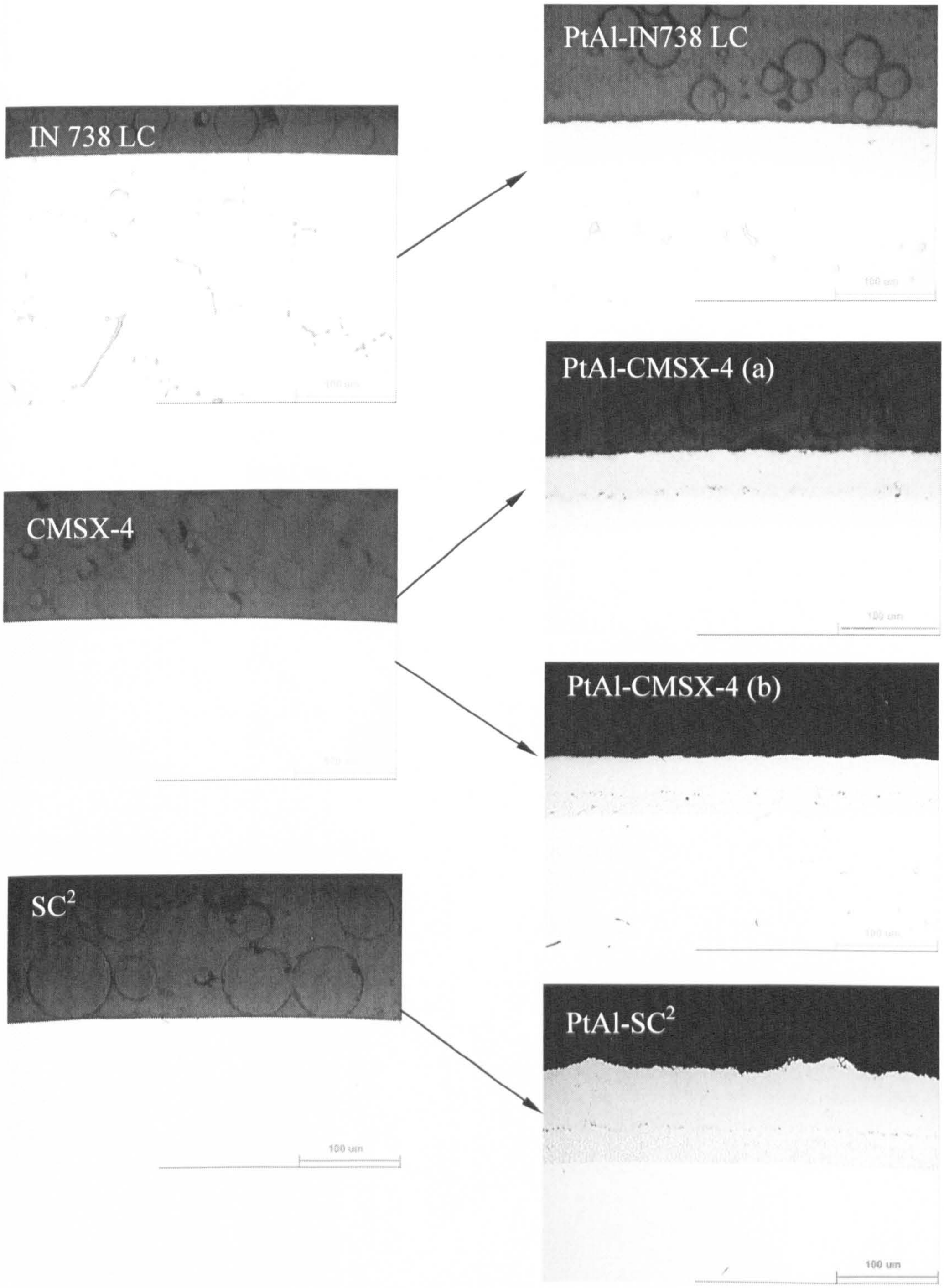

Figure 4.29: Optical micrographs of cross-sections of uncoated and PtAl coated unexposed materials systems. The PtAl/CMSX4 used in stage 1 (a) and in stage 2 (b) of this study.

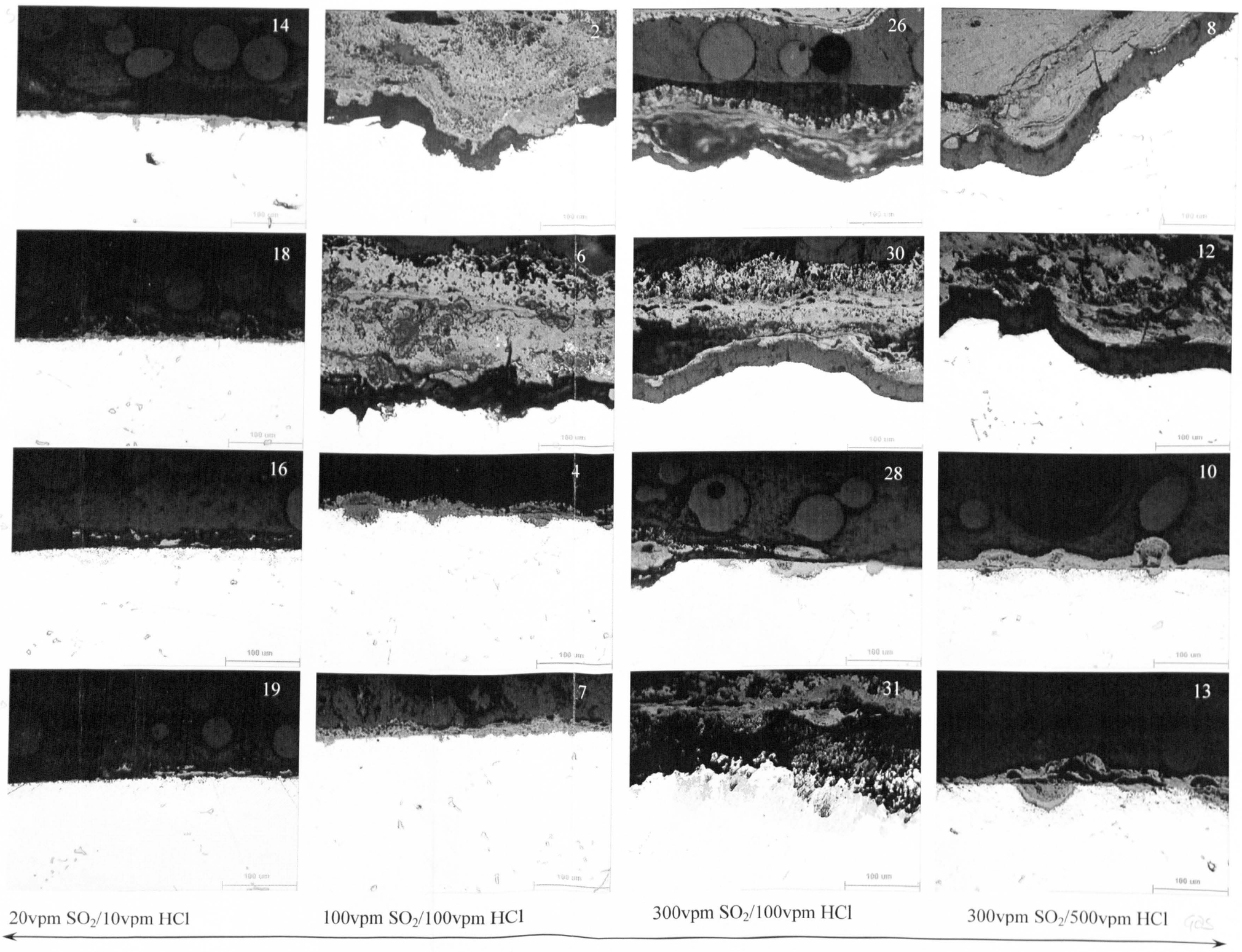

Figure 4.30: Effect on changing deposit composition: A, B, C and D (vertical) and effect of changing gas composition (horizontal) at 700° C on uncoated IN738 LC after 500h exposure.

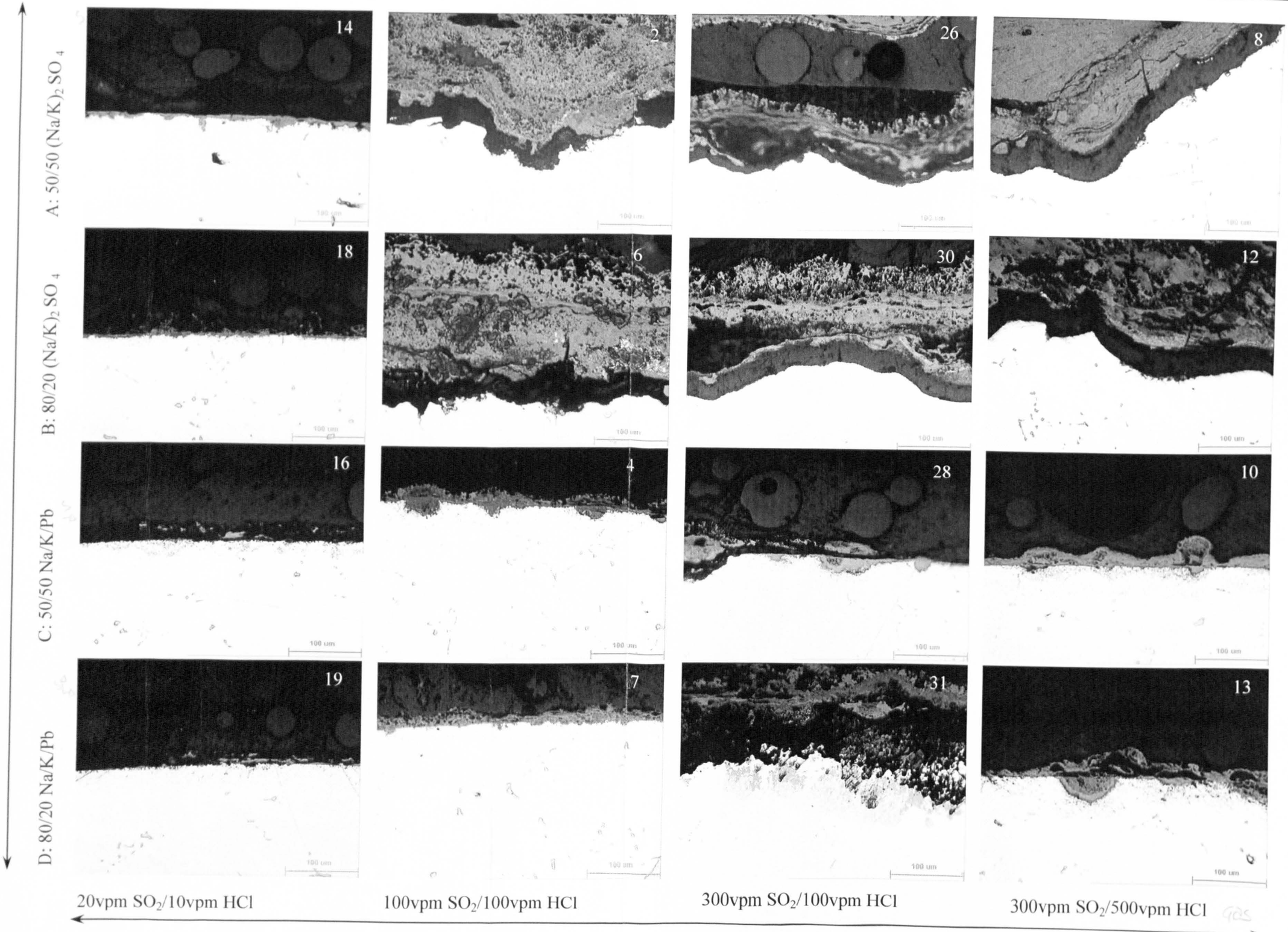

Figure 4.30: Effect on changing deposit composition: A, B, C and D (vertical) and effect of changing gas composition (horizontal) at 700° C on uncoated IN738 LC after 500h exposure.

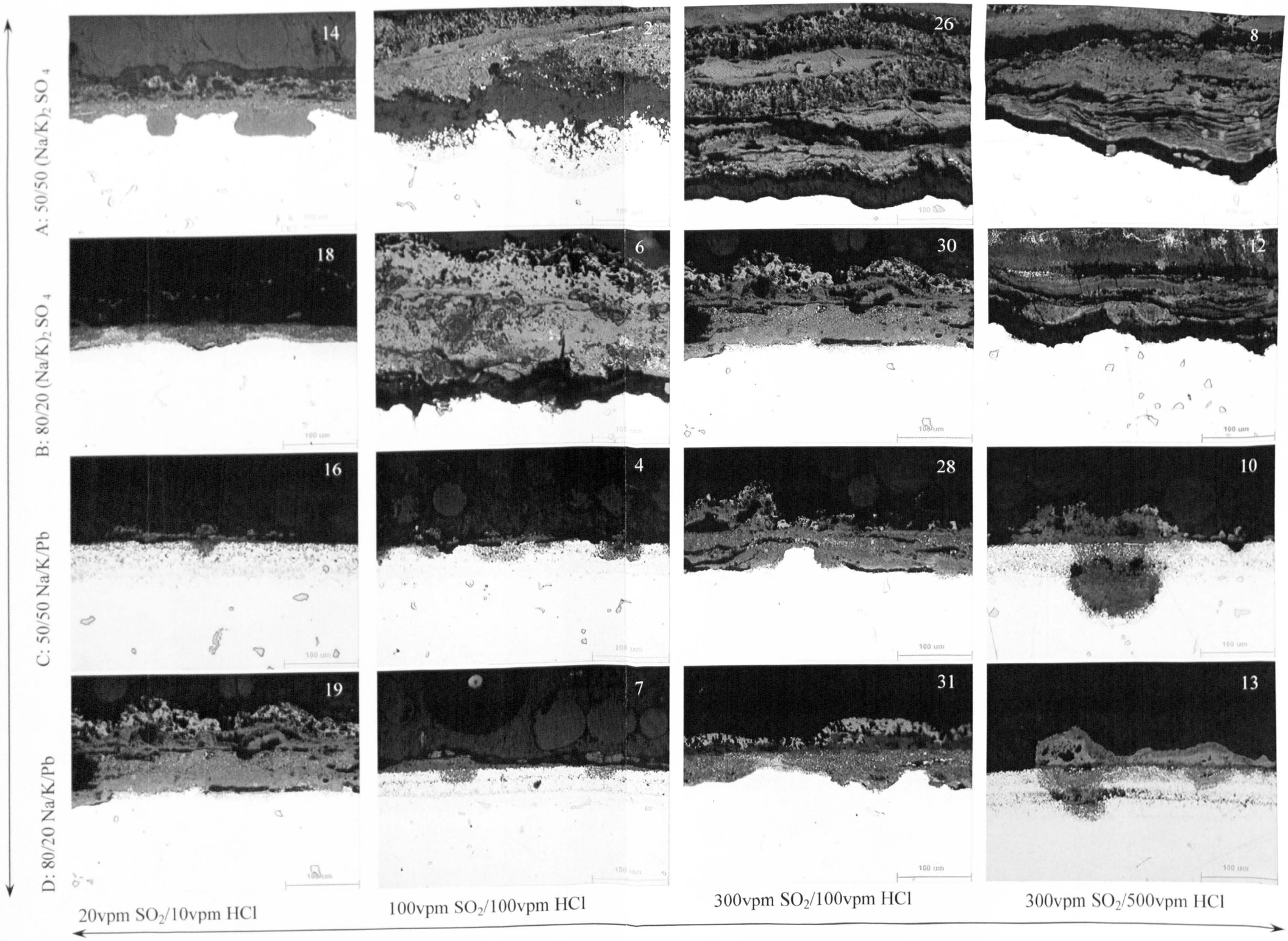

Figure 4.31: Effect on changing deposit composition: A, B, C and D (vertical) and effect of changing gas composition (horizontal) at 700° C on PtAl coated IN738 LC after 500h exposure.

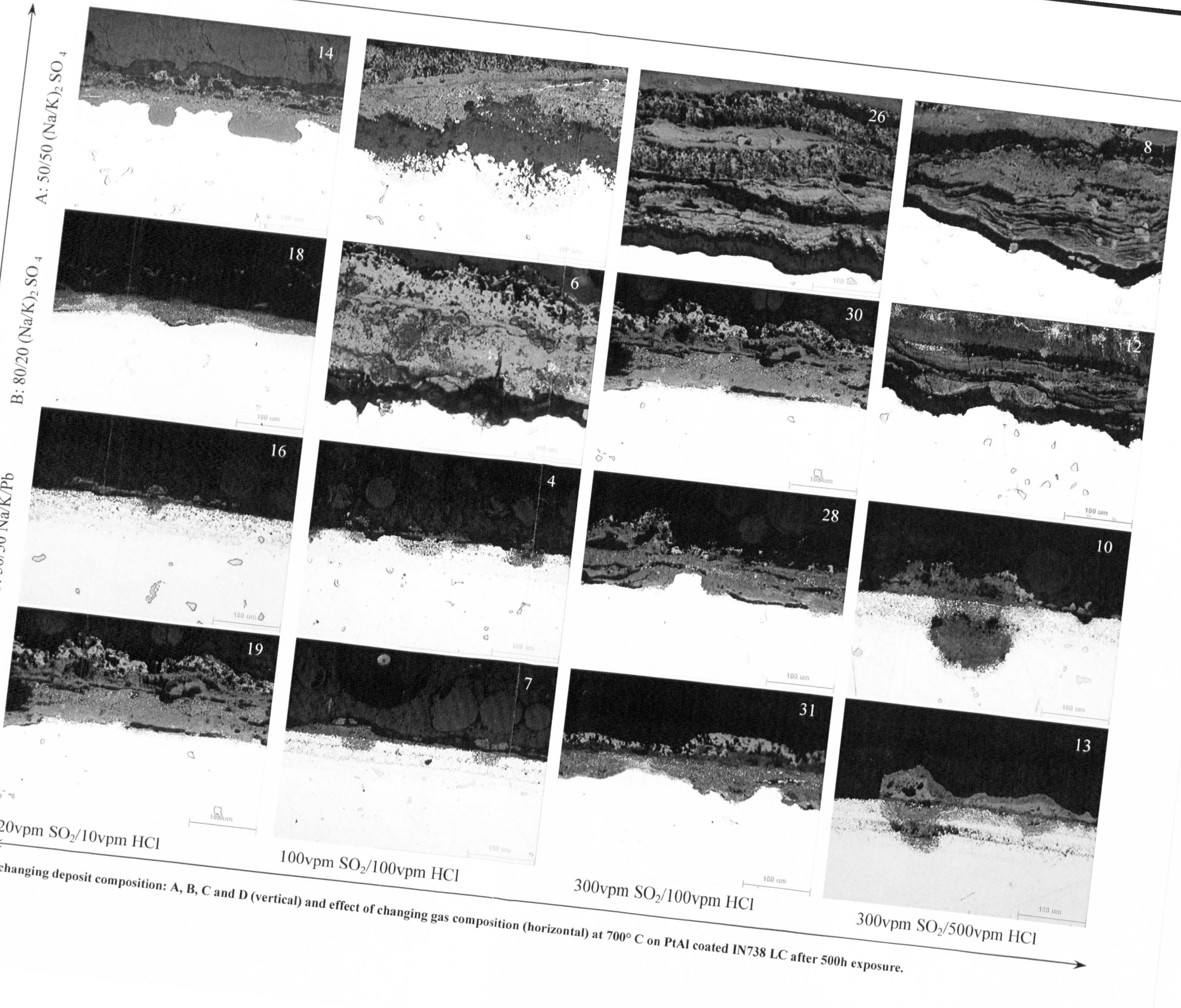

Figure 4.31: Effect on changing deposit composition: A, B, C and D (vertical) and effect of changing gas composition (horizontal) at 700° C on PtAl coated IN738 LC after 500h exposure.

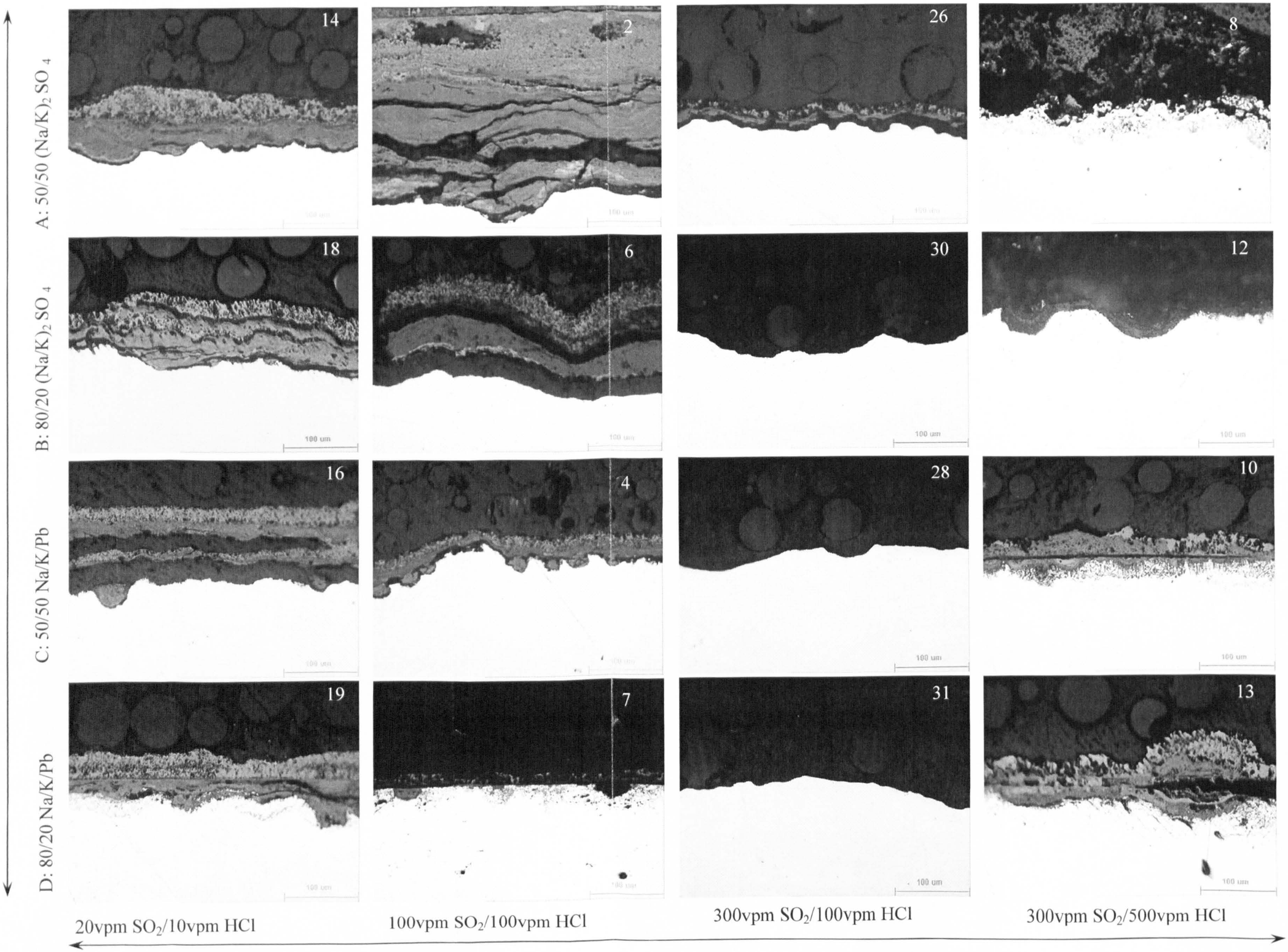

Figure 4.32: Effect on changing deposit composition: A, B, C and D (vertical) and effect of changing gas composition (horizontal) at 700° C on uncoated CMSX-4 after 500h exposure.

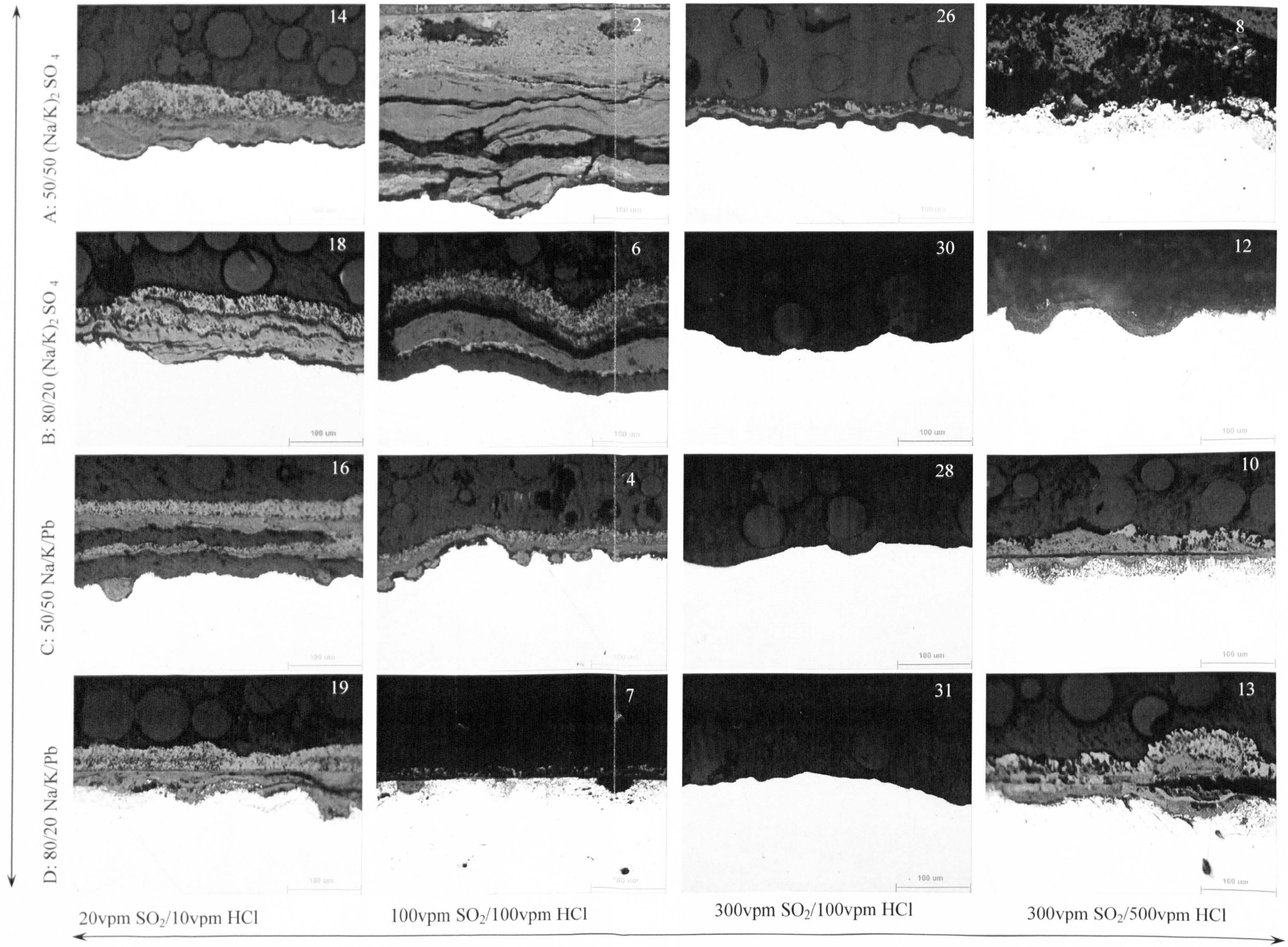

Figure 4.32: Effect on changing deposit composition: A, B, C and D (vertical) and effect of changing gas composition (horizontal) at 700° C on uncoated CMSX-4 after 500h exposure.

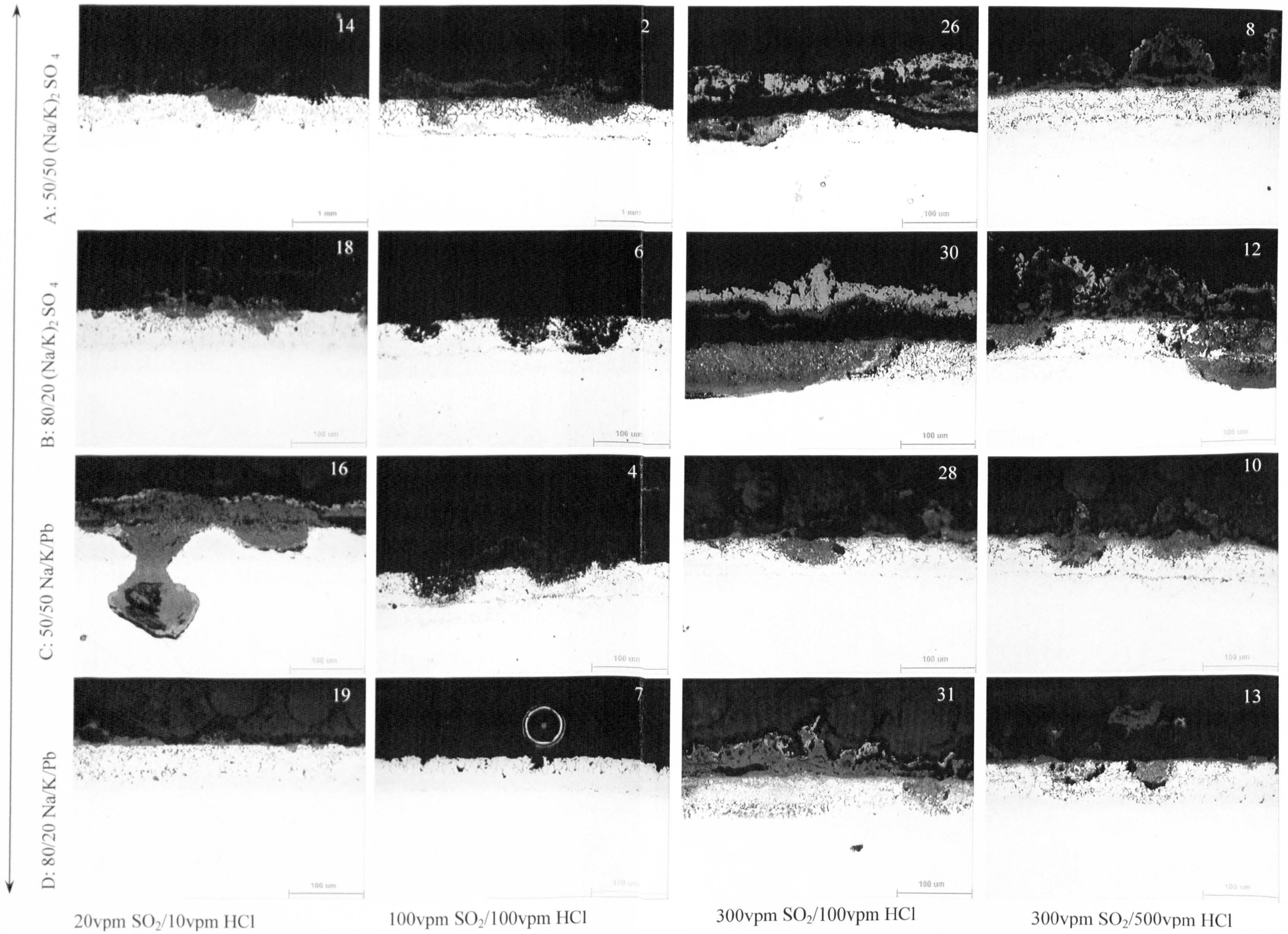

Figure 4.33: Effect on changing deposit composition: A, B, C and D (vertical) and effect of changing gas composition (horizontal) at 700° C on PtAl coated CMSX-4 after 500h exposure.

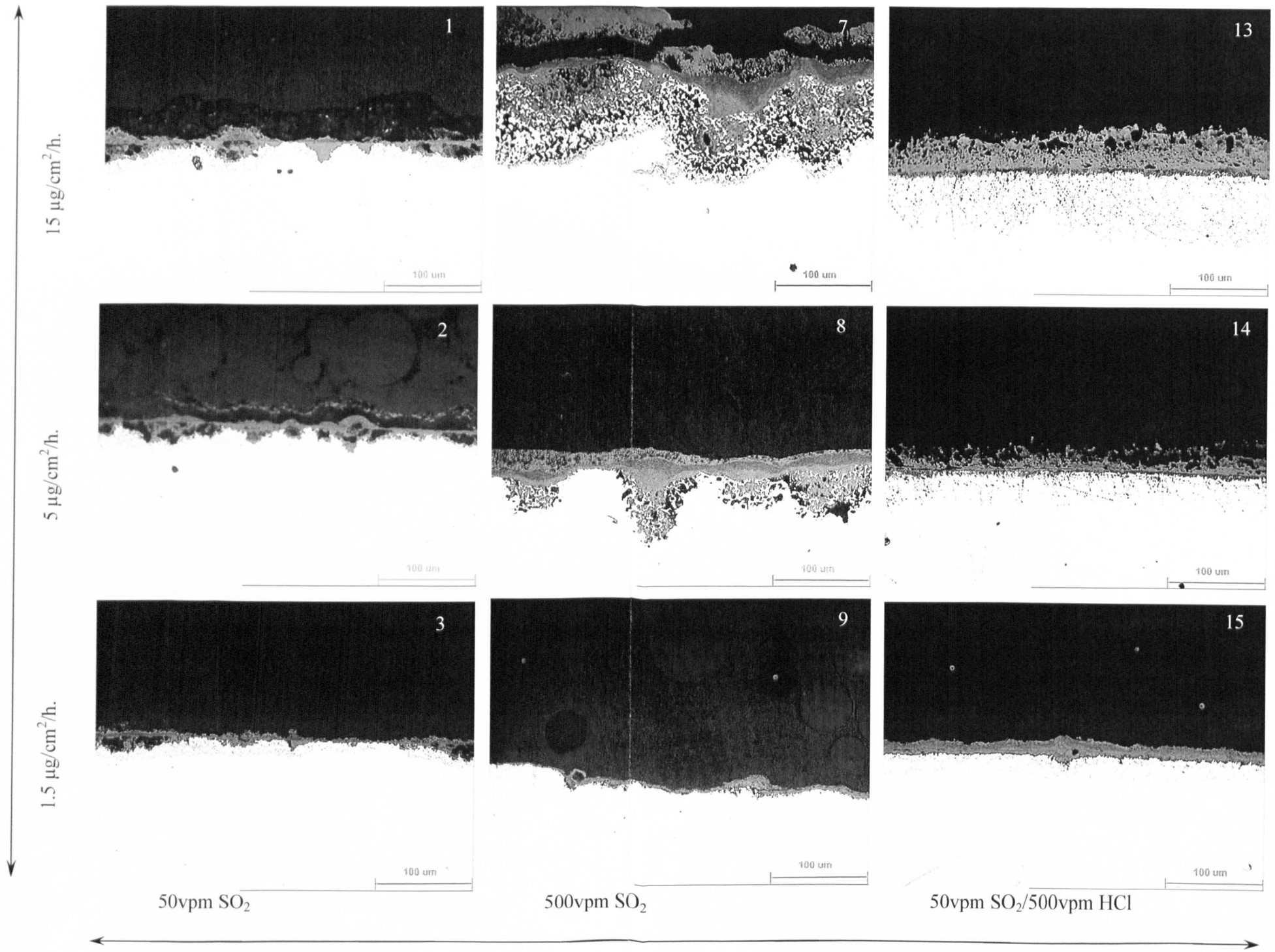

Figure 4.34: Effect on changing flux deposit from 1.5ug/cm²/h to 15µg/cm²/h of $(Na/K)_2 SO_4$ (vertical) and effect of changing gas composition (horizontal) at 700°C on uncoated SC²after 500h exposure.

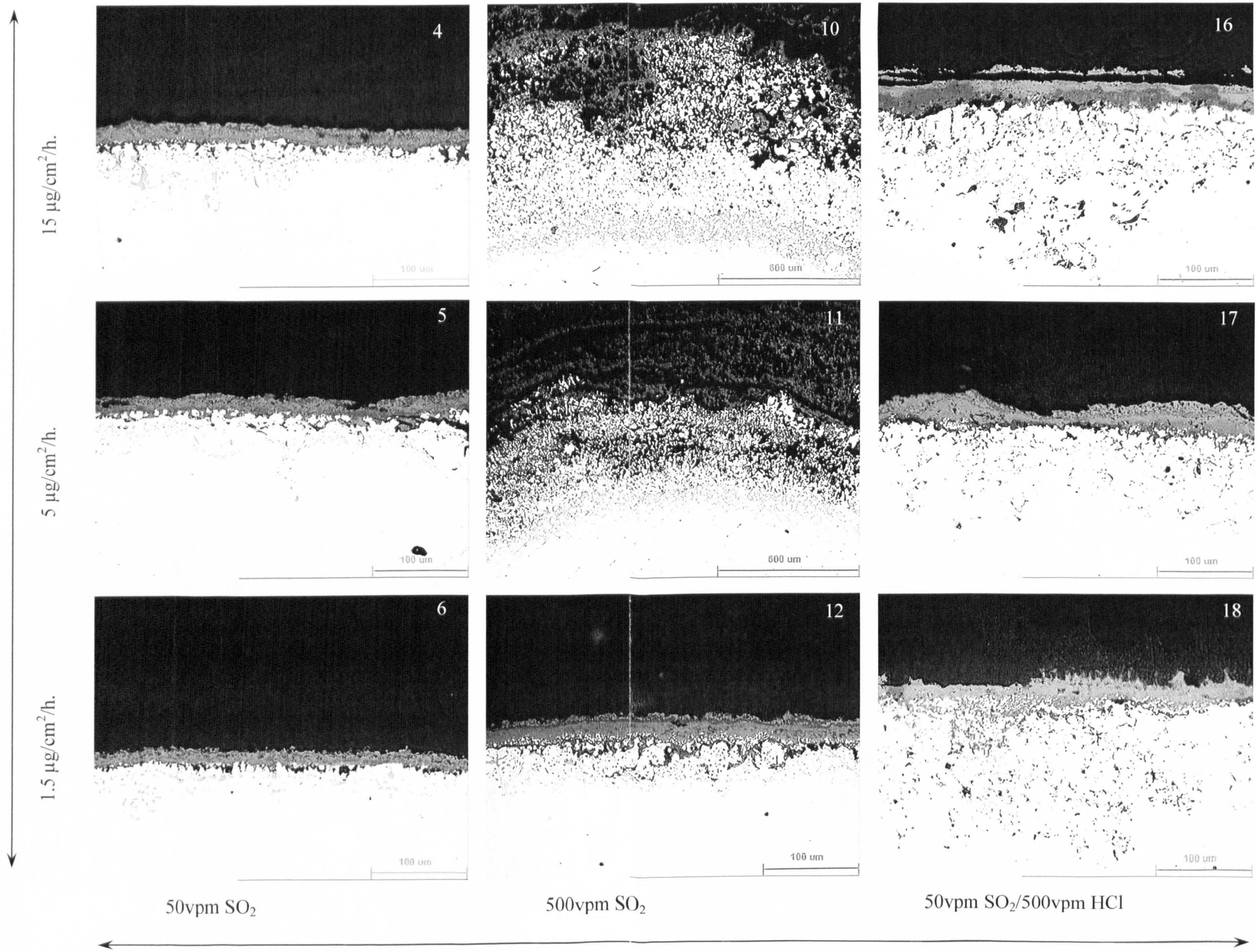

Figure 4.35: Effect on changing flux deposit from 1.5ug/cm²/h to 15µg/cm²/h of $(Na/K)_2 SO_4$ (vertical) and effect of changing gas composition (horizontal) at 900° C on uncoated SC² after 500h exposure.

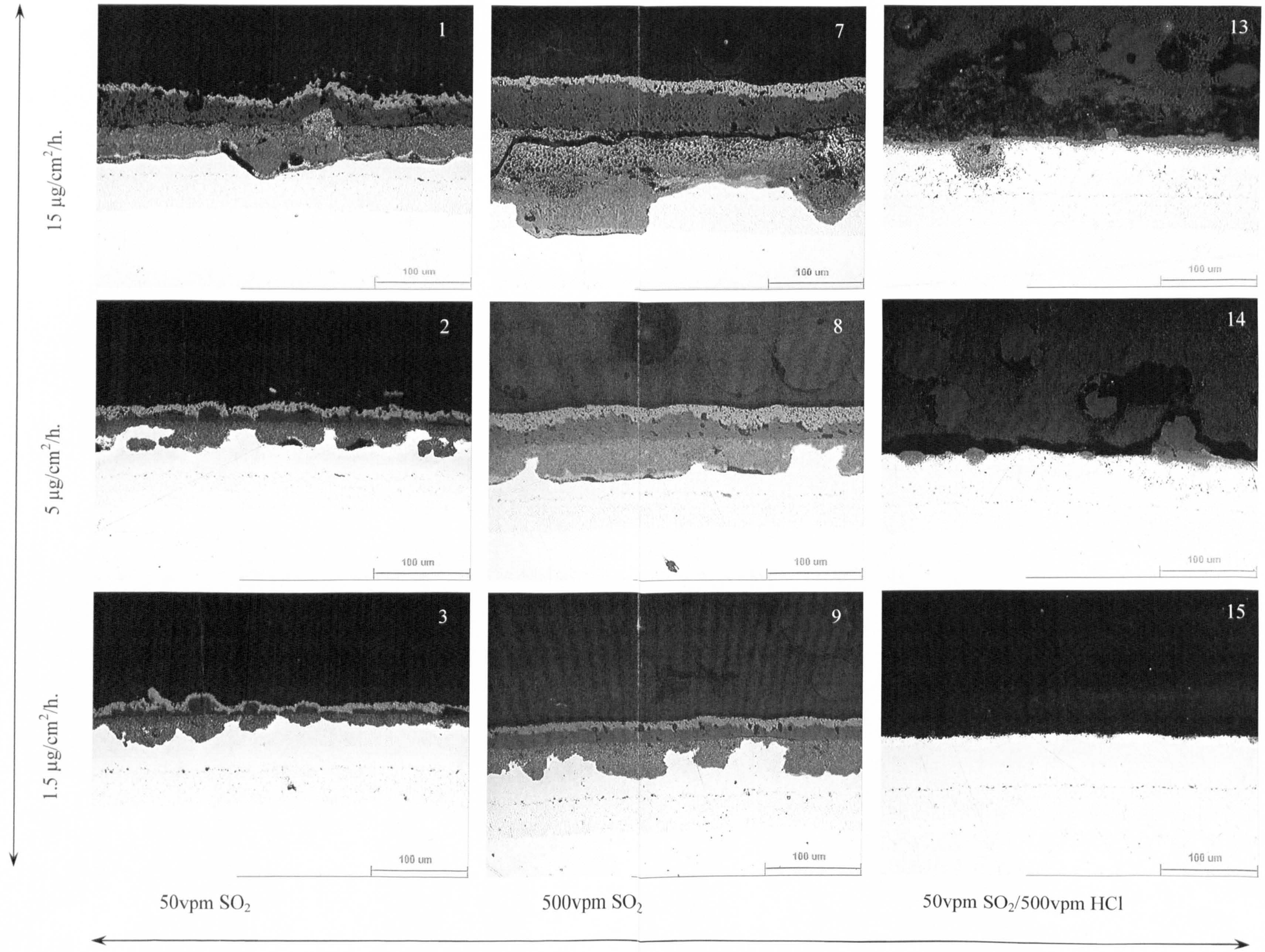

Figure 4.36: Effect on changing flux deposit from 1.5ug/cm^2/h to 15µg/cm^2/h of $(Na/K)_2 SO_4$ (vertical) and effect of changing gas composition (horizontal) at 700° C on PtAl coated SC^2 after 500h exposure.

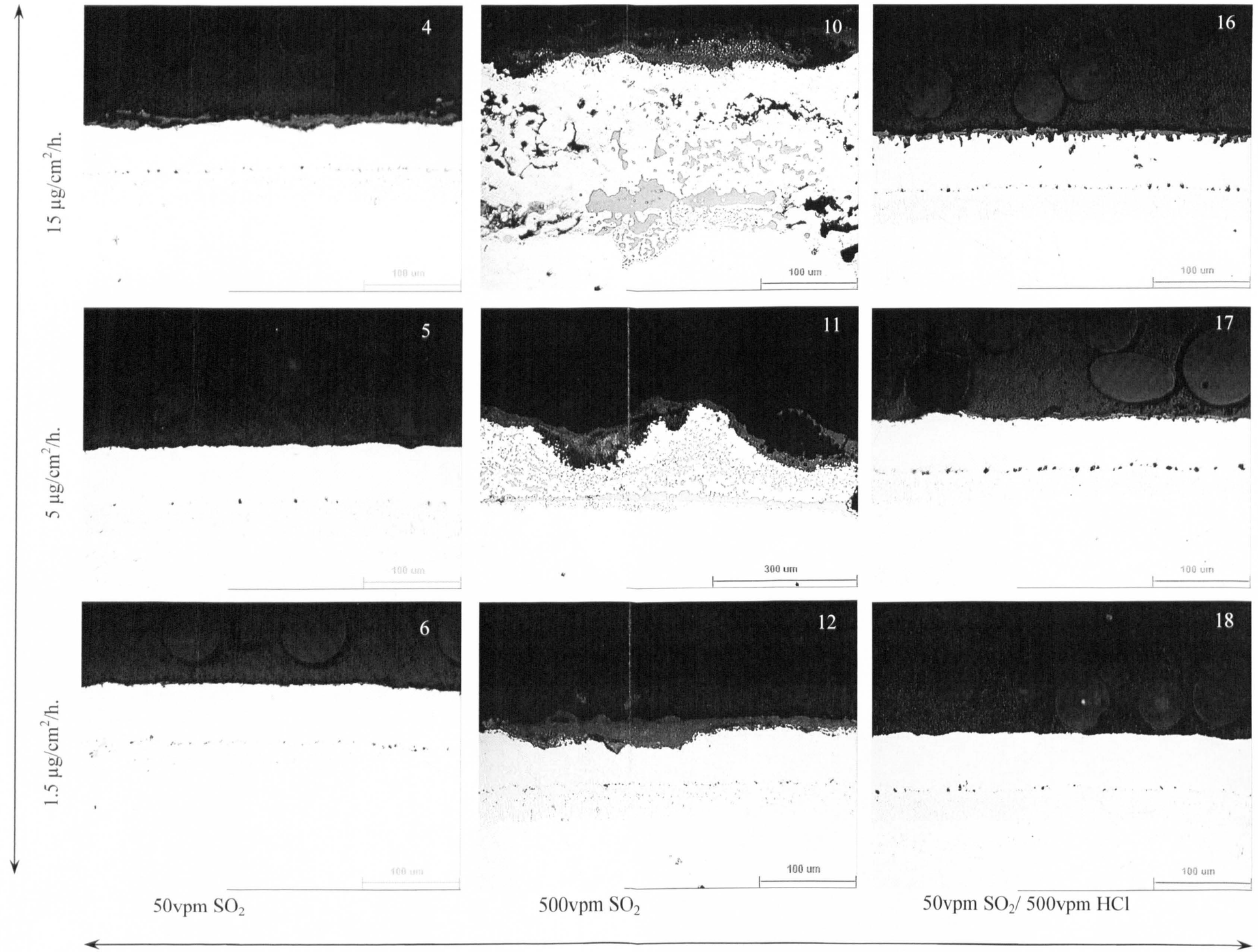

Figure 4.37: Effect on changing flux deposit from 1.5ug/cm^2/h to 15µg/cm^2/h of $(Na/K)_2 SO_4$ (vertical) and effect of changing gas composition (horizontal) at 900° C on PtAl coated SC^2 after 500h exposure.

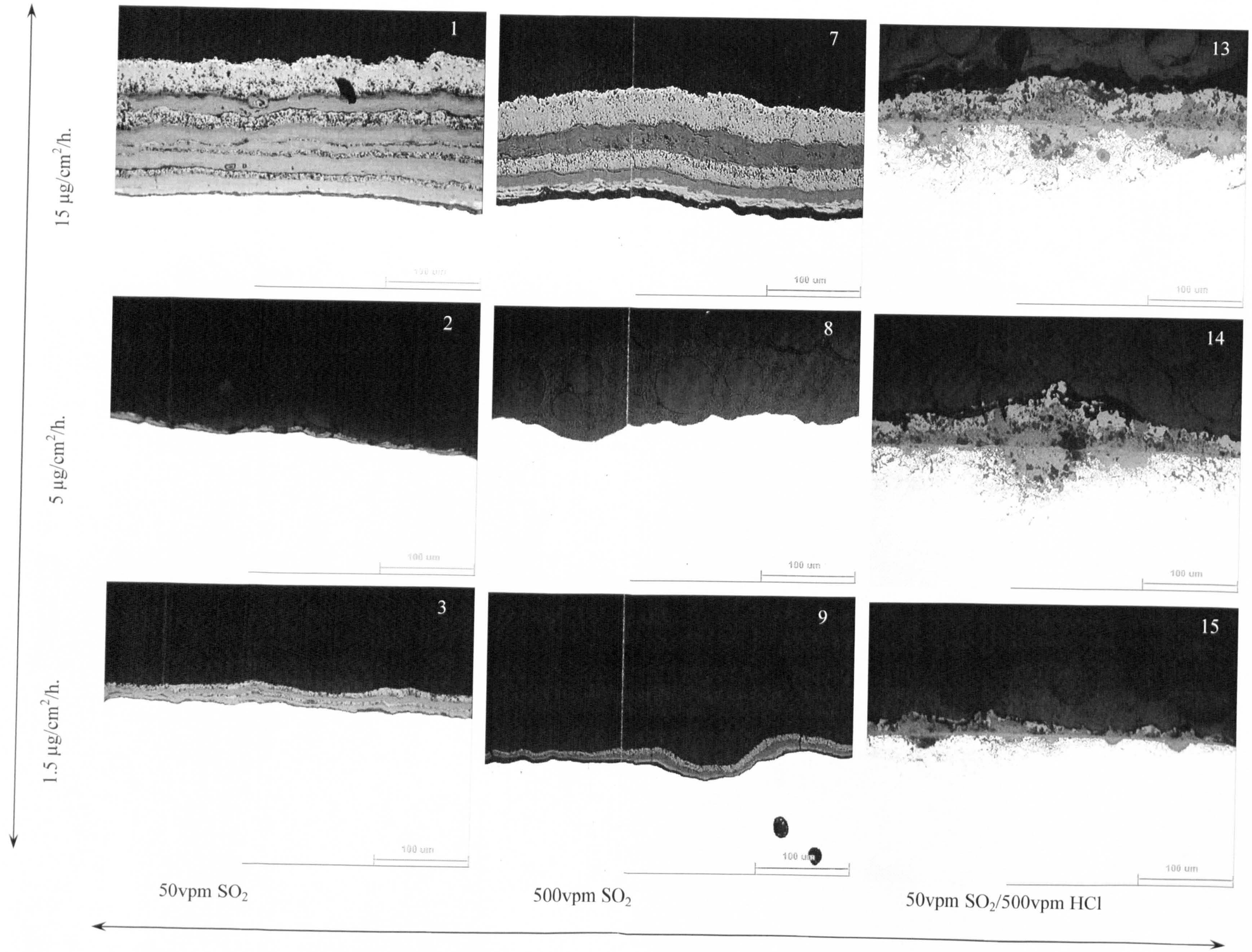

Figure 4.38: Effect on changing flux deposit from 1.5ug/cm²/h to 15µg/cm²/h of $(Na/K)_2 SO_4$ (vertical) and effect of changing gas composition (horizontal) at 700° C on uncoated CMSX-4 after 500h exposure.

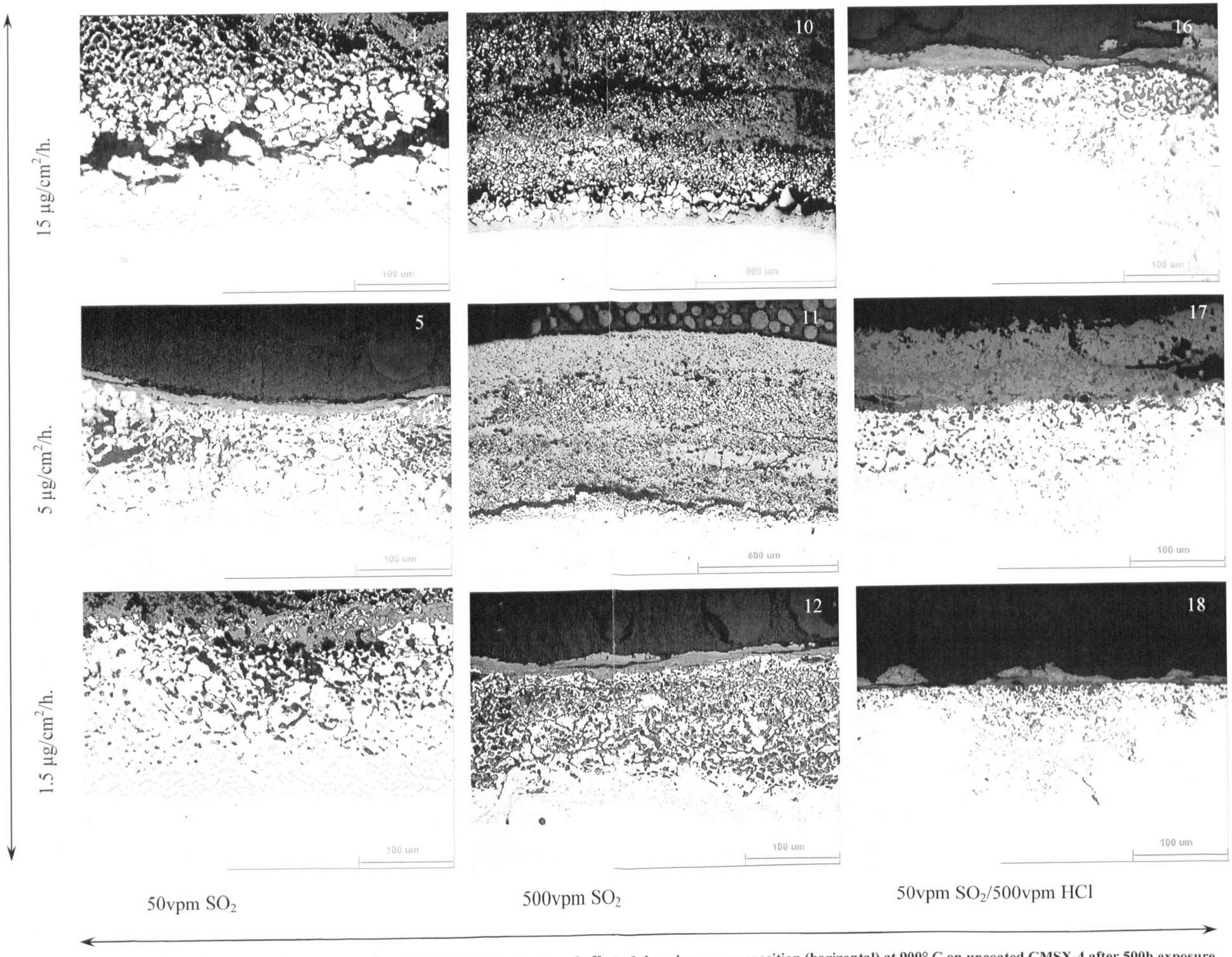

Figure 4.39: Effect on changing flux deposit from 1.5ug/cm²/h to 15µg/cm²/h of $(Na/K)_2 SO_4$ (vertical) and effect of changing gas composition (horizontal) at 900° C on uncoated CMSX-4 after 500h exposure.

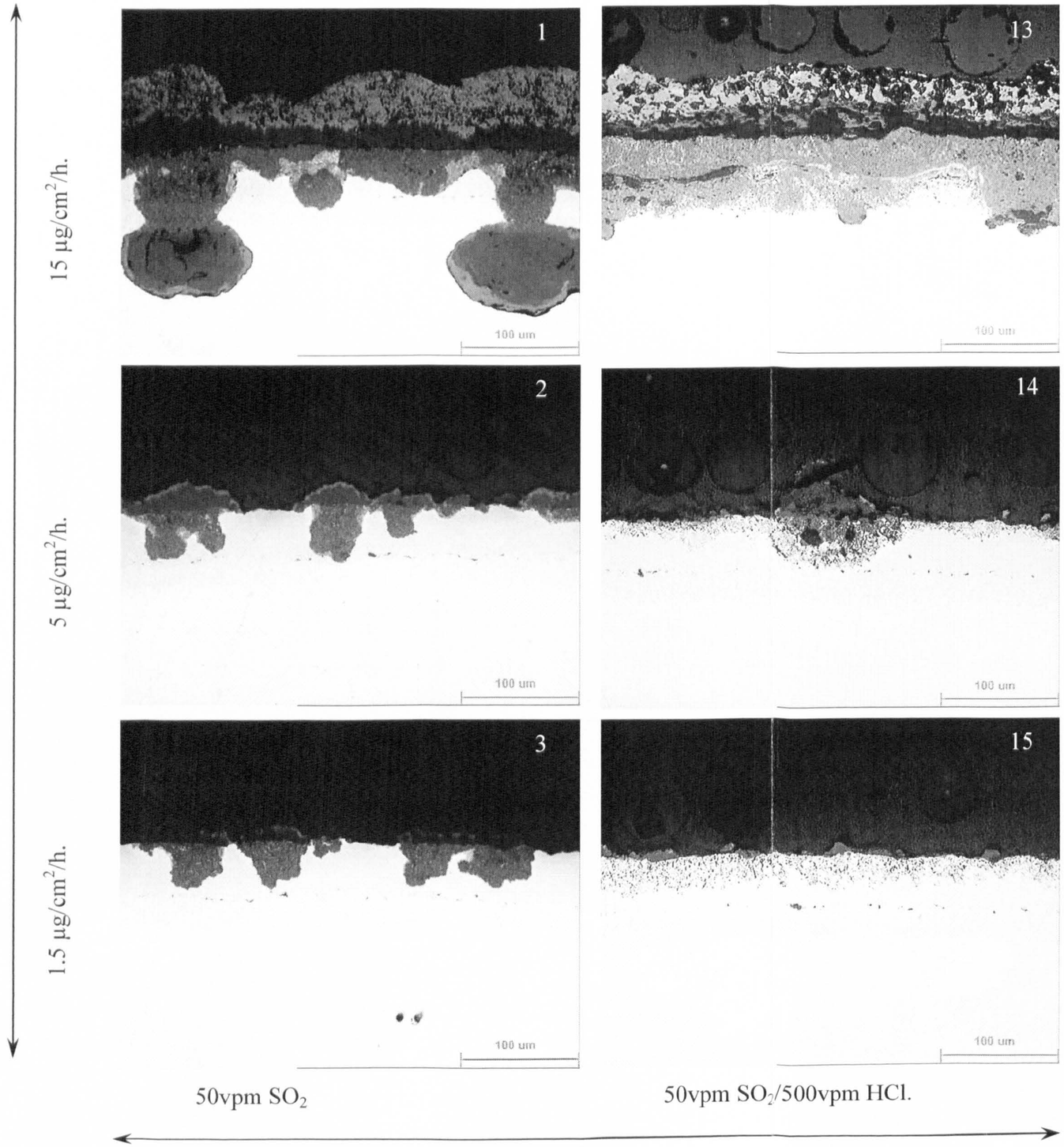

Figure 4.40: Effect on changing flux deposit from 1.5ug/cm^2/h to 15µg/cm^2/h of $(Na/K)_2 SO_4$ (vertical) and effect of changing gas composition (horizontal) at 700° C on PtAl coated CMSX-4 after 500h exposure.

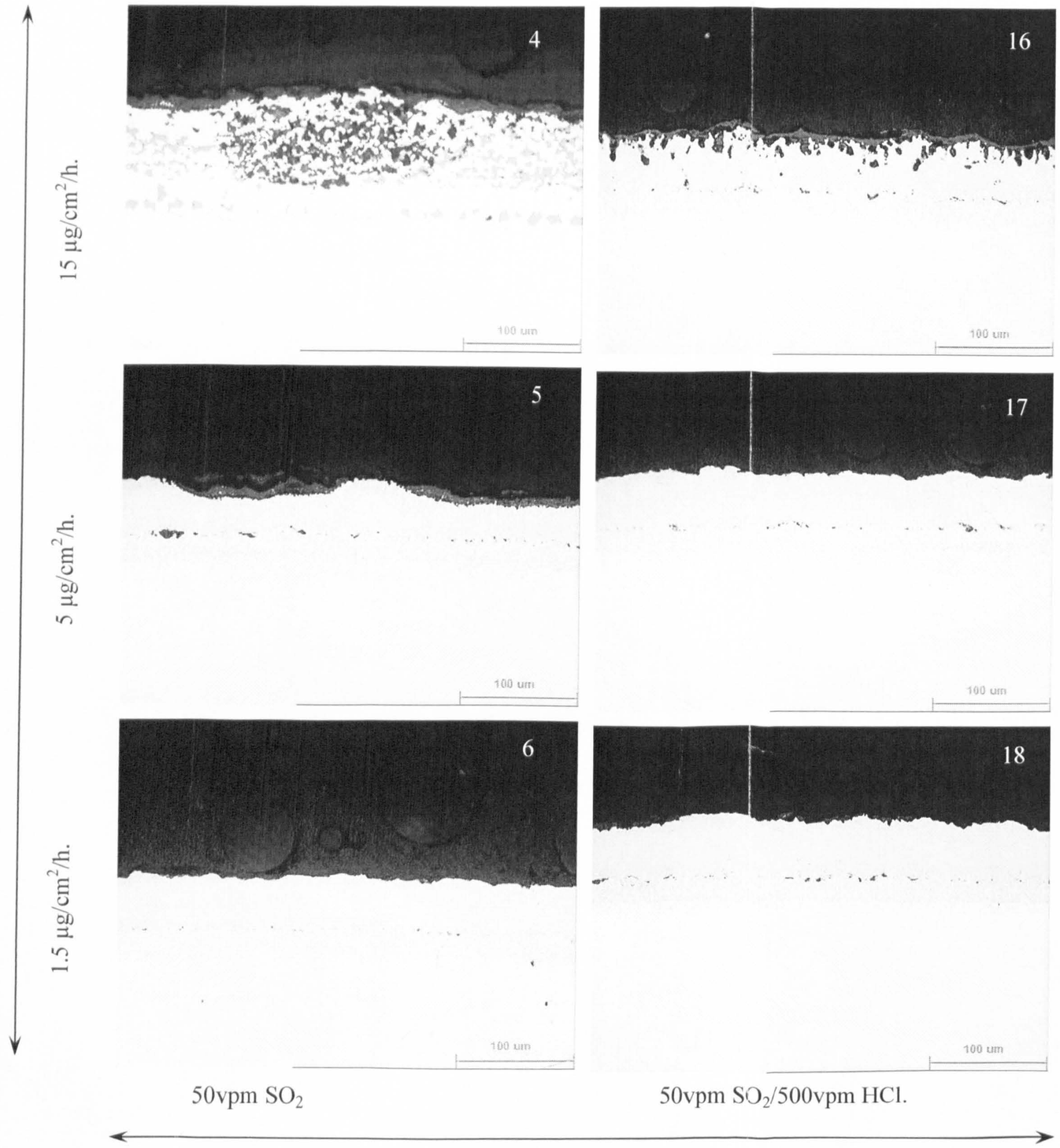

Figure 4.41: Effect on changing flux deposit from 1.5ug/cm^2/h to 15µg/cm^2/h of $(Na/K)_2 SO_4$ (vertical) and effect of changing gas composition (horizontal) at 900° C on PtAl coated CMSX-4 after 500h exposure.

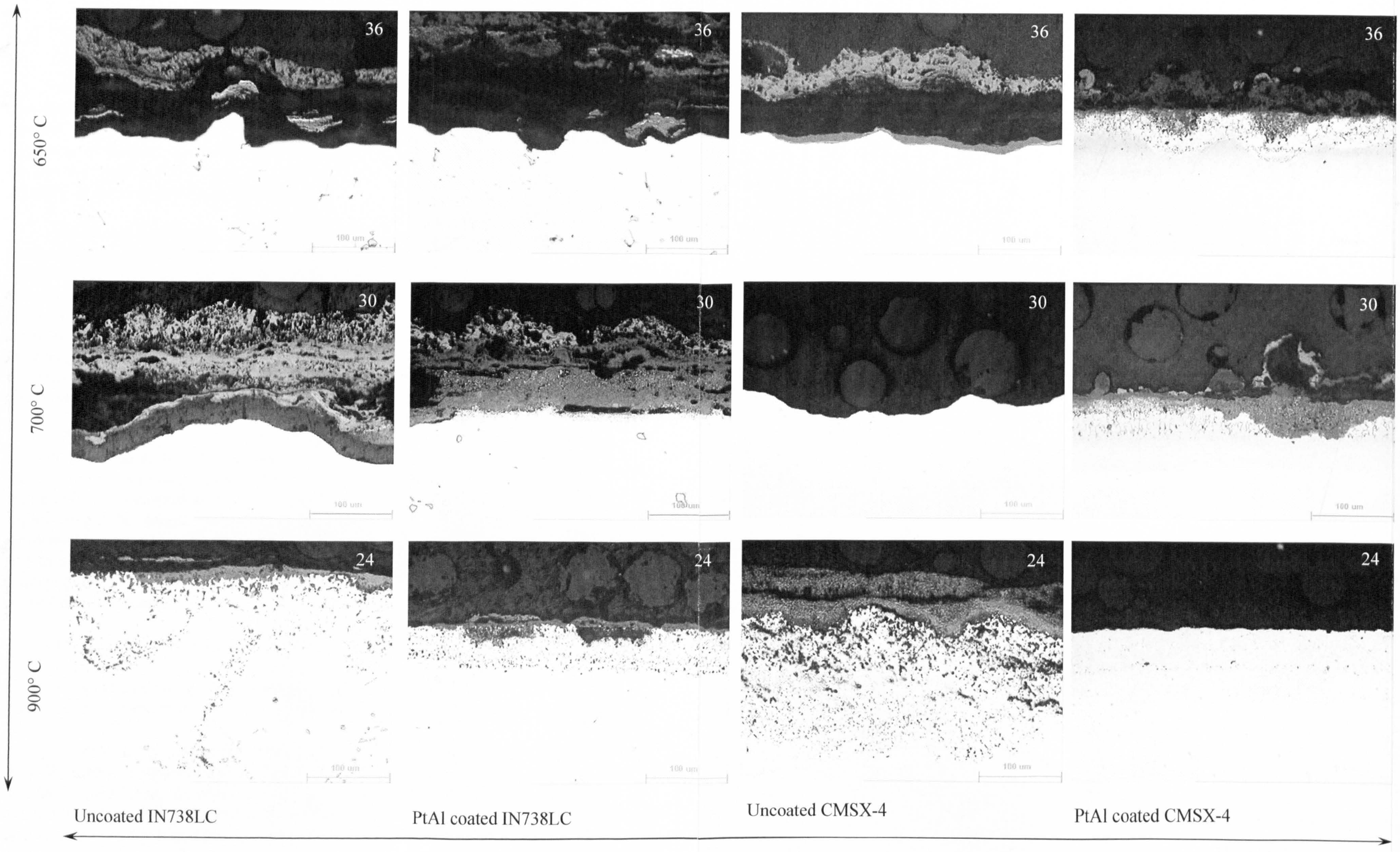

Figure 4.42: Effect on changing temperatures (vertical) on the different materials systems (horizontal) with 15µg/cm^2/h of $(Na/K)_2 SO_4$ in 300vpmSO_2/100vpm HCl after 500h exposure.

4.4 Statistical Assessment of Hot Corrosion Data

As explained in 3.5, the aim of the analysis of the pre-exposure and post-exposure dimensional measurements is to produce data sets of accurate material loss measurements. A key part of this data processing is the alignment of the two co-ordinate systems used for these measuring processes through the combination of reference points on the samples and reliance on the accuracy of the sample preparation process.

Additional parameters such as deposit thickness or depth of internal penetration are evaluated only from post-exposure measurement data. With the data generated from this process, statistical analysis can be carried out. The references were also prepared as cross-sections and used for repeatability checks of the overall metrology process: they were measured using the same metrology process as the exposed samples, three times each at different dates in order to establish a range of error over the accuracy of the image analysis system. For the cylindrical laboratory samples (Figure 3.6) only 24 measurement points are required to determine the variations in section loss.

The data obtained from the image analysis system are processed through a spreadsheet. This spreadsheet, developed by British Coal staff, matches the measurements of a particular sample before exposure (a series of diameters) vs. measurements after exposure (>24 x, y coordinates) using angles around the sample from the reference mark. As a part of this analysis, the non-exposure reference sample for each material system (uncoated alloy and /or alloy/coating) is processed through the spreadsheet, using these data as reference (each reference sample was measured three times on different times to consider measurement error).

Then, the processed data are plotted in the form of:

- Calculated and/or measured parameters at specific locations around a sample (e.g. metal loss, internal penetration, sound metal loss. See Figure 3.10).
- Probability plot of the same data in which the probability intervals are calculated as proportions of the "number of data points +1" and the metal loss data ordered from the smallest to the largest [130]. From these data, a new maximum value, i.e. the 4% probability of exeedence, on which the criteria for further assessment is based can be extracted (in fact, the spreadsheet calculates data for four confidence levels).

Figure 4.43 is an example of the results obtained for uncoated IN738LC illustrating the effects observed from different exposure conditions: gas and deposit composition, and temperature for this material.

These graphs illustrate the characteristic stochastic nature of hot corrosion around materials and, hence, the need for statistical analysis of such results.These raw data, obtained from combining the pre- and post-exposure metrology, have been further processed:

- by correcting for known errors (determined from reference samples)
- by ordering the data in terms of the decreasing extent of metal damage (or sound damage, i.e. metal damage + depth of internal penetration) to give probability distributions for each sample exposed in this study (reference [130]).

Groups of these probability plots are given in this section to permit comparisons between materials and conditions (Figure 4.44 to Figure 4.64). For example, Figure 4.62 (b) shows data for the uncoated SC^2 in 500vpm SO_2 at 900°C after 500h exposure. The non-straight line plot for the 1.5µg/cm^2/h deposition flux indicates that more that one mechanism could have operated around this sample since the line shows three regions: one, around 10%, is in propagation stage, the middle, ~80%, appears to be in the incubation stage, and the rest could represent oxidation.

On increasing the deposition flux to 5µg/cm^2/h, given the irregularity of the line and the range of change in sound metal (from ~600 to 1500µm), it is believed that the surface all around this sample is in the propagation stage. Similarly, the 15µg/cm^2/h line, shows even faster consumption of the sample, since the data are in the range from ~2100 to ~2800µm change in sound metal. This trend and the resulting damaged morphologies can be seen in Figure 4.35, photomicrographs 10, 11 and 12.

An example of two modes of attack that operate is given in Figure 4.64 (a), which shows the probability plot for CMSX4 in 500vpm SO_2 at 700°C after 500h exposure. The line corresponding to damage of 1.5µg/cm^2/h changes from a pitting mode (~60% of the sample surface) to a broad front attack, up to ~100µm of change in sound metal. Once the broad front attack has started, it moves forward with increasing flux deposit to 5µg/cm^2/h and, again at 15µg/cm^2/h. The resulting morphologies can be seen in Figure 4.38, photomicrographs 7, 8 and 9.

An example of a good normal distribution set is given by the straight lines for SC^2 at the three deposition fluxes in 50vpm SO_2 at 700°C after 500h exposure in Figure (a). The resulting morphologies can be seen in Figure 4.34, photomicrographs 1, 2 and 3.

The probability plots corroborate the relevance of statistical analysis: if, in Figure 4.62, the pure mean of the non-straight line corresponding to the 1.5µg/cm^2/h line were taken, the SC^2 in those conditions would be marked to have good performance, regardless of the deeper propagation values.

Straight probability lines are often observed for PtAl-coated samples, an indication of the protection by the coating on the substrate.

4.4.1 Probability Analysis Phase 1

4.4.1.1 Gas composition sensitivity

The sensitivity of uncoated IN738LC to gas composition with a deposit of 50/50 $(Na/K)_2 SO_4$ at 700°C is plotted in Figure 4.44 (a). These data show that, for this material, the SO_2/HCl combination cause higher general corrosion damage as the SO_2 and HCl concentration are increased from 20 to 300 vpm, and from 10 to 500 vpm respectively.

When PtAl-coated shown in Figure 4.44(b), there is no obvious protection improvement for IN738LC since the coating has been depleted in all cases, except when exposed to the lowest gas concentration. This effect may be also seen in the micrographs displayed in Figure 4.31.

In the case of the single crystal CMSX-4, the sensitivity towards the gas compositions shows the same trends as the reference material, IN738LC, although in different proportions (Figure 4.45 (a)). The general resistance to corrosion damage was improved by the PtAl coating (Figure 4.45 (b)). Unlike for the uncoated alloy, the higher concentration of HCl (500vpm) now appears beneficial.

The PtAl coating is not penetrated and does not seem to have been affected as much as for the 300vpm SO_2/100vpm HCl level; such effects can be visually appreciated in the micrographs in Figure 4.33. This tendency was also observed for IN738 LC when PtAl-coated.

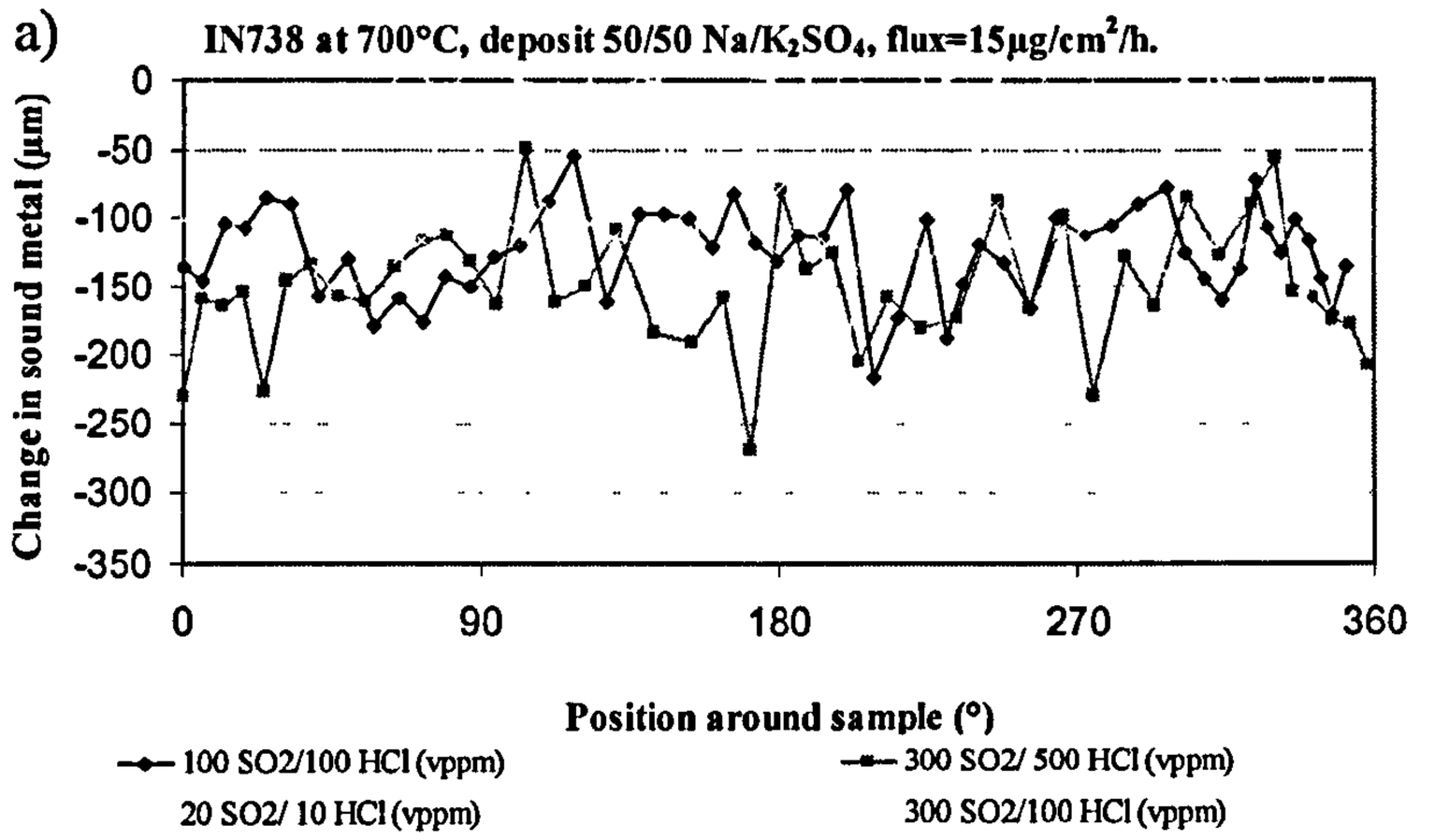

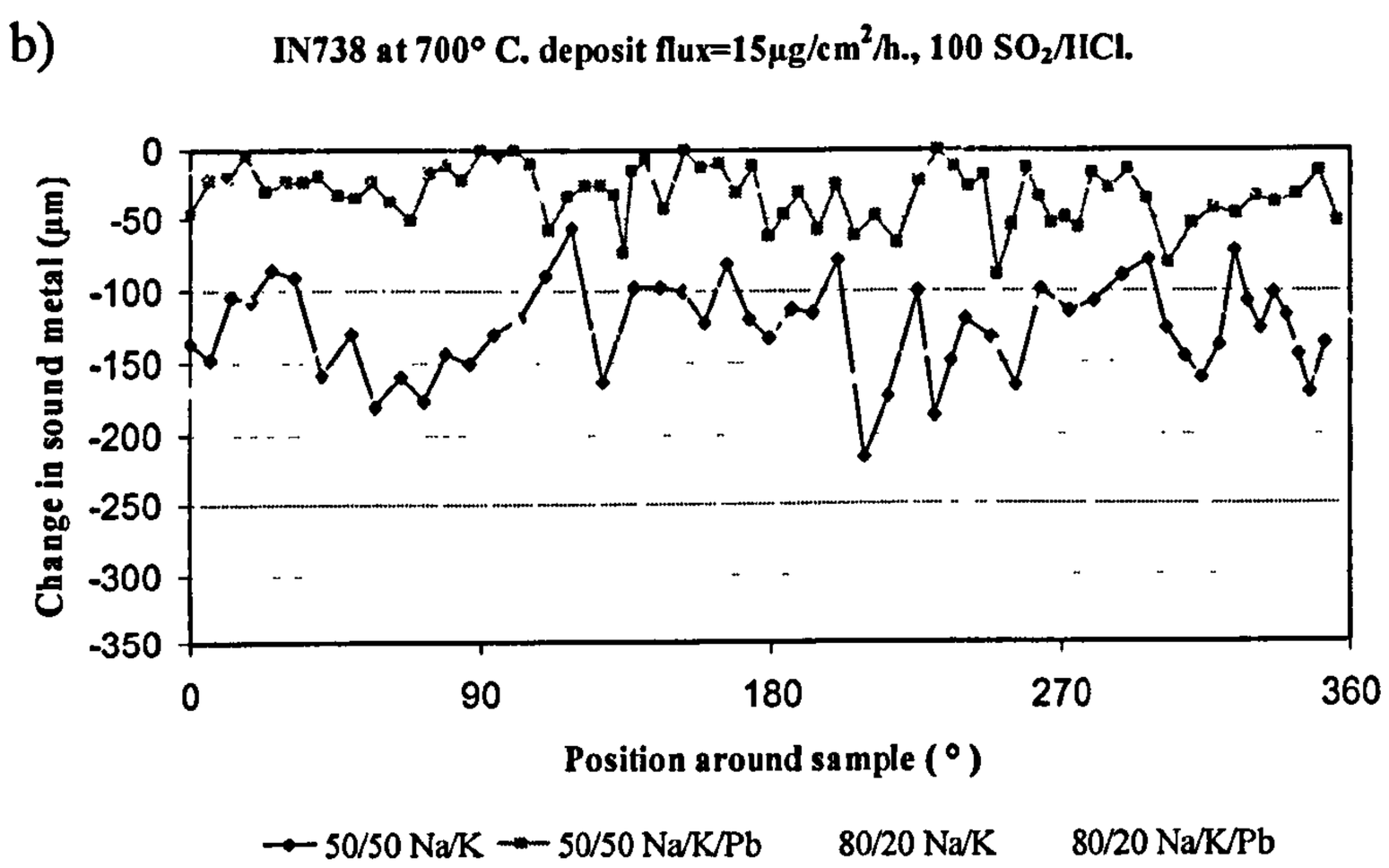

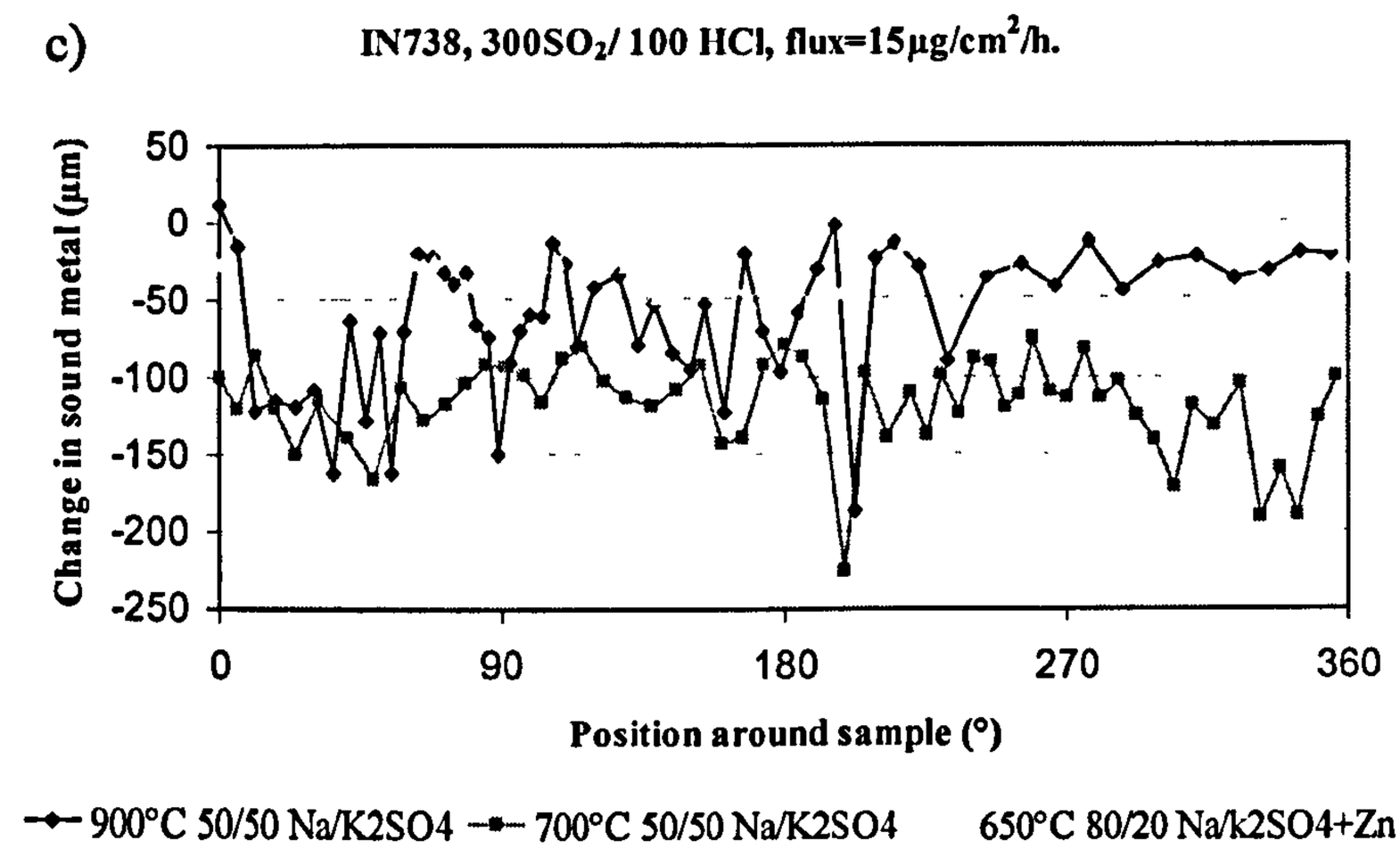

Figure 4.43: Sensitivity of measurements of sound metal loss in gas composition (a), deposit composition (b) and temperature (c) for uncoated IN738LC.

a) Uncoated IN738, 50/50 $(Na/K)_2SO_4$ flux 15µg/cm^2/h at 700° C.

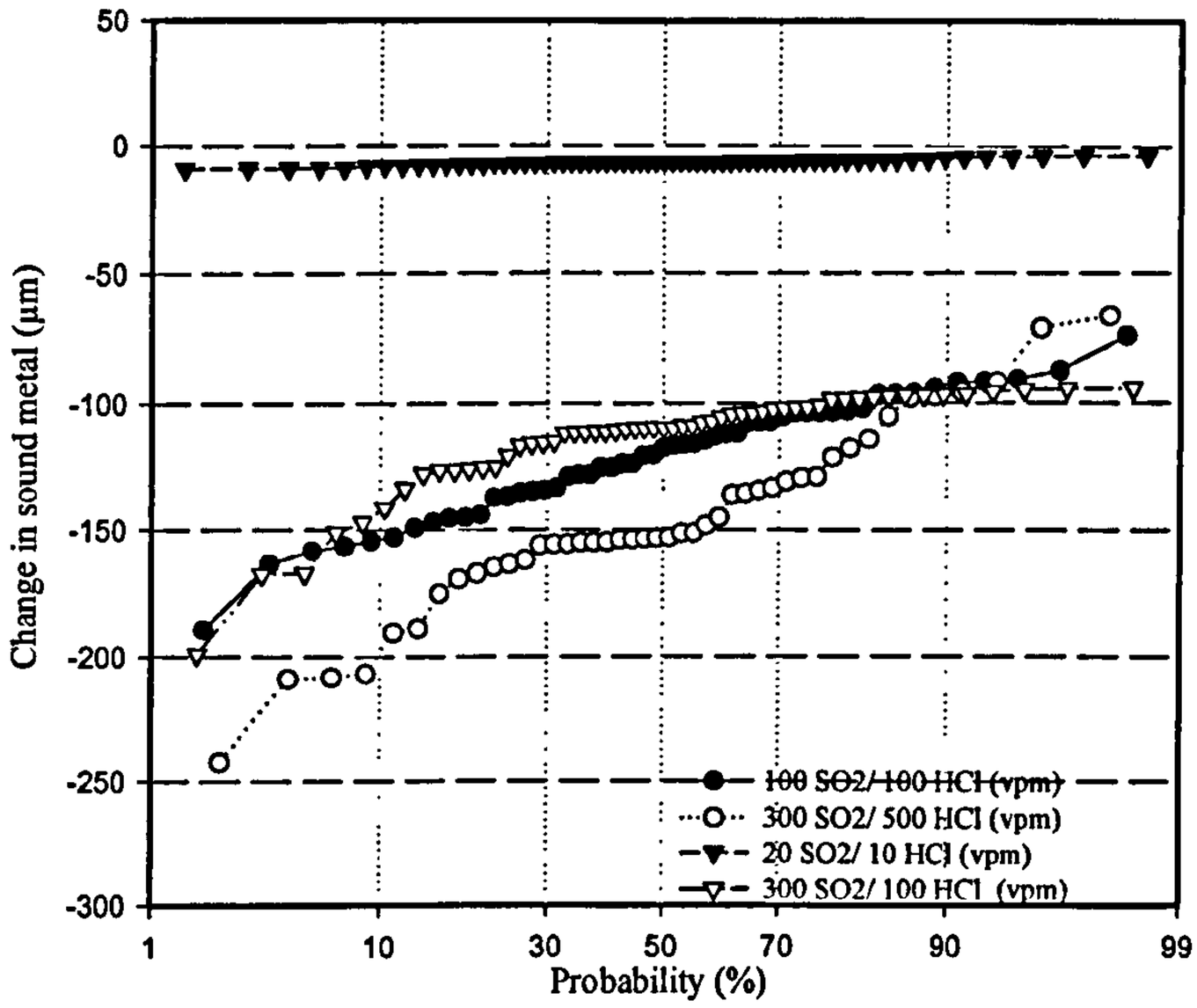

b) PtAl IN738, 50/50 $(Na/K)_2SO_4$, flux 15µg/cm^2/h at 700° C.

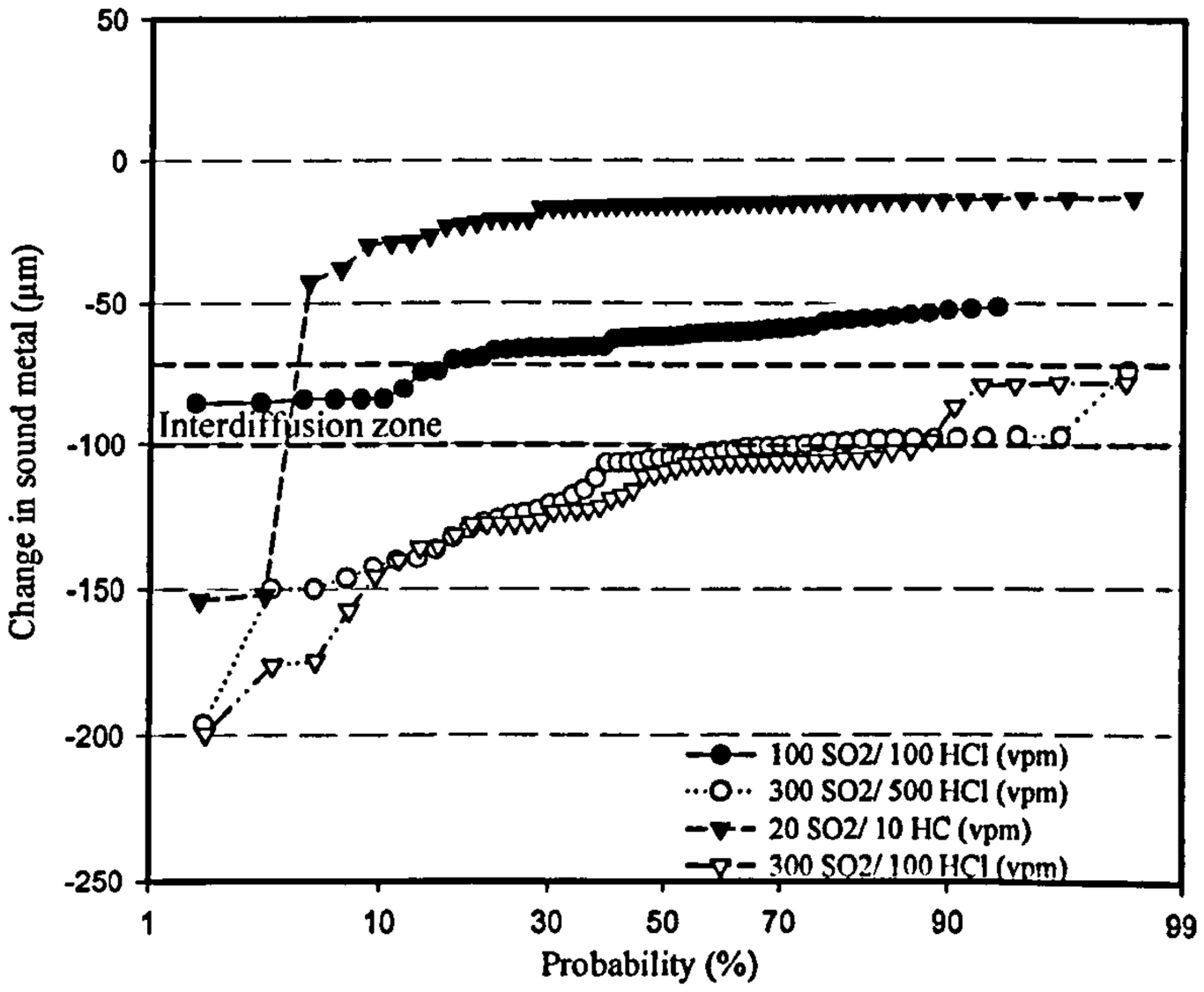

Figure 4.44: Change in sound metal as a function of the probability damage under different gas composition for uncoated IN738LC (a) and PtAl coated (b) after 500h exposure.

a) Uncoated CMSX-4, 50/50 $(Na/K)_2SO_4$, flux 15µg/cm^2/h at 700° C.

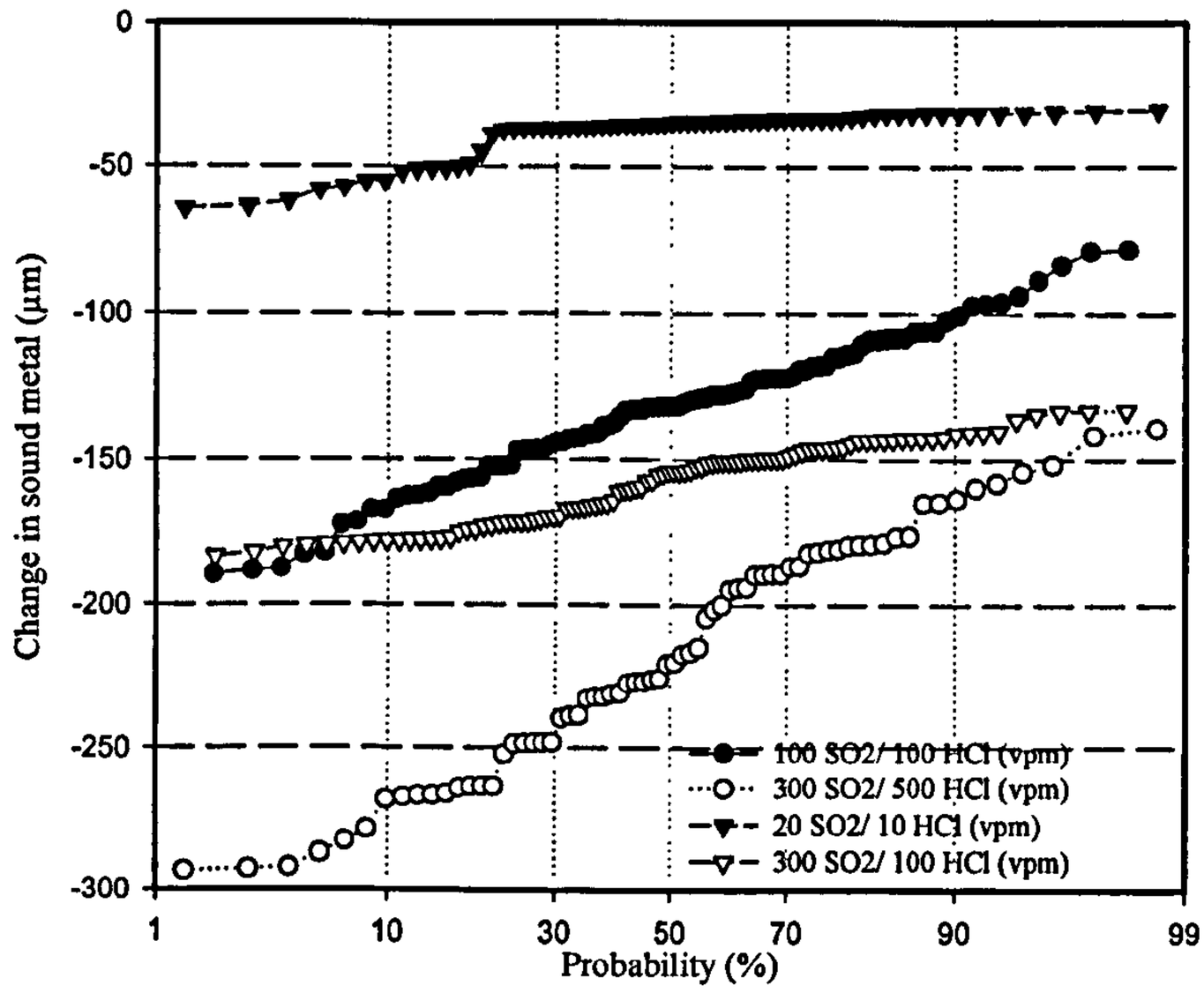

b) PtAl CMSX-4, 50/50 $(Na/K)_2SO_4$, flux 15µg/cm^2/h at 700° C.

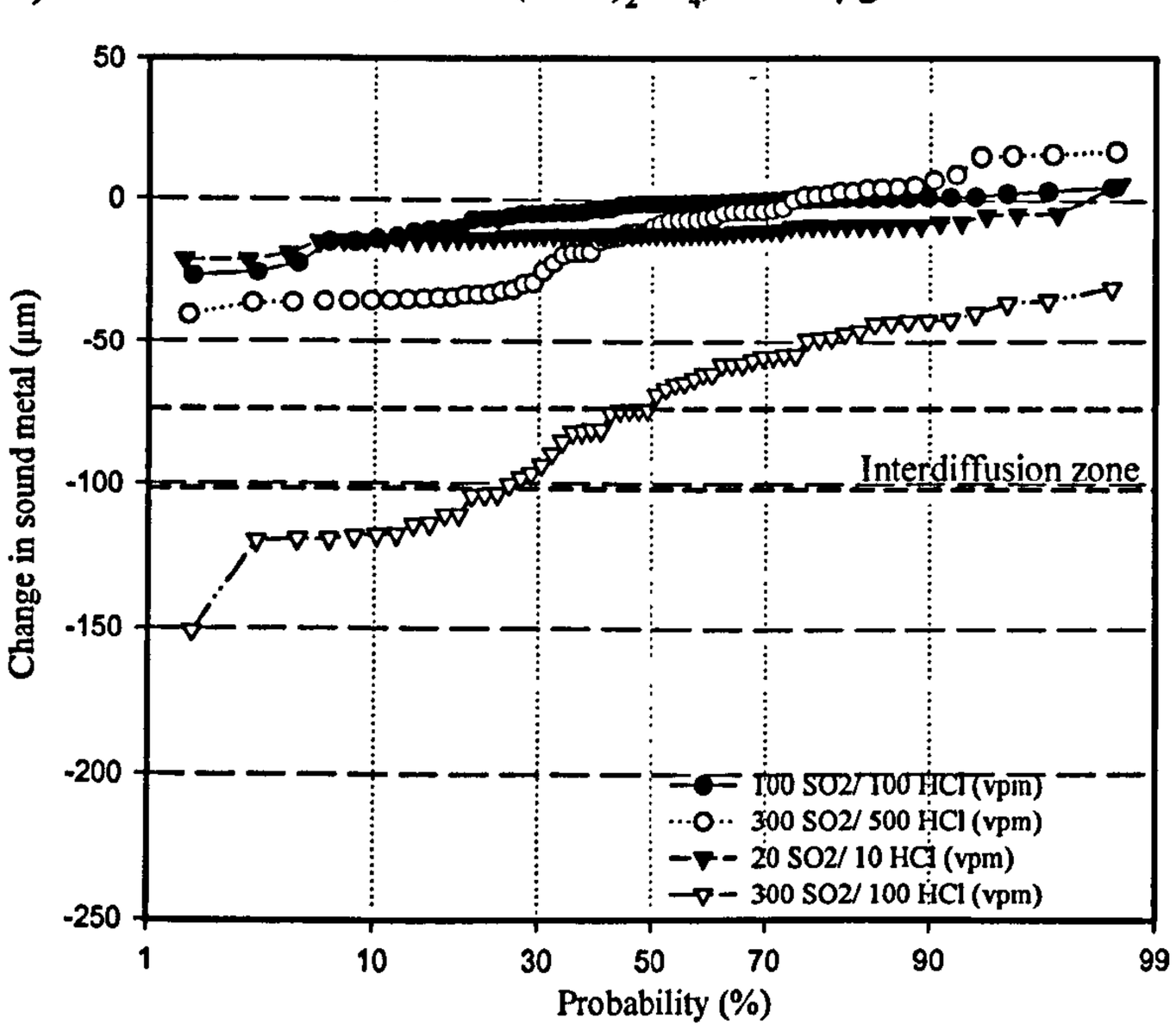

Figure 4.45: Change in sound metal as a function of the probability damage under different gas composition for uncoated CMSX4 (a) and PtAl coated (b) after 500h exposure.

a) Uncoated IN738, flux 15 µg/cm^2/h in 100 SO_2/HCl at 700°C.

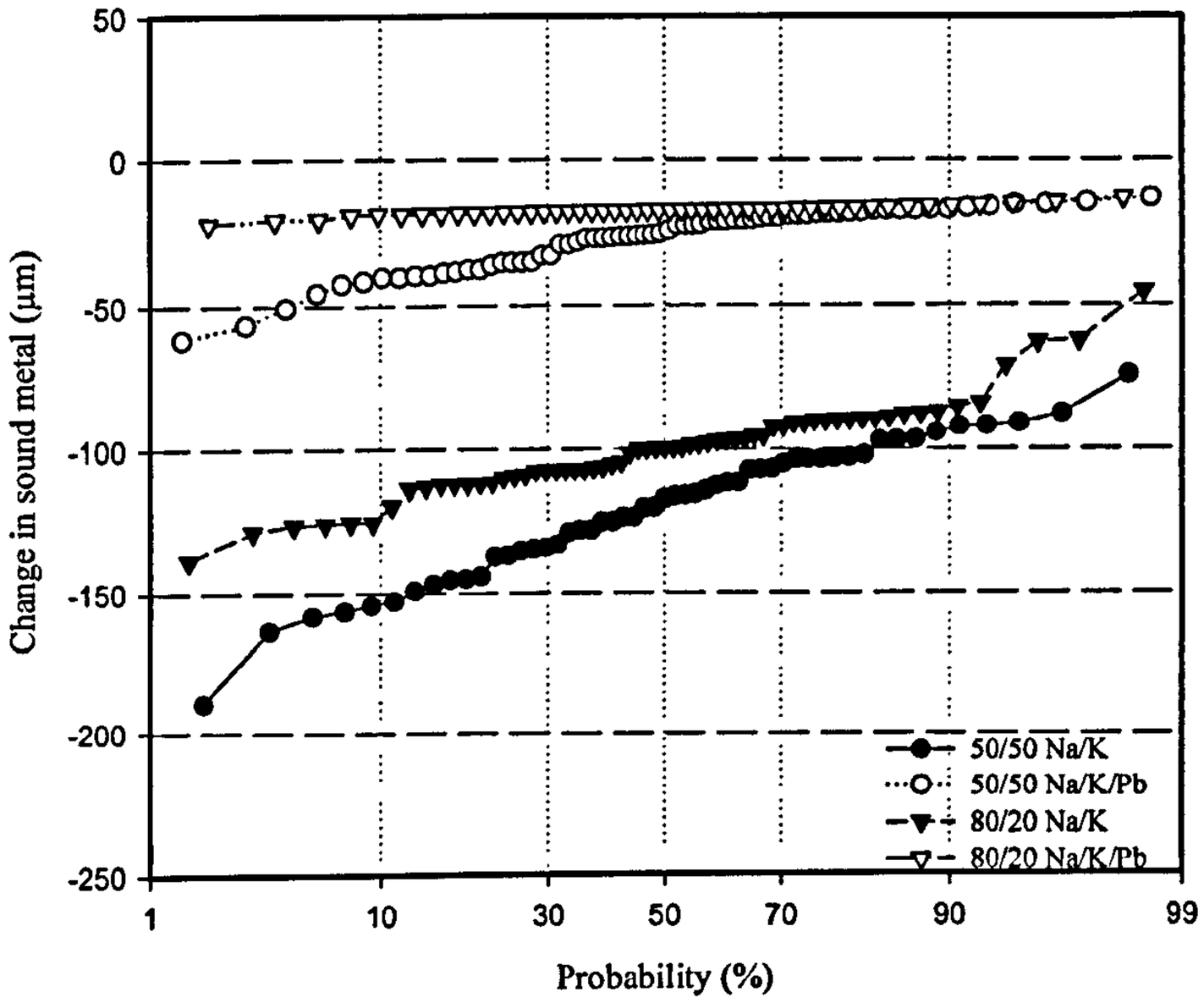

b) PtAl Coated IN738LC, flux 15µg/cm^2/h in 100 vpm SO_2/HCl at 700° C.

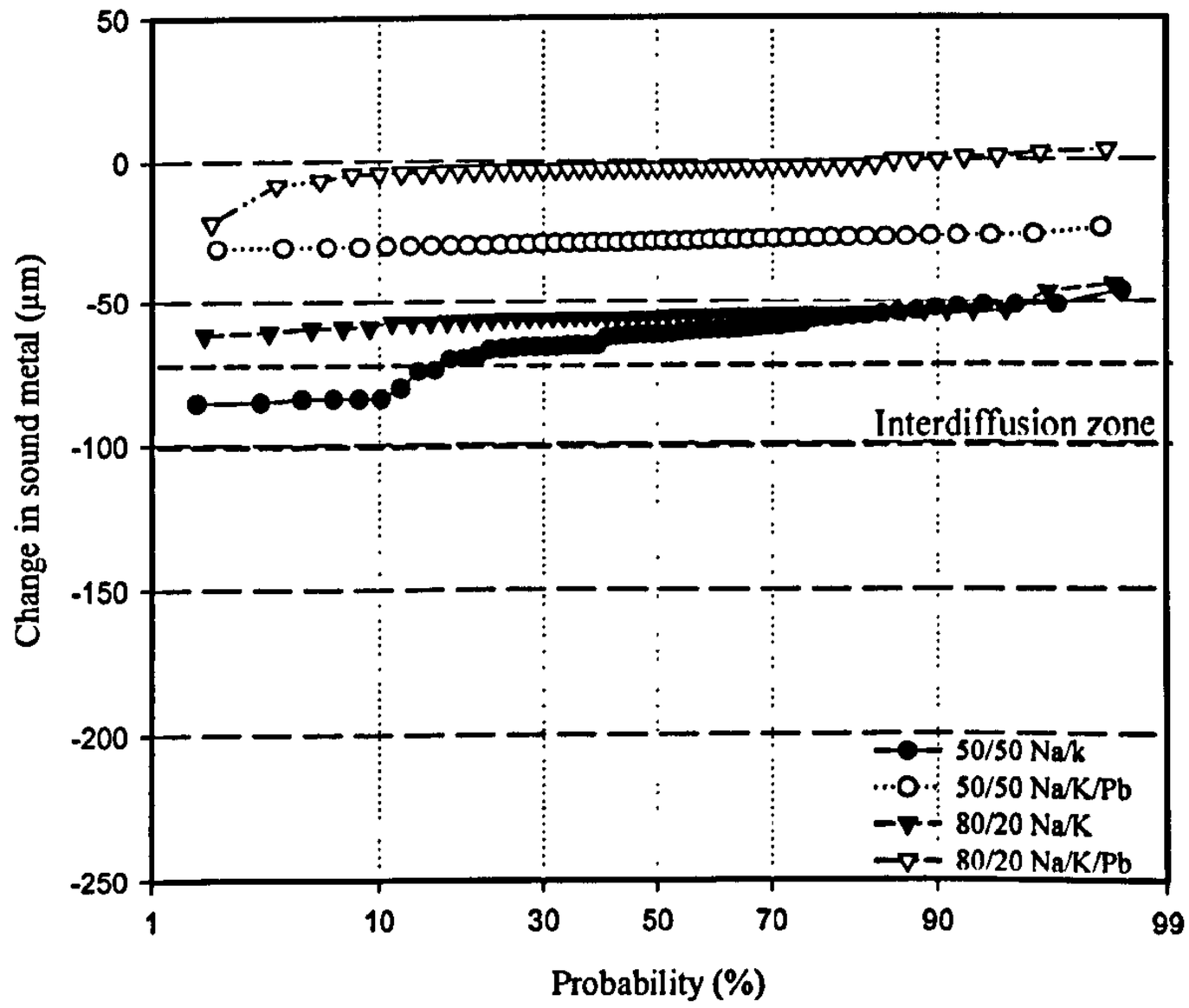

Figure 4.46: Change in sound metal as a function of the probability damage under different deposit composition for uncoated IN738LC (a) and PtAl coated (b) after 500h exposure.

a) Uncoated CMSX-4, flux 15μg/cm^2/h in 100 vpm SO_2/HCl at 700° C.

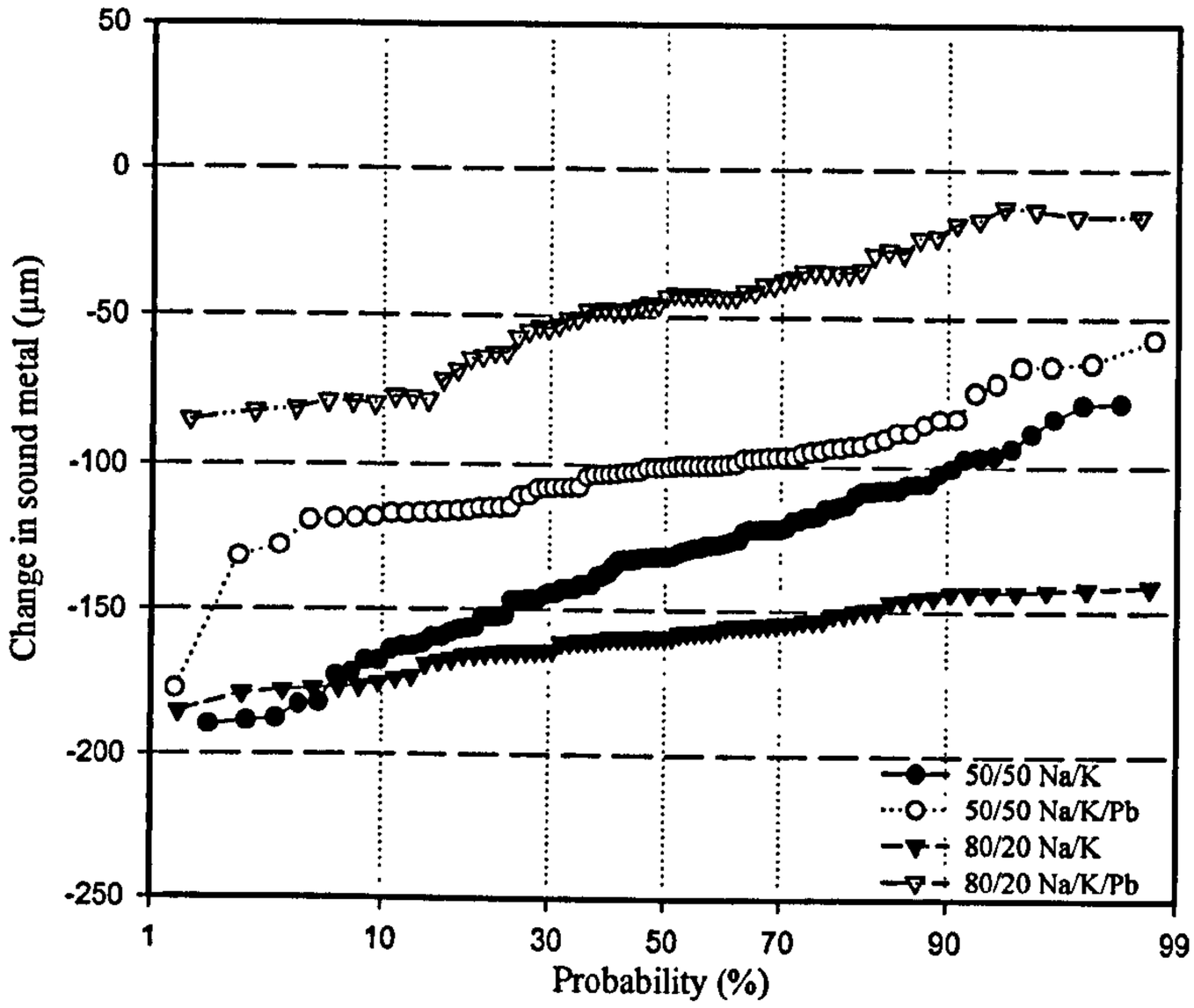

b) PtAl Coated CMSX-4, flux 15 μg/cm^2/h in 100 vpm SO_2/HCl at 700° C.

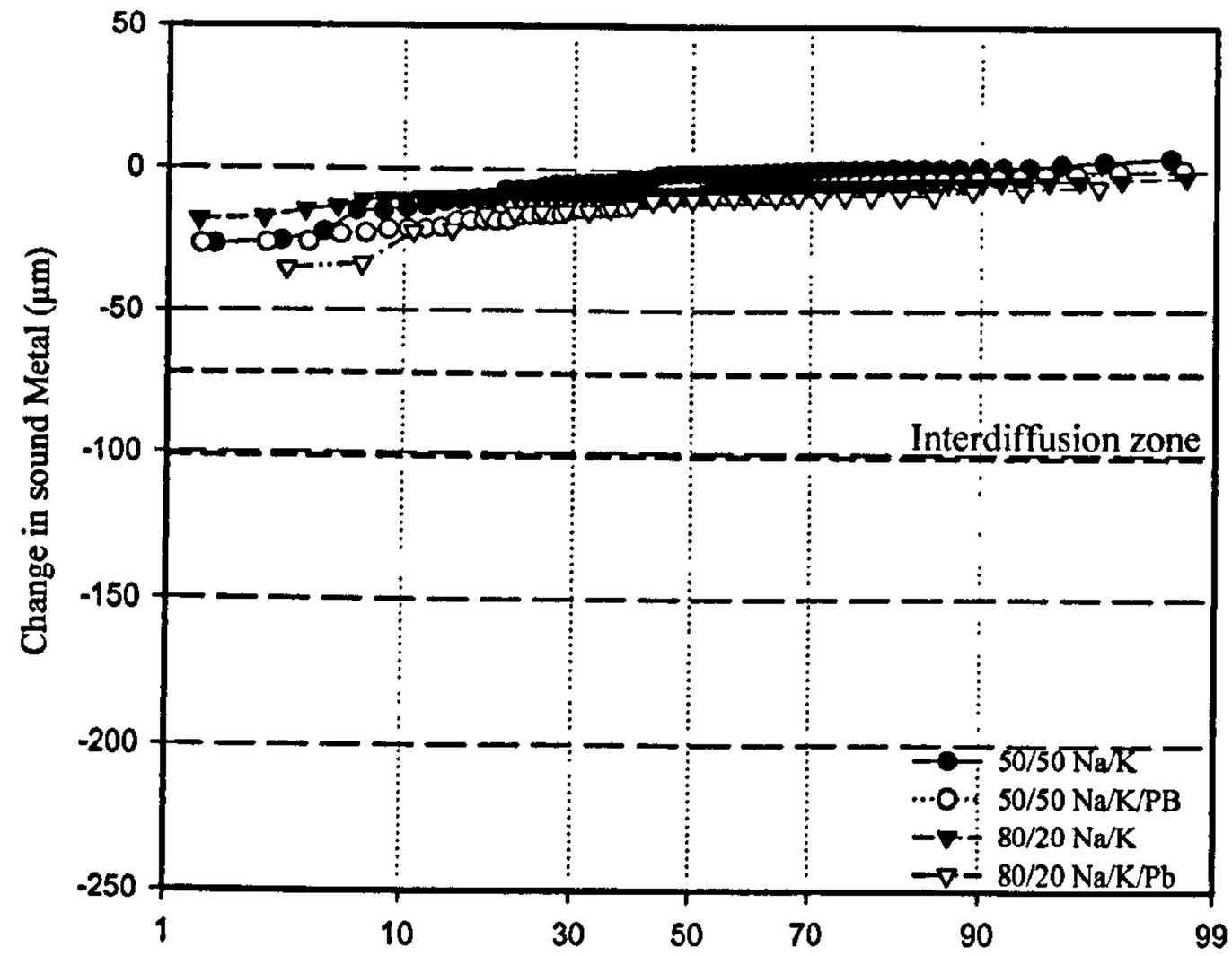

Figure 4.47: Change in sound metal as a function of the probability damage under different deposit composition for uncoated CMSX4 (a) and PtAl coated (b) after 500h exposure.

4.4.1.2 Deposit composition sensitivity

The next group of figures shows the sensitivity of the studied system materials to different deposit compositions i.e. $(Na/K)_2 SO_4$ and K_2SO_4, NaCl and $Pb(NO_3)_2$, in two different concentrations; 50/50 and 80/20, with a flux of 15μg/cm^2/h in 100 vpm SO_2/HCl at 700° C.

Figure 4.46 (a) shows that, for uncoated IN738LC, the alkali deposits caused much higher general corrosion damage (~200μm change in sound metal maximum penetration) than the deposits containing lead (~50μm change in sound metal maximum penetration).This trend is observed for PtAl-coated specimens except at different proportions; i.e. less general corrosion damage (~80μm change in sound metal), Figure 4.46 (b). However, little coating was left when either concentration of alkali deposits was applied; this is clear in the micrographs of Figure 4.31.

In a similar manner to that observed for the uncoated IN738 LC, the uncoated single crystal CMSX4, see Figure 4.47 (a), exhibited more general corrosion damage in the alkali metal solutions than in the deposits containing lead which, by comparison with the data for uncoated IN738 LC, seem to have had more effect (~150 μm change in sound metal) on this single crystal alloy. A visible improvement in performance can be seen in Figure 4.47 (b), when the single crystal is PtAl-coated. The general corrosion damage is no more than ~40 μm loss of sound metal, which is also better than observed for the PtAl-coated IN738LC (~80 μm). This improved performance can be seen in the photographs of Figure 4.33.

4.4.1.3 Temperature sensitivity

The sensitivities of hot corrosion of the materials to changing temperature are shown in the probability plots in Figure 4.48 and Figure 4.49. The uncoated IN738LC has been more extensively attacked at 700°C than at 650 and 900°C Figure 4.48 (a).

This susceptibility changes when the material is PtAl-coated (i.e., when coated, there is less general corrosion damage and this damage is less with increasing temperature from 650 to 900°C, Figure 4.48 (b)). As for the uncoated IN738LC, the CMSX4 was more affected at 700°C than at 650 and 900°C and the general corrosion damage was slightly larger than observed for IN738LC, Figure 4.49 (a). PtAl-coated CMSX4 again shows more attack at 700°C, Figure 4.49 (b), while at 700°C, the coating was penetrated and the substrate suffered severe attack.

a) Uncoated IN738, 80/20 $(Na/K)_2$ flux 15µg/cm^2/h in 300vpm SO_2/100 HCl.

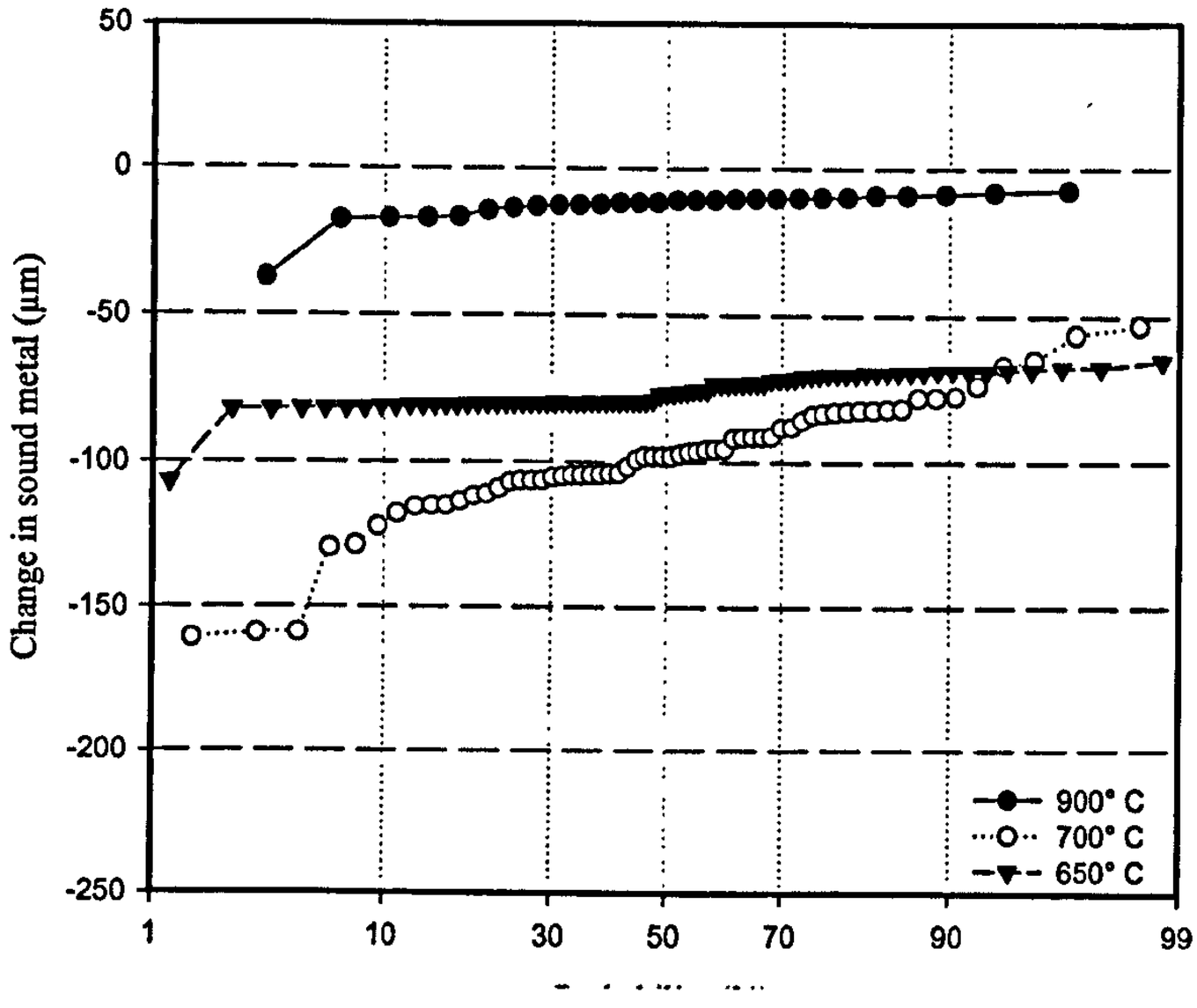

b) PtAl Coated IN738, 80/20 $(Na/K)_2SO_4$ flux 15µg/cm^2/h in 300 SO_2/100 HCl.

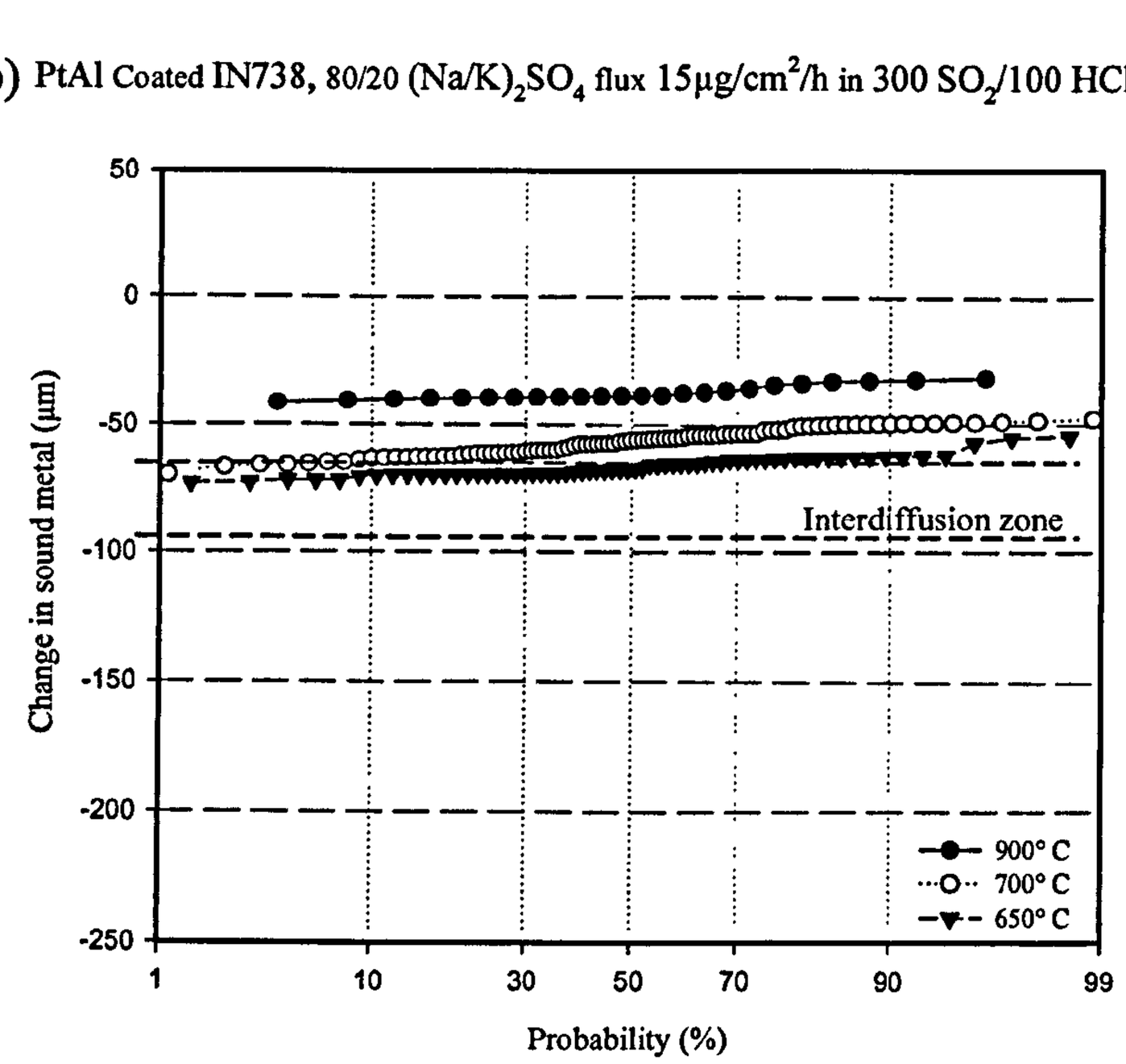

Figure 4.48: Change in sound metal as a function of the probability damage under different temperature of exposure for (a) uncoated IN738LC and (b) PtAl coated after 500h exposure.

a) Uncoated CMSX-4, 80/20 $(Na/K)_2$ flux 15µg/cm^2/h in 300vpm SO_2/100HCl.

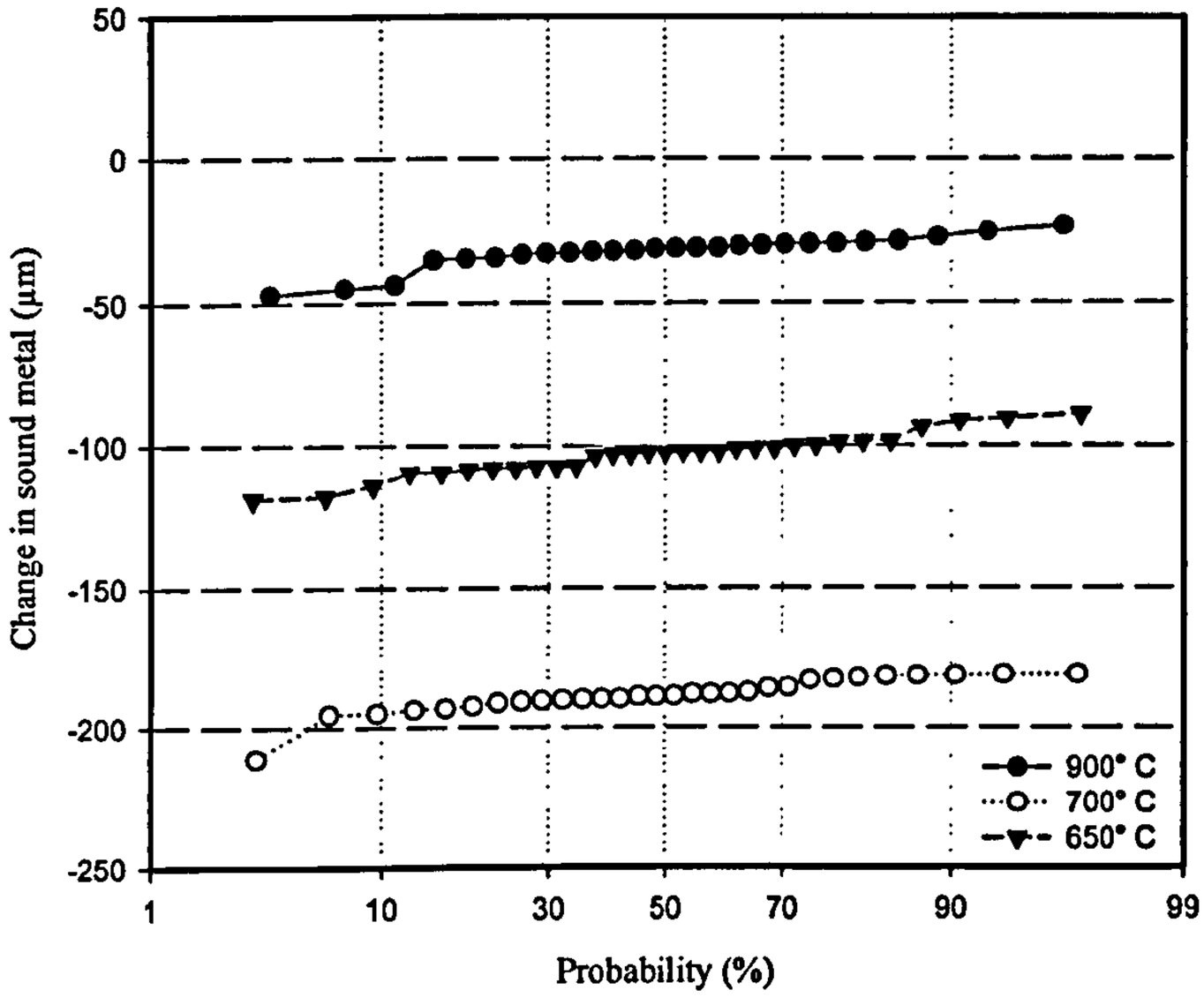

b) PtAl Coated CMSX-4, 80/20 $(Na/K)_2SO_4$ flux 15µg/cm^2/h in 300 SO_2/100 HCl.

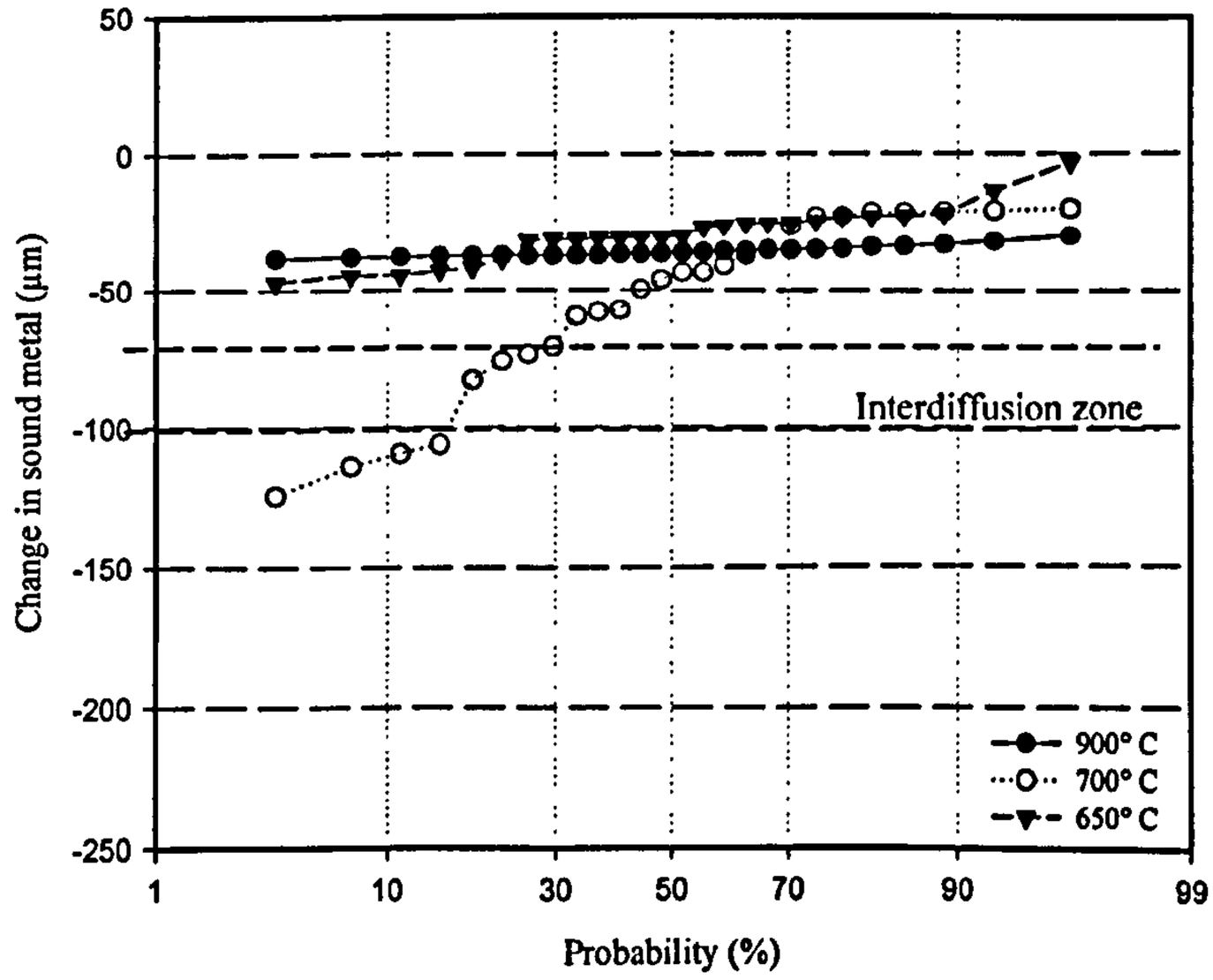

Figure 4.49: Change in sound metal as a function of the probability damage under different temperature of exposure for (a) uncoated CMSX4 and (b) PtAl coated after 500h exposure.

4.4.2 Probability Analysis Phase 2

4.4.2.1 Sensitivity to gas composition and temperature

The sensitivities of a new single crystal SC^2 and the commercial alloy CMSX-4 have been studied in the present work. Figure 4.50 to Figure 4.61 present the effects of three gas compositions: 50vpm SO_2, 500vpm SO_2 and 50vpmSO_2/500vpm HCl on uncoated and PtAl-coated material at 700 and 900°C, with the 80/20 $(Na/K)_2SO_4$ at fluxes of 1.5, 5 and 15µg/cm^2/h.

Figure 4.50 shows the effects of the three gas compositions with a flux of 1.5µg/cm^2/h on uncoated SC^2 at 700°C (a) and 900°C (b). The least aggressive environment for this material was 50vpmSO_2/500vpm HCl and uniform internal damage was observed, as well as sulphidation of the sample exposed in 50vpm SO_2 (Figure 4.34, photomicrograph 15 and 3 respectively). At 900°C, uncoated SC^2 was less sensitive to the gas containing 50vpm SO_2, and uneven internal sulphidation was observed (Figure 4.34 photomicrograph 6); more internal damage was observed in the 50vpm SO_2/500vpm HCl gas and internal oxidation/sulphidation occurred in the 500vpm SO_2 gas; such effects can be seen in Figure 4.34 (photomicrographs 18 and 12 respectively).

Figure 4.51 (a) and (b) show the improvement in performance of the SC^2 due to PtAl coating in the three hot corrosion environments, particularly at 900°C in the 500vpm SO_2 gas. Less damage was observed in those samples exposed in the environment with HCl addition at both temperatures. Features of the coating can be seen in Figure 4.36 (photomicrographs 3, 9, 15) for 700°C and in Figure 4.37 (photomicrograph 6, 12 and 18) for 900°C.

Figure 4.52 (a) and (b) show the results for uncoated SC^2 in identical conditions at 700 and 900°C respectively. The hot corrosion attack of CMSX4 increased considerably in the three environments at 900°C. At both temperatures, the least aggressive environment was the 50vpm SO_2/500vpm HCl gas. Typical type I hot corrosion, internal oxidation/sulphidation, was observed at 900°C (Figure 4.39 photomicrographs 6, 12, 18) and internal attack was also observed at 700°C in the sample exposed in the HCl addition environment (as seen in Figure 4.38, photomicrograph 15).

Figure 4.53 (a) and (b) show the results for the PtAl coated CMSX-4 at 700 and 900°C respectively. At both temperatures, the PtAl/CMSX-4 system was more sensitive in the 50vpm SO_2 gas; however, a significant improvement can be appreciated in (b) at 900°C in the two corrosive environments, due the PtAl coating. Typical type II hot corrosion morphology can be seen in Figure 4.40, photomicrograph 3, but not in photomicrograph 15, also at 700°C.

At 900°C, the coating is practically intact, as seen in Figure 4.41, photomicrographs 6 and 18. For uncoated SC^2 with a deposition flux of 5µg/cm^2/h, Figure 4.54 (a) shows a clear effect of a high concentration of SO_2 (500vpm), with much less damage from a low concentration of SO_2 (50vpm). The mixture of SO_2+HCl (50/500vpm) gas showed a slightly higher value of sound metal loss due to the extent of internal attack.

The distinct morphological characteristics may be appreciated in Figure 4.34, photomicrographs 2, 8 and 14. Comparing the differences in morphology between the uncoated SC^2 exposed at 700 and 900°C (Figure 4.54 (a) and (b)), there is an enormous increase in metal loss with internal attack in general but, especially, at the higher SO_2 concentration. This effect is shown in the micrographs in Figure 4.35 (photomicrographs 5, 11 and 17) where sulphidation in the alloy can also be seen. At 900°C, the low SO_2 gas concentration resulted in better performance in the presence of HCl.

SC^2 with PtAl coating exposed at 700°C was more resistant and had less sensitivity towards SO_2, in particular, as seen for the high gas concentration (Figure 4.55 (a)). A similar effect was observed at 900°C (Figure 4.55 (b)), although little protective coating was left after exposure in the 500vpm SO_2 environment. Figure 4.36 (photomicrographs 2, 8, 14) and Figure 4.37 (photomicrographs 5, 11 and 17) present the features of such attack for 700 and 900° C respectively.

In comparison with CMSX4, the uncoated SC^2 is, in general terms, less sensitive to the effect of the gaseous environment at 700°C (Figure 4.54 (a) vs. Figure 4.56 (a)). The 500 vpm SO_2 environment is the most damaging for the uncoated CMSX4. The least damaging environment is the low SO_2 in combination with HCl. These two materials at 900°C have reverse sensitivities from that at 700°C: i.e. the CMSX4 is less attacked at the high SO_2 concentration than the SC^2 which corrodes at approximately three times the rate of CMSX4, in terms of sound metal loss, i.e. section loss and internal sulphidation. In the 50vpm SO_2/500vpm HCl gas, SC^2 is more resistant to attack (Figure 4.54 (b) vs. Figure 4.56 (b)). An interesting change in morphologies is observed on comparing Figure 4.34 with Figure 4.38 and Figure 4.35 with Figure 4.39.

The PtAl coating on CMSX-4 provides some protection at both temperatures (700 and 900°C) (Figure 4.57 (a) and (b)).The coating provides good protection in the 50 vpm SO_2/500 vpm HCl environment at both 700°C and 900°C. The PtAl coating performs better on SC^2, as can be seen in Figure 4.55 (a) vs. Figure 4.57 (a).

Figure 4.58 shows the effect of the three gas compositions with a flux of 15μg/cm^2/h on uncoated SC^2 at 700°C (a) and 900°C (b).The greater effect was for the material exposed at 900°C in the three different environments. Catastrophic corrosion is observed for the SC^2 in the 500vpm SO_2 gas.

The resulting morphology can be seen in Figure 4.35 (photomicrographs 4, 10, 16) and, for the uncoated SC^2, at 700°C in Figure 4.34 (photomicrographs 1, 7 and 13). Less damage was observed in the PtAl-coated material at both temperatures, except in that exposed in the 50vpm SO_2 gas at 700°C. The resulting morphologies can be seen in Figure 4.36 (photomicrographs 1, 7, 13) and in Figure 4.37 (photomicrographs 4, 10 and 16).

The results for uncoated CMSX4 can be seen in Figure 4.60 (a) and (b). It can be seen that this material is very sensitive in the 500vpm SO_2 environment in both temperatures, but notably at 900°C. At 900°C, catastrophic sulphidation/oxidation damage is also observed for the uncoated CMSX4 in the 50vpm SO_2 gas and deep internal damage for the material exposed in the gas with the HCl addition. These results can also be seen in Figure 4.39 (photomicrographs 4, 10, 16) and, for 700°C, in Figure 4.38 (photomicrographs 1, 7 and 13).

Results from the PtAl-coated CMSX4 at 700°C, Figure 4.61 (a) and (b), show no improvement in any environment compared with the uncoated material; even in the 50vpm SO_2/500vpm HCl environment the coating was consumed (Figure 4.40 photomicrograph 13); however, at 900°C, a huge improvement is seen in the 50vpm SO_2/500vpm HCl environment.

In the 50vpm SO_2 environment at 900°C, some coating was left and in that same environment at 700°C, the coating was penetrated and the alloy was attacked locally; such features can be seen in Figure 4.41 (photomicrograph 4) and Figure 4.40 (photomicrograph 1) respectively.

a) Uncoated SC[2], 80/20 $(Na/K)_2SO_4$, flux 1.5µg/cm^2/h at 700°C.

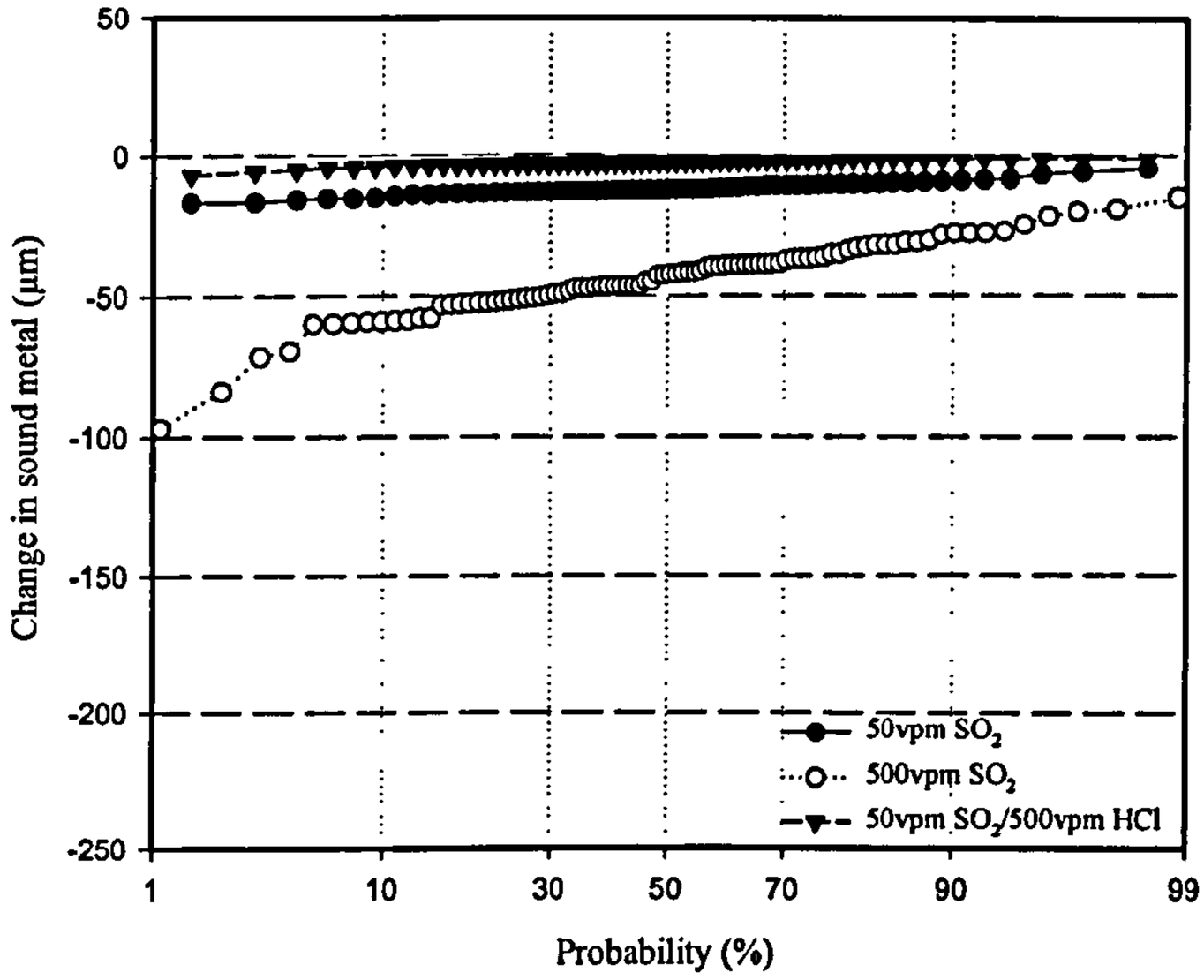

Uncoated SC[2], 80/20 $(Na/K)_2SO_4$, flux 1.5µg/cm^2/h at 900°C.

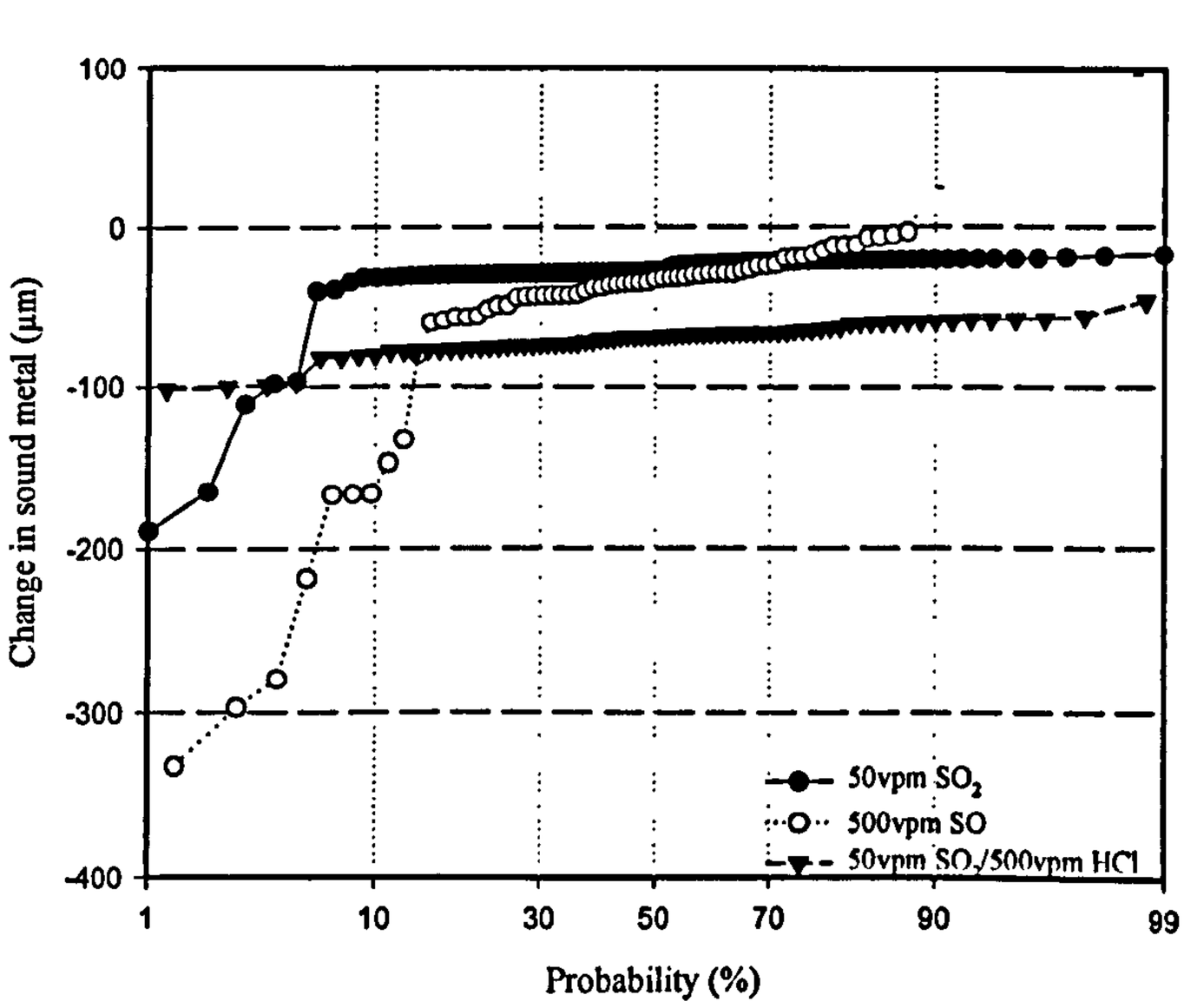

Figure 4.50: Change in sound metal as a function of the probability damage under different gas composition and deposit flux of 1.5µg/cm^2/h for uncoated SC[2] at (a) 700°C and (b) 900°C after 500h exposure.

a) PtAl Coated SC^2, 80/20 $(Na/K)_2SO_4$, flux 1.5µg/cm^2/h at 700°C.

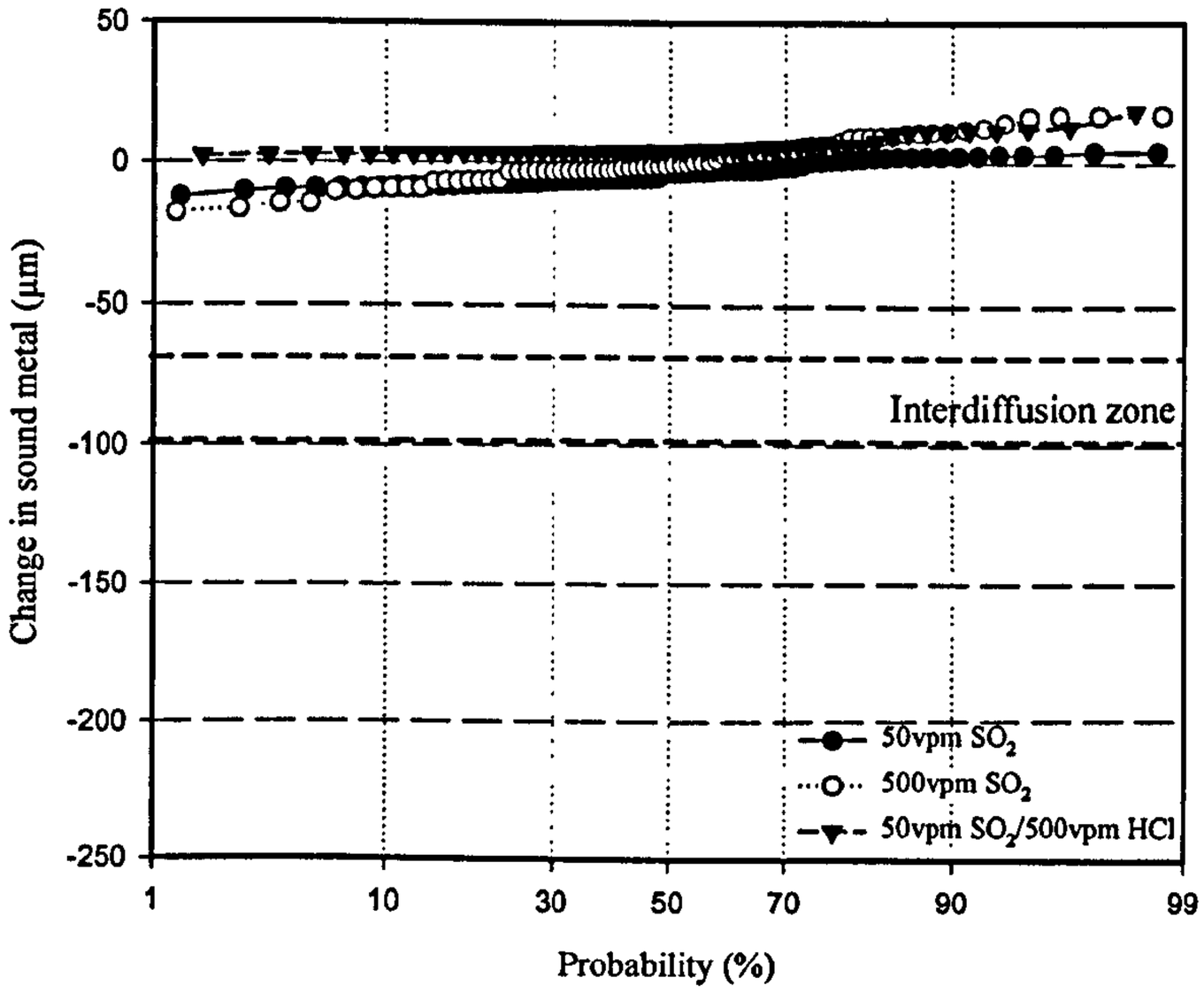

b) PtAl Coated SC^2, 80/20 $(Na/K)_2SO_2$, flux 1.5µg/cm^2/h at 900°C.

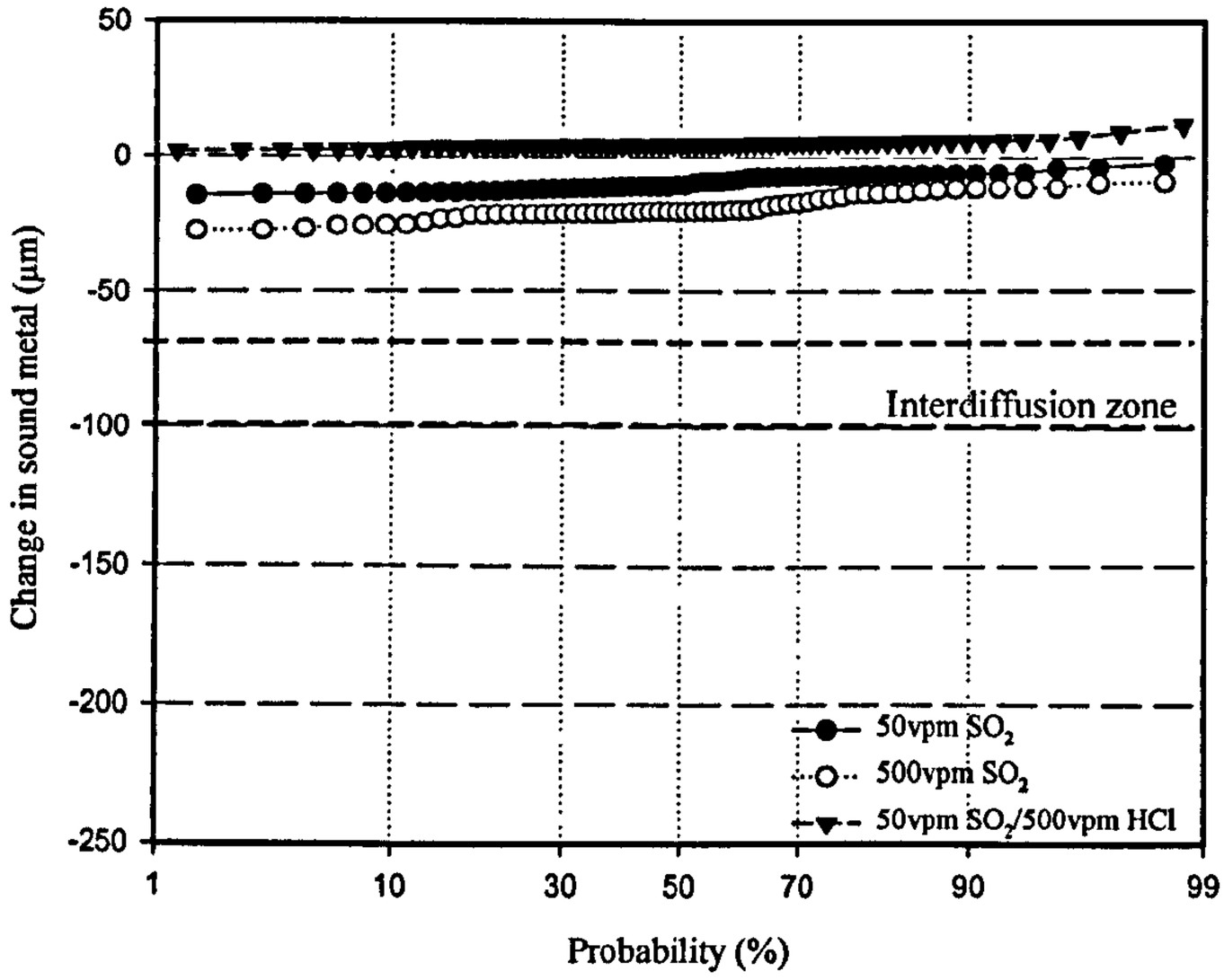

Figure 4.51: Change in sound metal as a function of the probability damage under different gas composition and deposit flux of 1.5µg/cm^2/h for PtAl coated SC^2 at (a) 700°C and (b) 900°C after 500h exposure .

a) Uncoated CMSX-4,80/20 $(Na/K)_2SO_4$, flux 1.5 µg/cm^2/h at 700°C.

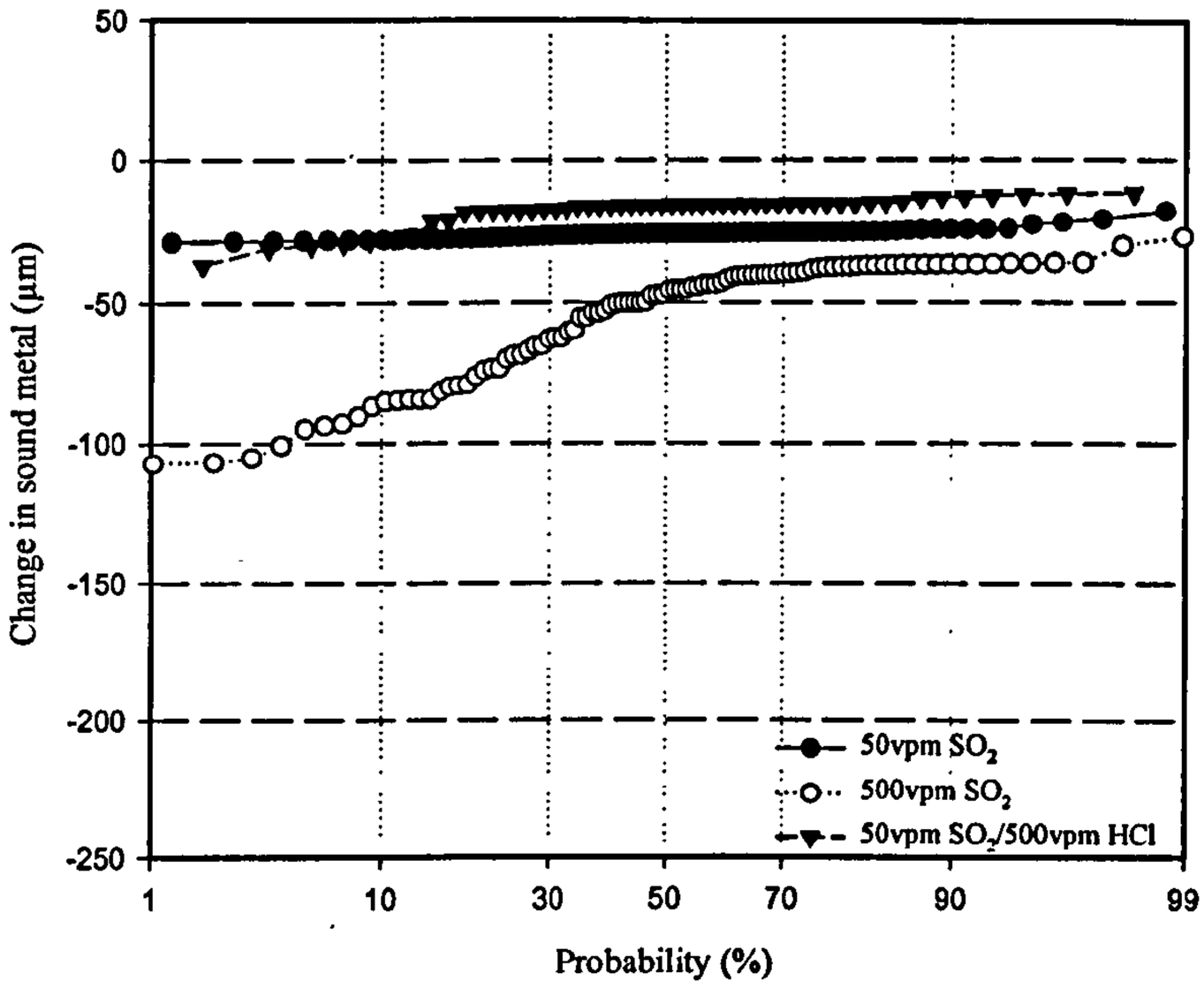

b) Uncoated CMSX-4, 80/20 $(Na/K)_2SO_4$, flux 1.5 µg/cm^2/h at 900°C.

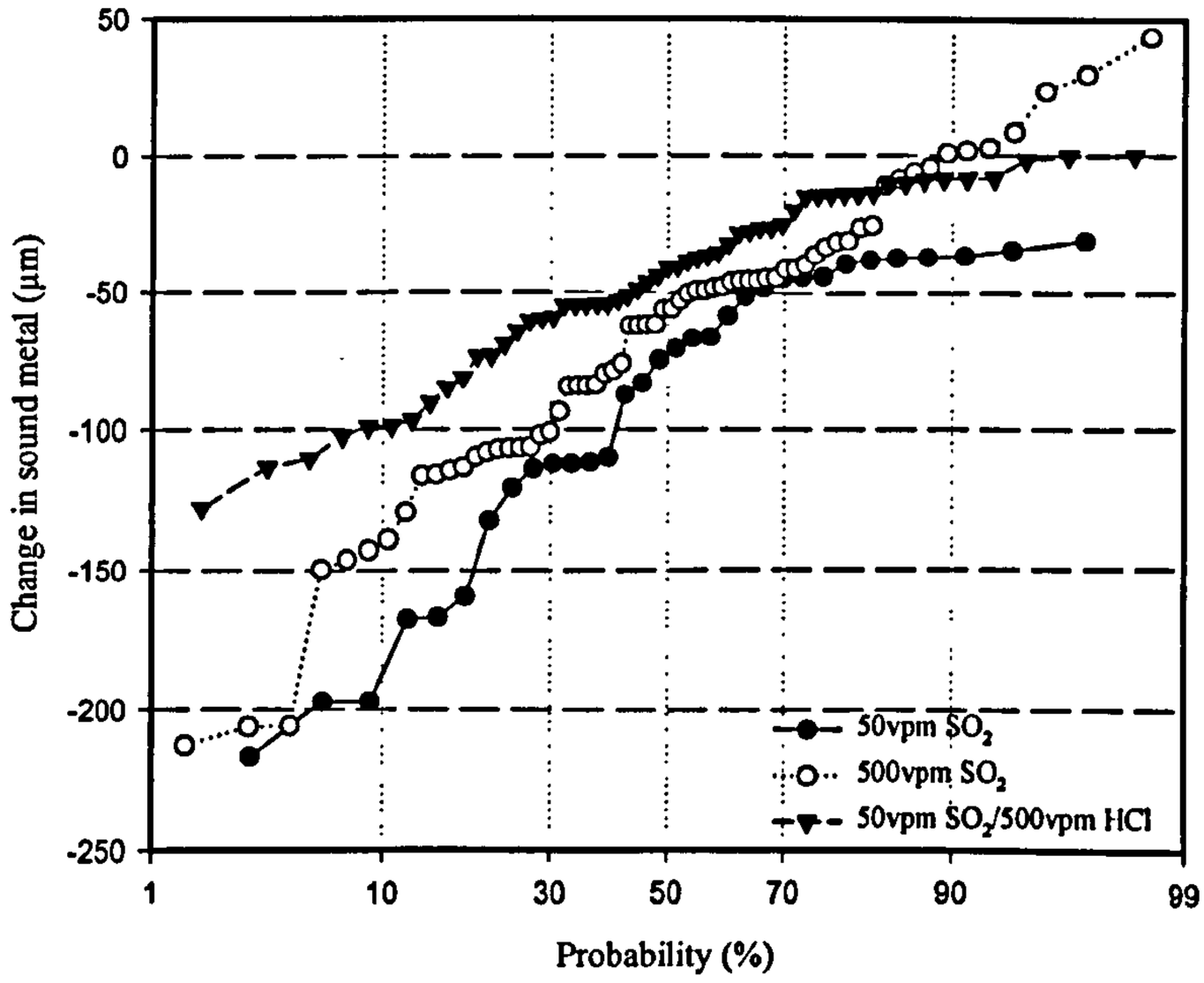

Figure 4.52: Change in sound metal as a function of the probability damage under different gas composition and deposit flux of 1.5µg/cm^2/h for uncoated CMSX4 at (a) 700°C and (b) 900°C after 500h exposure.

a) PtAl Coated CMSX-4, 80/20 $(Na/K)_2SO_4$, flux 1.5µg/cm^2/h at 700°C.

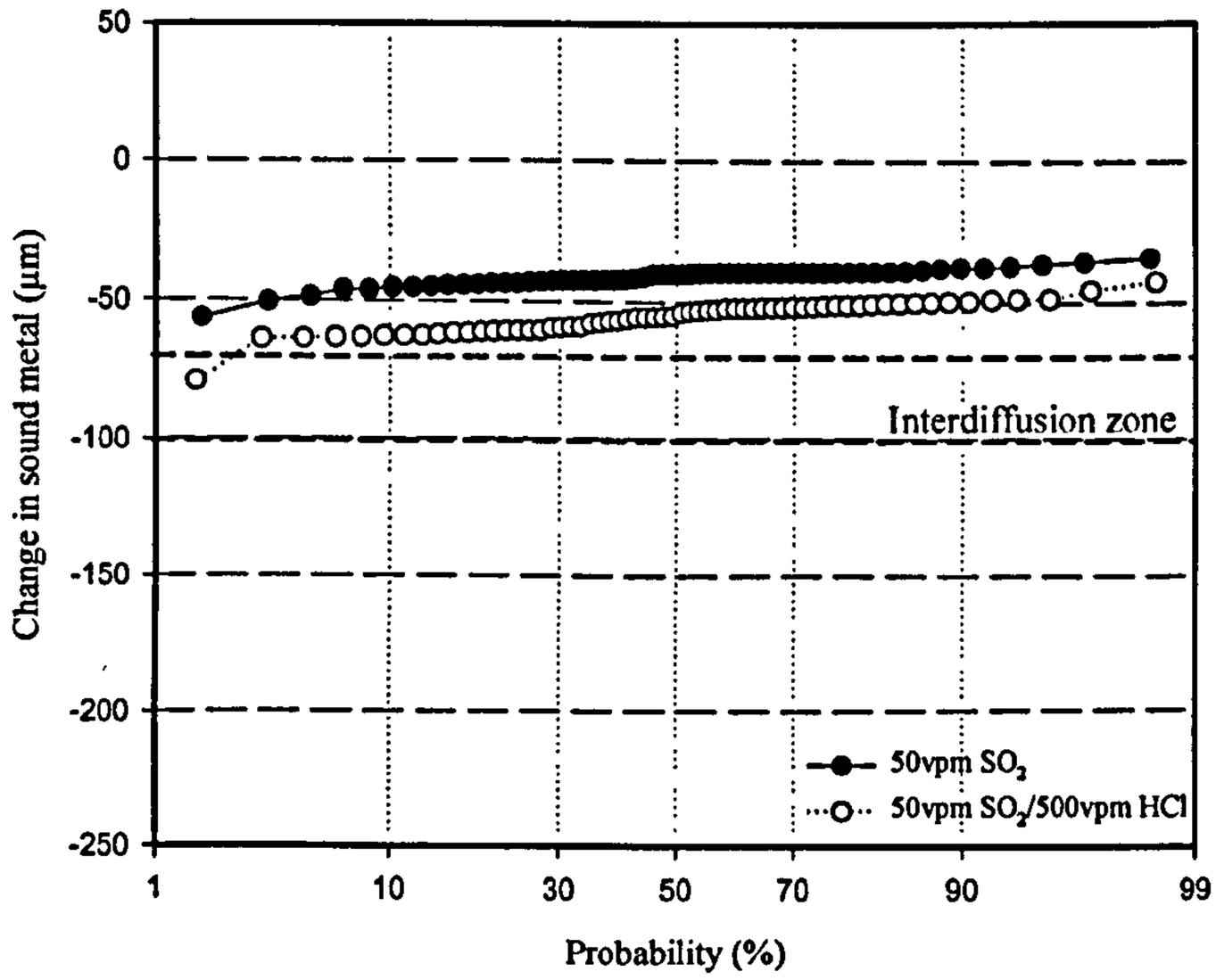

b) PtAl Coated CMSX-4, 80/20 $(Na/K)_2SO_4$, flux 1.5µg/cm^2/h at 900°C.

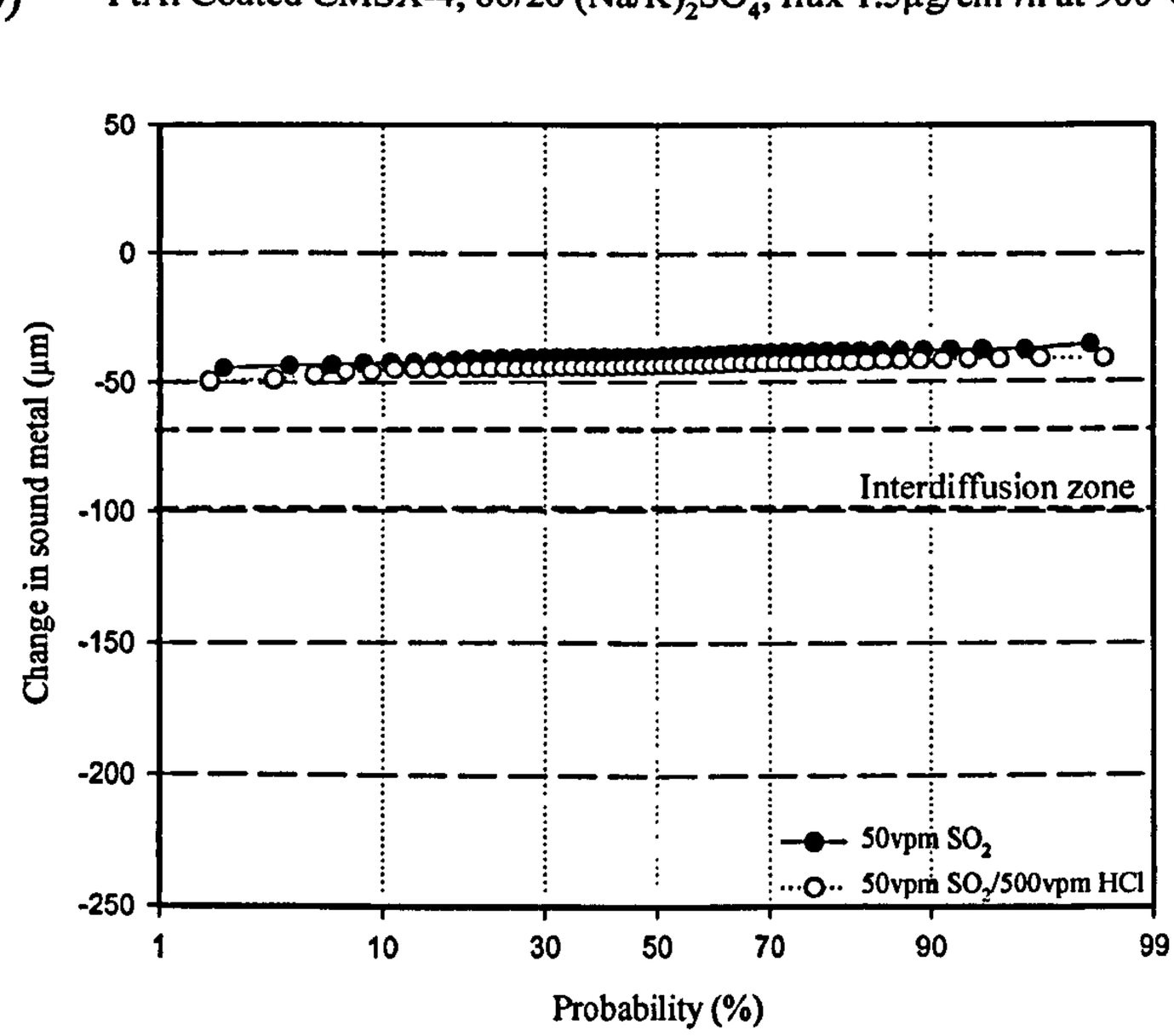

Figure 4.53: Change in sound metal as a function of the probability damage under different gas composition and deposit flux of 1.5µg/cm^2/h for PtAl coated CMSX4 at (a) 700°C and (b) 900°C after 500h exposure.

a) Uncoated SC[2], 80/20 $(Na/K)_2SO_4$, flux 5µg/cm^2/h at 700°C.

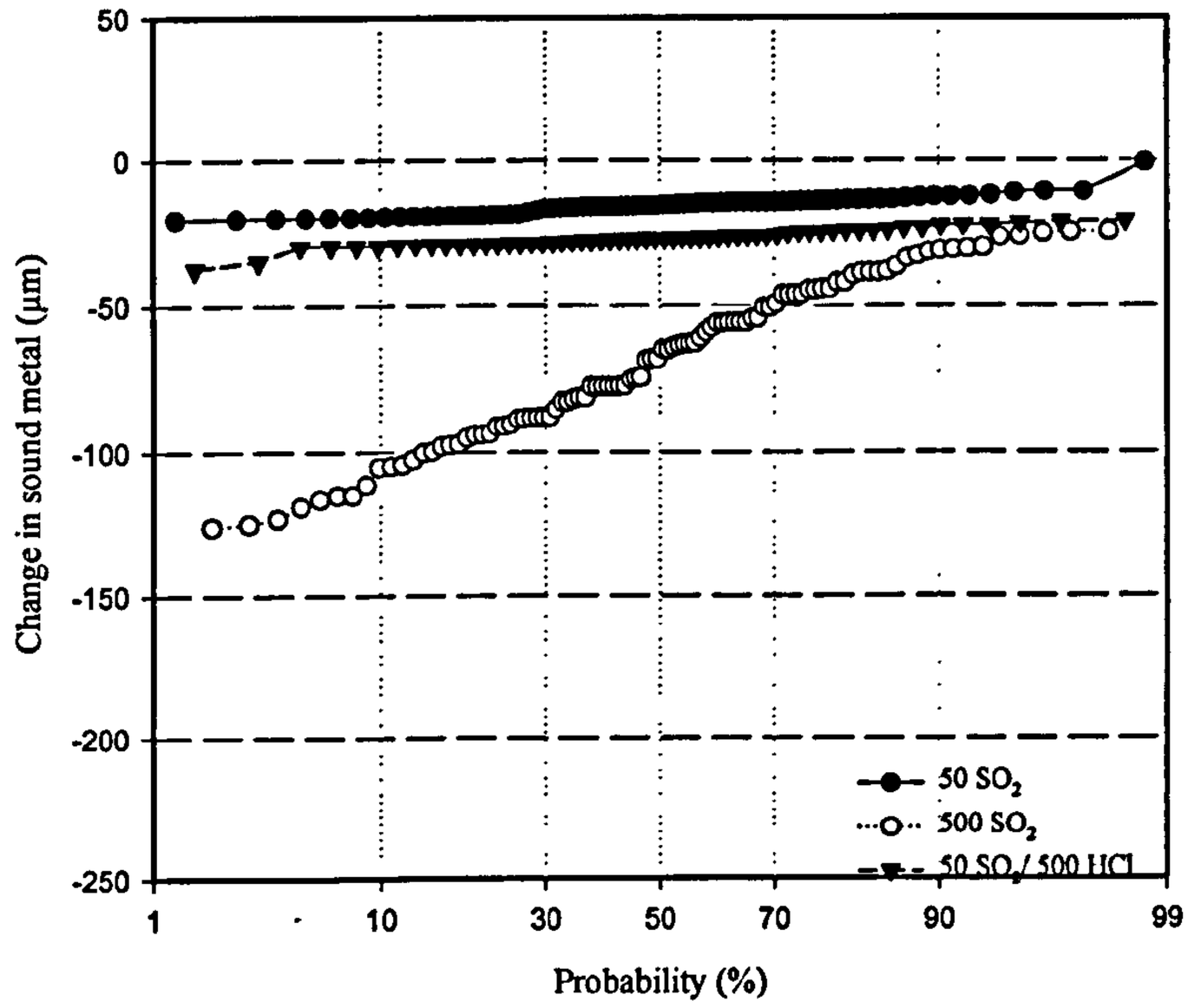

b) Uncoated SC[2], 80/20 $(Na/K)_2SO_4$, flux 5µg/cm^2/h at 900°C

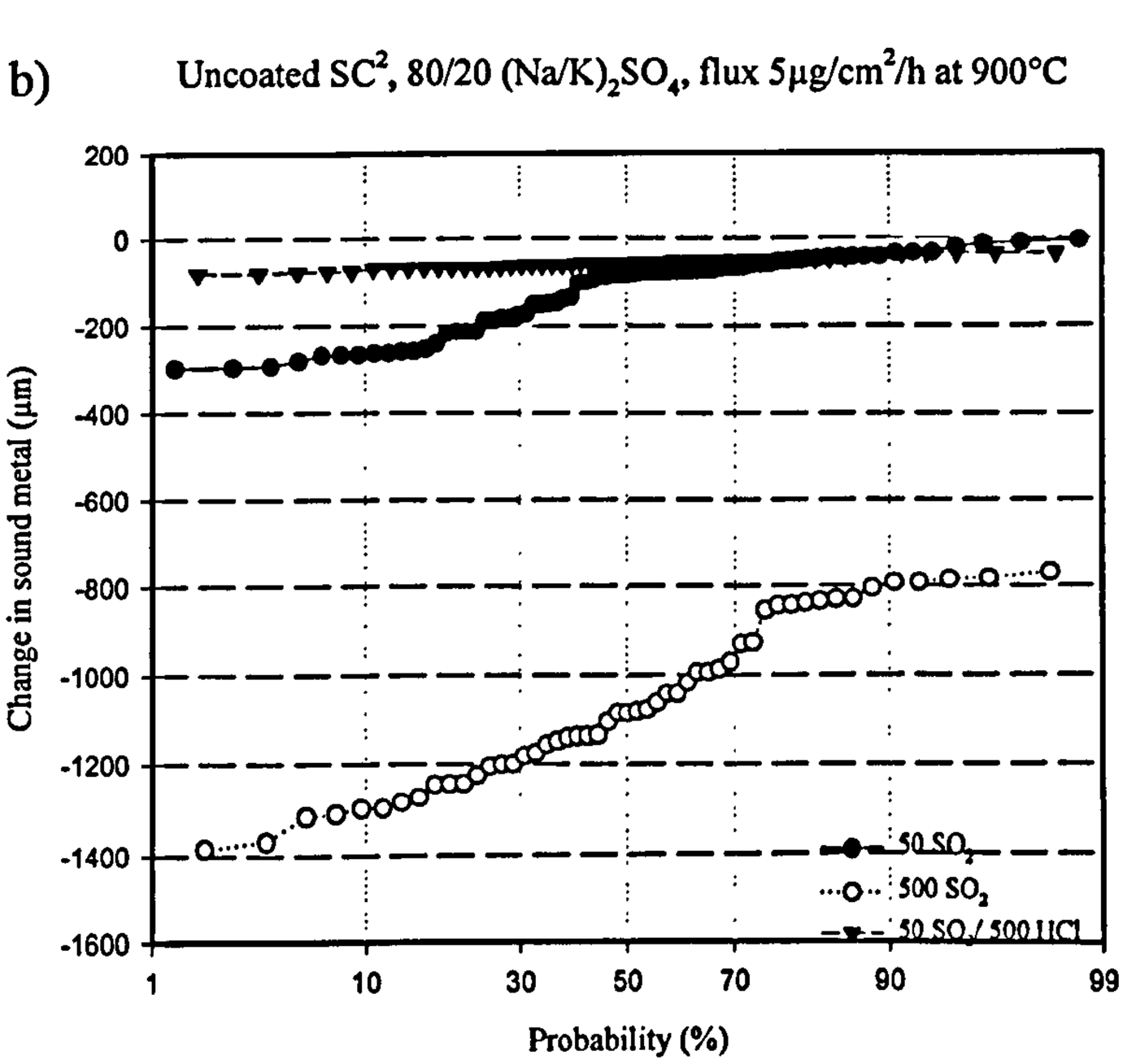

Figure 4.54: Change in sound metal as a function of the probability damage under different gas composition and deposit flux of 5µg/cm^2/h for uncoated SC[2] at 700°C (a) and 900°C (b) after 500h exposure.

a) PtAl Coated SC^2, 80/20 $(Na/K)_2SO_4$, flux 5µg/cm^2/h at 700°C.

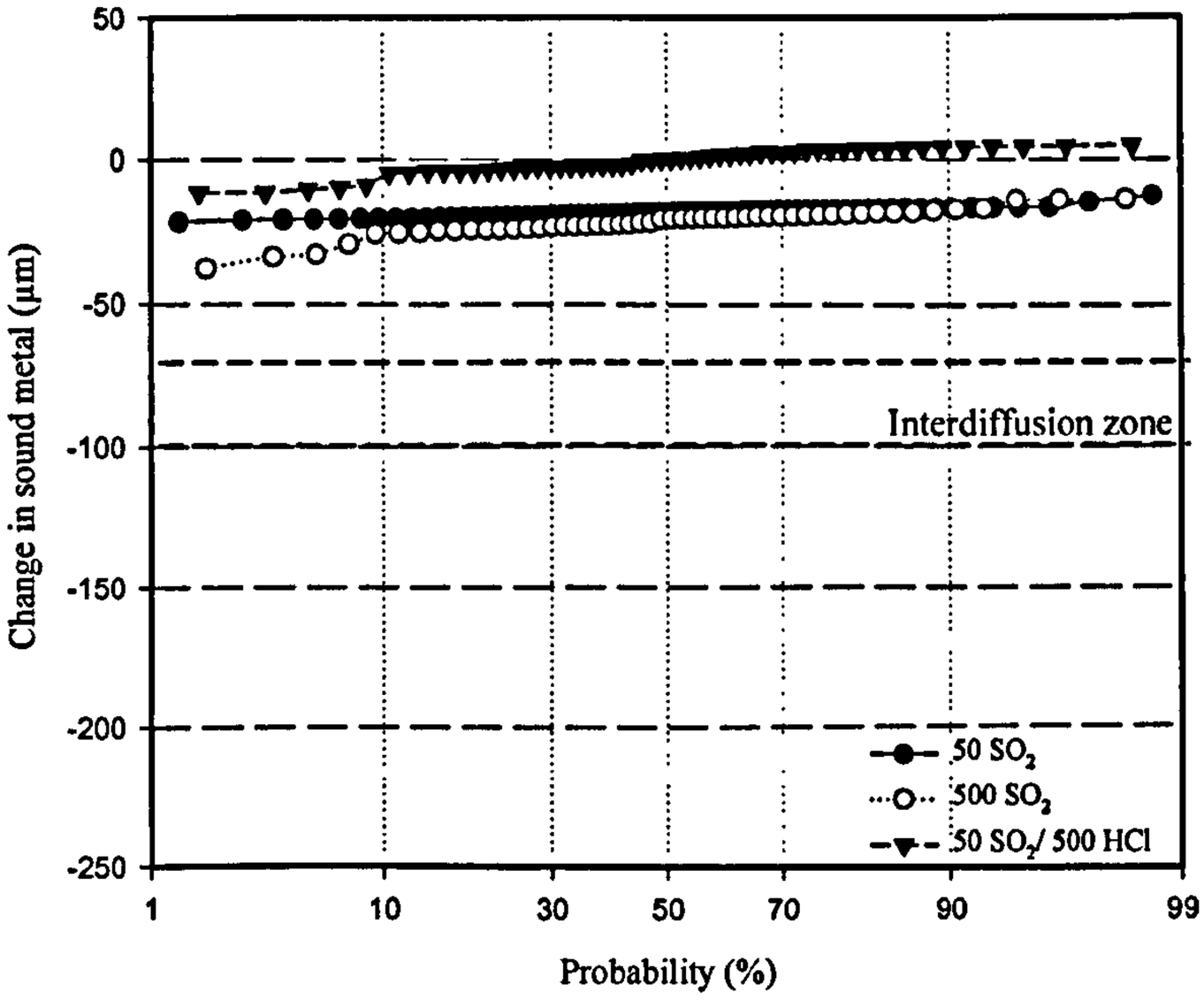

b) PtAl Coated SC^2, 80/20 $(Na/K)_2SO_4$, flux 5µm/cm^2/h at 900°C.

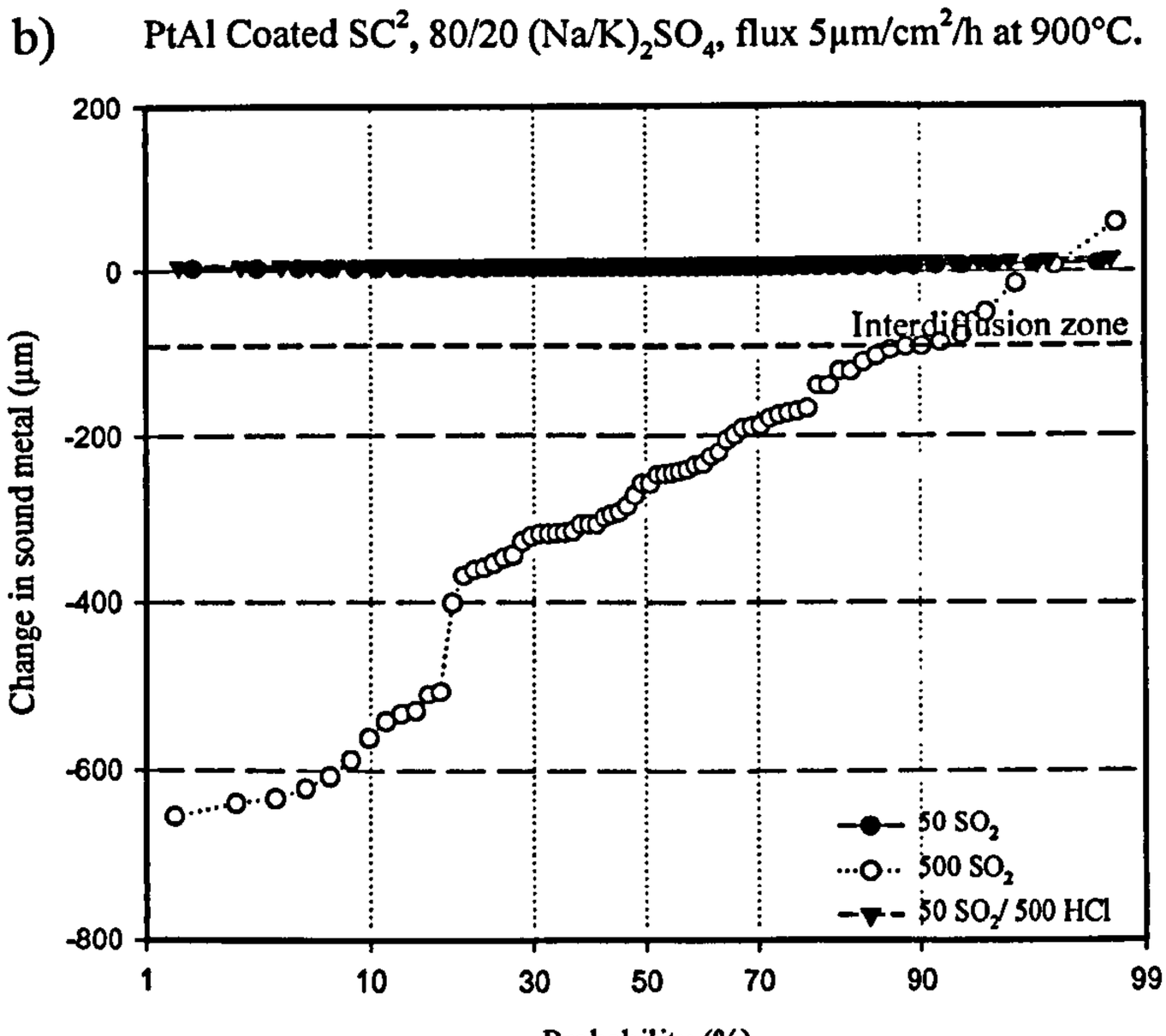

Figure 4.55: Change in sound metal as a function of the probability damage under different gas composition and deposit flux of 5µg/cm^2/h for PtAl coated SC^2 at (a) 700°C and (b 900°C) after 500h exposure.

a) Uncoated CMSX-4, 80/20 $(Na/K)_2SO_4$, flux 5µg/cm^2/h at 700°C.

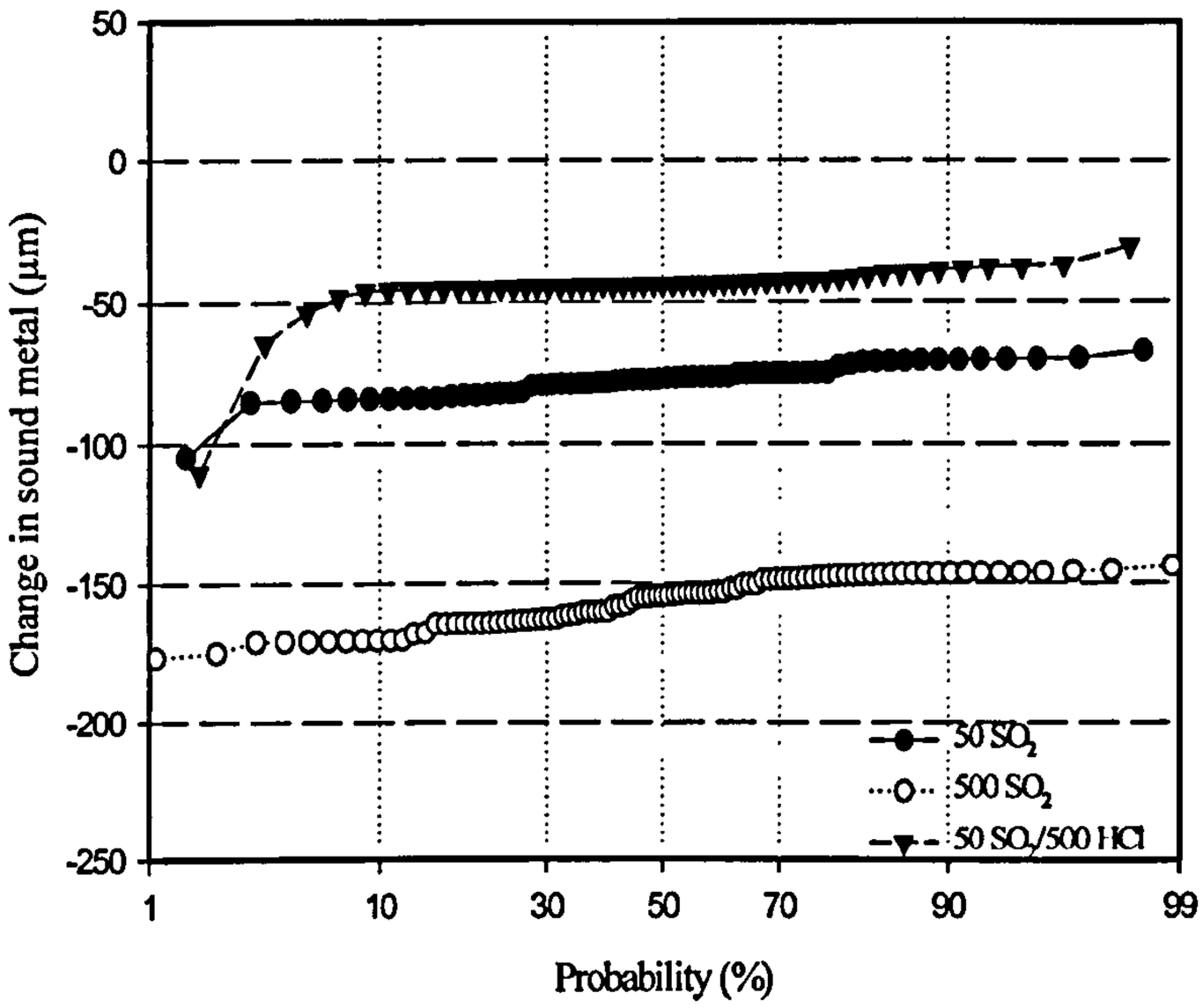

b) Uncoated CMSX-4, 80/20 $(Na/K)_2SO_4$, flux 5µg/cm^2/h at 900°C.

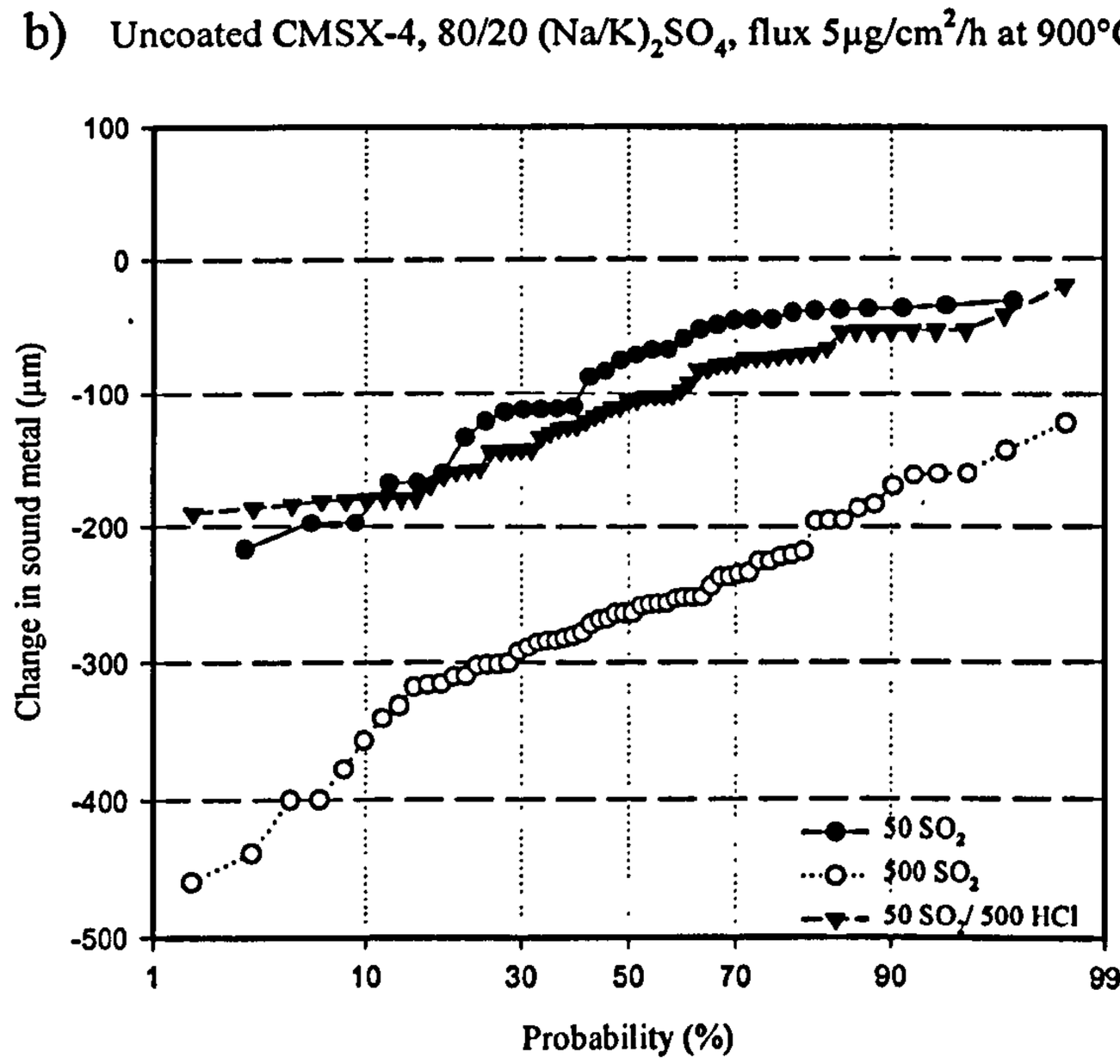

Figure 4.56: Change in sound metal as a function of the probability damage under different gas composition and deposit flux of 5µg/cm^2/h for uncoated CMSX4 at (a) 700°C and (b) 900°C after 500h exposure.

a) PtAl Coated CMSX-4, 80/20 $(Na/K)_2SO_4$, flux 5µg/cm^2/h at 700°C.

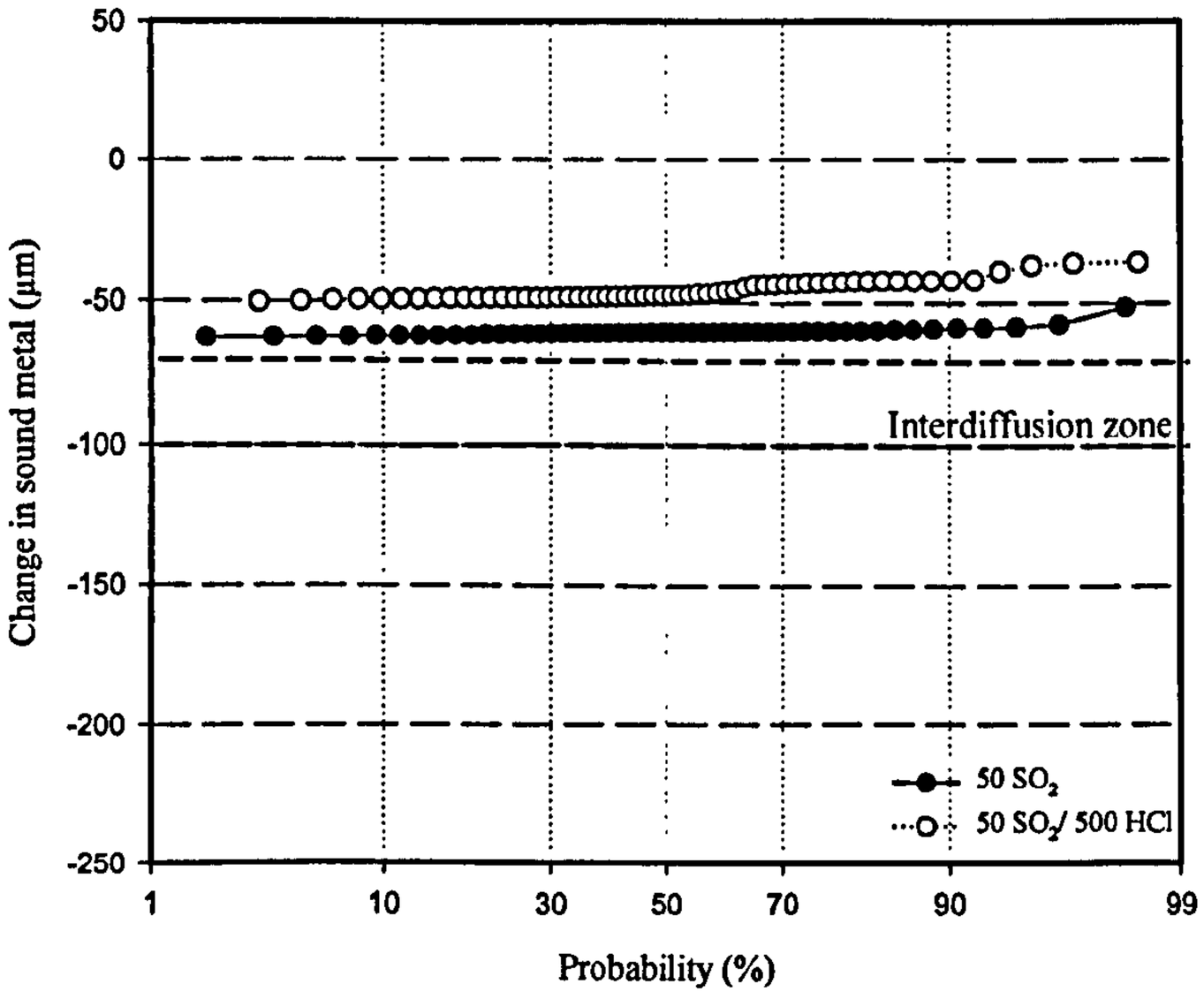

b) PtAl Coated CMSX-4, 80/20 $(Na/K)_2SO_4$, flux 5µm/cm^2/h at 900°C.

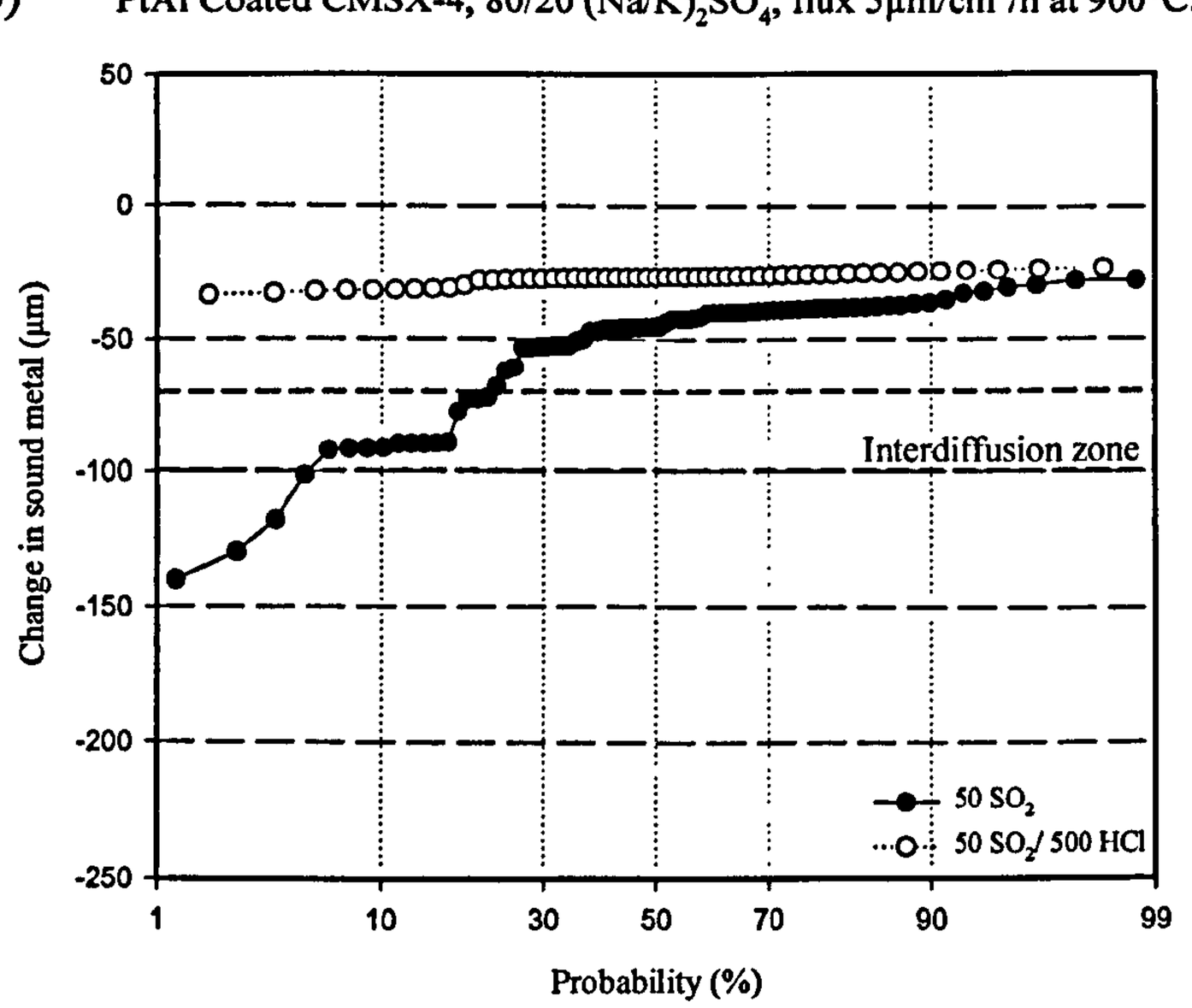

Figure 4.57: Change in sound metal as a function of the probability damage under different gas composition and deposit flux of 5µg/cm^2/h for PtAl coated CMSX4 at (a) 700°C (b) and 900°C after 500h exposure.

a) Unocated SC^2, 80/20 $(Na/K)_2SO_4$, flux 15µg/cm^2/h at 700°C.

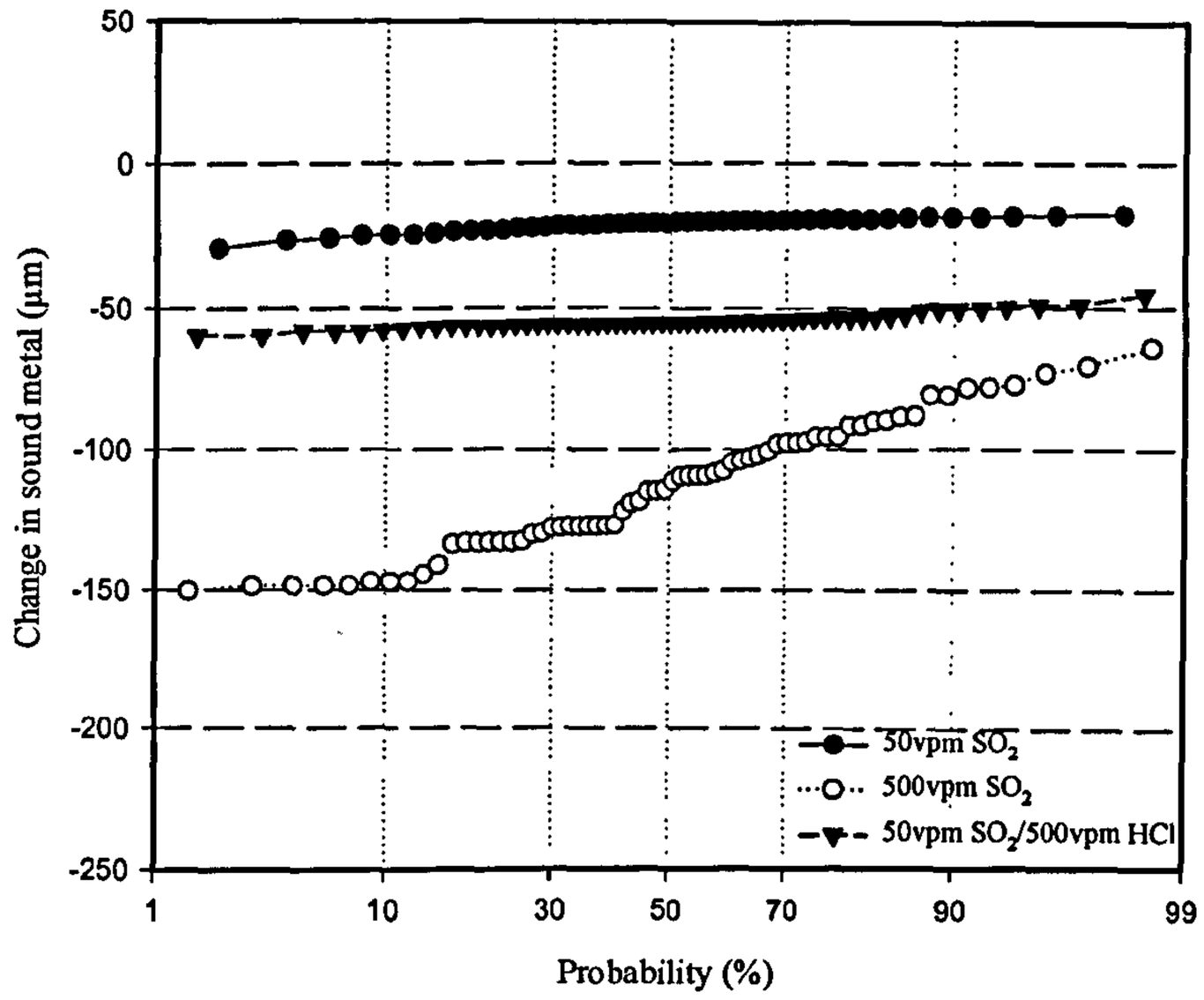

b) Uncoated SC^2, 80/20 $(Na/K)_2SO_4$, flux 15µg/cm^2/h at 900°C.

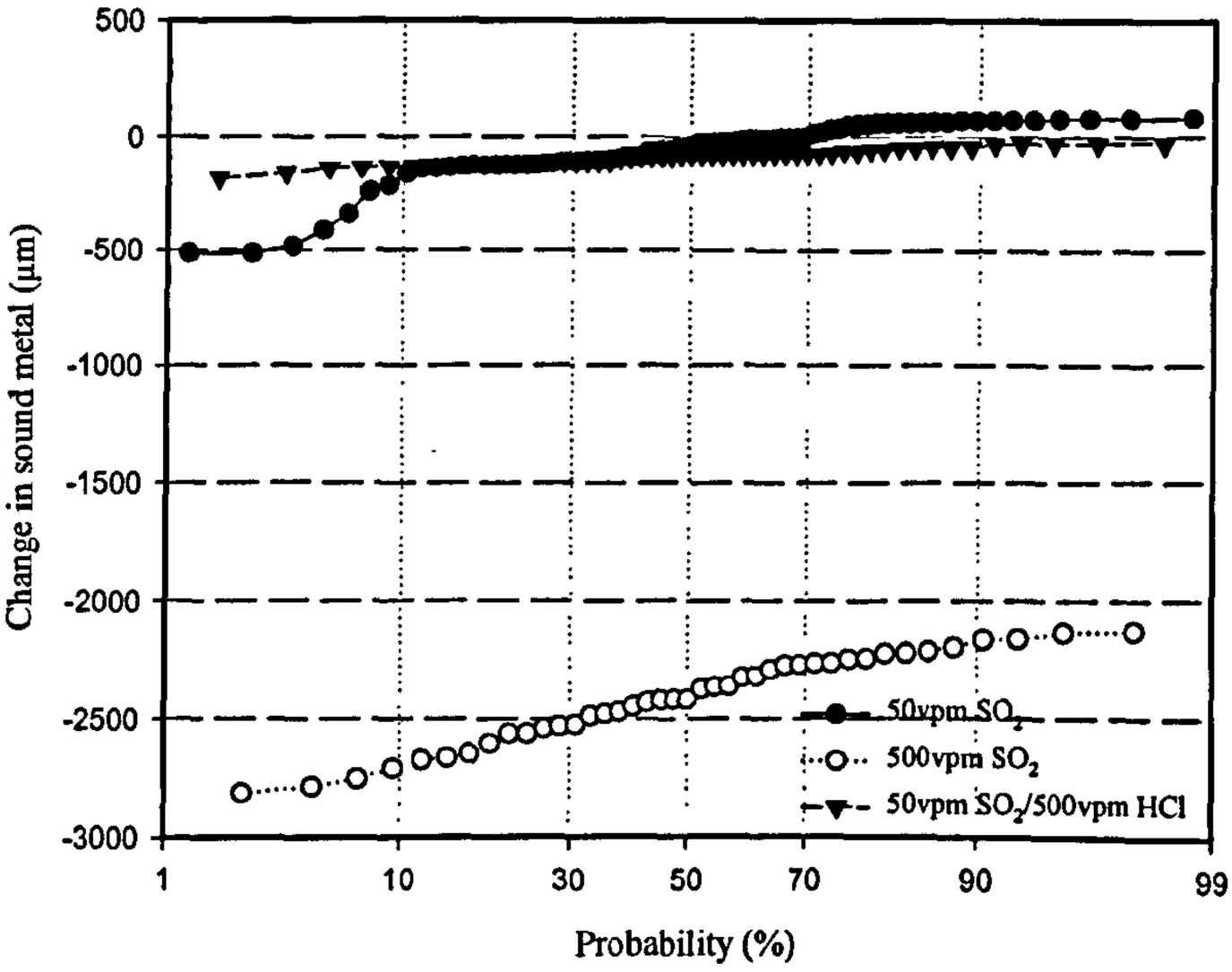

Figure 4.58: Change in sound metal as a function of the probability damage under different gas composition and deposit flux of 15µg/cm^2/h for uncoated SC^2 at (a) 700°C and (b) 900°C after 500h exposure.

PtAl Coated SC^2, 80/20 $(Na/K)_2SO_4$, flux 15µg/cm^2/h at 700°C.

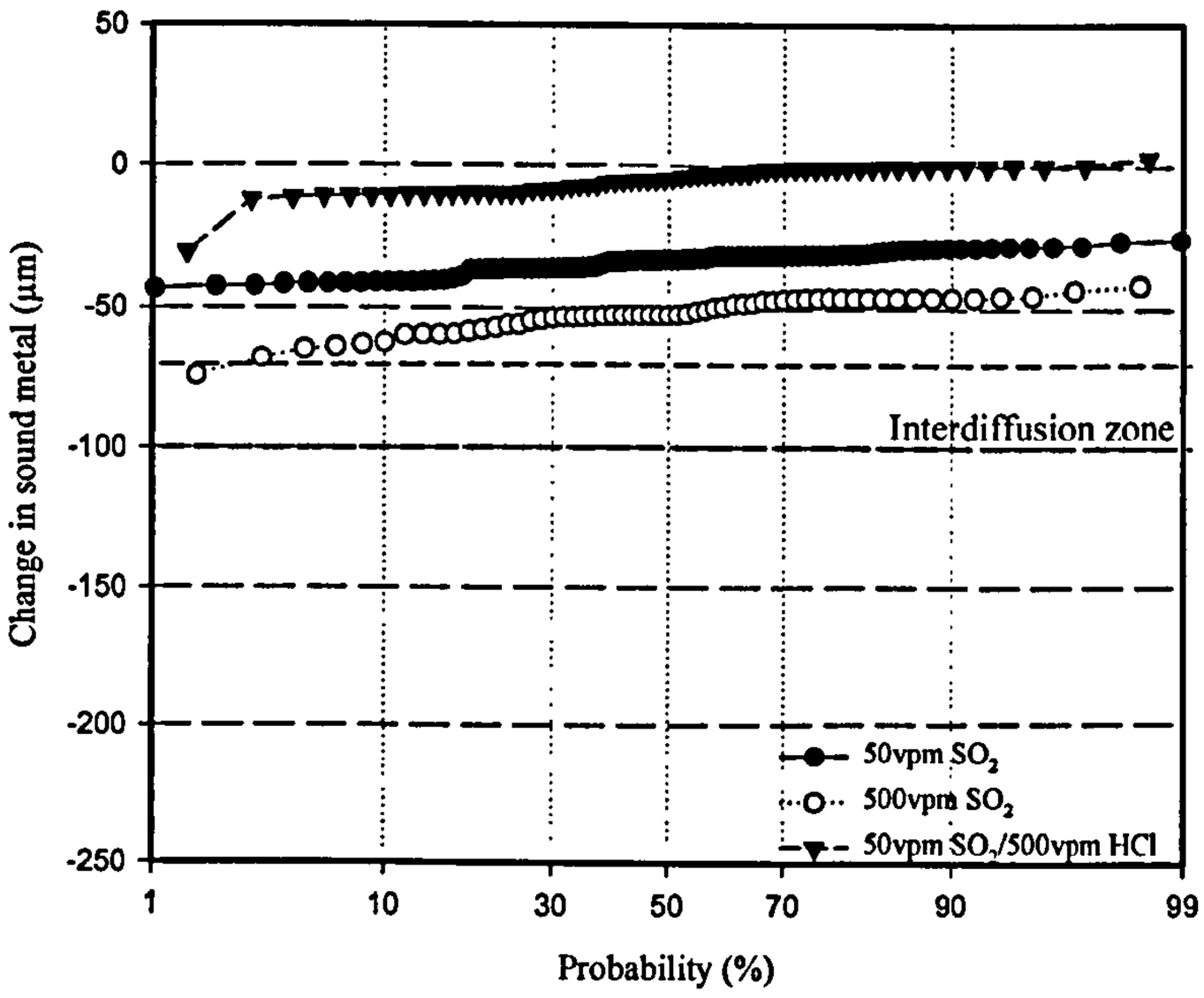

b) PtAl Coated SC_2, 80/20 $(Na/K)_2SO_4$, flux 15µg/cm^2/h at 900°C.

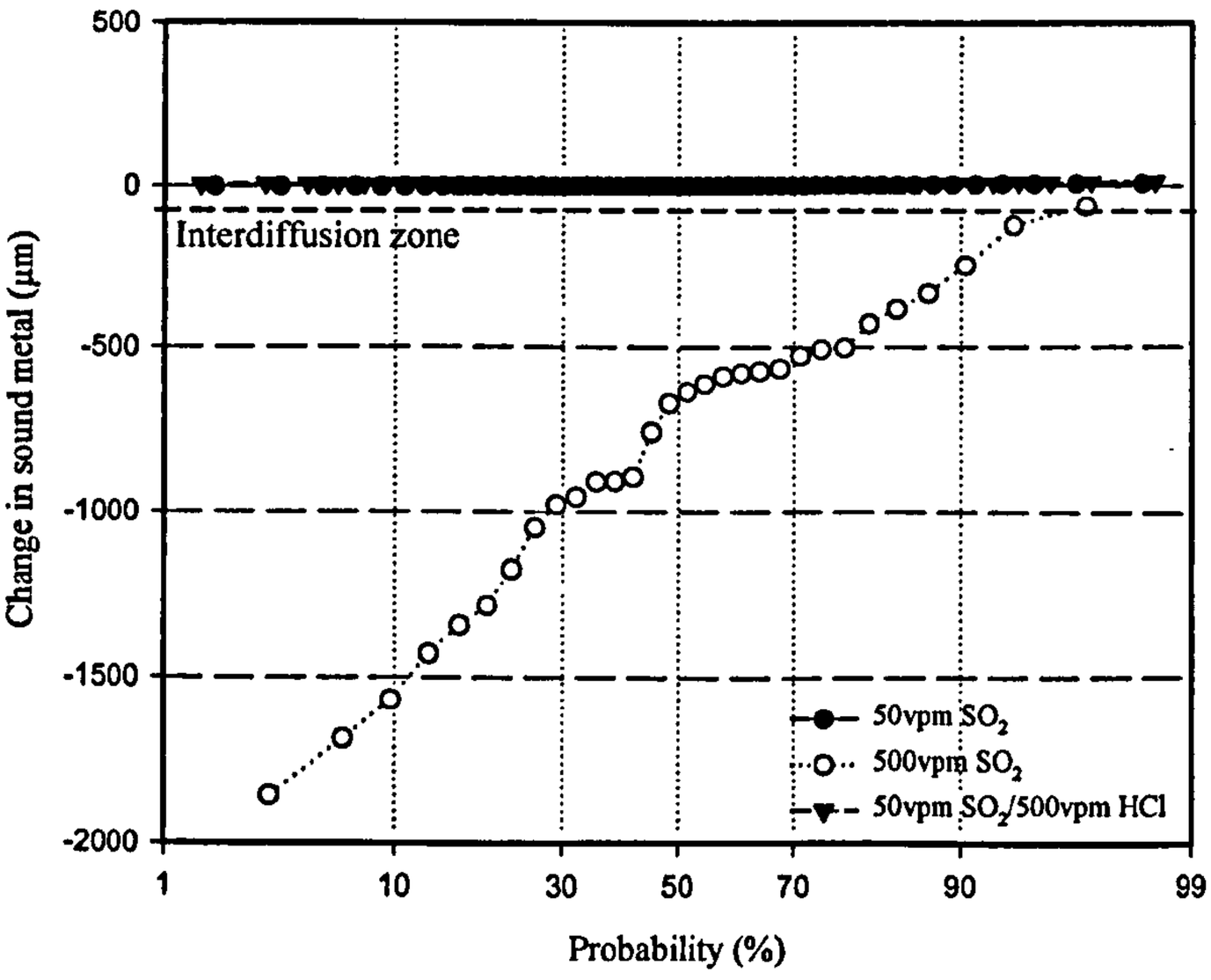

Figure 4.59: Change in sound metal as a function of the probability damage under different gas composition and deposit flux of 15µg/cm^2/h for PtAl coated SC^2 at (a) 700°C and (b) 900°C after 500h exposure.

a) Uncoated CMSX-4, 80/20 $(Na/K)_2SO_4$, flux 15µg/cm^2/h at 700°C.

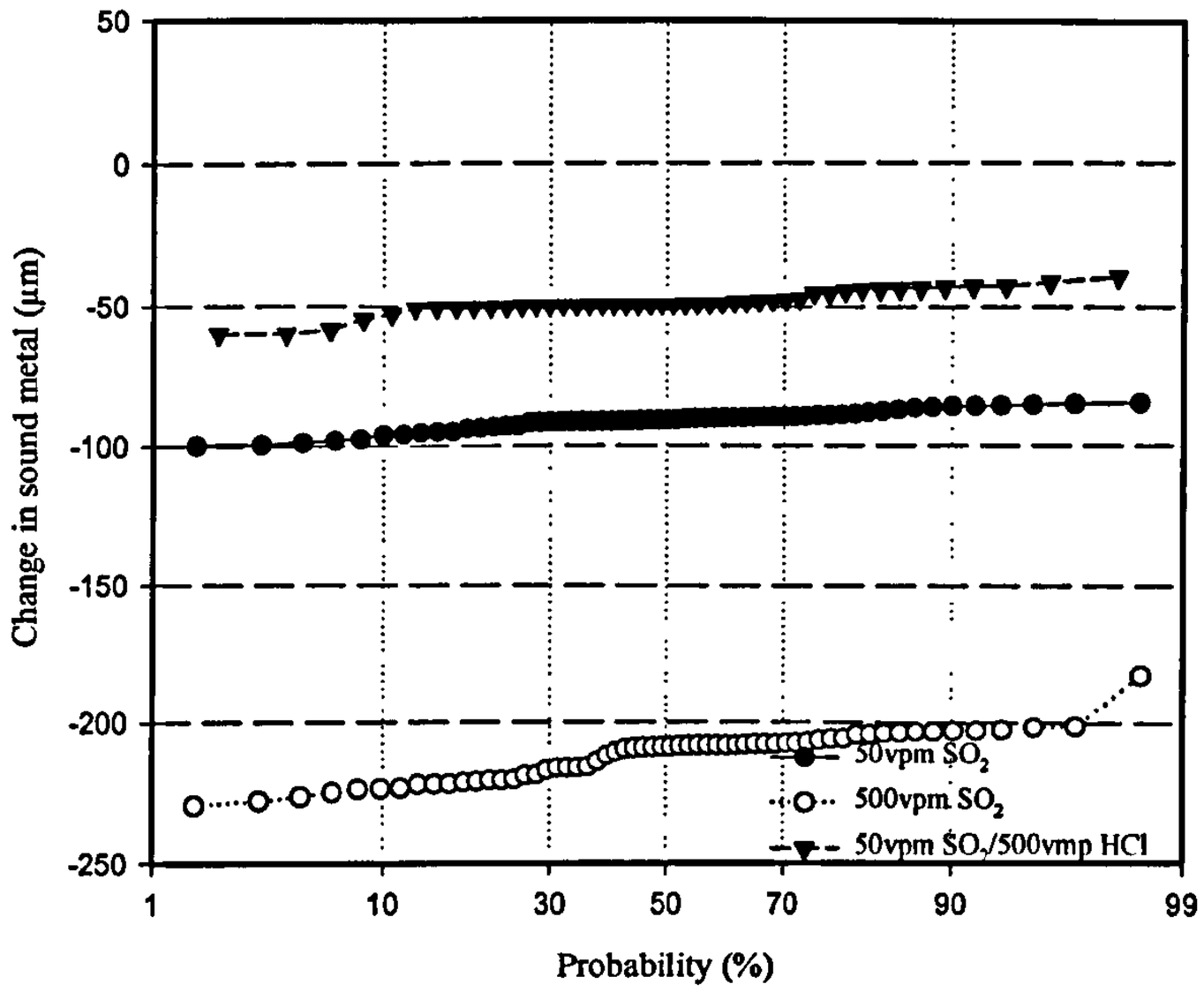

b) Uncoated CMSX-4, 80/20 $(Na/K)_2SO_4$, flux 15µg/cm^2/h at 900°C.

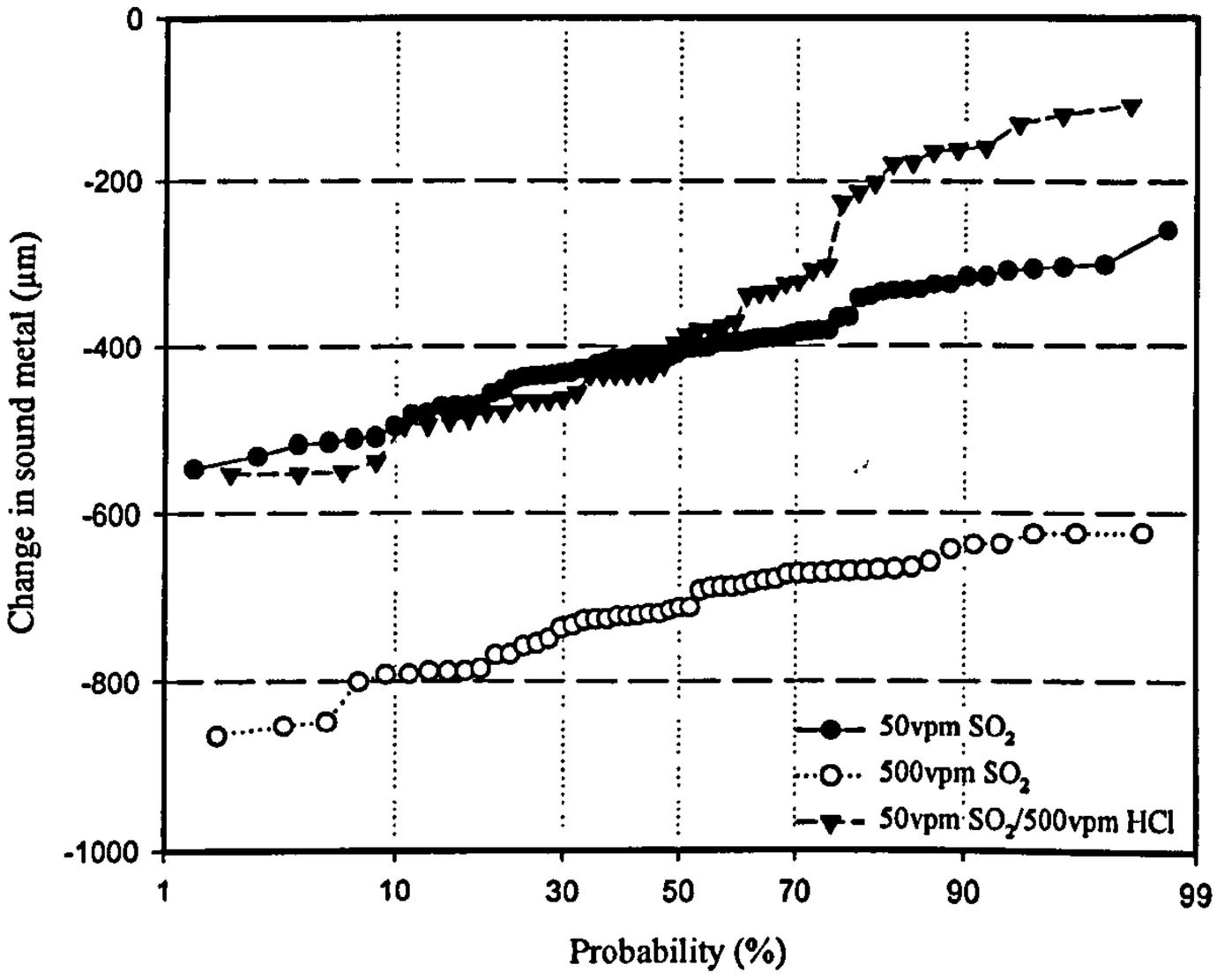

Figure 4.60: Change in sound metal as a function of the probability damage under different gas composition and deposit flux of 15µg/cm^2/h for uncoated CMSX4 at (a) 700°C and (b) 900°C after 500h exposure.

a) PtAl Coated CMSX-4, 80/20 $(Na/K)_2SO_4$, flux 15µg/cm^2/h at 700°C.

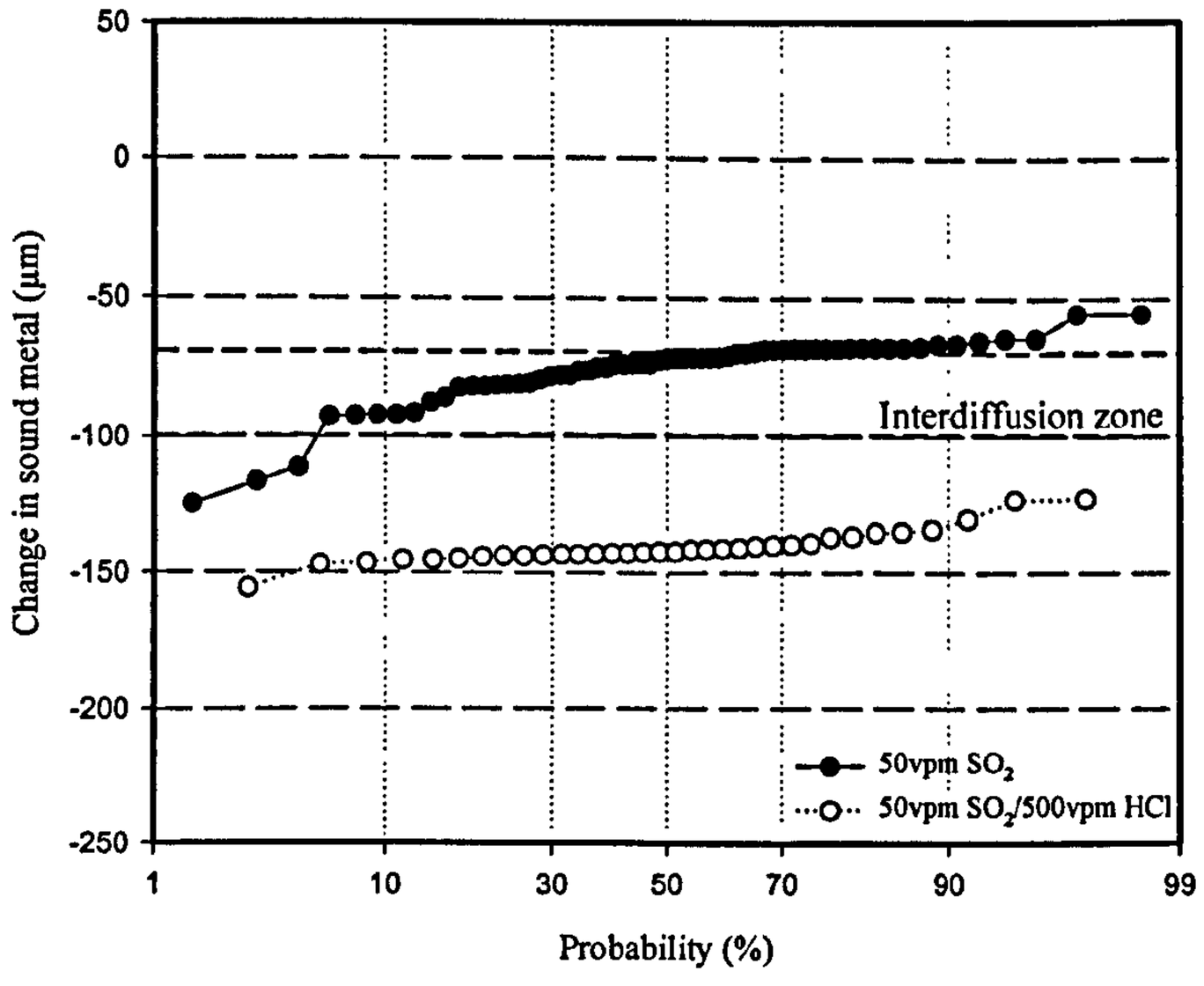

b) PtAl Coated CMSX-4, 80/20 $(Na/K)_2SO_4$, flux 15µg/cm^2/h at 900°C.

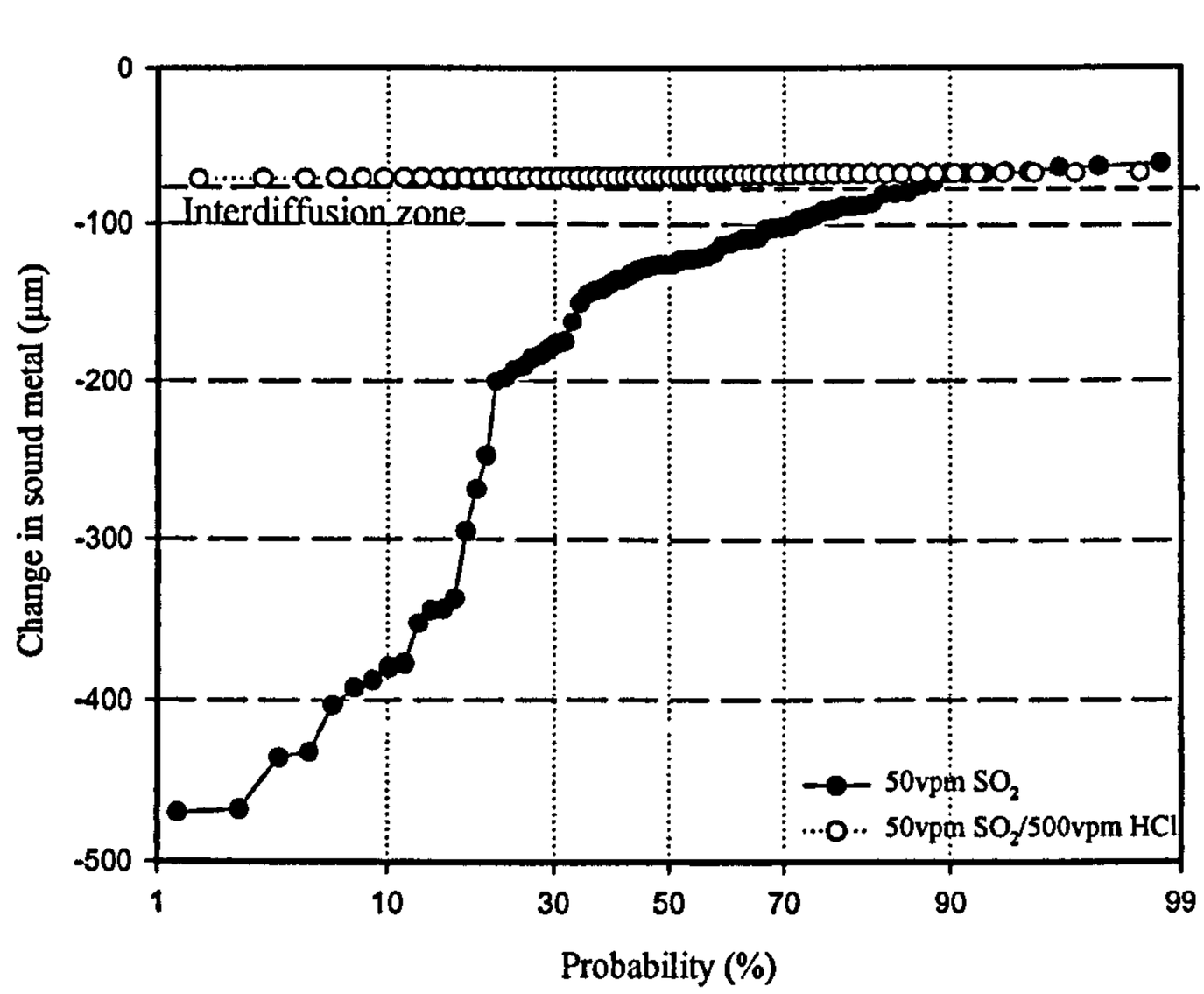

Figure 4.61: Change in sound metal as a function of the probability damage under different gas composition and deposit flux of 15µg/cm^2/h for PtAl coated CMSX4 at (a) 700°C and (b) 900°C after 500h exposure.

4.4.2.2 Sensitivity to deposition flux

For both single crystal superalloys, CMSX-4 and SC^2, the influence of varying the deposition flux in the range of 1.5, 5 and 15 μg/cm^2/h for 4/1 $(Na/K)_2SO_4$, has been also studied. Figure 4.62 to Figure 4.64 illustrate the effects observed during exposure in gas with the highest level of SO_2 (500 vpm) at 700 and 900°C. The hot corrosion of uncoated SC^2 is strongly dependent on the deposit flux; this affects corrosion damage significantly more at 900°C than 700°C. At 900°C, hot corrosion damage, up to 2800μm after 500h, has been measured. However, at 700°C, the damage (in this case type II pitting) only reached 150μm in the 500h exposure for otherwise identical test conditions (80/20 $(Na, K)_2$ SO_4 at a deposition rate of 15μm/cm^2/h in an air-500 vpm SO_x environment). This effect may be seen in Figure 4.62 (a), (b) and visually appreciated in Figure 4.34 (photomicrographs 7, 8, 9) and Figure 4.35 (photomicrographs 10, 11 and 12). A similar trend is observed at both temperatures for PtAl-coated SC^2, Figure 4.63 (a) and (b). The coating provides protection and gives an improvement in the general corrosion damage at 700°C. However, for the medium and high deposit fluxes, the coating has practically been destroyed at 900°C; only small areas of the surface have remnants of the PtAl coating, approximately 5-8% of the surface area, depending on the deposition flux. Examples of this level of damage are given in Figure 4.36 and Figure 4.37.

The uncoated CMSX4 at 700°C was more affected than the uncoated SC^2 (Figure 4.62 (a) vs. Figure 4.64 (a)). At 900°C, SC^2 was the more sensitive material (Figure 4.62 (b) vs. Figure 4.64(b)), with the extent of attack being 3x that of CMSX4 (excluding the lowest deposit flux). At both 700 and 900°C for uncoated CMSX-4, the observation of increasing corrosion damage with deposit flux, is clear (see Figure 4.62 and Figure 4.64), although this is not visually evident in Figure 4.38.

Figure 4.65 to Figure 4.68 illustrate the effects observed during exposure in the lowest SO_2 (50 vpm) gas at 700 and 900°C. The hot corrosion of uncoated SC^2 is quite uniform for each of the three deposition fluxes (1.5, 5 and 15μg/cm^2/h), with between zero and 50μm of damage. However, the dependency on the deposition flux is clear and slightly more damage can be seen with increasing deposition flux (Figure 4.65(a)). For uncoated SC^2 at 900°C, under the same test conditions as at 700°C, hot corrosion damage increased for the three deposit fluxes, up to ~500μm for the 15μg/cm^2/h concentration (Figure 4.65 (b)). This tendency can be seen in Figure 4.34 (photomicrographs 1, 2 and 3) for 700°C and in Figure 4.35 (photomicrograph 4, 5 and 6) for 900°C.

The PtAl-coated SC^2 showed only a little improvement at 700°C, with the 1.5 and 5 $\mu g/cm^2/h$ deposition fluxes. However, a huge improvement can be seen at 900°C; for example, for $15\mu/cm^2/h$ flux, the depth of hot corrosion damage is decreased from ~500μm when uncoated to ~20μm. Morphologies of the PtAl coating on SC^2 can be seen in Figure 4.36 (photomicrographs 1, 2, 3) for 700°C and in Figure 4.37 (photomicrographs 4, 5 and 6) for 900°C. The uncoated CMSX4 under identical test conditions to uncoated SC^2 at 700 and 900°C was more sensitive to the 50vpm SO_2 environment. It can be observed in Figure 4.67 (a) and (b) that the extent of hot corrosion increases with deposit flux concentration, with a gap between the $1.5\mu g/cm^2/h$ trend and the 5 and $15\mu g/cm^2/h$ trends. These results are not evident at first sight at 700°C in Figure 4.38 (photomicrographs 1, 2 and 3), but they are in the hot corrosion morphology in Figure 4.39 at 900°C.

The performance of the PtAl coating on CMSX4 is shown in Figure 4.68 (a) at 700°C and (b) at 900°C. At 700°C, the PtAl coating only improved the performance of the CMSX4 with a deposit flux of $5\mu g/cm^2/h$; at the $15\mu g/cm^2/h$ deposit flux, the coating was penetrated, damaging the alloy. At 900°C, an improvement can be seen for all the deposit flux concentrations; at both temperatures, the tendency of more damage with more deposit flux is observed and can be seen in Figure 4.40 (photomicrograph 1, 2, 3) and in Figure 4.41 (photomicrographs 4, 5 and 6).

Figure 4.59 to Figure 4.72 show the effects observed during exposure in 50vpm SO_2 plus 500vpm HCl gas at 700 and 900°C. The three different deposit concentrations were more corrosive at 900°C (up to ~200μm of metal loss) than at 700°C (up to~60μm). The dependency of the uncoated SC^2 on deposition fluxes is very clear at 700°C in Figure 4.69 (a), whereas, at 900°C, apparently the $5\mu g/cm^2/h$ flux had slightly less effect that the $1.5\mu g/cm^2/h$ deposit flux, Figure 4.69 (b). Typical type I internal damage is observed at 900°C, but the internal damage has a different appearance compared to that observed on those samples exposed at 700°C. These results can be seen in Figure 4.34 (photomicrographs 13, 14, 15) and in Figure 4.35 (photomicrographs 16, 17 and 18).

A significant improvement in performance is appreciable when the SC^2 is PtAl coated: at 700°C, hot corrosion damage was reduced for the three deposition fluxes to <~10μm of metal loss; at 900°C, the damage was reduced to ~0μm. The coating mode of damage can be seen in Figure 4.36 with internal damage at 700°C, (photomicrographs 13, 14, 15) and in Figure 4.37 (photomicrographs 16, 17 and 18) for 900°C with internal damage only in that sample for $15\mu g/cm^2/h$ deposit flux.

The uncoated CMSX-4 also showed a strong dependency on deposition flux both at 700 and 900°C Figure 4.71 (a) and (b). The greater damage was observed for the deposition fluxes at 900°C, up to ~550μm of metal loss for the 15μg/cm^2/h. Internal damage is observed not only in those samples exposed at 900°C, but also in those exposed at 700°C. Morphologies of this damage can be seen in Figure 4.38 (photomicrographs 13, 14, 15) and in Figure 4.39 (photomicrographs 16, 17 and 18).

No protection was observed for the PtAl-coated CMSX4 at 700°C, especially with the 15μg/cm^2/h deposit flux (as shown in Figure 4.72 (a)) since the coating was consumed. However, at 900°C, Figure 4.72 (b), the PtAl coating was more protective, particularly at the 15μg/cm^2/h deposit flux with an improvement of up to ~470μm of metal loss. Coating damage morphologies can be seen in Figure 4.40, showing the internal damage at 700°C in the HCl-containing environment (photomicrographs 13, 14, 15) and in Figure 4.41 (photomicrographs 16, 17 and 18) with internal damage in the sample exposed with a deposition flux of 15μg/cm^2/h at 900°C.

a) Uncoated SC^2, 80/20 $(Na/K)_2SO_4$ in 500 SO_2 at 700°C.

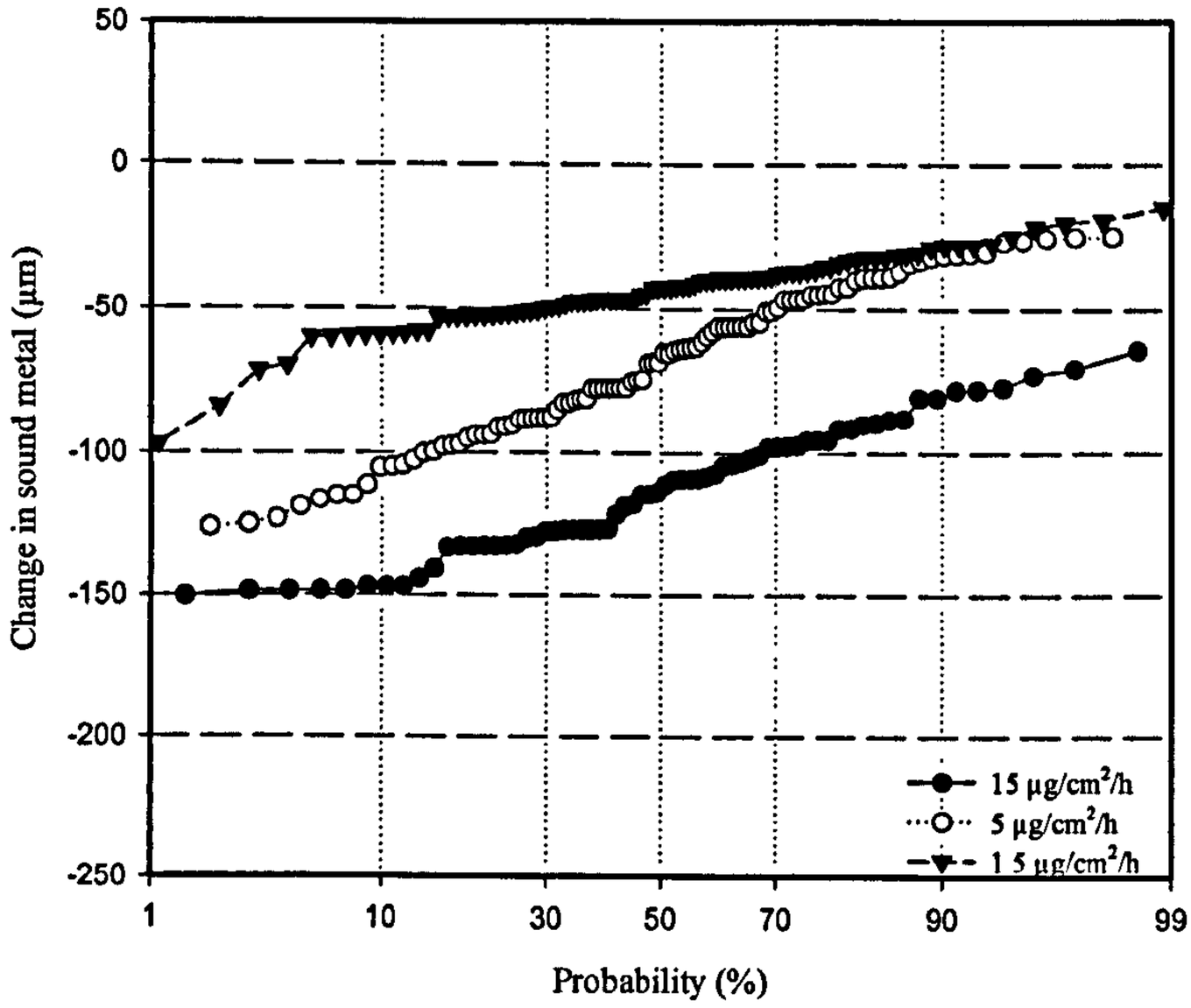

b) Uncoated SC^2, 80/20 $(Na/K)_2SO_4$ in 500 SO_2 at 900° C.

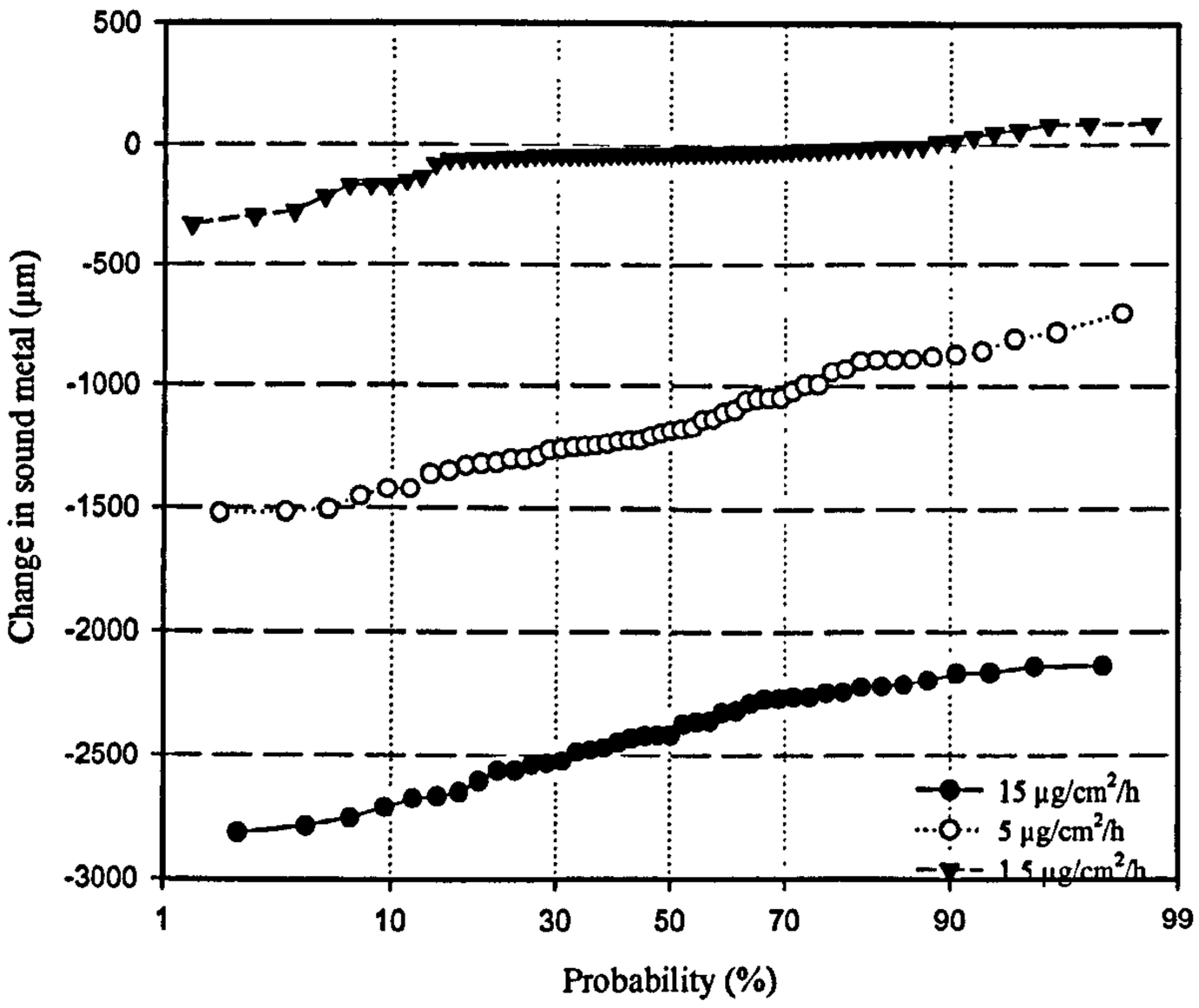

Figure 4.62: Change in sound metal as a function of the probability damage under different flux concentration for uncoated SC^2 in 500vpm SO_2 at (a) 700°C and (b) 900°C after 500h exposure.

a) PtAl Coated SC^2, 80/20 $(Na/K)_2SO_4$ in 500 SO_2 at 700° C.

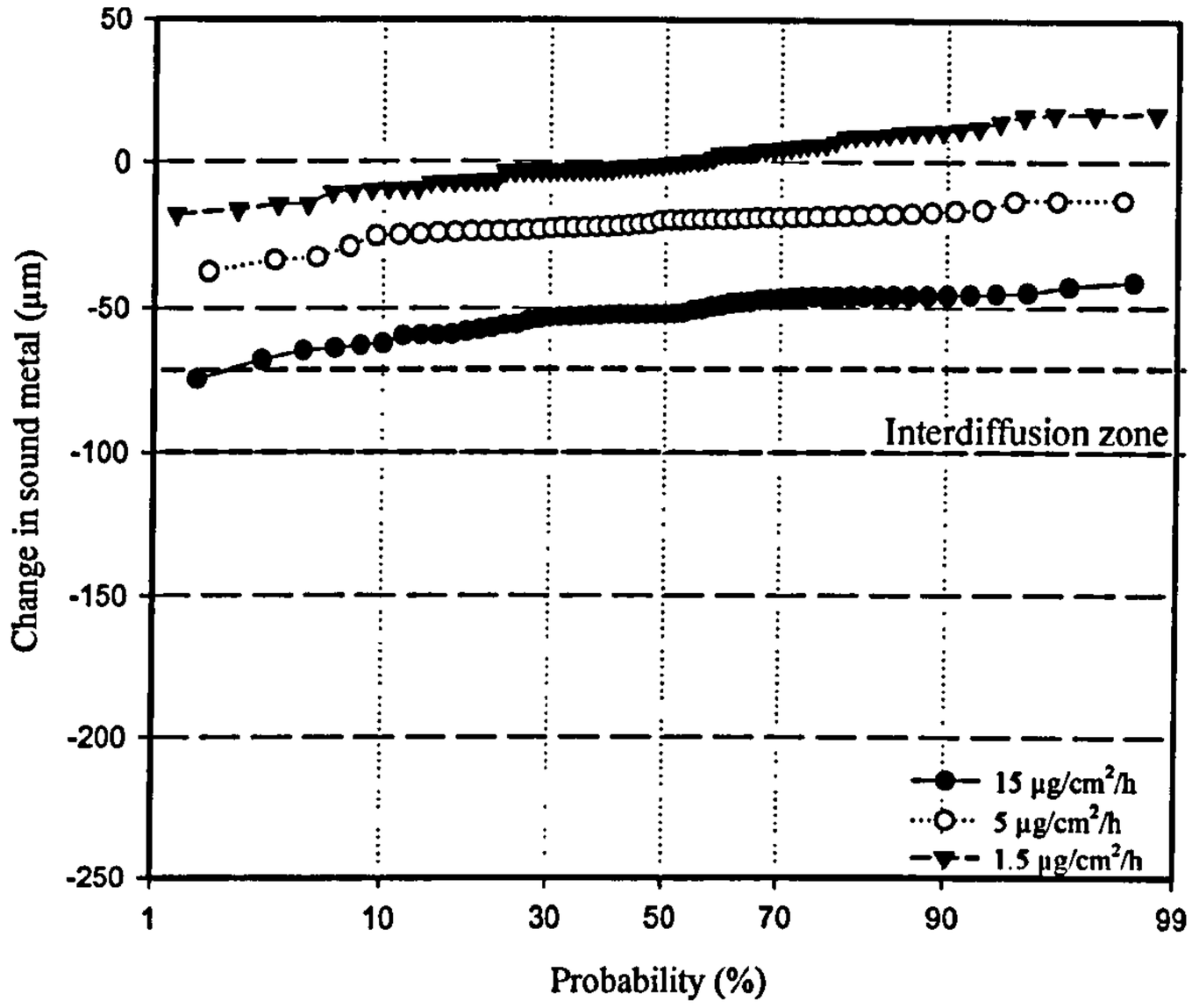

b) PtAl Coated SC^2, 80/20 $(Na/K)_2SO_4$ in 500 SO_2 at 900° C.

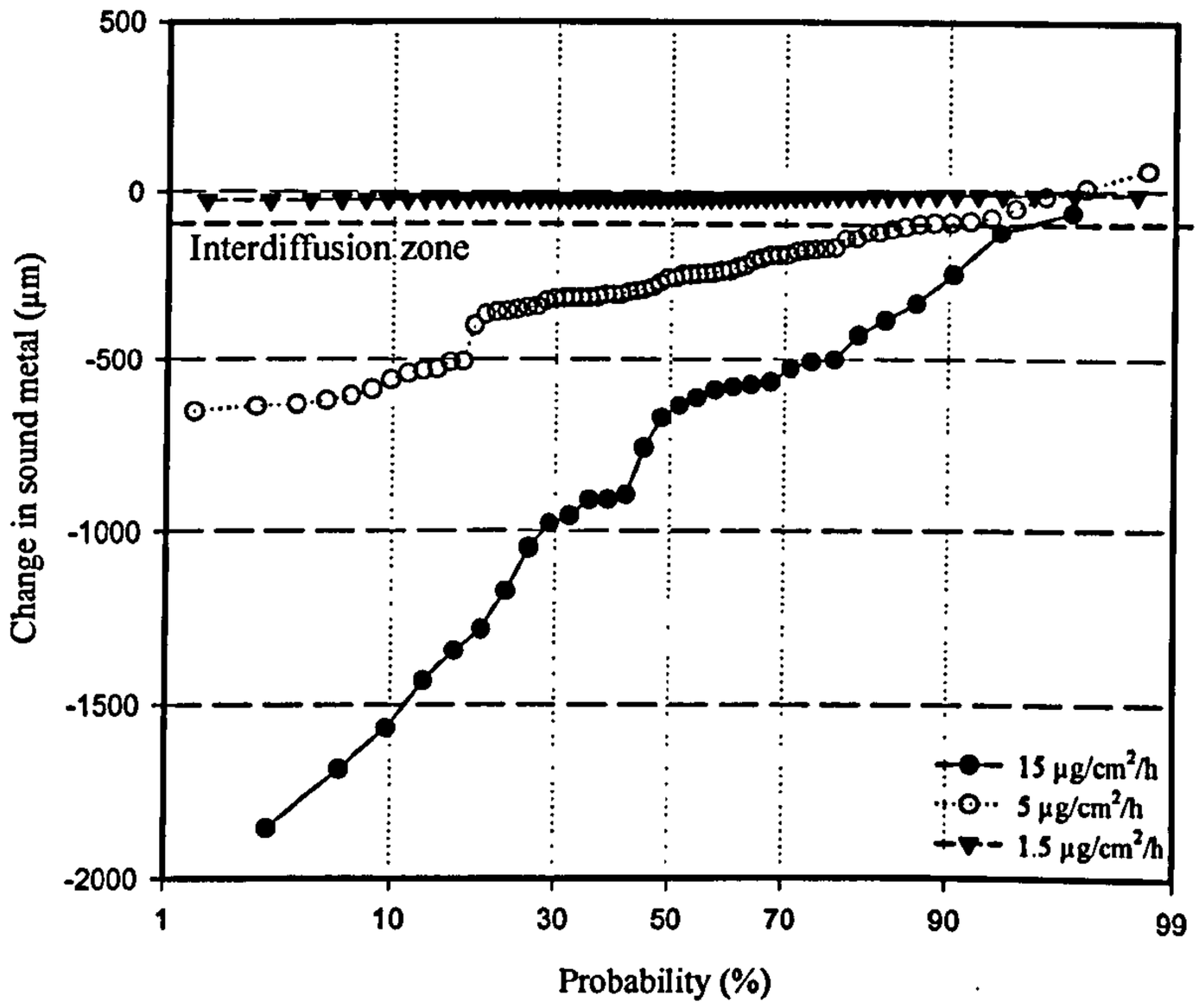

Figure 4.63: Change in sound metal as a function of the probability damage under different flux concentration for PtAl coated SC^2 in 500vpm SO_2 at (a) 700°C and (b) 900°C after 500h exposure.

a) Uncoated CMSX-4, 80/20 $(Na/K)_2SO_4$ in 500 vpm SO_2 at 700°C.

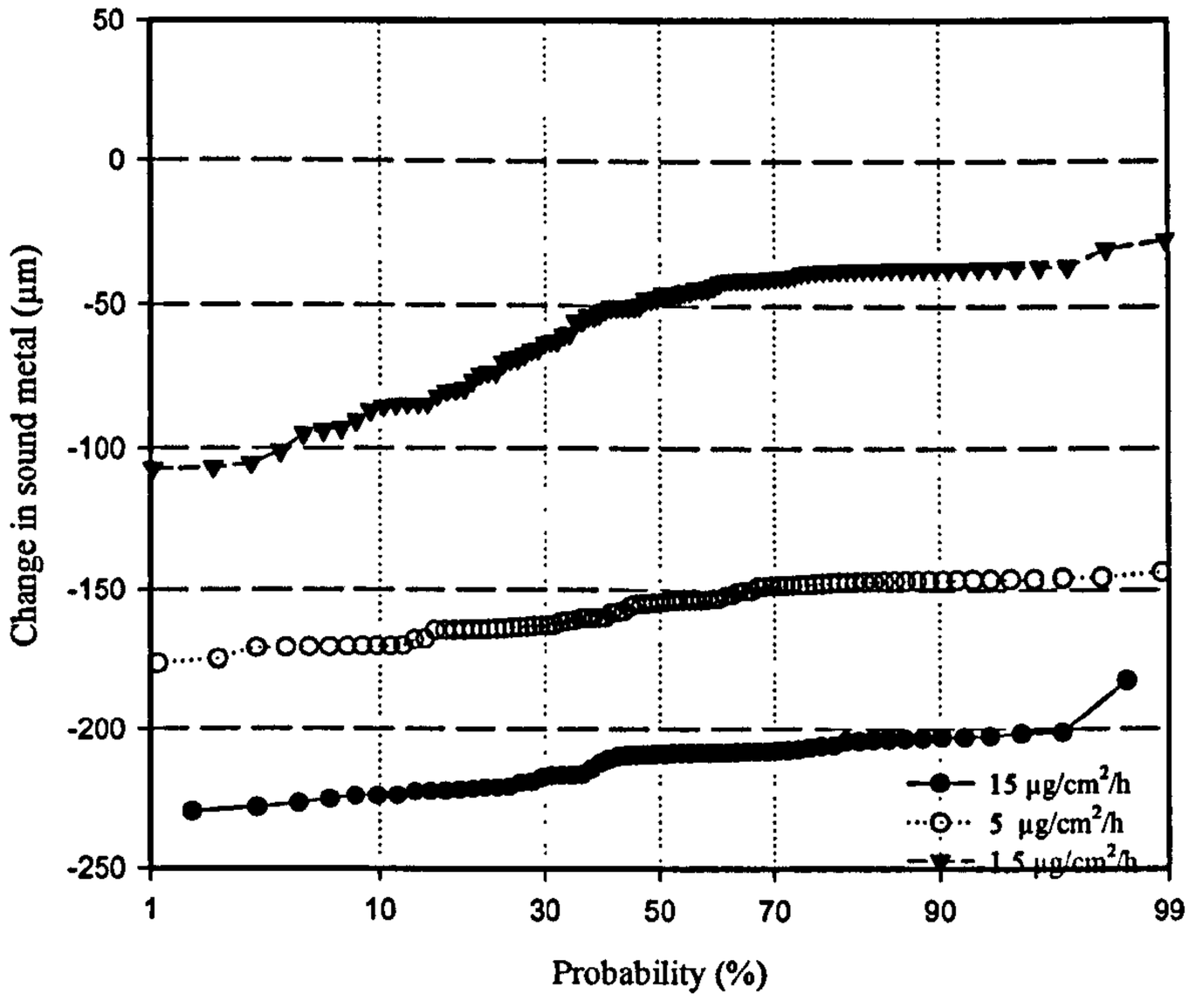

b) Uncoated CMSX-4, 80/20 $(Na/K)_2SO_4$ in 500 SO_2 at 900°C.

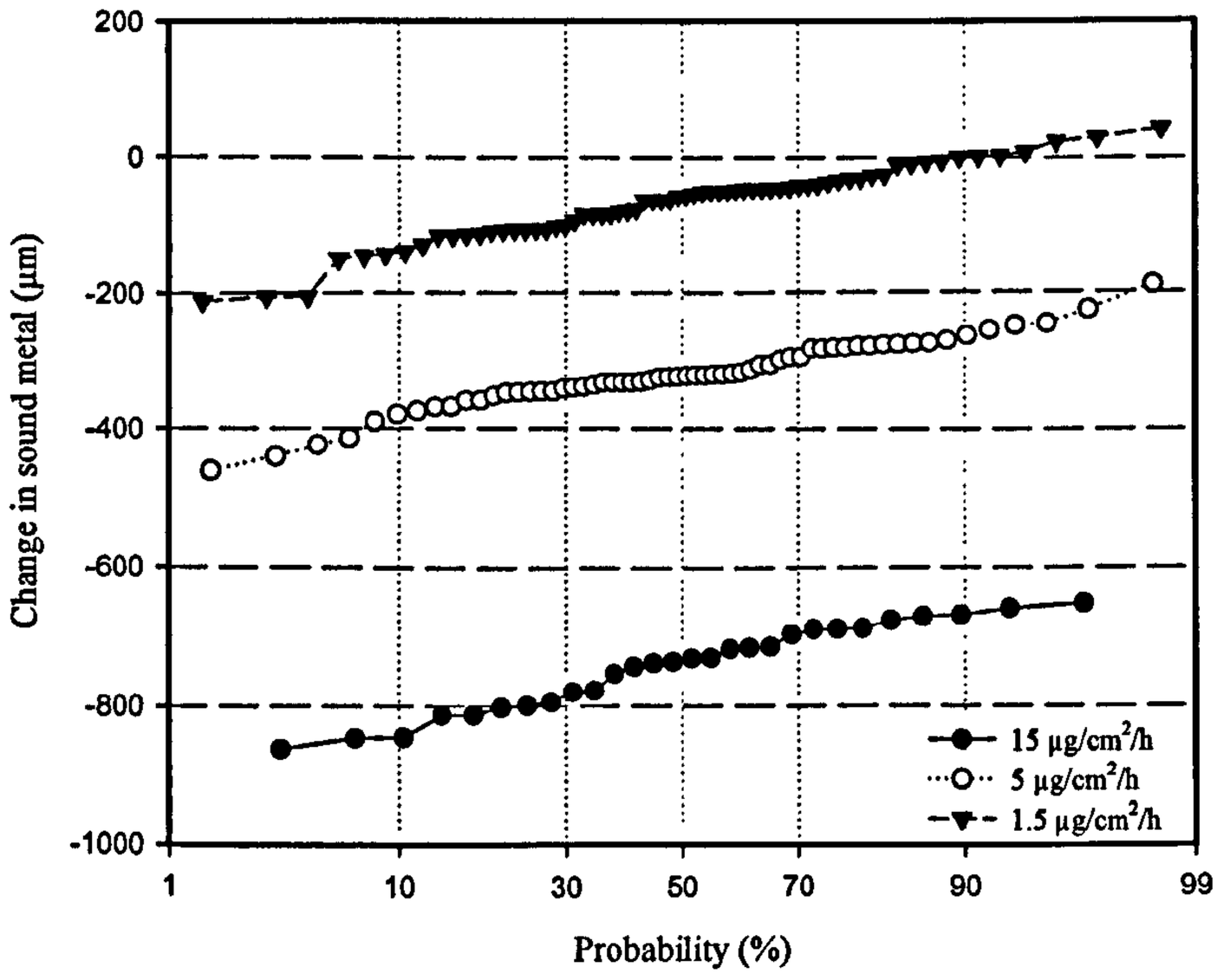

Figure 4.64: Change in sound metal as a function of the probability damage under different flux concentration for uncoated CMSX4 in 500vpm SO_2 at (a) 700°C and (b) 900°C after 500h exposure.

a) Uncoated SC^2 , 80/20 $(Na/K)_2SO_4$ in 50vpm SO_2 at 700°C.

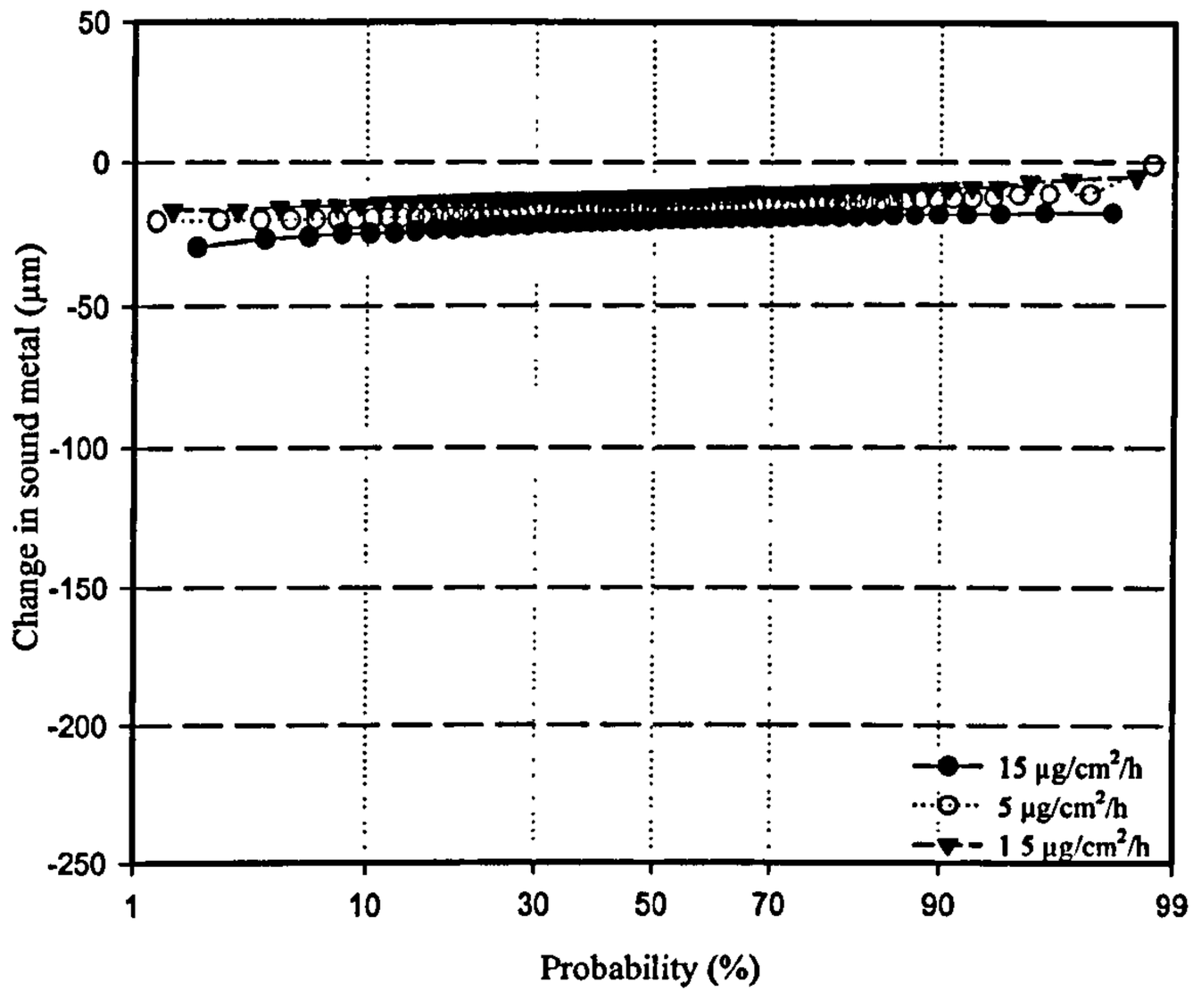

b) Uncoated SC^2 , 80/20 $(Na,K)_2SO_4$ in 50vpm SO_2 at 900°C.

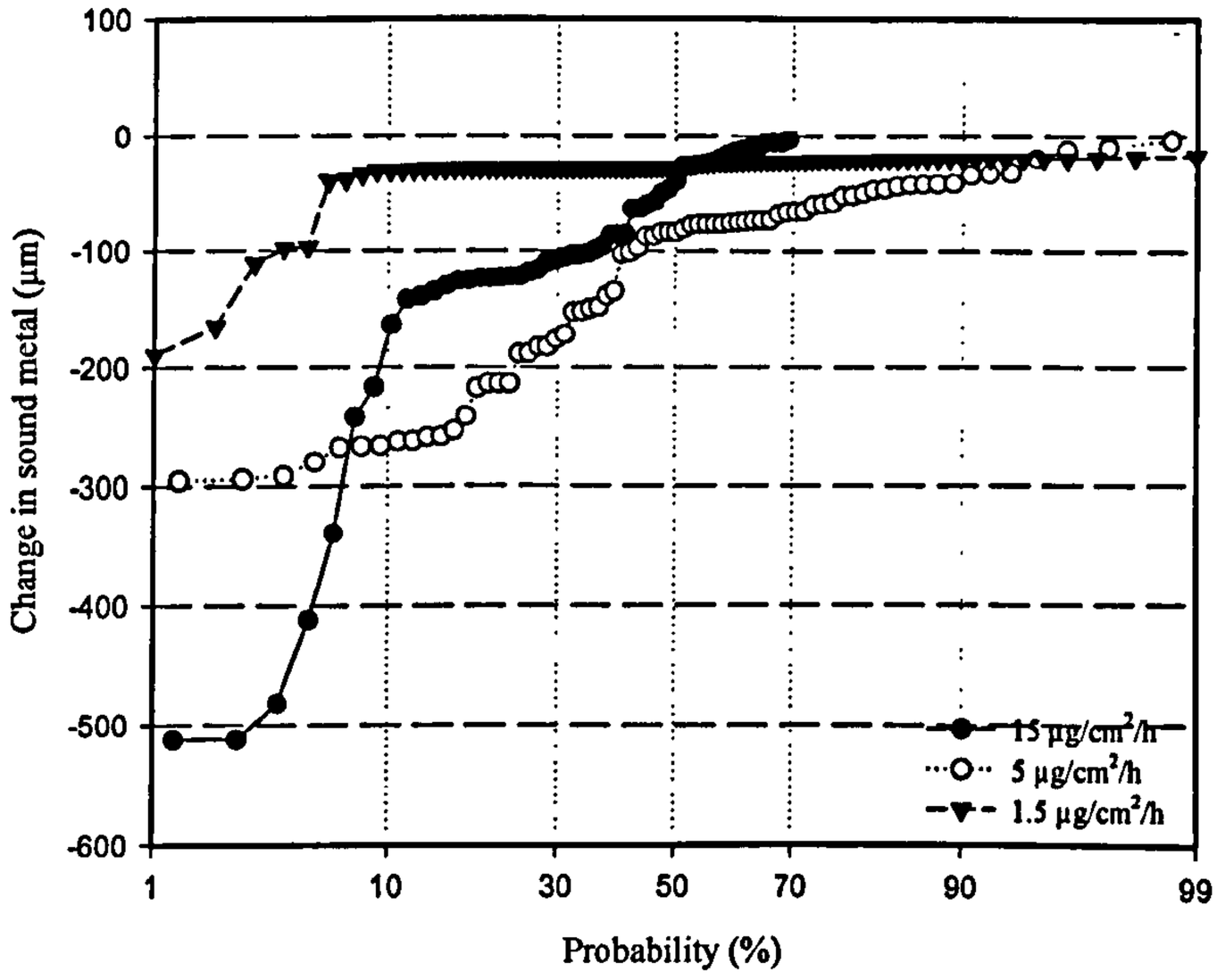

Figure 4.65: Change in sound metal as a function of the probability damage under different flux concentration for uncoated SC^2 in 50vpm SO_2 at (a) 700°C and (b) 900°C after 500h exposure.

a) PtAl Coated SC^2,80/20 $(Na/K)_2S)_4$ in 50vpm SO_2 at 700°C.

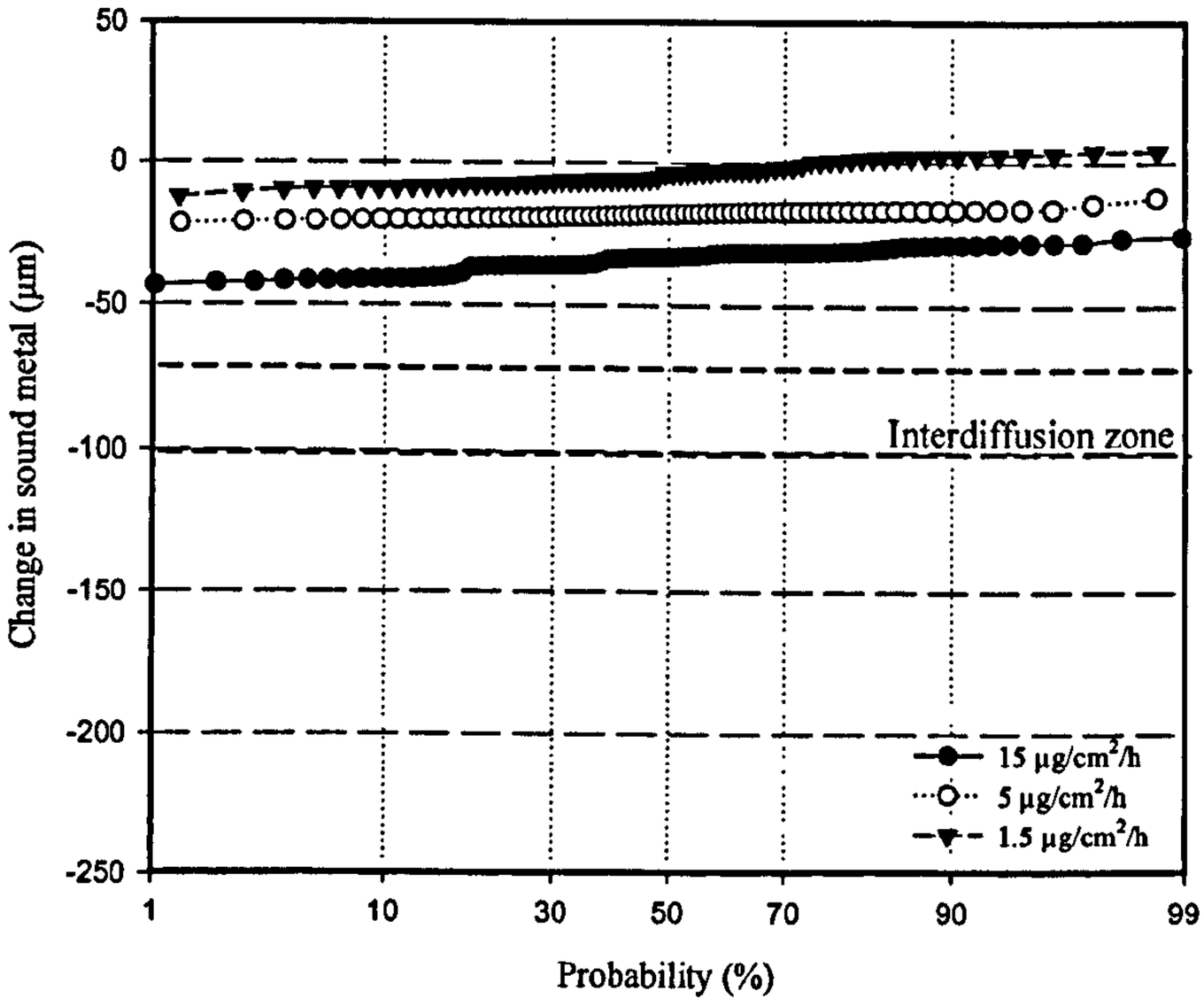

b) PtAl Coated SC^2, 80/20 $(Na/K)_2SO_4$ in 50vpm SO_2 at 900°C.

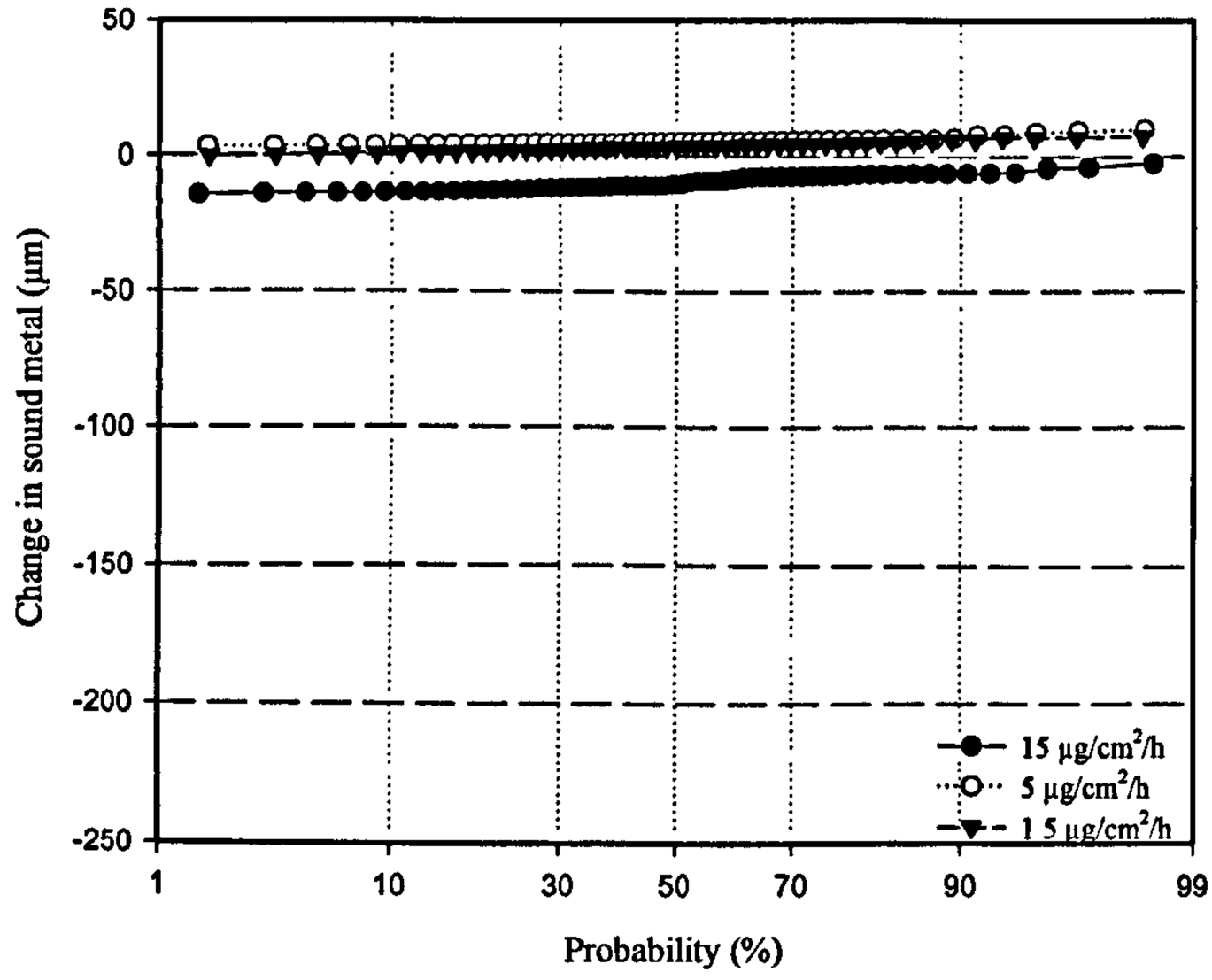

Figure 4.66: Change in sound metal as a function of the probability damage under different flux concentration for PtAl coated SC^2 in 50vpm SO_2 at (a) 700°C and (b) 900°C after 500h exposure.

a) Uncoated CMSX-4, 80/20 $(Na/K)_2SO_4$ in 50vpm SO_2 at 700°C.

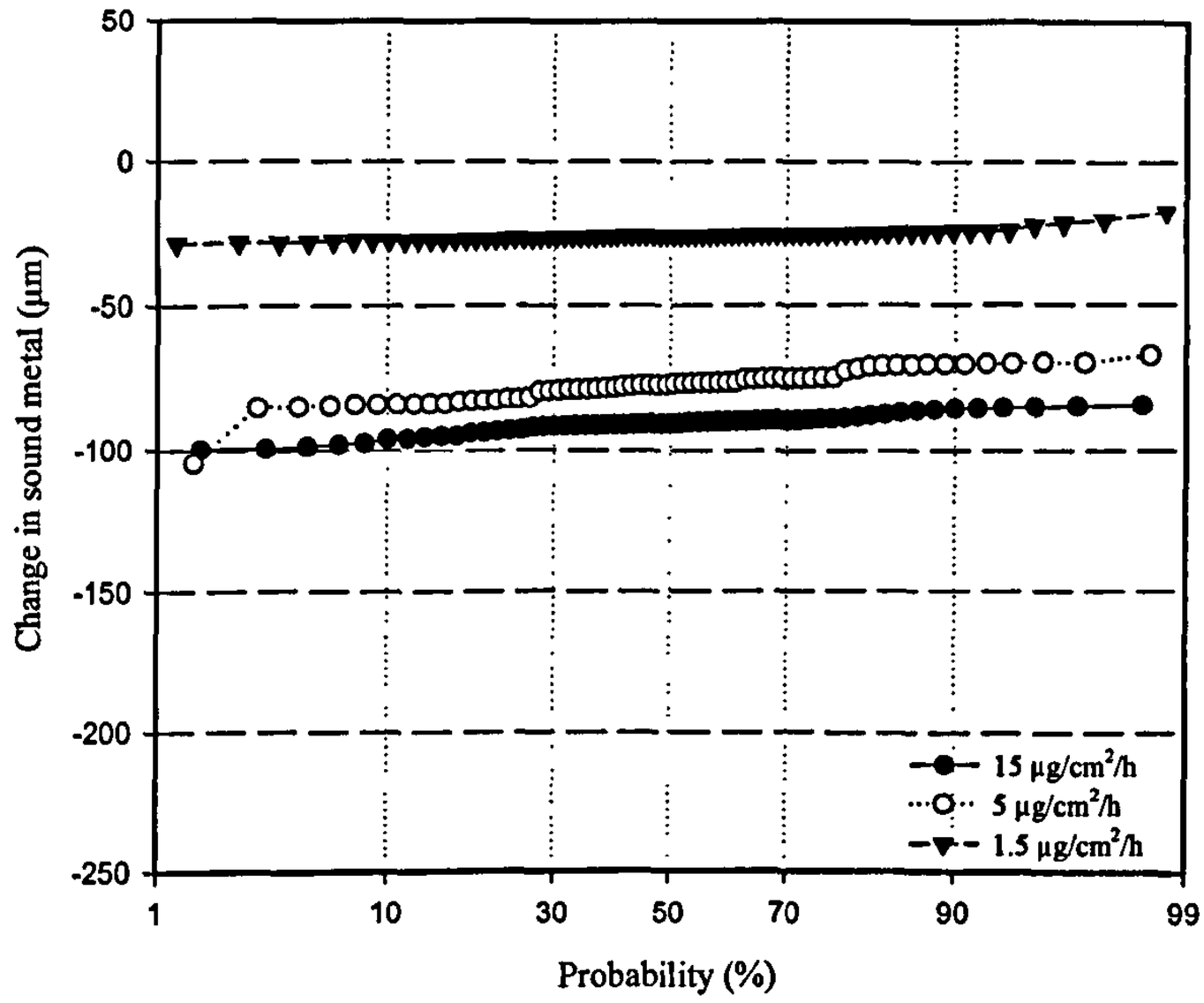

b) Uncoated CMSX-4, 80/20 $(Na/K)_2SO_4$ in 50vpm SO_2 at 900°C

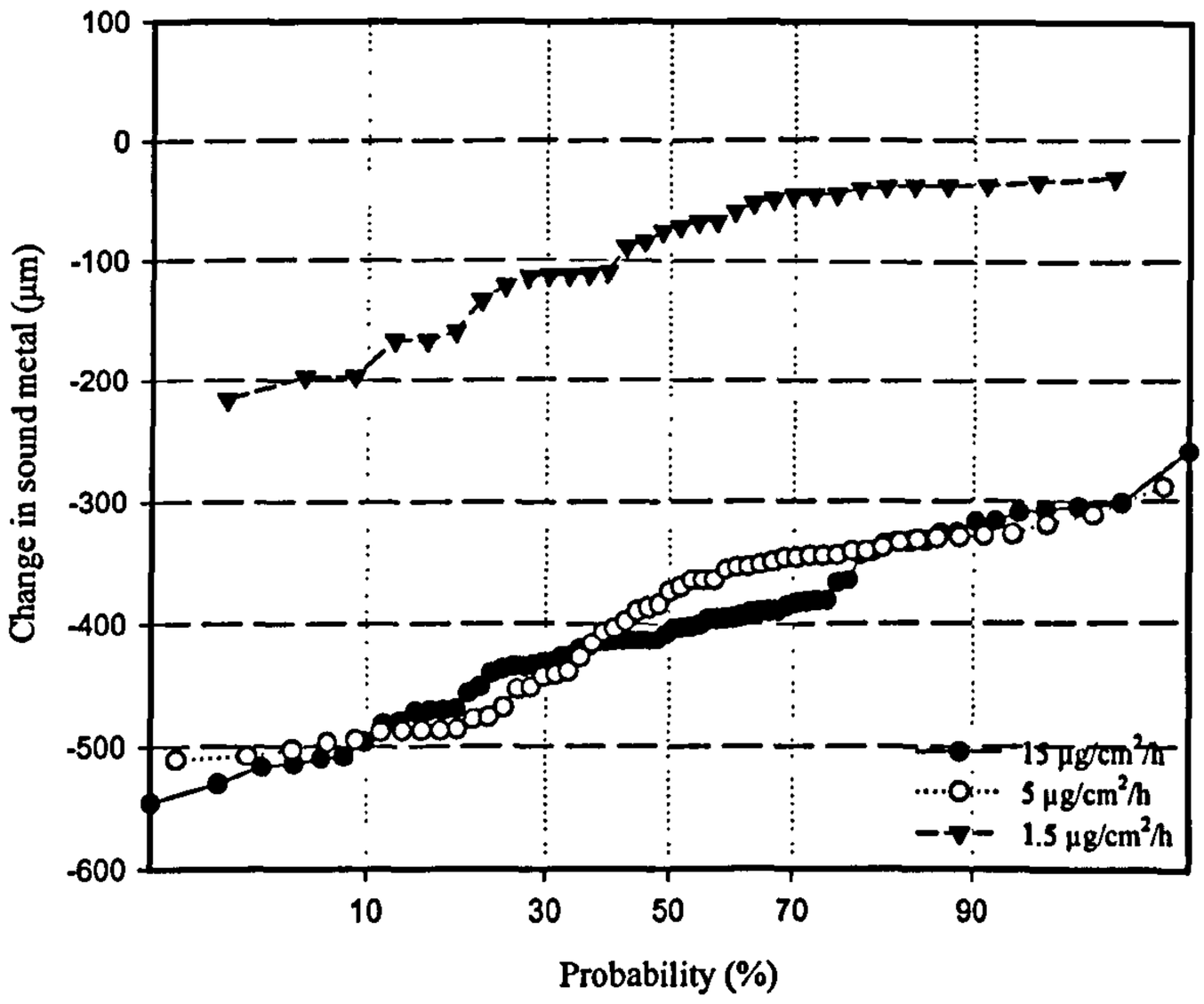

Figure 4.67: Change in sound metal as a function of the probability damage under different flux concentration for uncoated CMSX4 in 50vpm SO_2 at (a) 700°C and (b) 900°C after 500h exposure.

a) PtAl Coated CMSX-4, 80/20 $(Na/K)_2SO_4$ in 50vpm SO_2 at 700°C.

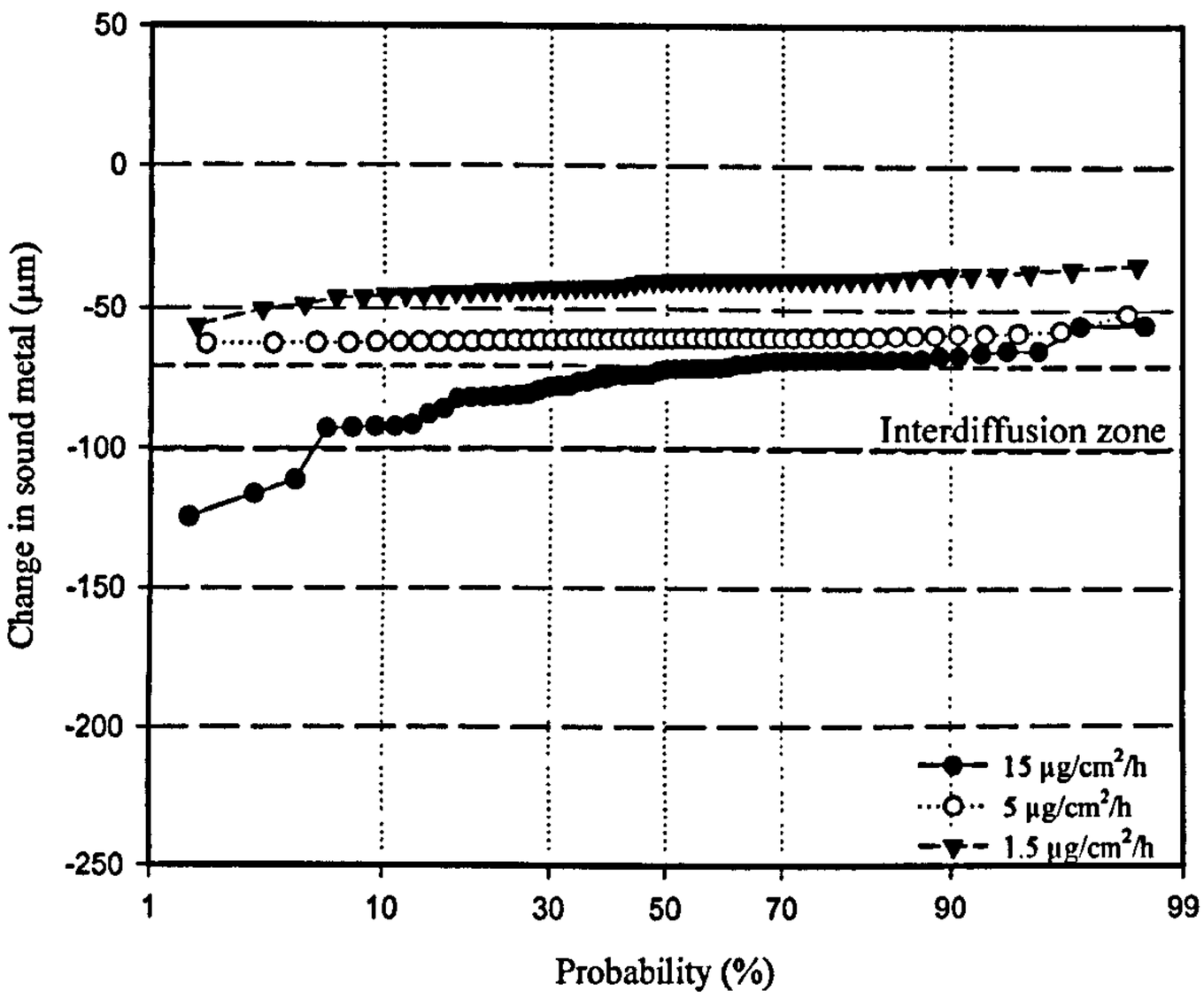

b) PtAl CMSX-4 Coated, 80/20 $(Na/K)_2SO_4$ in 50vpm SO_2 at 900°C.

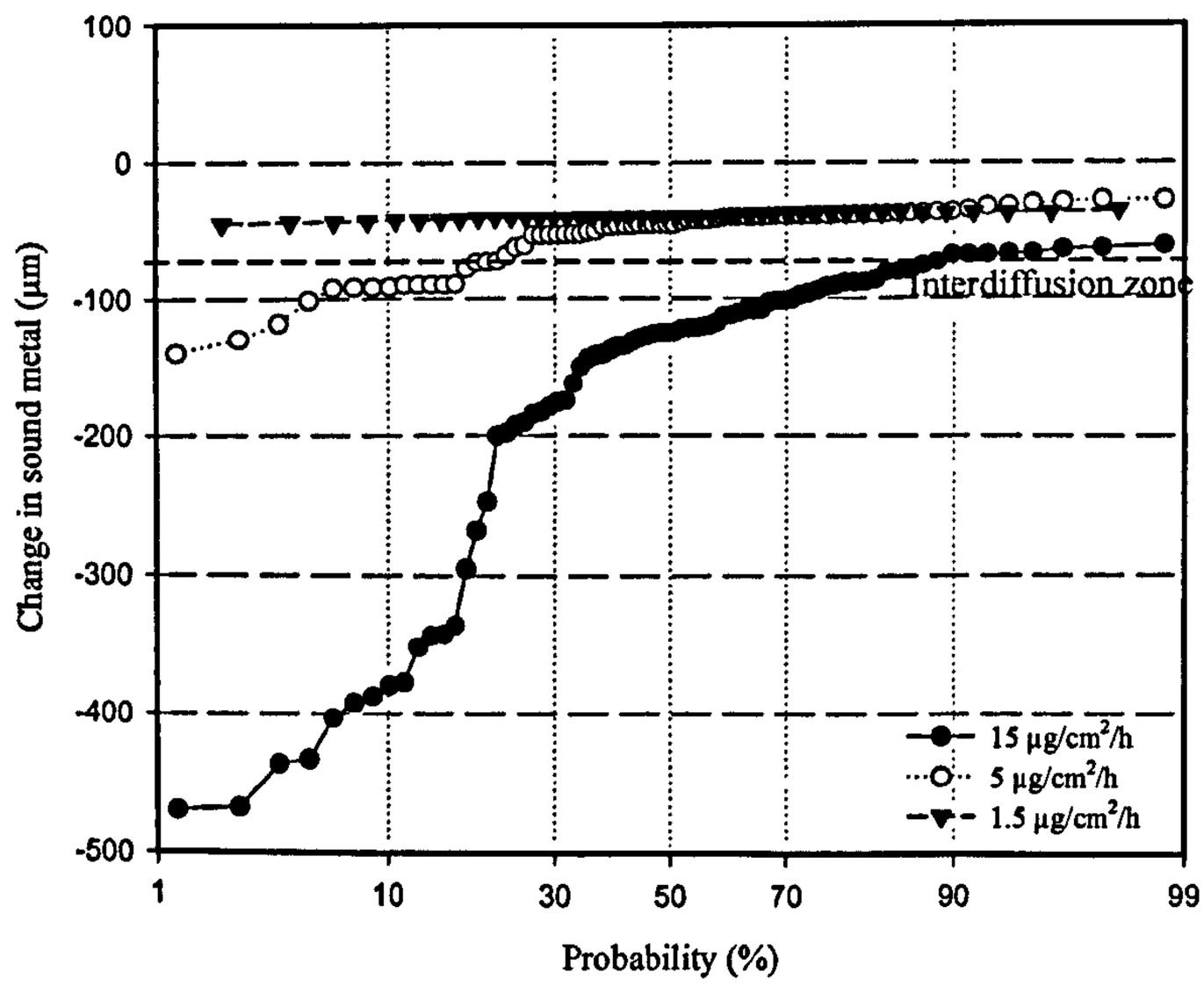

Figure 4.68: Change in sound metal as a function of the probability damage under different flux concentration for PtAl coated CMSX4 in 50vpm SO_2 at (a) 700°C and (b) 900°C after 500h exposure.

a) Uncoated SC^2, 80/20 $(Na/K)_2 SO_4$ in 50vpm SO_2/500vpm HCl at 700°C.

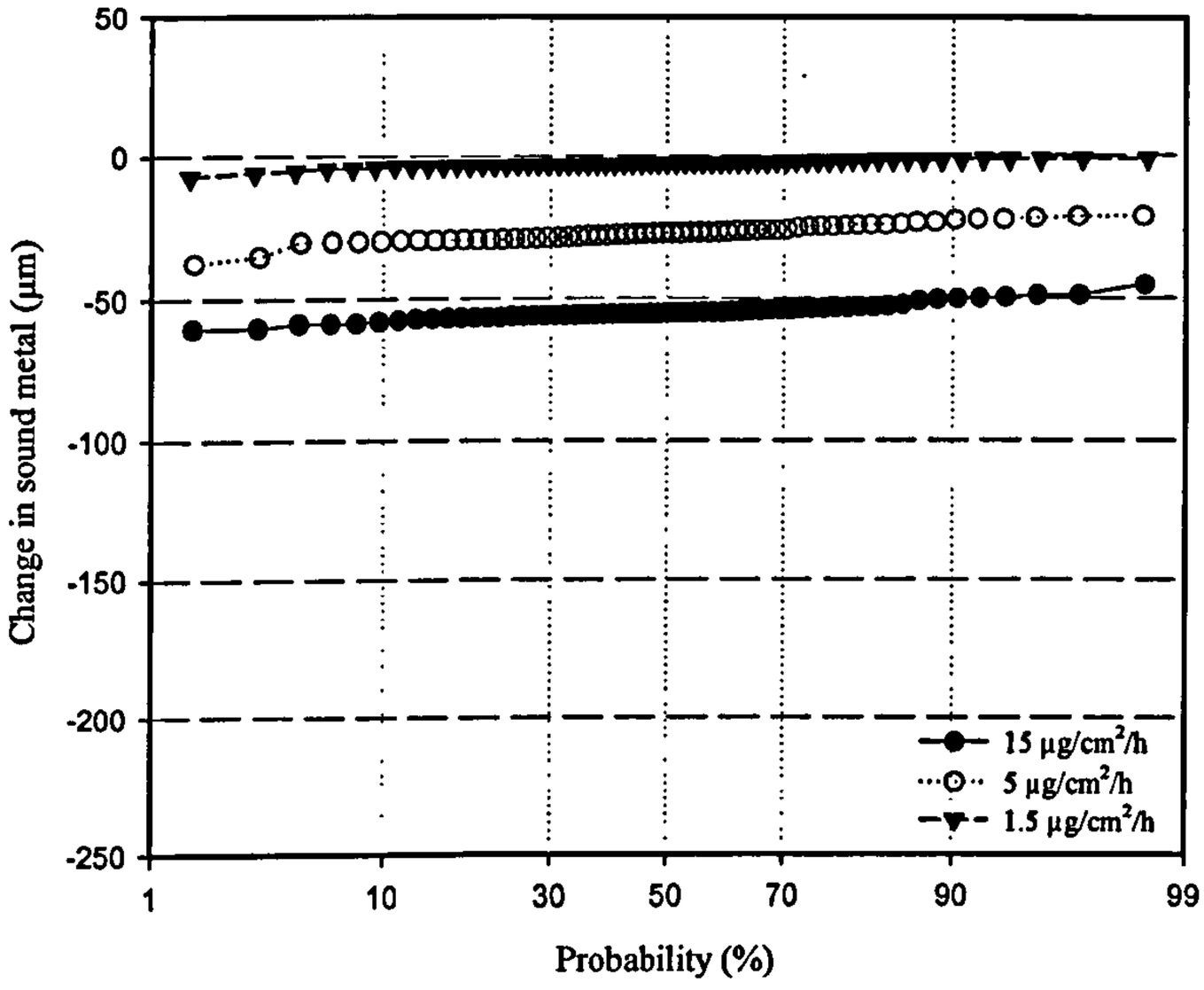

b) Uncoated SC^2, 80/20 $(Na/K)_2 SO_4$ in 50vpm SO_2/500vpm HCl at 900°C.

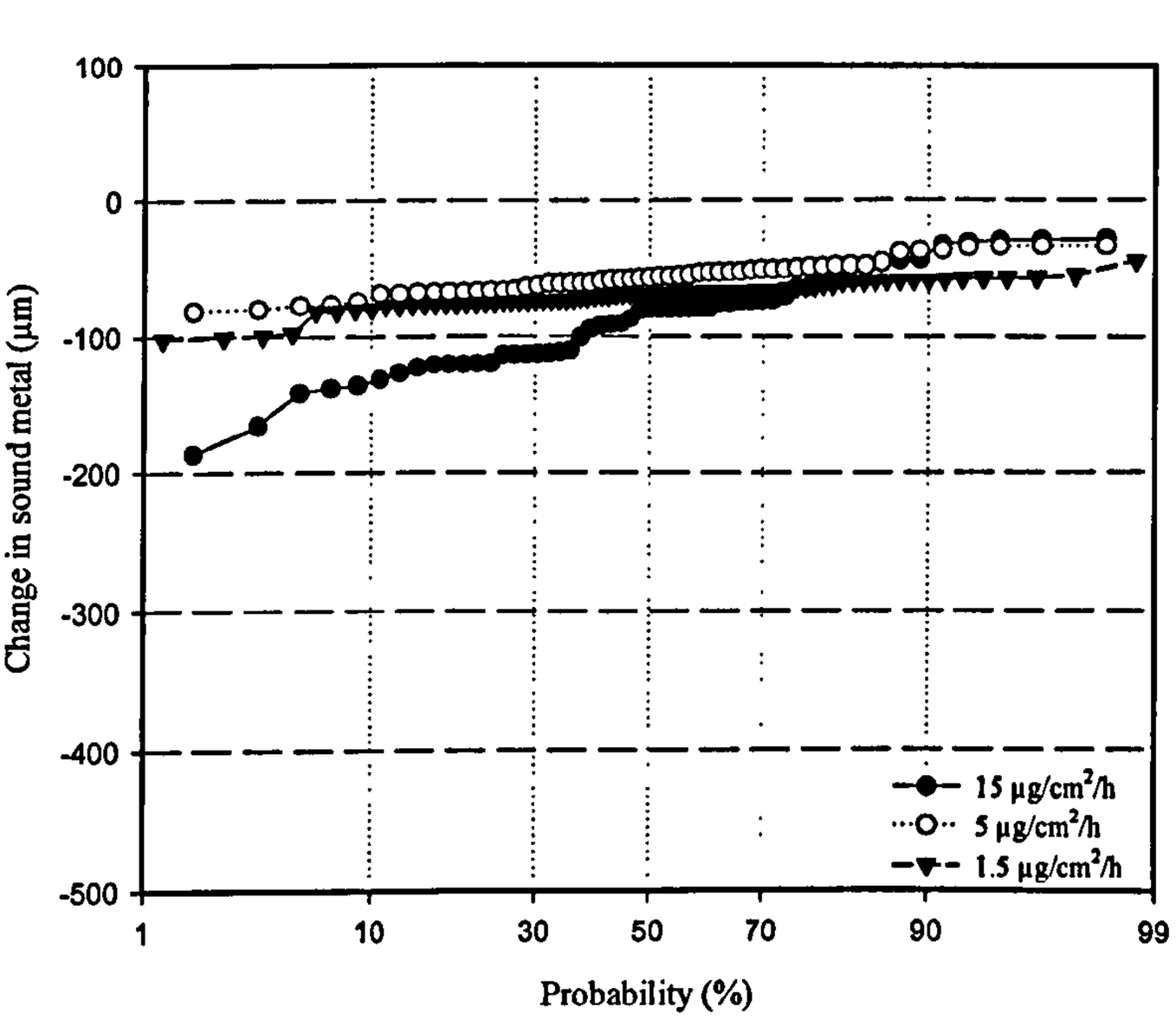

Figure 4.69: Change in sound metal as a function of the probability damage under different flux concentration for uncoated SC^2 in 50vpm SO_2/500vpm HCl at (a) 700°C and (b) 900°C after 500h exposure.

a) PtAl Coated SC^2, 80/20 $(Na/K)_2SO_4$ in 50vpm SO_2/500vpm HCl at 700°C.

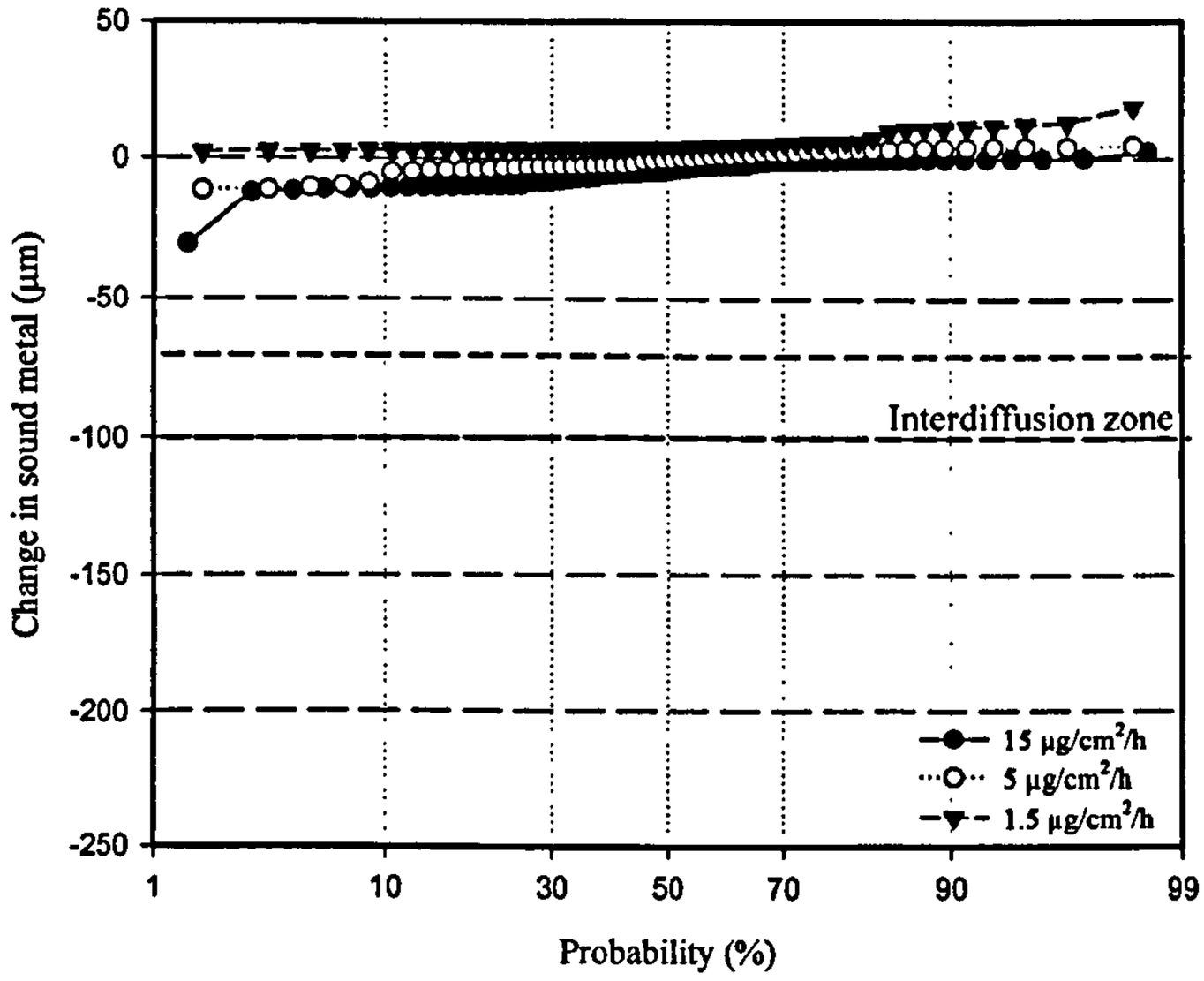

b) PtAl Coated SC^2, 80/20 $(Na/K)_2SO_4$ in 50vpm SO_2/500vpm HCl at 900°C.

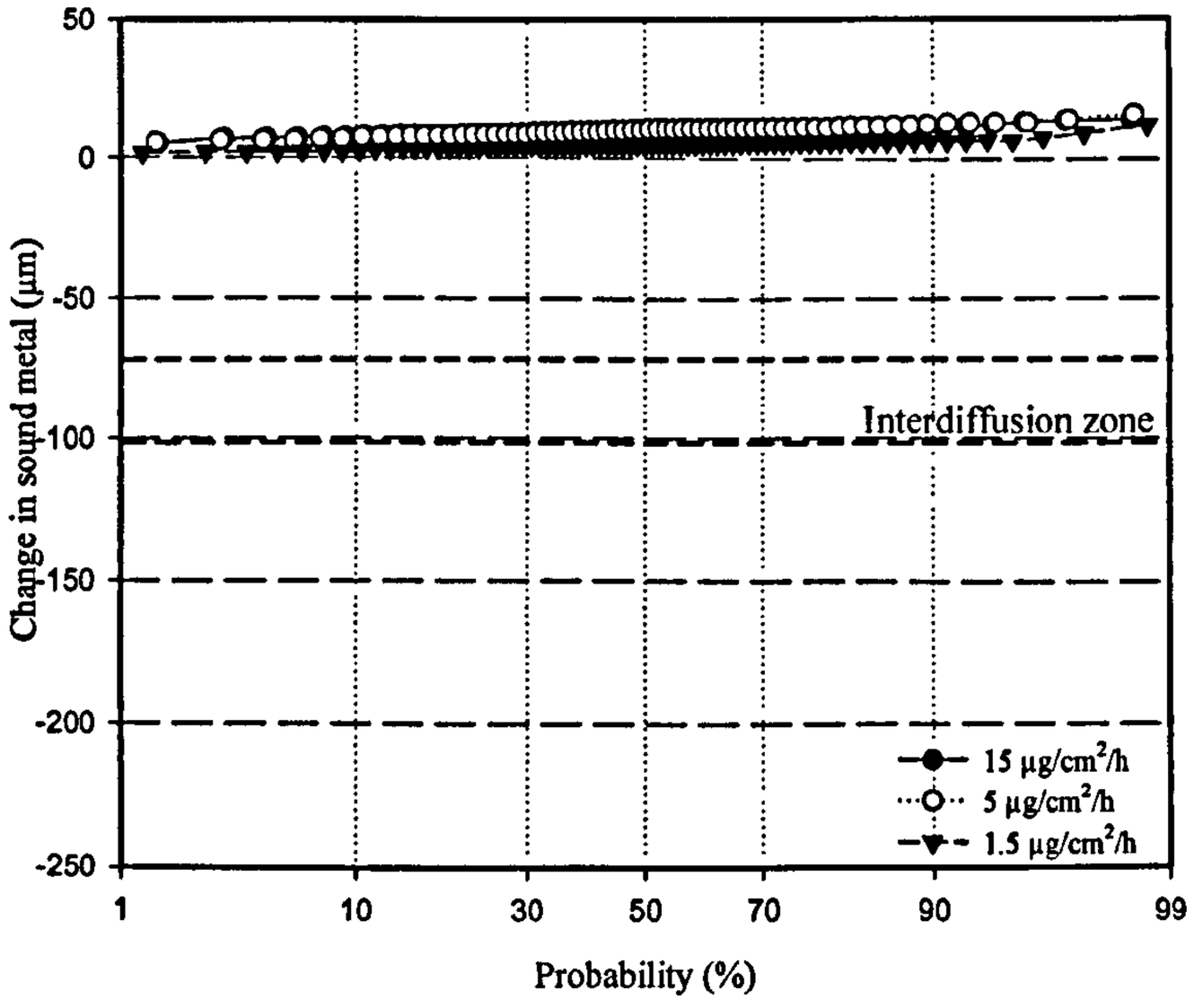

Figure 4.70: Change in sound metal as a function of the probability damage under different flux concentration for PtAl coated SC^2 in 50vpm SO_2/500 vpm HCl at (a) 700°C and (b) 900°C after 500h exposure.

a) Uncoated CMSX-4, 80/20 $(Na/K)_2SO_4$ in 50vpm SO_2/500vpm HCl at 700°C.

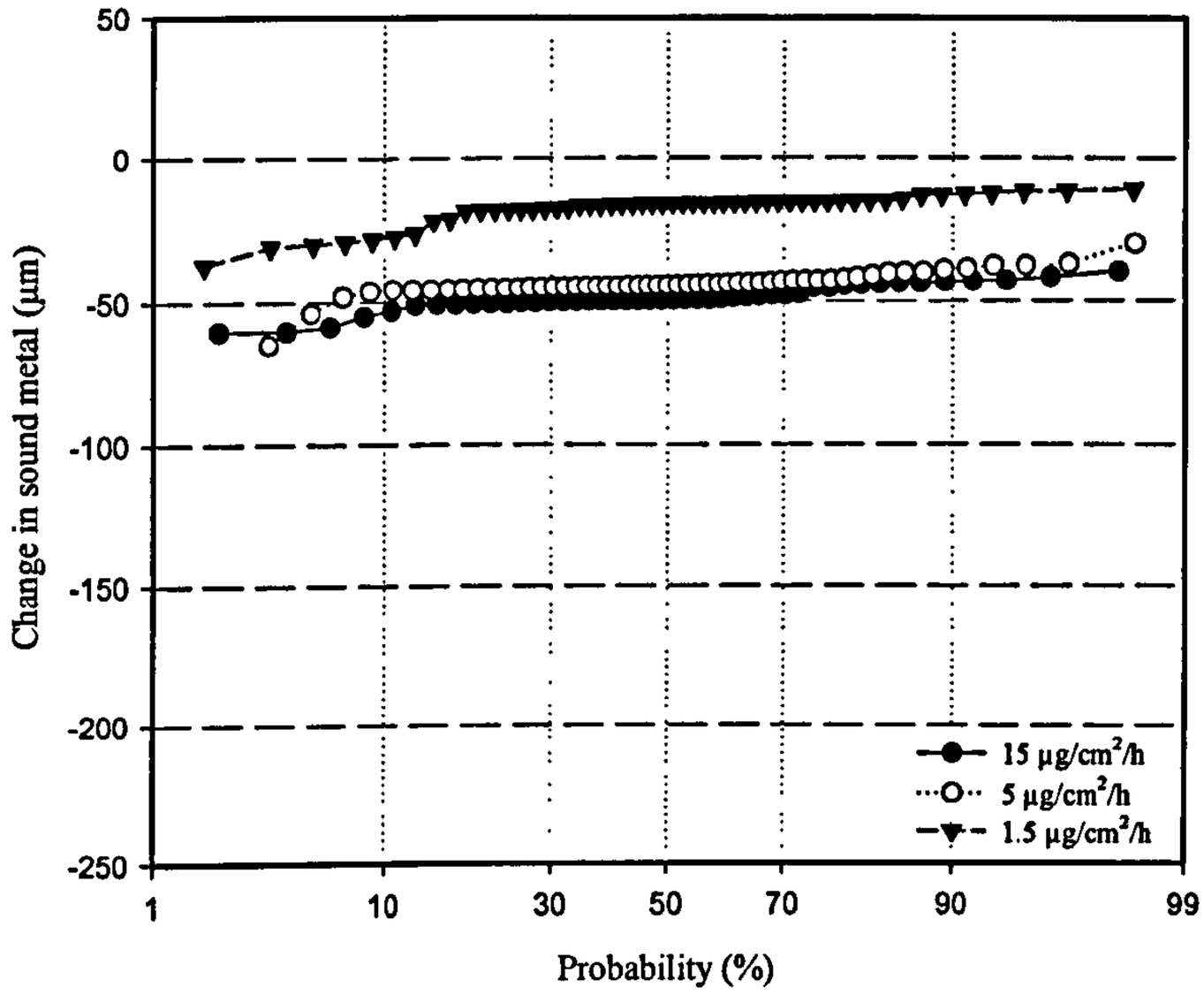

b) Uncoated CMSX-4, 80/20 $(Na/K)_2SO_4$ in 50vpm SO_2/500vpm HCl at 900°C.

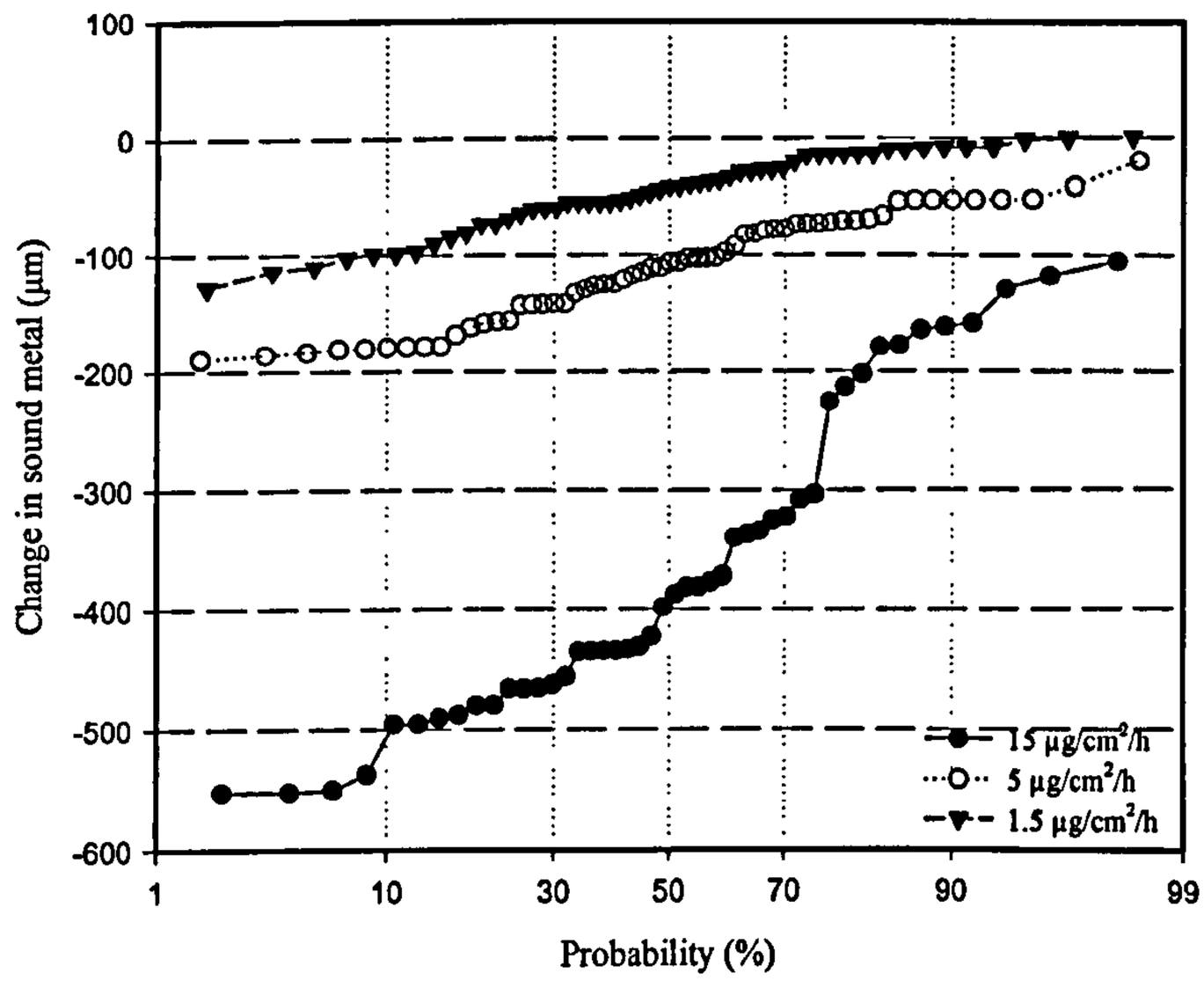

Figure 4.71: Change in sound metal as a function of the probability damage under different flux concentration for uncoated CMSX4 in 50vpm SO_2/500vpm HCl at (a) 700°C and (b) 900°C after 500h exposure.

a) PtAl CMSX4 Coated, 80/20$(Na/K)_2SO_4$ in 50vpm SO_2/500vpm HCl at 700°C.

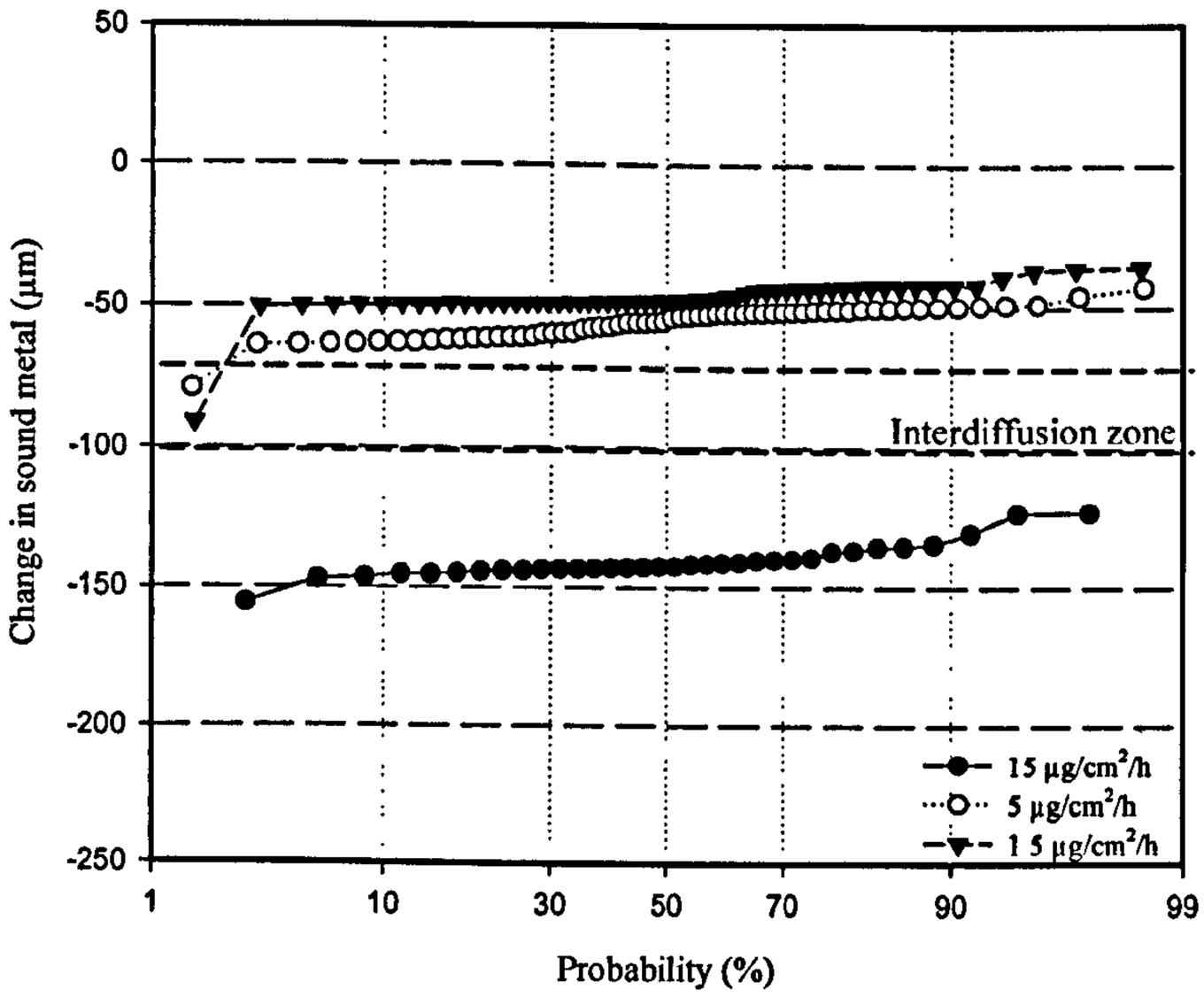

b)PtAl CMSX4 Coated, 80/20$(Na/K)_2SO_4$ in 50vpm SO_2/500vpm HCl at 900°C.

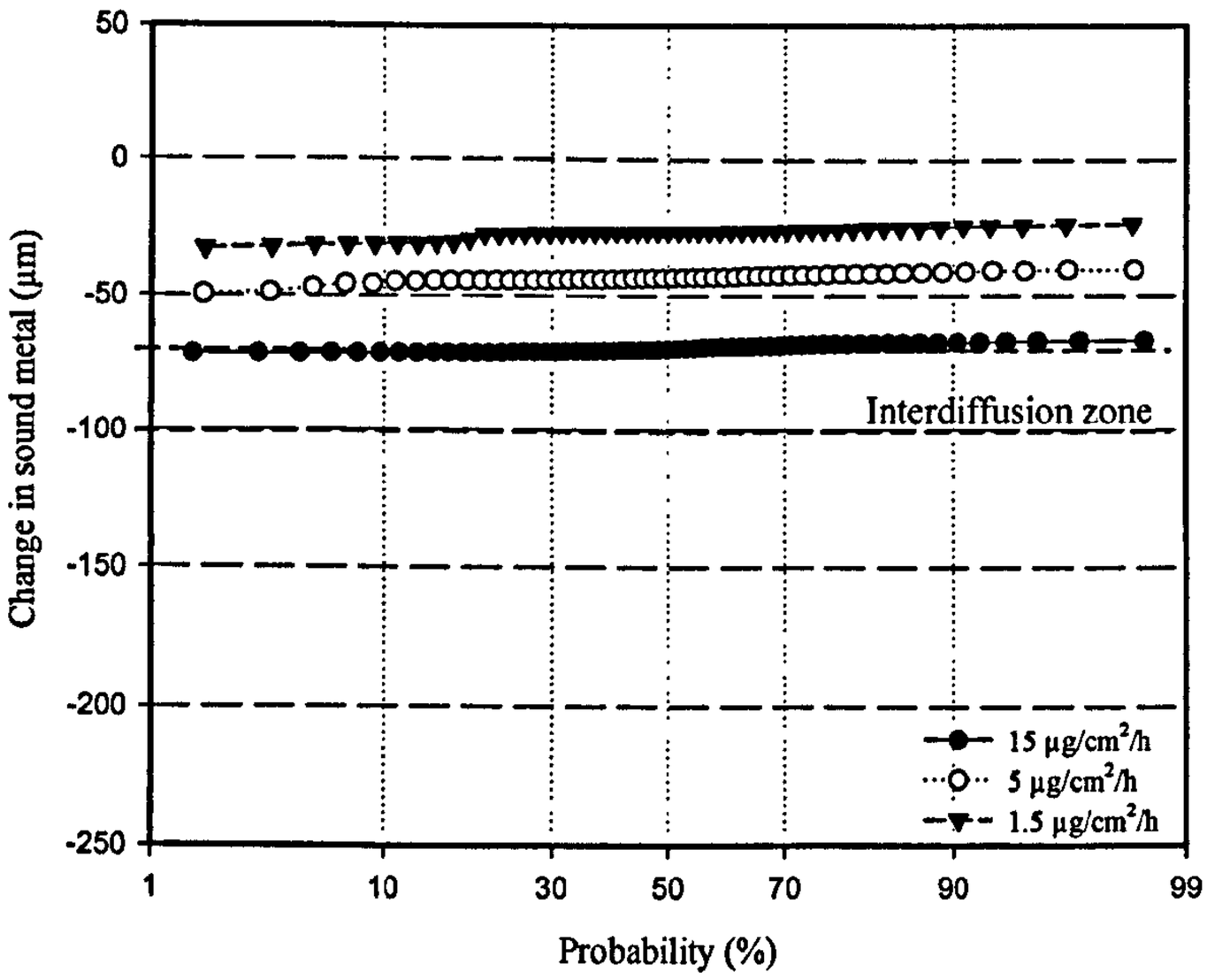

Figure 4.72: Change in sound metal as a function of the probability damage under different flux concentration for PtAl coated CMSX4 in 50vpm SO_2/500 vpm HCl at (a) 700°C and (b) 900°C after 500h exposure.

5 Discussion

5.1 Introduction

Industrial gas turbines are being developed to be used at higher firing temperatures and pressures to increase the efficiency of power generation (as explained in sections 2.1 and 2.2). The requirements for materials in the hot gas paths of gas turbine are very demanding; in particular the vane and blade materials for the hot combustion gas paths must give acceptable and predictable in-service lifetimes. Hot corrosion of turbine materials can occur very rapidly and can be an important life limiting factor. For hot corrosion to occur, a liquid (usually sulphate) deposit is required on the surface of components. The formation of these deposits depends on the presence of trace alkali, or other metal, species (e.g. sodium compounds) in the gas streams as well as other reactive gas species (e.g. sulphur dioxide (SO_2), sulphur trioxide (SO_3), HCl).

To explain the rates of corrosion, in 1979 a hot corrosion degradation sequence was proposed by Giggins and Petit in their Unified Theory [61] which remains true to this day. The basis for this theory is that hot corrosion data appear to indicate two stages of attack: an initial stage (initiation or incubation) during which the growth and dissolution of the protective oxide layer occurs and formation of deposits takes place and a second stage (propagation) where the attack rate increases considerably. The incubation stage can vary from seconds to thousands of hours and a number of factors have been identified upon which this phenomenon depends that are related to the service conditions, material composition and design.

1. Factors related to service conditions:

- Temperature (hot corrosion is a characteristic degradation mechanism in gas turbines in the metal temperature range of 600 to 950°C in a given environment).
- Gas composition and pressure (influence both the initiation and propagation mechanisms of hot corrosion attack, e.g. SO_3 presence).
- Deposit composition (two effects: one effect occurs because the deposit transforms from solid to liquid with compositional changes and another effect involves changes in the mechanism of the hot corrosion attack).
- Deposition flux (effect varies within the corrosion mechanism and flux level).

- Other factors include thermal cycles, physical state of the salts, erosion and gas velocity.

2. Factors related to the material and design are:

- Alloy composition (the length of the initiation stage can vary due to the aluminium content of nickel-chromium-aluminium or cobalt-chromium-aluminium alloys).
- Microstructural (the presence and/or removal of grain boundaries, e.g. in a single crystal superalloy)
- Geometry of the component (it is common to observe scale spalling at sharp angles of components)
- Other factors such as alloy fabrication conditions and methods.

Two general types of hot corrosion in gas turbine environments have been identified to date: Type I hot corrosion at ~ 750-900°C and Type II hot corrosion at ~ 600-800°C. Similar types of materials degradation can be expected in gas turbines using solid-derived fuels. The contaminant species of particular interest for corrosive degradation are those containing sulphur, chlorine, alkali metals (i.e. sodium and potassium) and other trace metals (e.g. lead). The levels of these contaminants are significantly different in the various potential solid fuels.

During the past approximately 40 years, efforts have been made to extend the incubation period of the material systems used in industrial gas turbines for power generation (development of new superalloys, coatings, surface treatments, etc.). As a part of these efforts, predicting the service life of new and known materials/coatings systems has become a relevant issue in the development of materials for power generation. In order to make precise prediction models, it is necessary to review the factors influencing the context and the material systems performance. Hence, this chapter discusses individually the corrosive effects of some of the factors related to service conditions of a gas turbine (i.e. deposition fluxes, deposit composition, temperature and gas composition) and those factors related to vane and blade materials and design (i.e. alloy composition and microstructure) on the initiation/incubation and propagation stages of the hot corrosion degradation sequence of the new single crystal superalloy SC^2, the already in use CMSX4 and the corrosion resistant IN738LC (as a reference), both uncoated and PtAl-coated.

The material performance data in terms of metal loss have been statistically interpreted in section 4.4 for each material system (alloy/coating) and form the basis for the development of corrosion models for platinum-aluminide coated/uncoated CMSX4 and SC^2 single crystals superalloys.

5.2 Effect of Varying Deposit Flux in Different Hot Corrosion Environments

As previously mentioned, among the factors that influence the incubation/propagation transition is the time of exposure (and thermal cycling); research on how this factor affects the hot corrosion of nickel-based superalloys has been carried out in the past. It has been observed for the alloy IN738LC, that up to 200h of exposure, there is low uniform damage, indicating an incubation time for the development of the pitting damage at low deposition flux, e.g. 1.5μg/cm^2/h. However, at a higher flux (e.g. 5μg/cm^2/h), the same uniform distribution of corrosion damage developing around the samples is observed, but in this case, from the start of the exposure, leaving no evidence of an incubation period [71]. Therefore, for IN738LC, with a deposition flux between 1.5 and 5μg/cm^2/h, the transition from incubation to propagation commences before 200h of exposure.

The corrosion damage levels were only measured are after 500h of exposure and therefore, no incubation periods could be seen. However, information on the incubation periods for the materials tested in this study can be deduced as a function of time from the mass change data presented in section 4.2. Approximate incubation times for all the materials/conditions tested are summarised in Table 5.5 and Table 5.6 in this chapter. By way of example for the uncoated CMSX4 material with a low deposit flux (1.5μg/cm^2/h) at 700°C in 50vpm SO_2/500vpm HCl environment (Figure 4.17) and in 50vpm SO_2 gas (Figure 4.18), an incubation period of no greater 50h can be seen. Slightly longer incubation periods are observed for SC^2 (no greater 100h) in the same corrosive environments (Figure 4.23 and Figure 4.24). As seen in the mass change data, incubation periods can be extended as a function of time by the application of coatings, in this study, the platinum/aluminium diffusion coating, the performance of which is discussed further in section 5.6.

Little research has been carried out to investigate the effect of changing the deposition flux for single crystal superalloys. However, a dependence of corrosion rate on the deposition flux has been observed in previous work for the nickel-based superalloy, IN738LC [71]. This dependence has an approximately sigmoidal shape and consists of three distinct characteristic behaviours: at low deposition fluxes (~0.25 to 1.5μg/cm^2/h) low corrosion rates are observed; at intermediate deposition fluxes (~ 5 to 15 μg/cm^2/h), much faster corrosion rates are found, with a dependence on deposit flux close to linear, the "flux limited hot corrosion regime"; and, at high deposition fluxes (>15μg/cm^2/h), a thick scale/deposit layer is found which effectively creates a buried-in-ash scenario and slightly reduces the corrosion rate with

further increases in flux. Despite IN738LC superalloy being a hot corrosion resistant superalloy, similar behaviour was observed for the two single crystal superalloys examined in this study, i.e. of the three distinct types of behaviour, they appear to fit into the "flux limited hot corrosion regime" under the conditions tested in this study, but with higher corrosion rates than IN738LC; this is possibly due to the different alloy compositions and/or microstructures, subjects that are discussed in section 5.4.

The effect of changing fluxes can be appreciated on specimens at first sight, as seen on the sets of photographs shown in Figure 5.1 for uncoated SC^2 samples recoated with the 80/20 $(Na/K)_2 SO_4$ solution. The pictures show an unexposed reference sample and samples coated with a low deposition flux ($1.5\mu g/cm^2/h$), an intermediate deposition flux ($5\mu g/cm^2/h$) and a high deposition flux ($15\mu g/cm^2/h$) exposed in air-500vpm SO_2 at temperatures of (a) 700°C and (b) 900°C after 500h of exposure and before being metallographically processed (the appearance of all samples tested was documented in such photo-sets).

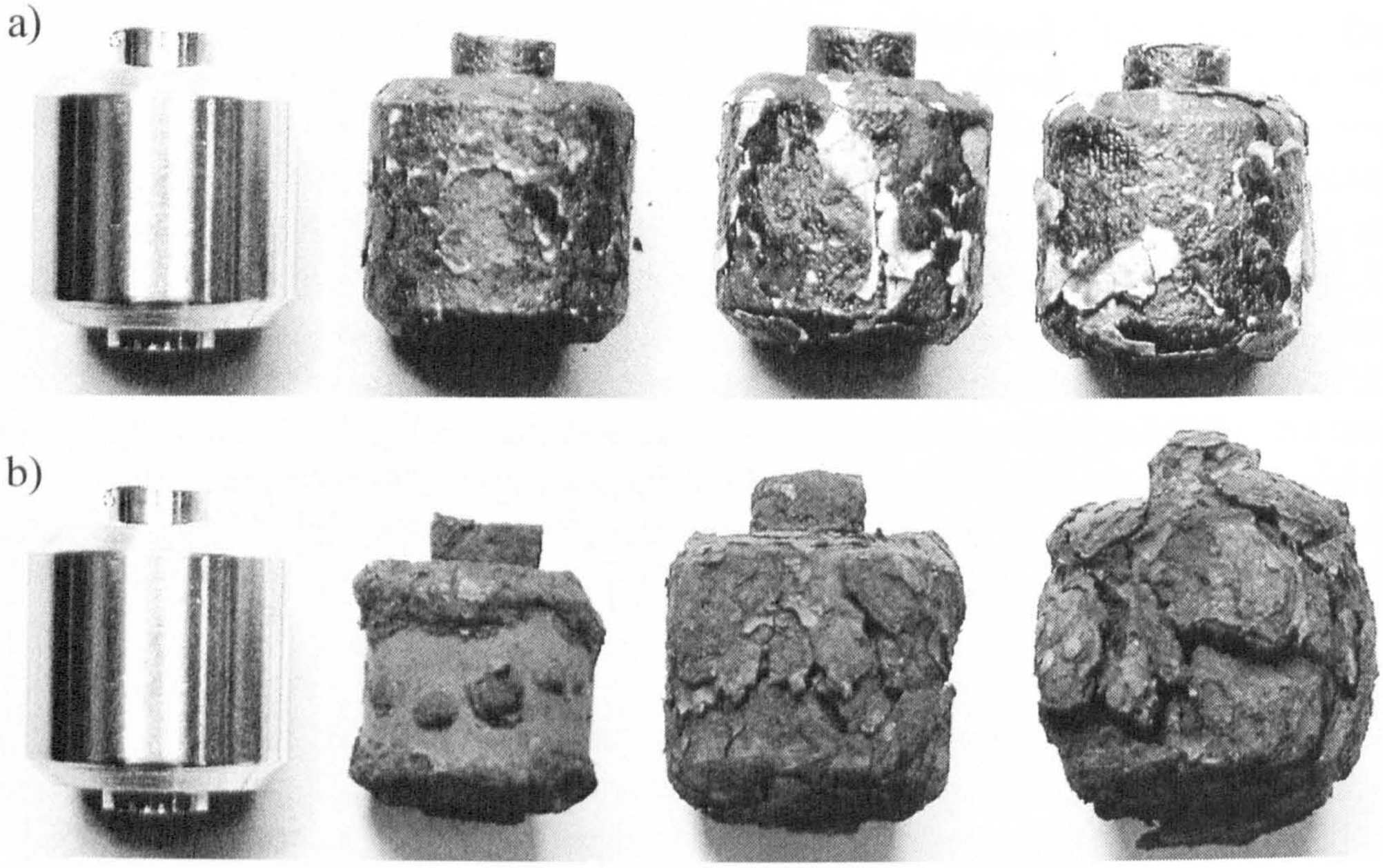

Figure 5.1: Deposit 80/20 $(Na/K)_2 SO_4$ from an unexposed reference sample to low deposition flux ($1.5\mu g/cm^2/h$), an intermediate deposition flux ($5\mu g/cm^2/h$) and a high deposition flux ($15\mu g/cm^2/h$) on uncoated SC^2, in 500vpm SO_2 at temperatures of (a) 700°C and (b) 900°C.

The corrosion damage of these uncoated single crystal superalloys, SC^2 and CMSX4, has been summarized in Figure 5.2 to Figure 5.5 by selecting a particular probability level of confidence (4% chance of being exceeded) from the ordered sound metal loss data presented in section 4.4. These illustrate the effects of varying the deposition flux of $80/20(Na/K)_2SO_4$ from a low deposition flux ($1.5\mu g/cm^2/h$), to an intermediate deposition flux ($5\mu g/cm^2/h$) and then a high deposition flux ($15\mu g/cm^2/h$) with changes in the various environmental parameters for three different SO_2 and HCl concentrations (50 vpm SO_2, 500vpm SO_2 and 50vpm SO_2/500 vpm HCl) at temperatures of 700 and 900°C.

The performance of uncoated SC^2 is presented in Figure 5.2 for the 700°C test conditions and shows the effect of the three different deposition fluxes, (1.5, 5 and 15 $\mu g/cm^2/h$) of 80/20 $(Na/K)_2SO_4$ in terms of sound metal loss with a 4% probability of being exceeded, after 500 hours in three different gas compositions (air-50vpm SO_2, 500vpm SO_2 and 50vpm SO_2/500vpm HCl).Uncoated SC^2 has corroded with a power law dependence on deposition flux, following an approximately straight line when plotted on a log axis when the flux deposit is increased from the lowest value, $1.5\mu g/cm^2/h$, to the intermediate value, $5\mu g/cm^2/h$ and then to the highest value, $15\mu g/cm^2/h$. Little increase in damage from flux to flux was seen in the line for the 50vpm SO_2/500HCl environment (only 4μm and 8μm respectively), still following a straight line but with a small gradient; this decrease in the total gradient could be due to changes in the gas composition, i.e. HCl addition on the correspondent environment; these effects are discussed in section 5.5 of this chapter. The hot corrosion damage seems to be lower only at the 1.5 $\mu g/cm^2/h$ flux with no HCl.

Changes in flux concentrations also have repercussions in the resulting damage morphologies, as can be seen in Figure 4.34 by comparing vertically the sets of photomicrographs 1, 2 and 3; 7, 8 and 9; 13, 14 and 15, where a progression of minor to major damage is seen due to the increase in deposition flux. This effect confirms the belief that some hot corrosion mechanisms are not self-sustaining and, therefore, the greater in the salt present, the greater is the attack. The salt reaches certain compositions, formed at the salt-alloy interface, by modifications of the as-deposited salt as a result of reaction with the alloy [61]. Typical hot corrosion type II morphologies can be appreciated in the photomicrographs 1 and 8 (Figure 4.34). However, the addition of HCl to the 50vpm SO_2 gas appears to suppress the typical pitting damage and leads to a broader front attack, with some internal damage. This can be seen in photomicrographs 13, 14 and 15 (Figure 4.34). Photomicrographs 1, 7 and 13 show the characteristic thick scale/deposit that resulted from a high deposit flux ($15\mu g/cm^2/h$).

Figure 5.3 shows the performance of uncoated SC^2 under the same test conditions as Figure 5.2 but at 900° C. Compared to the 700°C results, similar trends in behaviour were observed for the uncoated SC^2 at 900°C regarding sensitivity to deposition flux but the corrosion rates are much more severe (except the gradient from the 50vpm SO_2/500vpm HCl environment with a deposit flux of 5μg/cm^2/h, which showed a lower level of attack). The sensitivity of this uncoated single crystal material increases more significantly at 900°C than at 700°C for the three different hot corrosion environments. Very high corrosion rates, representing catastrophic hot corrosion, are observed with the intermediate and high deposit fluxes in the 500vpm SO_2 gas, the most aggressive environment (Figure 4.35, photomicrographs 10 and 11). Typical type I hot corrosion involving, internal oxidation/sulphidation damage is evident in all photomicrographs in Figure 4.35. Trends of increasing damage with increasing flux deposition can be seen by comparing vertically photomicrographs 4, 5 and 6; 10, 11 and 12; and 16, 17 and 18 (Figure 4.35).

Figure 5.4 shows the effect of deposition flux of 80/20 $(Na/K)_2 SO_4$ on the hot corrosion performance of uncoated CMSX-4 in terms of sound metal loss (with a 4% probability of being exceeded) after exposure at 700°C in the range of different gas compositions. This material shows practically the same corrosion rate with the 1.5μg/cm^2/h flux (only 2μm of metal loss difference) in the low SO_2/HCl environments. Increasing to the intermediate deposition flux, 5μg/cm^2/h, corrosion increased rapidly, especially in the 500vpm SO_2 environment. In the 50vpm SO_2 environment, the corrosion damage continues to increase, but more slowly, on increasing the deposit flux. However, with increasing flux in the 50vpm SO_2/500vpm HCl gas to 15μg/cm^2/h, the damage slightly decreases (4μm). This effect could be due to rapid formation of a thick scale/deposit layer which could reduce the corrosion rate at/after this particular flux concentration by burying the metal in a thick corrosion deposit [71]). This scale/deposit can be seen in Figure 4.38, photomicrograph 13, good examples of this effect can be seen in same figure in photomicrographs 1 and 7.

Figure 5.5 shows the effect of deposition flux for 80/20 $(Na/K)_2SO_4$ on the hot corrosion performance of uncoated CMSX-4 in terms of sound metal loss (with a 4% probability of being exceeded) after exposure at 900°C in the three different gas compositions. By comparing with Figure 5.4, the effect of changing temperature on the uncoated CMSX4 can be seen; clearly, at 900°C, this material is more sensitive than at 700°C and catastrophic corrosion was observed on those samples exposed in 500vpm SO_2 gas (Figure 4.39 photos 10, 11, 12) and deep internal damage in 50vpm SO_2/500 vpm HCl gas with flux of 15μg/cm^2/h (Figure 4.39 photo 16). As well as at 700°C, in the 50vpm SO_2 environment, the damage seems to be slightly more than in the other two environments when deposits are in the range of 1.5 and 5μg/cm^2/h but, with a

deposit flux of 15μg/cm^2/h, damage seem have stabilised (33μm of difference). Comparing the uncoated single crystals superalloys, CMSX-4 with SC^2 under the same tests conditions at 700°C (Figure 5.4 vs. Figure 5.2), in general, CMSX4 appears to have higher corrosion rates, whereas at 900°C, (Figure 5.5 vs. Figure 5.3) uncoated SC^2 is much more sensitive than CMSX4, showing excessive corrosion rates.

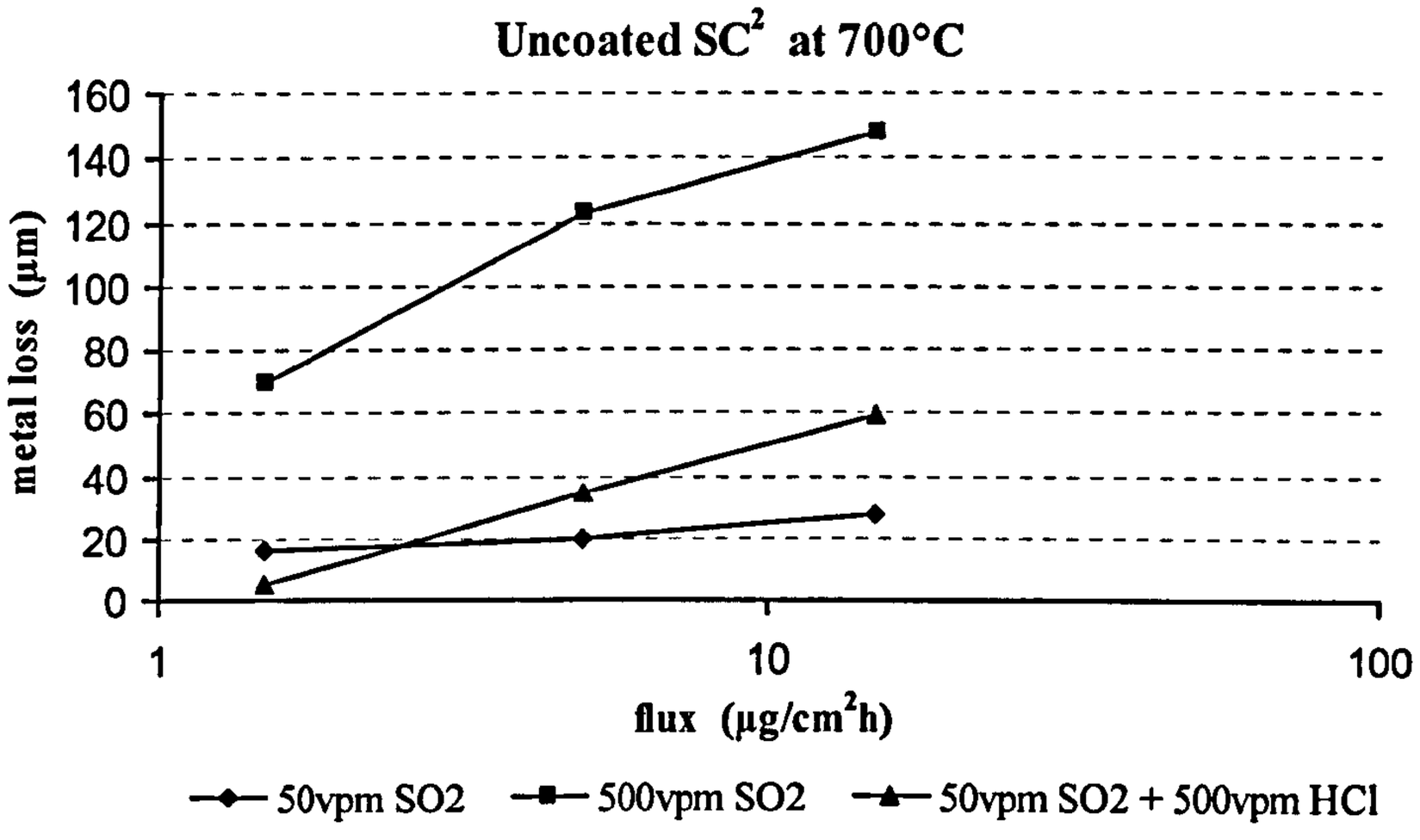

Figure 5.2:Effect of deposition flux of 80/20 $(Na/K)_2SO_4$ on the hot corrosion performance of uncoated SC^2 in terms of sound metal loss (with a 4% probability of being exceeded) after 500h of exposure at 700°C in a range of different gas composition.

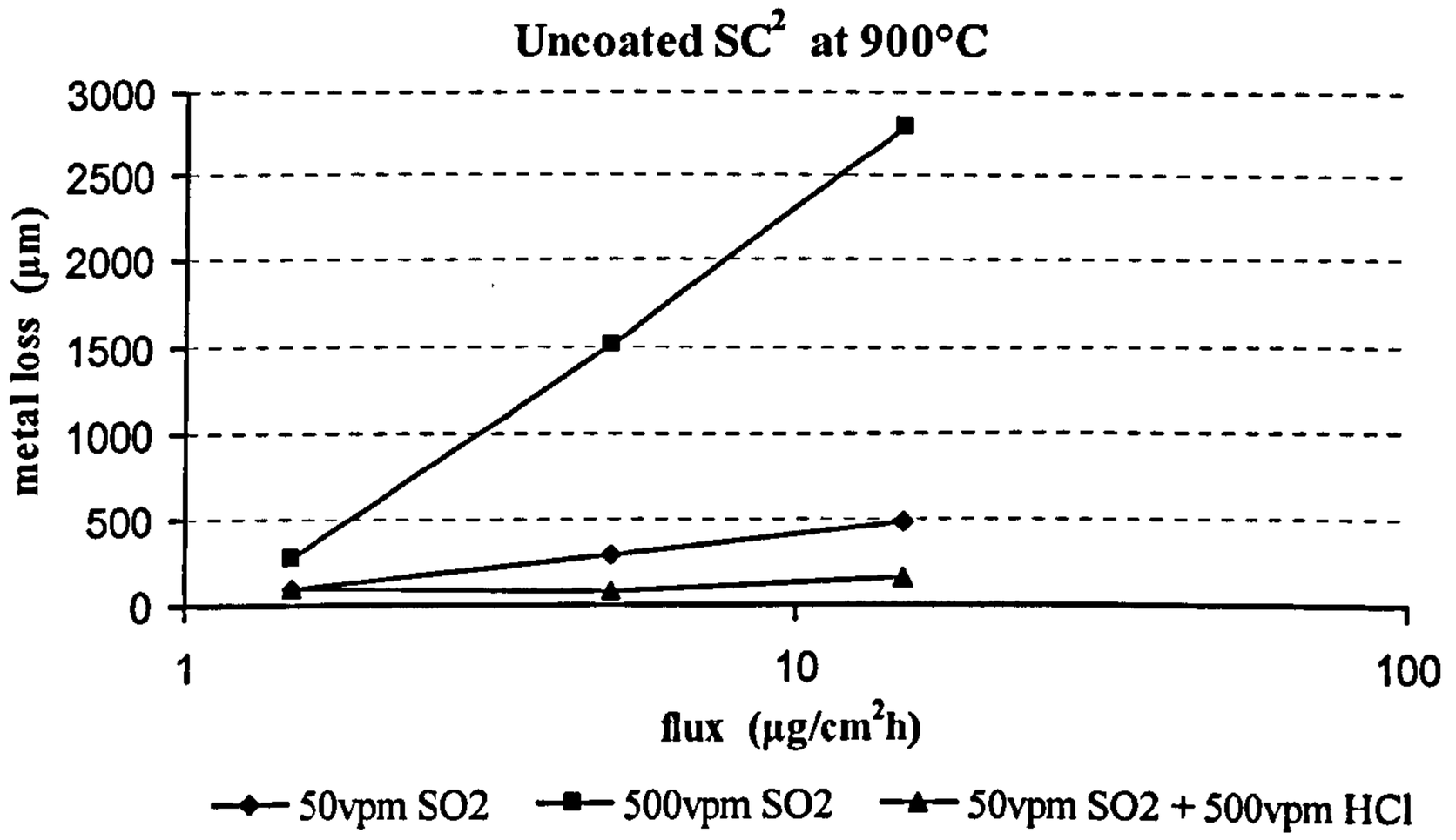

Figure 5.3: Effect of deposition flux of 80/20 $(Na/K)_2SO_4$ on the hot corrosion performance of uncoated SC^2 in terms of sound metal loss (with a 4% probability of being exceeded) after 500h exposure at 900°C in a range of different gas composition.

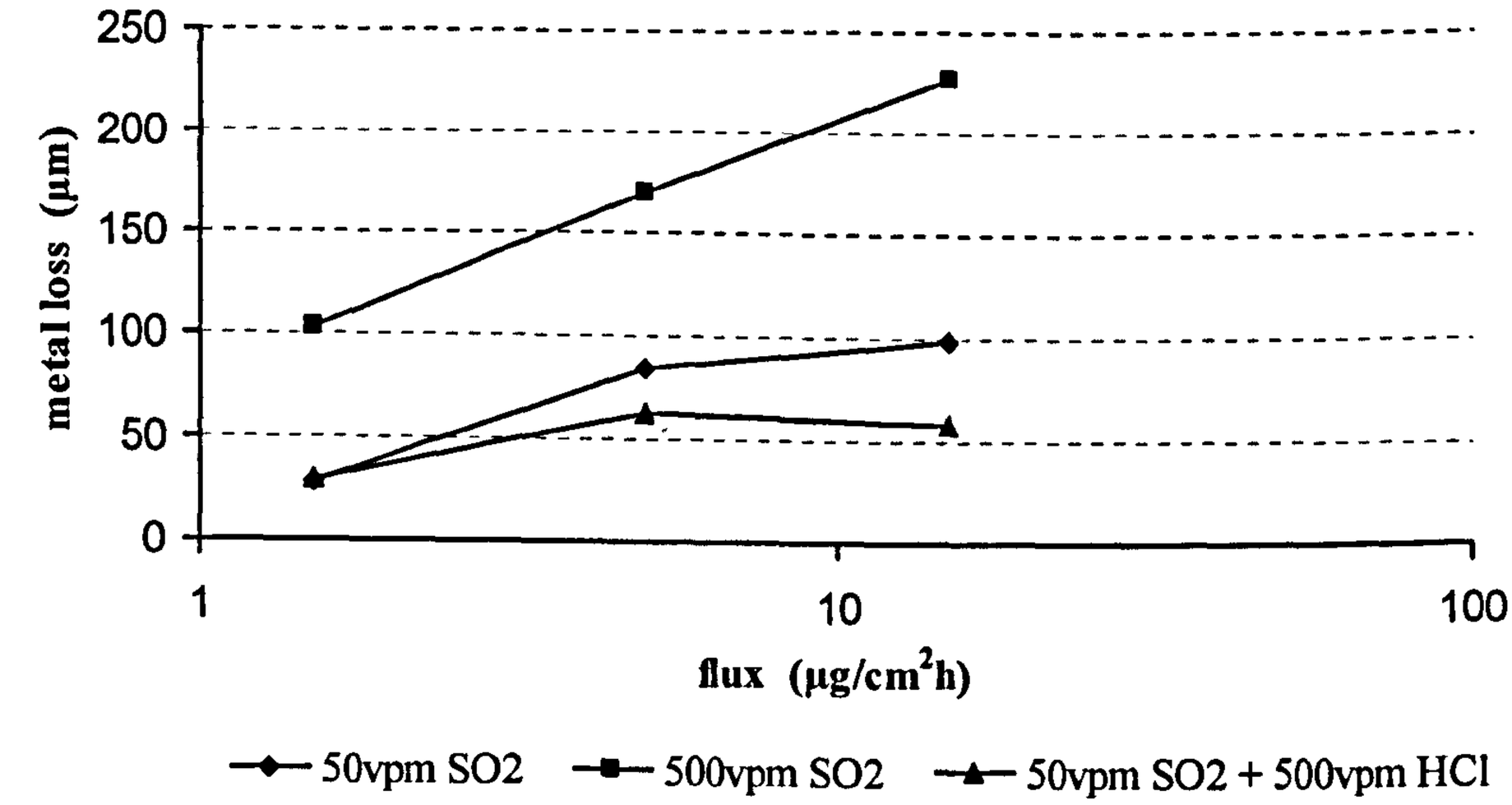

Figure 5.4: Effect of deposition flux of 80/20 $(Na/K)_2SO_4$ on the hot corrosion performance of uncoated CMSX-4 in terms of sound metal loss (with a 4% probability of being exceeded) after 500h exposure at 700°C in a range of different gas composition.

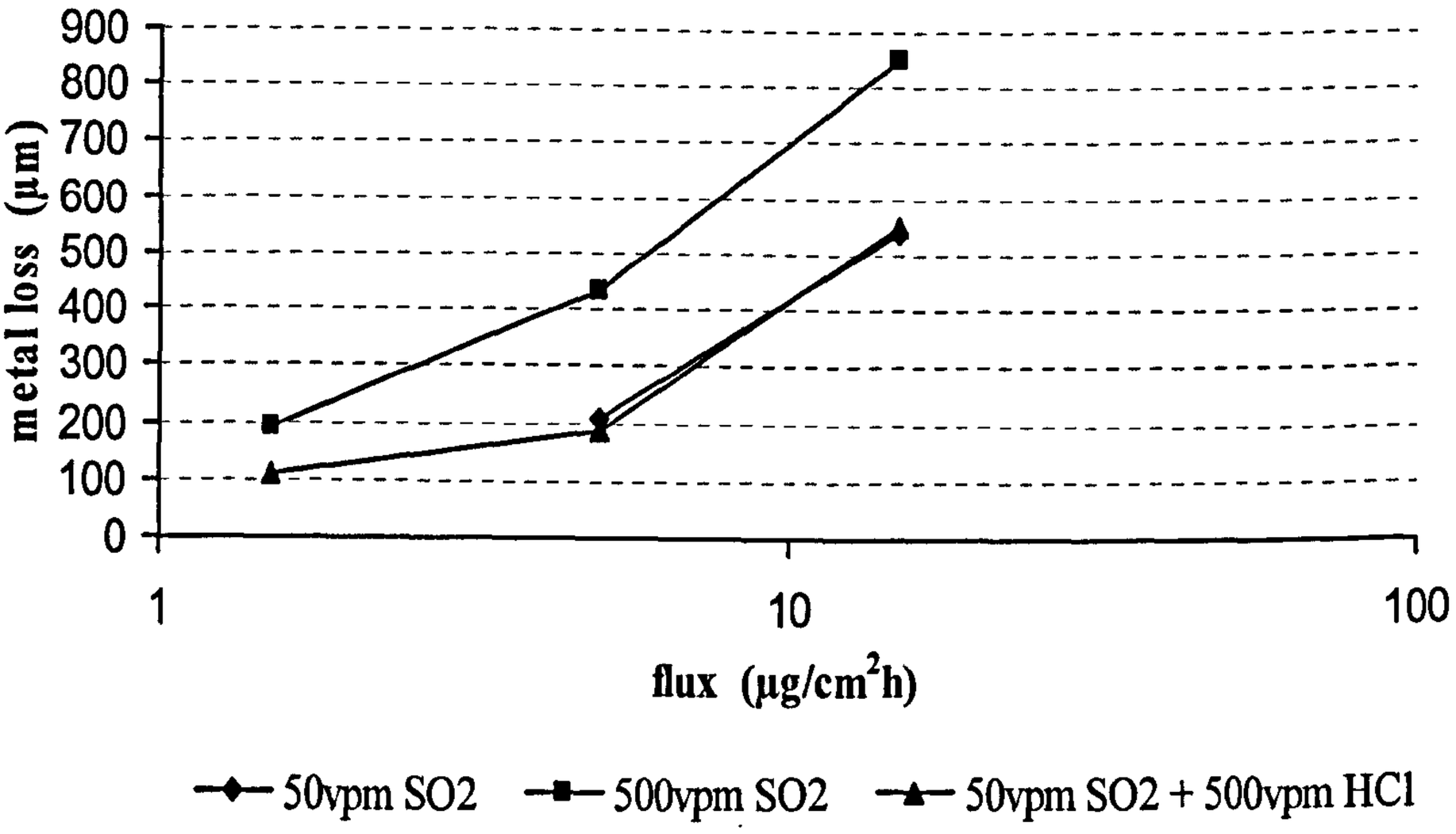

Figure 5.5: Effect of deposition flux of 80/20 $(Na/K)_2SO_4$ on the hot corrosion performance of uncoated CMSX-4 in terms of sound metal loss (with a 4% probability of being exceeded) after 500h exposure at 900°C in a range of different gas composition.

5.3 Effect of Varying the Deposit Composition

As explained in section 2.2, the environments found within the hot gas path of gas turbines depend on the contaminants present in the fuel and air entering the turbine. The levels of contaminants are different: fuel gases derived from coal, biomass and their mixes, release different contaminant levels of SO_x, HCl, Na, K, and of heavy metals such as Pb and Zn.

This section compares the effects observed by changing the levels of such contaminants (e.g. Na, K and Pb) with a deposition flux of 15µg/cm^2/h, on IN738LC and CMSX4, both platinum/aluminide coated and uncoated, in a 100vpm SO_2/100vpm HCl environment at 700°C after 500h exposure for damage levels which have a 4% probability of being exceeded. The values obtained from the statistical analysis methods explained in sections 4.4, illustrate the comparative performance of these deposit compositions in the form of histograms in Figure 5.6 for comparison with the alkali solutions, (50/50 $(Na/K)_2SO_4$ vs. 80/20 $(Na/K)_2SO_4$), and in Figure 5.7 for different levels of Pb; (50/50 $(Na/K)_2SO_4/PbCl_2$ vs. 80/20 $(Na/K)_2SO_4/PbCl_2$).

In both figures, similar trends can be observed, both for the different concentrations within alkali solutions, and for the different Pb concentrations:

- Damage is observed to be less for the 4:1 concentration of alkali sulphate solutions, (80/20$(Na/K)_2SO_4$ and 80/20 $(Na/K)_2SO_4/PbCl_2$), than for the 1:1 concentration (50/50$(Na/K)_2SO_4$ and 50/50 $(Na/K)_2SO_4/PbCl_2$).
- Uncoated CMSX4 is more sensitive to deposits than IN738LC.

The four material systems tested were more sensitive to the alkali solution concentrations ratio than to the addition of lead (Figure 5.6 vs. Figure 5.7).

- A significant improvement was observed when these materials were PtAl-coated.

The uncoated CMSX4 was more sensitive to changes in deposit compositions, possibly because this alloy was not originally designed to perform under 'dirty environments', but for aero-engines and, therefore, was intended to perform in cleaner environments, with different service-lives than land based gas turbines, (which are expected to run more continuously and with 'dirtier' hot gas environments). By comparing the chemical compositions of these two superalloys (see Table 2.2, section 2.3.2), significant differences can be seen: i.e., IN738LC contains practically ten times more Cr, known as an important element for corrosion resistance, for its capacity to form the auto-healing Cr_2O_3 layer. Low Cr concentrations will form external scales also containing NiO which are susceptible to the basic fluxing mode of attack.

Other elements (e.g. refractory metals, such as W and Ta), are in higher concentrations in CMSX4 (given it was designed to perform with strength).

As discussed in detail in the next section, the oxides of tungsten, molybdenum or vanadium can make the Na_2SO_4 too acidic such that a different corrosion mechanism is possible, i.e. degradation via alloy-induced acid fluxing. This is a result of the oxides of the metals tungsten, molybdenum and vanadium dissolving into the Na_2SO_4 to form tungstates, molybdates and vanadates, and displacing some SO_3 from the Na_2SO_4.

Both alkali solutions (50/50 and 80/20 Na_2SO_4) caused more damage to the four materials systems than lead-containing solutions. $PbCl_2$ has a very low melting point (497°C) and may have a higher vapour pressure at the test temperature, leading to a gradual loss of lead and so, effectively, giving a lower deposition flux to react with the samples. It is believed that the 50/50$(Na/K)_2SO_4$ concentration had more effect than the 80/20 concentration, because increasing the K level changes the melting point and so will change the solubility of gas phase species in the melt.

To compare the morphologies of the samples tested at 700°C for various alkali levels, as illustrated in Figure 5.6, compare photomicrographs 2 vs. 6 in: Figure 4.30 for uncoated IN738LC, Figure 4.31 for PtAl-coated IN738LC, Figure 4.32 for uncoated CMSX4 and Figure 4.33 for PtAl-coated CMSX4.To compare the morphology of the samples at 700°C tested in the lead-containing salts, as illustrated in Figure 5.7, compare photomicrographs 4 vs. 7 in Figure 4.30 for uncoated IN738LC, Figure 4.31 for PtAl-coated IN738LC, Figure 4.32 for uncoated CMSX4 and Figure 4.33 for PtAl-coated CMSX4.

Regardless of the lead content, the 50/50 deposit compositions produce more damage, even in the reference material IN738LC; the 80/20$(Na/K)_2SO_4$ solution was applied for stage 2 of the experimentation, since this is considered to be the standard solution for hot corrosion testing (near the eutectic composition).In order to define the propagation mode that took place in samples exposed to lead-containing salts, SEM/EDX element distribution mapping was carried out on one sample of each uncoated material (IN738LC and CMSX4). Such maps can be seen in Figure 5.8 and Figure 5.9. Figure 5.8, uncoated CMSX4 map, compares well with the type II hot corrosion element distributions reported in the literature (Figure 2.26 in section 2.5.5):

- There is a NiO-rich layer close to the deposit/corrosion product surface
- The reaction products in the pit are rich in Cr and Al (a zone rich in Al is at the base of the pit)
- Cr and Al have transformed into chromia and alumina scales on the product surface.

Similar features are observed for uncoated IN738LC in Figure 5.8, although, in this alloy, a thin sulphur-rich layer has formed in the base of the pit and the Al-rich layer in the pit is not as dense as that for CMSX4. These characteristics are consistent with the samples having undergone a gas-induced hot corrosion degradation mode.

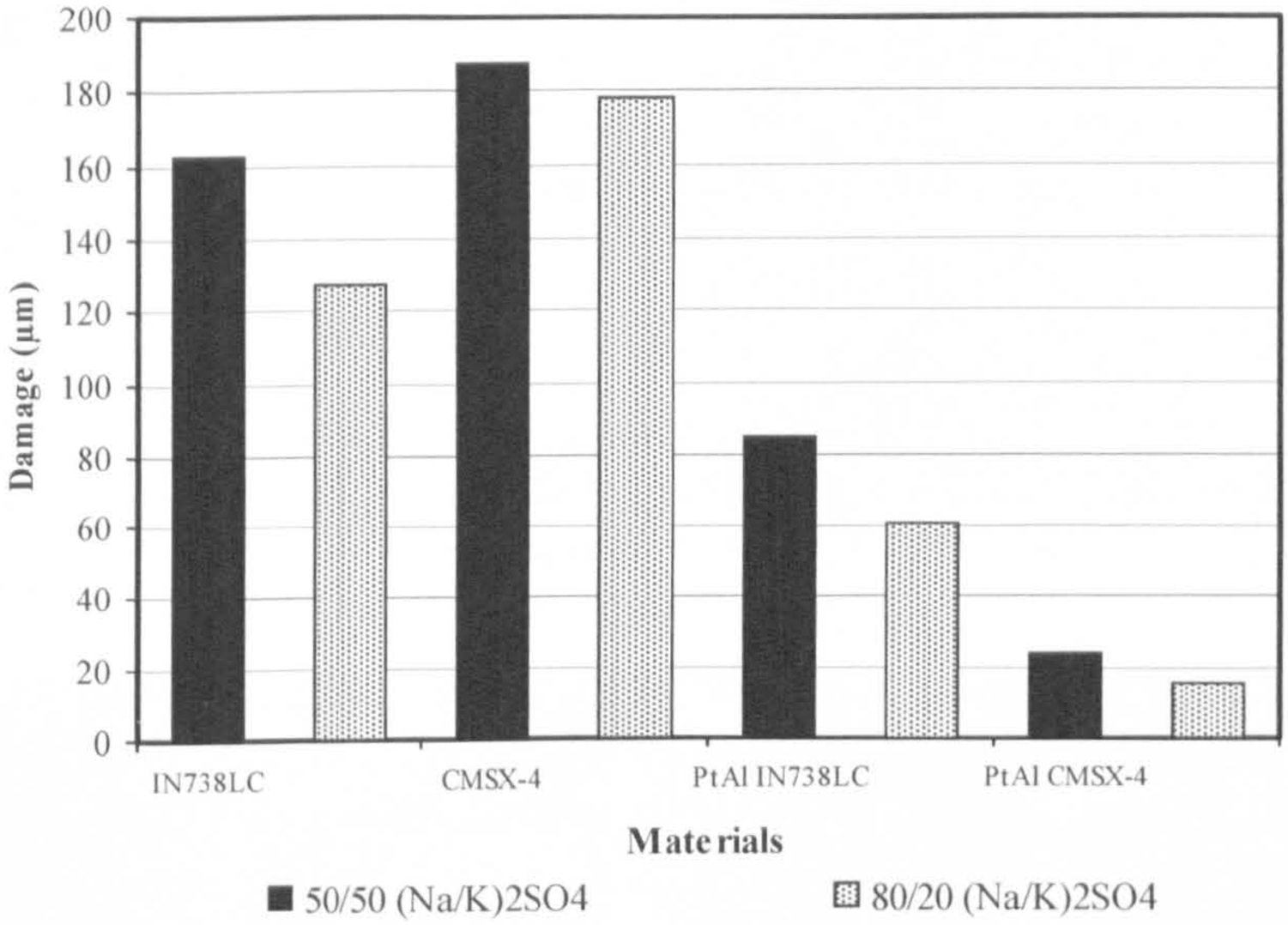

Figure 5.6: Effect of varying the Na and K concentration in the deposit composition on materials exposed for 500 h at 700°C with a deposit flux of 15µg/cm^2/h in air-100vpm SO_2/100vpm HCl.

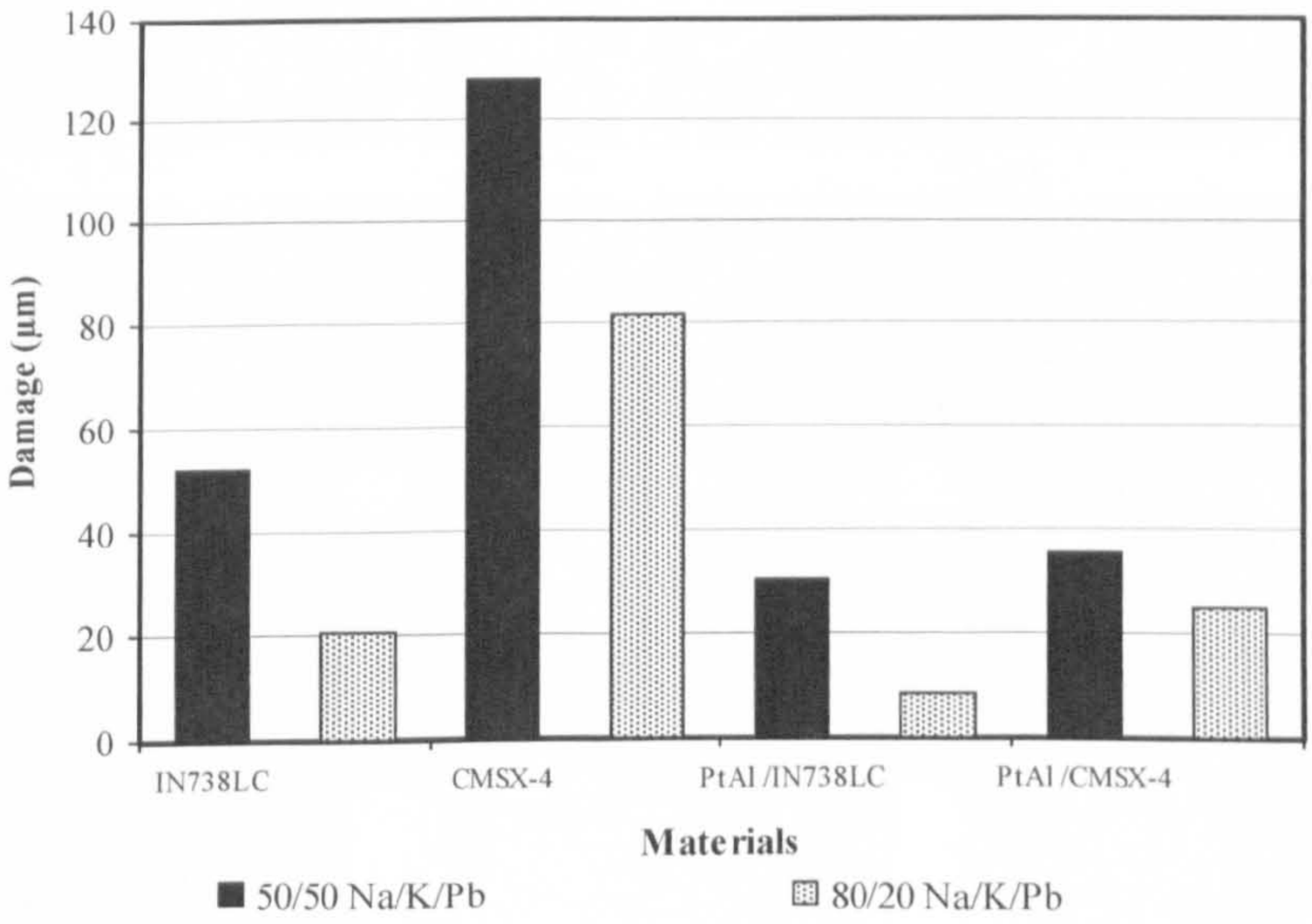

Figure 5.7: Effect of varying the lead concentration in the deposit composition on materials exposed for 500 h at 700°C with a deposit flux of 15µg/cm^2/h in air-100vpm SO_2/100vpm HCl.

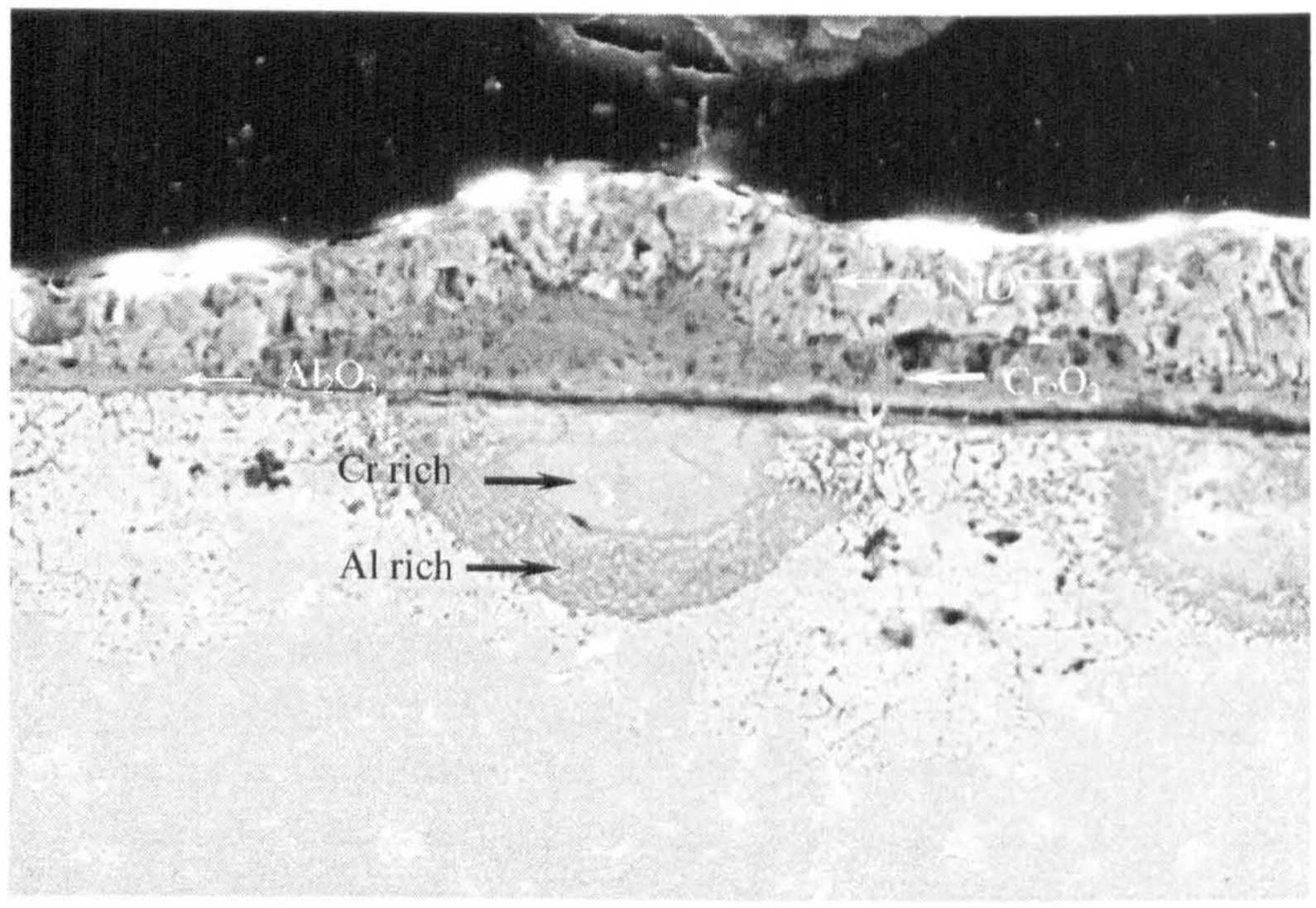

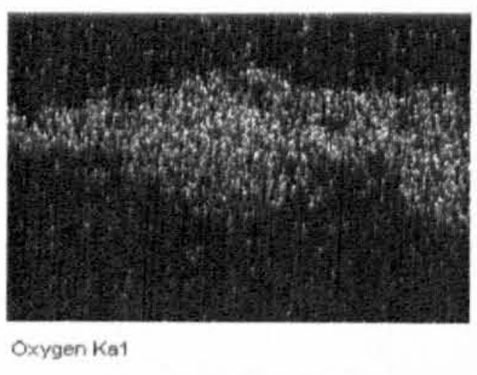
Oxygen Ka1

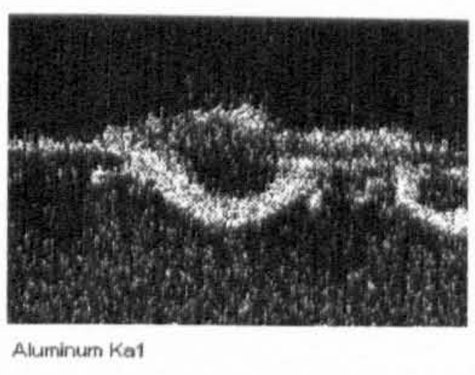
Aluminum Ka1

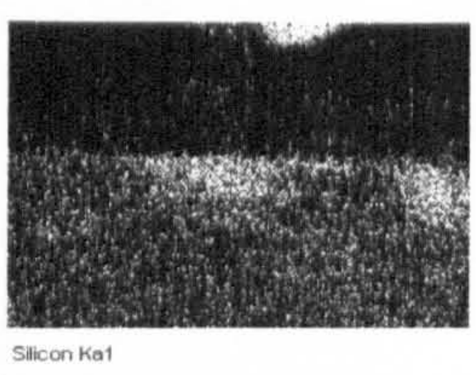
Silicon Ka1

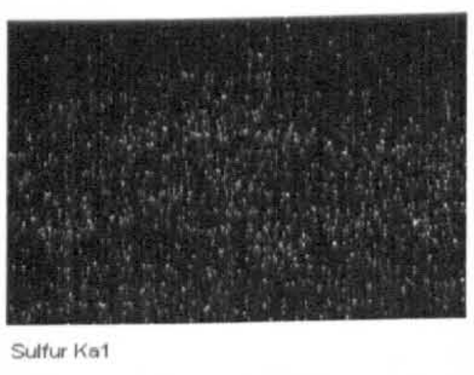
Sulfur Ka1

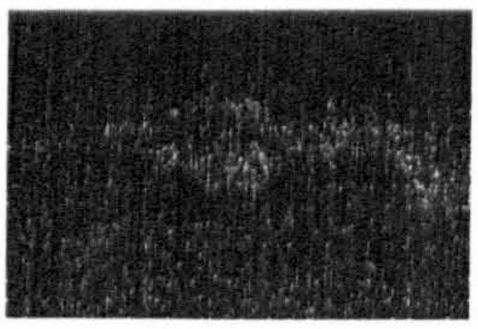
Titanium Ka1

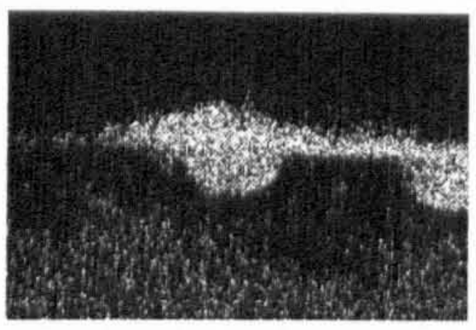
Chromium Ka1

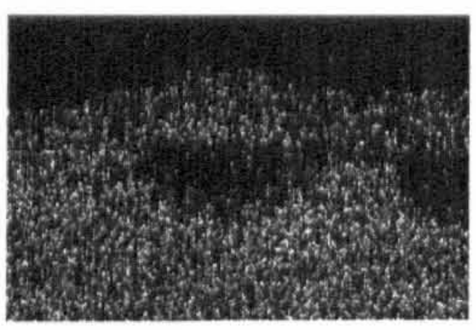
Cobalt Ka1

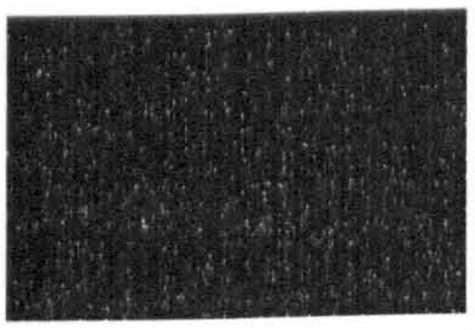
Chlorine Ka1

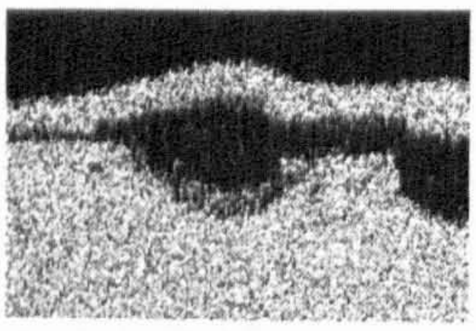
Nickel Ka1

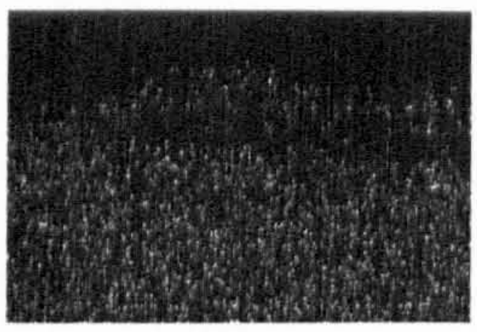
Tantalum La1

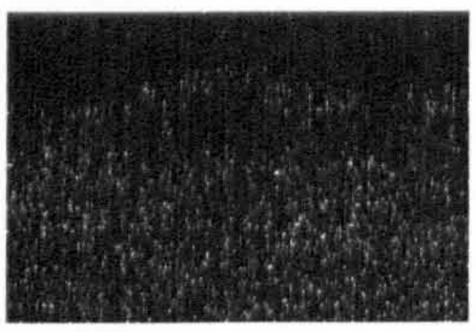
Tungsten La1

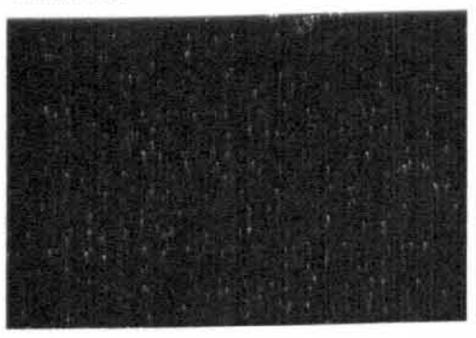
Sodium Ka1_2

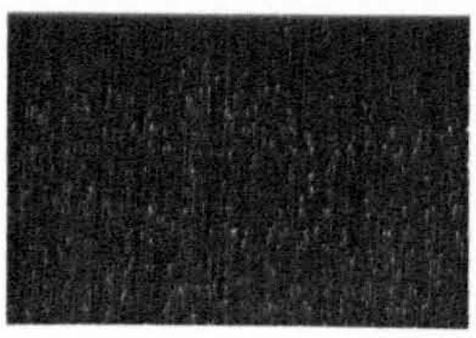
Potassium Ka1

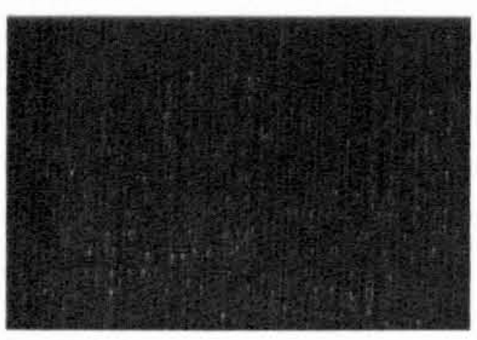
Lead La1

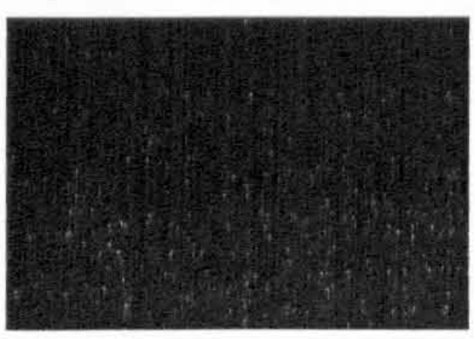
Rhenium La1

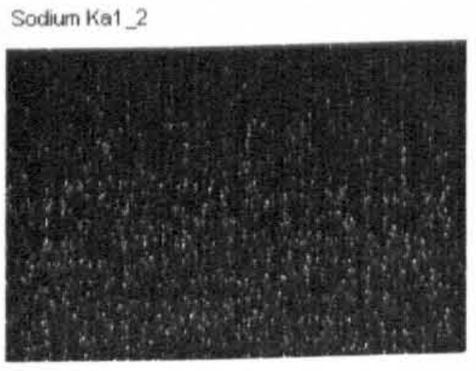
Yttrium La1

Figure 5.8: Example of gas phase induced hot corrosion attack in uncoated CMSX4 with 15µg/cm^2/h of 80/20 Na/K/Pb in 100vpm SO_2/100vpm HCl at 700°C after 500h exposure.

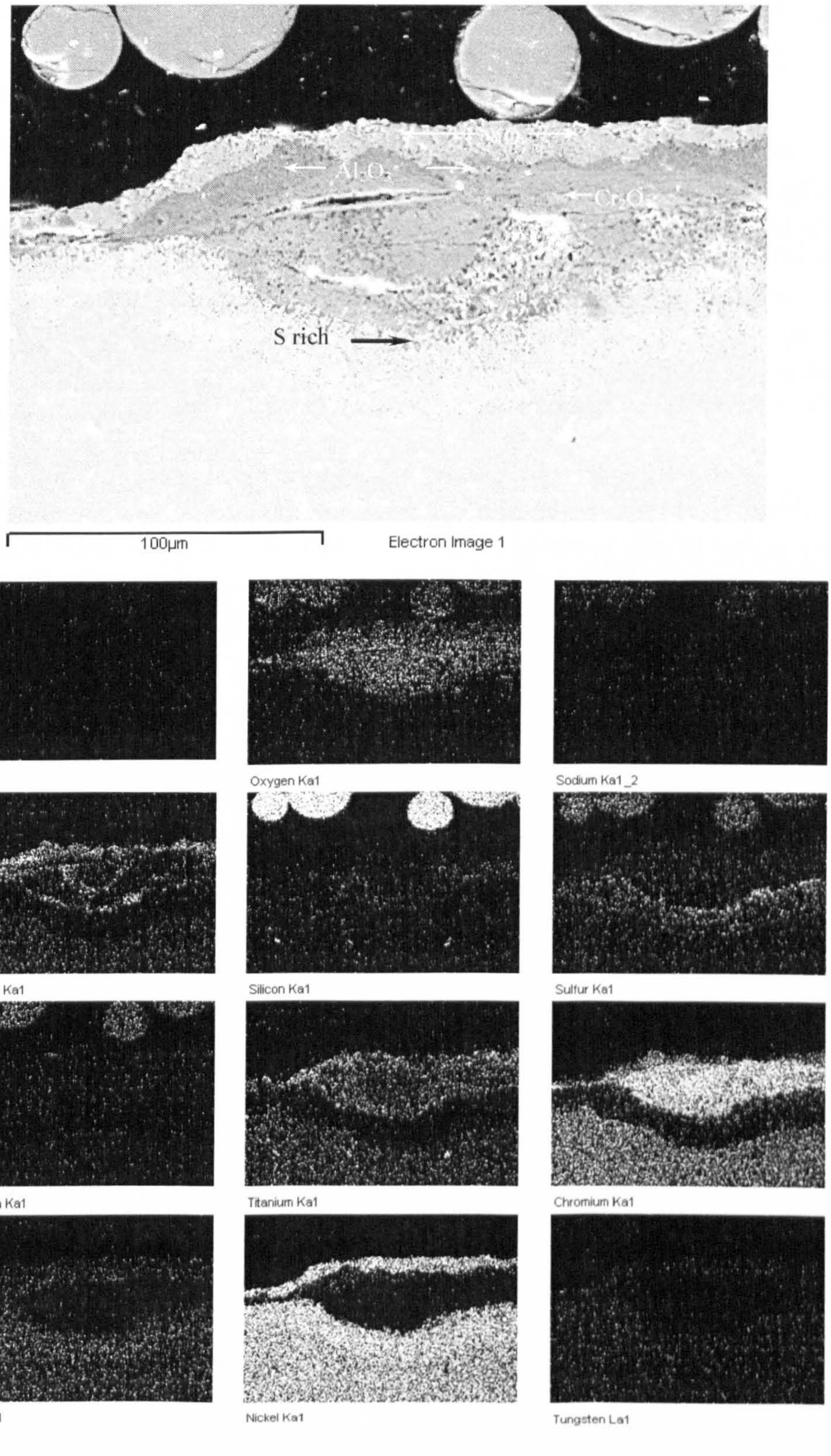

Figure 5.9: Example of gas phase induced hot corrosion attack in uncoated IN738LC with 15µg/cm^2/h of 50/50 Na/K/Pb in 100vpm SO_2/100vpm HCl at 700°C after 500h exposure.

5.4 Effect of Alloy Composition Different Hot Corrosion Environments

Alloy composition is an important factor in the performance of material systems, since the concentration of every element will modify the alloy characteristics needed to deal with the environment in which the material is exposed. The element/quantity will define (together with the deposit/gas composition, and temperature) the length of the initiation period and the propagation degradation mode i.e. basic fluxing, alloy/gas-induced acid fluxing or sulphur-induced hot corrosion. As a result, alloy behaviour prediction and future alloy improvements can be carried out.

The results shown in Figure 5.2, Figure 5.3, Figure 5.4 and Figure 5.5 are useful to compare the performance of the two uncoated single crystal alloys tested in this study (i.e. SC^2 vs. CMSX4), from the alloy composition point of view. From comparison of the uncoated materials under the same test conditions (i.e. deposit flux and gas composition) at 700°C (Figure 5.4 vs. Figure 5.2), and at 900°C (Figure 5.5 vs. Figure 5.3), in general it is observed that CMSX4 has higher corrosion rates than SC^2. However, in the 500vpm SO_2 environment at 900°C, the SC^2 is much more sensitive than the CMSX4 in showing excessive corrosion rates. Since this is believed to be mainly an effect of the high SO_2 concentration, it is discussed further in section 5.5 of this chapter.

SC^2, in general, shows lower corrosion rates than CMSX4, but these are still high compared with the reference material, IN792, because every alloy has been designed to perform in different contexts; different chemical elements/concentrations are chosen to satisfy the requirements of such conditions. For example, since efficiency enhancement is normally achieved by increasing the firing temperatures of the gas turbine, or reducing the level of cooling air required, the component temperatures are increased. Together with efficiency, the use of renewable sources of fuel gases, such as biogases and those derived from coal gasification, is desired (as explain in section 2.2); such fuel sources contain significant quantities of corrosive compounds. Thus, the single crystal SC^2 was designed for use as turbine blade material with higher strength and corrosion resistance after consideration of these two main drivers. SC^2 is a single crystal superalloy derived from SC16, a single crystal superalloy previously developed by ONERA for industrial gas turbine blade applications. SC^2 differs from SC16 in the wt% of chromium; with the aim of achieving sulphidation resistance comparable to that of IN738LC or IN792, in the temperature range 900-1000°C, but with creep strength significantly greater than that of IN792 [37].

CMSX4 is a superalloy developed for aero-engines and therefore, aimed at performing in different environments and with different service-lives than land-based gas turbines, which are expected to run more continuously and with 'dirtier' hot gas environments.

The chemical compositions of these two superalloys are given in Table 2.2 (section 2.3.2). It can be seen that SC^2 and CMSX4 are made from practically the same elements, but they vary in their contents [61]. SC^2 contains more:

Chromium and silicon: elements that promote the formation of slow growing and stable oxide scales (section 2, Figure 2.11).

- Nickel: an element that is very useful in combination with other elements and contributes to the alloy corrosion-resistance, excellent ductility, malleability and formability;
- Titanium: small additions of this element promote Cr_2O_3 formation on Ni-20Cr alloys (but do not significantly affect the Cr_2O_3 growth rate).

SC^2 contains less of the four refractory elements: vanadium, molybdenum, tungsten and tantalum. These elements could, under certain conditions, influence the corrosion degradation mechanism. The content of aluminium in SC^2 is also less. [148; 149]. Since the hot corrosion degradation modes affect each other and the interactions are also temperature-dependant, in order to understand the effect of varying the element contents in an alloy, it is necessary to review the hot corrosion mechanisms explained in section 2.5; by way of example, these are quoted generally in this section.

At the beginning of the attack, an O gradient develops across the Na_2SO_4 layer and an unstable oxide scale of Al_2O_3 and Cr_2O_3 is formed. The sulphate ions decompose forming oxygen ions (Equation 16) which react with the oxide scale (Al_2O_3 and Cr_2O_3); the sulphur is freed and forms sulphides with elements such as nickel at the surface of the alloy, leaving oxygen ions in the melt (Na_2O). Chromate and aluminate ions that form via basic fluxing (Equation 17 and Equation 18), diffuse away and, at higher oxygen pressures (i.e. towards the outer surface of the deposit), they precipitate out from the melt, realising oxide ions (Equation 19 and Equation 20) in exchange for sulphate ions.

When there is a supply of sulphate ions from the Na_2SO_4, the hot corrosion proceeds approximately at a linear rate (as in

Figure 2.22 in section 2.5.4) but, as the source of sulphate ions is depleted, the attack diminishes and oxygen becomes more plentiful in the corrosion product. The nickel sulphide particles in the scale are oxidized and some of the sulphur from this process moves deeper into the alloy where, for example, chromium sulphides can form (Figure 2.33 (b) section 2.5.8).

Thus, in order to keep this reaction going, a supply of oxygen/sulphur is needed. Hence, this type of mechanism, basic fluxing, common in type I hot corrosion, is not self-sustaining and needs to have more salt deposited to continue. The total amount of attack becomes greater as the amount of salt is increased, a feature discussed previously (in section 5.2 of this chapter). Since basic fluxing requires that an oxygen gradient be developed across the Na_2SO_4, the formation of oxide scales that grow slowly and consume as little oxygen as possible is an effective means to combat basic fluxing. The addition of more chromium and aluminium to alloys results in improved resistance to basic fluxing, provided continuous barriers of Al_2O_3 or Cr_2O_3 are formed.

It has been understood that the chromium content in an alloy composition can contribute to good hot corrosion resistant (although very high levels of chromium, to improve the hot corrosion resistant, have an adverse effect on the stress-rupture strength of the alloy). The IN738LC alloy, often used as a reference, as in part of this work, contains 16 wt% of chromium (a relatively high chromium content), CMSX4 contains 6.5 wt% (a low-chromium content alloy) and SC[2] contains 11.8 wt%. This content of chromium has influenced the performance of CMSX4. Such lower chromium-containing alloys tend to develop non-continuous layers of Cr_2O_3 and external scales, also containing NiO, which are susceptible to the basic fluxing mode of attack.

Other elements in binary nickel- and cobalt-based alloys can produce effects similar to chromium at low concentrations; aluminium, molybdenum or tungsten can be used to prevent attack of nickel-or cobalt-based alloys via basic fluxing. However, the oxides of molybdenum, tungsten or vanadium can make the Na_2SO_4 too acidic, such that a different corrosion mechanism is possible, i.e. degradation via alloy-induced acid fluxing. This is a result of the oxides of the metals: tungsten, molybdenum and vanadium dissolving into the Na_2SO_4 to form tungstates, molybdates and vanadates, displacing some SO_3 from the Na_2SO_4. A zone of liquid is formed immediately above the alloy due to the accumulation of the refractory metal oxides, e.g. MoO_3, WO_3 V_2O_5 in the Na_2SO_4 and the oxides normally relied upon for protection against attack, e.g. Al_2O_3, Cr_2O_3, NiO, CoO, become non-protective due a solution-reprecipitation process. This attack is self-sustaining because a small amount of salt appears adequate to cause the development of the refractory metal oxide zone.

Alloy-induced acidic fluxing results from the accumulation of oxides, such as MoO_3, WO_3 or V_2O_5, in salt deposit on alloys. This form of hot corrosion attack can be inhibited by decreasing the concentrations of the refractory elements, molybdenum, tungsten and vanadium.

Tantalum does not have the same effect as the other refractory metals, and therefore, appears to be a good replacement for Mo, W and V in the alloys [61]. SC^2 is thought to show lower corrosion rates than CMSX4 because the chromium is present in higher concentration. This, combined with aluminium (although aluminium concentration is less in SC^2 that CMSX4), makes SC^2 more resistant to basic fluxing degradation, which is a precursor to acidic fluxing; i.e. when basic fluxing eventually stops if the Na_2SO_4 is not replenished, the propagation mode may change to acidic fluxing as the activity of, for example, MoO_3 in the salt is increased to appropriate levels. The interaction between basic and acid fluxing has been modelled by Rapp [76] (Figure 2.31, section 2.5.5). The lower concentration of the refractory elements in SC^2 is thought to prolong the time before alloy-induced acid fluxing attack starts to take place.

When the oxygen pressure at the alloy/Na_2SO_4 or oxide-Na_2SO_4 interfaces is very low, the sulphur pressure can be high enough to form sulphides of aluminium and chromium (and, in some cases, even sulphides of cobalt, nickel and iron, unless the SO_3 pressure/content is very low), then the accumulation of these sulphides in the alloy (in alloys exposed to SO_2-O_2, sulphide formation occurs due to sulphur from the gas rather than from sulphur in the Na_2SO_4) can result in substantial degradation during subsequent oxidation as a result of the formation of less protective oxide scales; this mode of hot corrosion attack is sulphur-induced degradation.

Sulphide formation in the alloys can cause the formation of non-protective oxide scales by involving effects produced by internal sulphides on the selective oxidation process: i.e., when sulphur diffuses into the surface of an alloy, it usually reacts with the same elements that are diffusing to the surface, and combines with oxygen to form continuous oxide barriers. The formation of such sulphides causes the flux to the surface of the element being selectively oxidized to be decreased.

The greater susceptibility of nickel-based alloys to sulphur-induced attack, is generally observed only when aluminium is present in the alloy at levels between 1-6% wt. From previous work [61], it appears that nickel-based alloys with aluminium contents between 6 to 12 weight percent, are relatively resistant to this attack and that degradation takes place after the aluminium has been lost by oxide spallation in a cyclic test. Because the aluminium contain in SC^2 is less than in CMSX4 (4.2% and 5.6% respectively) and both are out of the beneficial range of aluminium content in nickel-based superalloys, these two alloys could have been degraded via sulphur-induced attack, but the CMSX4 with greater corrosion rates. Increased chromium concentrations are a very effective means to inhibit degradation via sulphidation.

An example of the sulphur-induced propagation mode, degraded by the mechanism previously explained, is the shown by the analysis for SC^2 after exposure at a flux of $5\mu g/cm^2/h$ in 500vpm SO_2 gas at 900°C in Figure 5.10 and, a higher magnification, in Figure 5.11:

- Traces of the oxidation/sulphidation progression are seen in the chromium map
- Sulphur is concentrated in the zone of lighter grey precipitates within the alloy.
- Aluminium levels are higher in the oxide scale
- Chromium levels are higher in the area of sulphide particles

Another example of the sulphur-induced propagation mode, degraded by the same mechanism shown by the analysis for SC^2 after exposure at a flux of $5\mu g/cm^2/h$ in 50vpm SO_2 gas at 700°C in Figure 5.12 and Figure 5.13:

- Sulphur-rich particles are present in the alloy underneath the oxide scale.

Gas phase-induced acid fluxing is a propagation mode that becomes more evident in the presence of SO_3 in the environment and thus, is observed at lower temperatures (peak concentrations of SO_3 are generated at temperatures between 650-700°C); further discussion about the effects of this propagation mode is given in section 5.5. From the corrosion rate data obtained by the methods described in section 3.5, it is possible to carry out an analysis as a function of alloy composition by using multiple linear regression to calculate a straight line that best fits the data by the least square method; thus returns an equation that describes the line. The equation for the line is:

$$y = m_1x_1 + m_2x_2 + m_3x_3 + b$$

Equation 22

where the dependent y-value, corrosion damage, is a function of the independent x-values, relevant elements that influence the hot corrosion mechanisms, i.e. chromium, aluminium, molybdenum and tungsten. The m-values are coefficients corresponding to each x-value, and b is a constant value. The corrosion damage (y-value) considered was that with a confidence level of 4% of being exceeded (i.e. the maximum rate of attack expected).

Materials		CMSX4/SC^2/IN792					
Temperature		700°C			900°C		
Gas (vpm)	Flux µg/cm^2/h	Cr ($m1$)	Al ($m2$)	Mo/W ($m3$)	Cr ($m1$)	Al ($m2$)	Mo/W ($m3$)
50SO_2	1.5	1	4	6	0.45	85	-11
	5	0.3	25	16	74	-679	1001
	15	5	-9	68	1	301	-242
500SO_2	1.5	5	17	17	5	16	-43
	5	9	8	49	53	199	-662
	15	15	9	86	4	708	-1811
50SO_2/ 500HCl	1.5	0.06	9	7	-1	47	-40
	5	4	0	29	0.3	50	15
	15	3	-29	36	15	137	146

Table 5.1: Corrosion coefficients as a function of alloy composition for the uncoated CMSX4, SC^2 and IN792 in type I and type II hot corrosion.

Thus, it is possible to assess the influence that each element had on the type I and type II hot corrosion environments under each test condition carried out in stage 2 of this study. Such coefficients (m values) are displayed in Table 5.1.

A high value of m is indicative of a negative influence of that element on alloy corrosion. For example; at 700°C, the m value for the effects of molybdenum/tungsten is always higher that the m value for the effect of chromium in the three environments with the three different deposition fluxes. At 900°C, aluminium shows, in general, higher m values than the refractory metals, making aluminium the element with most negative influence.

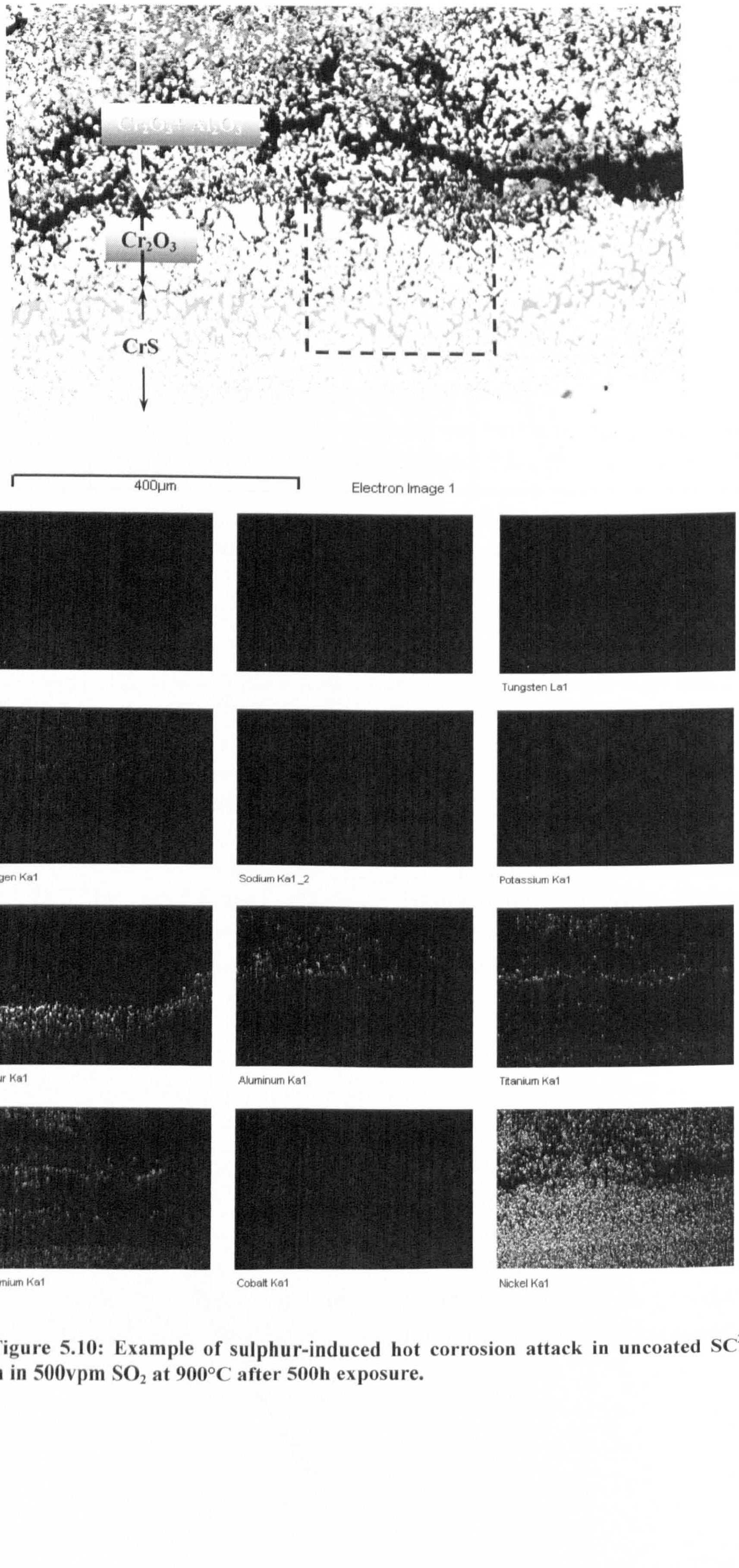

Figure 5.10: Example of sulphur-induced hot corrosion attack in uncoated SC^2 with $5\mu g/cm^2/h$ in 500vpm SO_2 at 900°C after 500h exposure.

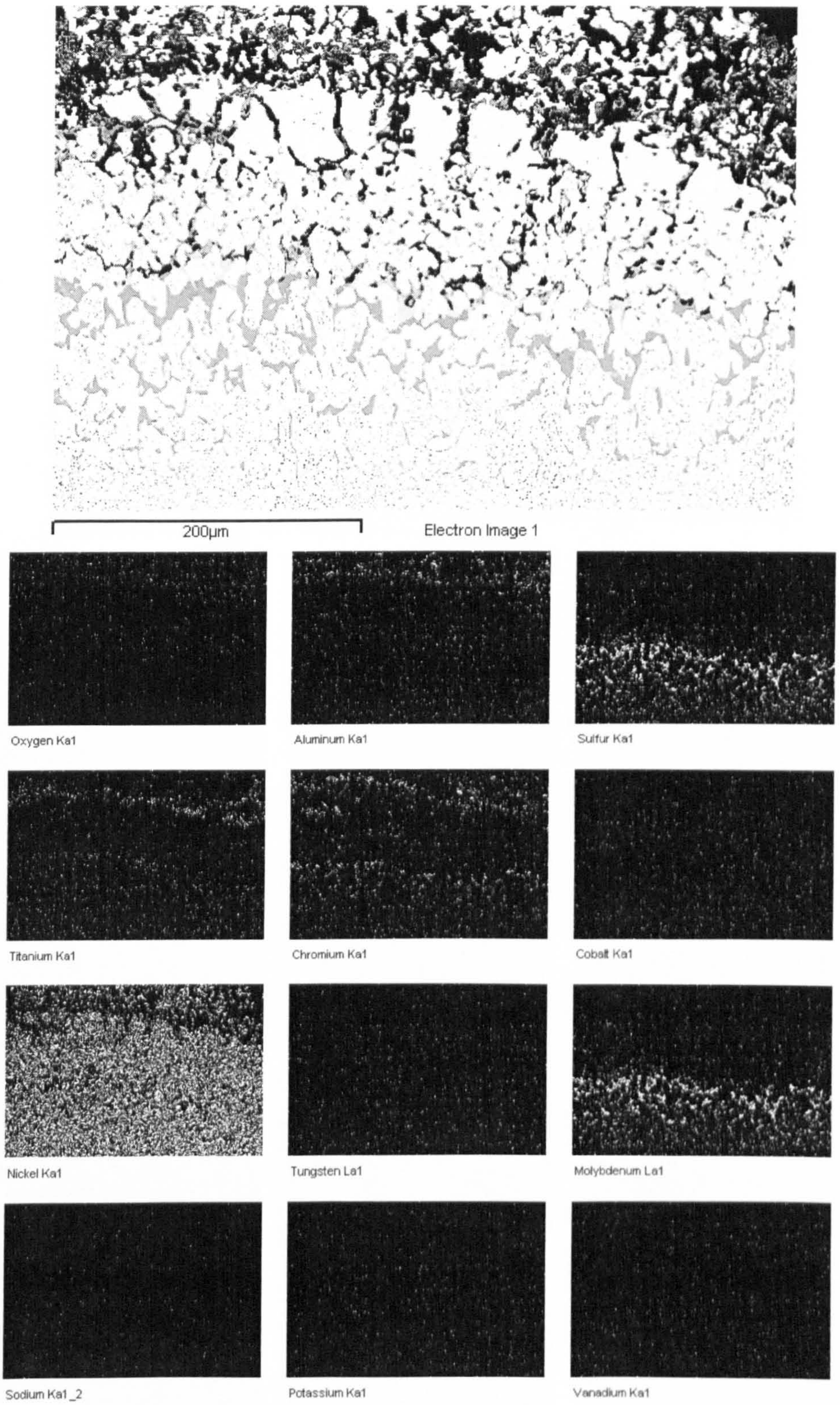

Figure 5.11: Higher magnification of the example of sulphur-induced hot corrosion attack in uncoated SC[2] with 5µg/cm^2/h in 500vpm SO_2 at 900°C after 500h exposure.

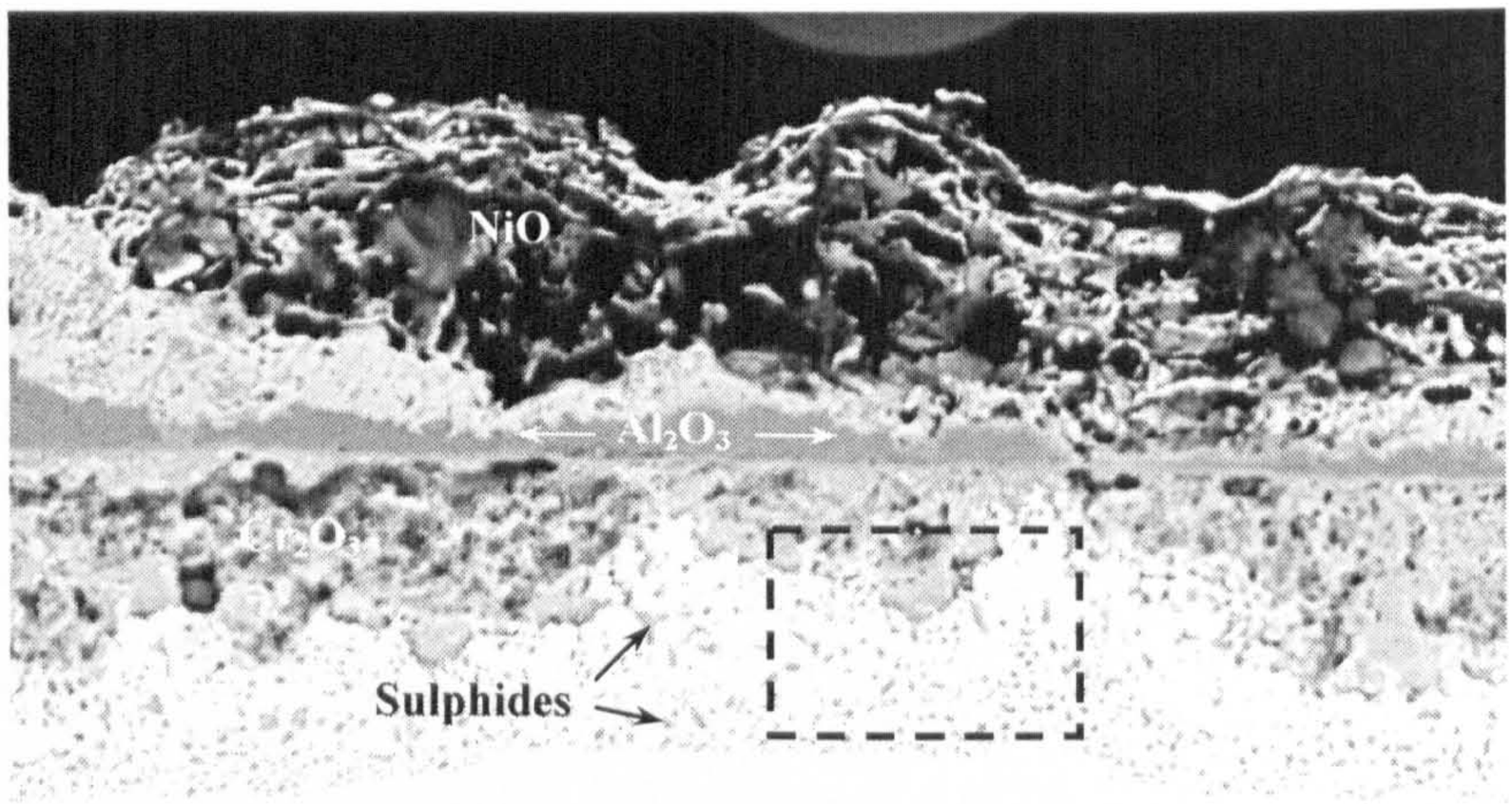

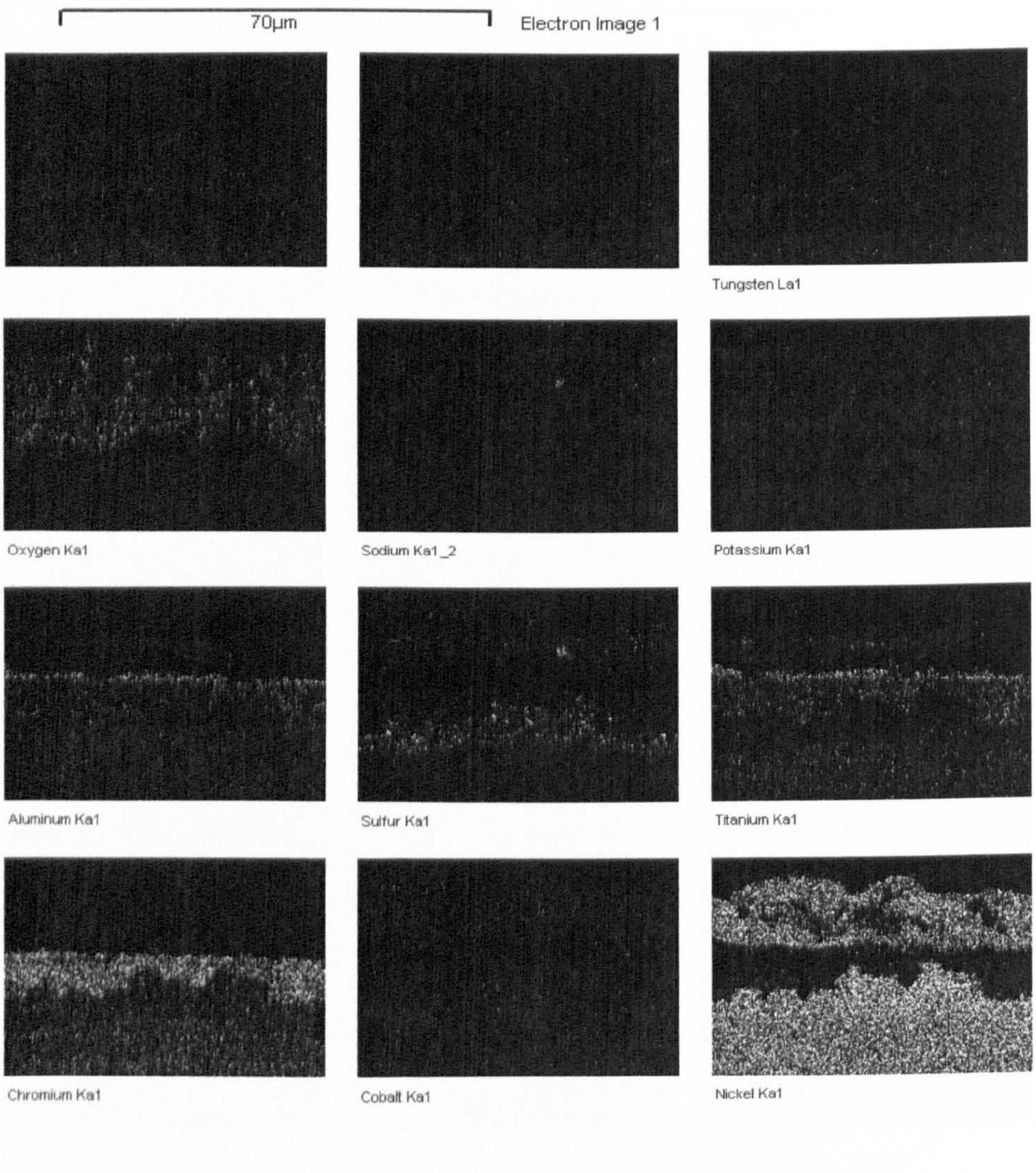

Figure 5.12: Example of mixed mode hot corrosion attack in uncoated SC^2 with $5\mu g/cm^2/h$ in 50vpm SO_2 at 700°C after 500h exposure.

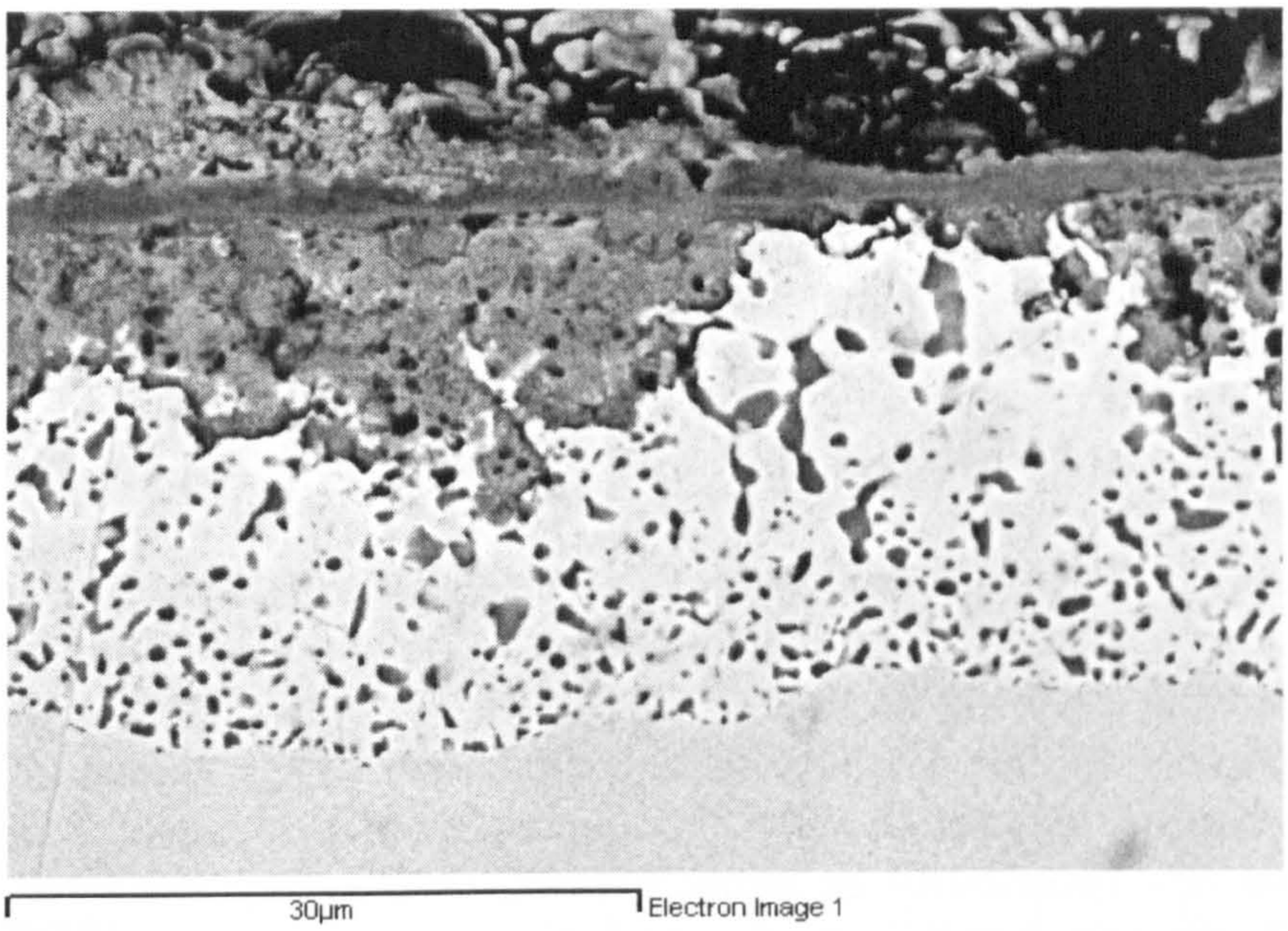

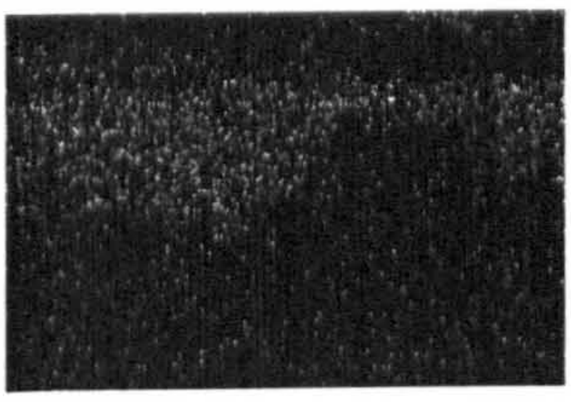
Oxygen Ka1

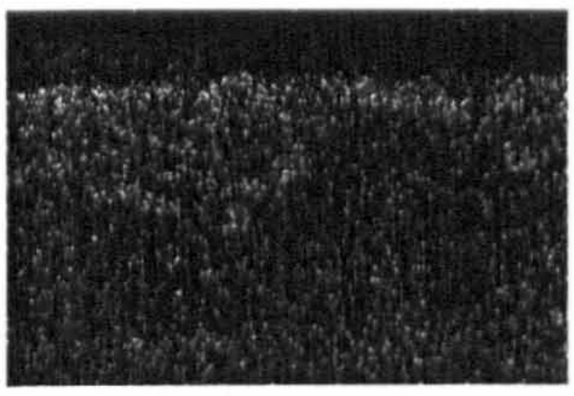
Aluminum Ka1

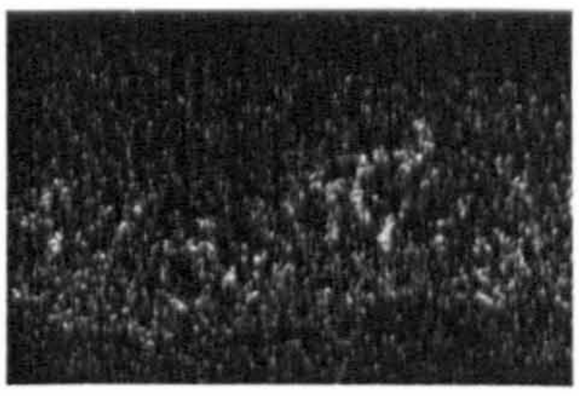
Sulfur Ka1

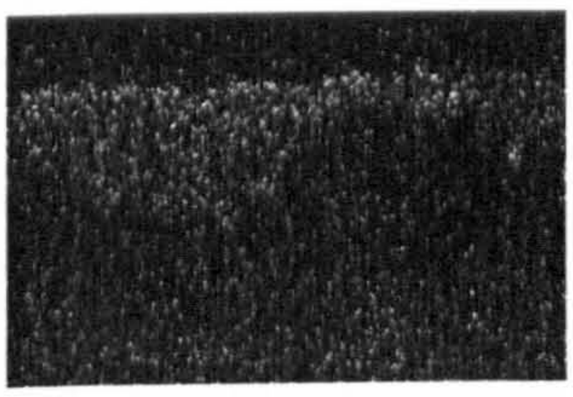
Titanium Ka1

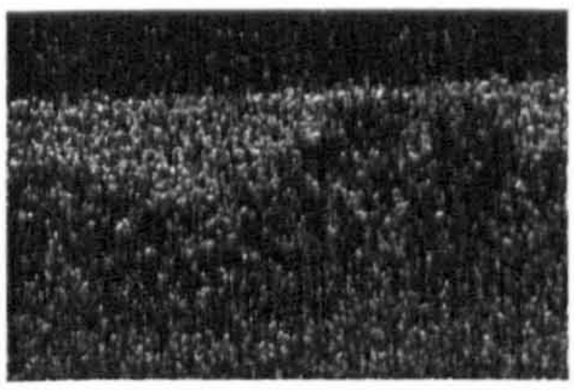
Chromium Ka1

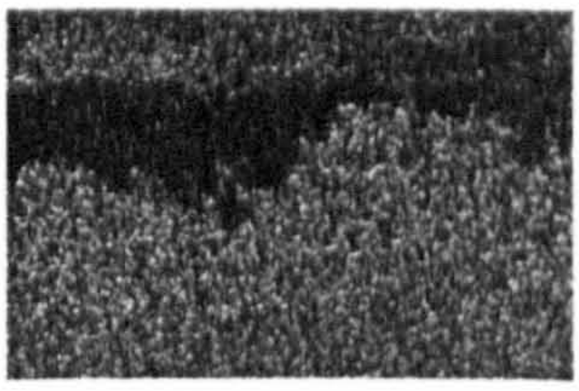
Nickel Ka1

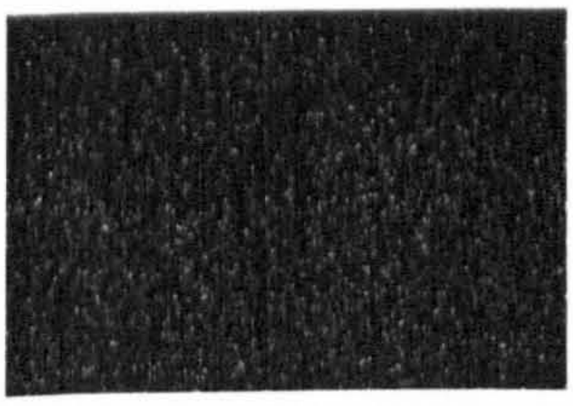
Tungsten La1

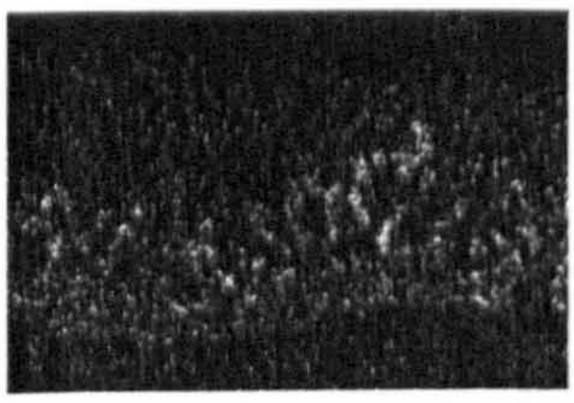
Molybdenum La1

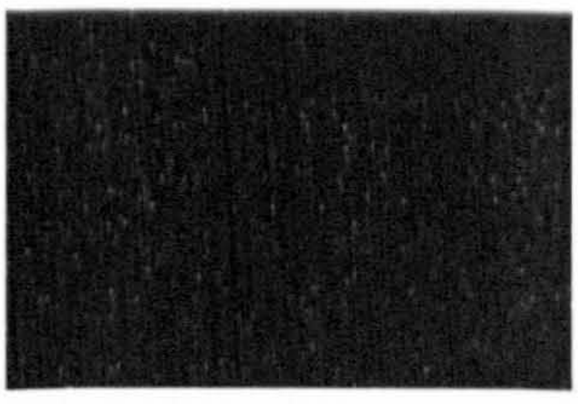
Sodium Ka1_2

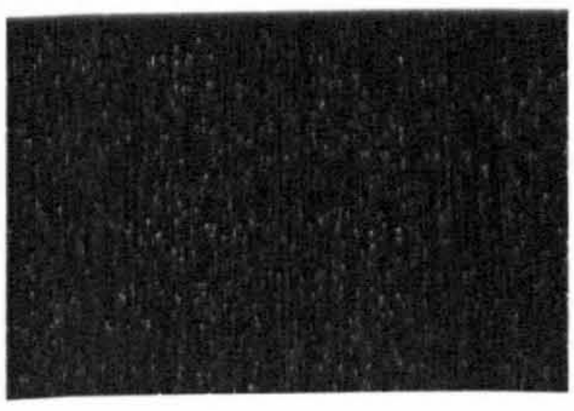
Potassium Ka1


Cobalt Ka1


Vanadium Ka1

Figure 5.13: Higher magnification of the example of mixed mode hot corrosion attack in uncoated SC^2 with 5µg/cm^2/h in 50vpm SO_2 at 700°C after 500h exposure.

5.5 Effect of the Gas Composition in Different Hot Corrosion Environments

In the results shown in Figure 5.2, Figure 5.3, Figure 5.4 and Figure 5.5, a comparison on the effect of changing the gas composition on the performance of the two uncoated single crystal alloys tested in this study, i.e. SC^2 vs. CMSX4, can be seen.

The uncoated materials under the same test conditions of deposit flux and gas composition at 700°C are shown in Figure 5.4 vs. Figure 5.2 and at 900°C in Figure 5.5 vs. Figure 5.3. However, for easier interpretation of the effect of changing the gas composition, Table 5.2 for type II and Table 5.3 for type I hot corrosion, summarise the values of corrosion loss, at a confidence level with 4% probability of being exceed, for the two uncoated materials under all the test conditions. A comparison between the values has been carried out, marked as positive (✓), negative (×) or neutral (O) (a tolerance of +- 10μm was given to mark a difference as neutral). Two main effects are noted:

- It can be seen that the 500vpm SO_2 gas is the most aggressive environment for both CMSX4 and SC^2 at 700 and 900°C when exposed with the lowest, medium and highest deposit fluxes (1.5, 5 and 15μg/cm^2/h).

- The addition of HCl to the 50vpm SO_2 environment could be beneficial, detrimental or neutral; it appears beneficial/neutral under type I hot corrosion conditions (Figure 5.3), but may be detrimental under type II conditions. In Table 5.2, type II, it seems that the HCl addition has a rather positive effect on the uncoated CMSX4, since it showed a beneficial effect when exposed to the medium and high deposit flux concentrations (5 and 15μg/cm^2/h) and no apparent effect with the lowest deposit flux concentration (1.5μg/cm^2/h).

In contrast, SC^2 generally had a negative performance due the HCl addition in the environment when exposed with same deposit fluxes as CMSX4, although it was beneficial with the 1.5 μg/cm^2/h flux concentration. Thus, there is a double effect (and neutral) by the addition of HCl to the environment, apparently depending upon alloy composition and temperature. At 900°C, internal oxidation/sulphidation damage that is typical of type I hot corrosion is observed. However, at 700°C, the typical type II pitting damage appears to be suppressed leading to a broader front attack and internal damage.

Temp. °C	Material/Gas (vpm)	CMSX4	SC^2	The SC^2 performs better than CMSX4	CMSX4	SC^2	The SC^2 performs better than CMSX4	CMSX4	SC^2	The SC^2 performs better than CMSX4
700	Flux ($\mu g/cm^2/h$)	1.5			5			15		
	$50SO_2$	28	16	✓	85	20	✓	99	28	✓
	500 SO_2	103	70	✓	171	123	✓	227	148	✓
	$50SO_2$/ 500HCl	30	60	✓	63	34	✓	59	60	O
	The HCl addition to the environment is beneficial	O	✓		✓	✖		✓	✖	
	The 500vpm SO_2 is the most aggressive environment	✓	✓		✓	✓		✓	✓	

Table 5.2: Values of corrosion loss (with the confidence level of the 4% probability of being exceed) from type II hot corrosion for the uncoated CMSX4 and SC^2 materials under all the test conditions; marking as positive (✓), negative (✖) or neutral (O) result (a tolerance of +- 10μm was given to consider a difference as neutral).

Temp. °C	Material/Gas (vpm)	CMSX4	SC^2	The SC^2 performs better than CMSX4	CMSX4	SC^2	The SC^2 performs better than CMSX4	CMSX4	SC^2	The SC^2 performs better than CMSX4
900	Flux ($\mu g/cm^2/h$)	1.5			5			15		
	$50SO_2$	-	96		210	288	✓	540	474	✓
	500 SO_2	194	268	✖	433	1513	✖	849	2794	✖
	$50SO_2$/ 500HCl	112	98	✓	185	79	✓	548	163	✓
	The HCl addition to the environment is beneficial	-	O		✓	✓		O	✓	
	The 500vpm SO_2 is the most aggressive environment	(✓)	✓		✓	✓		✓	✓	

Table 5.3: Values of corrosion loss (with a confidence level of the 4% probability of being exceed from type I hot corrosion for the uncoated CMSX4 and SC^2 materials under all the test conditions; marking as positive (✓), negative (✖) or neutral (O) result (a tolerance of +- 10μm was given to consider a difference as neutral). ((✓) assuming HCl additions are neutral or beneficial).

Varying the gas concentrations is another factor that can alter the gas-deposit-alloy reaction. It is known that the combination of Na_2SO_4 and SO_3 is very effective in producing attack (a significant amount of attack at 649°C is not observed for Na_2SO_4 or SO_3 acting independently). The Na_2SO_4 deposit could become more acidic (sulphides of aluminium and chromium can be formed) [61].

Comparing the results obtained with data from the literature, it is believed that some samples were degraded by the propagation mode of sulphur-induced hot corrosion and/or gas-phase induced hot corrosion. For example, Figure 4.34 photomicrograph 8, illustrates a sample that was further studied in the scanning electron microscope (SEM) by energy dispersive X-ray (EDX) to analyse the distribution of elements in the corrosion product. This analysis can be seen in Figure 5.14. Some characteristics of gas-phase induced hot corrosion can be seen:

- Na_2SO_4 is distributed throughout the corrosion product; cobalt/nickel diffuse through the deposit/corrosion product to the gas interface where oxides and sulphates of these elements are formed
- Non-uniform appearance, growth of pits and sulphur-rich precipitates around their edges
- NiO-rich layer close to the deposit/corrosion product surface
- Reaction products in the pits are Cr (and Al)-rich
- Evidence of a residual Cr_2O_3/ Al_2O_3 surface scale above the pits

The distribution of Na_2SO_4 uniformly throughout the corrosion product indicates that the Na_2SO_4 was liquid at the temperature where hot corrosion took place. Thermodynamic considerations can show that liquid deposits may form with moderate SO_3 levels in the gas, i.e., liquid solutions of Na_2SO_4 and $NiSO_4$ or $CoSO_4$. Na_2SO_4+$NiSO_4$ has a melting point of 671°C which is lower that of pure Na_2SO_4 (884°C); at temperatures below 884°C, very low corrosion rates would be observed for SO_3 levels below the minimum required to stabilized the liquid (see Figure 2.37 section 2.5.9). At higher SO_3 levels, the liquid phase can form, thereby accelerating the corrosion process, in other words, accelerating the transition from the incubation to the propagation stage. Thus, the increased corrosion rates observed of this work by increasing the SO_2 concentration from 50 to 500vpm SO_2 can be understood. If the exposed temperature exceeds the pure Na_2SO_4 melting point of 884°C, even at low SO_3 levels, high corrosion rates could be expected since, as seen in Figure 2.37, that is above of the minimum required to stabilize the liquid. By comparing the corrosion values in 500vpm SO_2 gas in Table 5.2 with Table 5.3, it can be seen that the values for the two single crystal materials are higher at 900°C than at 700°C. An identical effect is observed for those values in the 50vpm SO_2 environment for the two materials.

The excessive corrosion rates observed on SC^2 vs. CMSX4 in the 500vpm SO_2 gas at 900°C are due to both degrading via sulphur-induced attack. The greater susceptibility of the nickel-based alloys to sulphur-induced attack, is generally observed only when aluminium is present in the alloys; although both alloys contain aluminium, the SC^2 concentration of 4.02 wt%, is further from the beneficial range of 6-12 w% than the 5.6tw% of CMSX4. An indication of the less beneficial effect of the aluminium for SC^2 in the 500vpm SO_2 gas at 900°C can be seen in results of the multiple regression analysis showed in Table 5.1, section 5.4.

The mechanisms and characteristics of the gas-induced acid attack are explained and referred in section 2.5.9 (Chapter 2). The significant features are:

- The hot corrosion attack is non-uniform and has a pitting-like appearance
- Liquid solutions of Na_2SO_4+MSO_4 (M=nickel or cobalt) are present on, or in, the scale in the regions of local attack
- Sulphur, in the form of sulphides, is present at or near the interface of the metal and the reaction products
- The reaction products in the pits consist of the sulphate mixture, Cr_2O_3 and/or Al_2O_3 (depending upon the alloy composition).
- The external region of the reaction products (corrosion-gas interface) mainly comprises NiO and CoO/Co_3O_4 on nickel- and cobalt-based alloys respectively (a schematic representation of these features from the literature is show in Figure 2.26).

Regarding the effects of the HCl addition to the 50vpm SO_2 gas previously mentioned, which have been shown to have beneficial/detrimental/neutral effect, depending on the environment and the alloy/coating system being studied. This effect together with the morphological features, is a result of the effect of HCl on the acid/base balance of the deposit. Selected uncoated samples exposed to the 50vpm SO_2/500vpm HCl gas with 5µg/cm^2/h deposition flux were analysed by EDX analysis in the SEM to identify the effects on the propagation degradation modes of the HCl addition to the environment. For example, Figure 5.15 displays a backscattered image and mapping for SC^2 at 700°C. Figure 5.16 displays the results under same test conditions for CMSX4, and Figure 5.17, an SC^2 sample at 900°C.

It is believed that SC^2 in Figure 5.15 could have undergone HCl-induced attack, giving an internal damage zone underneath the scale that is not common at 700°C (similar internal damage has been observed in the Al-Khyat work [150]). $AlCl_3$, $CrCl_3$ and $TiCl_4$ vapour chlorides are formed in the alloy-depletion zone.

Thus, chlorine could remove the species from the alloy by vapour transport outward into scale. Thus the Al, Cr and Ti have been removed from the alloy; leaving pores and channels behind, the alloy could then oxidize.

Figure 5.16, shows that CMSX4 could undergo, unlike SC^2 in Figure 5.15 in identical test conditions, SO_2/SO_3 gas-phase-induced acid fluxing since the corrosion morphology has the same typical characteristics of Figure 5.14. However, the pit internal damage of these two samples is different, i.e. in CMSX4 (Figure 5.16) precipitates in the internal damage have a 'dispersed whisker' appearance throughout the alloy edge (see also photomicrograph 14 in Figure 4.38); whereas in SC^2 (Figure 5.14), internal damage seems to be more localized.

This may be in part be due to the presence of the HCl. Preferred depletion channels/pores may be formed initially, which later oxidized to give alumina filled channels, providing a short circuit diffusion path for sulphur inward. Thus, it may started as type II corrosion but propagating as type I; possibly depending on the quantity of SO_x to which it was exposed.

Gas (vpm)	Flux $\mu g/cm^2/h$	SC^2		CMSX4	
Temp.(°C)		700	900	700	900
$50SO_2$	1.5 5 15	Mixed Mode	Sulphur-induced	Gas phase-induced	Sulphur-induced
500 SO_2	1.5 5 15	Gas-phase-induced	Sulphur-induced	Gas-phase-induced	Sulphur-induced
$50SO_2$/ 500HCl	1.5 5 15	HCl-induced	Basic fluxing	Gas-phase-induced	Sulphur-induced

Table 5.4: Final propagation modes in uncoated SC^2 and CMSX4 materials considering test conditions of the stage 2 of this work based in morphologies and SEM/EDX analysis.

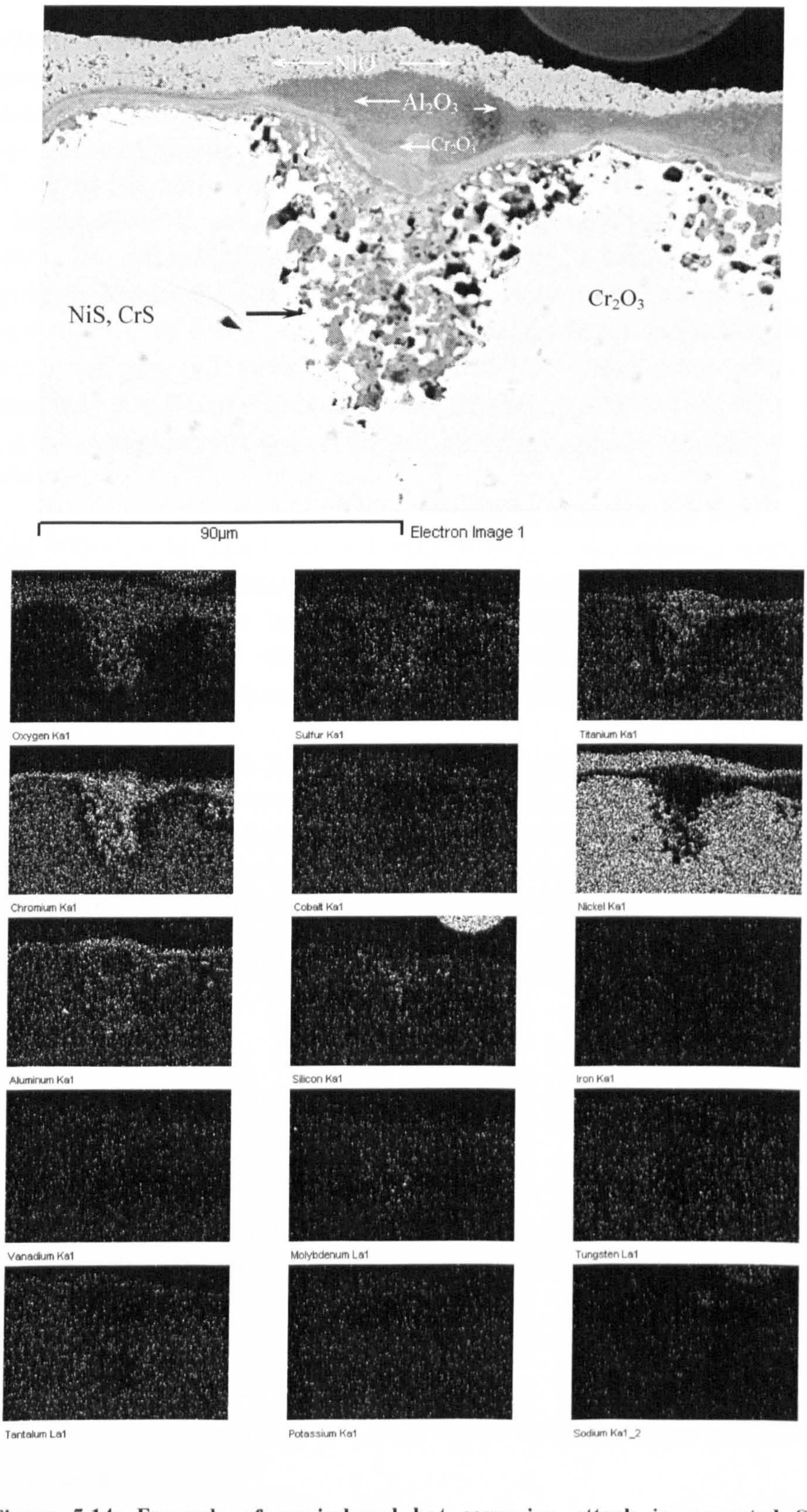

Figure 5.14: Example of gas-induced hot corrosion attack in uncoated SC[2] with 5µg/cm^2/h in 500vpm SO_2 at 700°C after 500h exposure.

The alloy composition could also have influenced the damage; since the high concentrated layer of Al observed in SC^2 (Figure 5.15) is not observed in CMSX4, Figure 5.16. However, a morphological comparison between the photomicrographs sets 1, 2, 3 and 13, 14 and 15 in Figure 4.38, provides evidence of the HCl benefit in the 50vpm SO_2 environment; in the first set (photos 1, 2 and 3), pit progression is well advanced, whereas, in the second set (photos 13, 14 and 15), pits are progressing (values of this in terms of metal loss are summarized in Table 5.2). Figure 5.17 seems to show basic fluxing degradation; based on these features:

- Deposit/corrosion product contains Cr_2O_3 and Al_2O_3 rich layers
- Internal damage zone with mostly Al_2O_3 precipitates in a nickel-rich matrix
- Test temperature of 900°C

Further SEM/EDX analysis at higher magnification (dotted square) was carried out to determine the nature of the internal damage. Sulphate ions may have diffused through the deposit, towards the alloy surface and nickel sulphides (NiS) had also formed. These sulphides (NiS) can be seen in Figure 5.18.

In a normal hot corrosion environment at 700°C, SO_3 is formed and is in equilibrium with the melt (gas/deposit/alloy); it reacts with the NiO in the oxide scale to form $NiSO_4$, decreasing the melting point of the deposit corrosion product, making it liquid and more susceptible of degradation. The SO_3 also reacts with the deposit, e.g. $(Na/K)_2SO_4$ to form $(Na/K)_2S_2O_7$ (Equation 23), making the deposit more acidic and so dissolving the alloy elements and their oxides.

$$(Na/K)_2SO_4 + SO_3 \rightarrow (K/Na)_2S_2O_7$$

Equation 23

When HCl is added to the system, it could react with the deposit in the surface, forming sodium/potassium chloride, water and SO_3 that could go back to the environment.

$$Na_2SO_4 + HCl \Leftrightarrow NaCl + H_2O + SO_3 \uparrow$$

Equation 24

Thus, Equation 23 and Equation 24 could take place at the same time in the deposit. By varying the concentration of SO_2 or HCl in the environment, either Equation 23 or Equation 24 will govern the degradation mode and the partial pressure of sulphur available for internal sulphidation.

Thus, at 700°C with higher HCl concentrations, the levels of SO_3 in the deposit may be decreased due to the displacement of Equation 24 to the right, leaving less SO_3 in the deposit to attack the alloy but would result in an increased solution of NaCl in the deposit. As a result, no sulphides are formed underneath the pits and, rather, internal oxidation attack takes place. Excess chlorine/chloride species can lead to more rapid breakdown of the protective oxides, plus outward transport of $AlCl_3$ or $CrCl_2$ vapour chlorides, where they then oxidise.

At 900°C, with much lower levels of SO_3 in the gaseous environment, the HCl addition could increase the extent of internal oxidation by further reducing the SO_3 levels in the deposit via Equation 24. The negative effect of the HCl addition observed on SC^2 samples exposed at 700°C, is perhaps due to the influence of temperature and the different alloy composition.

Having considered the main factors that influence the hot corrosion degradation modes (alloy composition, deposition rates, gas composition, and temperature), the resulting morphologies can be analysed to determine the final propagation modes that took place in the materials exposed in this study, considering all test conditions. Table 5.4 summarizes such information based on the morphologies shown in Figure 4.34, Figure 4.35, Figure 4.38, Figure 4.36 and the SEM/EDX analyse reported in this chapter.

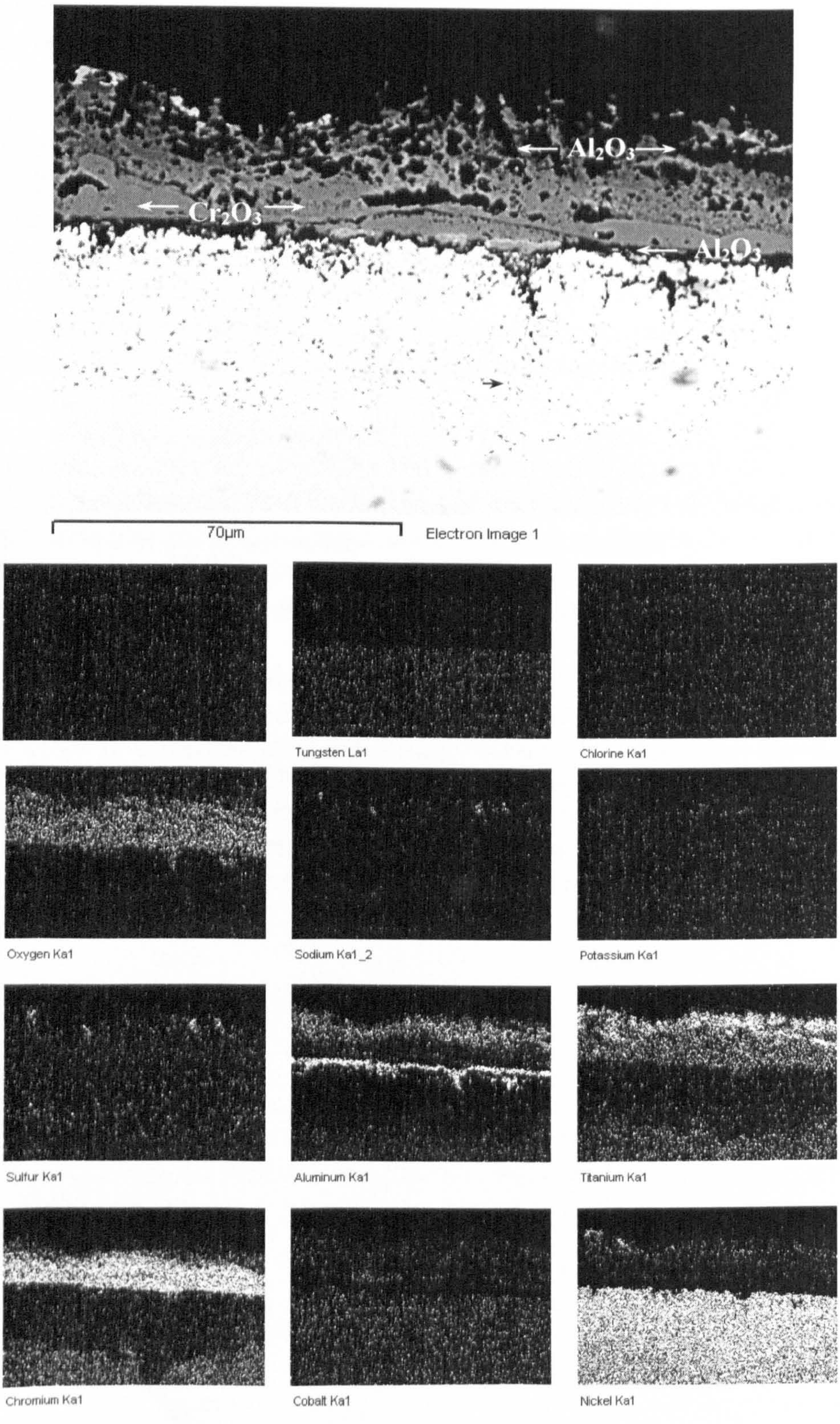

Figure 5.15: Example of chlorine-induced hot corrosion in uncoated SC^2 with 5µg/cm^2/h in 50vpm SO_2/500vpm HCl at 700°C after 500h exposure.

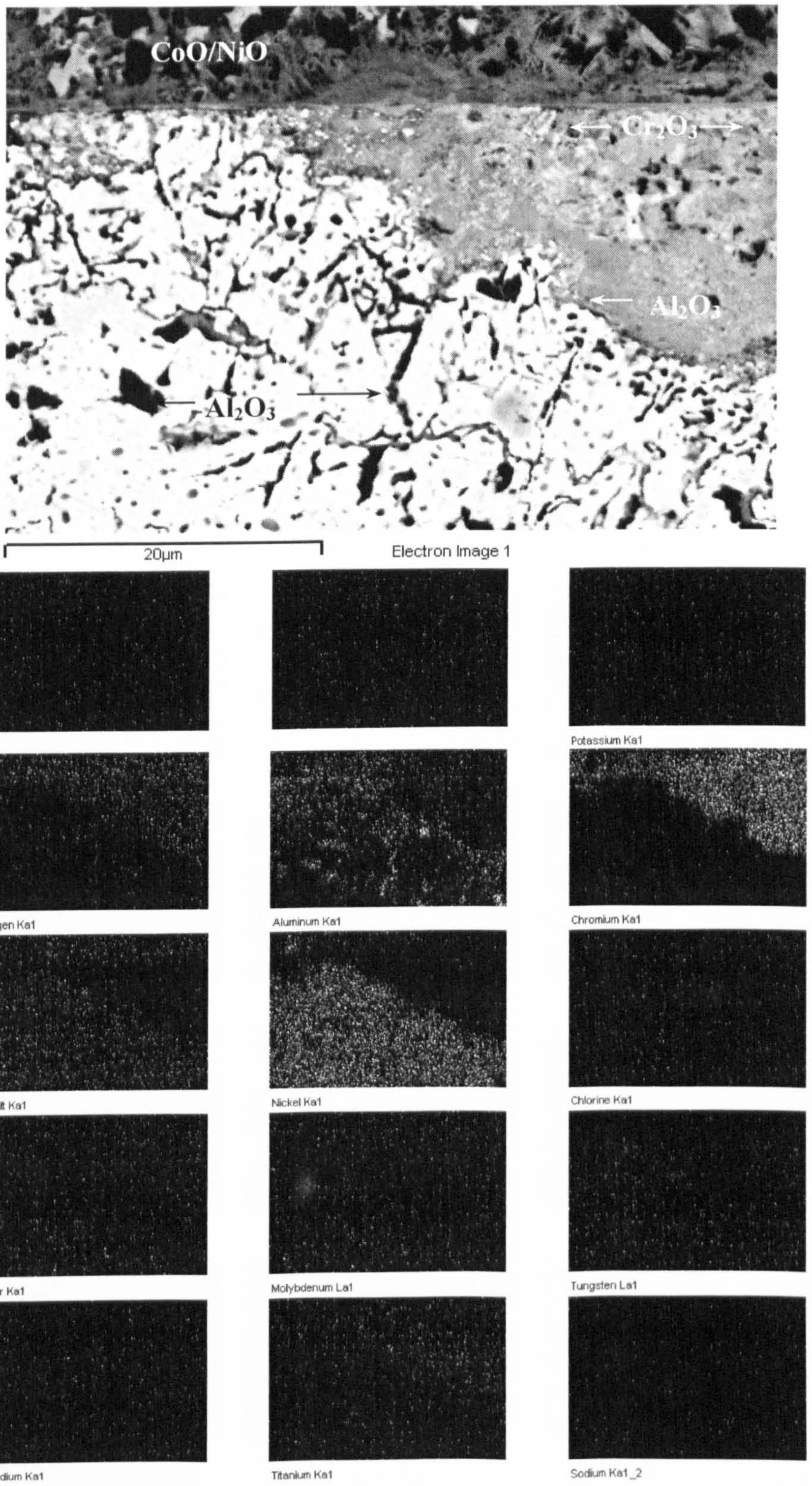

Figure 5.16: Example of gas phase-induced hot corrosion attack in uncoated CMSX4 after 500h exposure with 5µg/cm^2/h in 50vpm SO_2/500vpm HCl at 700°C.

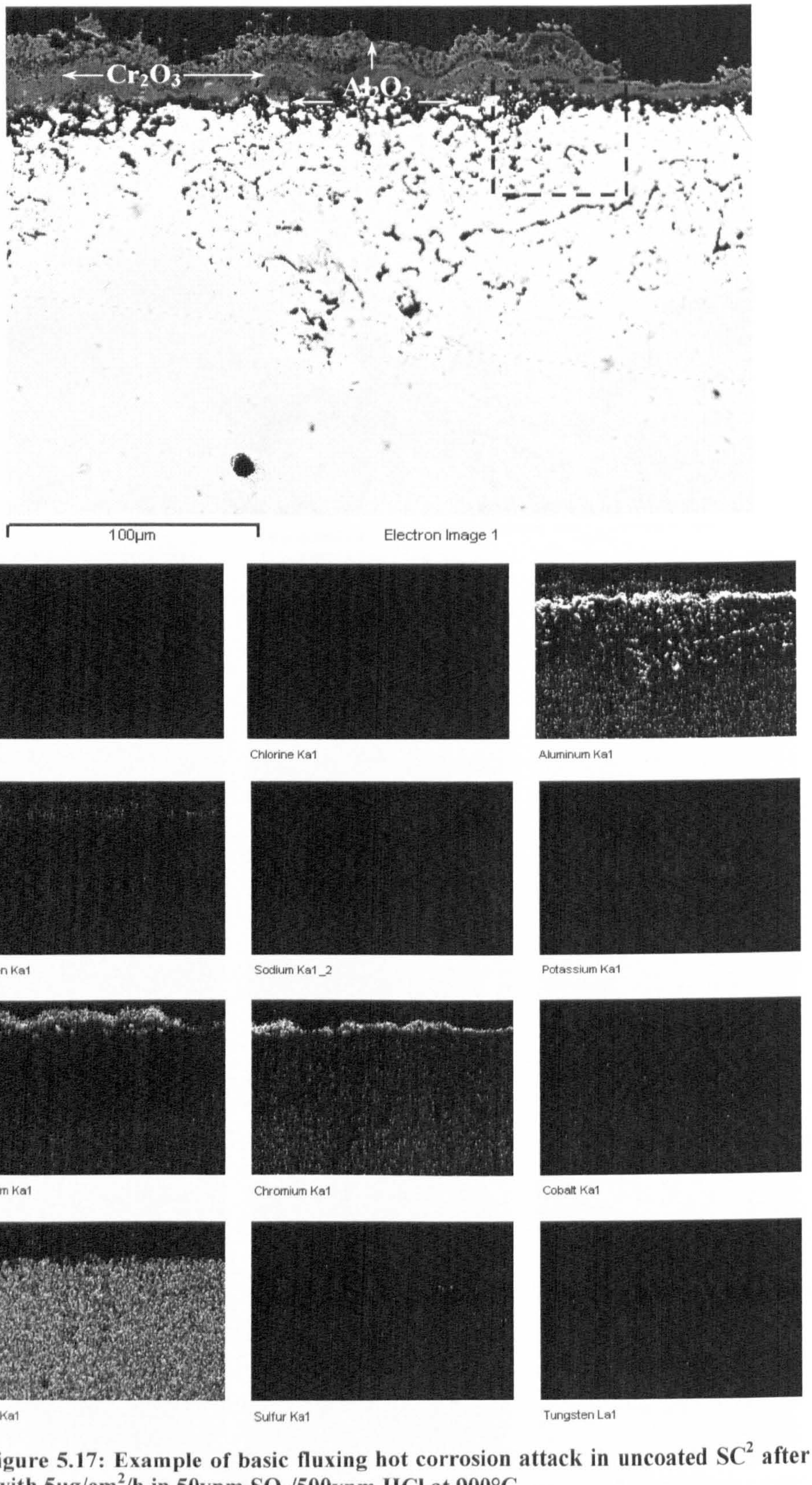

Figure 5.17: Example of basic fluxing hot corrosion attack in uncoated SC^2 after 500h exposure with 5µg/cm^2/h in 50vpm SO_2/500vpm HCl at 900°C.

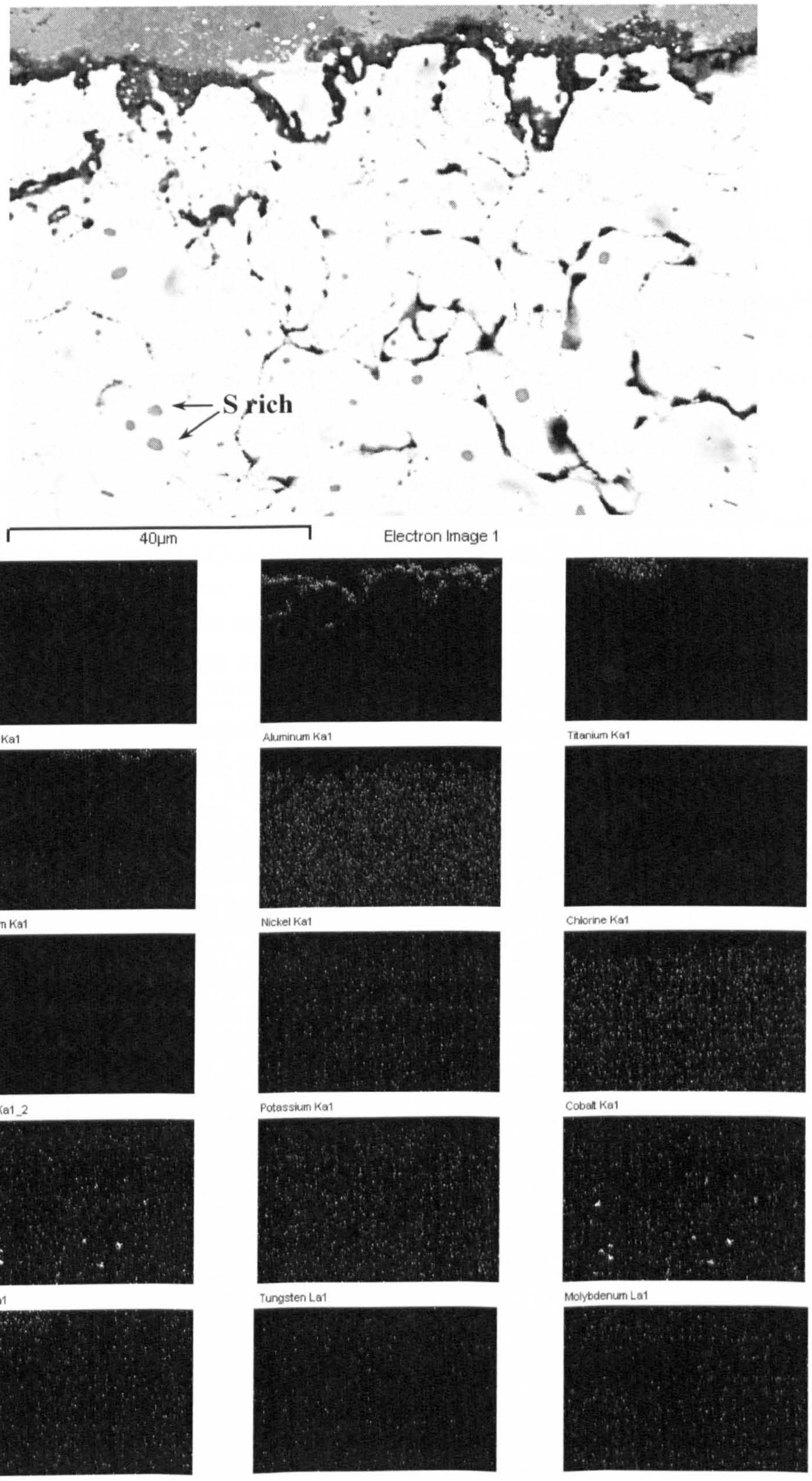

Figure 5.18: Higher magnification of the example of basic fluxing hot corrosion attack in uncoated SC[2] after 500h exposure with 5µg/cm^2/h in 50vpm SO_2/500vpm HCl at 900°C.

5.6 PtAl Coatings Performance in Different Hot Corrosion Environments

The corrosion rates of CMSX4 and SC^2 with PtAl coatings are shown in Figure 5.19 and Figure 5.20 respectively for the three different environments (50vpm SO_2, 500vpm SO_2 and 50vpmSO_2/500 vpm HCl) with the three deposition fluxes (1.5, 5 and 15 $\mu g/cm^2/h$), at 700°C at a particular level of confidence (4% of exceedance). Corrosion rates under identical test conditions at 900°C are shown in Figure 5.21 and Figure 5.22.

As for the previous section, for easier interpretation of the results, the values (4% of exceedance) for the main features of the PtAl coating have been summarized in Table 5.5 and Table 5.6. These data give a comparison between CMSX4 vs. SC^2, both with and without a PtAl coating, on whether or not the coating was protective for the base alloy, i.e., if the coating showed a deposition flux dependence and extended the incubation time of the based materials (marking as positive (✓), negative (✗) or neutral(○)).

Five main features of the PtAl coating performance are observed:

- Corrosion damage to the single crystal alloy/PtAl coating systems increased with increasing flux deposition.
- On the CMSX4, the PtAl coating was protective at 900°C but not at 700°C. (one exception was observed in the 50vpm SO_2 gas). On SC^2, the PtAl coating was protective at both 700 and 900°C (one exception was observed in the 50vpm SO_2 gas)
- The PtAl coating on SC^2 showed lower corrosion rates than the PtAl coating on CMSX4 in all the cases (it was not possible to compare the excessive corrosion rates of this system in the 500vpm SO_2 gas, due a lack of PtAl/CMSX4 samples being provided)
- Comparing the corrosion values for each PtAl/alloy system in terms of temperature, at 900°C, often the values are lower than those at 700°C
- The PtAl coating appears to extend the incubation time period for the CMSX4 and SC^2 alloys (observations based on the mass change data in Figure 4.17 to Figure 4.28, presented in section 4.2.2).

The dependence of corrosion rate on deposition flux for the PtAl coating appears to be within the characteristics of the "flux limited hot corrosion regime"[71] (discussed in section 5.2). In general, the corrosion rates for the coated materials have a lower dependence on flux than those of uncoated materials. Qualitatively, an indication of these changes in corrosion rate as a function of deposition flux for the PtAl/single crystal samples, as well as when uncoated, can be seen on the sets of photographs in Figure 5.23.

This figure shows the surface appearance of damage from the unexposed sample, and samples with the lowest deposition flux (1.5µg/cm^2/h), the medium (5µg/cm^2/h) and the highest flux (15µg/cm^2/h) on SC^2 coated with PtAl at 700°C in (a) 500vpm SO_2 gas and (b) in 50vpm SO_2 gas after 500h exposure (and before being metallographically processed).

The protective effect of the PtAl coating on SC^2 in the most aggressive environment (500vpm SO_2 gas) at 700°C can be seen by comparing the set of photos in Figure 5.23 (a) with that in Figure 5.1.

Alloy	CMSX4								
Gas vpm	Flux µg/cm²/h	700°C		uncoated Vs. PtAl coated	Incubation time uncoated Vs. coated	900°C		uncoated Vs PtAl coated	Incubation time uncoated Vs. coated
		uncoated	coated			uncoated	coated		
	1.5	28	50	✖	10 vs. 65	-	44	-	30vs 180
50SO_2	5	85	62	✓	2 vs. 45	210	117	✓	5 vs. 45
	15	99	112	✖	3 vs. 35	540	434	✓	10 vs. 50
	1.5	103	-	-	0-	194	-		10-
500SO_2	5	171	-	-	0-	433	-		7-
	15	227	-	-	0-	849	-		3-
	1.5	30	50	✖	10 vs180	112	32	✓	35vs100
50SO_2/ 500HCl	5	63	64	O	10 vs. 90	185	49	✓	0 vs. 0
	15	59	154	✖	7 vs. 30	548	71	✓	0 vs. 0
PtAl Corrosion Rate dependant on deposition flux			✓				✓		

Table 5.5: Values of the confidence level with the 4% probability of being exceed from type I and type II hot corrosion for the comparison of theCMSX4 PtAl coated material under all the test conditions; marking as positive (✓), negative (✖) or neutral (O) result (a tolerance of +- 10µm was given to consider a difference as neutral).

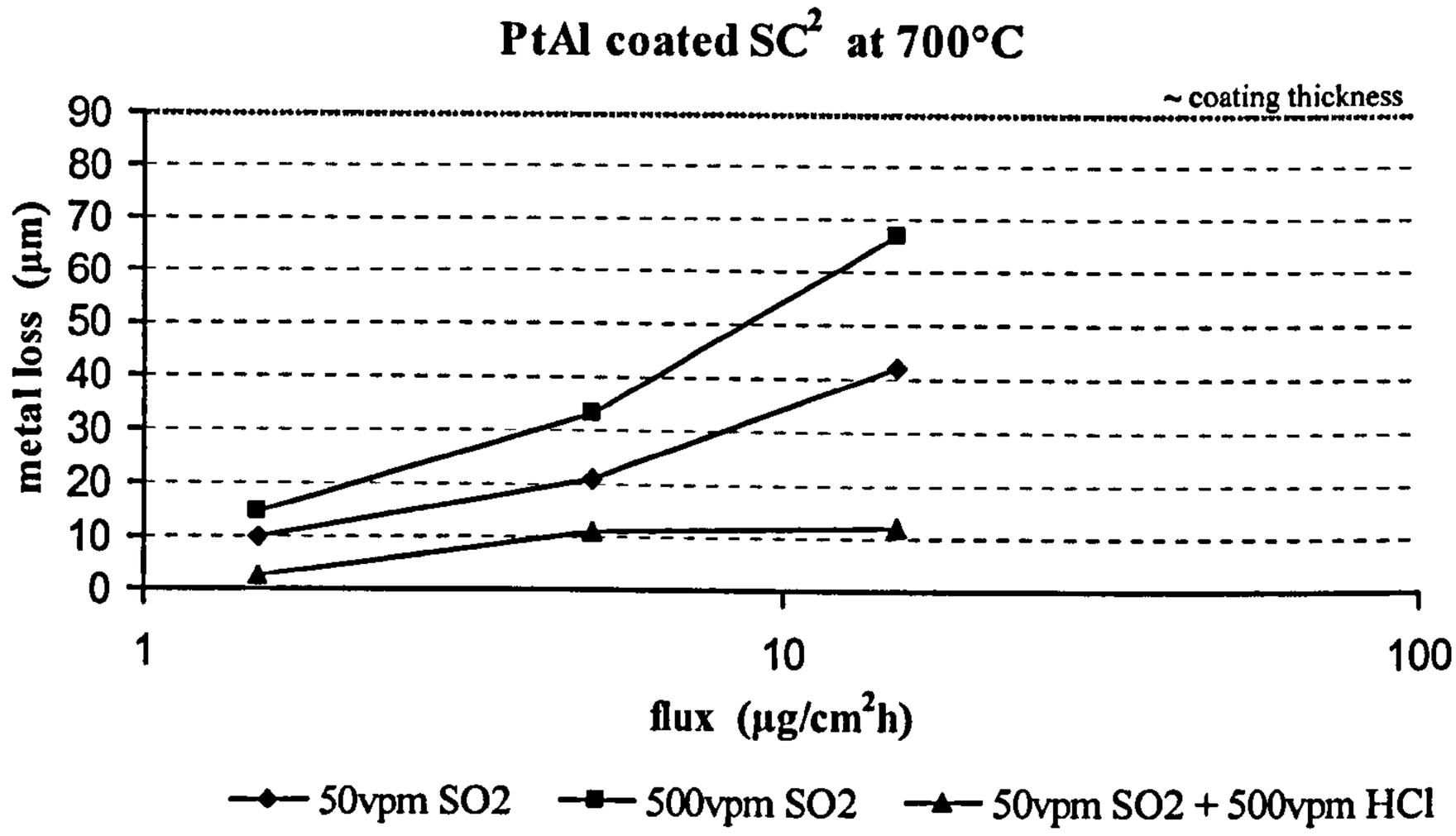

Figure 5.19: Effect of deposition flux of 80/20 $(Na/K)_2SO_4$ on the hot corrosion performance of PtAl coated SC^2 in terms of sound metal loss (with a 4% probability of being exceeded) after 500h exposure at 700°C in a range of different gas composition (red dashed line indicates ~ coating thickness).

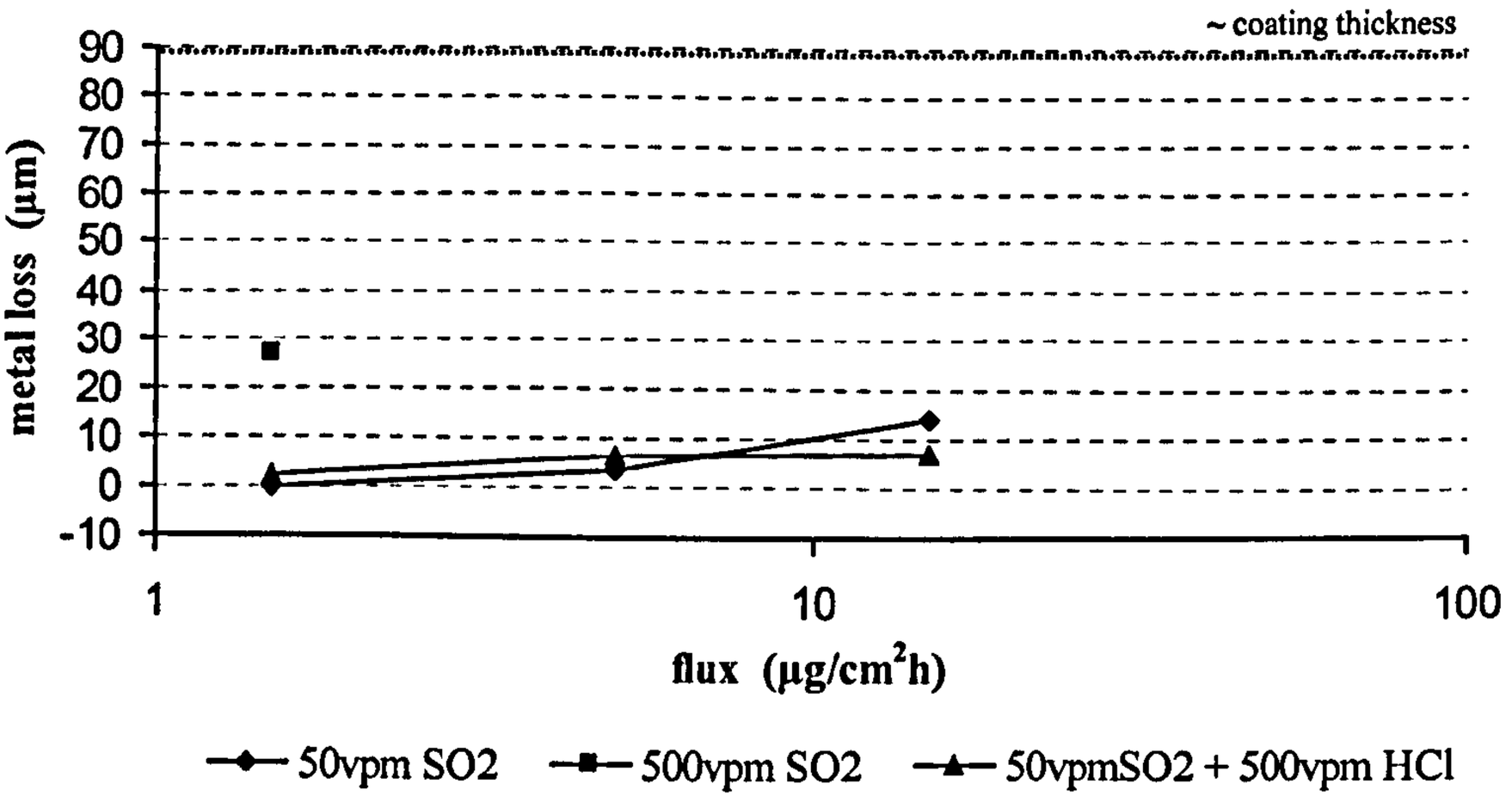

Figure 5.20: Effect of deposition flux of 80/20 $(Na/K)_2SO_4$ on the hot corrosion performance of PtAl coated SC^2 in terms of sound metal loss (with a 4% probability of being exceeded) after 500h exposure at 900°C in a range of different gas composition (red dashed line indicates ~ coating thickness) .Only the 1.5µg/cm²/h value of the 500vpm SO_2 plotted due catastrophic corrosion rates of the other two values.

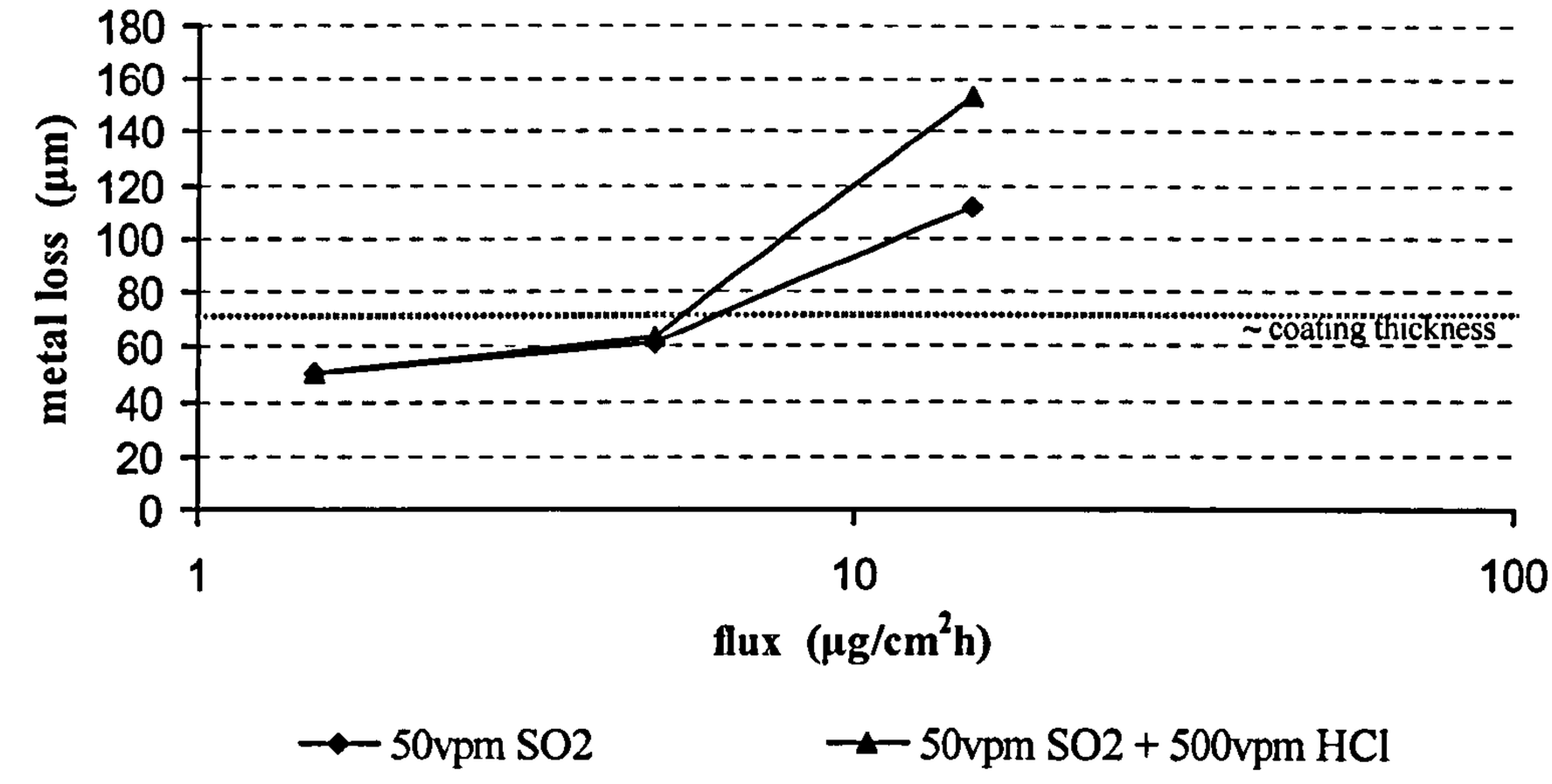

Figure 5.21: Effect of deposition flux of 80/20 $(Na/K)_2SO_4$ on the hot corrosion performance of PtAl coated CMSX-4 in terms of sound metal loss (with a 4% probability of being exceeded) after 500h exposure at 700°C in a range of different gas composition (red dashed line indicates ~ coating thickness).

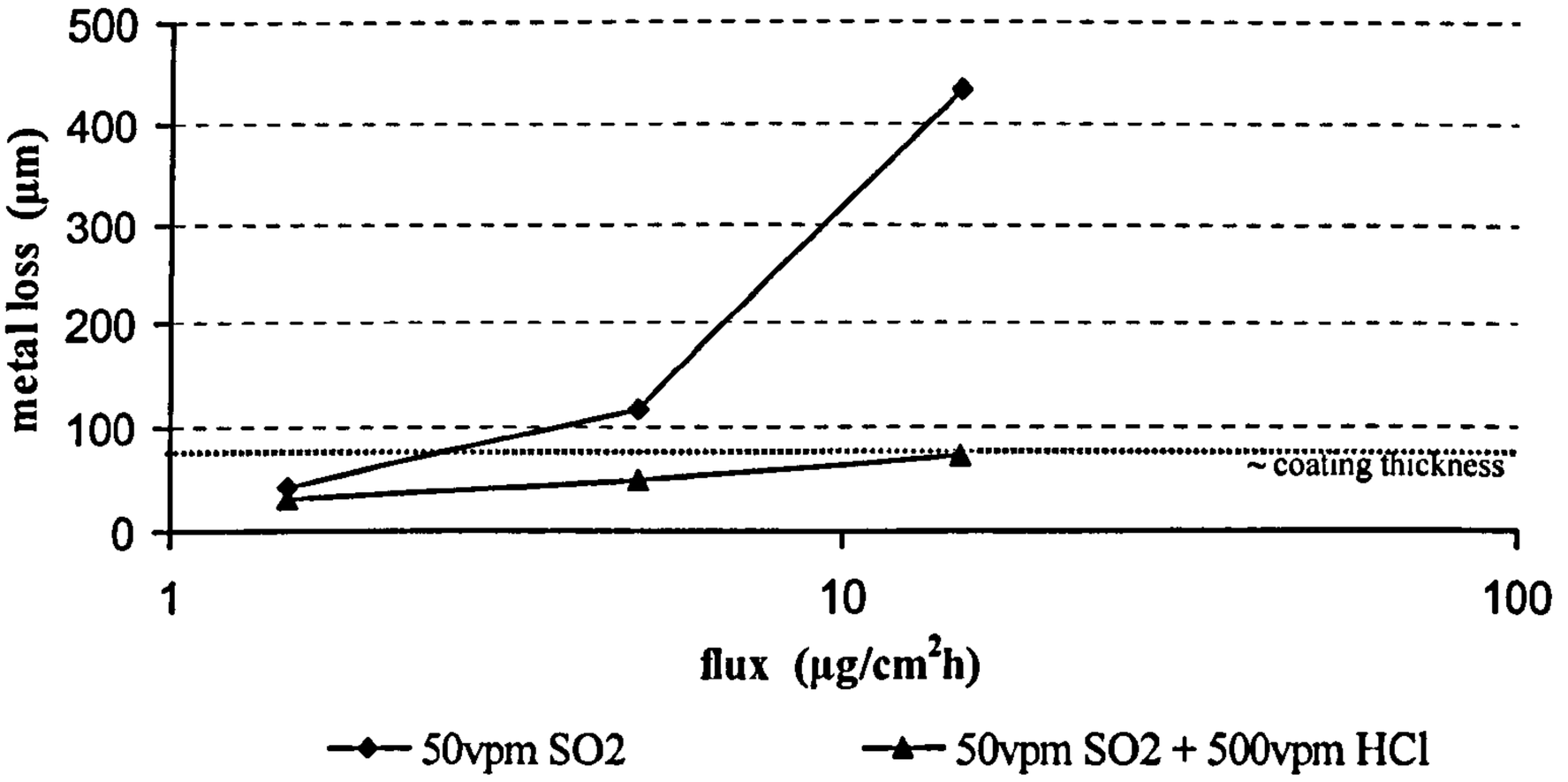

Figure 5.22: Effect of deposition flux of 80/20 $(Na/K)_2SO_4$ on the hot corrosion performance of PtAl coated CMSX-4 in terms of sound metal loss (with a 4% probability of being exceeded) after 500h exposure at 900°C in a range of different gas composition (red dashed line indicates ~ coating thickness).

Alloy	SC²								
Gas vpm	Flux µg/cm²/h	700°C		uncoated Vs. PtAl coated	Incubation time uncoated Vs. Coated	900°C		uncoated Vs PtAl coated	Incubation time uncoated Vs. coated
		uncoated	coated			uncoated	coated		
	1.5	16	10	✓	50 vs. 40	96	0	✓	20 vs200
$50SO_2$	5	20	21	○	25 vs. 5	288	3	✓	5 vs. 400
	15	28	42	✗	35 vs. 3	474	14	✓	5 vs. 40
	1.5	70	15	✓	0 vs. 20	268	27	✓	5 vs. 15
$500SO_2$	5	123	33	✓	3 vs. 4	1513	627	✓	4 vs. 10
	15	148	67	✓	3 vs. 2	2794	1814	✓	2 vs. 7
	1.5	6	3	✓	35 vs. 20	98	2	✓	35 vs400
$50SO_2$/ 500HCl	5	34	11	✓	15 vs. 10	79	6	✓	30 vs. 50
	15	60	12	✓	10 vs. 7	163	7	✓	0 vs. 0
PtAl Corrosion Rate dependant on deposition flux			✓				✓		

Table 5.6: Values of the confidence level with the 4% probability of being exceed from type I and type II hot corrosion for the comparison of theSC² PtAl coated material under all the test conditions; marking as positive (✓), negative (✗) or neutral (○) result (a tolerance of +- 10µm was given to consider a difference as neutral).

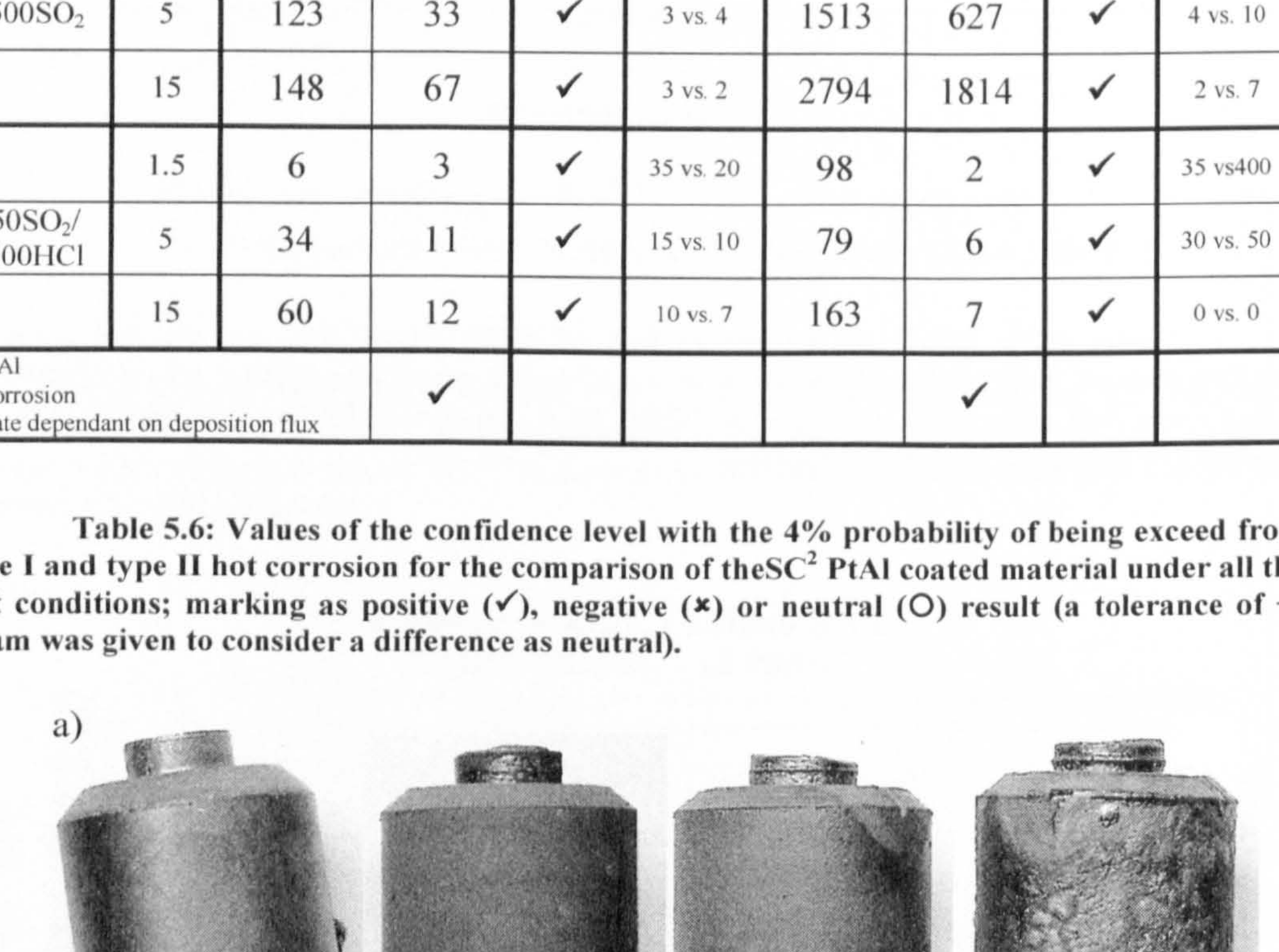

Figure 5.23: Deposit 80/20 $(Na/K)_2 SO_4$ from a non exposed reference sample to low deposition flux (1.5µg/cm²/h), an intermediate deposition flux (5µg/cm²/h) and a high deposition flux (15µg/cm²/h) on uncoated SC² at 700°C in 500vpm SO_2 (a) and in 50vpm SO_2 (b), after 500h exposed.

The progression from minor to major damage due increasing deposition fluxes, can also be seen in the resulting morphologies, by comparing vertically the sets of photomicrographs in Figure 4.36, Figure 4.37, Figure 4.40 and Figure 4.41. The morphologies/structures of the unexposed reference PtAl samples used in this study can be seen in Figure 4.29 (section 4.3.3). By comparing these figures, different thickness and appearance can be noticed within the samples.

This is due to the three different base alloys (IN738LC, CMSX4 and SC^2); therefore, different structure/morphology characteristics of the PtAl coating were obtained. These PtAl coating morphologies, as explained in section 2.6, are dependant on pack activity (the rate at which Al is released); this determines the direction of diffusion of the elements forming the coating. Inward diffusion of Al, from a high activity pack where an outer layer of $PtAl_2$+ β(Ni, Pt)Al forms, or outward diffusion of Ni, from a low activity pack. In this study, the PtAl coatings were applied as high activity coatings on the IN738LC, CMSX4 and SC^2 alloys. Prior to aluminising, platinum was electro-deposited on all samples (details of the PtAl coatings are given in section 2.6.6).

However, the PtAl coating on CMSX4 tested in stage 1 of this study differs in structure from that tested in stage 2, because they were supplied from different batches. Regardless of the aluminising processes carried out for different times/conditions, it is believed that the different morphologies/structures obtained could have influenced the hot corrosion resistance of the PtAl coating for only a short period of time at the start of the exposure. Comparative studies of different PtAl coatings on CMSX4 carried out by Angenete [38; 151], show that, after 20h oxidation with different PtAl coatings, the dominant oxide phase appears to be α-Al_2O_3 and no spinel grains were observed. An example of an optical image of a sample from each batch can be seen in Figure 4.29, section 4.3.3. A backscattered image from a sample from the batch used in stage 2 is shown in Figure 5.25.

The performance of the PtAl coating at 700°C is different on each alloy because the properties of a diffusion coating depend not only on the processing conditions, but also on the substrate composition and subsequent heat treatment. As the PtAl is applied as a platinum electro-deposition process heat treatment, followed by a diffusion aluminizing process, a consequence of the inward growth will be that slowly diffusing alloying elements from the substrate will be entrapped in the coating. The result is that the Cr concentration is different and elements such as W, Mo, Ta, Re, etc, may be present in precipitates and/or in solid solution in the coating matrix. Thus the PtAl coating composition will not be the same on each substrate.

Interdiffusion of the coating and substrate elements will continue during exposure in the corrosion environments, although at lower rates than in coating processing (900 to 1100°C) due to the lower exposure temperatures (≤900°C). Since the coating composition that forms is influenced by the substrate elements, amongst other factors, the result of having different concentrations of the refractory elements, as well as different concentrations of Cr and Al, will be that, in different corrosion environments, different degradation modes and corrosion rates on the coating/alloy system could be expected.

Corrosion data for the coated samples displayed in Table 5.5 vs. Table 5.6 show that this is the case. At 700°C, the PtAl coating on SC^2 showed lower corrosion rates for all the different exposure conditions (deposition flux, gas composition and temperature) in comparison with the PtAl coating on CMSX4. The PtAl coating was protective practically for all the SC^2 uncoated samples under the two temperatures (700 and 900°C), but on CMSX4, showed little effective protection at 700°C (only two exceptions, see Table 5.5). This could be, as when uncoated, due to the alloy composition, i.e. the different element contents, in particular the protective oxide formers chromium and aluminium. It is known that the presence of chromium decreases the minimum aluminium content needed to form a continuous alumina scale. In the NiAl system, the minimum concentration of Al at which alumina is the dominant oxide is about 35 at%, but, with the addition of 5 at% chromium, the limit for Al_2O_3 is pushed to about 12 at% [39; 38]. This mechanism is explained in detail in section 2.3.6.

Thus, chromium has an important effect on the selective oxidation of aluminium and formation of a continuous Al_2O_3 scale. Since the corrosion resistance of the coating relies on the formation of a protective Al_2O_3 scale (with a reservoir of Al, typically in excess of 30wt% aluminium deposited to thicknesses of 30-100μm), the alloy with higher concentration of Cr (that gives a higher Cr containing PtAl coating), i.e. with SC^2 as substrate, is likely to form and maintain more stable Al_2O_3 and Cr_2O_3 oxide scales than the system PtAl/CMSX4, thereby making the PtAl/SC^2 system more resistant to the corrosive environments.

The PtAl coatings on both alloys were more protective at 900°C than at 700°C. This is believed to be a result of the formation of a more protective oxide scale at the higher temperature; alumina grows fast enough at 900°C to allow the formation of thicker alumina-rich scale. At 700°C, the slower growth of alumina will result in a thinner scale with a more mixed composition (chromia/alumina), giving less protection. This effect is greater (i.e. gives less protection) for CMSX4 than SC^2 at 700°C, as the lower Cr content of CMSX4 reduces the stability of Al_2O_3 growth (as described above).

The hot corrosion propagation modes will degrade the coating/superalloy systems according to the substrate and gas compositions, the deposition fluxes and the temperature. The mode(s) by which the coating is consumed may vary: for example, as suggested in section 4.3.2, the progression of damage, removing the coating layer by layer, suggest an electrochemical form of attack, with the underlying material layer being protected until the outer layer has been removed. The resulting morphologies will remain with the typical hot corrosion characteristics, e.g. localized pitting attack at low temperatures (700°C) or broad internal sulphidation/oxidation at higher temperatures (900°C).

A representative example of the substrate influence can be seen by comparing photomicrographs 1 in both Figure 4.36 vs. Figure 4.40. Backscattered image /SEM mapping analysis were carried out on these two samples, as well as on the unexposed coated reference samples. Unexposed PtAl coating on SC^2 is shown in Figure 5.24 and PtAl coating on CMSX4 in Figure 5.25. Comparing the unexposed PtAl coatings on CMSX4 and SC^2 in Figure 5.24 vs. Figure 5.25 respectively, the differences between the morphology/structure due the influence of the base alloy can be seen:

- SC^2 has a bright layer of β(Pt, Ni)Al outer layer.
- CMSX4 has a $PtAl_2$+β(Pt, Ni)Al outer layer.
- In CMSX4, the Cr that is present is scattered at a low level through the alloy/coating, whereas in SC^2, Cr is additionally concentrated in the interdiffusion/alloy zone.

To compare the elemental distributions and identify the degradation modes for the systems, SEM mapping analysis can be seen in Figure 5.26 and Figure 5.27. In Figure 5.27, corrosion damage has commenced in the outer layer of the coating and continued to penetrate inwards through the coating towards the substrate, producing deep localized damage in the alloy, CMSX4. The mapping analysis indicates that the propagation mode was gas phase-induced acid fluxing, given the characteristics:

- Non-uniform pits around the sample surface
- Cr_2O_3 and Al_3O_3 in the pit
- External regions of NiO and CoO
- A sulphur-rich reaction product layer along the boundary of the pit

In comparison with Figure 5.26, corrosion damage did not penetrate the interdiffusion zone of the coating. This is evidence for benefit provided by the SC^2 alloying elements to the PtAl coating under these test conditions.

The elemental distribution from mapping analysis of this system, PtAl/SC^2, showed the same characteristics previously listed, suggesting that its

degradation mode was gas phase-induced acid fluxing. Regarding the effects of different gas compositions on the PtAl coating, reference is made to Figure 5.28, Figure 5.29 and Figure 5.30; the same deposition flux of 5µg/cm^2/h was applied on these samples and they were all exposed at 700°C.

Figure 5.28 shows the effect of the 50vpm SO_2 environment on the PtAl coating (at a lower flux than Figure 5.26). It is believed that this sample was attacked via gas phase-induced acid fluxing, given the characteristics listed above, but, in this case:

- Chromium was left mainly in the interdiffusion zone
- Sulphur is present in a thin layer on the pit/coating boundary, and also in thick outer layer.
- Al is depleted below corrosion boundary.
- Ni is enriched in the outer corrosion product/deposit layer.

Figure 5.29 shows the effect of increasing the SO_2 concentration ten times (i.e. to 500vpm SO_2). The sample has undergone the same degradation mode (i.e. gas phase-induced acidic fluxing) as that exposed to 50vpm SO_2 but the reaction is more severe.

Figure 5.30 shows the result of adding 500vpm HCl to the 50vpm SO_2 environment. It can be seen that the HCl addition has changed the propagation mode from gas phase-induced acid fluxing to basic fluxing. The mapping analysis shows the following features of basic fluxing attack:

- Oxygen, chromium and aluminium are concentrated in the exterior region of the corrosion scale/deposits; this may be because the aluminate and chromate ions diffuse away from the alloy and are precipitated at higher oxygen pressure as Al_2O_3 and Cr_2O_3, together with oxide ions that diffuse out into the bulk of Na_2SO_4 in exchange for sulphate ions
- Nickel is left in the coating/alloy

The means by which HCl could have changed the acid/basic balance of the deposit corrosion product system are believed to be the same as when samples were uncoated; these are discussed in section 5.5 of this chapter.

Figure 5.31 shows an example of the damage to the PtAl/SC^2 system for a flux of 5µg/cm^2/h in 500vpm gas at 900°C. This sample underwent uneven catastrophic corrosion which consumed most of the coating. However, the only bit of the PtAl remaining was analysed. Probably this sample was degraded by sulphur-induced corrosion since it shows:

- Clear traces of chromium sulphide in a thin layer in the interdiffusion zone and in the alloy.
- Cr_2O_3 and Al_2O_3 in the corrosion product layer.

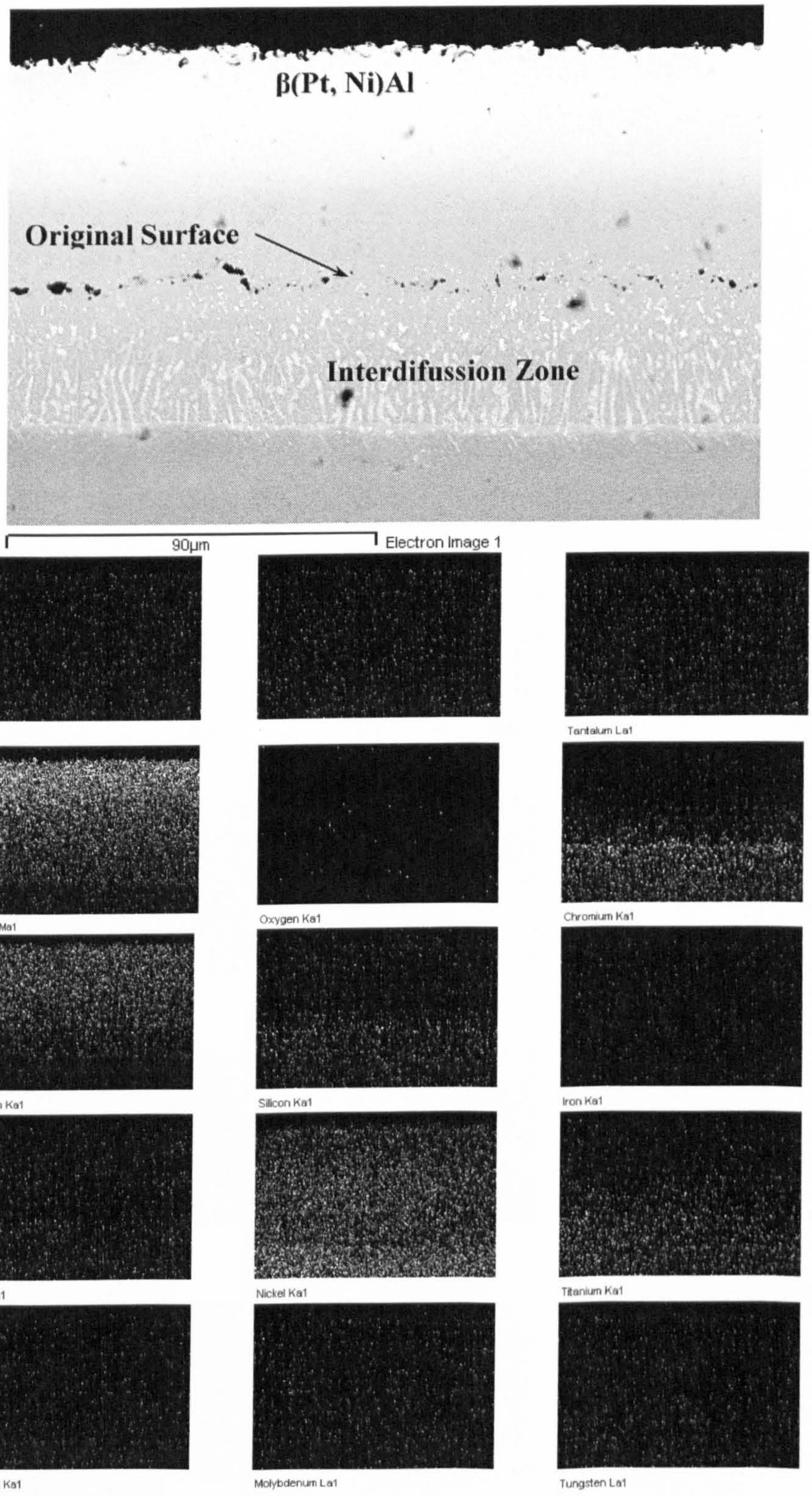

Figure 5.24: Backscattered image/mapping of the un-exposure reference sample SC^2 PtAl coated.

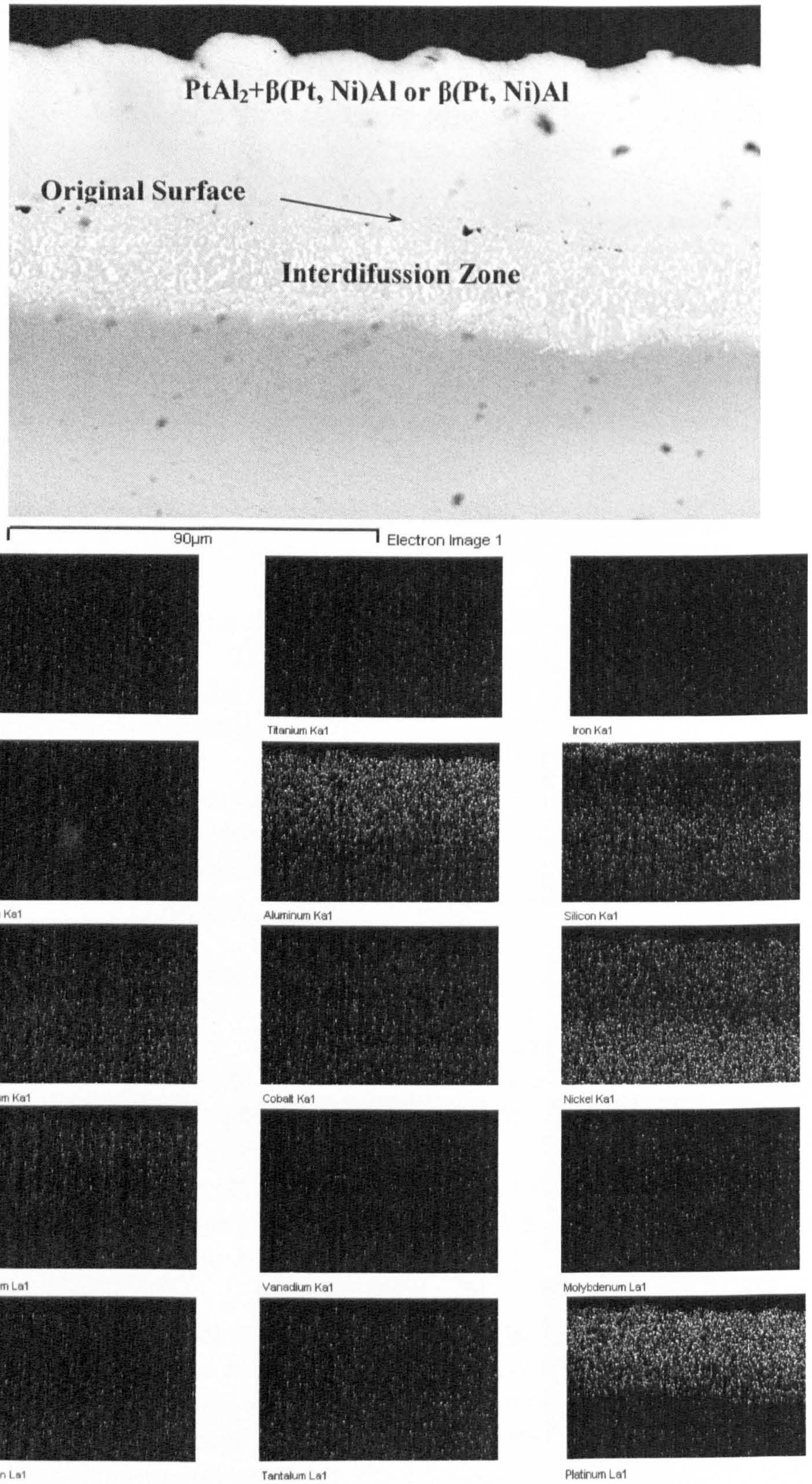

Figure 5.25: Backscattered image/mapping of the un-exposure reference sample CMSX4 PtAl coated.

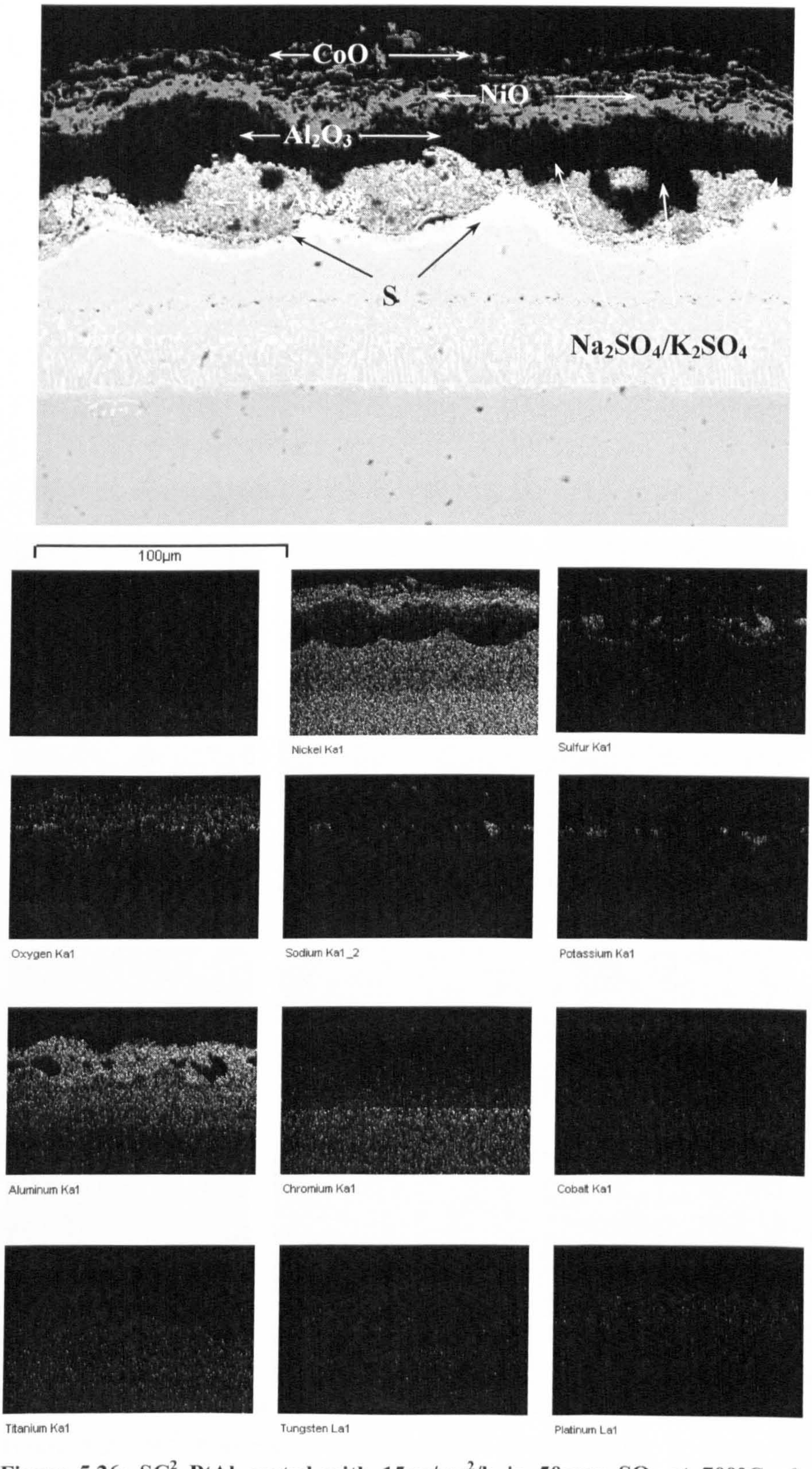

Figure 5.26: SC^2 PtAl coated with 15µg/cm^2/h in 50vpm SO_2 at 700°C after 500h exposure.

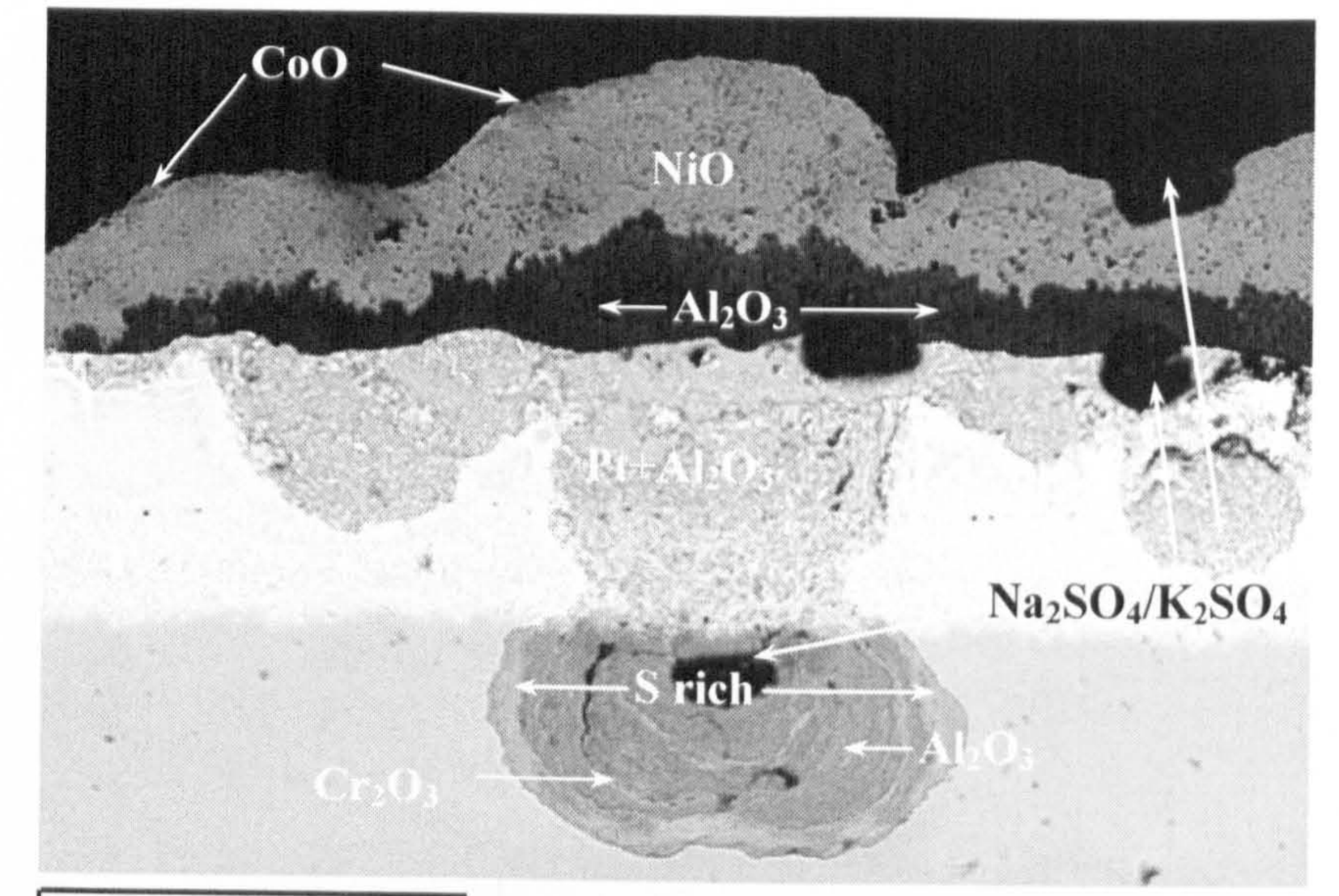

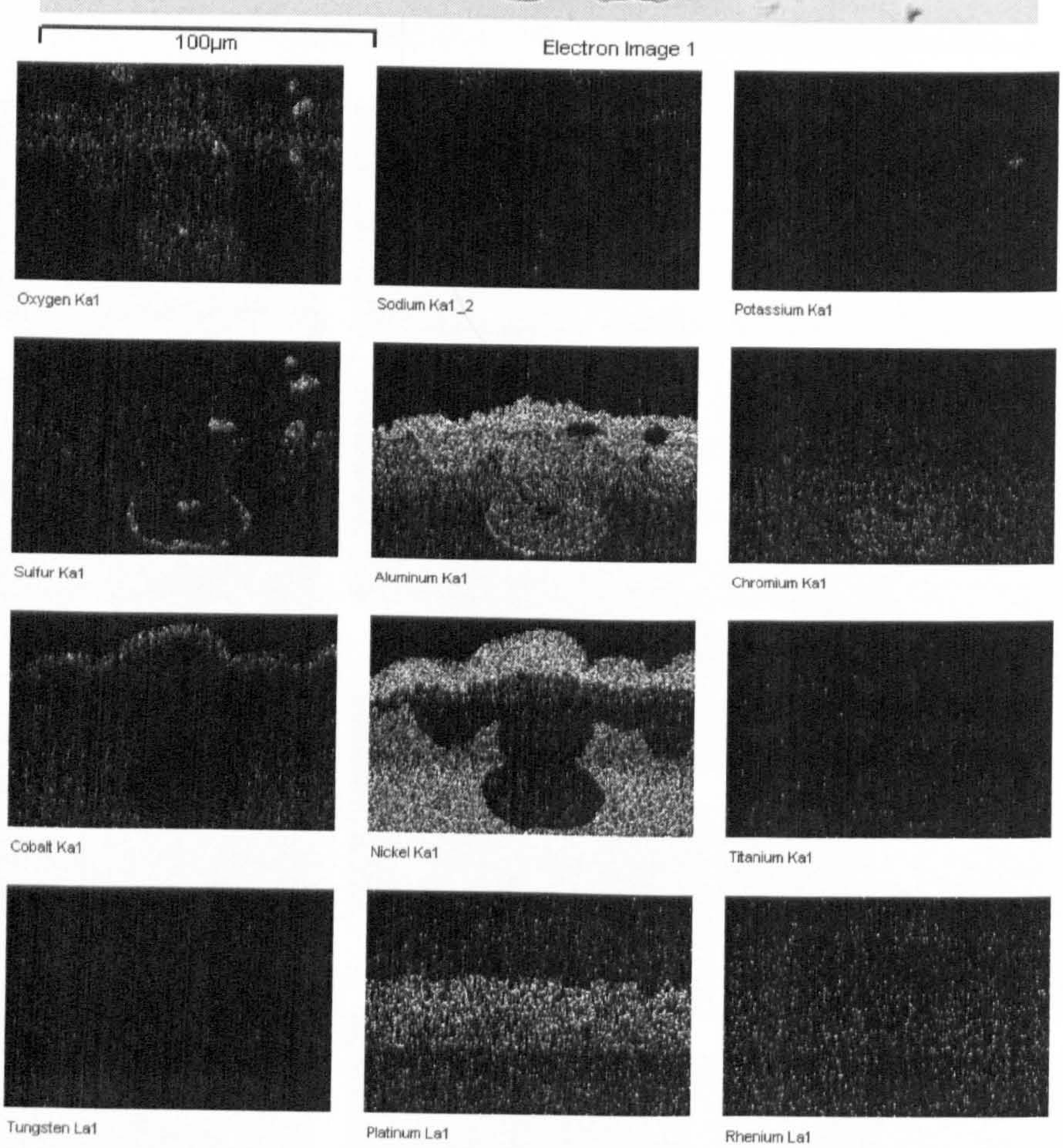

Figure 5.27: CMSX4 PtAl coated with 15µg/cm^2/h in 50vpm SO_2 at 700°C after 500h exposure.

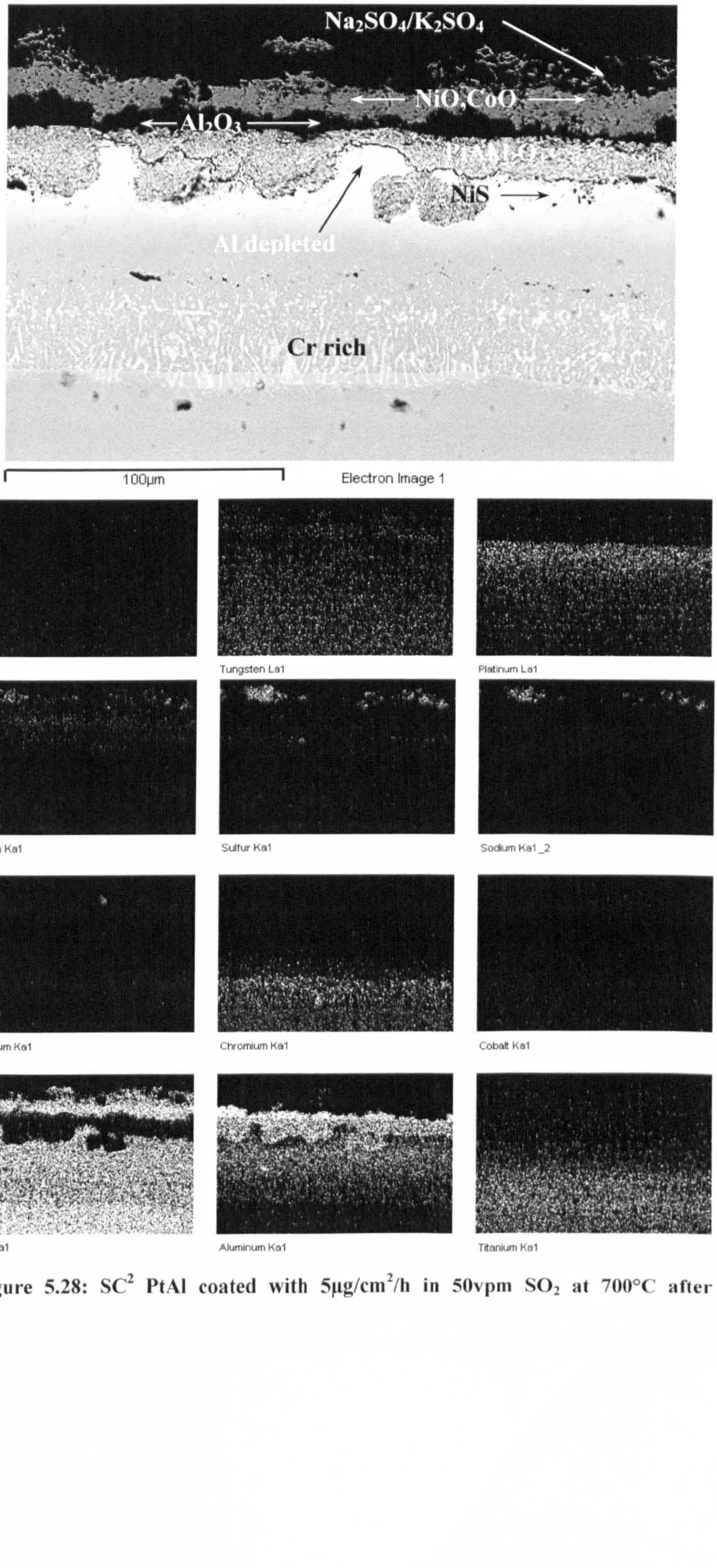

Figure 5.28: SC^2 PtAl coated with 5µg/cm^2/h in 50vpm SO_2 at 700°C after 500h exposure.

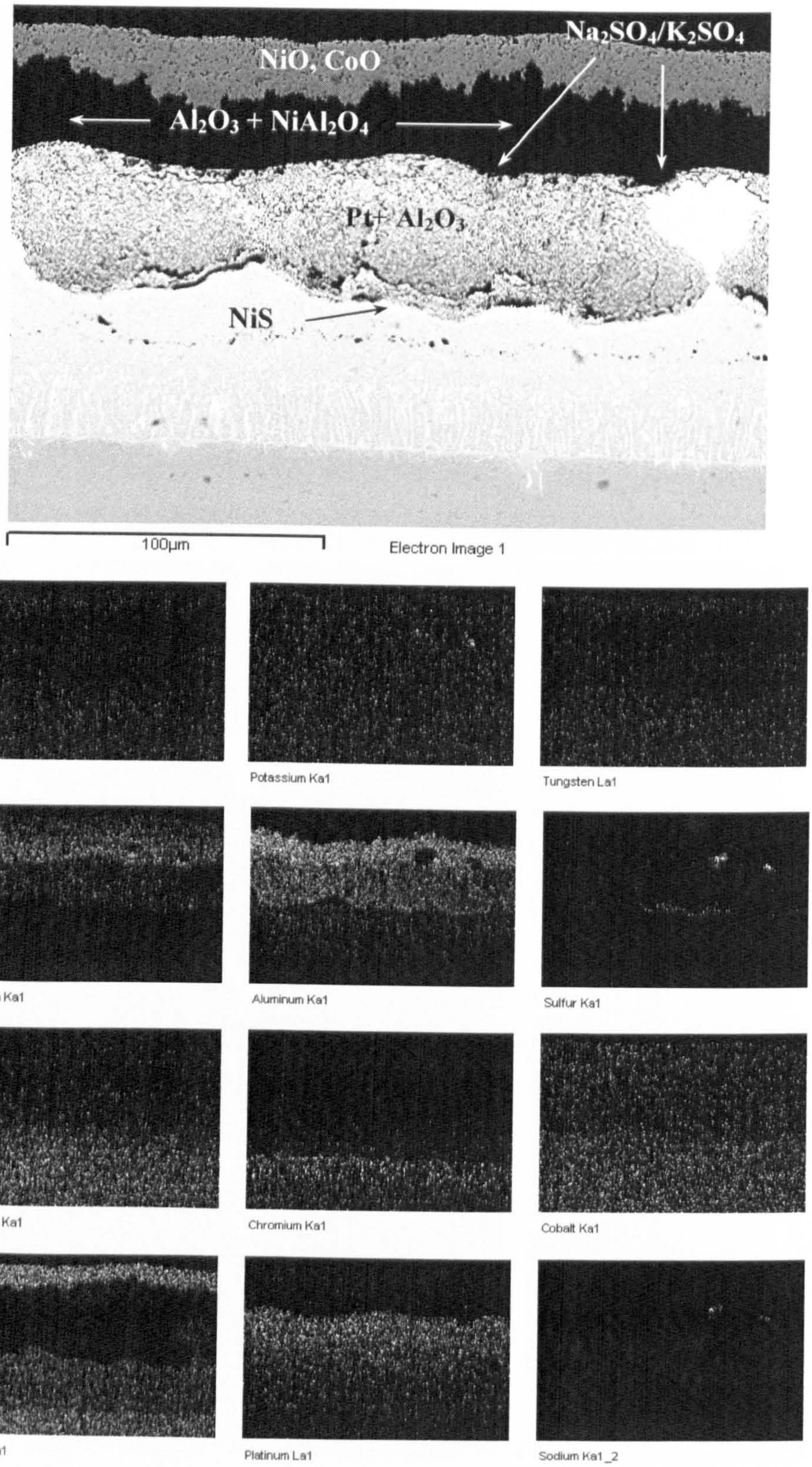

Figure 5.29: SC^2 PtAl coated with 5µg/cm^2/h in 500vpm SO_2 at 700°C after 500h exposure.

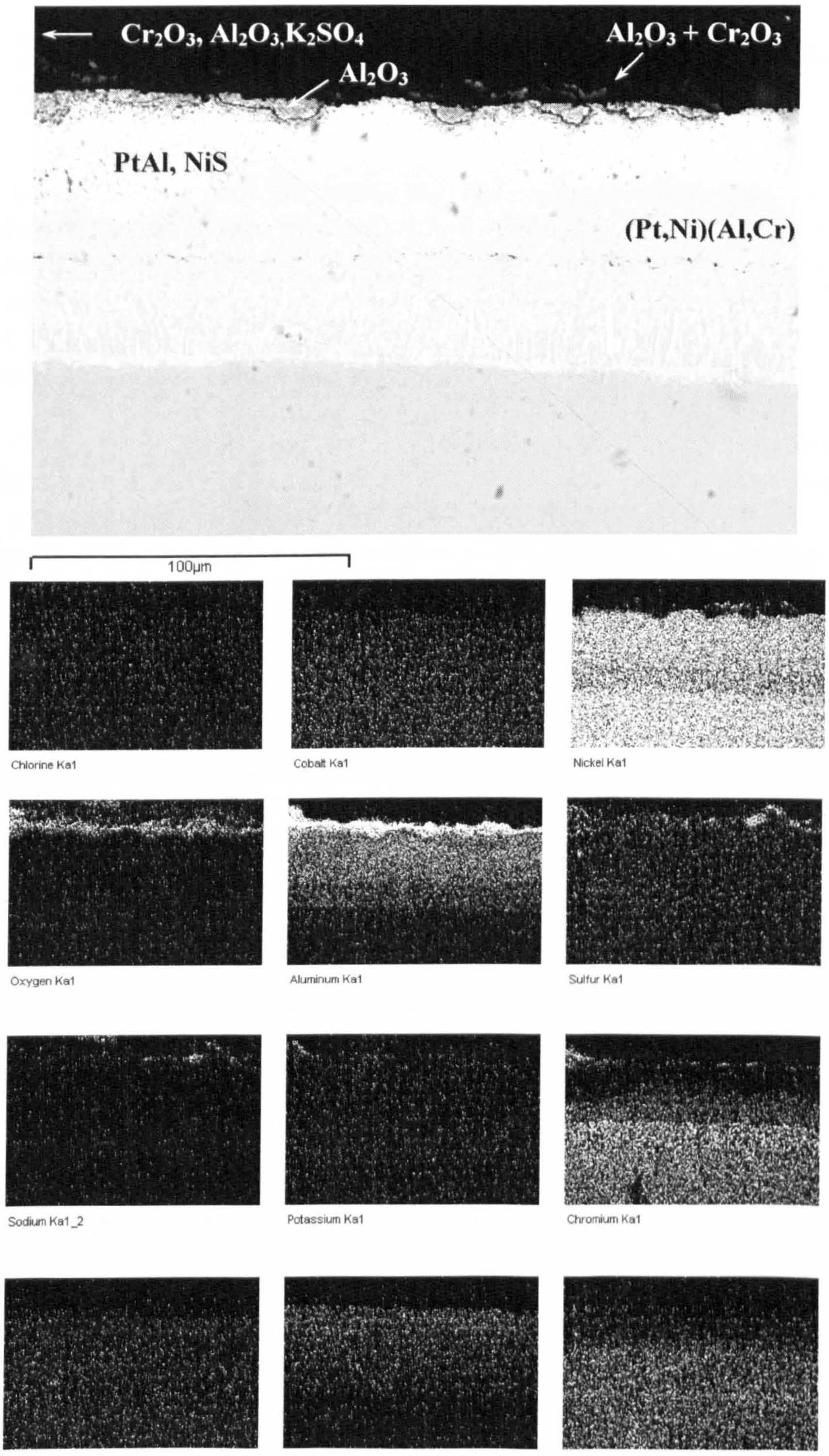

Figure 5.30: SC^2 PtAl coated with 5µg/cm^2/h in 50vpm SO_2/500vpm HCl at 700°C after 500h exposure.

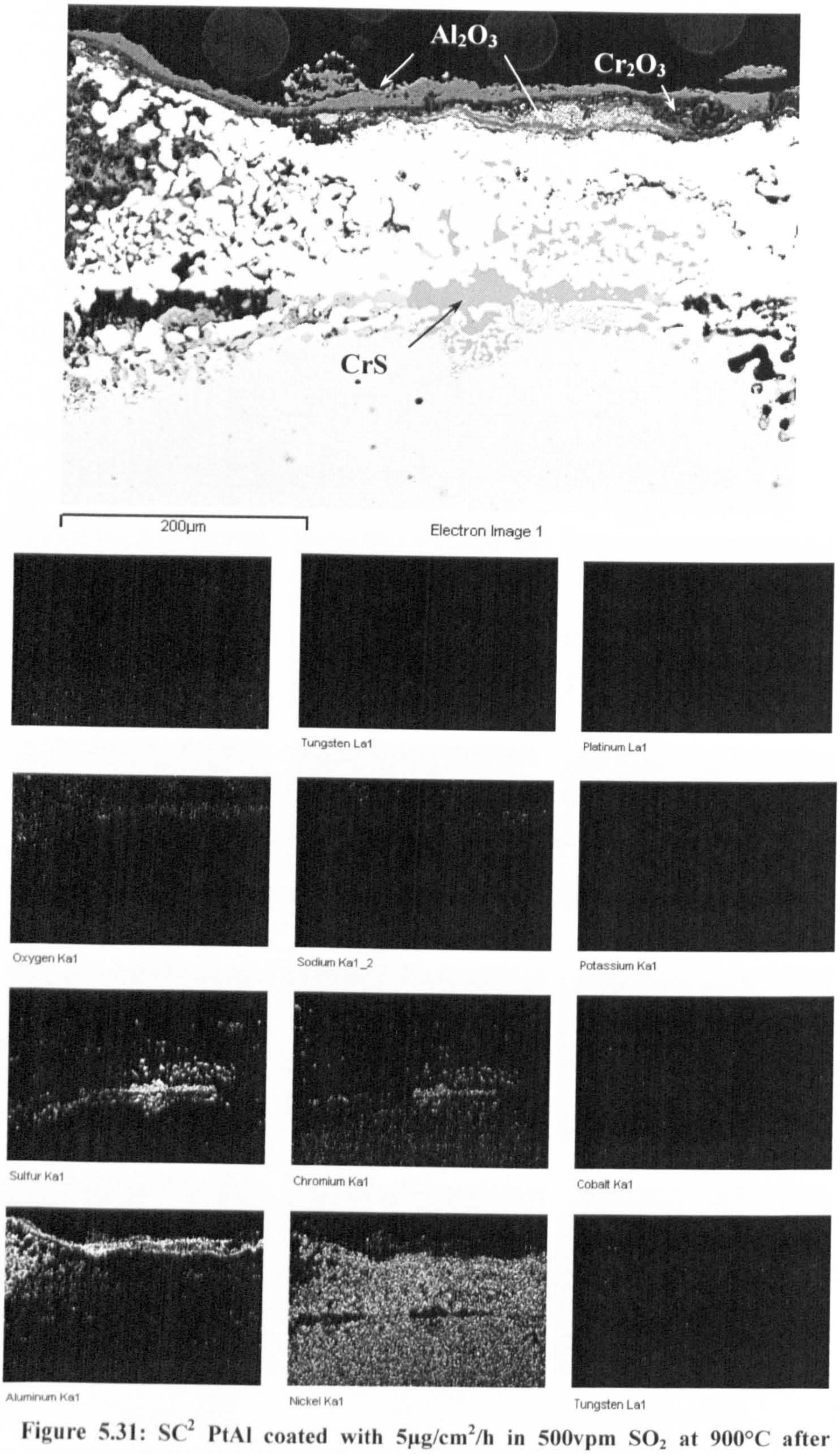

Figure 5.31: SC^2 PtAl coated with 5µg/cm^2/h in 500vpm SO_2 at 900°C after 500h exposure.

5.7 Life Prediction Models in Hot Corrosion Environments

Having addressed the main factors influencing the hot corrosion degradation sequence (i.e. incubation and then propagation periods) which describe the hot corrosion phenomena, it is now possible to derive models that allow predictions of the service life of both uncoated and PtAl coated CMSX4 and SC^2. These models are based on an analysis of the quantitative data obtained during the course of this research.

Options for improving the high-temperature corrosion resistance of material systems include extension of the incubation period and/or reduction of the propagations rates of hot corrosion. Future alloy/coating improvements are possible if quantitative information is available on the sensitivity of alloys/coating corrosion rates to changes in exposure conditions. Thus, this section discusses the results obtained and an analysis using the methods explained in section 4.4, to produce models that allow prediction of the life of the single crystals studied:

- Firstly, models that describe the incubation period in terms of time (hours) as a function of deposition flux, SO_x and HCl levels, for each single crystal/PtAl coating/temperature combination.
- Models that describe the propagation rate are then discussed in terms of metal loss rate (μm/h, at 4% probability of exceedance) as functions of deposition flux, SO_x and HCl levels for each single crystal/PtAl coating/temperature combination.

5.7.1 Incubation Models

To generate the incubation period models, an oxide scale break down value was taken from the mass change data (graphs presented in section 4.2) from the intersection point of the mass change trend with 0.1 $\mu g/cm^2$ (a value chosen to correspond to an oxide scale of approximately 0.5μm thick). The incubation times that have been calculated are summarized in Table 5.5 and Table 5.6 for the CMSX4 and SC^2 systems respectively. These values for incubation times were analysed using multiple linear regression of the logarithms of flux, SO_x and HCl to calculate a power law that best fits the data by the least square method. The generic equation for the incubation times is:

$$t = (flux)^a * (SO_x + 1)^b * (HCl + 1)^c * K$$

Equation 25

The unit corrections to the SO_x level and HCl level permit zero levels of SO_x and HCl to be modelled. The incubation time, t, is modelled as a function of the factors that have been discussed in sections 5.2 and 5.5: i.e. deposition flux and gas composition (i.e. SO_x and HCl concentrations). The a, b, c values are coefficients corresponding to the power law exponent of each factor and K is a constant. The coefficients, constants and correlation coefficient (r^2) values for all the single crystal/PtAl coating/temperature combinations are summarized in Table 5.7. Thus, the calculated incubation time can be plotted as a function of deposition flux for each gas composition environment to describe the behaviour of the materials/coating systems studied: Figure 2.1 is an example of such a plot.

Incubation										
Materials/ Temp.	700°C					900°C				
	Flux (a)	SO_x (b)	HCl (c)	K	r^2	Flux (a)	SO_x (b)	HCl (c)	K	r^2
CMSX4	-0.22	-0.90	0.13	194	0.92	-0.28	-0.28	0.21	55	0.79
SC[2]	0.02	-1.3	-0.11	6545	0.82	-0.28	-0.36	0.24	53	0.88
PtAl/CMSX4	-0.52	n/a	0.08	106	0.82	-1.41	n/a	-0.27	692	0.67
PtAl/SC[2]	-0.86	-0.19	0.04	70	0.85	-1.30	-0.83	-0.18	14267	0.61

Table 5.7: Incubation time exponents (a, b, c), constants (K) and correlation r^2 for all materials systems at 700 and 900°C. (n/a = no sample to analyse).

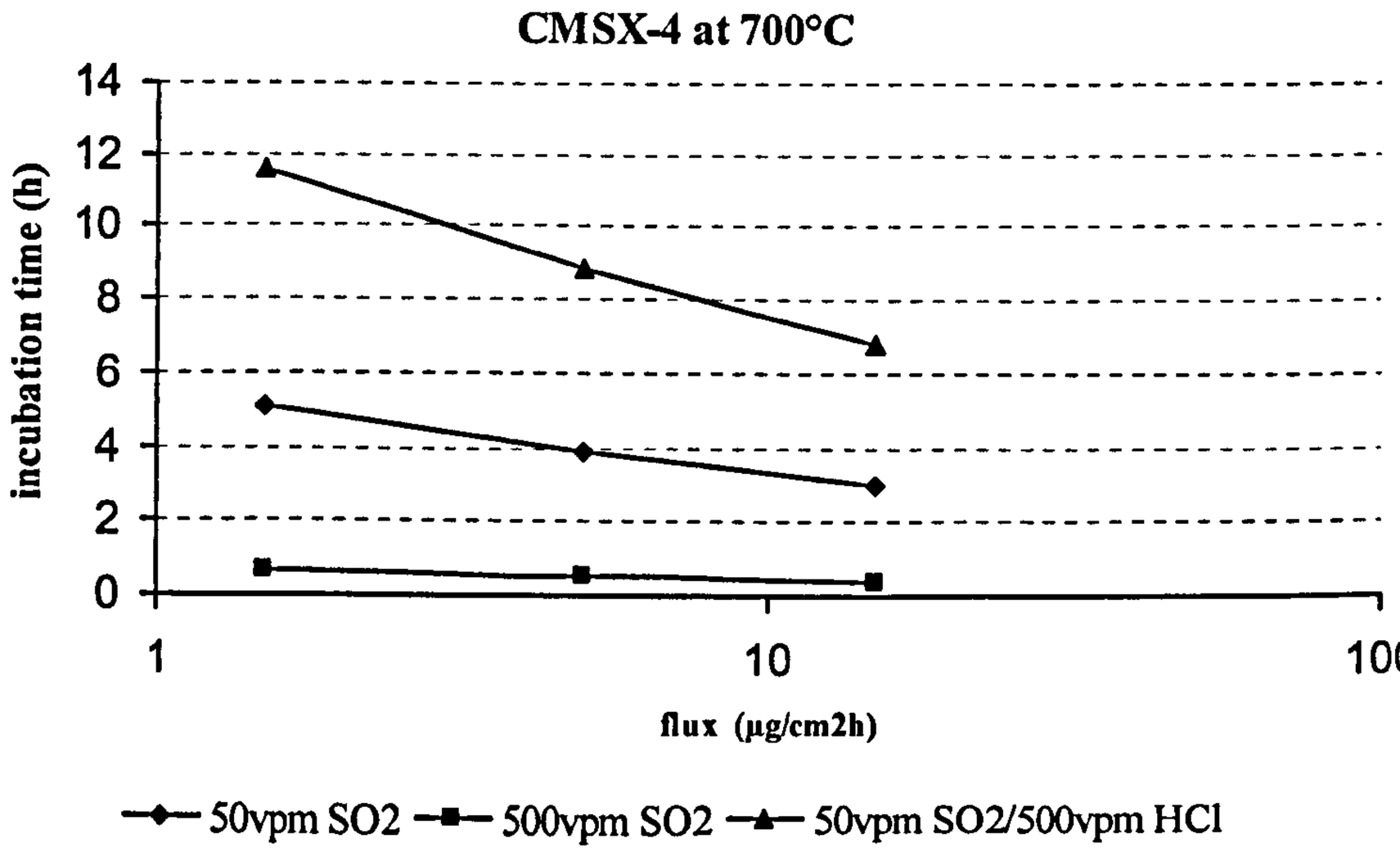

Figure 5.32: Example of the calculated incubation times for the CMSX4 at 700°C.

The trends in the incubation time described by the models can be summarized as follows:

- Uncoated CMSX4 and SC^2 at 700°C:

- The incubation time depends on deposition flux: it decreases as the deposition flux increases from the lower, to medium and then the maximum flux (the ten times change in deposition flux gave 0 to 0.5x change in the incubation time for CMSX4 and no change in incubation time for SC^2).
- The incubation time decreases by changing the gas concentration from 50vpm SO_2 to 500 vpm SO_2 (the ten times change in gas concentration gave 2-3 times change for CMSX4 and 3 times change for SC^2).
- For CMSX4, an increase in the incubation time by the addition of 500vpm HCl to the 50vpm SO_2 environment is observed (the HCl addition gives a 2x change in the incubation time with gas composition).

- Uncoated CMSX4 and SC^2 at 900°C:

- The same deposition flux dependency is observed at 900°C as at 700°C (the ten times change in deposition flux gave 2 times decrease for the both alloys).
- The same sensitivity to the change in SO_2 concentration is observed (the ten times change in gas concentration gave 2 times change for both alloys).
- HCl increased the incubation time for both materials in a 50vpm SO_2 environment (the HCl addition to the gas gave 2-3 times improvement for both alloys).

- PtAl/ CMSX4 and PtAl/SC^2 at 700°C:

- The incubation time dependence on deposition flux decreases with increasing deposition flux from the lower, medium and to the maximum flux (the ten times change in deposition flux gave 3-6 times decrease in incubation time for the Pt/Al SC^2).
- The incubation time decreases by changing the gas concentration from 50vpm SO_2 to 500 vpm SO_2 (the ten times change in gas concentration gave 1-2 times change for the PtAl/SC^2).
- For the PtAl/CMSX4 system, a decrease in the incubation time is observed by the addition of 500vpm HCl to the 50vpm SO_2 environment (this HCl addition gave a 0.5-1 times decrease for both alloys)

- PtAl/ CMSX4 and PtAl/SC^2 at 900°C:

- A similar deposition flux dependency is observed as that at 700°C (the ten times change in deposition flux gave 1-6 times change for the PtAl/ SC^2 system).

- The sensitivity to the change of SO_2 concentration is similar to that at 700°C (the ten times change in gas concentration gave 6 times change for the PtAl/SC^2 system).
- The PtAl/CMSX4 alloy showed an increased incubation time through the addition of HCl to the 50vpm SO_2 environment (this HCl addition gave between 1-10 times change for both alloys).

5.7.2 Propagation Models

To produce the propagation period models, the propagation rate was calculated as follows:

$$PR = (CR - 0.5) \div (500 - t)$$

Equation 26

This assumes that, during the incubation period 0.5µm of metal/coating is lost in the incubation time (t). CR is the sound metal loss at particular confidence level of 4% probability of being exceeded after 500 hours of exposure (summarized in Table 5.5 and Table 5.6). 0.5 is the equivalent of 0.1 mg/cm^2 mass gain expressed in µm. Having calculated the corrosion rate values, in the same way as for the incubation time, the main factors that determine the propagation rate were analysed by multiple linear regression to $\log(flux), \log(SO_x)$ and $\log(HCl)+1)$ to calculate a straight line by the least square method. The equation used for describing the propagation period is:

$$PR = (flux)^a * (SO_x + 1)^b * (HCl + 1)^c * K$$

Equation 27

The propagation rate, PR is a function of the various factors discussed in sections 5.2 and 5.5 that influence the propagation modes: i.e. deposition flux and gas composition, i.e. SO_x and HCl concentrations. The exponents a, b, c are independant coefficients corresponding to each factor and K is a constant. The coefficients, constants and correlation coefficient (r^2) values for all the materials are summarized in Table 5.8.

Propagation										
Materials/ Temp.	700°C					900°C				
	Flux (a)	SO_x (b)	HCl (c)	K	r^2	Flux (a)	SO_x (b)	HCl (c)	K	r^2
CMSX4	0.39	0.41	-0.03	0.01	0.91	0.59	0.17	-0.02	0.11	0.91
SC^2	0.52	0.70	0.00	0.001	0.85	0.64	0.64	-0.11	0.01	0.89
PtAl/CMSX4	0.32	n/a	0.04	0.09	0.82	0.54	n/a	-0.17	0.13	0.85
PtAl/SC^2	0.63	0.19	-0.17	0.00	0.96	0.83	n/a	0.05	0.00	0.78

Table 5.8: Propagation rates exponents (a, b, c), constants (K) and correlation r^2 values for all materials systems at 700 and 900°C. (n/a = no sample analysed).

The trends in the propagation rates described by the models are shown in Figure 5.33 to Figure 5.40 and can be summarized as follows:

- Uncoated CMSX4 and SC^2 at 700°C (Figure 5.33 and Figure 5.34)
  - The propagation rate depends on deposition flux: it increases with increasing deposition flux from the lower, to medium and then maximum flux (this ten times change in deposition flux gave 2-3 times change in propagation rate for the CMSX4 and 1.5-2.5 times for the SC^2).
  - The propagation rate increases by changing the gas concentration from 50vpm SO_2 to 500 vpm SO_2 (this ten times change in gas concentration gave 2-4 times change for the CMSX4 and 6-35 times for the SC^2)
  - For CMSX4, the propagation rate decreases with the addition of 500vpm HCl to the 50vpm SO_2 environment (this HCl addition to the gas composition gave no change to 2 times reduction in propagation rate for the CMSX4 and 2 times decrease for the SC^2).

- Uncoated CMSX4 and SC^2 at 900°C (Figure 5.35 and Figure 5.36)
  - A similar deposition flux dependency is observed to that at 700°C (the ten times change in deposition flux gave a 5 times increased in propagation rate for the CMSX4 and 2-5 increase for the SC^2)
  - The sensitivity to the change of SO_2 concentration was also similar to that observed at 700°C (the ten times change in the gas concentration gave 1-4 times change for the CMSX4 and 0.5-4.5 times change for the SC^2).
  - For both materials a decrease in the propagation rate was observed for the addition of 500vpm HCl to the 50vpm SO_2 environment (this HCl addition gave 0.5-1 times change for the CMSX4 and no change to 0.75 times increase for the SC^2).

For the Pt/Al coatings, in several cases, the corrosion damage had penetrated through the coating and progressed into the substrate. For these cases, the propagation damage rate calculated consisted of a mixture of damage to the coating and damage to the substrate. Therefore, these values could not be used in the models. These data on the graphs (in Figure 5.37 to Figure 5.40) are shown by open symbols and linked to the true coating data by dashed lines.

- PtAl/ CMSX4 and PtAl/SC^2 systems at 700°C (Figure 5.37 and Figure 5.38).
  - The propagation rate depends on deposition flux; it increases with increasing deposition flux from the lower, to medium and then maximum flux. (this ten times change in deposition flux gave between no change and 0.5 times change for the CMSX4 and 4-100 times for the SC^2).
  - The propagation rate also increases by changing the gas concentration from 50vpm SO_2 to 500 vpm SO_2 (this ten times change in the gas concentration gave 0.5-2 times for the SC^2).
  - For the PtAl/SC^2 system, a decrease in the propagation rate by the addition of 500vpm HCl to the 50vpm SO_2 environment is observed (this HCl addition to the gas composition gave 0.5-4 times change in propagation rate).

- PtAl/ CMSX4 and PtAl/SC^2 systems at 900°C (Figure 5.39 and Figure 5.40)
  - At 900°C, the same deposition flux dependency as observed at 700°C was found (a ten times change in deposition flux gave a 2 times increase in propagation rate for the CMSX4 and 2-10 times for the SC^2).
  - For the PtAl/CMSX4 alloy system, a decrease in the propagation rate was observed by the addition of HCl to the 50vpm SO_2 environment (this HCl addition gave a 2 times decrease in propagation rate).

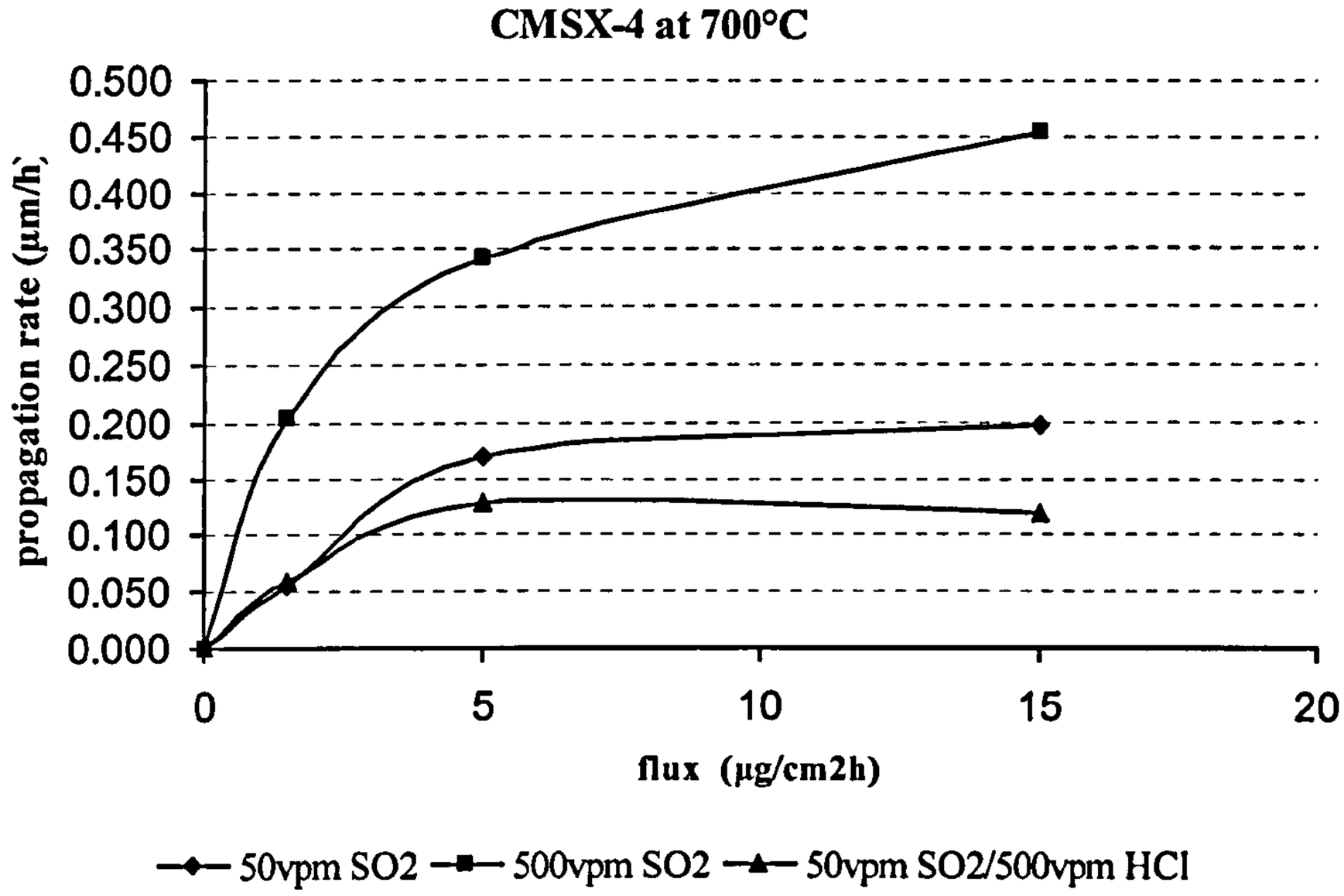

Figure 5.33: Propagation rate model of the uncoated CMSX4 at 700°C as a function of deposition flux and gas composition.

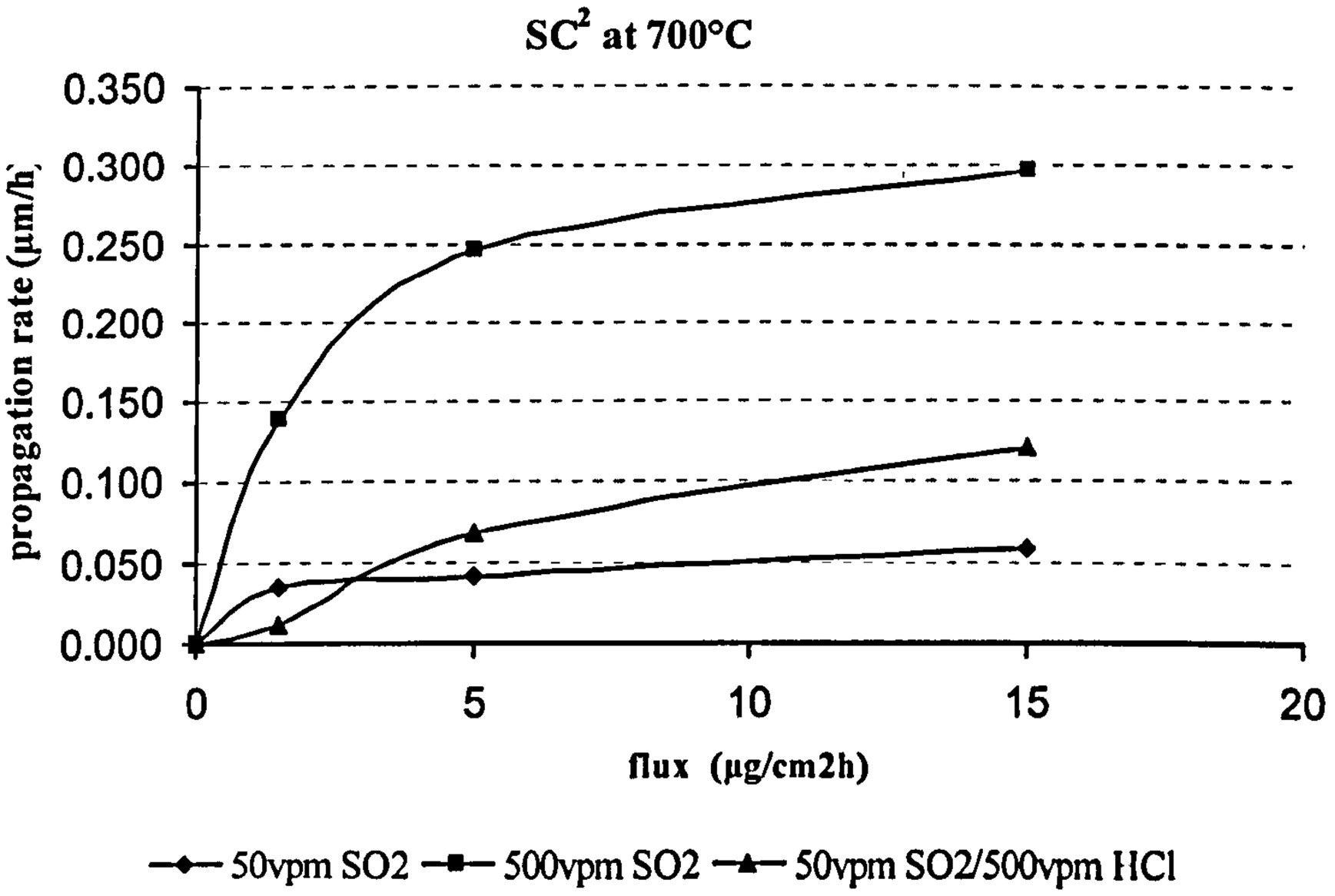

Figure 5.34: Propagation rate model of the uncoated SC^2 at 700°C as a function of deposition flux and gas composition.

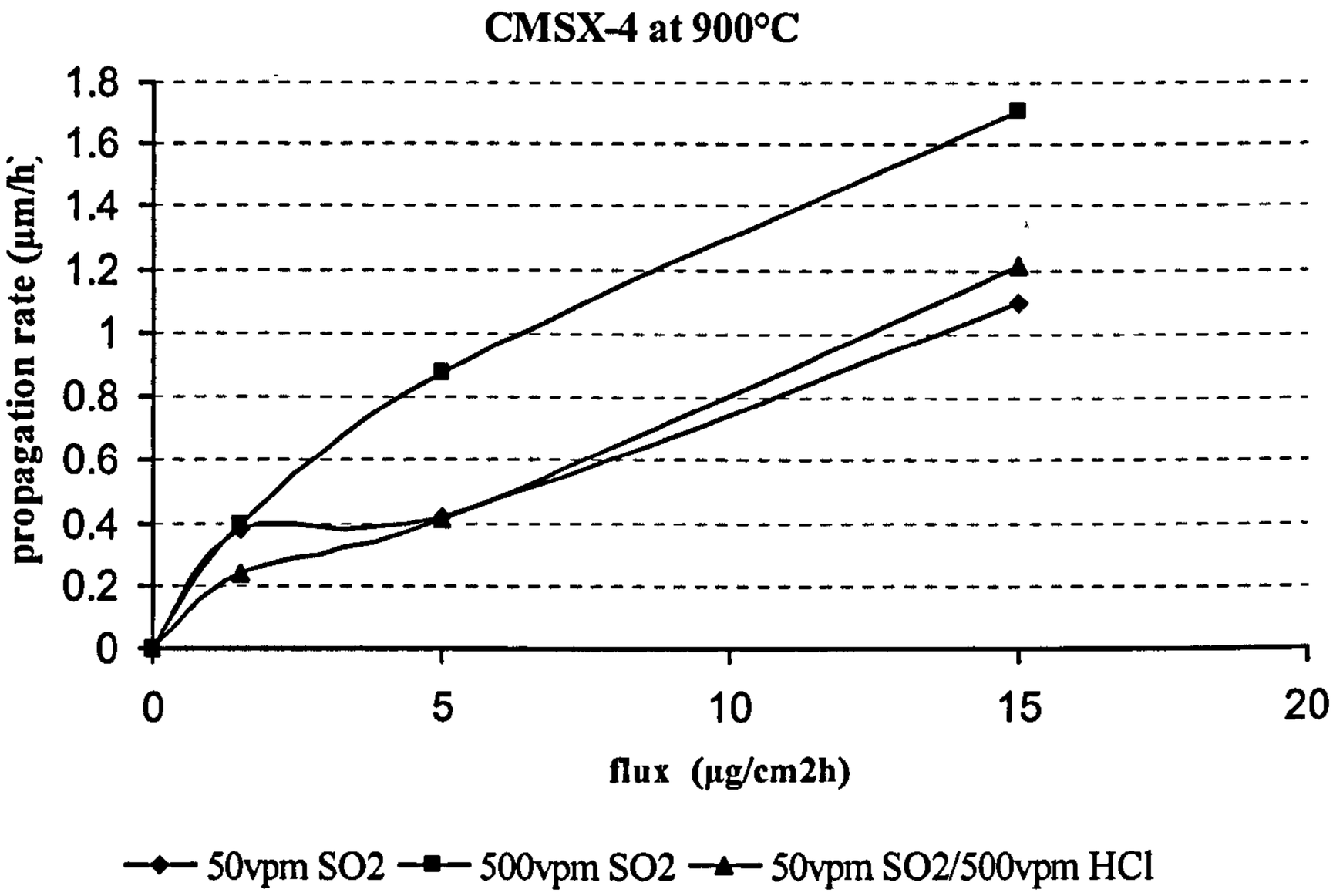

Figure 5.35: Propagation rate model of the uncoated CMSX4 at 900°C as a function of deposition flux and gas composition.

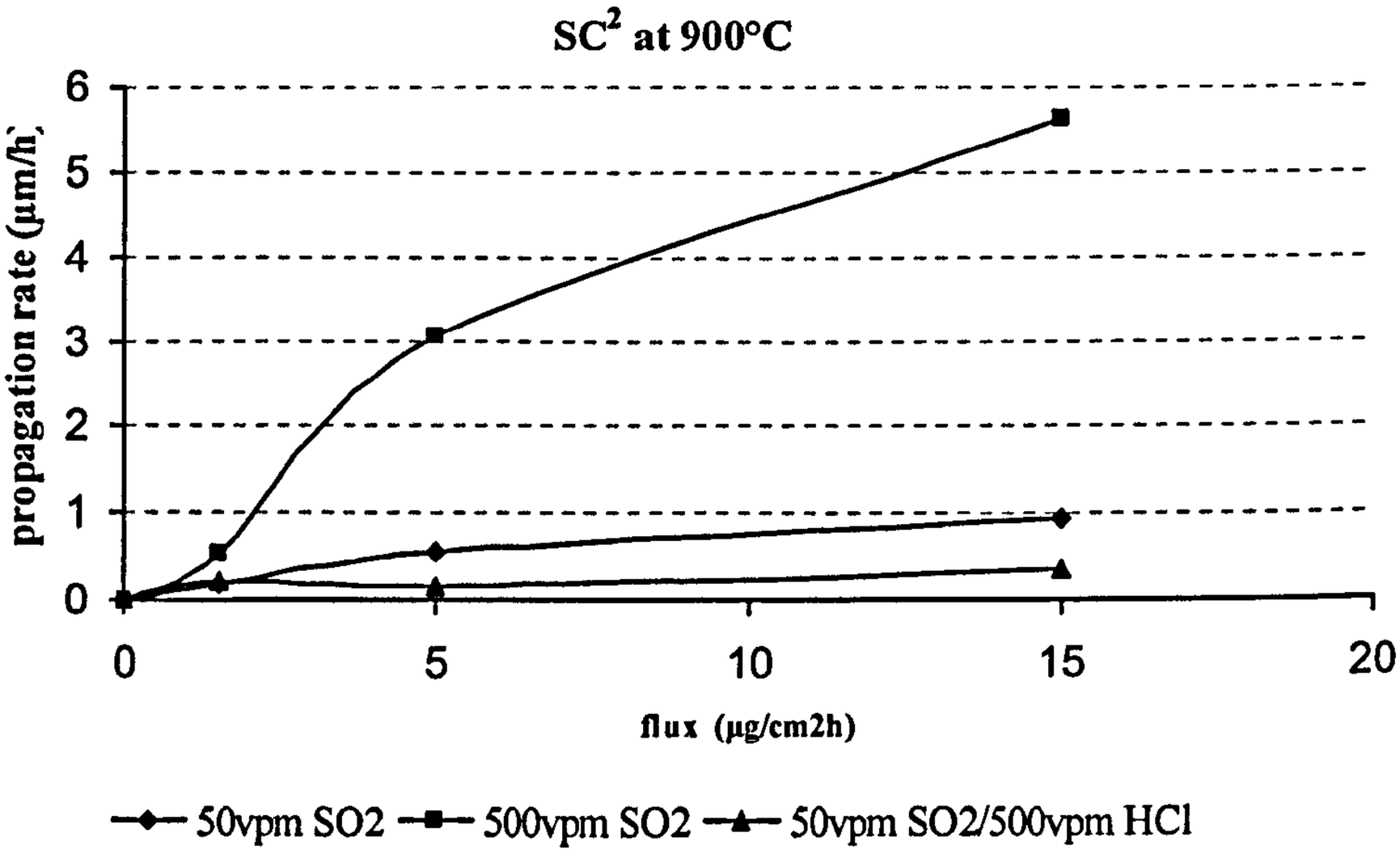

Figure 5.36: Propagation rate model of the uncoated SC^2 at 900°C as a function of deposition flux and gas composition.

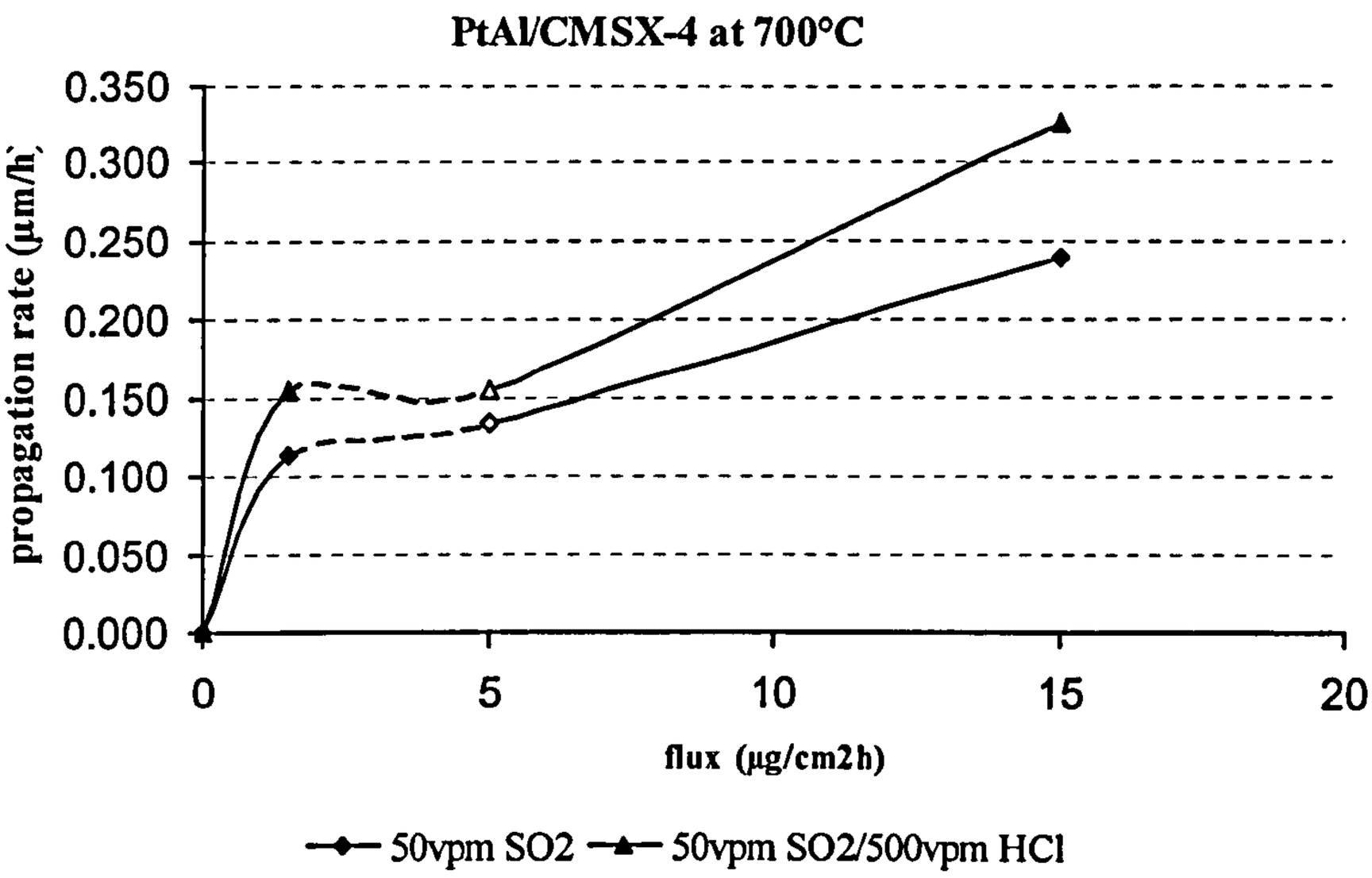

Figure 5.37: Propagation rate model of the PtAl coated CMSX4 at 700°C as a function of deposition flux and gas composition.

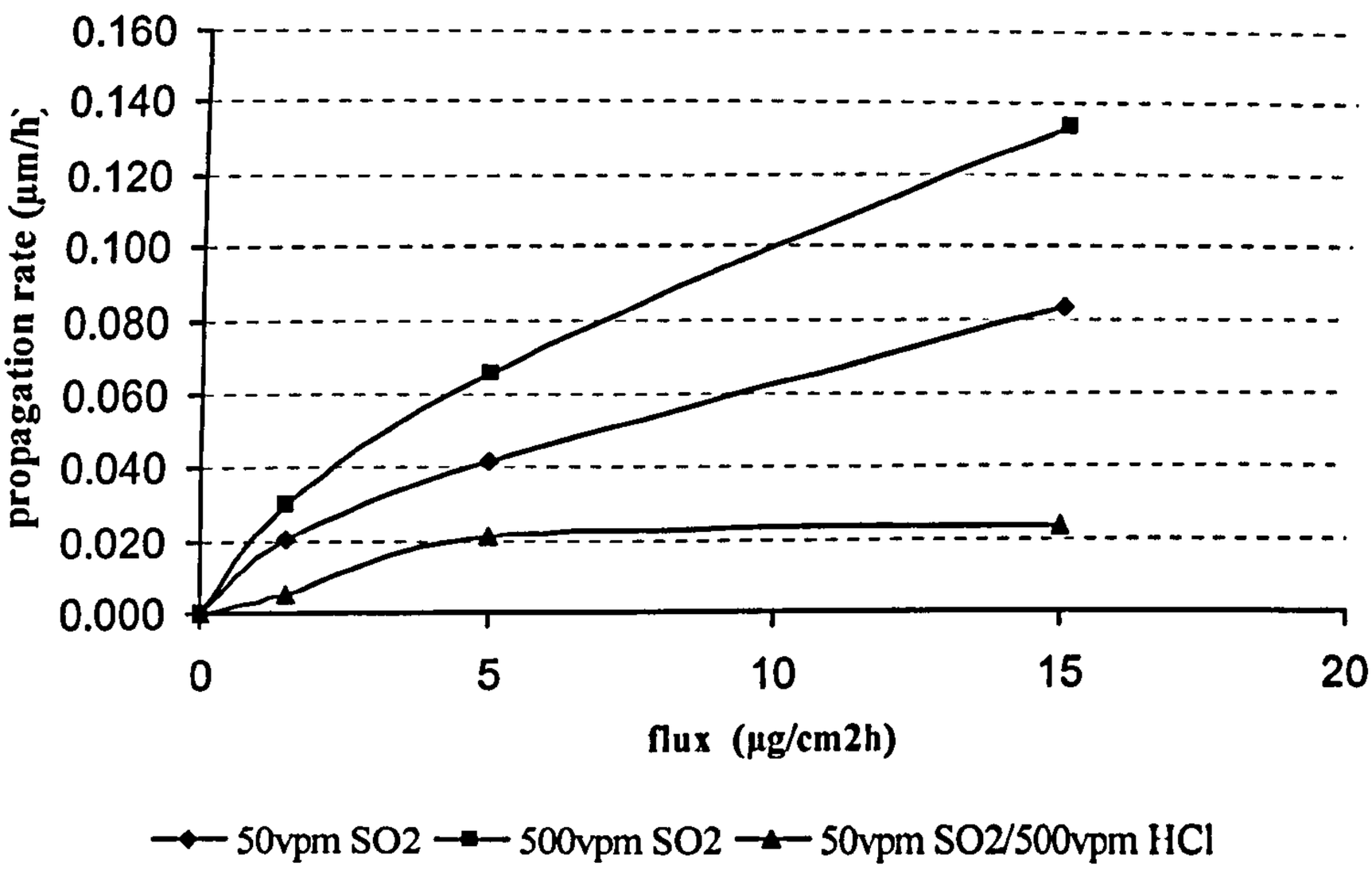

Figure 5.38: Propagation rate model of the PtAl coated SC^2 at 700°C as a function of deposition flux and gas composition.

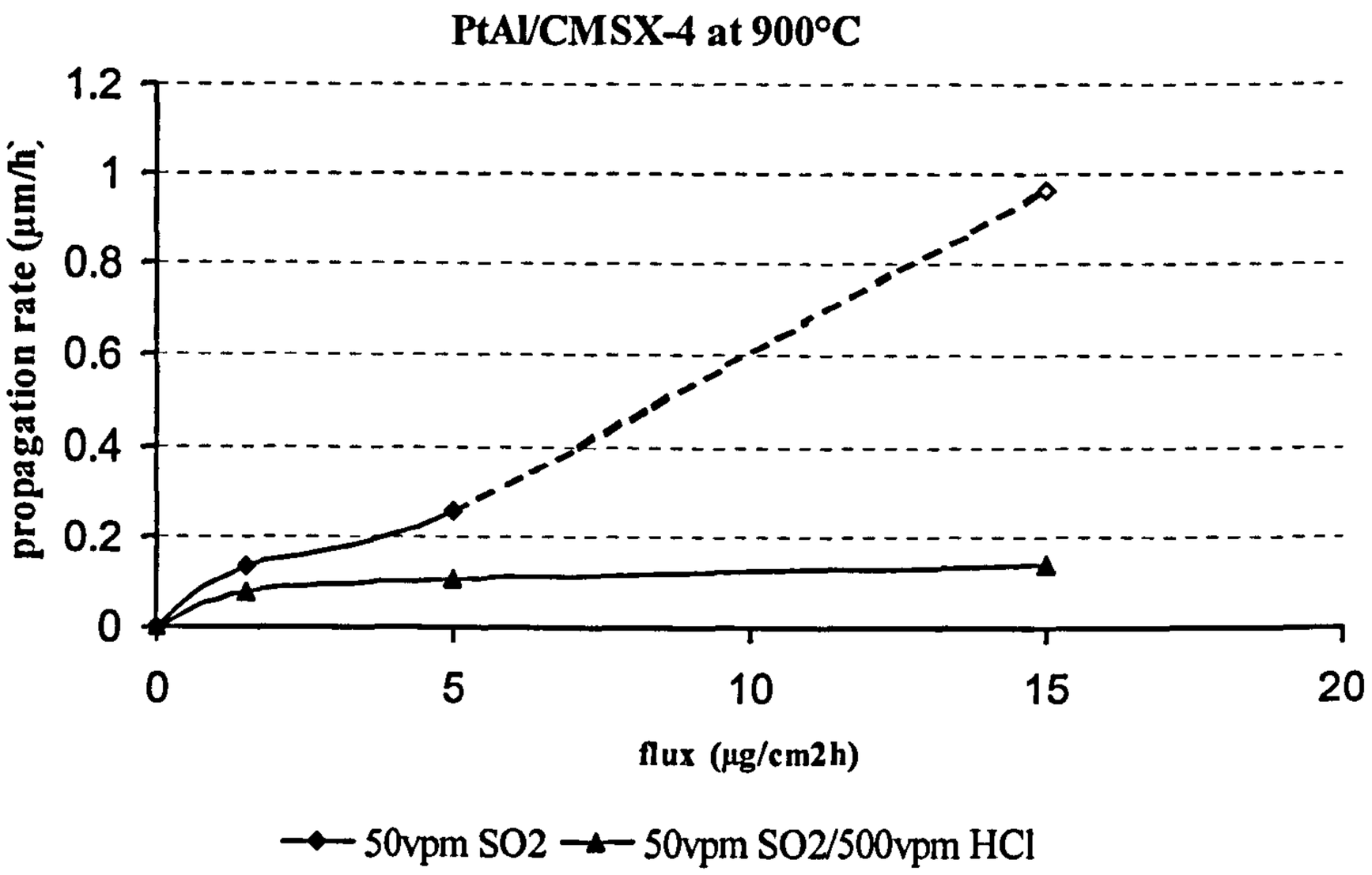

Figure 5.39: Propagation rate model of the PtAl/coated CMSX4 at 900°C as a function of deposition flux and gas composition.

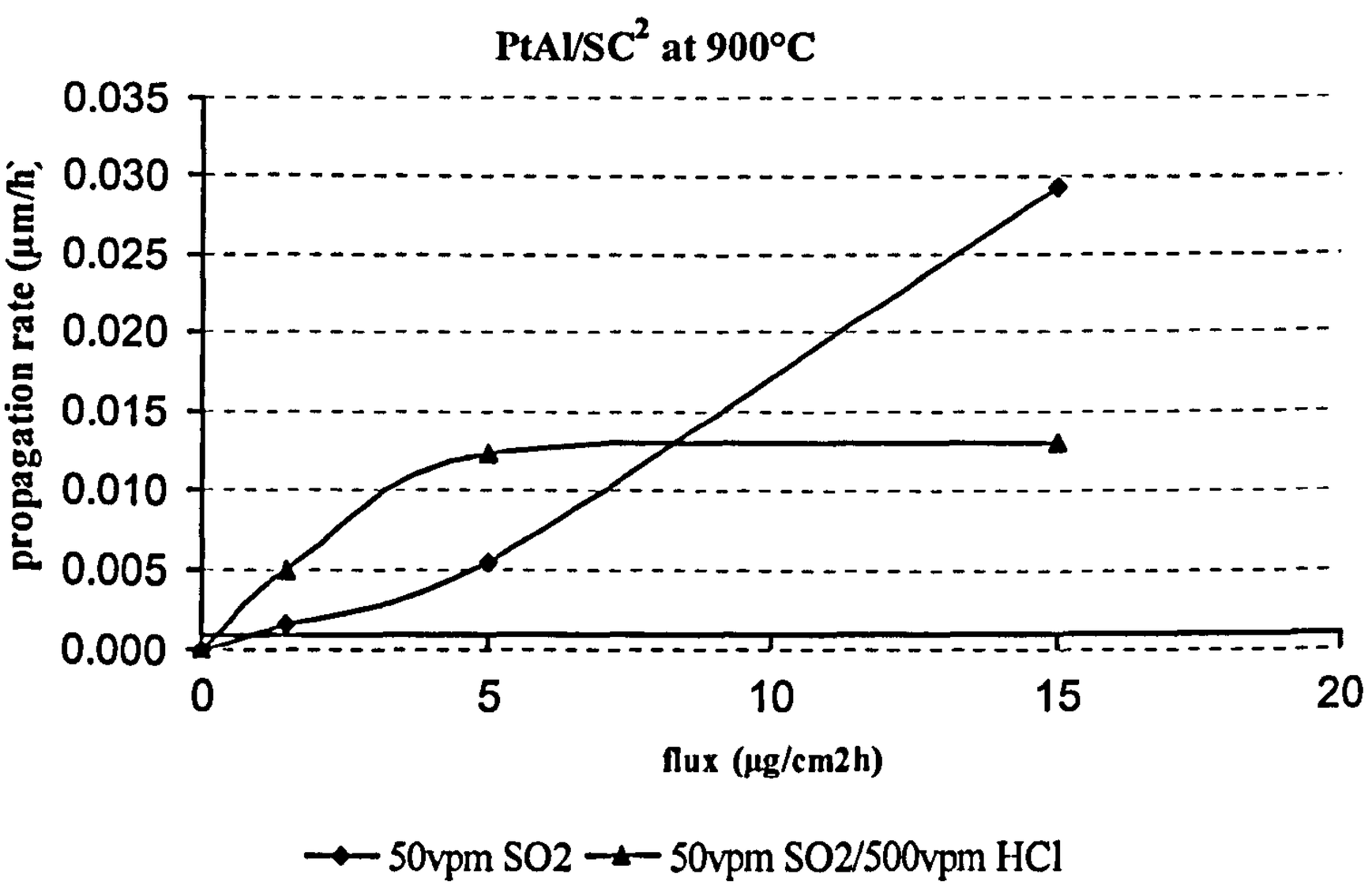

Figure 5.40: Propagation rate model of the PtAl coated at 900°C as a function of deposition flux and gas composition.

6 Conclusions

- The main factors that determine the hot corrosion degradation of materials were successfully reproduced in laboratory tests, i.e. variations in deposition fluxes and compositions, gases concentrations and compositions, and temperatures by the methods described in this work.

- The methods used and data collected from these tests have allowed a systematic study of the hot corrosion process and both a qualitative and quantitative assessment of the materials systems performance.

- Typical type I hot corrosion morphologies were observed; broad non-uniform distributions of pits around the sample surfaces.

- The typical type II morphologies were not observed on those materials exposed with an HCl addition to the environment; these tended to show more damage.

- From these quantitative metal loss and qualitative mass change data, life prediction models for CMSX4 and SC^2, both PtAl coated and uncoated, have been developed to describe/predict the commencement of hot corrosion failure under the different conditions in the type I and type II hot corrosion temperature ranges.

- All material systems investigated showed that the hot corrosion regime, and corrosion rates, directly depend on the deposition flux: corrosion rates increased from the low flux to the medium flux approximately by a factor of 1-2, and then to maximum flux approximately by a factor 2-3, for both type I and type II hot corrosion.

- The alloying element contents define the modes of attack under the hot corrosion conditions. Elements such as chromium are shown to have an important role in the hot corrosion resistance of the materials, both for PtAl coated and uncoated materials.

- Materials/coatings have been shown to be very sensitive to changes in their environment: corrosion rates increased significantly (approximately as a factor of 2-7 times) with a ten times increase in the SO_2 gas concentration. This SO_2 increment influenced the mechanism of attack only for SC^2, at both type I and type II hot corrosion temperatures.

- The HCl addition to the environment proved to be beneficial for the uncoated materials at 900°C. This effect is believed to be due to the HCl reducing the amount of SO_2 in the deposit/surface.

- In most cases, the Pt/Al coating extended the incubation time of the material/systems, approximately by a factor of 2-10 times.

- Separate models have been developed for the two single crystals superalloys: CMSX4 and SC[2], in both the uncoated and platinum aluminide coated condition. The goodness of fit as defined by the regression coefficient varies from 0.88 to 0.99 for the propagation models at 700 and 900°C. The incubation models are as precise at 700°C but less precise at 900°C with regression coefficients of 0.78-0.94.

- The corrosion rates of the uncoated single crystals, CMSX4 and SC[2], are too high for them to be used with confidence in gas turbines fired with gases derived form coal and/or biomass, without some form of protective coating.

- Platinum/aluminium coating provided protection in the most mild environments studied i.e. a flux of 1.5 $\mu g/cm^2/h$ flux for 50vpm SO_2 gas and 50vpm SO_2/500vpm HCl gas mixtures.

- Under the more severe combinations of gas composition, deposition flux and metal temperature, the corrosion rates of these single crystals with platinum/aluminium coatings are also excessive and, therefore, the coatings do not provide sufficient protection. This high lights the need for improved coating designs to combat highly corrosive conditions.

7 Suggestions for Future Work

- The HCl beneficial/neutral effect on the hot corrosion reactions should be fully investigated to establish a more detailed mechanism model.

- The incubation times could be thoroughly investigated by examining specimens after 20, 20 and 100 h of exposure in cycles of 20, 50 and 100 hours.

- To extend the studies on the effects of contaminants from biomass- and waste-fired gas turbine generation. For example, the increase in corrosion rates from the 50/50 $(Na/K)_2SO_4$, or the decrease corrosion rates by the presence of lead.

- Other coating systems, e.g. silica-modified aluminides and/or overlay coatings (e.g. smart coatings), could be investigated under a range of hot corrosion conditions.

- For exposure in severe hot corrosion conditions, single crystals alloys could be developed that have more inherent corrosion resistance, by increasing the chromium levels and redistributing the other elements.

Reference List

?[1] Simms N.J., Oakey J.E., and Smith M.A. (1991), 'Materials Issues for Coal-Fired Combined Cycle Power Plants', in *Materials for Combined Cycle Power Plan* , Vol. 229-240 at Sheffield, UK; Institute of Metals,

[2] Allen D.H., Oakey J.E., and Scarlin B. (1998), Lecomte-Beckers J *Materials for Advanced Power Engineering* pp. 1825-1839.

[3] Schulenberg T. (1998), 'New Development in Land-Based Gas Turbine Technology', in Lecomte-Beckers J *Materials for Advanced Power Engineering* pp. 849-859 .

[4] Van Liere J. (1997), 'Present Status of Advanced Coal-Fired Power Plants. ', in *Corrosion in Advanced Power Plants. Proceedings of the Second International Workshop on Corrosion in Advanced Power Plants. Materials at High Temperature.* Vol. 7 at Tampa, Florida;

[5] Energy Consumption in The United Kingdom. *Dep. of Trade and Industry. National Statistics.*,

[6] Holt N.A.H. (2003), 'Operating Experience and Improvement Opportunities for Coal-Based IGCC Plants', in Norton J.F. et al. *Life Cycle Issues in Advanced Energy Systems. Materials at High Temperature* at Woburn; UK,

[7] Ruth L.A (2003), 'Advanced Clean Coal Technology in the USA.', in Norton J.F. et al. *Life Cycle Issues in Advanced Energy Systems. Materials at High Temperature* at Woburn; UK,

x [8] Market Trends (1990), *Gas Turbine World Handbook*, pp. 2-5.

[9] Schlachter W. and Gessiger G.H. (1990), 'Innovation in Power Engineering Role of Materials', in *High Temperature Materials for Power Engineering 1990. Part 1* , Vol. 1 Kluwer, pp. 1-24.

? [10] Gyarmathy G. (1991), 'Technical Aspects of Combined-Cycle Plants', in *Materials for Combined Cycle Power Plan* at Sheffield, UK; Institute of Metals, pp. 1-16.

? [11] Allen J. and Stringer J. (1991), 'Materials Experience in the United States With Large Gas-Fired Combined Cycle Plants', in *Materials for Combined Cycle Power Plan* at Sheffield, UK; Institute of Metals, pp. 17-24.

[12] Yamamoto K. , Kajigaya I., and Umaki H. (2003), 'Operational Experience of USC Steam Condition Plant and PFBC Combined Cycle System With Material Performance', in Norton J.F. et al. *Life Cycle Issues in Advanced Energy Systems. Materials at High Temperature* at Woburn; UK,

[13] Wilson C. L. (1977), *Report of the Workshop on Alternative Energy Strategies. Energy: Global Prospects 1985-2000*, McGraw Hill,

[14] Salo K. (1998), 'Kotka Ecopower IGCC-Project, the Attempt to Transfer the Biocycle Project to Finland', *Biomass and Bioenergy* , Vol. 15, No. 3, pp. 225-228.

[15] Radcliff A.S. (1987), 'Factors Influencing Gas Turbine Use and Performance', *Material Science and Technology* , Vol. 3, pp. 554-561.

[16] Simms N.J., Oakey J.E., Stephenson D.J., Smith P.J., and Nicholls J.R. (1995), 'Erosion-Corrosion Modelling of Gas Turbine Materials', *Wear*, Vol. 186-187, pp. 248-255.

[17] Stoiber J and Singheiser L. 'Case Study of Sulphate Induced Hot Corrosion in a Modern Industrial Gas Turbine', in *Materials Ageing and Component Life Extension* at Milan, Italy; pp. 1377-1386.

[18] Kilgallon P., Simms N.J., and Oakey J.E. (2002), 'Fate of Trace Contaminants From Biomass Fuels in Gasification Systems', in Lecomte-Beckers J et al. *Materials for Advanced Power Engineering 2002. Proceedings of the 7th Liege Conference Part II,* Vol. 21 Forschungszentrum Julich GmbH, pp. 903-911.

[19] Tschinkel J.G. (1972), 'Formation of Sodium Sulphate in Gas Turbine Combustors', *Corrosion*, Vol. 28, No. 5, pp. 161-169.

[20] Gibb W.H. (1983), 'The Nature of Chlorine in Coal and Its Behaviour During Combustion', in Meadowcroft D. B. and Manning M.I. *Corrosion Resistant Materials for Coal Conversion Systems*, Applied Science, London, pp. 25-45.

[21] Spacil H.S. and Luthra K.L. (1982), 'Volatization/Condensation of Alkali Salts in a Pressurized Fluidized Bed Coal Combustor/Gas Turbine Combined Cycle', *Journal of the Electrochemical Society*, Vol. 129, No. 9, pp. 2119-2126.

[22] Stringer J. (1977), 'Hot Corrosion of High Temperature Alloys', *Annual Review Material Science*, Vol. 9, pp. 447-509.

[23] Stringer J. (1995), 'Practical Experience With Wastage at Elevated Temperatures in Coal Combustion Systems', in Hutchings I.M. and Little J.A. *Erosion by Liquid and Solid Impact,* Vol. 186-187 no.2 at Cambridge; ELSEVIER, Amsterdam, pp. 11-27.

[24] Meadowcroft D. B. and Stringer J. (1987), 'Corrosion in Coal-Fired Gas Turbines', *Material Science and Technology*, Vol. 3, pp. 562-570.

[25] Simms N.J., Encinas-Oropesa A., Kilgallon P., and Oakey J.E. (2002), 'Performance of Gas Turbine Materials in "Dirty Fuel" Environments', in Lecomte-Beckers J et al. *Materials for Advanced Power Engineering 2002. Proceedings of the 7th Liege Conference Part II,* Vol. 21 Forschungszentrum Julich GmbH, pp. 923-932.

[26] Simms N.J., Smith P.J., Nicholls J.R., and Oakey J.E. (1994), Grimethorpe Toping Cycle Project. Corrosion Modelling.,

[27] Cabrillac C., Leach J. S. L., Marcus P., and Pourbaix A (1983), 'The Cost of Corrosion in the EEC', *Met. Materials*, Vol. 3, No. 9, pp. 533.

[28] Cost of Corrosion: $300 Billion a Year (1995), *Materials Performance*, pp. 5.

[29] NACE and NBS Enter a Cooperative Corrosion Data Agreement (1983), *NACE News*, pp. 57.

[30] Sims C.T., Stoloff N.S., and Hagel W.H. (1987), *Superalloys II. High Temperature Materials for Aerospace and Industrial Power.*, J. Wiley , New York.

[31] Molloy W.J. (1990), 'Investment Cast Superalloys a Good Investment', *Advanced Materials and Processes*, Vol. 138, No. 4, pp. 23-30.

[32] E.W.Ross and C.T.Sims (1987), 'Nickel-Based Alloys', in *Superalloys II. High Temperature Materials for Aerospace and Industrial Power.* J Wiley, New York, pp. 97-134.

[33] Sims C.T. and Hagel W.H. (1972), 'The Superalloys. Vital High Temperature Gas Turbine Materials for Aerospace and Industrial Power', USA, pp. 595.

[34] Mercier S, Bacos M-P, and Josso P (2004), 'Innovative Coating for Aggressive Environments: Land-Based Turbine Applications.', in *6th International Symposium on High-Temperature Corrosion and Protection of Materials* at Les Embiez Fr;

[35] Gleeson B. (2000), 'High Temperature Corrosion of Metallic Alloys and Coatings.', in Schutze M. *Materials Science and Technology. Corrosion and Environmental Degradation Vol II.*, Wiley-vch, N.Y., pp. 174-228.

[36] Stringer J. and Wright I. (1995), 'Current Limitations of High Temperature Alloys in Practical Applications', *Oxidation of Metal*, Vol. 44 , No. 1/2, pp. 271-308.

[37] Caron P., Escale A., McColvin G., Blackler M., Wahi R., and Lelait L. *Proceedings of the 5th International Charles Parsons Turbine Conference: PARSONS 2000- Advanced Materials for 21st Century Turbines and Power Plant.* at Cambridge; pp. 847-864.

[38] Angenete J. (2002), *Aluminide Diffusion Coatings for Ni Based Superalloys. Coating and Oxide Microstructure.* Department of Experimental Physics. Chalmers University of Technology. Goteborg University, Goteborg, Sweden.

[39] Giggins C.S. and Pettit F.S. (1971), 'Oxidation of Ni-Cr-Al Alloys Between 1000° and 1200°C', *Journal of the Electrochemical Society*, Vol. 118, pp. 1782-1790 .

[40] Vogel D., Newman L., Deb P., and Boone D.H. (1987), 'Ductile-to-Brittle Transition Temperature Behaviour of Platinum-Modified Coatings', in *High Temperature Corrosion of Materials and Coatings for Energy Systems and Turboengines* , Vol. II at Marseille, France; ELSEVIER, pp. 227-231.

[41] Smialek J.L. and Meier G.H. (1987), 'High Temperature Oxidation', in *Superalloys II. High Temperature Materials for Aerospace and Industrial Power.* J. Wiley , New York, pp. 293-326.

[42] Bradford S.A. (1987), 'Fundamentals of Corrosion in Gases', in *Metals Handbook* (9 edition), Vol. 13, ASM International, U.S.A., pp. 61.

[43] Richardson F.D. and Jeffes H.E. (1952), 'The Thermodynamics of Substances of Interest in Iron and Steel Making. III Sulphides', *Journal of the Iron and Steel Institute*, pp. 165-175.

[44] Ellingham J.H.T. (1944), 'Reducibility of Oxides and Sulphides in Metallurgical Processes', *Journal of the Society of Chemical Industry*, Vol. 63 , No. 125, pp. 125-133.

[45] Kofstad P. (1988), *High Temperature Corrosion*, Elsevier Applied Science, London & New York.

[46] Kofstad P. (1966), *High Temperature Oxidation of Metals*, Wiley, New York.

[47] Kubaschewski O. and Hopkins B.E. (1967), *Oxidation of Metals and Alloys* (2 edition), Butterworth, London.

[48] Evans U.R (1961), *The Corrosion and Oxidation of Metals*, Edward Arnold Ltd., London.

[49] Birks N. and Meier G.H. (1983), *Introduction to High Temperature Oxidation of Metals*, Edward Arnold, London.

[50] Kofstad P. (1981), 'Oxidation Mechanisms for Pure Metal in Single Oxidant Gases', in Rapp R.A. *High Temperature Corrosion* at San Diego, California; National Association of Corrosion Engineers, Houston Texas, pp. 123-138.

[51] Hsu H.S. (1987), 'Review of the Development and Breakdown of Protective Oxide Scales on Alloys Exposed to Coal-Derived Atmospheres', *Oxidation of Metal*, Vol. 28 , No. 3/4, pp. 213-235.

[52] Wagner C. (1951), 'Diffusion and High Temperature Oxidation of Metals', in *Atom Movements* , The American Society for Metals, pp. 153.

[53] Wagner C. (1975), 'Equations for Transport in Solid State Chemistry.', *Progress in Solid State Chemistry*, Vol. 10 part 1, pp. 3-16.

[54] Corrosion Control (1979), in Frank N. Kemmer *The NALCO Water Handbook*, McGraw-Hill , pp. 1-15.

[55] Pettit F.S. and Giggins C.S. (1987), 'Hot Corrosion', in *Superalloys II* , J. Wiley, U.S.A., pp. 327-357.

[56] Johnson D.M., Whittle D.P., and Stringer J. (1975), 'Mechanisms of Na_2SO_4 -Induced Accelerated Oxidation', *Corrosion Science*, Vol. 15, pp. 721-739.

[57] Bornstein N.S. and DeCrescente M.A. (1971), 'The Role of Sodium in the Accelerated Oxidation Phenomenon Termed Sulfidation', *Metallurgical Transactions*, Vol. 2, pp. 2875-2883.

[58] Bornstein N.S. and DeCrescente M.A. (1969), 'The Relationship Between Compounds of Sodium and Sulfur and Sulfidation', *Transactions of the Metallurgical Society of AIME*, Vol. 245, pp. 1947-1952.

[59] Goebel J.A. , Pettit F.S., and Goward G.W. (1973), 'Mechanism for the Hot Corrosion of Nickel-Base Alloys', *Metallurgical Transactions*, Vol. 4, pp. 261-278.

[60] Goebel J.A. and Pettit F.S. (1970), 'Na_2SO_4- Induced Accelerated Oxidation (Hot Corrosion) of Nickel', *Metallurgical Transactions*, Vol. 1, pp. 1943-1954.

[61] (1979), Hot Corrosion Degradations of Metals. A Unified Theory Final Scientific Report., Pratt & Whitney Aircraft Group, Florida, USA.

[62] Conde J.F.C., Erdos E., and Rahmel A 'Mechanisms of Hot Corrosion', in *Proceedings of High Temperature Alloys for Gas Turbines* at Belgium; pp. 99-148.

[63] Khanna, A. S. and Jha S.K. (1998), 'Degradation of Materials Under Hot Corrosion Conditions', *Transactions of the Indian Institute of Metals*, Vol. 51, No. 5, pp. 279-290.

[64] *Handbook of Chemistry and Physics* (1973), (53 edition), The Chemical Rubber Co., Cleveland, Ohio.

[65] Roth R.S., Negas T., and Cook L.P. (1981), *Phase Diagrams for Ceramist*, Vol. IV. Completed at the National Bureau of Standards, The American Ceramic Society, U.S.A.

[66] Singh P. and Birks N. (1978), 'Reaction of Cobalt in Ar-SO_2 Atmospheres at 500-900°C', *Oxidation of Metals*, Vol. 12, No. 1, pp. 23-34.

[67] Mckee D.W., Shores A., and Luthra K.L. (1978), 'The Effect of SO_2 and NaCl on High Temperature Hot Corrosion', *Journal of the Electrochemical Society. Solid-State Science and Technology*, Vol. 125, No. 3, pp. 411-419.

[68] Giggins C.S. and Pettit F.S. (1980), 'Corrosion of Metals and Alloys in Mixed Gas Environments at Elevated Temperatures', *Oxidation of Metals*, Vol. 14, pp. 363-413.

[69] Meier G.H., Birks N., Pettit F.S., and Giggins C.S. (1981), 'Thermodynamic Analyses of the High Temperature Corrosion of Alloys in Gases Containing More Than One Reactant', in Rapp R.A. *High Temperature Corrosion* at San Diego, California; National Association of Corrosion Engineers, Houston Texas, pp. 327-335.

[70] Hancock P. (1982), 'The Use of Laboratory and Test Rigs to Simulate Gas Turbine Corrosion Problems', *Corrosion Science*, Vol. 22, No. 1, pp. 51-64.

[71] Simms N.J., Smith P.J., Encinas-Oropesa A., Ryder S., Nicholls J.R., and Oakey J.E. (2001), 'Development of Type II Hot Corrosion in Solid Fuel Fired Gas Turbine', in *Life Time Modelling of High Temperature Corrosion Processes. Proceedings of an EFC Workshop 2001* , Vol. 34 Maney Publishing, London, pp. 247-260.

[72] Duret-Thual C., Morbioli R., and Steinmetz P (1986), *A Guide to the Control of High Temperature Corrosion and Protection of Gas Turbine Materials.*, Commission of the European Communities, Belgium .

[73] Beltran A. and Shores A. (1972), 'Hot Corrosion', in *The Superalloys* , J. Wiley, New York, pp. 317.

[74] Rapp R.A. and Goto K.S. (1981), 'The Hot Corrosion of Metals by Molten Salts ', in Braunstein J. and Selman J.R. *Molten Salts*, The Electrochemical Society, NJ, pp. 159-177.

[75] Gupta K. and Rapp R.A. (1980), 'The Solubilities of NiO, CO_3O_4 and Ternary Oxides in Fused Na_2SO_4 at 1200° K', *Journal of the Electrochemical Society*, Vol. 127 , No. 10, pp. 2194-2201.

[76] Rapp R.A. (1987), 'Chemistry and Electrochemistry of Hot Corrosion of Metals', *Materials Science and Engineering*, Vol. 87, pp. 319.

[77] Bornstein N.S. and DeCrescente M.A. (1970), 'The Role of Sodium and Sulfur in the Accelerated Oxidation Phenomena-Sulfidation', *Corrosion*, Vol. 26, no. 7, pp. 209-214.

[78] Wootton M.R. and Birks N. (1972), 'The Oxidation of Nickel in Atmospheres Containing Sulphur Dioxide', *Corrosion Science*, Vol. 12, pp. 829-841.

[79] Chang D.R., Nemoto R, and Wagner J.B., Jr. (1976), 'The Diffusion of Sulfur-35 in NiO', *Metallurgical Transactions*, Vol. 7A, pp. 803-806.

[80] Luthra K.L. and Shores A. (1980), 'Mechanism of Na_2SO_4 Induced Corrosion at 600°- 900° C', *Journal of the Electrochemical Society*, Vol. 127 no.10, pp. 2202-2210.

[81] LeBlanc O. and Shores A. (1982), 'Thermodynamics of Molten $NiSO_4$-Na_2SO_4 at 1000 °-1300° K', in *Extended Abstracts, Fall Meet of the Electrochemical Society* at Montreal; Electro Chemical Society, Pennington NJ, pp. 416-417.

[82] Misra A.K., Whittle D.P., and Worrell W.L. (1982), 'Thermodynamics of Molten Sulfate Mixtures', *Journal of the Electrochemical Society*, Vol. 129 no.8, pp. 1840-1845.

[83] Lillerud K.P., Haflan B., and Kofstad P. (1984), 'On the Reaction Mechanism of Nickel With SO_2+O_2/SO_3', *Oxidation of Metal*, Vol. 21 nos.3, 4, pp. 119-134.

[84] Luthra K.L. and LeBlanc O. (1987), 'Low Temperature Hot Corrosion of Co-Cr-Al Alloys', *Materials Science and Engineering*, Vol. 87, pp. 329-335.

[85] Levin E.M., Robbins C.R., and McMurdie H.F. (1964), *Phase Diagrams for Ceramist*, The American Ceramic Society, U.S.A.

[86] LeBlanc O., Luthra K.L., and Haskell R.W (1989), 'Thermodynamics of the Na_2SO_4 -K_2SO_4-$CoSO_4$ System and Their Relevance to Low-Temperature Hot Corrosion', *Oxidation of Metals*, Vol. 31, No. 5/6, pp. 393-413.

[87] Hocking MG. and Sidky P.S. (1987), 'The Corrosion of Nickel-Based Ternary Alloys and Superalloys for Gas Turbine Applications-II. The Mechanism of Corrosion in SO_2/O_2 Atmospheres', *Corrosion Science*, Vol. 27 , No. 2, pp. 205-214.

[88] Luthra K.L. (1981), 'Mechanism of Low Temperature Hot Corrosion.', in Rapp R.A. *High Temperature Corrosion* at San Diego, California; National Association of Corrosion Engineers, U.S.A., pp. 507-512.

[89] Luthra K.L. (1982), 'Low Temperature Hot Corrosion of Cobalt-Base Alloys: Part I. Morphology of the Reaction Product.', *Metallurgical Transactions*, Vol. 13A, pp. 1843-1852.

[90] Luthra K.L. (1982), 'Low Temperature Hot Corrosion of Cobalt-Base Alloys: Part II. Reaction Mechanism.', *Metallurgical Transactions*, Vol. 13A, pp. 1853-1864.

[91] Luthra K.L. (1985), 'Kinetics of the Low Temperature Hot Corrosion of Co-Cr-Al Alloys', *Journal of the Electrochemical Society*, Vol. 132 , No. 6, pp. 1293-1298.

[92] Kaufman M. 'Hot Corrosion Reactions in Nickel, Cobalt and Nickel-Aluminide-Based Alloys', *Transactions of the ASM*, pp. 590-606.

[93] Chiang K.T. , Pettit F.S., and Meier G.H. (1981), 'Low Temperature Hot Corrosion', in Rapp R.A. *High Temperature Corrosion* at San Diego, California; National Association of Corrosion Engineers, U.S.A., pp. 519-530.

[94] Hossain M.K and Saunders S.R.J. (1978), 'A Microstructural Study of the Influence of NaCl Vapour on the Oxidation of a Ni-Cr-Al Alloy at 850 °C', *Oxidation of Metals*, Vol. 12, No. 1, pp. 1-21.

[95] Bourhis Y. and John C. St. (1975), 'Na_2SO_4 and NaCl-Induced Hot Corrosion of Six Nickel-Based Superalloys', *Oxidation of Metals*, Vol. 9, No. 6, pp. 507-527.

[96] Hancock P. (1978), 'The Role of Halides in Gas Temperature Hot Corrosion', in D.L. Hildenbrand and D.D. Cubicciotti *Proceedings of the Symposium on High Temperature Metal Halide Chemistry* The Electrochemical Society, Princeton, N.J., pp. 645-663.

[97] Shores A., Luthra K.L., and Mckee D.W. (1978), 'The Effect of Small Concentrations of NaCl on Hot Corrosion.', in D.L. Hildenbrand and D.D. Cubicciotti *Proceedings of the Symposium on High Temperature Metal Halide Chemistry.* The Electrochemical Society, Princeton, N.J., pp. 538-554.

[98] Stringer J. , Nagarajan V., and Whittle D.P. (1978), 'The Role of Chlorides in the Hot Corrosion of Cobalt-Base Alloys.', in D.L. Hildenbrand and D.D. Cubicciotti *Proceedings of the Symposium on High Temperature Metal Halide Chemistry* The Electrochemical Society, Princeton, N.J., pp. 509-520.

[99] Malik A. U. , Asrar N., Ahmad S., and Siddiqi N. A. (1988), 'Hot Corrosion Behaviour of Some Industrially Important Nickel-Base Alloys in Presence of Na2SO4 (s) and NaCl (s)', *Z. Metallkde*, Vol. 79 no.5, pp. 285.

[100] Sharma R.N. and Prakash S. (1996), 'Hot Corrosion of a Nickel Base Superalloy in Varying Salt Atmosphere Between 700°-950°C.', *Transactions of the Metal Finishers Association of India*, Vol. 5, No. 1, pp. 47-54.

[101] Advances in Corrosion Science and Technology (1976), in Daniel P.L. and Rapp R.A. *Halogen Corrosion of Metals*, Plenum Press N.Y., pp. 55-172.

[102] Jacobson N.S., MacNallan M.J., and Kreidler E.R. (1990), 'High Temperature Reactions of Ceramics and Metals With Chlorine and Oxygen', in *Materials Chemistry at High Temperatures* , Humana, pp. 381-392.

[103] Chang N.Y. and Wei F.I. (1991), 'High Temperature Chlorine Corrosion of Metals and Alloys', *Journal of Materials Science*, Vol. 26, pp. 3693-3698.

[104] Foroulis Z.A. (1988), 'Corrosion in Chlorine Environments', *Anti-Corrosion*, Vol. 35, pp. 4-12.

[105] Stott F. H., Prescott R., and Elliot P. (1990), 'Corrosion Resistance of High Temperature Alloys in Gas Containing Hydrogen Chloride', *Material Science and Technology*, Vol. 6, pp. 364-370.

[106] Prescott R., Stott F. H., and Elliot P. (1989), 'The Degradation of Metals in a Hydrogen Chloride-Containing Gas at High Temperature', *Corrosion Science*, Vol. 29 , No. 4, pp. 465-474.

[107] Rhee M.H., McNallan M.J., and Rothman M.F. (1985), 'Long Term High Temperature Corrosion Studies of High Temperature Alloys in Chlorine Contaminated Environments', in Rothman M.F. *High Temperature Corrosion in Energy Systems* The Metallurgical Society of AIME, USA, pp. 483-499.

[108] Ihara Y., Ohame H., Sakiyama K, and Hashimoto K. (1982), 'The Corrosion Behaviour of Nickel in Hydrogen Chloride Gas and Gas Mixtures of Hydrogen Chloride and Oxygen at High Temperatures', *Corrosion Science*, Vol. 22 , No. 10, pp. 901-912.

[109] Hossain M.K, Rhoades-Brown J.E., and Saunders S.R.J. (1980), 'The Effects of HCl and NaCl on Hot Corrosion', in *Behaviour of High Temperature Alloy in Aggressive Environments* at Petten, The Netherlands; pp. 483-496.

[110] McNallan M.J., Liang W.W, Oh J.M., and Kang C.T. (1982), 'Morphology of Corrosion Products Formed on Cobalt and Nickel in Argon-Oxygen-Chlorine Mixtures at 1000 °K ', *Oxidation of Metals*, Vol. 17, pp. 371-390.

[111] Hurst R.C. , Johnson J.B., Davies M., and Hancock P. (1973), 'Sulphate and Chloride Attack of Nickel-Based Alloys and Mild Steels', in Hart A.B. and Cutler A.J.B. *Depositions and Corrosion in Gas Turbines*, John Willey & Sons, New York, pp. 143-157.

[112] Nicholls J.R. (2000), Review of Coatings for Gas Turbines, Cranfield University,

[113] Nicholls J.R. (2003), 'Advances in Coating Design for High-Performance Gas Turbines', *MRS Bulletin*, pp. 659-670.

[114] Nicholls J.R. and Hancock P. (1987), 'Advanced High Temperature Coatings for Gas Turbines', *Industrial Corrosion*, Vol. 5, No. 4, pp. 8-17.

[115] Goward G.W. (1981), 'Recent Developments in High Temperature Coatings for Gas Turbine Airfoils', in *High Temperature Corrosion* at San Diego, California; National Association of Corrosion Engineers, U.S.A., pp. 553-560.

[116] Goward G.W. (1983), 'Protective Coatings for High Temperature Gas Turbine Alloys: A Review of The State of Technology.', in *Surface Engineering: Surface Modification of Materials* at Les Arcs, France; Martinus Nijhoff Publishers, pp. 408-426.

[117] Goward G.W. (1986), 'Low-Temperature Hot Corrosion in Gas Turbines: a Review of Causes and Coatings Therefor', *Journal of Engineering for Gas Turbines and Power*, Vol. 108, pp. 421-425.

[118] Goward G.W. and Canon L.W. (1988), 'Pack Cementation Coatings for Superalloys: a Review of History, Theory, and Practice', *Journal of Engineering for Gas Turbines and Power. Transactions of the ASME*, Vol. 110, pp. 150-154.

[119] McMinn A. (1987), *Coatings Technology for Hot Components of Industrial Combustion Turbines: A Review of the State of the Art*, AP-5078, Research Project 2388-3, San Antonio, Texas.

[120] Nicholls J.R. (2000), 'Designing Oxidation Resistant Coatings', *JOM*, Vol. 52, No. 1, pp. 28-35.

[121] Saunders S.R.J. and Nicholls J.R. (1989), 'Coatings and Surface Treatments for High Temperature Oxidation Resistant', *Material Science and Technology*, Vol. 5, No. 8, pp. 780-798.

[122] Godlewsky K and Godlewska E. 'The Effect of Chromium on the Corrosion Resistance of Aluminide Coatings on Nickel and Nickel-Based Superalloys.', in *High Temperature Corrosion of Materials and Coatings for Energy Systems and Turboengines* , Vol. II at Marseille, France; ELSEVIER, pp. 103-110.

[123] Bauer R, Schneider K., and Grunling H.W. (1985), 'Experience With Platinum Aluminide Coatings in Land-Based Gas Turbine', *High Temperature Technology*, Vol. 3, No. 2, pp. 59-64.

[124] Wu W.T., Rahmel A., and Schorr M. (1984), 'Role of Platinum in the Na_2SO_4- Induced Hot Corrosion Resistance of Aluminium Diffusion Coatings', *Oxidation of Metals*, Vol. 22, No. 1/2, pp. 59-81.

[125] Malik M., Morbioli R., and Huber P. (1982), 'The Corrosion Resistance of Protective Coatings', in *High Temperature Alloys for Gas Turbines 1982* at Liege, Belgium; The Netherlands, pp. 87-98.

[126] Barkalow R. H. and Goward G.W. 'Microstructural Features of Low Temperature Hot Corrosion in Nickel and Cobalt Base MCrAlY Coatings Alloys', in Rapp R. *High Temperature Corrosion* at San Diego, Ca; Houston, Texas, pp. 502-507.

[127] Stringer J. (1998), 'Coatings in the Electricity Supply Industry: Past, Present and Opportunities for the Future', *Surface and Coatings Technology*, Vol. 108-109, pp. 1-9.

[128] Nicholls J.R., Simms N.J., and Oakey J.E. (2001), 'Statistical Assessment of Corrosion Morphologies for High Temperature Component Life Prediction.', in Strang A. and Cawley J. *Quantitative Microscopy of High Temperature Materials* Institute of Materials,

[129] Meier G.H. and Pettit F.S. (1989), 'High Temperature Corrosion of Alumina-Forming Coatings for Superalloys', *Surface and Coatings Technology*, Vol. 39, No. 40, pp. 1-17.

[130] Nicholls J.R. and Hancock P. (1983), 'The Analysis of Oxidation and Hot Corrosion Data-A Statistical Approach', in Rapp R.A. *High Temperature Corrosion* at San Diego, California; National Association of corrosion Engineers Houston, Texas, pp. 198-210.

[131] Nicholls J.R. and Hancock P. (1987), 'Prediction of High Temperature Corrosion Performance Using Statistical Analysis Techniques', in *Plant Corrosion* , Ellis Horwood, pp. 257-273.

[132] Nicholls J.R. and Stephenson D.J. (1992), 'A Life Prediction Model for Coatings Based on the Statistical Analysis of Hot Slat Corrosion Performance', *Corrosion Science*, Vol. 33, No. 8, pp. 1313-1325.

[133] Strutt J.E., Nicholls J.R., and Barbier B. (1985), 'The Prediction of Corrosion by Statistical Analysis of Corrosion Profiles', *Corrosion Science*, Vol. 25, No. 5, pp. 305-315.

[134] Nicholls J.R. and Triner D.A. (1990), 'The Influence of Fuel Composition on Lives of Current Valve Materials-Parametric Equations for Valve Prediction', in *Diesel Engine Combustion Chamber Materials for Heavy Fuel Operation* DTI/ Industry Valve Project, pp. 121-129.

[135] Nicholls J.R. and Stephenson D.J. (1990), 'Hot Corrosion Tests on Candidate Diesel Valve Materials-Paper 5', in *Diesel Engine Combustor Chamber Materials for Heavy Fuel Operation* pp. 47-60.

[136] Nicholls J.R., Smith P.J., and Oakey J.E. (1994), 'Prediction of Hot Salt Corrosion Within Utility Gas Turbines', in D Coutsouradis et al *Materials for Advanced Power Engineering* at Liege, Belgium; Kluwer, pp. 1237-1289.

[137] Simms N., Nicholls J.R, and Oakey J.E. (2001), 'Corrosion and Lifetime Modelling of Components in Coal Fired Combined Cycle Power Systems', in *Life Time Modelling of High Temperature Corrosion Processes. Proceedings of an EFC Workshop 2001* , Vol. 34 Maney Publishing, London, pp. 379-397.

[138] Nicholls J.R (1993), 'A Life Prediction Model for The Corrosion of Hot Section Components and Coatings', in *4th European Propulsion Forum* The Royal Aeronautical Society, pp. 1-18.

[139] Bacos M-P, Josso p., Vialas N., Poquillon D., Pieraggi B., Monceau D., Nicholls J.R, Simms N., Encinas-Oropesa A., Ericsson T., and Stekovic S. (2004), 'ALLBATROS Advanced Long Life Blade Turbine Coating System', *Applied Thermal Engineering*, Vol. 24, pp. 1745-1753.

[140] Nicholls J.R. (1995), 'Guidelines for Methods of Testing and Research in High Temperature Corrosion', in *Discontinuous Measurements of High Temperature Corrosion.* The European Federation of Corrosion by The Institute of Materials., UK, pp. 11-36.

[141] (2001), Draft Code of Practice for "Discontinuous Corrosion Testing in High Temperature Gaseous Atmospheres", ERA Technology,

[142] Hot Salt Corrosion Standard Test Procedures and Performance (1989), *Special Issue of High Temperature Technology*, Vol. 7, No. 4,

[143] (2002), Final Report on Gas Turbines in Advanced Co-fired Energy Systems,

[144] Simms N.J. , Oakey J.E., and Nicholls J.R. (2000), 'Development and Application of a Methodology for the Measurement of Corrosion and Erosion Damage in Laboratory, Burner Rig and Plant Environments', *Materials at High Temperatures*, Vol. 17, No. 2, pp. 355-362.

[145] Simms N.J. and Oakey J.E. (1997), 'Measurement of Corrosion Damage in Coal-Fired Combined Cycle Power Systems', in *Microscopy of Oxidation 3- Third International Conference on the Microscopy of Oxidation* at University of Cambridge ; The Institute of Materials, U.K., pp. 657-668.

[146] Simms N.J. , Oakey J.E., and Nicholls J.R. 'A Methodology for the Quantification of Corrosion and Erosion Damage in Laboratory, Burner Rig and Plant Environments.', in *High Temperature Corrosion and Materials Chemistry. Proceedings of the Per Koftad Memorial Symposium.* Vol. 99-38 The Electrochemical Society, U.S.A., pp. 305-316.

[147] Samuels L.E. (1967), in *Metallographic Polishing by Mechanical Methods* U.K., pp. 7.

[148] Rebak R.B. (2000), 'Corrosion of Non-Ferrous Alloys I Nickel, Cobalt, Copper, Zirconium and Titanium Base Alloys.', in Schutze M. *Materials Science and Technology. Corrosion and Environmental Degradation Vol II.*, Wiley-vch, N.Y., pp. 71-111.

[149] Bray J.L. (1962), *Metalurgia Extractiva De Los Metales No Ferreos*, Ediciones Interciencia, Madrid.

[150] Al-Khyat A.I.M. (1991), *High Temperature Chloride Induced Corrosion of Nickel and Nickel-Based Alloys* (unpublished PhD thesis), Cranfield University, Cranfield, UK.

[151] Angenete J., Stiller K., and Langer V. (2003), 'Oxidation of Simple and Pt Modified Aluminide Diffusion Coatings on Ni Based Superalloys-I. Oxide Scale Microstructure', *Oxidation of Metals*, Vol. 60, No. 1/2, pp. 47-82.

Appendix

Papers published incorporating part of this work are:

"Hot Corrosion of Coated Single Crystal Superalloys".
NJ Simms, A. Encinas-Oropesa and J. Nicholls. Eurocorr 2004, Nice 2004. European Corrosion Federation (to be published)

"Development of Hot Corrosion on coated Single Crystal Superalloys".
NJ Simms, A. Encinas-Oropesa and J. Nicholls. Les Embiez, May 2004. Materials Science Forum (to be published)

"ALLBATROS Advanced Long Life Blade Turbine Coating Systems".
M-P Bacos, P.Josso, N.Vialas, D.Poquillon, B.Pieraggi, D.Monceau, J.R.Nicholls, N.Simms, A.Encinas-Oropesa,T.Ericsson, S.Stekovic. Applied Thermal Engineering 24, 2004. p.1745-1753.

"Predicting Hot Corrosion in Industrial Gas Turbines".
NJ Simms, L Heikinheimo, A Encinas-Oropesa, S Tuurna, PJ Kilgallon, JR Nicholls and J Oakey. Corrosion Science in the 21st Century, Manchester Jun. 2003

"Performance of Gas Turbine Materials in Dirty Fuel Environments".
NJ Simms, A. Encinas-Oropesa, P Kilgallon and JE Oakey. Materials for Advanced Power Engineering 2002, Liege, Oct. 2002.

"The Development of Type II Hot Corrosion in Solid Fuel Fired Gas Turbines".
NJ Simms, PJ Smith, A Encinas-Oropesa, S Ryder, J Nicholls and J Okay. European Federation of Corrosion Workshop: Life time Modelling of High Temperature Corrosion Processes, Frankfurt, Feb. 2001.